

MECHANISTIC INVESTIGATIONS OF ON-DEMAND LIGHT DEGRADABLE POLYMERIC MATERIALS

Zur Erlangung des akademischen Grades eines
DOKTORS DER NATURWISSENSCHAFTEN

(Dr. rer. nat.)

von der KIT-Fakultät für Chemie und Biowissenschaften
des Karlsruher Instituts für Technologie (KIT)

genehmigte

DISSERTATION

von

M. Sc. Julian Bachmann

Referent: Prof. Dr. Andreas-Neil Unterreiner

Korreferenten: Prof. Dr. Christopher Barner-Kowollik

Prof. Dr. Patrick Théato

Tag der mündlichen Prüfung: 25. Oktober 2022



Dieses Werk ist lizenziert unter einer Creative Commons Namensnennung -
Nicht kommerziell - Keine Bearbeitungen 4.0 International Lizenz (CC BY-NC-ND 4.0 DE):
<https://creativecommons.org/licenses/by-nc-nd/4.0/deed.de>

The herein presented thesis was developed between May 2019 and September 2022 in a binational PhD agreement ('cotutelle de these') between the Queensland University of Technology (QUT, Australia) and the Karlsruhe Institute of Technology (KIT, Germany) under the supervision of Prof. Dr. Christopher Barner-Kowollik (QUT) and Prof. Dr. Andreas-Neil Unterreiner (KIT).

“May it be a light to you in dark places, when all other lights go out.”

- J. R. R. Tolkien, *The Fellowship of the Ring*

Abstract

Polymers – or vernacularly called ‘plastics’ – are an interesting material class. Polymers are long chains of repeating or alternating building blocks, constituted of a backbone and any pending side chains. Characteristics such as mechanical properties or stimuli-mediated responsiveness of a polymer can be varied by adjusting their molecular structure, sequence and reaction conditions under which they are generated. The critical role of polymers in many aspects of society is owed to the characteristics they possess. However, their resistance against degradation also evokes key global concern, since accumulation of plastic waste in terrestrial and aquatic ecosystems affects all biological life. Conventionally, plastic waste is subjected to chemical treatment or heat, allowing recycling or ‘waste-to-energy’ strategies. Recycling always entails some level of degradation and can manifest as fragmentation, backbone modification or crosslinking. Ideally, degradation is desired after its intended use, but usually polymers lack the feature of ‘on-demand’ degradability. Light would be an ideal trigger medium given its abundance and spatiotemporal control, thus constituting a suitable stimulus to induce degradation on demand.

In the present thesis, the trigger ‘light’ was explored to provide a powerful tool for on-demand degradation scenarios. Several model systems were selected and their mechanism of action investigated. Initially, *ortho*-nitrobenzyl (*o*NB) chemistry was employed. *o*NB compounds are usually utilized in drug release applications or protection group chemistry and undergo photocleavage upon ultraviolet (UV) light irradiation. An *o*NB motif was synthesised, featuring blue-visible light degradability, and readily incorporated into polyurethanes – a polymer class notoriously known for its poor degradability. A ns-laser setup was employed, allowing to determine the wavelength-resolved reactivity of photolabile units. The used *o*NB compound displayed reactivity up to 420 nm, yet disclosed an unexpected reactivity shape compared to its absorption spectrum. Femtosecond spectroscopy revealed energy dissipation dynamics for the employed irradiation wavelength, comparable to UV light excitation conditions. A critical key intermediate, the *aci*-nitro tautomer, is generated via two different pathways, depending on the irradiation wavelength. The direct

generation of the tautomer is allowed via 325 nm irradiation while a biradical intermediate is formed upon 400 nm irradiation. Studying the solvent influence discloses stabilisation of either the biradical intermediate or the *aci*-nitro tautomer. To establish a connection between reactivity and absorptivity, substantial effort was directed into investigating donor-acceptor systems. For this purpose, other *o*NB compounds were synthesised, allowing for greater tunability thanks to an aldehyde motif. It was found that non-stabilized systems possess the highest reactivity, but the lowest selectivity due to their propensity to undergo side reactions and *vice versa*. *o*NB containing polyurethanes were exposed to UV light and the evolution of degradation traced via size exclusion chromatography (SEC). It was found that longer chains seem to fragment more rapidly, and a shift towards higher retention time was observed throughout the entire series.

Inspired by these previous findings, *o*NB motives were placed as on demand degradation points in mid-chain position of polymer chains, revealing a clear trend towards chain-length dependent cleavage rates. Depending on the size of the polymer, different degradation kinetics were obtained. The trend was correlated to a physical model which relates the total entropy to the degree of polymerisation and was found to agree well with the experimental data.

Backbone modification such as oxidation can occur as degradation as well, which was investigated in the visible light region. The high-energetic molecule class of tetrazines, an hexatomic aromatic system with four nitrogen atoms distributed at positions 1, 2, 4 and 5 was probed for its mechanism of action. Wavelength resolved reactivity studies revealed poor degradability throughout the visible light window, but significant improvement upon addition of oxidation agents was found. It was hypothesised that the combination of both hydrogen peroxide and green light allowed tetrazine to undergo nitrogen-oxygen exchange thus shifting its polarity. The molecular composition was hereby determined via nuclear magnetic resonance spectroscopy and mass spectrometry methods. Tetrazines were incorporated into linear thiol-acrylate polymers by employing a tetrazine diacrylate and a commercially available dithiol. Polymer degradation was investigated via a combinatory study of exposing the system to both triggers, i.e. an oxidation agent and green light, isolated, simultaneously and in sequence. Accelerated oxidation upon green light irradiation was confirmed.

Crosslinking via [2+2] cycloaddition was studied on a new styrylpyrido pyrazine chromophore. The reaction proceeded even with long-range visible light close to $\lambda = 540$ nm, constituting the longest wavelength employed in [2+2] cycloadditions in water as far as the author is aware at the time of writing. Crosslinking occurred at neutral pH-values and could be tuned by changing acidity of the solvent. Additionally, a blue light responsive photoacid generator can be used to tune the acidity by irradiation. The chromophore was embedded into a multidimensional network by exploiting an 8-arm linker. The obtained hydrogel was responsive to pH-value and irradiation conditions.

Zusammenfassung

Polymere – umgangssprachlich als „Plastik“ bezeichnet – sind eine interessante Materialklasse. Polymere sind lange Ketten von sich wiederholenden oder alterniert auftretenden Baueinheiten, welche das Rückgrat der Kette und etwaige Seitenketten formen. Charakteristika wie mechanische Eigenschaften oder Stimulus-verursachtes Reaktionsvermögen eines Polymers können durch die molekulare Struktur, die Sequenz und Reaktionsbedingungen festgelegt werden. Die Allgegenwärtigkeit von Polymeren in sowohl Industrie- als auch Haushaltssektor ist den besonderen charakteristischen Eigenschaften von Polymeren zu verdanken. Resistenz gegenüber äußeren Einflüssen machen Polymere zu einem Problem auf globaler Ebene, da Akkumulierung von Plastikabfall in terrestrischen und aquatischen Ökosystemen biologisches Leben beeinflusst. Konventionell erfolgt die Behandlung von Plastikabfall entweder chemisch oder pyrolytisch, welche die Rückführung von Materie oder Energie erlauben. Recycling führt allerdings zu einem gewissen Grad an Degradationsphänomenen, entweder manifestiert als Fragmentierung, Rückgratsmodifikation oder Nachvernetzung. Idealerweise ist Degradation erwünscht nach der Nutzung, allerdings fehlt Polymeren die Implementierung einer „Bei Bedarf“-Degradierbarkeit. Licht wäre das perfekte Auslösemedium, um Degradierbarkeit bei Bedarf hervorzurufen, da es im Überfluss auftritt und sowohl räumlich als auch zeitlich kontrollierbar ist.

In der vorliegenden Arbeit wurde das Auslösemedium „Licht“ erforscht, um ein leistungsstarkes Werkzeug für „Bei Bedarf“-Degradierungsszenarios bereitzustellen. Mehrere Modellsysteme wurden ausgesucht und ihr Reaktionsverhalten untersucht. Zuerst wurden *ortho*-nitrobenzyl (*o*NB)-Systeme eingesetzt. *o*NB-Verbindungen finden üblicherweise Verwendung bei Wirkstofffreisetzungen oder in der Schutzgruppenchemie und erleiden einen lichtausgelösten Bindungsbruch bei ultravioletter Lichtbestrahlung. Ein *o*NB-Molekül wurde synthetisiert, welches Absorptionseigenschaften im blau-sichtbaren Wellenlängenbereich zeigt und anschließend in lineare Polyurethane eingebaut – eine Polymerklasse mit mangelnder Degradierbarkeit. Ein Aufbau mit einem durchstimmbaren Nanosekundenlaser erlaubt die Beobachtung von Wellenlängen-abhängigem Reaktionsverhalten. Eine atypische

Form des Reaktionsverhalten der untersuchten *o*NB-Verbindung wurde festgestellt, welches sich bis zu 420 nm erstreckt. Ultraschnelle Femtosekundenspektroskopie enthüllte eine Relaxationsdynamik unter sichtbarer Lichteinstrahlung, welche stark der Dynamik bei UV-Lichtanregung ähnelt. Wesentliche Mühe wurde auf die Untersuchung von Donor-Akzeptor-Systemen und deren Reaktivität gelenkt. Es wurde gefunden, dass nicht stabilisierte Systeme die höchste Reaktivität, aber auch die niedrigste Selektivität aufweisen, da sie eher zu Nebenreaktionen neigen und vice versa. *o*NB-inkorporierte Polyurethane wurden UV-Licht ausgesetzt und deren Morphologieänderung mithilfe Größenausschlusschromatographie und weiteren standardisierten Verfahren verfolgt. Es wurde gefunden, dass längere Ketten schneller fragmentieren und eine Elutionsverschiebung zu höheren Retentionszeiten bei unterschiedlichen Polymergrößen festgestellt.

Inspiziert von den vorangegangenen Ergebnissen war die räumliche Position des *o*NB-Motivs von besonderem Interesse. Eine bifunktionelle *o*NB-Verbindung ermöglichte kontrolliertes Wachstum an beiden Endgruppen, welches die Isolierung von unterschiedlich langen Polymerketten mit einem zentral lokalisierten *o*NB-Molekül ermöglichte. Abhängig von der Polymerlänge wurde eine unterschiedliche Degradierungskinetik erhalten. Diese Tendenz wurde in Zusammenhang mit einem physikalischen Modell gesetzt, welches die gesamte Entropie mit dem Grad der Polymerisation in guter Übereinstimmung mit experimentellen Befunden verknüpft.

Da Degradierung im UV- oder blau-sichtbaren Wellenlängenbereich von Fragmentierungsmechanismen beherrscht wird, wurde logischerweise eine Verschiebung in den grün-sichtbaren Wellenlängenbereich überlegt. Ein Derivat der hochenergetischen Molekülklasse der Tetrazine, ein sechsatomiges aromatisches System mit vier Stickstoffatomen verteilt an den Positionen 1, 2, 4 und 5, wurde auf seine Reaktivität untersucht. Eine Wellenlängen-aufgelöste Reaktivitätsstudie zeigte schwache Degradierbarkeit über das gesamte sichtbare Wellenlängenspektrum hinweg, konnte jedoch signifikant durch Zugabe eines Oxidationsmittels gesteigert werden. Es wurde herausgefunden, dass die Kombination von sowohl Wasserstoffperoxid als auch grünem Licht einen Stickstoff-Sauerstoff Austausch und damit eine Polaritätsänderung verursacht. Die atomare Änderung wurde mittels Kernspinresonanz- und massenspektrometrischen Untersuchungen aufgeklärt werden. Tetrazin wurde anschließend als Tetrazin-Diakrylat in lineare Thiol-Akrylat-

Polymere eingebaut unter Verwendung eines kommerziell erhältlichen Dithiols. Die Morphologieentwicklung wurde untersucht mithilfe einer kombinatorischen Studie, bei dem die Polymere beiden Auslösemedien gleichzeitig, isoliert und hintereinander ausgesetzt wurden. Dabei wurde eine beschleunigte Oxidation unter Bestrahlung mit grünem Licht festgestellt.

Vernetzung mithilfe einer [2+2]-Cycloaddition wurde an einem neuartigen Styrylpyridylpyrazin Chromophor untersucht. Die Reaktion verlief selbst unter langwellig sichtbarem Licht ($\lambda = 540 \text{ nm}$) und markiert die längste Wellenlänge in Wasser für solche Reaktionen, zumindest nach Kenntnisstand des Autors zum Verfassungszeitpunkt. Die Vernetzung trat unter neutralen pH-Bedingungen auf und konnte durch Änderung des pH-Werts verändert werden. Zusätzlich wurde ein mit blauem Licht auslösbarer Photosäuregenerator eingesetzt, welcher den pH-Wert durch Bestrahlung mit blauem Licht beeinflussen konnte. Das Chromophor wurde in mehrdimensionale Netzwerke eingebaut unter Benutzung eines achtarmigen Vernetzers. Die Bildung des Hydrogels wurde beeinflusst durch pH-Wert und Bestrahlungsbedingungen.

Keywords

Action Plot, chain growth polymerisation, dual-trigger, entropy, femtosecond spectroscopy, fragmentation, laser, light, light emitting diode, light-induced chemistry, (macro-) molecular analysis, mass spectrometry, mechanism of action, photochemistry, photodegradation, photoligation, photophysics, polymer chemistry, polymer degradation, polymer design, relaxation dynamics, spectroscopy, reversible deactivation radical polymerisation (RDRP), step-growth polymerisation, synthesis, ultrafast, ultraviolet, visible, wavelength-resolved reactivity

Table of Contents

Abstract	i
Zusammenfassung	iv
Keywords	vii
Table of Contents	viii
List of Figures	x
List of Tables.....	xxxvi
List of Abbreviations.....	xlii
List of Symbols	xlvi
List of Equations	xlvi
Academic Output.....	li
Acknowledgements	lv
Chapter 1: Introduction	1
1.1 Background.....	1
1.2 Purpose and Context.....	3
Chapter 2: Theoretical Fundamentals	7
2.1 Photophysics	7
2.2 Photochemistry	14
2.3 Polymerisation	20
Chapter 3: Exploring the photochemistry of <i>ortho</i>-nitrobenzyl alcohols and incorporation in polyurethanes.....	33
3.1 Abstract.....	33
3.2 Introduction.....	34
3.3 Results and Discussion	34
3.4 Conclusion	76

Chapter 4: Chain-Length-Dependent Photolysis of <i>ortho</i>-nitrobenzyl-Centered Polymers	77
4.1 Abstract	77
4.2 Introduction	78
4.3 Results and Discussion	79
4.4 Conclusion.....	93
Chapter 5: Peroxide-accelerated photodegradation of tetrazine-bearing thiol-acrylate polymers via green light.....	95
5.1 Abstract	95
5.2 Introduction	95
5.3 Results and Discussion	96
5.4 Conclusion.....	108
Chapter 6: Wavelength-Orthogonal Stiffening and Inhibition of Hydrogel Networks with Visible Light.....	111
6.1 Abstract	111
6.2 Introduction	112
6.3 Results and Discussion	113
6.4 Conclusion.....	129
Chapter 7: Conclusion and Outlook	131
Chapter 8: Experimental Part	141
8.1 Materials	141
8.2 Analysis and instrumentation	143
8.3 Laser Setups	149
8.4 Experimental procedures	153
8.5 Synthetical procedures	185
Appendices	205
Bibliography	284

List of Figures

Figure 1-1: Scope of this PhD thesis.	5
Figure 2-1: Franck-Condon interpretation of transitions between two electronic states (lower and upper black curves). Vibrational modes of electronic excited and ground state are represented as ν_0 , ν_1 , etc. Transitions occur from the vibronic ground state into a state similar to the nuclear vibrational wavefunction, as depicted by the vertical dashed line. The reader is referred to the text for further explanation. Adapted from literature. ^[26]	9
Figure 2-2: General structure of <i>o</i> NB compounds.	15
Figure 2-3: Left: Aromatic structure of <i>ortho</i> -nitro toluene (<i>o</i> NT). Right: Proposed structure after hydrogen abstraction resembling quinonoid species. Figure adapted with permission from G. Wettermark, <i>J. Phys. Chem.</i> 1962 , <i>66</i> (12), 2560-2562. Copyright 1962 American Chemical Society.....	16
Figure 2-4: Different tetrazine isomers.	18
Figure 3-1: ¹ H-NMR spectrum of 4 before (black solid) and after (red solid) chromatographic purification in DMSO- <i>d</i> ₆ (*).	36
Figure 3-2: UV/Vis absorption spectra of the <i>o</i> NB dialcohol 4 and its precursors (Scheme 3-2) at 25 °C in acetonitrile. <i>d</i> = 10 mm. Reproduced from Ref. 200 with permission from the Royal Society of Chemistry. Modified representation.	38
Figure 3-3: Left: Simplified <i>o</i> NB degradation mechanism. Right: Experimental (red) and simulated (purple) EPR spectra of the <i>o</i> NB dialcohol 4 in deuterated chloroform after 395 nm irradiation. Reproduced from Ref. 200 with permission from the Royal Society of Chemistry. Modified representation.	39
Figure 3-4: a) FT-IR spectra before (black) and after irradiation (red) of 4 in acetonitrile. Disappearance of characteristic frequency bands of	

nitroaromatics as well as appearance of the carbonyl frequency are highlighted. b) $^1\text{H-NMR}$ spectra of the *o*NB dialcohol before (top, **4**) and after (bottom, **4d**) irradiation. The protons *a* and *b* are assigned to the methyl group in alpha position of the secondary alcohol and carbonyl group, respectively. Irradiation parameters: 365 nm LED, 60 minutes, acetonitrile- d_3 . Reproduced from Ref. 200 with permission from the Royal Society of Chemistry. Modified representation..... 41

Figure 3-5: Top: Degradation reaction of **4**. The red boxes indicate the protons investigated for determination of conversion and yield. Bottom: Action plot of **4** in acetonitrile. Extinction (black), conversion X_4 (red), yield Y_{4d} (blue). Reproduced from Ref. 200 with permission from the Royal Society of Chemistry. Modified representation..... 41

Figure 3-6: Extracted single transients from pure solvent (acetonitrile) after excitation. $\lambda_{\text{ex}} = 400 \text{ nm}$, $E_{\text{ex}} = 2 \mu\text{J}$, $d = 1 \text{ mm}$. The transients extracted range in the entire visible spectrum and chirp can be observed in all transient responses..... 43

Figure 3-7: UV/Vis absorption spectrum of **4** before (black solid) and after (red solid) transient fs-laser experiment. $\lambda_{\text{ex}} = 400 \text{ nm}$, $E_{\text{ex}} = 2 \mu\text{J}$, $d = 1 \text{ mm}$, acetonitrile and zoom on the absorption shoulder..... 45

Figure 3-8: Contour plot of **4** with stationary UV/Vis absorption spectrum (top). $\lambda_{\text{ex}} = 400 \text{ nm}$, $E_{\text{ex}} = 2 \mu\text{J}$, $\lambda_{\text{probe}} = \text{supercontinuum}$, $d = 1 \text{ mm}$, $c = 72 \text{ mmol L}^{-1}$, acetonitrile. Transient response around 400 nm is neglected due to pump pulse scattering. 45

Figure 3-9: TA spectra of **4** between -2.8 and 2.1 ps (left) as well as between 2.1 and 980 ps (right). $\lambda_{\text{ex}} = 400 \text{ nm}$, $E_{\text{ex}} = 2 \mu\text{J}$, $\lambda_{\text{probe}} = \text{supercontinuum}$, $d = 1 \text{ mm}$, $c = 72 \text{ mmol L}^{-1}$, acetonitrile. Transient response around 400 nm is neglected due to pump pulse scattering..... 46

Figure 3-10: Extracted single transient responses for the features at 460, 490, 520 and 600 nm. Experimental data was fit with a biexponential fit, starting from the maximum response..... 47

- Figure 3-11:** TA spectra (solid lines) of **4** between -2.8 and 100 ps.
 $\lambda_{\text{ex}} = 400 \text{ nm}$, $E_{\text{ex}} = 2 \mu\text{J}$, $\lambda_{\text{probe}} = \text{supercontinuum}$, $d = 1 \text{ mm}$,
 $c = 72 \text{ mmol L}^{-1}$, acetonitrile. Transient response around 400 nm is neglected due to pump pulse scattering. Stationary absorption (Abs.) and emission spectra (Em.) are depicted in black and red. Parameters for acquisition emission spectrum: $\lambda_{\text{ex}} = 400 \text{ nm}$, *slit size* = 5, EtOH..... 49
- Figure 3-12:** Contour plot of **4** with respective stationary UV/Vis absorption spectrum (top) in THF (left) and EtOH (right). $\lambda_{\text{ex}} = 400 \text{ nm}$,
 $E_{\text{ex}} = 2 \mu\text{J}$, $\lambda_{\text{probe}} = \text{supercontinuum}$, $d = 1 \text{ mm}$, $OD_{400 \text{ nm, THF}} \sim 1.2$,
 $OD_{400 \text{ nm, EtOH}} \sim 1.4$. Transient response around 400 nm is neglected due to pump pulse scattering. The legend on the right applies to both contour plots. Absorption spectra before and after the experiment are appended in **Figure S3-23**. 52
- Figure 3-13:** TA spectra of **4** between -2.8 and 100 ps in THF (left) and EtOH (right). $\lambda_{\text{ex}} = 400 \text{ nm}$, $E_{\text{ex}} = 2 \mu\text{J}$, $\lambda_{\text{probe}} = \text{supercontinuum}$,
 $d = 1 \text{ mm}$, $OD_{400 \text{ nm, THF}} \sim 1.2$, $OD_{400 \text{ nm, EtOH}} \sim 1.4$. Transient response around 400 nm is neglected due to pump pulse scattering. 52
- Figure 3-14:** Contour plot of **4** with respective stationary UV/Vis absorption spectrum (top). $\lambda_{\text{ex}} = 325 \text{ nm}$, $E_{\text{ex}} = 0.5 \mu\text{J}$,
 $\lambda_{\text{probe}} = \text{supercontinuum}$, $d = 1 \text{ mm}$, $OD_{325 \text{ nm, AcN}} \sim 2.5$,
acetonitrile. UV/Vis spectra before and after acquisition are available in **Figure S3-25**..... 53
- Figure 3-15:** Selected TA spectra of **4**. Experimental parameters, refer to **Figure 3-14**. 54
- Figure 3-16:** Contour plot profile of **4** with respective stationary UV/Vis absorption spectrum (top) in THF (left) and EtOH (right).
 $\lambda_{\text{ex}} = 325 \text{ nm}$, $E_{\text{ex}} = 0.4 \mu\text{J}$, $\lambda_{\text{probe}} = \text{supercontinuum}$, $d = 1 \text{ mm}$,
 $OD_{325 \text{ nm, THF}} \sim 3.1$, $OD_{325 \text{ nm, EtOH}} \sim 1.9$. The legend on the right applies to both TA profiles. Absorption spectra before and after the experiment are appended in **Figure S3-27**. 55

Figure 3-17: Contour plots of 3 with respective stationary UV/Vis absorption spectrum (top) in AcN. Left panel: $\lambda_{\text{ex}} = 400 \text{ nm}$, $E_{\text{ex}} = 2 \mu\text{J}$, $\lambda_{\text{probe}} = \text{supercontinuum}$, $d = 1 \text{ mm}$, $OD_{400 \text{ nm,AcN}} \sim 2.7$. Right panel: $\lambda_{\text{ex}} = 325 \text{ nm}$, $E_{\text{ex}} = 0.5 \mu\text{J}$, $\lambda_{\text{probe}} = \text{supercontinuum}$, $d = 1 \text{ mm}$, $OD_{325 \text{ nm,AcN}} \sim 0.4$. Transient response around 400 nm is neglected due to pump pulse scattering. Absorption spectra before and after the experiment are appended in Figure S3-29	58
Figure 3-18: TA spectra after $\lambda_{\text{ex}} = 400 \text{ nm}$ (left) and $\lambda_{\text{ex}} = 325 \text{ nm}$ (right) in acetonitrile. Experimental parameters, refer to Figure 3-17	59
Figure 3-19: TA spectra (scattered) at 0.51 ps (purple) and 982 ps (ochre) and deconvolution with three gaussian functions (thin dashed lines). Cumulative representation is given in solid purple or ochre lines. Spectra were recorded at $\lambda_{\text{ex}} = 400 \text{ nm}$ (left) and $\lambda_{\text{ex}} = 325 \text{ nm}$ (right) in acetonitrile.	60
Figure 3-20: UV/Vis absorption spectra of the primary alcohol systems 2,5-H1 (green), 2,5-H2 (yellow) and 2,5-H3 (red). Spectra were recorded in acetonitrile. $d = 10 \text{ mm}$	64
Figure 3-21: Top: Suggested degradation of 2,5-H2 . The red boxes indicate the protons investigated for determination of conversion and yield. Bottom: Action plot of 2,5-H2 measured in acetonitrile. Black solid line: absorption spectrum measured in acetonitrile ($d = 10 \text{ mm}$). Red: Conversion of 2,5-H2 . Blue: Yield of 2,5-H2d	65
Figure 3-22: Top: Suggested degradation of 2,5-H3 . The red boxes indicate the protons investigated for determination of conversion and yield. Bottom: Action plot of 2,5-H3 measured in acetonitrile. Black solid line: absorption spectrum measured in acetonitrile ($d = 10 \text{ mm}$). Red: Conversion of 2,5-H3 . Blue: Yield of 2,5-H3d	66
Figure 3-23: UV/Vis absorption spectra of all investigated molecules (right) in acetonitrile. $d = 10 \text{ mm}$. Molecular structures are listed in Table 3-9 and Scheme 3-2	67

- Figure 3-24:** Top: Suggested degradation of **2,5-Ph2**. The red boxes indicate the protons investigated for determination of conversion and yield. Bottom: Action plot of **2,5-Ph2** measured in acetonitrile. Black solid line: absorption spectrum measured in acetonitrile ($d = 10$ mm). Red: Conversion of **2,5-Ph2**. Blue: Yield of **2,5-Ph2d**..... 68
- Figure 3-25:** Top: Suggested degradation of **2,5-Ph3**. The red boxes indicate the protons investigated for determination of conversion and yield. Bottom: Action plot of **2,5-Ph3** measured in acetonitrile. Black solid line: absorption spectrum measured in acetonitrile ($d = 10$ mm). Red: Conversion of **2,5-Ph3**. Blue: Yield of **2,5-Ph3d**..... 69
- Figure 3-26:** Action Plots of all compounds investigated in this chapter. Action plots were determined in acetonitrile. Solid coloured lines: extinction coefficient ϵ . Coloured Scatter-line plots: Conversion X (squares). Coloured dashed lines: Yield Y (diamonds)..... 69
- Figure 3-27:** $^1\text{H-NMR}$ spectrum of polyurethane formed in $\text{THF-}d_8$ (*) after a reaction period of 20 minutes (see Experimental section). + marks catalyst present. Reproduced from Ref. 200 with permission from the Royal Society of Chemistry. Modified representation..... 70
- Figure 3-28:** SEC-ESI mass spectra of poly(urethane-*o*NB) (20 min) averaged over retention times of single charged polymer from 18.8 to 20.6 min. The isocyanate unit ($m/z = 168.09$) is displayed in green, the hydrolysed isocyanate unit ($m/z = 142.11$) in blue and the *o*NB unit ($m/z = 257.09$) in red. Reproduced from Ref. 200 with permission from the Royal Society of Chemistry.. 71
- Figure 3-29.** SEC traces of PUs in THF after 2 to 20 min reaction time at 70 °C. 360 nm absorbance was used for detection. Traces were normalized to the same area. Reproduced from Ref. 200 with permission from the Royal Society of Chemistry. Modified representation. 72
- Figure 3-30:** SEC traces of polymers after treatment with 365 nm photons (solid coloured lines). The polymers were allowed to form within a) two minutes, b) five minutes, c) ten minutes, d) 17 minutes, e) 20

- minutes. Dashed black line resembles the isolated polymer.
 Reproduced from Ref. 200 with permission from the Royal Society of
 Chemistry. Modified representation. 74
- Figure 3-31:** Frequency change of quartz crystal coated with 10 mL of a 7 mg mL⁻¹ polymer solution (PU-20 min) in dioxane (red) and DMSO (blue) and irradiated with a 365 nm LED from $t = 0$ min. Data obtained using a quartz crystal microbalance at 25 °C with a constant flow of water. Reproduced from Ref. 200 with permission from the Royal Society of Chemistry. Modified representation. 75
- Figure 3-32:** X-ray photoelectron spectroscopy of a silica slide coated with 10 mL of a 7 mg mL⁻¹ polymer solution (20 minutes cured PU) in DMSO, irradiated with a 365 nm LED and washed out with water. Wide scans are available in **Figure S3-51**. Reproduced from Ref. 200 with permission from the Royal Society of Chemistry. Modified representation. 75
- Figure 4-1:** ¹H-NMR spectra of sample **2** in acetonitrile-*d*₃ before (black) and after (red) irradiation. $\lambda = 340$ nm, $U = 4.2$ V, $I = 0.25$ A, $dist = 0.5$ cm. Reprinted with permission from J. Bachmann *et al.* *ACS Macro Lett.* **2021**, *10*, 4, 447-452. Copyright 2021 American Chemical Society. Modified representation. 81
- Figure 4-2:** UV/Vis spectra of irradiated sample **2** in acetonitrile-*d*₃ before (black) and after (red) irradiation. $\lambda = 340$ nm, $U = 4.2$ V, $I = 0.25$ A, $dist = 0.5$ cm, $d = 10$ mm. Reprinted with permission from J. Bachmann *et al.* *ACS Macro Lett.* **2021**, *10*, 4, 447-452. Copyright 2021 American Chemical Society. Modified representation. 82
- Figure 4-3:** Top: Photodegradation of **2** leading to the nitrosobenzaldehyde **2d**. Bottom: Action plot of **2** in acetonitrile-*d*₃ showing the Conversion X_2 (red) and Yield Y_{2d} (blue). Reprinted with permission from J. Bachmann *et al.* *ACS Macro Lett.* **2021**, *10*, 4, 447-452. Copyright 2021 American Chemical Society. Modified representation. 83
- Figure 4-4:** Plot of molar amount of photoproduct **2d** versus the number of incident photons. The linear fit (red) describes the experimental data

well, but deviation at prolonged exposure can be observed. The intercept of the fit was set to zero. Reprinted with permission from J. Bachmann *et al. ACS Macro Lett.* **2021**, *10*, 4, 447-452. Copyright 2021 American Chemical Society. Modified representation. 84

Figure 4-5: Molecular weight distributions of **T1** and **P1** to **P4** in DMAc. Molecular weight averages and polydispersity indices are collated in **Table 4-1**. Reprinted with permission from J. Bachmann *et al. ACS Macro Lett.* **2021**, *10*, 4, 447-452. Copyright 2021 American Chemical Society. Modified representation. 86

Figure 4-6: a) SEC traces of **T1** before and after irradiation (UV-A) in DMAc. b) SEC traces of **P4** at different residence times in DMAc. Reprinted with permission from J. Bachmann *et al. ACS Macro Lett.* **2021**, *10*, 4, 447-452. Copyright 2021 American Chemical Society. Modified representation. 87

Figure 4-7: Evolution of number distribution of **P4** during irradiation in DMAc. The decrease of the species with higher molecular weight and the increase of the species of lower molecular weight is noted. Reprinted with permission from J. Bachmann *et al. ACS Macro Lett.* **2021**, *10*, 4, 447-452. Copyright 2021 American Chemical Society. Modified representation. 88

Figure 4-8: a) Exemplarily deconvolutional analysis of **P4** after 2.5 min of UV-A irradiation. Depicted are the experimental (black), and deconvoluted Lorentzian functions of assigned **P4** (red) and **P_F** (green). The cumulative trace is indicated in blue colour. b) Evolution of area of **P_F** during UV-A irradiation in DMAc for the full irradiation period. The fit described in the text is coloured in red. Reprinted with permission from J. Bachmann *et al. ACS Macro Lett.* **2021**, *10*, 4, 447-452. Copyright 2021 American Chemical Society. Modified representation. 89

Figure 4-9: Relative fragment area evolution of **P1** to **P4** under UV-A irradiation in DMAc. The shaded zoom shows the evolution over the first 10 minutes. The solid lines are to guide the eye and do not

represent the first-order decay. Reprinted with permission from J. Bachmann <i>et al. ACS Macro Lett.</i> 2021 , <i>10</i> , 4, 447-452. Copyright 2021 American Chemical Society. Modified representation.	90
Figure 4-10: Evolution of apparent rate coefficient k_{apparent} for a first order decay versus the experimental M_n for the polymers P1-P4 (2.0 mg mL ⁻¹). The fit result for the small molecule 4 was added. It is noted that k_{app} for 4 was not determined via deconvolutional SEC analysis but via ¹ H-NMR spectroscopy (DMSO- <i>d</i> ₆) instead. Reprinted with permission from J. Bachmann <i>et al. ACS Macro Lett.</i> 2021 , <i>10</i> , 4, 447-452. Copyright 2021 American Chemical Society. Modified representation.	91
Figure 4-11: Obtained k_{apparent} for P2-P4 versus the used mass concentrations. Note that the values for 2.0 mg mL ⁻¹ have been derived from Figure S4-19-Figure S4-22 . Reprinted with permission from J. Bachmann <i>et al. ACS Macro Lett.</i> 2021 , <i>10</i> , 4, 447-452. Copyright 2021 American Chemical Society.	92
Figure 5-1: Action Plot in absence (red) and presence (blue) of hydrogen peroxide (H ₂ O ₂). Solid lines depict the extinction coefficient and scatter illustrate conversion X of TzDA	98
Figure 5-2: ¹ H-(a) and ¹³ C-(b) NMR spectra of TzDA in acetonitrile- <i>d</i> ₃ before treatment (olive), after exposure to H ₂ O ₂ (black) and after exposure to H ₂ O ₂ and green light ($\lambda = 525$ nm).	100
Figure 5-3: a) Liquid chromatograms of TzDA in acetonitrile at different conditions. Olive: before treatment, black: after exposure to H ₂ O ₂ , ochre: After green light irradiation. b) Assigned structure of the most prominent tetrazine peak in each retention panel.	100
Figure 5-4: a) UV/Vis absorption spectra and b) SEC traces of P1 in THF under exposure of both hydrogen peroxide and 525 nm light.	104
Figure 5-5: a) UV/Vis absorption spectra and b) SEC traces of P5 in THF under exposure of only hydrogen peroxide. c) UV/Vis absorption spectra and d) SEC traces of P5 in THF under exposure of only 525 nm light.	104

- Figure 5-6:** a) UV/Vis absorption spectra and b) SEC traces of **P5** in THF under exposure of both hydrogen peroxide and 525 nm light. 106
- Figure 5-7:** a) $A_{520\text{ nm}}$ and b) M_n evolution of **P1** and **P5** under various triggers. ... 106
- Figure 5-8:** a) $A_{520\text{ nm}}$ and b) M_n evolution of **P1-P5** in presence of H_2O_2 and under green light irradiation..... 107
- Figure 5-9:** a) UV/Vis spectra and b) SEC traces of **P5** in a sequence-driven exposure experiment upon exposure to H_2O_2 and subsequently green light. Extracted absorbance at 520 nm (c) and M_n (d) during the course of exposure. The green-shaded area marks exposure with 525 nm light. *: Data point which has been exposed to H_2O_2 only for 120 minutes. The dotted line is a guide for the eye. 109
- Figure 6-1:** A) MeO-PEG-SPP undergoes photocycloaddition by visible light at 400–550 nm and $\text{pH} \geq 7$. In the presence of a PAG ($\lambda_{\text{activation}} = 400 - 510\text{ nm}$), the photoreactivity of the SPP is inhibited; however, green light at 520 – 550 nm can still activate the photocycloaddition. Thus, the PAG effectively restricts the photoreactivity of MeO-PEG-SPP in the 400 – 510 nm window. B) The SPP group is attached to an 8-arm PEG together with a non-halochromic acrylamidylpyrene (AP) chromophore, which undergoes photocycloaddition by blue light ($\lambda_{\text{activation}} = 400 - 470\text{ nm}$). The photoreactivity of AP is not compromised in presence of PAG. Thus, the 8-arm PEG-AP-SPP can crosslink by either blue or green light via photocycloaddition of the AP or SPP group, respectively. Reproduced with permission. © 2022 The Authors. *Angewandte Chemie International Edition* published by Wiley-VCH GmbH. 113
- Figure 6-2:** SEC data (calibrated against pMMA) of MeO-PEG-SPP and $(\text{MeO-PEG-SPP})_2$ after laser irradiation at 480 nm ($6.32 \pm 0.18 \cdot 10^{19}$ photons which result in a pulse energy of 848 μJ) in water (10 mg mL^{-1}). B) SEC-ESI-MS analysis of the dimerization of MeO-PEG-SPP after irradiation at 480 nm. Zoom into the mass spectra of experimental and simulated isotopic patterns, indicating their excellent agreement. Detailed SEC-ESI-MS analysis is appended in the

- appendix, **Figure S6-7, Figure S6-8.** Reproduced with permission. © 2022 The Authors. *Angewandte Chemie International Edition* published by Wiley-VCH GmbH..... 116
- Figure 6-3:** UV/Vis absorption spectrum of MeO-PEG-SPP (black solid) in water and the corresponding conversion (red solid) for the cycloaddition in water ($c = 10 \text{ mg mL}^{-1}$). Reproduced with permission. © 2022 The Authors. *Angewandte Chemie International Edition* published by Wiley-VCH GmbH..... 117
- Figure 6-4:** UV/Vis spectra of MeO-PEG-SPP in different organic solvents. Spectra were normalised to the absorbance at 400 nm. $d = 10 \text{ mm}$. Reproduced with permission. © 2022 The Authors. *Angewandte Chemie International Edition* published by Wiley-VCH GmbH..... 118
- Figure 6-5:** UV/Vis spectra of MeO-PEG-SPP and corresponding action plots under various pH conditions (green squares: aqueous, yellow circles: pH = 5, orange triangles: pH = 3, red diamonds: pH = 1). In all experiments, approximately $105 \mu\text{mol}$ of photons were deposited (**Table 8-23-Table 8-26**). $d = 10 \text{ mm}$. Reproduced with permission. © 2022 The Authors. *Angewandte Chemie International Edition* published by Wiley-VCH GmbH..... 119
- Figure 6-6:** A) Picture of MeO-PEG-SPP in water at different pH values before irradiation. B) UV/Vis absorption spectra of MeO-PEG-SPP reaction mixtures in water before (solid) and after (dashed) irradiation with $\lambda = 480 \text{ nm}$ ($6.32 \pm 0.18 \cdot 10^{19}$ photons). $d = 10 \text{ mm}$. Reproduced with permission. © 2022 The Authors. *Angewandte Chemie International Edition* published by Wiley-VCH GmbH. 120
- Figure 6-7:** Absorption spectra of MeO-PEG-AP reaction mixtures in water before (solid) and after (dashed) irradiation with $\lambda = 420 \text{ nm}$ ($6.38 \pm 0.36 \cdot 10^{19}$ photons). Spectra were normalised to 371 nm before and 350 nm after irradiation. $d = 10 \text{ mm}$. Reproduced with permission. © 2022 The Authors. *Angewandte Chemie International Edition* published by Wiley-VCH GmbH..... 121

Figure 6-8: Conversion to cycloaddition products as a function of pH for MeO-PEG-SPP (black squares, $\lambda = 480$ nm, $6.32 \pm 0.18 \cdot 10^{19}$ photons) and MeO-PEG-AP (red circles, $\lambda = 420$ nm, $6.38 \pm 0.36 \cdot 10^{19}$ photons). Reproduced with permission. © 2022 The Authors. *Angewandte Chemie International Edition* published by Wiley-VCH GmbH..... 122

Figure 6-9: UV/Vis absorption spectra of the MeO-PEG-SPP in water in before and after irradiation with blue light at $\lambda = 445$ nm in A) absence of PAG or B) presence of PAG. C) $^1\text{H-NMR}$ spectra (600 MHz, CDCl_3) of MeO-PEG-SPP before (top spectrum) and after irradiation by green light at 525 nm with PAG, blue light at $\lambda = 445$ nm, and blue light at $\lambda = 445$ nm with PAG (bottom spectrum, irradiation conditions: $I_L = 3 \text{ W cm}^{-2}$, $t = 1 \text{ h}$); the highlighted area indicates the resonances from styryl $\text{CH}=\text{CH}$ protons. Reproduced with permission. © 2022 The Authors. *Angewandte Chemie International Edition* published by Wiley-VCH GmbH..... 124

Figure 6-10: UV/Vis absorption spectra of PAG (black) and MeO-PEG-SPP (red) in water. $d = 10$ mm..... 125

Figure 6-11: UV/Vis spectra and corresponding action plots of MeO-PEG-SPP and PAG in different concentrations of PAG in water. Violet squares: No PAG, green circles: $[\text{PAG}] = 1.71 \text{ mg mL}^{-1}$, red triangles: $[\text{PAG}] = 4.00 \text{ mg mL}^{-1}$. $d = 10$ mm..... 125

Figure 6-12: A) Schematic crosslinking of MeO-PEG-SPP in acidic environments. B) Evolution of storage modulus of PEG-(SPP)₈ solution ($c = 5 \text{ mM}$) under blue light conditions ($\lambda = 445$ nm, $I_L = 20 \text{ mW cm}^{-2}$) at different pH values. C) Evolution of storage modulus of PEG-(AP)₈ solution ($c = 5 \text{ mM}$) under blue light conditions ($\lambda = 445$ nm, $I_L = 20 \text{ mW cm}^{-2}$) at different pH values. D) and E) Sequence-defined irradiation conditions of PEG-(SPP)₃(AP)₄ solution ($c = 5 \text{ mM}$, 10 wt%) display λ -orthogonal crosslinking of the polymer by either blue (445 nm) or green (525 nm) light ($I_L = 20 \text{ mW cm}^{-2}$). F) Schematic presentation of photomask experiments

demonstrating the spatial control over the stiffening process. G) Strain sweep rheological data of two different areas of the hydrogel, initially formed by green light and selectively stiffened by blue light. H) Strain sweep rheological data of two different areas of the hydrogel, first formed by blue light and selectively stiffened by green light.

Reproduced with permission. © 2022 The Authors. *Angewandte Chemie International Edition* published by Wiley-VCH GmbH..... 127

- Figure 8-1:** Transmittance of the bottom of the glass vials used in the current study. Transmittance of the bottom of the glass vials used in the current study..... 150
- Figure 8-2:** Experimental setup for the photoreactor-based irradiation experiments. Reprinted with permission from J. Bachmann *et al. ACS Macro Lett.* **2021**, *10*, 4, 447-452. Copyright 2021 American Chemical Society. 163
- Figure 8-3:** Emission spectrum of the employed UV-A lamps. Reprinted with permission from J. Bachmann *et al. ACS Macro Lett.* **2021**, *10*, 4, 447-452. Copyright 2021 American Chemical Society. 164
- Figure 8-4:** LED Irradiation setup with a) photobox enclosure and b) without enclosure. 175
- Figure 8-5:** Emission spectrum of the employed green light LED. 175
- Figure S3-1:** ^1H -NMR spectrum of **2** in $\text{DMSO-}d_6$ (*). Reproduced from Ref. 200 with permission from the Royal Society of Chemistry. Modified representation. 205
- Figure S3-2:** ^{13}C -NMR spectrum of **2** in $\text{DMSO-}d_6$ (*). Reproduced from Ref. 200 with permission from the Royal Society of Chemistry. Modified representation. 206
- Figure S3-3:** ^1H -NMR spectrum of **3** in $\text{DMSO-}d_6$ (*). Reproduced from Ref. 200 with permission from the Royal Society of Chemistry. Modified representation. 206

Figure S3-4: ^{13}C -NMR spectrum of 3 in $\text{DMSO-}d_6$ (*). Reproduced from Ref. 200 with permission from the Royal Society of Chemistry. Modified representation.	207
Figure S3-5: ^1H -NMR spectrum of 4 in $\text{DMSO-}d_6$ (*). Reproduced from Ref. 200 with permission from the Royal Society of Chemistry. Modified representation.	207
Figure S3-6: ^{13}C -NMR spectrum of 4 in $\text{DMSO-}d_6$ (*). Reproduced from Ref. 200 with permission from the Royal Society of Chemistry. Modified representation.	208
Figure S3-7: a) Extracted simulated spectra of N3, C1, the convolution of C1 and N3 and the experimental spectrum (from top to bottom). b) Assumed coupling pattern for the systems N3 (left) and C1 (right). The arrow indicates position of the radical, boxes represent coupling nuclei. c) Superimposed simulated and experimental spectra. Reproduced from Ref. 200 with permission from the Royal Society of Chemistry. Modified representation.	210
Figure S3-8: ^1H -NMR spectra (in acetonitrile- d_3) illustrating the analysis process for the action plot. Due to simplicity, only the first entry of every wavelength is shown. The reader is referred to Figure 3-4 b for emphasized resonances and Chapter 8.4.1.3 for analysis. No irradiation experiment is depicted in solid black. Reproduced from Ref. 200 with permission from the Royal Society of Chemistry. Modified representation.	210
Figure S3-9: Setup for LED irradiation experiments. The heat generated by the LED is dissipated by heat sink and fan. The NMR tube is placed in 2 cm distance. Reproduced from Ref. 200 with permission from the Royal Society of Chemistry.	211
Figure S3-10: Emission spectra of the used LED's and the extinction coefficient ϵ of 4 in acetonitrile in comparison. Reproduced from Ref. 200 with permission from the Royal Society of Chemistry. Modified representation.	211

- Figure S3-11:** a) $^1\text{H-NMR}$ spectra of **4** in acetonitrile- d_3 with 340 nm irradiation in different exposure times. b) Plot of conversion and yield versus time for **4** (black) and **4d** (red) according to resonances *a* and *b*. Reproduced from Ref. 200 with permission from the Royal Society of Chemistry. Modified representation. 212
- Figure S3-12:** a) $^1\text{H-NMR}$ spectra of **4** in acetonitrile- d_3 with 365 nm irradiation in different exposure times. b) Plot of conversion and yield versus time for **4** (black) and **4d** (red) according to resonances *a* and *b*. Reproduced from Ref. 200 with permission from the Royal Society of Chemistry. Modified representation. 213
- Figure S3-13:** a) $^1\text{H-NMR}$ spectra of **4** in acetonitrile- d_3 with 390 nm irradiation in different exposure times. b) Plot of conversion and yield versus time for **4** (black) and **4d** (red) according to resonances *a* and *b*. Reproduced from Ref. 200 with permission from the Royal Society of Chemistry. Modified representation. 214
- Figure S3-14:** a) $^1\text{H-NMR}$ spectra of **4** in acetonitrile- d_3 with 415 nm irradiation in different exposure times. b) Plot of conversion and yield versus time for **4** (black) and **4d** (red) according to resonances *a* and *b*. Reproduced from Ref. 200 with permission from the Royal Society of Chemistry. Modified representation. 215
- Figure S3-15:** UV/Vis absorption spectra of **3** in acetonitrile. $d = 10$ mm. 216
- Figure S3-16:** Determination of extinction coefficient ϵ of **3** in acetonitrile at 325 nm (left) and 400 nm (right). $\epsilon_{325 \text{ nm}} = (3700 \pm 210) \text{ L mol}^{-1} \text{ cm}^{-1}$, $\epsilon_{400 \text{ nm}} = (309 \pm 19) \text{ L mol}^{-1} \text{ cm}^{-1}$ 216
- Figure S3-17:** UV/Vis absorption spectra of **4** in acetonitrile. $d = 10$ mm. 217
- Figure S3-18:** Determination of extinction coefficient ϵ of **4** in acetonitrile at 325 nm (left) and 400 nm (right). $\epsilon_{325 \text{ nm}} = (3300 \pm 40) \text{ L mol}^{-1} \text{ cm}^{-1}$, $\epsilon_{400 \text{ nm}} = (554 \pm 5) \text{ L mol}^{-1} \text{ cm}^{-1}$ 217
- Figure S3-19:** Contour plot of **4** with respective stationary in the first 2 ps. (top). $\lambda_{\text{ex}} = 400 \text{ nm}$, $E_{\text{ex}} = 2 \mu\text{J}$, $\lambda_{\text{probe}} = \text{supercontinuum}$, $d = 1 \text{ mm}$,

acetonitrile. Transient response around 400 nm is neglected due to pump pulse scattering.....	218
Figure S3-20: Single transients of the 600 nm response. Figure S3-19 for parameters.	218
Figure S3-21: Single transients of the 460 nm response. Figure S3-19 for parameters.	219
Figure S3-22: Single transients of the 520 nm response. Figure S3-19 for parameters.	220
Figure S3-23: UV/Vis absorption spectra of 4 before and after transient fs-laser experiment. $\lambda_{\text{ex}} = 400$ nm, $E_{\text{ex}} = 2$ μJ , $d = 1$ mm, THF (left), EtOH (right).	220
Figure S3-24: Single transients of the 460, 490, 520 and 600 nm responses in different solvents (THF left, EtOH right). Figure 3-12 for parameters. ...	221
Figure S3-25: UV/Vis absorption spectrum of 4 before and after transient fs-laser experiment. $\lambda_{\text{ex}} = 325$ nm, $E_{\text{ex}} = 0.5$ μJ , $d = 1$ mm, acetonitrile, $d = 1$ mm.	222
Figure S3-26: Single transients of the 420, 490 and 520 nm responses in acetonitrile. Figure 3-14 for parameters.	222
Figure S3-27: UV/Vis absorption spectra of 4 before and after transient fs-laser experiment. $\lambda_{\text{ex}} = 325$ nm, $E_{\text{ex}} = 0.4$ μJ , $d = 1$ mm, THF (left), EtOH (right).	223
Figure S3-28: Single transients of the 460, 490, 520 and 600 nm responses in different solvents (THF left, EtOH right). Figure 3-14 for parameters. ...	224
Figure S3-29: UV/Vis absorption spectra of 3 before and after transient fs-laser experiment. experiment. $\lambda_{\text{ex}} = 400$ nm, $E_{\text{ex}} = 2.0$ μJ , $d = 1$ mm (left), $\lambda_{\text{ex}} = 325$ nm, $E_{\text{ex}} = 0.5$ μJ , $d = 1$ mm (right).	224
Figure S3-30: Single transients of 3 the 430, 510 and 640 nm responses at different excitation conditions. $\lambda_{\text{ex}} = 400$ nm, $E_{\text{ex}} = 2.0$ μJ , $d = 1$ mm, acetonitrile (left), $\lambda_{\text{ex}} = 325$ nm, $E_{\text{ex}} = 0.5$ μJ , $d = 1$ mm, acetonitrile (right).	225

Figure S3-31: ^1H -NMR spectrum of 2,5-H2 in $\text{DMSO-}d_6$ (*).	226
Figure S3-32: ^{19}F -NMR spectrum of 2,5-H2 in $\text{DMSO-}d_6$.	226
Figure S3-33: ^{13}C -NMR spectrum of 2,5-H2 in $\text{DMSO-}d_6$ (*).	227
Figure S3-34: ^1H -NMR spectrum of 2,5-H3 in $\text{DMSO-}d_6$ (*).	227
Figure S3-35: ^{13}C -NMR spectrum of 2,5-H3 in $\text{DMSO-}d_6$ (*).	228
Figure S3-36: ^1H -NMR spectrum of 2,5-Ph2 in $\text{DMSO-}d_6$ (*).	228
Figure S3-37: ^{19}F -NMR spectrum of 2,5-Ph2 in $\text{DMSO-}d_6$.	229
Figure S3-38: ^{13}C -NMR spectrum of 2,5-Ph2 in $\text{DMSO-}d_6$ (*).	229
Figure S3-39: ^1H -NMR spectrum of 2,5-Ph3 in $\text{DMSO-}d_6$ (*).	230
Figure S3-40: ^{13}C -NMR spectrum of 2,5-Ph3 in $\text{DMSO-}d_6$ (*).	230
Figure S3-41: UV/Vis absorption spectra of 2,5-H2 in acetonitrile. $d = 10$ mm.	231
Figure S3-42: Determination of extinction coefficient ϵ of 2,5-H2 in acetonitrile at 221, 267 and 350 nm (from left to right). $\epsilon_{221 \text{ nm}} = (6670 \pm 50) \text{ L mol}^{-1} \text{ cm}^{-1}$, $\epsilon_{267 \text{ nm}} = (5770 \pm 50) \text{ L mol}^{-1} \text{ cm}^{-1}$, $\epsilon_{350 \text{ nm}} = (315 \pm 8) \text{ L mol}^{-1} \text{ cm}^{-1}$.	231
Figure S3-43: UV/Vis absorption spectra of 2,5-H3 in acetonitrile. $d = 10$ mm.	232
Figure S3-44: Determination of extinction coefficient ϵ of 2,5-H3 in acetonitrile at 343 (left) and 250 nm (right). $\epsilon_{343 \text{ nm}} = (9700 \pm 100) \text{ L mol}^{-1} \text{ cm}^{-1}$, $\epsilon_{250 \text{ nm}} = (4200 \pm 60) \text{ L mol}^{-1} \text{ cm}^{-1}$.	232
Figure S3-45: UV/Vis absorption spectra of 2,5-Ph2 in acetonitrile. $d = 10$ mm.	233
Figure S3-46: Determination of extinction coefficient ϵ of 2,5-Ph2 in acetonitrile at 350 (left) and 263 nm (right). $\epsilon_{350 \text{ nm}} = (428 \pm 5) \text{ L mol}^{-1} \text{ cm}^{-1}$, $\epsilon_{263 \text{ nm}} = (5060 \pm 40) \text{ L mol}^{-1} \text{ cm}^{-1}$.	233
Figure S3-47: UV/Vis absorption spectra of 2,5-Ph3 in acetonitrile. $d = 10$ mm.	234

Figure S3-48: Determination of extinction coefficient ϵ of 2,5-Ph3 in acetonitrile at 343 (left) and 252 nm (right). $\epsilon_{343 \text{ nm}} = (8330 \pm 60) \text{ L mol}^{-1} \text{ cm}^{-1}$, $\epsilon_{252 \text{ nm}} = (5410 \pm 50) \text{ L mol}^{-1} \text{ cm}^{-1}$	234
Figure S3-49: SEC traces in THF of polyurethanes formed (solid lines) and their deconvoluted Gaussians in dashed line. Reproduced from Ref. 200 with permission from the Royal Society of Chemistry. Modified representation.	235
Figure S3-50: Top: Full HSQC-NMR spectrum of the 2 min cured polymer in THF- d_8 . Bottom: Zoomed spectrum between 2.5 and 0.5 ppm. The ^1H -NMR resonances at 1.53 ppm, suspected to be the result of an amine group, and its correlated ^{13}C resonance are highlighted in orange. ~ residual catalyst. Reproduced from Ref. 200 with permission from the Royal Society of Chemistry. Modified representation.....	236
Figure S3-51: Wide scan XPS spectra of thin films of <i>o</i> NB-Polyurethane before (black) and after (blue) UV irradiation. Reproduced from Ref. 200 with permission from the Royal Society of Chemistry. Modified representation.	237
Figure S4-1: ^1H -NMR spectrum of 1 in DMSO- d_6 (*). Reprinted with permission from J. Bachmann <i>et al. ACS Macro Lett.</i> 2021 , <i>10</i> , 4, 447-452. Copyright 2021 American Chemical Society.	238
Figure S4-2: ^{13}C -NMR spectrum of 1 in DMSO- d_6 (*). Reprinted with permission from J. Bachmann <i>et al. ACS Macro Lett.</i> 2021 , <i>10</i> , 4, 447-452. Copyright 2021 American Chemical Society.	238
Figure S4-3: ^1H -NMR spectrum of 2 in DMSO- d_6 (*). Reprinted with permission from J. Bachmann <i>et al. ACS Macro Lett.</i> 2021 , <i>10</i> , 4, 447-452. Copyright 2021 American Chemical Society.	239
Figure S4-4: ^{13}C -NMR spectrum of 2 in DMSO- d_6 (*). Reprinted with permission from J. Bachmann <i>et al. ACS Macro Lett.</i> 2021 , <i>10</i> , 4, 447-452. Copyright 2021 American Chemical Society.	239
Figure S4-5: ^1H -NMR spectrum of 3 in DMSO- d_6 (*).	240
Figure S4-6: ^{13}C -NMR spectrum of 3 in DMSO- d_6 (*).	240

- Figure S4-7:** ^1H -NMR spectrum of **4** in $\text{DMSO-}d_6$ (*). Reprinted with permission from J. Bachmann *et al. ACS Macro Lett.* **2021**, *10*, 4, 447-452. Copyright 2021 American Chemical Society. 241
- Figure S4-8:** ^{13}C -NMR spectrum of **4** in $\text{DMSO-}d_6$ (*). Reprinted with permission from J. Bachmann *et al. ACS Macro Lett.* **2021**, *10*, 4, 447-452. Copyright 2021 American Chemical Society. 241
- Figure S4-9:** Full Gradient selected HSQC (HSQCEDET)-NMR spectrum of **4** in $\text{DMSO-}d_6$ (*). Reprinted with permission from J. Bachmann *et al. ACS Macro Lett.* **2021**, *10*, 4, 447-452. Copyright 2021 American Chemical Society. Modified representation. 242
- Figure S4-10:** ^1H -NMR spectrum of non-degradable core in $\text{DMSO-}d_6$ (*). Reprinted with permission from J. Bachmann *et al. ACS Macro Lett.* **2021**, *10*, 4, 447-452. Copyright 2021 American Chemical Society. 242
- Figure S4-11:** ^{13}C -NMR spectrum of non-degradable core in $\text{DMSO-}d_6$ (*). Reprinted with permission from J. Bachmann *et al. ACS Macro Lett.* **2021**, *10*, 4, 447-452. Copyright 2021 American Chemical Society. 243
- Figure S4-12:** Full Gradient selected HSQC (HSQCEDET)-NMR spectrum of nondegradable core in $\text{DMSO-}d_6$ (*). Reprinted with permission from J. Bachmann *et al. ACS Macro Lett.* **2021**, *10*, 4, 447-452. Copyright 2021 American Chemical Society. Modified representation. 243
- Figure S4-13:** UV/Vis absorption spectra of **2** at different concentrations in acetonitrile. $d = 10$ mm. Reprinted with permission from J. Bachmann *et al. ACS Macro Lett.* **2021**, *10*, 4, 447-452. Copyright 2021 American Chemical Society. Modified representation. 244
- Figure S4-14:** Determination of extinction coefficient ϵ of **2** in acetonitrile at 360, 340 and 257 nm (from left to right). $\epsilon_{360 \text{ nm}} = (225 \pm 2) \text{ L mol}^{-1} \text{ cm}^{-1}$, $\epsilon_{340 \text{ nm}} = (369 \pm 2) \text{ L mol}^{-1} \text{ cm}^{-1}$, $\epsilon_{257 \text{ nm}} = (1601 \pm 6) \text{ L mol}^{-1} \text{ cm}^{-1}$. Reprinted with permission from J. Bachmann *et al. ACS Macro Lett.* **2021**, *10*, 4, 447-452. Copyright 2021 American Chemical Society. Modified representation. 244

- Figure S4-15:** Operated UV-A photoreactor lamps. Left axis: Emission spectrum. Right axis: Conversion of **2** as a function of wavelength. Reprinted with permission from J. Bachmann *et al.* *ACS Macro Lett.* **2021**, *10*, 4, 447-452. Copyright 2021 American Chemical Society. 245
- Figure S4-16:** Evolution of resonances of **2** irradiated with a distinct number of photons at 350 nm in acetonitrile-*d*₃. The resonances *b* and *d* relate to characteristic resonances of molecule **2** and its photoproduct as depicted in **Scheme 4-2**. All resonances were referenced to the TMB resonance. Due to simplicity, only one spectrum per time increment is shown. Reprinted with permission from J. Bachmann *et al.* *ACS Macro Lett.* **2021**, *10*, 4, 447-452. Copyright 2021 American Chemical Society. Modified representation. 245
- Figure S4-17:** a) Proposed cleavage reaction of **4**. b) Conversion *X* of **4**, monitored via ¹H-NMR spectroscopy and monoexponential fit (line). The calculation was performed identical to the action plot studies (**Figure S4-16**) and qualitative degradation experiments. *k*_{apparent} was obtained as $k_{app,4,c=2.0} = 0.025 \pm 0.005 \text{ min}^{-1}$. Reprinted with permission from J. Bachmann *et al.* *ACS Macro Lett.* **2021**, *10*, 4, 447-452. Copyright 2021 American Chemical Society. Modified representation. 246
- Figure S4-18:** SEC traces in THF of **T2** before (black) and after (red) attempted endgroup removal. Synthetical protocol is appended in Chapter 8.5.2.7. Reprinted with permission from J. Bachmann *et al.* *ACS Macro Lett.* **2021**, *10*, 4, 447-452. Copyright 2021 American Chemical Society. 247
- Figure S4-19:** a) Number distribution of **P1** for all time periods in a mass concentration of 2.0 mg mL⁻¹. b) Deconvolution plots of single SEC traces for every time increment from 0 to 240 min. c) Evolution of Fragment area over time and fit of physical model. Reprinted with permission from J. Bachmann *et al.* *ACS Macro Lett.* **2021**, *10*, 4, 447-452. Copyright 2021 American Chemical Society. 248

- Figure S4-20:** a) Number distribution of **P2** for all time periods in a mass concentration of 2.0 mg mL⁻¹. b) Deconvolution plots of single SEC traces for every time increment from 0 to 240 min. c) Evolution of Fragment area over time and fit of physical model. Reprinted with permission from J. Bachmann *et al. ACS Macro Lett.* **2021**, *10*, 4, 447-452. Copyright 2021 American Chemical Society. 249
- Figure S4-21:** a) Number distribution of **P3** for all time periods in a mass concentration of 2.0 mg mL⁻¹. b) Deconvolution plots of single SEC traces for every time increment from 0 to 240 min. c) Evolution of Fragment area over time and fit of physical model. Reprinted with permission from J. Bachmann *et al. ACS Macro Lett.* **2021**, *10*, 4, 447-452. Copyright 2021 American Chemical Society. 250
- Figure S4-22:** a) Number distribution of **P4** for all time periods in a mass concentration of 2.0 mg mL⁻¹. b) Deconvolution plots of single SEC traces for every time increment from 0 to 240 min. c) Evolution of Fragment area over time and fit of physical model. Reprinted with permission from J. Bachmann *et al. ACS Macro Lett.* **2021**, *10*, 4, 447-452. Copyright 2021 American Chemical Society. 251
- Figure S4-23:** a) Number distribution of **P2** in a mass concentration of 0.5 mg mL⁻¹ for all time periods. b) Deconvolution plots of single SEC traces for every time increment from 0 to 240 min. c) Evolution of Fragment area over time and fit of physical model. Note that this experiment was performed during the revision process. The polymer, although stored at 5 °C in the dark, showed an increased level of cleavage compared to the initial polymer. Reprinted with permission from J. Bachmann *et al. ACS Macro Lett.* **2021**, *10*, 4, 447-452. Copyright 2021 American Chemical Society. 252
- Figure S4-24:** a) Number distribution of **P2** in a mass concentration of 1.0 mg mL⁻¹ for all time periods. b) Deconvolution plots of single SEC traces for every time increment from 0 to 240 min. c) Evolution of Fragment area over time and fit of physical model. Note that this experiment was per-formed during the revision process. The polymer, although stored at 5 °C in the dark, showed an increased level of cleavage

compared to the initial polymer. Reprinted with permission from J. Bachmann *et al. ACS Macro Lett.* **2021**, *10*, 4, 447-452. Copyright 2021 American Chemical Society..... 253

Figure S4-25: a) Number distribution of **P3** in a mass concentration of 0.5 mg mL⁻¹ for all time periods. b) Deconvolution plots of single SEC traces for every time increment from 0 to 240 min. c) Evolution of Fragment area over time and fit of physical model. Note that this experiment was performed during the revision process. The polymer, although stored at 5 °C in the dark, showed an increased level of cleavage compared to the initial polymer. Reprinted with permission from J. Bachmann *et al. ACS Macro Lett.* **2021**, *10*, 4, 447-452. Copyright 2021 American Chemical Society..... 254

Figure S4-26: a) Number distribution of **P3** in a mass concentration of 1.0 mg mL⁻¹ for all time periods. b) Deconvolution plots of single SEC traces for every time increment from 0 to 240 min. c) Evolution of Fragment area over time and fit of physical model. Note that this experiment was performed during the revision process. The polymer, although stored at 5 °C in the dark, showed an increased level of cleavage compared to the initial polymer. Reprinted with permission from J. Bachmann *et al. ACS Macro Lett.* **2021**, *10*, 4, 447-452. Copyright 2021 American Chemical Society..... 255

Figure S4-27: a) Number distribution of **P4** in a mass concentration of 0.5 mg mL⁻¹ for all time periods. b) Deconvolution plots of single SEC traces for every time increment from 0 to 60 min. c) Evolution of Fragment area over time and fit of physical model. Note that this experiment was performed during the revision process. The polymer, although stored at 5 °C in the dark, showed an increased level of cleavage compared to the initial polymer. Reprinted with permission from J. Bachmann *et al. ACS Macro Lett.* **2021**, *10*, 4, 447-452. Copyright 2021 American Chemical Society..... 256

Figure S4-28: a) Number distribution of **P4** in a mass concentration of 1.0 mg mL⁻¹ for all time periods. b) Deconvolution plots of single SEC traces for every time increment from 0 to 60 min. c) Evolution of Fragment

area over time and fit of physical model. Note that this experiment was performed during the revision process. The polymer, although stored at 5 °C in the dark, showed an increased level of cleavage compared to the initial polymer. Reprinted with permission from J. Bachmann *et al. ACS Macro Lett.* **2021**, *10*, 4, 447-452. Copyright 2021 American Chemical Society. 257

Figure S4-29: Obtained SEC-MS traces of **P2**. TIC: Total ion count, RI: Refractive index, Absorption traces at 254 and 360 nm. Different mass-to-charge regions for $z = 1, 2, 3$ are color-coded. Reprinted with permission from J. Bachmann *et al. ACS Macro Lett.* **2021**, *10*, 4, 447-452. Copyright 2021 American Chemical Society. 258

Figure S4-30: a) Experimental mass spectrum of **P2** for $z = 1$ region. b) Superimposed spectra and assigned counter ions. c) Enlarged view of the shaded area and assignment of found species. Reprinted with permission from J. Bachmann *et al. ACS Macro Lett.* **2021**, *10*, 4, 447-452. Copyright 2021 American Chemical Society. 259

Figure S4-31: a) Experimental mass spectrum of **P2** for $z = 2$ region. b) Superimposed spectra and assigned counter ions. c) Enlarged view of the shaded area and assignment of found species. Reprinted with permission from J. Bachmann *et al. ACS Macro Lett.* **2021**, *10*, 4, 447-452. Copyright 2021 American Chemical Society. 261

Figure S4-32: a) Experimental mass spectrum of **P2** for $z = 3$ region. b) Superimposed spectra and as-signed counter ions. c) Enlarged view of the shaded area and assignment of found species. Reprinted with permission from J. Bachmann *et al. ACS Macro Lett.* **2021**, *10*, 4, 447-452. Copyright 2021 American Chemical Society. 263

Figure S5-1: $^1\text{H-NMR}$ spectrum of TzDA in $\text{DMSO-}d_6$ (*). 265

Figure S5-2: $^{13}\text{C-NMR}$ spectrum of TzDA in $\text{DMSO-}d_6$ (*). Inlet shows the two resonances at approximately 166 ppm. 265

Figure S5-3: $^1\text{H-NMR}$ spectrum of TEGDA in $\text{DMSO-}d_6$ (*). 266

Figure S5-4: ^{13}C -NMR spectrum of TEGDA in $\text{DMSO-}d_6$ (*). Inlet shows the two resonances at approximately 70 ppm.	266
Figure S5-5: ^1H -NMR spectrum of TEGAS in acetonitrile- d_3 (*). Inlets show resonances around 3.6 (left) and 2.7 ppm (right).	267
Figure S5-6: ^{13}C -NMR spectrum of TEGAS in acetonitrile- d_3 (*). Inlet shows the resonances at approximately 72 ppm.	267
Figure S5-7: ^1H -NMR spectra of glycidyl methacrylate (top) and the product thiiran-2-ylmethyl methacrylate (bottom) in $\text{DMSO-}d_6$ (*).	268
Figure S5-8: ^{13}C -NMR spectrum of thiiran-2-ylmethyl methacrylate in $\text{DMSO-}d_6$ (*).	268
Figure S5-9: Full scale ^1H - (a) and ^{13}C - (b) NMR spectra of TzDA before treatment (olive), after exposure to H_2O_2 (black) and after green light irradiation in presence of H_2O_2 (ochre) in acetonitrile- d_3	269
Figure S5-10: LC-ESI mass spectra of TzDA under various conditions. Olive: before treatment, black: after exposure to H_2O_2 , ochre: after green light irradiation. The top left panel depicts the chromatograms of each experiment. a) Mass spectrum of peak A and assignment to theoretically derived species. b) Mass spectrum of peak B and assignment to theoretically derived species. c) Mass spectrum of peak C and assignment to theoretically derived species.	270
Figure S5-11: Exemplarily ^1H -NMR analysis of P3 in $\text{DMSO-}d_6$ (*). Assignment of resonances of monomers, the formulation used before polymerisation and the purified polymer after drying (from top to bottom). Enlarged overview of acrylic resonances on the left hand side.	271
Figure S5-12: a) ^1H -NMR spectra of isolated polymers in $\text{DMSO-}d_6$ (*). b) Enlarged spectra with the resonances of TzDA (b) and TEGDA (c) highlighted in blue (markings are referred to Figure S5-11 bottom).	272
Figure S5-13: UV/Vis absorption spectra of TzDA in absence (solid line) and presence of hydrogen peroxide (H_2O_2 , 6 v%, dashed line). Different solvents were investigated: Acetonitrile (AcN, green), dimethyl	

<p>sulfoxide (DMSO, ochre), ethanol (EtOH, orange), tetrahydrofuran (THF, red). Inlet shows enlarged absorption band around 500 nm.</p>	272
<p>Figure S5-14: LC-ESI-MS analysis of TEGAS after oxidation. UV Chromatograms (254 nm absorbance) of a) TEGAS and b) its oxidation product. Mass spectra for c) TEGAS and d) its oxidation product. Mass spectra were extracted from the increment and compared to simulated isotopic data (top to bottom). A gaussian shape with a deviation of 5 ppm for the simulated species was assumed.....</p>	273
<p>Figure S5-15: ¹H-NMR spectra of TEGAS in acetonitrile-<i>d</i>₃ (*) before (blue) and after (red) oxidation.....</p>	274
<p>Figure S5-16: P2 in presence of H₂O₂ under green light conditions (λ = 525 nm). a) UV/Vis absorption spectra, recorded at indicated irradiation times. b) SEC traces in THF, recorded at indicated irradiation times. c) Evolution of the 520 nm absorbance. d) Evolution of <i>M</i>_n. <i>M</i>_n was determined according to pMMA calibration.....</p>	275
<p>Figure S5-17: P3 in presence of H₂O₂ under green light conditions (λ = 525 nm). a) UV/Vis absorption spectra, recorded at indicated irradiation times. b) SEC traces in THF, recorded at indicated irradiation times. c) Evolution of the 520 nm absorbance. d) Evolution of <i>M</i>_n. <i>M</i>_n was determined according to pMMA calibration.....</p>	275
<p>Figure S5-18: P4 in presence of H₂O₂ under green light conditions (λ = 525 nm). a) UV/Vis absorption spectra, recorded at indicated irradiation times. b) SEC traces in THF, recorded at indicated irradiation times. c) Evolution of the 520 nm absorbance. d) Evolution of <i>M</i>_n. <i>M</i>_n was determined according to pMMA calibration.....</p>	276
<p>Figure S6-1: Emission spectra of the LED lights used in the rheometer irradiation experiments. Reproduced with permission. © 2022 The Authors. Angewandte Chemie International Edition published by Wiley-VCH GmbH.</p>	277
<p>Figure S6-2: ¹H-NMR spectrum of S3 in DMSO-<i>d</i>₆ (*). Reproduced with permission. © 2022 The Authors. Angewandte Chemie International Edition published by Wiley-VCH GmbH.....</p>	277

- Figure S6-3:** $^1\text{H-NMR}$ spectrum of **S4** in CD_2Cl_2 (*). Reproduced with permission. © 2022 The Authors. *Angewandte Chemie International Edition* published by Wiley-VCH GmbH. 278
- Figure S6-4:** $^1\text{H-NMR}$ spectrum of MeO-PEG-SPP in acetonitrile- d_3 (*). Reproduced with permission. © 2022 The Authors. *Angewandte Chemie International Edition* published by Wiley-VCH GmbH. 278
- Figure S6-5:** $^1\text{H-NMR}$ spectrum of PEG-(AP) $_8$ in acetonitrile- d_3 (*). Reproduced with permission. © 2022 The Authors. *Angewandte Chemie International Edition* published by Wiley-VCH GmbH. 279
- Figure S6-6:** $^1\text{H-NMR}$ spectrum of PAG in DMSO- d_6 (*). Reproduced with permission. © 2022 The Authors. *Angewandte Chemie International Edition* published by Wiley-VCH GmbH. 279
- Figure S6-7:** a) Refractive Index (RI) SEC trace of MeO-PEG-SPP before irradiation. b) Extracted mass spectrum from the increment and assigned species with $m/z = 3$ and $m/z = 4$. c) Enlarged mass spectrum of the most abundant $m/z = 4$ species and comparison with simulated isotopic data. d) Enlarged mass spectrum of the most abundant peak close to 657 and comparison with isotopic data. e) Assignment of the experimental mass of intact MeO-PEG-SPP to its simulation, alongside its derived error and composition. Reproduced with permission. © 2022 The Authors. *Angewandte Chemie International Edition* published by Wiley-VCH GmbH. 280
- Figure S6-8:** A) Refractive Index (RI) SEC trace of MeO-PEG-SPP and (MeO-PEG-SPP) $_2$ after irradiation. B) Extracted mass spectrum from the increment and assigned species between $m/z = 5$ and $m/z = 8$. C) Enlarged mass spectrum of the most abundant $m/z = 7$ species and comparison with simulated isotopic distribution for the same species. D) Enlarged mass spectrum of the most abundant peak close to 698 and comparison with simulated isotopic distribution for the same species. E) Assignment of the experimental mass of intact (MeO-PEG-SPP) $_2$ and theoretical mass, as well as its associated derived error and composition. Reproduced with permission. © 2022 The

Authors. Angewandte Chemie International Edition published by
Wiley-VCH GmbH. 281

Figure S6-9: Rheology data of PEG-(SPP)₃(AP)₄ solution (5 mM) under irradiation of blue and green light ($I_L = 20 \text{ mW cm}^{-2}$). Reproduced with permission. © 2022 The Authors. Angewandte Chemie International Edition published by Wiley-VCH GmbH. 282

Figure S6-10: A) Photoswitching of the synthesised merocyanine PAG generator by visible light (400-510 nm) to its spiropyran form, releasing a proton during the process. The spiropyran form is rapidly reversed (in 5 min) to the merocyanine form in the dark. B) UV/Vis absorbance spectra of the PAG in the merocyanine and spiropyran forms, respectively. C) The reversible switching of the PAG by light (at 445 nm, 2 min of irradiation) and in the dark (30 min) for up to 6 cycles in a solution having initial pH value of 6.8, displaying the changes in pH after each switch. Reproduced with permission. © 2022 The Authors. Angewandte Chemie International Edition published by Wiley-VCH GmbH. 283

Figure S6-11: From left to right: In the first experiment, hydrogel was formed by irradiating the PEG-(SPP)₃(AP)₄ solution (10wt%, ca. 4.7 mM) and PAG (0.5 mM) with blue light, during which the PAG was switched from its merocyanine form (red) to its spiropyran form (colourless), revealing the yellow colour of the AP and SPP dimer; irradiation of green light, partly covered by a mask, enabling the stiffening of the gel only on the irradiated part, during this time the spiropyran form was reverted back to the merocyanine form. In the second experiment, the gel was initially formed by irradiation with green light, causing no change to the merocyanine; blue light irradiation on the selected part of the gel triggered the second gelation and photobleaching of PAG. Reproduced with permission. © 2022 The Authors. Angewandte Chemie International Edition published by Wiley-VCH GmbH. 283

List of Tables

Table 2-1: Several spectral regions and their respective wavelengths. Adapted from literature. ^[23]	7
Table 2-2: Comparison of FRP and RDRP. ^[131]	29
Table 3-1: Extracted amplitudes and time constants from the fits shown in Figure 3-10	47
Table 3-2: Several isolated transients of the 460 nm response. The fits are appended in Figure S3-21	48
Table 3-3: Several isolated transients of the 600 nm response. The fits are appended in Figure S3-20	48
Table 3-4: Several isolated transients of the 520 nm response. The fits are appended in Figure S3-22	50
Table 3-5: Extracted transients and influence of solvent. The fits are appended in Figure S3-24	51
Table 3-6: Several isolated transients of the entire transient response of 4 in acetonitrile. The fits are appended in Figure S3-26	55
Table 3-7: Several isolated transients of the entire transient response of 3 in acetonitrile. The fits are appended in Figure S3-30	60
Table 3-8: Classification of molecules investigated.	62
Table 3-9: Tabularized overview of chemical compounds synthesised and their names.	63
Table 4-1: Molecular data of the polymers T1 and P1–P4	85
Table 5-1: Obtained tetrazine-bearing polymers and their proposition.	102
Table 8-1: Parameters for the Action-Plot experiment. *: When conversion is determined to < 0 , resolution limit of the NMR spectrometer is assumed. I_{IS} : Integral internal standard, I_4 : Integral of resonance for 4 , I_{4d} : Integral of resonance for 4d , X_4 : Conversion of 4 , Y_{4d} : Yield of 4d . ..	154

Table 8-2: Experimental parameters for the performed irradiation experiments. (*: performed in photovial to compensate UV absorption of ordinary glass).	155
Table 8-3: Parameters for PLD-SEC experiments. Entries are denoted as curing time_ irradiation time	156
Table 8-4: Irradiation parameters for the undegassed action plot of compound 2,5-H2 . I_{1s} : Integral internal standard, I_2 : Integral of resonance for 2 , I_{2a} : Integral of resonance for 2d , X_2 : Conversion of 2 , Y_{2a} : Yield of 2d . ..	157
Table 8-5: Irradiation parameters for the undegassed action plot of compound 2,5-H3 . I_{1s} : Integral internal standard, I_3 : Integral of resonance for 3 , I_{3a} : Integral of resonance for 3d , X_3 : Conversion of 3 , Y_{3a} : Yield of 3d . ..	158
Table 8-6: Irradiation parameters for the undegassed action plot of compound 2,5-Ph2 . I_{1s} : Integral internal standard, I_2 : Integral of resonance for 2 , I_{2a} : Integral of resonance for 2d , X_2 : Conversion of 2 , Y_{2a} : Yield of 2d . ..	159
Table 8-7: Irradiation parameters for the undegassed action plot of compound 2,5-Ph3 . I_{1s} : Integral internal standard, I_3 : Integral of resonance for 3 , I_{3a} : Integral of resonance for 3d , X_3 : Conversion of 3 , Y_{3a} : Yield of 3d . ..	161
Table 8-8: Experimental parameters for the action plot of compound 2 . I_{1s} : Integral internal standard, I_b : Integral of resonance <i>b</i> , I_d : Integral of resonance <i>d</i> , X_2 : Conversion of 2 , Y_{2a} : Yield of 2d	164
Table 8-9: Irradiation data for the determination of Φ in acetonitrile- d_3 . I_{1s} : Integral internal standard, I_2 : Integral of resonance for 2 , I_{2d} : Integral of resonance for 2d , n_{2a} : Molar amount of 2	166
Table 8-10: Obtained areas of parent and fragment of P1 ($c = 2.0 \text{ mg mL}^{-1}$) and calculations of the Relative Fragment Abundance, <i>RFA</i>	168
Table 8-11: Obtained areas of parent and fragment of P2 ($c = 2.0 \text{ mg mL}^{-1}$) and calculations of the Relative Fragment Abundance, <i>RFA</i>	169
Table 8-12: Obtained areas of parent and fragment of P3 ($c = 2.0 \text{ mg mL}^{-1}$) and calculations of the Relative Fragment Abundance, <i>RFA</i>	169

Table 8-13: Obtained areas of parent and fragment of P4 ($c = 2.0 \text{ mg mL}^{-1}$) and calculations of the Relative Fragment, Abundance, <i>RFA</i>	170
Table 8-14: Obtained areas of parent and fragment of P2 ($c = 0.5 \text{ mg mL}^{-1}$).	171
Table 8-15: Obtained areas of parent and fragment of P2 ($c = 1.0 \text{ mg mL}^{-1}$).	171
Table 8-16: Obtained areas of parent and fragment of P3 ($c = 0.5 \text{ mg mL}^{-1}$).	172
Table 8-17: Obtained areas of parent and fragment of P3 ($c = 1.0 \text{ mg mL}^{-1}$).	172
Table 8-18: Obtained areas of parent and fragment of P4 ($c = 0.5 \text{ mg mL}^{-1}$).	173
Table 8-19: Obtained areas of parent and fragment of P4 ($c = 1.0 \text{ mg mL}^{-1}$).	173
Table 8-20: parameters fulfilling the fit conditions.	174
Table 8-21: Experimental parameters for the laser-based irradiation of TzDA in pure H ₂ O. λ : Wavelength of incident light; E : Energy per pulse; ΔE : Error in energy per pulse; k : Number of pulses; N_p : Number of photons deposited; $A_{511 \text{ nm}}$: Absorbance of solution at 511 nm after irradiation; X : Conversion; ΔX : Error in conversion.	176
Table 8-22: Experimental parameters for the laser-based irradiation of TzDA in a H ₂ O:H ₂ O ₂ mixture. λ : Wavelength of incident light; E : Energy per pulse; ΔE : Error in energy per pulse; k : Number of pulses; N_p : Number of photons deposited; $A_{511 \text{ nm}}$: Absorbance of solution at 511 nm after irradiation; X : Conversion; ΔX : Error in conversion.	177
Table 8-23: Experimental data for the irradiation of MeO-PEG-SPP in aqueous solution. λ : Wavelength, E_{pulse} : Measured pulse energy at the sample holder of the laser setup (Figure 8-1), ΔE_{pulse} : Error in measured pulse energy, t : Irradiation time, T_λ : Transmittance of the glass vial at respective wavelength, N_p : Deposited number of photons according to Equation 8-5, ΔN_p : Error in deposited number of photons, X : Conversion according to Equation 8-29, ΔX : Error in conversion according to Equation 8-30.	180
Table 8-24: Experimental data for the irradiation of MeO-PEG-SPP in aqueous solution (pH = 5). λ : Wavelength, E_{pulse} : Measured pulse energy at the sample holder of the laser setup (Figure 8-1), ΔE_{pulse} : Error in	

measured pulse energy, t : Irradiation time, T_λ : Transmittance of the glass vial at respective wavelength, N_P : Deposited number of photons according to Equation 8-5, ΔN_P : Error in deposited number of photons, X : Conversion according to Equation 8-29, ΔX : Error in conversion according to Equation 8-30. 180

Table 8-25: Experimental data for the irradiation of MeO-PEG-SPP in aqueous solution (pH = 3). λ : Wavelength, E_{pulse} : Measured pulse energy at the sample holder of the laser setup (**Figure 8-1**), ΔE_{pulse} : Error in measured pulse energy, t : Irradiation time, T_λ : Transmittance of the glass vial at respective wavelength, N_P : Deposited number of photons according to Equation 8-5, ΔN_P : Error in deposited number of photons, X : Conversion according to Equation 8-29, ΔX : Error in conversion according to Equation 8-30. 181

Table 8-26: Experimental data for the irradiation of MeO-PEG-SPP in aqueous solution (pH = 1). λ : Wavelength, E_{pulse} : Measured pulse energy at the sample holder of the laser setup (**Figure 8-1**), ΔE_{pulse} : Error in measured pulse energy, t : Irradiation time, T_λ : Transmittance of the glass vial at respective wavelength, N_P : Deposited number of photons according to Equation 8-5, ΔN_P : Error in deposited number of photons, X : Conversion according to Equation 8-29, ΔX : Error in conversion according to Equation 8-30. 181

Table 8-27: Experimental data for the irradiation of MeO-PEG-SPP in H₂O in the presence of PAG in $[PAG] = 1.71 \text{ mg mL}^{-1}$ (stoichiometric amount). λ : Wavelength, E_{pulse} : Measured pulse energy at the sample holder of the laser setup (**Figure 8-1**), ΔE_{pulse} : Error in measured pulse energy, t : Irradiation time, T_λ : Transmittance of the glass vial at respective wavelength, N_P : Deposited number of photons according to Equation 8-5, ΔN_P : Error in deposited number of photons, X : Conversion according to Equation 8-29, ΔX : Error in conversion according to Equation 8-30. 182

Table 8-28: Experimental data for the irradiation of MeO-PEG-SPP in H₂O in the presence of PAG in $[PAG]=4.00 \text{ mg mL}^{-1}$. λ : Wavelength, E_{pulse} : Measured pulse energy at the sample holder of the laser setup (**Figure**

8-1), ΔE_{pulse} : Error in measured pulse energy, t : Irradiation time, T_{λ} : Transmittance of the glass vial at respective wavelength, N_{P} : Deposited number of photons according to Equation 8-5, ΔN_{P} : Error in deposited number of photons, X : Conversion according to Equation 8-29, ΔX : Error in conversion according to Equation 8-30.	183
Table 8-29: Conversion of MeO-PEG-SPP and MeO-PEG-AP after single- wavelength (480 nm for SPP, 420 nm for AP) irradiation in different aqueous solutions. *: Conversion value for pH = 7 for MeO-PEG-SPP was obtained from Table 8-23 . pH: pH value determined via pH sensor, X : Conversion according to Equation 8-29, ΔX : Error in conversion according to Equation 8-30.	183
Table 8-30: Polymerisation protocol. *: Only T1 was used with a non- degradable core.	193
Table 8-31: Polymerisation details. ^a values obtained after calibration against <i>p</i> MMA standard for RI detection. ^b Yield of recovered polymer.	199
Table 8-32: Investigation of polymer composition. ^a Experimental equivalents are provided from ¹ H-NMR spectra of the respective polymer after isolation.	199
Table S3-1: Detailed overview of found species in the mass spectrum of 2 , comparison with theoretically expected m/z values and derived error Δ	208
Table S3-2: Detailed overview of found species in the mass spectrum of 3 , comparison with theoretically expected m/z values and derived error Δ	208
Table S3-3: Detailed overview of found species in the mass spectrum of 4 , comparison with theoretically expected m/z values and derived error Δ	209
Table S3-4: Settings for the acquisition of shown EPR spectrum.	209
Table S3-5: Parameters obtained by the simulation of two radical species via the <i>garlic</i> function.	209

Table S3-6: Extracted transients and influence of solvent. The fits are appended in Figure S3-28	223
Table S4-1: Detailed overview of identified signals in the mass spectrum Figure S4-30 , comparison with theoretically expected m/z values, derived error Δ and α , ω -group.	260
Table S4-2: Detailed overview of identified signals in the mass spectrum Figure S4-31 , comparison with theoretically expected m/z values, derived error Δ and α , ω -group.	261
Table S4-3: Detailed overview of identified signals in the mass spectrum Figure S4-32 , comparison with theoretically expected m/z values, derived error Δ and α , ω -group.	263
Table S5-1: Detailed overview of identified signals in mass spectra Figure S5-10 , comparison with theoretically expected m/z values, derived error Δ and composition.	271
Table S5-2: Assignment of the experimental mass of TEGAS and TEGASO to its simulation, alongside its derived error and composition.	273

List of Abbreviations

Abbreviation	Full notation
A	Absorption
AI	Artificial Intelligence
AIBN	Azobisisobutyronitrile
AP	Acrylpyrene
ARC	Australian Research Council
ATRP	Atom Transfer Radical Polymerisation
BH ₃	Borane
BODIPY	Dipyrometheneboron difluoride
CA	Cycloaddition
CCD	Charge-coupled device
D/A	Donor/Acceptor
DBTL	Dibutyl tin dilaurate
EPR	Electron Paramagnetic Resonance
ESA	Excited State Absorption
ESI	Electrospray Ionisation
ESIPT	Excited State Intramolecular Proton Transfer
EU	European Union
F	Fluorescence
FRP	Free Radical Polymerisation
GSB	Ground State Bleaching
GVD	Group Velocity Dispersion
GVM	Group Velocity Mismatch
HDI	Hexamethylene Diisocyanate
HEA	Hydroxyethyl Acrylate
HGSA	Hot Ground State Absorption
HOMO	Highest Occupied Molecular Orbital
HSQC	Heteronuclear Single-Quantum Coherence
IC	Internal Conversion
ICT	Intramolecular Charge Transfer

IEDDA	Inverse Electron Deficient Diels-Alder
IP	Ionic Polymerisation
IR	Infrared
ISC	Intersystem Crossing
IVR	Intermolecular Vibrational Redistribution
KIT	Karlsruhe Institute of Technology
L	Luminescence
LC	Liquid Chromatography
LCAO	Linear Combination of Atomic Orbitals
LG	Leaving Group
LED	Light Emitting Diode
LUMO	Lowest Unoccupied Molecular Orbital
MO	Molecular Orbital
MS	Mass Spectrometry
NHS	N-hydroxysuccinimide
NMP	Nitroxide Mediated Polymerisation
NMR	Nuclear Magnetic Resonance
NOPA	Noncollinear Optical Parametric Amplification
NPEOC	[2-(2-nitrophenyl)ethoxy]carbonyl
NPPOC	[2-(2-nitrophenyl)-propoxy]carbonyl
OKE	Optical Kerr Effect
<i>o</i> NB	<i>ortho</i> -nitrobenzyl
<i>o</i> NT	<i>ortho</i> -nitrotoluene
OPA	Optical Parametric Amplification
OPO	Optical Parametric Oscillation
P	Phosphorescence
PAG	Photoacid Generator
PDI	Polydispersity Index
PEG	Polyethylene Glycol
PLA	Poly lactide
PLD	Pulsed Laser Degradation
PPG	Photolabile Protecting Group
PU	Polyurethane

QCM	Quartz Crystal Microbalance
QUT	Queensland University of Technology
QY	Quantum Yield
RLA	Relative Fragment Abundance
RAFT	Reversible Addition-Fragmentation chain Transfer
RDRP	Reversible Deactivation Radical Polymerisation
ROS	Reactive Oxygen Species
SDG	Sustainable Development Goals
SE	Stimulated Emission
SEC	Size Exclusion Chromatography
SFG	Sum Frequency Generation
SHG	Second Harmonic Generation
SOC	Spin-Orbit-Coupling
SPM	Self-Phase-Modulation
SPP	Styrylpyrido[2,3-b]pyrazine
SQ	Styrylquinoxaline
TEGDA	Tetraethylene Glycol Diacrylate
TEMPO	2,2,6,6-tetramethylpiperidinyloxy
TICT	Twisted Intramolecular Charge Transfer
Tz	Tetrazine
TzDA	Tetrazine Diacrylate
UN	United Nations
UV	Ultraviolet
UV/Vis	Ultraviolet-visible (range)
VR	Vibrational Relaxation
XPS	X-ray Photoelectron Spectroscopy

List of Symbols

Symbol	Full notation
t_{acq}	Acquisition time
N_t	Amount of endgroups at time t
ω	Angular frequency
k_{app}	Apparent rate constant of cleavage
θ_i	Atomic orbital
k_B	Boltzmann constant
P_{calc}	Calculated Power
z_i	Charge
B_0	Center of magnetic field
c	Concentration
$[A]$	Concentration of absorber A
X	Conversion
I	Current
d	Cuvette diameter
ϵ_0	Dielectric coefficient in vacuum
$B_{\epsilon' \leftarrow \epsilon''}$	Einsteinian coefficient for stimulation absorption
G'	Elastic modulus
μ	Electric dipole moment operator
E	Electric field vector
S_e	Electron spin
\vec{R}	End-to-end vector
$S(\vec{R})$	Entropy
E_{ex}	Excitation energy
λ_{ex}	Excitation wavelength
Φ	Fluorescence quantum yield
P_F	Fragment polymer
$S(v', v'')$	Franck-Condon factors
ν	Frequency
G_e	Gain exponent

G_n	Gain mantisse
g	Gyromagnetic constant
A_H	Hyperfine constant
$P(\vec{R})$	ideal chain probability density function
I_L	Intensity of light
t_{irr}	Irradiation time
ν_p	Kinetic chain length for propagation
ν_t	Kinetic chain length for termination
f_{rep}	Laser repetition rate
lw	Line width
pK_a	Logarithmic acid dissociation constant
R_i	Location of nucleus i
G''	Loss modulus
m	Mass
n	Molar amount
$\varepsilon(\nu)$	Molar extinction coefficient
X_i	Molar fraction
M	Molecular Weight
r_{ns}	Nonstoichiometric factor
$\Omega(\vec{R})$	Number of microstates
N_p	Number of photons
k_{pulse}	Number of pulses
N_R	Number of repetitions
P_n	Number-averaged Degree of Polymerisation (chain growth)
DP_n	Number-averaged Degree of Polymerisation (step growth)
M_n	Number-averaged molecular weight
OD	Optical Density
η_0	Ordinary refractive index
P	Parent polymer
l	Path length
P_l	Polarisation vector (linear)
P_{nl}	Polarisation vector (nonlinear)
D	Polydispersity

λ_{probe}	Probe wavelength
ζ	Progress of medium propagation
$P\bullet$	Propagating polymer chain
E_{pulse}	Pulse energy
Φ	Quantum Yield
R	Range of recorded EPR spectrum
k	Rate constant
\vec{k}_i	Rate constant of chain initiation
\vec{k}_p	Rate constant of chain propagation
\vec{k}_t	Rate constant of chain termination
\vec{k}_d	Rate constant of initiator generation
η	Refractive index
τ_{TM}	Relaxation time transparent medium
χ	Susceptibility
$T\bullet$	Stable Radical
G'	Storage Modulus
t	Time
T_λ	Transmittance of glass
z_p	Travelling photon trajectory
ν	Vibrational mode
G''	Viscous modulus
U	Voltage
k_i	Wave vector
Ψ	Wave function
λ	Wavelength
w_i	Weight fraction
M_w	Weight-averaged molecular weight
h	Planck constant
\vec{k}_{pump}	Wave vector for OPA (Pump)
\vec{k}_{signal}	Wave vector for OPA (Signal)
\vec{k}_{idler}	Wave vector for OPA (Idler)
Y	Yield

List of Equations

Equation 2-1	8
Equation 2-2	8
Equation 2-3	8
Equation 2-4	9
Equation 2-5	9
Equation 2-6	10
Equation 2-7	10
Equation 2-8	10
Equation 2-9	10
Equation 2-10	10
Equation 2-11	11
Equation 2-12	12
Equation 2-13	12
Equation 2-14	12
Equation 2-15	13
Equation 2-16	13
Equation 2-17	14
Equation 2-18	14
Equation 2-19	14
Equation 2-20	22
Equation 2-21	22
Equation 2-22	22
Equation 2-23	23
Equation 2-24	23

Equation 2-25	23
Equation 2-26	23
Equation 2-27	23
Equation 2-28	23
Equation 2-29	24
Equation 2-30	24
Equation 2-31	24
Equation 2-32	24
Equation 2-33	24
Equation 2-34	25
Equation 2-35	25
Equation 2-36	26
Equation 2-37	26
Equation 2-38	26
Equation 2-39	26
Equation 2-40	26
Equation 2-41	27
Equation 2-42	27
Equation 3-1	50
Equation 4-1	78
Equation 8-1	144
Equation 8-2	144
Equation 8-3	144
Equation 8-4	146
Equation 8-5	149
Equation 8-6	149

Equation 8-7	151
Equation 8-8	153
Equation 8-9	153
Equation 8-10	154
Equation 8-11	156
Equation 8-12	156
Equation 8-13	167
Equation 8-14	167
Equation 8-15	167
Equation 8-16	168
Equation 8-17	168
Equation 8-18	168
Equation 8-19	168
Equation 8-20	168
Equation 8-21	168
Equation 8-22	174
Equation 8-23	174
Equation 8-24	174
Equation 8-25	174
Equation 8-26	176
Equation 8-27	176
Equation 8-28	179
Equation 8-29	179
Equation 8-30	179

Academic Output

Publications in peer-reviewed journals:

- *UV-induced photolysis of polyurethanes*

C. Petit,⁺ J. Bachmann,⁺ L. Michalek, Y. Catel, E. Blasco, J. P. Blinco, A.-N. Unterreiner, C. Barner-Kowollik *Chem. Commun.* **2021**, 57, 2911.

Contributor	Statement of Contribution
Julian Bachmann	Research design, experimental conceptualization, monomer synthesis, execution all light-mediated degradation experiments, analysis and interpretation of all acquired data, simulation EPR spectra, writing and editing original manuscript, processing revisions.
Charlotte Petit	Research design, experimental conceptualization, monomer and polymer synthesis, assistance in QCM and XPS measurements, analysis and interpretation of acquired data, writing and editing original manuscript, processing revisions.
Lukas Michalek	Execution QCM and XPS measurements, assistance in analysis and interpretation of acquired data, assistance in editing original manuscript.

- *Chain-Length-Dependent Photolysis of ortho-Nitrobenzyl-Centered Polymers*
J. Bachmann,⁺ C. Petit,⁺ L. Michalek, Y. Catel, E. Blasco, J. P. Blinco,
A.-N. Unterreiner, C. Barner-Kowollik *ACS Macro Lett.* **2021**, *10*, 4, 447-452.

Contributor	Statement of Contribution
Julian Bachmann	Research design, experimental conceptualization, execution of all experiments, monomer and polymer synthesis, execution light-mediated degradation experiments, modelling kinetic data set, analysis and interpretation of all acquired data, writing and editing original manuscript, processing revisions.
Charlotte Petit	Research design, assistance in experimental conceptualization, assistance in analysis and interpretation of acquired data, assistance in writing and editing original manuscript, assistance in processing revisions.
Lukas Michalek	Ideal chain model, assistance in analysis and interpretation of acquired data, assistance in editing original manuscript.

- *Wavelength-Orthogonal Stiffening of Hydrogel Networks with Visible Light*
V. X. Truong,⁺ J. Bachmann,⁺ A.-N. Unterreiner, J. P. Blinco, C. Barner-Kowollik *Angew. Chem. Int. Ed.* **2022**, *61* (15), e202113076.

Contributor	Statement of Contribution
Julian Bachmann	Research design, experimental conceptualization, execution light-mediated ligation experiments, action plots, analysis of all acquired data, writing and editing original manuscript, processing revisions.
Vinh X. Truong	Research design, experimental conceptualization, execution of material study (rheology), monomer and polymer synthesis, analysis and interpretation of acquired data, writing and editing original manuscript, processing revisions.

Conference contributions:

- *In-depth study of light-induced depolymerisation of polyurethanes*
J. Bachmann, J. P. Blinco, A.-N. Unterreiner, C. Barner-Kowollik
Pacifichem **2021**, Honolulu, USA (oral presentation)
- *Chain-Length-Dependent Photolysis of ortho-Nitrobenzyl-Centered Polymers*
J. Bachmann, J. P. Blinco, A.-N. Unterreiner, C. Barner-Kowollik
Queensland Student Chemistry Symposium (QSCS) **2021**, Townsville, Australia (oral presentation)

⁺contributed equally

Acknowledgements

I could not have taken this journey without my two principal supervisors, Prof. Christopher Barner-Kowollik and Prof. Andreas-Neil Unterreiner. I am deeply indebted to the opportunity they gave me, for their guidance, superb feedback and the continuous support over the last years. I am grateful for their encouragement and patience which made me thrive in the best way possible. Their wisdom and knowledge are unprecedented and I am thankful for experiencing this first hand.

Words cannot express my gratitude to my secondary supervisors Prof. Eva Blasco, Prof. James Blinco, Dr. Charlotte Petit and Dr. Yohann Catel for their invaluable support, their helpful advice and the opportunity to shine some light into this interesting topic. I would like to extend my sincere thanks to my collaborators Dr. Lukas Michalek and Dr. Vinh X. Truong for their support. Further, I want to thank Mr. Bronson Keays and Mr. Jan Veit for the assistance during their capstone project and bachelor thesis, respectively. Financial support from the Australian Research Council (ARC) and Ivoclar Vivadent AG as well as the infrastructure provided by QUT and KIT are gratefully acknowledged.

I would like to express my deepest appreciation to my colleagues and coworkers at both working nodes. Although Germany and Australia can (almost) not be any more distant, I never felt apart. I want to thank the Soft Matter Materials Laboratory for the incredible time I had in Brisbane. I want to thank my co-workers and friends for their contributions to my project, their always positive attitude and the awesome time I had in- and outside working hours. With this, I also want to thank my colleagues at KIT for their input and fruitful discussions.

My thanks also go to the most incredible people I met in Australia. I want to thank my travel partners for the overwhelming moments while travelling. Not even tropical storms, flooding or bushfires kept us from having a wonderful time in this beautiful country. Many thanks to my friends for all the fun we had, the time we could spend and the memories we could share together. Last but definitely not least, I want to thank my family across the globe. You were the light in the darkest hours and an even brighter inspiration to me. Thank you for always being there and not letting me down.

Chapter 1: Introduction

1.1 BACKGROUND

Hermann Staudinger initial proposal that polymers are long sequences of equal building blocks, marked the birth of a new scientific field and allowed for unprecedented economic growth.^[1] Polymers (or vernacularly called ‘plastics’) are long chains of small molecules. These small molecules are purposely called monomers since they are a single part of the entire chain. Monomers can be linked to each other by covalent bond forming reactions during macromolecular chain growth. Most often, a carbon-carbon bond is formed and represents the backbone of the chain. Molecular design of a monomer, the sequence in which they are added and general reaction conditions allow for a plethora of different plastics, many of which can be found in any day-to-day task today.^[2]

Polymers are omnipresent and can be found in many industrial or domestic sectors.^[2] Construction highly benefits from rapid and low-cost production as well as their outstanding mechanical properties. Traditional construction materials like timber or steel often require laborious manufacturing. Additionally, plastics are light-weight and can be readily moulded in any shape, easing transportation and use. However, not only (sometimes meter-long) construction tools profit from the existence of plastics. Since polymers consist of (often) identical building blocks, plastic materials are highly reproducible and thus decoupled from occurring invariances found in nature.^[3] Depending on the molecular architecture, polymers often fulfil biologically relevant criteria such as being aseptic and resistant to enzymatic destruction.^[4] This inertness makes plastics ideal for the medical sector. Consumables such as syringes, tubing material and single-use personal protective equipment are often manufactured using plastics. More importantly, plastics find application in wound-healing, implants and prosthetics, given their low-weight and bioavailability. Restorative dentistry unites all superior characteristics plastic can feature. Repair or restorative operations in the oral cavity often require materials which offer pH resistance and are biocompatible, yet have outstanding mechanical properties and low leaching performance.^[5]

Despite all these advantages, using polymers to the current extent comes at a high cost. It is their very resistance to external influences or general conception of stability which renders plastics problematic. The current accumulation of solid plastic waste found in terrestrial and aquatic ecosystems raises concerns on a global level.^[6] Reducing plastic pollution is an integral part of the United Nations Sustainable Development Goals (UN SDG's)^[7]. A 'Business As Usual' strategy results in an annual release of approximately 60-90 megatons (Mt) into maritime ecosystems, significantly missing a target emission of 8 Mt by 2030.^[8] The European Union (EU) implemented the EU waste hierarchy which is integrated in the EU Waste Framework Directive.^[9] The EU prioritizes prevention of plastic use, and landfill disposal is avoided while recycling strategies are heavily promoted.^[10-11] Recycling strategies include 'Waste-to-Energy' (incineration) processes as well as chemical and mechanical engineering.^[10] In the latter two, the plastic is either treated with acid and bases or heat for reshaping purposes. However, all recycling operations induce some level of degradation to a polymer, affecting its overall quality.

Polymer degradation describes induced changes in chemical composition, which in return affects a polymers' performance. In general, many different pathways of polymer degradation have been established in the scientific community.^[12-13] Established pathways include mechanochemical, oxidative thermal or photolytic degradation.^[13] Mechanochemical recycling induces a high level of stress by shearing to a polymer. Labile bonds such as crosslinking sites are prone to cleavage, forming radical species. Since oxygen is omnipresent, the addition of reactive oxygen species to a polymers backbone or sidechain often occurs. Reactive sites such as vinylic termini or CH₂ groups are especially prone to oxygen addition, forming peroxides or inducing random scission reactions. Generally, oxidative degradation is often accompanied by thermal or photolytic degradation. Thermal degradation simply describes the cleavage of bonds of lowest energy with heat. These bonds will cleave upon passing a certain energy threshold, again forming radicals. Photodegradation mainly involves either the presence of reactive oxygen species such as ozone or random bond cleavage due to high energetic ultraviolet irradiation.^[14] Additionally, photoresponsive moieties such as carbonyl or carboxyl groups can absorb light quanta to generate radicals. UV light has sufficient energy to break various chemical bonds, causing the untargeted frequent generation of radicals. Thus, the applicability of

photodegradable polymers in medical fields is limited. The difference between thermal and photolytic degradation lies in the transportation of energy. While heat can be applied on a bulk material simultaneously, high energy light only acts on the surface and is barely matter penetrating. Most often, degradation is superimposed by several degradation processes. Exemplarily, melt extrusion is a common practice in recycling and often faces oxidative, thermal and mechanochemical degradation simultaneously. Mechanical properties are often designed for either stability, which makes a plastic robust and enduring, or instability, which makes the plastic prone to degradation. Plastics as a material must withstand external influences until its purpose has been fulfilled. After its intended use, one may consider it beneficial to remove all stability-granting characteristics, thus making plastic simple to degrade or easy to discard. However, this is not state of the art, since a plastics' properties are typically determined and set during its fabrication. Consequently, the implementation of 'on-demand' characteristics, i.e. a sudden change in a material's likeliness to undergo facile and specific degradation, is highly beneficial.

1.2 PURPOSE AND CONTEXT

Light is an abundant resource and can be found (almost) anywhere on the globe's surface. Its role as energy and illumination source^[15-16] as well as navigation support^[17] underpins its usefulness. Most critically, life on our planet would not be possible without light. Thanks to the advent and rise of the scientific field of photochemistry, powerful tools to conveniently manipulate molecules via light are at hand. Popular examples like photosynthesis^[18] and the process of vision^[19] rely on discrete photochemical and -physical steps. All these aspects are naturally taken for granted but in fact allow for a high degree of precision thanks to the spatiotemporal control offered by light^[20] and the low cost of operation^[21] compared to temperature-driven chemistry. However, considering the removal of polymeric material such as filling or adhesives from complex biological systems like the oral cavity remains challenging, since ultraviolet light is harmful for organic tissue. Thus, visible light as a trigger medium to allow tailored polymer degradation would be highly desirable.

In the current thesis, 'On-Demand' characteristics are imparted onto polymers, thus allowing for degradability, while investigating the key underpinning mechanistic

steps. Here, light as a possible technology platform is envisaged to act as the controlled trigger to change a polymers morphology and structure (**Figure 1-1**). Instead of using heat as a conventional degradation medium, light allows a degradation on demand due to its spatiotemporal resolution. Different polymer techniques and morphologies were realized in order to demonstrate the advantages of a light-driven degradation. The thesis at hand comprises several stand-alone chapters, depicting the usefulness of light for degradable polymers. Exemplarily, a complete backbone breakdown as well as a controlled centric scission were investigated. Further examinations include backbone oxidation as a possible pathway as well as light-induced crosslinking phenomena. Note that any considerations regarding mechanical processing or engineering are beyond the scope of the current thesis. Instead, the thesis seeks to lay the ground work of fundamental principles that could be applied in practice. Thus, the synthesis of photoresponsive monomers and polymers are in focus. Further, particular emphasis was placed on light-matter interactions, the wavelength resolved reactivity screening, as well as tracking the change of polymers' morphology. Consequently, a variety of magnetic, spectroscopic and spectrometric methods were used, which are applicable on both the small molecule and the polymer level.

Chapter 3 provides a first prototype study for the degradation via ultraviolet light and aims for fragmentation of a polymer. First, significant efforts were focused on the photochemistry of the photolabile group before polymer aspects were investigated. The small molecule studies involved complex analysis, such as femtosecond spectroscopy and wavelength-resolved reactivity studies. A polymer class notoriously known for its lack of degradation was selected specifically for this purpose. Polyurethanes can be formed upon condensation of a diisocyanate and a dialcohol. A photoresponsive dialcohol was synthesised and a linear polymer based on a commercially available diisocyanate formed. Upon ultraviolet light irradiation, two characteristic fragments, namely a carboxylic acid and a nitrosoketone were generated. The backbone fragmentation was hereby traced via chromatographic, spectroscopic and spectrometric methods.

Chapter 4 investigates the effect of polymer morphology on light-driven degradation. Here, the polymer is no longer simply fragmented into molecular blocks but instead cleaved in half. A polymer chain with a single light-cleavable center was investigated. A bifunctional linker with photoresponsive functionality allows for controlled two-

arm growth. Depending on the obtained chain length, different photolysis kinetics were determined, a general trend estimated and compared to a theoretical model.

Chapter 5 extends the term ‘degradation’ by modifying the polymers morphology. The oxidation of the backbone was investigated. The modification was achieved by exploiting a dual-trigger mechanism with visible light which may extend its applicability into the realm of ultraviolet-sensitive environments. A photocleavable tetrazine motif was selected which undergoes nitrogen-oxygen substitution. The oxidation was traced via spectroscopic, spectrometric and magnetic methods.

Chapter 6 constitutes a feasibility study and pushes the definition of degradation. Degradation was introduced as any significant change of the backbone, be it complete fragmentation (Chapter 3), spatially targeted fragmentation of the center (Chapter 4) or backbone oxidation (Chapter 5). One form of downgrading polymeric material is crosslinking which occurs due to backbone-backbone recombination. This degradation process often results in stiffer and more brittle materials. Chapter 6 establishes visible light crosslinking and inhibition thereof under acidic conditions via [2+2] cycloadditions.

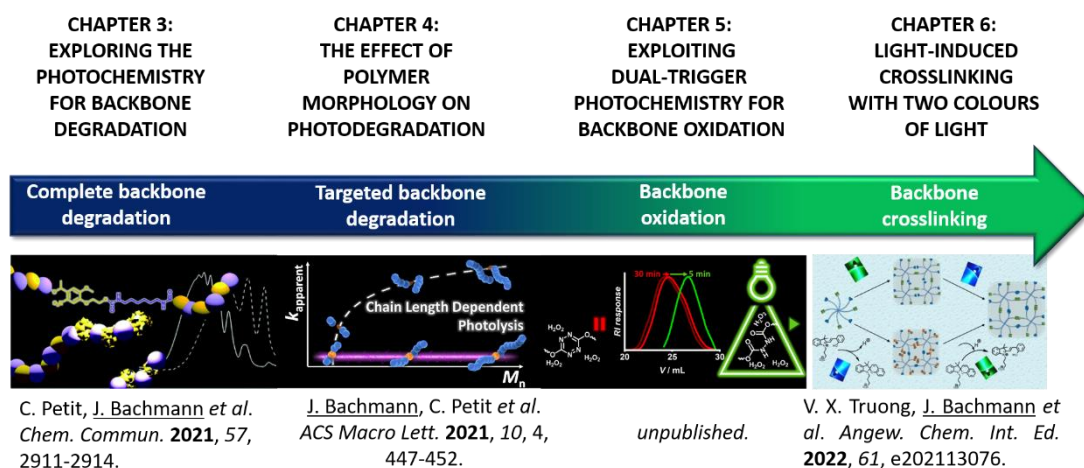


Figure 1-1: Scope of this PhD thesis.

Each chapter introduces its objective and intentions briefly prior to discussing the findings. A short summary is given at the end of each chapter. However, an overarching summary and outlook section will encompass the general findings, encountered drawbacks and a possible future in this field.

Chapter 2: Theoretical Fundamentals

2.1 PHOTOPHYSICS

2.1.1 Electronic transitions in molecules

Light is a form of electromagnetic radiation. It is mostly characterized by its wavelength and thus can be classified according to its spectral region (**Table 2-1**). Notably, human vision can capture only the Near-IR (NIR), visible and UV-A parts of light due to excitation of retinal cones.^[22] After processing, the human brain attributes these to specific colours, usually ranging from deep purple (UV-A) to red (NIR).

Table 2-1: Several spectral regions and their respective wavelengths. Adapted from literature.^[23]

Region	Wavelength interval / nm
	10 ⁶ – 25000 (Far-IR)
Infrared (IR)	25000 – 2500 (Middle-IR)
	2500 – 770 (Near-IR)
Visible (Vis)	770 – 390
	390 – 320 (UV-A)
	320 – 290 (UV-B)
Ultraviolet (UV)	290 – 200 (UV-C)
	200 – 10 (Far-UV)

An important aspect of light is the possibility to excite certain (e.g. organic) molecules. Especially the UV-visible light region ($320 < \lambda < 770$ nm) allows for electronic excitation which changes the electron distribution of a molecule significantly, allowing for photochemical transformations.^[24] In general, the electron density is determined by the population of its molecular orbitals Ψ (MO) which are approximated by the linear combination of atomic orbitals θ_i (LCAO).^[25] Atomic orbitals take internal coordinates of electrons and nuclei into account. For a given MO, LCAO gives:

$$\Psi = \sum_i c_i \theta_i \quad \text{Equation 2-1}$$

MO's represent the electronic landscape of a molecule. However, LCAO requires the formation of accessible, yet at ambient conditions unpopulated electronic states. Of particular interest in organic chemistry are the frontier orbitals, the highest occupied molecular orbital (HOMO) and the lowest unoccupied molecular orbital (LUMO).^[25] Many excitation processes in organic photochemistry occur between HOMO and LUMO or even higher-lying states which can be denoted by e.g. LUMO₊₁, LUMO₊₂. A transition usually occurs when location and momentum of nuclei in the electronic ground state can be preserved. A so called 'vertical' transition thus happens when the nuclear wave functions remain unaltered.^[25] Although excitation usually arises from the lowest vibrational state of the electronic ground state, the final vibrational state can differ, depending on the overlap of final and initial wave function. **Figure 2-1** depicts vertical transitions between two electronic states. As a quantum mechanical descriptor for the probability of transition, the electric dipole moment operator μ , is introduced.^[25]

$$\mu = -e \sum_i r_i + e \sum_i Z_i R_i = \mu_\epsilon + \mu_N \quad \text{Equation 2-2}$$

Hereby, μ corresponds to locations of electrons (first addend) as well as charges (Z_i) and location of nuclei (R_i). According to the Born-Oppenheimer approximation, operator as well as wavefunctions of nuclei and electrons can be separated. A vibrational state is then described by the wavefunction product $\Psi_\epsilon(r, R)\Psi_\nu(R)$ which separates the electronic (depending on both location of electrons and nuclei) and the vibrational wavefunction (depending on the location of nuclei).

The transition moment between two vibrational modes (ν) of the initial and final electronic state (ϵ), $|\epsilon''\nu''\rangle$ and $|\epsilon'\nu'\rangle$, in full notation quotes:^[25]

$$\begin{aligned} < \epsilon'\nu' | \mu | \epsilon''\nu'' > \\ &\geq \int \int \Psi_{\epsilon'}^*(r; R) \Psi_{\nu'}^*(R) [\mu_\epsilon \\ &+ \mu_N] \Psi_{\epsilon''}(r; R) \Psi_{\nu''}(R) d\tau_\epsilon d\tau_N \end{aligned} \quad \text{Equation 2-3}$$

Since orthogonality of the wavefunction product $\Psi_\epsilon^* \Psi_{\epsilon''}$ applies, the volume element of the electronic integral equals zero. The transition moment between two electronic

states thus only depends on the overlap of initial and final wave function of the vibrational modes, as stated by Equation 2-4:

$$\begin{aligned} \langle \varepsilon'v' | \mu | \varepsilon''v'' \rangle \\ = \mu_{\varepsilon'\varepsilon''} \int \Psi_{v'}^*(R) \Psi_{v''}(R) d\tau_N = \mu_{\varepsilon'\varepsilon''} S(v', v'') \end{aligned} \quad \text{Equation 2-4}$$

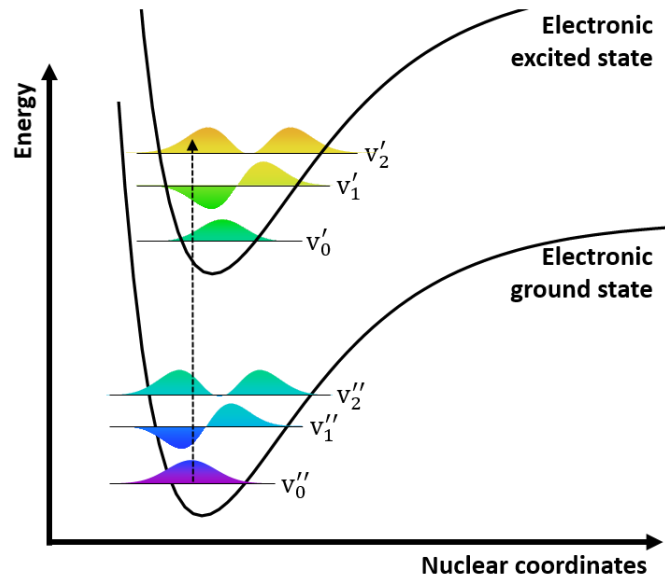


Figure 2-1: Franck-Condon interpretation of transitions between two electronic states (lower and upper black curves). Vibrational modes of electronic excited and ground state are represented as v_0, v_1 , etc. Transitions occur from the vibronic ground state into a state similar to the nuclear vibrational wavefunction, as depicted by the vertical dashed line. The reader is referred to the text for further explanation. Adapted from literature.^[26]

A transition is allowed when the integral of nuclear vibronic wavefunctions is not zero which manifests in the Franck-Condon factors $S(v', v'')$. The Einsteinian coefficient for absorption $B_{\varepsilon' \leftarrow \varepsilon''}$ correlates with the squared transition dipole moment and the Franck-Condon factors:^[27]

$$B_{\varepsilon' \leftarrow \varepsilon''} \propto \mu_{\varepsilon'\varepsilon''}^2 S^2(v', v'') = \frac{8\pi^3}{3h^2} |\mu_{\varepsilon'\varepsilon''}^2 S^2(v', v'')| \quad \text{Equation 2-5}$$

The attenuation of photon intensity from I_L to $I_L - dI$ passing through an absorbing medium in concentration $[A]$ along the pathway distance dl can be expressed as Equation 2-6:^[25]

$$dI_L = -\frac{n(\nu)h\nu}{c} \cdot B_{\varepsilon' \leftarrow \varepsilon''} I_L dl \quad \text{Equation 2-6}$$

The molar extinction coefficient $\varepsilon(\nu)$ correlates to the Einstein coefficient and is thus introduced as Equation 2-7:

$$\varepsilon = \frac{n(\nu)h\nu}{c} \cdot \frac{B_{\varepsilon' \leftarrow \varepsilon''}}{[A]} \quad \text{Equation 2-7}$$

Combining Equation 2-6 and Equation 2-7 gives the differential rate equation for reduction in light intensity (Equation 2-8) which results in the universally applicable Beer-Lambert law Equation 2-9 and describes the effect of absorbance A :^[25]

$$\frac{1}{I} dI = -\varepsilon(\nu)[A]dl \quad \text{Equation 2-8}$$

$$\ln\left(\frac{I_0}{I}\right) = A = \varepsilon(\nu) \cdot c \cdot l \quad \text{Equation 2-9}$$

Alternatively, the absorbance is related to the transmittance T in the following manner:

$$T = 10^{-A} \quad \text{Equation 2-10}$$

2.1.2 Relaxation pathways of molecules after photoexcitation

After completion of the electronic transition, the nuclei respond to the newly orientated electronic density by populating new vibrational modes. This reorientation is one of possible relaxation mechanisms which determine the fate of molecules after photoexcitation. The understanding of energy dissipation processes was investigated by Aleksander Jabłoński in 1933^[28] whose work will be described in this chapter.

The eponymous Jabłoński diagram exemplifies the different pathways on a three-level energy landscape, as illustrated in **Scheme 2-1**. After vertical excitation (Absorption, A) into an electronic excited singlet state (S_n with $n > 0$), nuclei respond to the readjusted electron density by reorientation of nuclear coordinates into several vibrational modes. This process is called intermolecular vibrational redistribution (IVR) and usually completes on a picosecond timescale.^[29-30] After redistribution, the system is located on the lowest vibrational mode of the electronically excited energy surface. Here, the system is allowed to undergo spin-allowed transitions between states consisting of the same spin multiplicity.^[31] Such transitions include Internal

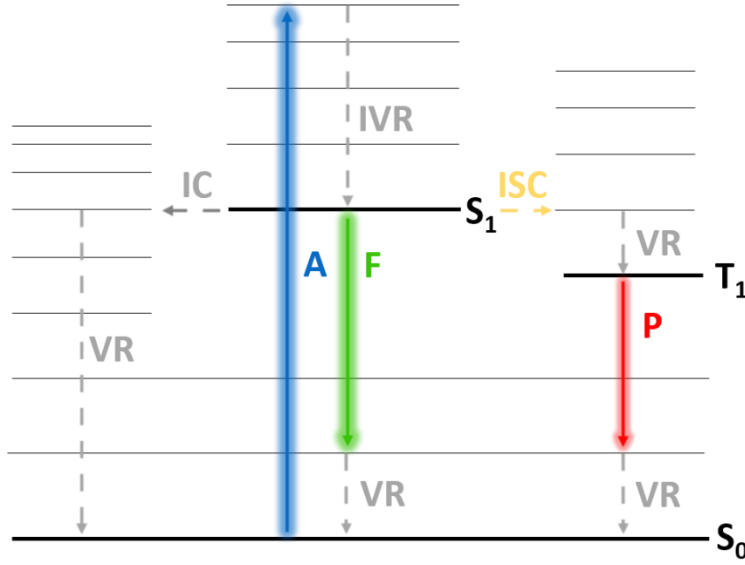
Conversion (IC) or emission of radiation in form of Fluorescence (F). The former usually proceeds within picoseconds,^[32] while radiative processes (fluorescence) proceed from the lowest vibrational mode according to Kasha's rule^[33] within nanoseconds.^[34] Classically, a transition onto the triplet energy surface is forbidden.^[35] However, Spin-Orbit-Coupling (SOC) can induce a perturbation which allows mixing of electronic states with different multiplicity.^[25] Typically, the coupling efficiency scales with the fourth power of nuclear charge^[31] and thus mostly found when heavy atoms contribute to the molecular structure. This transition is then called intersystem crossing (ISC) and can occur on a rapid time scale, even up to femtoseconds in the presence of heavy metals.^[36] Further, the El-Sayed rule states that SOC amplifies upon change in configuration of states participating in transition.^[37] From an electronic triplet surface, nonradiative vibrational relaxation to other triplet states or radiative phosphorescence to the singlet state can occur. Phosphorescence can only occur under spin inversion which is forbidden.^[27] However, SOC allows for a transition matrix element unequal zero, thus attributing long lifetimes of milliseconds.^[38] A plethora of various chemical transformations are based on the simple presence of two unpaired electrons in a triplet state. Many photochemical reactions proceed from a triplet state, such as generation of photoinitiated radicals,^[39-40] the radical photoinduced deprotection of nitrobenzyl compounds^[41-42] or [2+2] cycloadditions.^[43-45] The latter two are of paramount significance to this thesis, thus owed their own section.

2.1.3 Nonlinear optics

The motion of light can ideally be described as a travelling wave in vacuum, characterized by angular frequency ω ($= 2\pi\nu$) and amplitude of its electrical field \vec{E} .^[46] Molecules interacting with such an electric field experience temporary displacement of charge and nuclei, thus inducing a second electric field which is described as polarization \vec{P} . It gives Equation 2-11:^[46]

$$\vec{P}_l = \epsilon_0 \chi^{(1)} \cdot \vec{E} \quad \text{Equation 2-11}$$

Here, ϵ_0 is the dielectric coefficient in vacuum and χ is the susceptibility. In intense light fields, commonly found in laser spectroscopy, the induced electric field \vec{P} has to be extended by terms of higher order, as depicted in Equation 2-12.^[46]



Scheme 2-1: Jabłoński diagram illustrating several relaxation pathways on a three-level system. After vertical photoexcitation (A, blue), the system undergoes intermolecular vibrational energy redistribution (IVR, grey). Afterwards, the system is allowed to dissipate energy in the following manner: Internal conversion (IC) to transition into a (vibrationally) hot ground state, fluorescence (F, green) or intersystem crossing (ISC; yellow). From a triplet surface, phosphorescence (P, red) is possible. Often, the aforementioned processes are accompanied by vibrational relaxation (VR, grey). The reader is referred to the text for further explanation. Adapted from ref.^[28]

$$\vec{P}_{nl} = \varepsilon_0\chi^{(1)} \cdot \vec{E} + \varepsilon_0\chi^{(2)} : \vec{E}\vec{E} + \varepsilon_0\chi^{(3)} \vdots \vec{E}\vec{E}\vec{E} + \dots \quad \text{Equation 2-12}$$

Susceptibilities can be of linear order (1) or of nonlinear, higher order, denoted as (2), (3) and so on. \vec{P} and \vec{E} are vectors which require tensor multiplication operations, denoted as \cdot , $:$ and \vdots , respectively. One notes that polarization of higher order is proportional to the squared, cubic, quartic degree of incident light \vec{E} .^[46]

$$\vec{P}^{(2)} = \varepsilon_0\chi^{(2)} |\vec{E}| \vec{E} \quad \text{Equation 2-13}$$

$$\vec{P}^{(3)} = \varepsilon_0\chi^{(3)} |\vec{E}|^2 \vec{E} \quad \text{Equation 2-14}$$

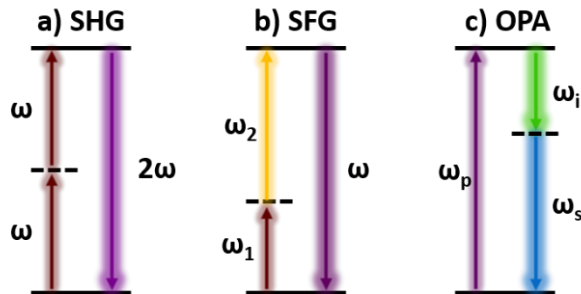
Nonlinear crystals with susceptibilities unequal zero allow different degrees of polarizations to be induced. New waves are generated which fulfil the condition Equation 2-15:^[47]

$$\omega = \omega_1 \pm \omega_2 \quad \text{Equation 2-15}$$

Upon travelling through a nonlinear medium, vectors of propagating waves \vec{k} can be realized if those match the displacement vectors of atoms in the nonlinear medium. Taking the condition of Equation 2-15 into account, one considers phase-matching conditions for new waves,

$$\vec{k}(\omega_1 \pm \omega_2) = \vec{k}(\omega_1) \pm \vec{k}(\omega_2) \quad \text{Equation 2-16}$$

which also considers the conservation of momentum for three photons. Many nonlinear processes derive from these simple considerations, like second harmonic generation (SHG, $\vec{k}(2\omega) = 2\vec{k}(\omega)$), sum frequency generation (SFG, $\vec{k}(\omega_1 + \omega_2) = \vec{k}(\omega_1) + \vec{k}(\omega_2)$) or optical parametric amplification (OPA, $\vec{k}_{\text{signal}} = \vec{k}_{\text{pump}} - \vec{k}_{\text{idler}}$). The latter allows for tuneable output waves, since both signal and idler waves are generated from the pump wave (**Scheme 2-2**). If OPA occurs in a resonator cavity environment, signal or idler are allowed to oscillate in the cavity, which is then called Optical Parametric Oscillation (OPO).^[46]



Scheme 2-2: Two-level diagram depicting frequency generation processes. It is noted that incoming waves are depicted on the left while outgoing waves are illustrated on the right-hand side. a) SHG, b) SFG, c) OPA.^[46]

Although laser pulses can be spectrally tuned by exploiting phase matching conditions (Equation 2-16), group velocities do not necessarily match. In short, the propagation through a transparent medium is dependent on the spectral characteristics, e.g. its wavelength of the pump pulse. Inevitably, this leads to an increase of pulse duration. By using a non-collinear geometry of the vectors of signal and idler, both amplify each other in transparent media, a continuous seed source provided. This process is called

Noncollinear Optical Parametric Amplification (NOPA)^[48] which is used in ultrafast laser applications such as pump-probe spectroscopy.

Another important aspect found in the field of nonlinear optics is the presence of high (laser) light intensity I_L . The ordinary refractive index η_0 has to be expanded by a term η_2 which is then dependent on high light irradiances. Equation 2-17 is known as the optical Kerr effect (OKE):^[47]

$$\eta(\omega, I_L) = \eta_0(\omega) + \eta_2(\omega, I_L) \quad \text{Equation 2-17}$$

A different notation links the change of susceptibility to the alternation of refractive index.^[49]

$$\Delta\eta = \frac{2\pi}{\eta_0} \cdot \Delta\chi \quad \text{Equation 2-18}$$

Consequently, the transparent media encounters different alternations of η along the photons' travelling trajectory z_p . If one considers pulse duration to be comparable to the relaxation time of transparent media τ_{tM} , the progress of medium propagation ζ alters η to be according to Equation 2-19

$$\Delta\eta(z_p, \zeta) = \frac{1}{\tau_{tM}} \int_{-\infty}^{\zeta} \eta_2 |E(z_p, \zeta')|^2 \cdot e^{-\frac{\zeta-\zeta'}{\tau_{tM}}} d\zeta' \quad \text{Equation 2-19}$$

with $\zeta = t - \frac{z_p \eta_0}{c_0}$ and c_0 being the speed of light in vacuum.^[49] In essence, the later parts of a light pulse will experience a larger $\Delta\eta$ than the (spectrally) earlier parts of the pulse which results in significant spectral broadening. Transparent media such as CaF₂ can be used to generate supercontinuum light with a spectral range of $350 < \lambda < 720$ nm.^[50]

2.2 PHOTOCHEMISTRY

2.2.1 *ortho*-nitrobenzyl

The photodeprotection of *ortho*-nitrobenzyl (*o*NB) acetate was firstly reported in the 1960s.^[51] *o*NB compounds comprise of an aliphatic aromatic system with an adjacent nitro group in *ortho* position. Structures of exemplary *o*NB compounds are displayed in **Figure 2-2**. *o*NB compounds can easily be afforded by nitrating the aromatic system in a single reaction step. In general, an electrophilic aromatic substitution is performed,

with an *in situ* generated or directly present nitronium cation acting as the electrophile.^[52-53] Initial studies investigated the nitration of alkylbenzenes, such as toluene in detail.^[54] Substitution at ortho or para positions are preferred, with little selectivity at the meta position since the distribution of afforded isomers predominantly depends on the substrate and its directing substitutes.^[55]

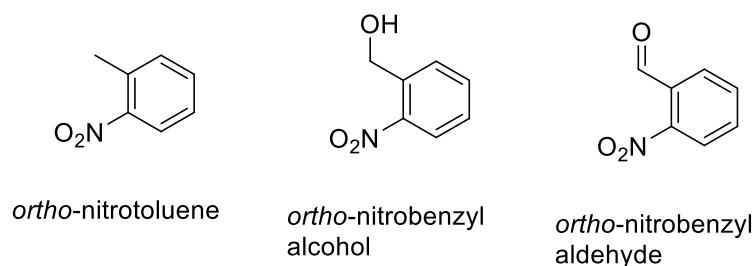


Figure 2-2: General structure of *o*NB compounds.

However, the isomer distribution also depends on the nitrating agents used, such as nitric acid,^[56-57] dinitrogen pentoxide,^[58] nityl chloride,^[59] tetranitromethane,^[60-61] N-nitropyridinium^[62] or nitronium^[63] salts. *ortho*-nitro aliphatic compounds can undergo hydrogen transfer under UV light irradiation. First reports indicate the *in situ* generation of a short lived triplet state which resembles a quinonoid intermediate (see **Figure 2-3**).^[64]

Interestingly, hydrogen abstraction triggers a reaction cascade and internally oxidizes the aliphatic substituent in the final step. It is noted that the oxidation mechanism of *ortho*-nitroalkanes (or aldehyde derivatives) features significant resemblance to the degradation mechanism of *o*NB's, hence described here in detail.^[42] Both *ortho*-nitrobenzaldehyde^[65-66] and *ortho*-nitrotoluene^[67] can be oxidized to their acid and alcohol analogue, respectively.

After photoexcitation (**Scheme 2-3**, IIa), vibrationally cooling occurs prior to population of a triplet state of *o*NB's. Population of the triplet state is then followed by a hydrogen-transfer (IIb). γ -hydrogen abstraction is considered a critical reaction step after excitation of certain chromophores. It was identified by Norrish and thus is classified a Norrish type II reaction which often occurs in the presence of biradicals.^[68-69] The generation of the quinonoid *aci*-form (IIc) is ambiguous and somewhat concerted, since transformation from both a triplet or an excited singlet state has been

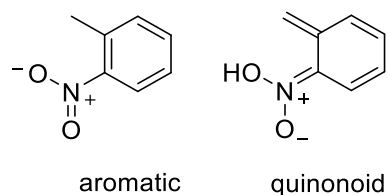
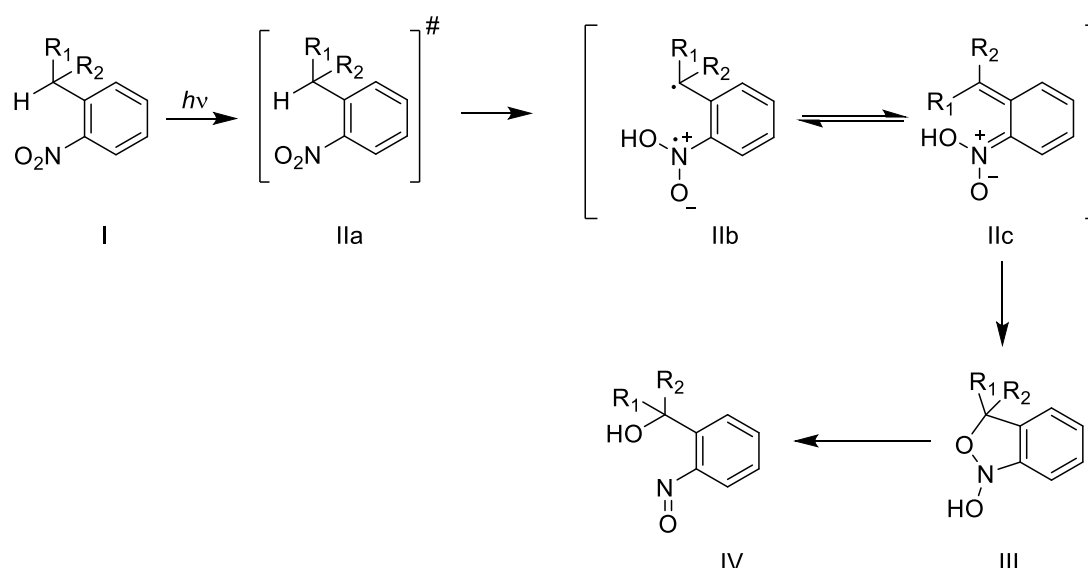


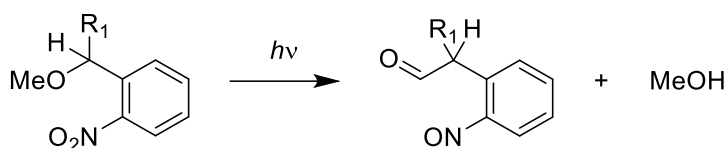
Figure 2-3: Left: Aromatic structure of *ortho*-nitro toluene (*o*NT). Right: Proposed structure after hydrogen abstraction resembling quinonoid species. Figure adapted with permission from G. Wettermark, *J. Phys. Chem.* **1962**, 66 (12), 2560-2562. Copyright 1962 American Chemical Society.

reported.^[41] However, rearomatization leads to a five-membered benzoisoxazolidine-like structure (III). After ring opening, the former benzylic (aldehydic) position was oxidized, while the nitro group transformed into a nitroso group (IV). Indeed, this reaction can be considered an intramolecular redox reaction, as the total oxidation state remains unchanged. Upon prolonged irradiation, the afforded nitroso compounds can be afforded as dimers. Nitroso dimers are azodioxy compounds and possess azobenzene-like characteristics such as strong color and appearance as *E*- and *Z*-isomer.^[70-72] As azobenzenes are strong light absorber, an internal light filter effect is usually encountered when handling *o*NB compounds, preventing any efficient photochemical transformation.^[73]



Scheme 2-3: Degradation scheme of *ortho*-nitrobenzyl compounds. For further details, the reader is referred to the text. Figure adapted with permission from R. W. Yip, D. K. Sharma, R. Giasson and D. Gravel, *The Journal of Physical Chemistry* **1985**, 89 (25), 5328-5330.

In the presence of a possible leaving group, such as a carboxylate or an alcoholate, *o*NB compounds can release the leaving group upon photoexcitation. This crucial characteristic classifies *o*NB's as photolabile protecting groups (PPG). Instead of oxidizing the benzylic position, the -ONOH-oxygen (**Scheme 2-3**, IV) is transferred onto the benzylic (alcohol or ester) position, then the leaving group is released in the process (see **Scheme 2-4**).^[74] The photodeprotection strategy marks an important chapter in peptide synthesis^[75] and biochemical applications,^[76] since it is orthogonal to classic triggers such as heat or change of pH which is harmful to living systems or sensitive molecules. Unsurprisingly, *o*NB's are widely employed due to their ease of synthesis, their tunability and their simple photolytic removal conditions. Nowadays, *o*NB compounds overcame the limitations of simple molecular deprotection chemistry and are employed in self-reporting systems,^[77] light-responsive material,^[78-80] micelles^[81] and drug delivery design.^[82-83]



Scheme 2-4: Release of leaving group (here: MeOH).

Nevertheless, *o*NB chemistry underlies significant drawbacks. As photoexcitation of the $n\pi^*$ band marks the first step in photodegradation, usually harsh UV light is employed which prohibits its applicability to any living system. Current efforts are directed onto significant manipulation of this absorption band. Using different substituent on the aromatic ring improves e.g. the UV sensitivity.^[84] Often, expanding the donor-acceptor system results in improvements of photophysical properties, such as higher absorption wavelength or higher extinction.^[85-86] The photoactivity can be improved further upon incorporation of additional methyl and veratryl-based groups.^[87]

2.2.2 *s*-Tetrazines

Tetrazines (Tz) are a class of heterocycles containing four nitrogen atoms distributed into an aromatic, six-membered ring structure. Possible isomers, such as

1, 2, 4, 5^[88] or 1, 2, 3, 4^[89] are known and have been isolated; however, the 1, 2, 3, 5 isomer^[90] has been reported as well (**Figure 2-4**). The latter two have been reported as several derivatives, such as condensed aromatic systems,^[91-92] with stabilizing substituents^[93] or even as monocyclic aromatic rings.^[94] Although of particular interest in modern organic chemistry, the 1,2,3,4 and 1,2,3,5 isomers are highly unstable due to two consecutive nitrogen-nitrogen bonds, hence not further described in detail.

1, 2, 4, 5-tetrazine (henceforth termed ‘Tz’) is the most stable isomer and was already isolated by Pinner in the late 18th century.^[95] Nowadays, a variety of 3, 6-disubstituted tetrazines can be afforded via different synthetic protocols; but hydrazine or a hydrazide is usually involved in the synthesis, forming di- or tetrahydrotetrazines.^[96-97] New functionalities can easily be introduced in the tetrazine junction at its 3, 6-position. Depending on the nature of the substituents, derivatives are either isolated by entering an existing Tz ring^[98] or the substituents build up the Tz structure during the dimerization reaction.^[99-100]

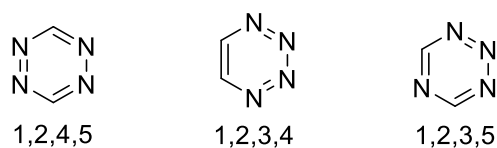


Figure 2-4: Different tetrazine isomers.

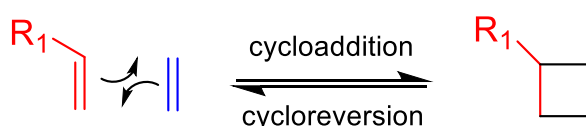
s-Tetrazines are an interesting class of heterocycles, owing their unique characteristics to the arranged nitrogen nuclei. Tz’s are electron-poor,^[101-102] attributing them extraordinary performance in inverse electron deficient Diels-Alder (IEDDA) reactions.^[96-97, 103] Further, all tetrazines exhibit weak absorption in the green-visible range due to an improbable $n\pi^*$ transition.^[104] Although the presence of an $n\pi^*$ band is similar to aforementioned *o*NB compounds (Chapter 2.2.1), photodynamics of s-tetrazines occur on singlet energy surfaces.^[105] Indeed, upon direct excitation of the $n\pi^*$ band, the molecule undergoes internal conversion from the S_1 into a hot (vibrationally excited) S_0 state before unimolecular dissociation under dinitrogen release occurs.^[106-108]

Interestingly, tetrazines not only stand out regarding their photophysical properties, but their thermodynamic characteristics are also worth mentioning. A high heat of

reaction can be achieved due to the molecular nitrogen and carbon balance^[109] which makes tetrazine chemistry applicable for use in photopropellants or -explosives.^[110]

2.2.3 [2+2] Cycloadditions

Cycloadditions (CA's) are common ligation practices among many synthetic disciplines. Simply, electrocyclic reactions proceed via breaking of π - and formation of σ -bonds, hence most π -bond bearing molecules such as carbonyl, enol(-ates), vinylic monomers or alkenes can participate in cycloadditions (**Scheme 2-5**). Prominent examples include the [4+2] (Diels-Alder) and the [2+2] cycloaddition. Generally, cycloaddition can be induced either photochemically (under excitation of electronic states) or thermally (under excitation of vibrational nodes). Whether an electrocyclic reaction is permitted, is manifested in the Woodward-Hoffmann rule.^[111] Photochemically, $[2_s+2_s]$ cycloadditions are permitted, while $[4_s+2_s]$ cycloadditions are forbidden.^[112-113] The superscript *s* indicates a suprafacial approximation of the HOMO and LUMO orbitals participating in the reaction. Analogously, $[4_s+2_a]$ are photochemically permitted as well, with the superscript *a* indicating an antarafacial approximation of the frontier orbitals.



Scheme 2-5: Representation of two vinylic compounds undergoing a [2+2] cycloaddition and cycloreversion. For simplicity reasons, stereochemistry and all substituents are omitted.

Depending on the substituents along the vinylic bond, different wavelengths can be used for the cycloaddition but often, harsh UV light conditions are necessary ($< 300\text{nm}^{[114]}$, $> 300\text{ nm}^{[115-116]}$).

Even more blue-shifted wavelengths have to be employed for the cycloreversion which renders the [2+2] dimerization strategy impracticable for any biological or living application. The isolation of head-to-head or tail-to-tail isomers has been observed upon cycloreversion and is usually undesired.^[117] Further, the fate of electronically excited molecules is not distinct: Instead of reacting in a [2+2] fashion, cis-trans-

isomerization instead can occur if molecular structure allows rotation along the critical bond.^[43, 118] Interestingly, excited state relaxation dynamics differ significantly, depending on the fate of the excited molecule. Exemplarily, cis-trans isomerization are governed by an ultrafast $S_1 \rightarrow S_0$ conical intersection,^[19, 119] whereas [2+2] CA can proceed via a 1,4-biradical intermediate on a triplet surface (e.g. enones) or via an excited singlet state (e.g. styrenes and stilbenes).^[43]

But despite these limitations, [2+2] CA still attract significant attention, due to their easy implementation and realization, even in absence of a catalyst or sensitizer.^[120] By extending the conjugated electron system, the reaction conditions were tuned to allow for implementation into living systems. Exemplarily and one of the more famous examples is the styrylpyrene system. By introducing the styrylpyrene moiety, a visible light linkable (and low-energy UV reverting) system was established.^[121] Styrylpyrene^[120] and similar systems^[122] were employed for wavelength-dependent reaction screening or in responsive material design.^[123-124]

2.3 POLYMERISATION

2.3.1 Introduction

The release of Staudinger's works in 1929 marks the birth of the term 'polymer'.^[125-126] Staudinger's claims, a polymer (from Greek, *poly-* 'many' and *-mer* 'part') being a covalently bonded macromolecule of high molecular weight was regarded as extremely controversial at the time. Rightfully, however, Staudinger was awarded with the Nobel Prize in 1953.^[127] Prior to Staudinger's studies and the in-depth understanding of the nature of polymers, substantial effort was, however, directed towards modifications of polymer systems, e.g. the vulcanization of rubber^[128] or imitations of natural fibres such as ivory.^[129] Although naturally occurring polymers such as cellulose or keratin are known, growth of these materials proceeds naturally and their production is not in line with current material demands. On the other hand, the rapid manufacturing of such materials on a synthetic level was either not achieved or afforded materials of inferior quality.

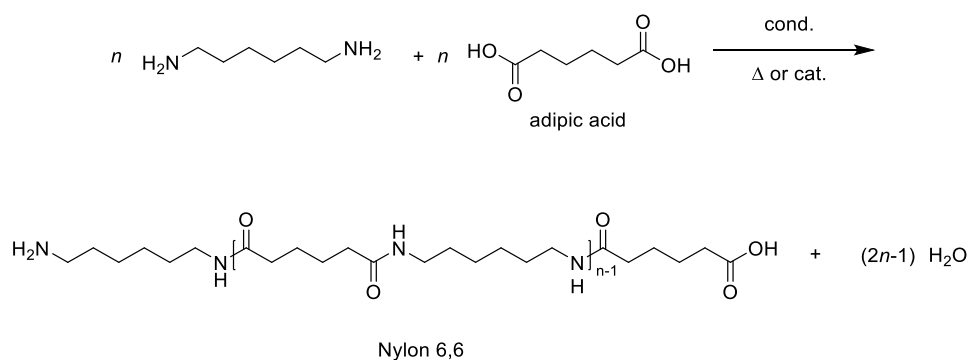
Plastics are highly versatile, usually low-cost and light materials, owing their unique characteristics the plethora of combinations of different building blocks.^[130] Although

the bonding mode is similar in many types of polymers, i.e. is a covalently bonded carbon chain, the properties of the polymers can be altered in many ways. The composition of a polymer such as length, alternating monomer sequence, degree of branching, presence of polar or hydrogen bonds, type of monomer and type of reaction mechanism, all critically contribute to the properties obtained.^[131] Naturally, reaction conditions, blending procedures or manufacturing conditions impact the properties significantly as well.^[132-133]

The high demand and lack of natural resources during World War II led to a surge in the mass production of plastics.^[134] Demand as well as production has only expanded ever since. The impact of polymers (or the consumer-friendlier term ‘plastics’) on society, humankind, the environment and civilization is unprecedented. The contributions to consumer health and safety, such as food and water packaging, are of paramount significance for society, including the health sector in need of sterile and ‘single-use’ equipment, as well as polymer-based therapeutics benefitting massively from the advent of plastics.^[135-136]

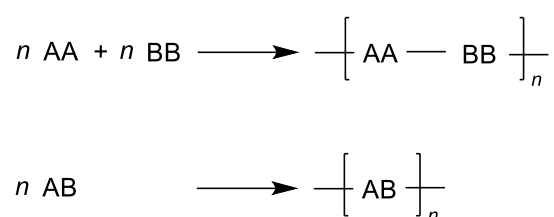
2.3.2 Step-growth polymerisation

Polymers are classified with regard to their mechanism into step-growth and chain-growth. This classification was introduced by Flory^[137] and Carothers,^[138] which is still in use today. Both mechanisms can be further differentiated. Step-growth polymerisation is a distinct type of polymerisation. **Scheme 2-6** illustrates a textbook example, i.e. the reaction of a diamine and diacid forming Nylon 6,6.^[131]



Scheme 2-6: Step-growth polymerisation of a diamine and a diacid. The reader is referred to the text for details.

Chemical activation is the first reaction step in a step-growth reaction, initiated either by heat (Δ) or via a catalyst. Since all functional groups (every diamine and diacid in **Scheme 2-6**) are simultaneously activated, there is no separation between actively and passively participating molecules. For example, the synthesis of Nylon 6,6 (**Scheme 2-6**) involves the reaction of AA and BB monomers, with the letters indicating identical functional end groups. However, AB monomers used in step growth reaction also exist, e.g. amino acids in the synthesis of polypeptides (**Scheme 2-7**).



Scheme 2-7: Examples of step-growth polymerisations. Top: Two monomers with different end groups, AA and BB, participate in a step-growth reaction. Bottom: One single species with a self-polymerisable pair of end groups, AB.

Formally, the conversion X indicates the remaining relative fraction of end groups N_t in a reaction mixture, Equation 2-20.

$$X = 1 - \frac{N_t}{N_{t=0}} \quad \text{Equation 2-20}$$

It is noted that monomers do not necessarily depict a definite number of end groups, i.e. in presence of bi- and multifunctional monomers or in mixtures thereof. The number-average degree of polymerisation DP_n , is the fraction of residual to initial amount of endgroups.

$$DP_n = \frac{N_0}{N_t} = \frac{1}{1 - X} \quad \text{Equation 2-21}$$

If A and B end groups are not used in stoichiometric conditions, Equation 2-21 is expanded and the non-stoichiometric factor r_{ns} is introduced.^[131]

$$\frac{N_{A,t=0}}{N_{B,t=0}} = r_{ns} \leq 1 \quad \text{Equation 2-22}$$

$$DP_n = \frac{N_{A,t=0} + N_{B,t=0}}{N_{A,t} + N_{B,t}} = \frac{N_{A,t=0} \left(1 + \frac{1}{r_{ns}}\right)}{N_{A,t} + N_{B,t}} \quad \text{Equation 2-23}$$

Thus, it follows for the amount of unconverted endgroups A or B at any time t :

$$N_{A,t} = (1 - X)N_{A,t=0} \quad \text{Equation 2-24}$$

$$N_{B,t} = (1 - r_{ns}X)N_{B,t=0} \quad \text{Equation 2-25}$$

The total number of end groups gives:

$$N_{A,t} + N_{B,t} = \frac{N_{A,t=0}}{r_{ns}} (r_{ns} - 2r_{ns}X + 1) \quad \text{Equation 2-26}$$

Merging Equation 2-23 and Equation 2-26 gives the most well-known version of Carothers' equation:

$$DP_n = \frac{r_{ns} + 1}{r_{ns} - 2r_{ns}X + 1} \quad \text{Equation 2-27}$$

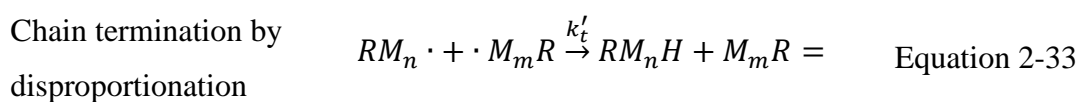
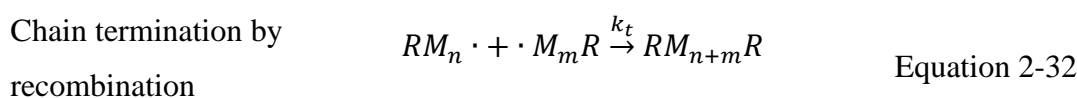
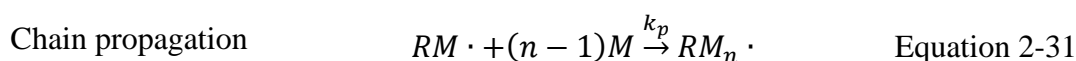
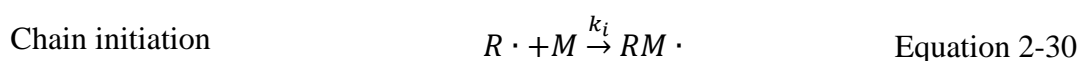
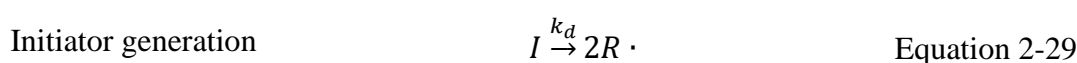
As all monomers (and also the constructed small chains of such) are equally active in a step-growth polymerisation, high molecular weight polymers can only be achieved at very high degrees of polymerisations if the monomers are stoichiometrically employed ($r_{ns} = 1$). To control DP_n , substoichiometric conditions can be used ($X = 1, r < 1$), resulting in Equation 2-28. Exemplarily, evaporation of one or all components in step-growth polymerisation is common due to operation at elevated temperature.^[139]

$$DP_n = \frac{r_{ns} + 1}{r_{ns} - 2r_{ns} + 1} = \frac{1 + r_{ns}}{1 - r_{ns}} \quad \text{Equation 2-28}$$

2.3.3 Chain-growth polymerisation

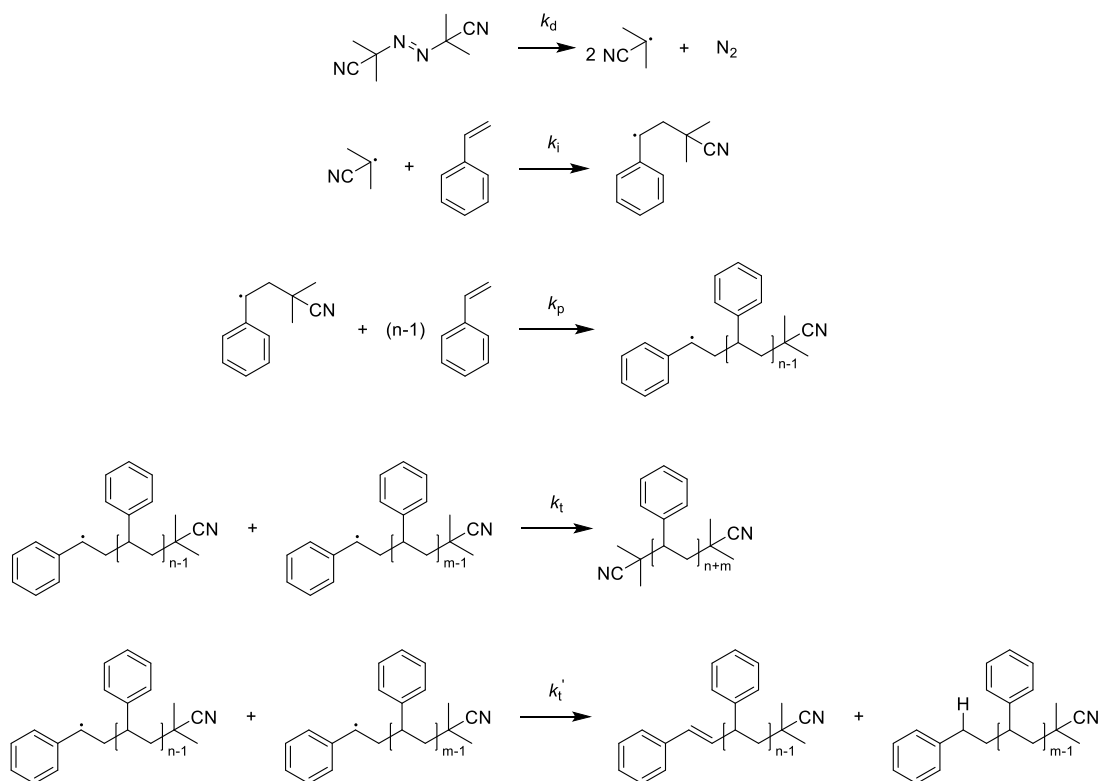
Fundamentally different are the mechanisms of growth in Chain-growth and step-growth polymerisations. While step-growth proceeds *stepwise*, i.e. the combination of growing chains, chain-growth proceeds via the continuous addition of monomer. For the latter, the concentration of active sites is usually small. Active sites can be formed differently, either by introducing charges (Ionic Polymerisation, IP) or radicals (Free Radical Polymerisation, FRP). In ionic polymerisations, the activation energy is small since dissociation of the initiator occurs even under ambient conditions.^[140] Further,

termination cannot proceed via recombination. Propagating chains grow thanks to their charge (positive or negative) and thus cannot react with each other. Instead, termination occurs via recombination with impurities (water, oxygen) or inactivating ions. Brønsted or Lewis acids or metalorganic compounds can be used as initiators. Ionic polymerisation is prone to impurities, thus requires the usage of highly purified solvents and agents. In return, IP features low polydispersity and a high rate of reaction. On the opposite, Free Radical Polymerisation (FRP) proceeds via generation of an initiating species, such as a radical and adds to a vinyl bond of a monomer. The addition results in a new radical which can add to another monomer allowing for chain propagation. The reaction steps are the following:



Scheme 2-8 describes the polymerisation of styrene under thermal decomposition of azobisisobutyronitrile (AIBN). AIBN decomposes at elevated temperature, however, photoinitiators cleavable by light can be employed as well. The formed radical $R\cdot$ subsequently adds onto an available vinylic monomer, M , thus forming a propagating radical as well ($RM\cdot$). The net concentration of active sites after addition remains unchanged, since one radical is consumed and one is formed in the process. The propagating chain ($RM_n\cdot$) grows by adding to other monomer units and can only terminate by reaction with another radical-carrying species, such as an initiator radical or a different propagating chain. Upon termination, the two species recombine or disproportionate, resulting in a saturated and unsaturated species. Naturally, polymer chains grow in a statistical fashion, e.g., the chains are distributed over a length spectrum. Thus, it is important to categorize an obtained polymer by its average molecular weights. As the name implies, the number-average molecular weight of a

polymer, M_n , is the sum of all polymer masses, M_i , weighted and averaged according to their molar amount n_i (Equation 2-34).



Scheme 2-8: Summary of reaction steps in a chain-growth polymerisation: k_d : Initiator generation. k_i : Chain initiation. k_p : Chain propagation. k_t : Chain termination by recombination. k_t' : Chain termination by disproportionation. The reader is referred to the text for further details.

$$\bar{M}_n = \frac{\sum_i n_i M_i}{\sum_i n_i} = \sum_i \left(\frac{n_i}{\sum_i n_i} M_i \right) = \sum_i x_i M_i \quad \text{Equation 2-34}$$

Similar considerations are applied for the weight-average molecular weight of a polymer, M_w , with x_i and w_i being the molar and weight fractions, respectively.

$$\bar{M}_w = \frac{\sum_i m_i M_i}{\sum_i m_i} = \sum_i w_i M_i \quad \text{Equation 2-35}$$

The polydispersity index (D) is defined as the fraction of M_n and M_w as stated in Equation 2-36. The value of D is associated with the molar mass distribution and provides important information such as the degree of control in chain growth polymerisations.

$$\bar{D} = \frac{\bar{M}_w}{\bar{M}_n} \quad \text{Equation 2-36}$$

The differences in polymerisation mechanisms between chain-growth and step-growth polymerisation require a different expression for the degree of polymerisation, here P_n :

$$P_n = \frac{\bar{M}_n}{M_m} \quad \text{Equation 2-37}$$

Since P_n is only determined by the number of propagating events prior to termination, the kinetic chain length ν can be introduced as governing kinetic parameter and expressed in a rate law equation according to the probabilities of propagation p versus termination t :^[131]

$$\nu = \frac{v_p}{v_t} = \frac{k_p[M][P \cdot]}{k_t[P \cdot]^2} = \frac{k_p[M]}{k_t[P \cdot]} \quad \text{Equation 2-38}$$

With $[M]$ and $[P \cdot]$ the concentrations of monomer and radical, respectively. For a termination event via disproportionation, it reads $P_n = \nu$, thus:

$$P_n = \frac{k_p[M]}{\sqrt{k_t \cdot 2k_d[I]}} \quad \text{Equation 2-39}$$

If termination by combination occurs, it reads $P_n = 2\nu$, thus:

$$P_n = 2 \frac{k_p[M]}{\sqrt{k_t \cdot 2k_d[I]}} \quad \text{Equation 2-40}$$

Reaction control can be gained by either increasing the concentration of monomer $[M]$ or decreasing the concentration of initiating species $[I]$.

2.3.4 Reversible Deactivation Radical Polymerisation

Most commercially available polymers are either generated by chain or step growth polymerisations. However, undesired termination events such as chain transfer and recombination prevent efficient growth, in fact, they form ‘dead’ polymers. Such effect reduces the properties obtainable, since inhomogeneous growth can result in weaker, less crosslinked areas of a bulk material. Further, building block functionalities cannot be introduced which lowers applicability. Indeed, in the realm of chain-growth polymerisation, reaction control is a critical metric to consider. Chains do not

propagate in a controlled fashion which causes inhomogeneous growth. I.e., termination occurs upon reaction with another species and results in uncontrolled polymerisation with a complex product distribution. Control is desirable in chain-growth systems since macromolecular properties (such as dispersity) impact the material properties, such as glass transition temperature, brittleness and elasticity modulus.^[131] Some fundamentals of reversible deactivation radical polymerisation are provided in further detail.

Several characteristics were introduced in Chapter 2.3.3, describing the polymer distribution regarding their molecular weight, which will be continued on. Considering Equation 2-29 to Equation 2-33, the mass distribution of a conventional radical polymerisation is broad, since chains continuously form, propagate and eventually terminate.^[131] Interestingly, the rate of reaction ν for propagation ν_p and termination ν_t is of different order with regard to the total radical concentration $[P\bullet]$:

$$\nu_p \sim [P\bullet]^1 \quad \text{Equation 2-41}$$

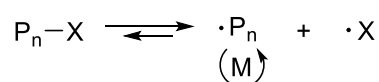
$$\nu_t \sim [P\bullet]^2 \quad \text{Equation 2-42}$$

Theoretically, minimizing the radical concentration $[P\bullet]$ will affect ν_t to a greater degree than ν_p . If one considers $[P\bullet] \rightarrow 0$, ν_t will be reduced significantly. Since a certain level of radical concentration is needed, the general directive is to keep $[P\bullet]$ low by establishing an equilibrium between deactivated and activated radicals. This way, not only termination is reduced but also other undesired side reaction like chain transfer to solvent molecules. Exemplarily, the addition of a stable radical ($T\bullet$) allows for reaction with a propagating chain $P\bullet$ which reversibly deactivates the propagating radical. The bond can be reversibly broken and formed. Alternatively, one considers a rapid transfer of radicals onto the chains to allow for little growth before the radical ‘shuttles’ onto other chains again. Such degenerative chain transfer does not require reduced radical concentration. Living character often can be achieved via several fundamental mechanisms which are schematized in **Scheme 2-9**.^[141]

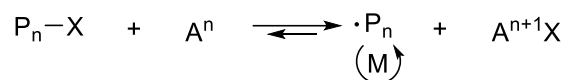
Commonly, these mechanisms allow for simultaneous growth of polymers.^[142] The Dissociation-Combination mechanism relies on the formation of a relatively weak inactivating bond. Most prominently, 2,2,6,6-tetramethylpiperidinyloxy (TEMPO) can be used to impart livingness on the polymerisation of styrene.^[143] This most prominent example was developed in the early stages of Nitroxide-mediated

polymerisations (NMP). Initially, the NMP technique was limited to styrene since styrene undergoes autoinitiation at elevated temperatures. The continuous development of new nitroxide derivatives and alkoxyamines provides a plethora of possibilities to use NMP for a variety of monomers. Alternatively, redox systems can be used to impart livingness on a polymer system. A halide X can be transferred on a redox component A (**Scheme 2-9**), forming a transient radical $P_n\cdot$ which participates in propagation.^[144] The persistent radical effect causes a consumption of transient radicals thus contributing to an enrichment of X . Eventually, halide termination is favoured over self-termination, narrowing the polymer distribution. Atom Transfer Radical Polymerisation (ATRP) employs a transition metal catalyst (i.e. Cu^I , Cu^{II} systems) as the deactivating species.

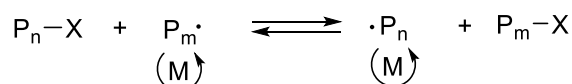
Dissociation-Combination



Atom Transfer



Degenerate Transfer Mechanism



Scheme 2-9: Fundamental mechanisms in RDRP techniques.

Degenerate transfer allows for rapid transfer of radical capabilities on chains. The transformations are termed degenerate since only functionalities are exchanged and chains only differ in degree of polymerisation (**Scheme 2-9**). Importantly, the rate of transfer must be equal or larger than the rate of propagation to ensure equilibrium. Several degenerative transfer mechanisms were reported, and most prominent examples include the use of dithioesters and trithiocarbonates. Most prominently, Reversible Addition-Fragmentation chain Transfer agents (RAFT) impart living character on a polymer system. **Table 2-2** collates some differences between a free-radical (non-controlled) and a living (controlled) polymerisation.

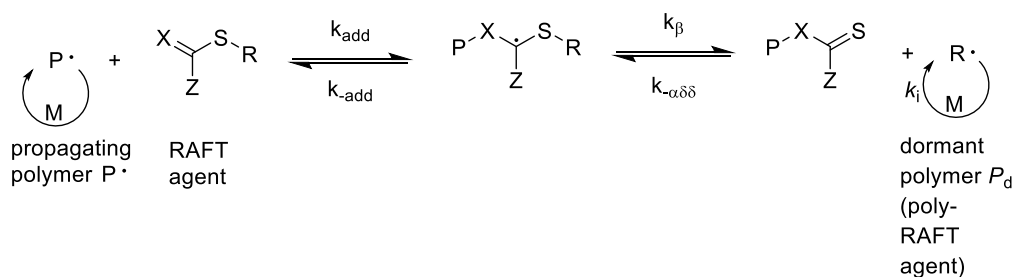
Table 2-2: Comparison of FRP and RDRP.^[131]

Parameter	FRP	RDRP
D	1.5 - 2.0	1.1
Dependency on conversion	Linearly	Rapid increase at low conversion
Sensitivity to contaminations	Low	High

Nowadays, many synthetic techniques are available to impart living character onto a polymerisation process. While NMP^[145-147] and ATRP^[148-151] induce living character by reducing the radical concentration via deactivation, RAFT polymerisation relies on the shuttle effect of the chain transfer effect.^[152-153] Since RAFT is employed in the current thesis, it will be discussed in a stand-alone chapter.

2.3.4.1 Reversible Addition-Fragmentation chain Transfer polymerisation

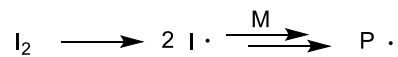
The simplified mechanism for Reversible Addition-Fragmentation chain Transfer (RAFT) polymerisation is depicted in **Scheme 2-10**.^[154] Trapping of propagating polymer chains $P_n\cdot$ is achieved by thioester compounds^[155] of the form $X=C(Z)SR$ with X being a methylene or sulphur adjacent. The resulting RAFT-adduct is a tertiary carbon-centred radical. The R and Z groups are carefully designed for efficient addition/cleavage reversibility. After β -scission, the previously propagating polymer is in a dormant state, while $R\cdot$ is able to reinitiate dormant polymer chains. Such a transfer reaction is called degenerate as the net sum of functionalities remains constant, and the only difference is in molecular weight of the propagating species (**Scheme 2-10** left and right). A vital aspect lies in the efficient reactivation of the dormant polymer P_d (**Scheme 2-10** right).

**Scheme 2-10:** Simplified RAFT mechanism.

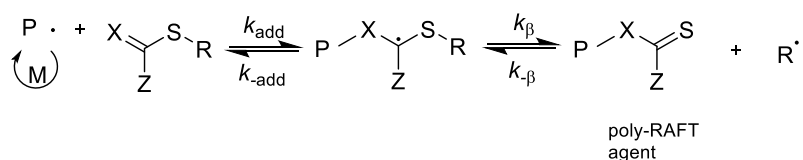
To generate living character via a RAFT polymerisation, the dormant polymer P_d must participate in the degenerate transfer at least similarly to the RAFT agent (**Scheme 2-10** left). The transfer is thus called degenerate since molecular structure of P_d and the RAFT agent is similar, the only difference being their molecular weight. However, the molecular weight should be similar as well in an efficient RAFT process. Eventually, the chain transfer of P^\bullet and R^\bullet onto the RAFT agent occurs in an equilibrium. No radicals are formed or consumed as part of its mechanism, making RAFT distinctively different from ATRP and NMP. The persistent radical effect observed in ATRP does not occur in RAFT, since RAFT does not rely on a reduced radical concentration to impart living character. In a typical RAFT mechanism, a mechanistic separation between the pre-equilibrium and a main-equilibrium is common. The detailed RAFT mechanism is presented in **Scheme 2-11**. Initiation, propagation and termination are identical to a conventional free-radical polymerisation. However, formation of the dormant poly-RAFT agent requires efficient addition of the chain, stabilisation of the tertiary radical and release of the leaving group. Several factors impact the performance of the RAFT process, e.g. the selection of R and Z groups. During the pre-equilibrium phase, the RAFT agent is converted to the polymeric RAFT agent. Sometimes, inhibition to a certain degree is observed due to slow reinitiation and/or fragmentation.^[156] Thus, it is critical to tailor the molecular structure of the RAFT agent since R and Z group determine the activity of the RAFT agent. Careful matching to the activity of the employed monomer is necessary.^[157] For example, Z groups such as naphthyl and phenyl act as activators and stabilize the tertiary radical while heteroaromatics act as deactivators. R groups are selected with weak SR bond characteristics and high reinitiation efficiency.^[158] The main equilibrium phase promotes equal and consistent growth of polymer chains. The reversible release and re-addition of polymer chains to the dormant (or unconsumed small molecule) RAFT agent allows for a statistically narrow distribution of propagation events; thus, all chains will grow approximately equally until all monomer is consumed. Ideally, the propagating chains are frequently capped to minimize their probability to undergo termination which allows for the synthesis of block copolymers upon addition of a second monomer species. Compared to other RDRP techniques, RAFT is highly interesting for precision polymer generation since an ideal RAFT polymerisation does not limit the rate of polymerisation, as the overall

radical concentration is unchanged compared to an identical conventional free radical polymerisation.

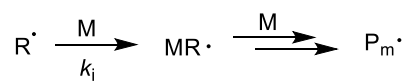
Initiation and propagation



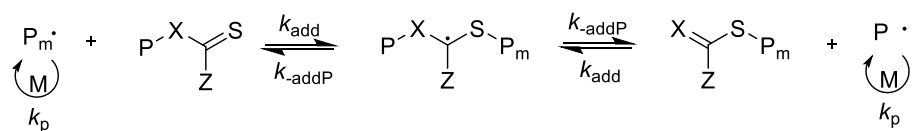
Pre-equilibrium



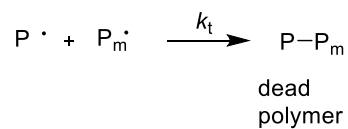
Reinitiation



Main equilibrium



Termination



Scheme 2-11: Detailed RAFT mechanism.

Chapter 3: Exploring the photochemistry of *ortho*-nitrobenzyl alcohols and incorporation in polyurethanes

Parts of this chapter were adapted and reproduced with permission from the Royal Society of Chemistry from C. Petit, J. Bachmann, L. Michalek, Y. Catel, E. Blasco, J. P. Blinco, A.-N. Unterreiner, C. Barner-Kowollik *Chem. Commun.* **2021**, 57, 2911. The candidate conceptualized research and experimental design, performed all small molecule syntheses, performed all UV/Vis studies, executed all light-mediated degradation experiments, analysed and interpreted all acquired datasets, simulated EPR spectra, performed all PLD-SEC experiments, contributed to writing the initial draft and editing the original manuscript, processed revisions. Charlotte Petit performed the polymer synthesis, conceptualized research and experimental design and supervised the candidate in all stages.

3.1 ABSTRACT

One of the oldest and most popular examples of photolabile protecting groups are *ortho*-nitrobenzyl (*o*NB) compounds.^[51] A combinatory study on a small molecule and polymer level was conducted to investigate the degradation of *o*NB's. Interestingly, *o*NB are often exposed to UV light conditions. However, visible light can be employed as well but it is questionable if the mechanism at hand differs when employing different irradiation sources. A visible light-degradable *o*NB compound was investigated. Ultrafast transient absorption spectroscopy, as well as structure-reactivity-correlation studies were performed in order to unravel *o*NB chemistry in the visible light regime. Afterwards, *o*NB's were incorporated into polymeric material to represent a possible solution for plastic pollution. Plastic waste and the use of non-degradable materials in packaging is a growing cause of environmental concern, with the polyurethane (PU) class being known for their lack of degradability. Herein, we investigate photosensitive *ortho*-nitrobenzyl units on a fundamental molecular level

and achieved incorporation into PUs to allow for controlled photodegradation. Photodegradation was explored in solution and on thin films which give additional insights on the design of degradable adhesives.

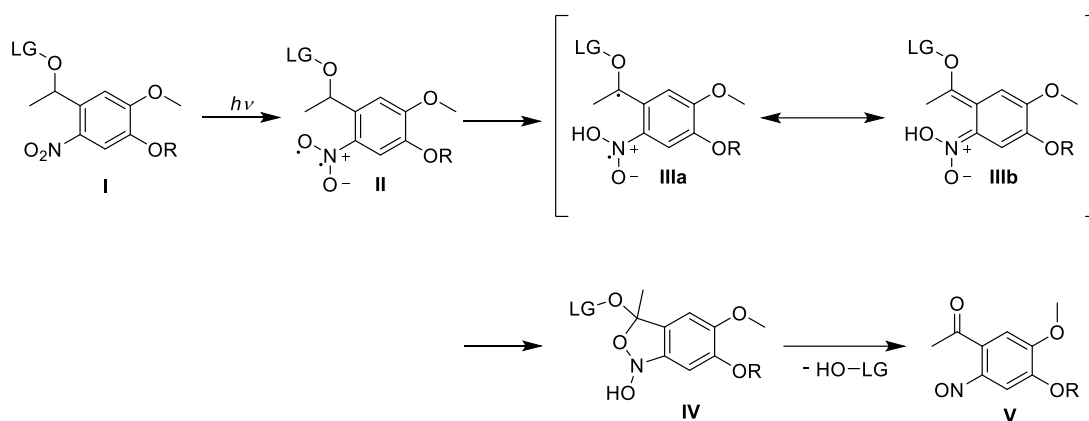
3.2 INTRODUCTION

Polyurethanes (PUs) are employed in a wide variety of applications, ranging from industrial products such as shoe soles, wheels, construction, packaging, and adhesives^[159-160] to drug delivery as well as for *in vitro* and *in vivo* biocompatibility studies for enzymatic, tissue and cellular responses to the material.^[161-166] The Bayer chemical company greatly contributed to expand the types of PUs in industry, particularly with the invention of the diisocyanate polyaddition technique, thus leading to the establishment of the PU industry in 1937.^[167] The properties of PU resulting from the reaction of polyols and isocyanates depend mainly on the nature of starting compounds they are made of.^[160] For example, long and flexible polyols usually generate soft elastic polymers, while highly crosslinked polymers lead to rigid and hard materials.^[168] Despite their outstanding mechanical, physical, and chemical properties, PUs' main challenge remains achieving degradability. This extensive range of applicability gives rise to high levels of waste unable to be recycled. High temperature treatment is the most used technology for the waste management of PUs.^[169] However, incineration is not only energy intensive, but also generates harmful gas emissions.^[170] On the other hand, light can trigger degradation and is a powerful tool as it allows for spatial and temporal control.

3.3 RESULTS AND DISCUSSION

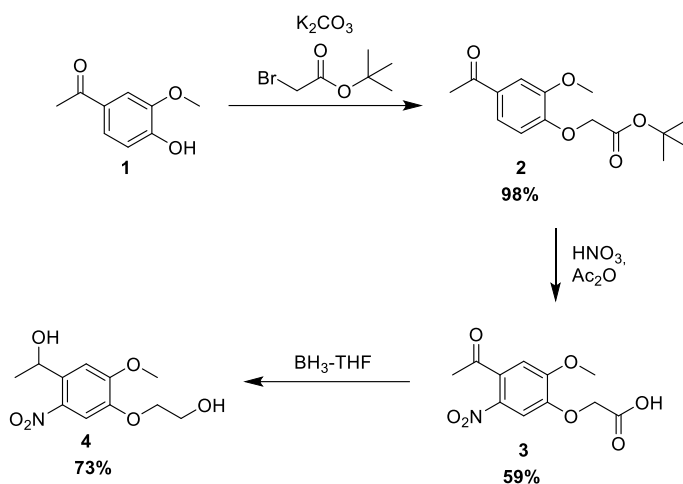
3.3.1 Approach

ortho-nitrobenzyl (*o*NB) derivatives are commonly used in photochemistry and -biology owing to their capability to cleave upon light irradiation.^[171-175] Indeed, under ultraviolet (UV) light, *o*NB moieties undergo a Norrish type II reaction, leading to the formation of a nitroso compound and the release of a carboxylic acid.^[81, 176-179] The degradation scheme is depicted in **Scheme 3-1**.



Scheme 3-1: Degradation mechanism of *o*NB's. Adapted from literature.^[179]

An *o*NB compound (**Scheme 3-1**, I) is exposed to UV light conditions ($h\nu$) and undergoes cleavage of the N=O π -bond (II). The formation of either a biradical after hydrogen abstraction (IIIa) or formation of an *aci*-nitro tautomer (IIIb) is considered simultaneously. Reorganisation to a five-membered benzoisoxazol structure (IV) is followed by reorganisation to the nitrosoketone under liberation of the leaving group (LG) as an alcohol or an acid (V). Generally, *o*NB compounds are exposed to UV light but its reactivity can be extended into the visible light region. Interestingly, it is ambiguous if the established mechanism holds true under such visible light irradiation condition. Thus, investigation on a small-molecule level with ultrafast transient absorption spectroscopy may give insight on the relaxation dynamics present. Afterwards, the studied photodegradable moieties were incorporated into PU polymer chains (**Scheme 3-3**). A step-growth polymerisation with *o*NB-containing dialcohol and diisocyanates readily allows for the insertion of these photodegradable moieties into every second monomer unit. After investigating the light-induced degradation of the photosensitive monomer, the polymer photolysis was performed in diluted conditions as well as on thin films. An *o*NB-based dialcohol (**Scheme 3-3**, orange) was synthesised via a 3-step procedure as depicted in **Scheme 3-2**. Synthetic procedures are available in Chapter 8.5.1. The first step consists of the formation of tert-butyl 2-(4-acetyl-2-methoxyphenoxy)acetate from acetovanillone, followed by a nitration step to afford the carboxylic acid **3** and a final reduction driven by BH_3 , allowing for the formation of the *o*NB dialcohol monomer **4** (**Scheme 3-2**). Due to the presence of boric acid as byproduct, a purification step via ion exchange chromatography



Scheme 3-2: Synthetical route towards the *o*NB dialcohol **4**. Percentages illustrate respective yield after each step.

through amberlite 743 was carried out to obtain the *o*NB dialcohol in high purity. The ^1H - and ^{13}C -Nuclear Magnetic Resonance (NMR) spectra, as well as mass spectrometric (MS) analysis of precursors, are available in the appendix (**Figure S3-1-Figure S3-6**). Prior to the ion exchange chromatographic purification (**Figure 3-1**), a single resonance arising at 6.5 ppm was easily assigned to the acidic protons of boric acid. After the purification, however, the impurity completely disappeared while leaving all other resonances unaltered.

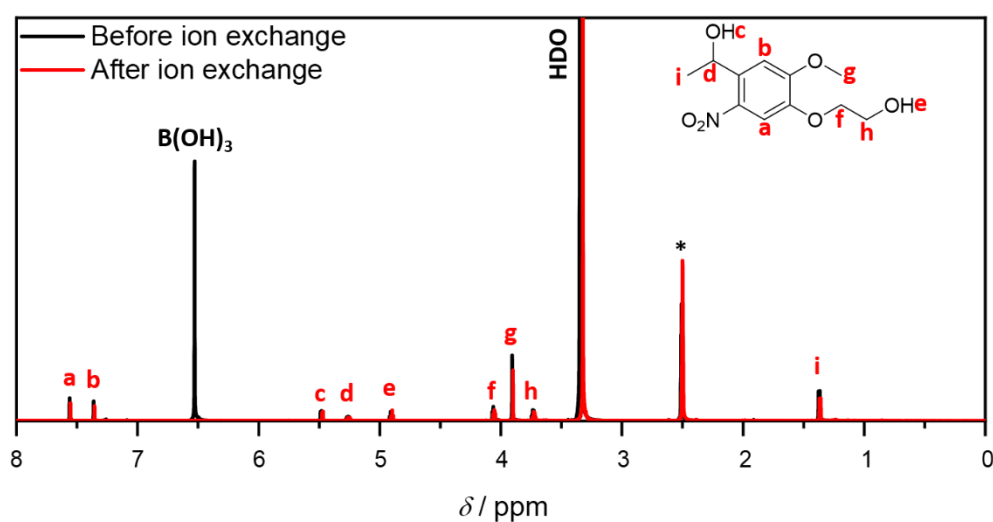
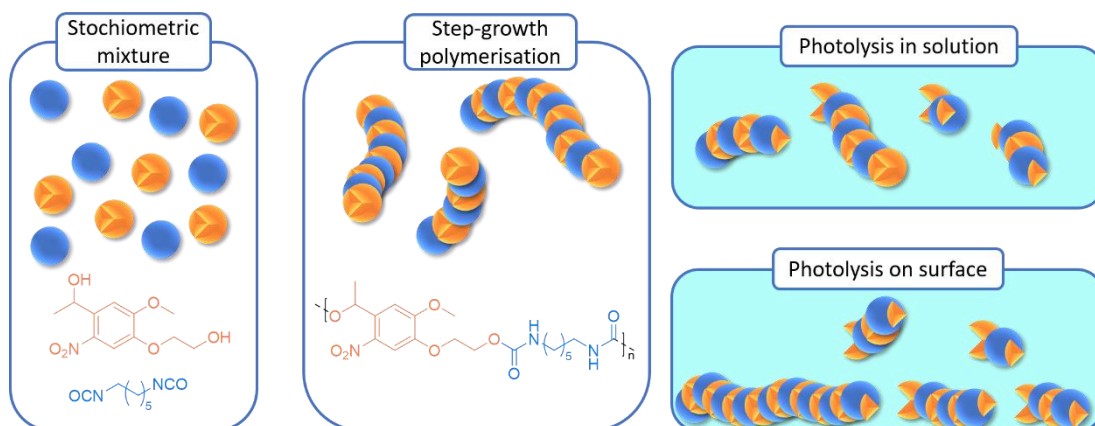


Figure 3-1: ^1H -NMR spectrum of **4** before (black solid) and after (red solid) chromatographic purification in $\text{DMSO-}d_6$ (*).



Scheme 3-3: Overall scheme of the step-growth polymerisation of *o*NB dialcohol and hexamethylene diisocyanate (HDI) followed by the photolysis performed in solution and on thin film. The step-growth polymerisation of an *o*NB dialcohol (orange) with hexamethyl diisocyanate (HDI, blue) is performed in stoichiometric amounts. The photolysis of the resulting polymers is then achieved in solution or on thin film. Reproduced from Ref. 200 with permission from the Royal Society of Chemistry. Modified representation.

3.3.2 Light attenuation evolution of a light-degradable linker

In order to verify the *o*NB cleavage when exposed to near visible light (close to 400 nm), its photochemical properties are assessed. Stationary UV/Vis absorption studies of the *o*NB dialcohol precursors were performed in acetonitrile at 25 °C. The addition of the *tert*-butyl moiety (**Figure 3-2**, 1 - 2) leads to an increase in absorbance in the region around 330 nm. However, both the acetovanillone and its ester derivatives exhibit no absorbance at 350 nm or higher. Insertion of a nitro group (**Figure 3-2**, 2 - 3) induces an absorbance band around 400 nm. This feature is of key importance, as the transmittance of typical plastic materials is usually below 350 nm.^[180] The final reduction step (**Figure 3-2**, 3 - 4) further increases the absorbance. As a result, the *o*NB dialcohol absorbs light mainly below 400 nm, an essential feature for degrading coloured polymeric material. It is expected that the photolysis of the *o*NB moiety occurs between 350 and 400 nm, according to the newly introduced absorption band in this region.

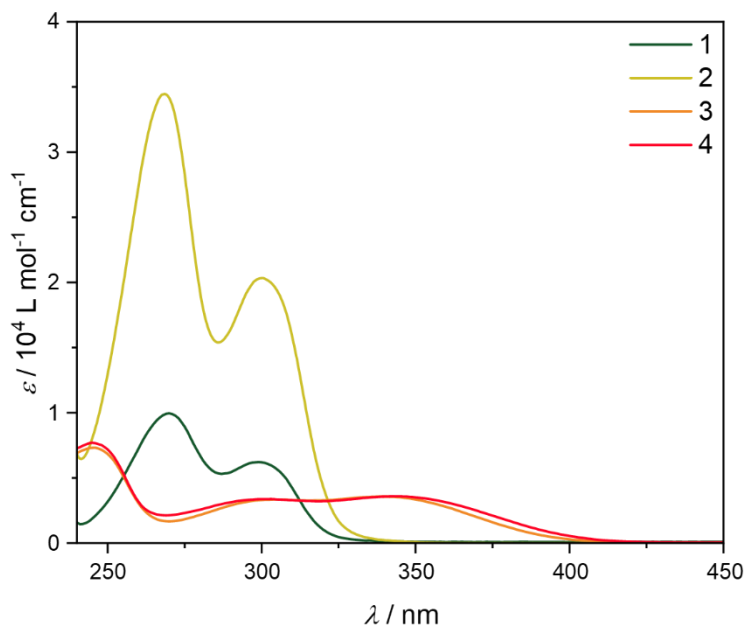


Figure 3-2: UV/Vis absorption spectra of the *o*NB dialcohol **4** and its precursors (**Scheme 3-2**) at 25 °C in acetonitrile. $d = 10$ mm. Reproduced from Ref. 200 with permission from the Royal Society of Chemistry. Modified representation.

3.3.3 Light degradation of a small molecule light degradable linker

The understanding of the *o*NB cleavage mechanism is essential from the perspective of a multi-component-material used in an industrial environment. Indeed, to achieve the effective photodegradation of an *o*NB-based adhesive material, side-reactions must be avoided in favour of the photolysis process. The photolysis of nitrobenzyl compounds studied by electron paramagnetic resonance (EPR) has been reported in the literature.^[181-184] EPR spectra of many *para*-substituted compounds have been studied and the mechanism of the splitting patterns is well understood,^[181-182] but to date few examples involving *ortho*-substituted compounds are described.^[183-184] To the best of our knowledge, all examples with *o*NB moiety describe the photolysis in an aqueous environment. To allow for further in-depth analysis via Size Exclusion Chromatography (SEC) and hyphenated Mass Spectrometry (SEC-ESI-MS), the polymer formed from nitrobenzyl-based monomeric units must be soluble in organic solvents. Even though the splitting pattern of *ortho*-nitrobenzyl relies on the position of the main substituent group in relation to the NO₂ group on the aromatic ring, the observed EPR spectrum is also dependent on the

experimental conditions (e.g. solvent). An EPR spectrum of **4** in CDCl₃ was recorded after irradiation with 395 nm (**Figure 3-3** right). Information regarding EPR setup and analysis are appended in Chapter 8.2.6 and Chapter 8.4.1.1 (**Figure S3-7**). Halogenated as well as deuterated solvents were found to improve the signal to noise ratio. Consulting the *o*NB degradation mechanism, simplified in **Figure 3-3** left, the light-induced degradation of the *o*NB moiety leads to the heterolytic cleavage of the N=O bond, thus generating free radicals on both the N and one of the O atoms. The abstraction of a proton from the N by the O atom induces the transfer of a free radical to the carbon holding the secondary alcohol function (**Scheme 3-1**, IIIa).

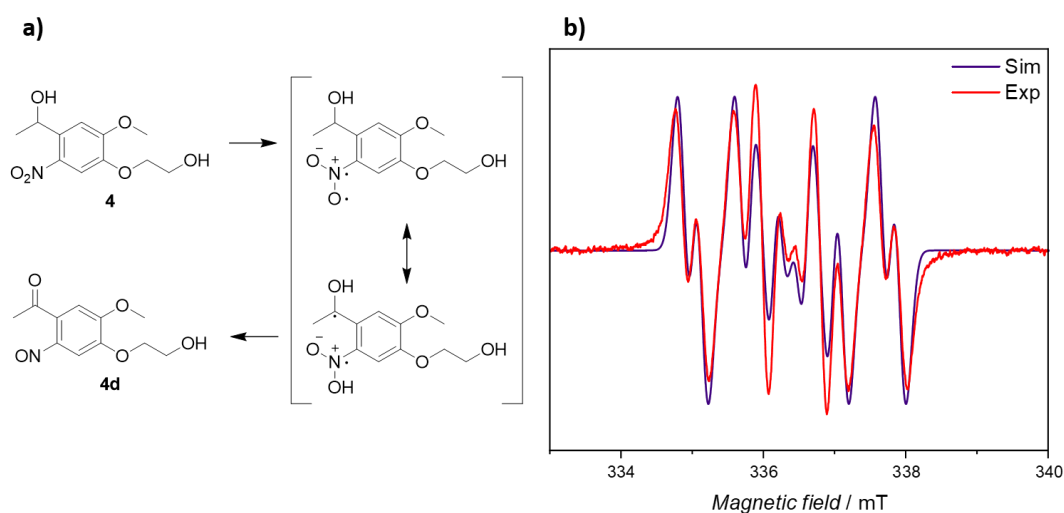


Figure 3-3: Left: Simplified *o*NB degradation mechanism. Right: Experimental (red) and simulated (purple) EPR spectra of the *o*NB dialcohol **4** in deuterated chloroform after 395 nm irradiation. Reproduced from Ref. 200 with permission from the Royal Society of Chemistry. Modified representation.

Indeed, **Figure 3-3** shows a clustered response of at least two components. Briefly, the EPR spectrum was simulated with the EasySpin package (Chapter 8.4.1.1, **Table S3-4**, **Table S3-5**, **Figure S3-7**) and spectra of an electron coupling to adjacent nuclei are calculated. It was found that the experimental spectrum is convoluted by two spectra. An electron is positioned at the nitrogen atom of the Nitro group coupling to adjacent H atoms. Unsurprisingly the other electron is located at the benzylic carbon atom. The structure found has most resemblance to structure IIIa (**Scheme 3-1**). Nevertheless however, radical formation represents only the first chemical step of the degradation

process. To achieve an in-depth understanding of the overall degradation of *o*NB dialcohol to a nitroso-ketone compound, the presence of the latter requires further confirmation. Fourier-transformed infrared (FT-IR) and ¹H-NMR spectroscopy were used purposely. The IR spectrum provides insight into changes of functional groups before and after irradiation (**Figure 3-4 a**). Indeed, frequency bands at 1520 and 1340 cm⁻¹ are characteristic for nitroaromatics (**Figure 3-4 a**). A carbonyl group would appear as a broad band between 1650 and 1750 cm⁻¹. After irradiation, the NO₂ bands have decreased in strength. Particularly both the asymmetric stretch vibration (1520 cm⁻¹) and the symmetric stretch vibration (1340 cm⁻¹) band of a NO₂-group lost some strength. On the opposite, the rise of a broad band at 1700 cm⁻¹ suggests formation of a carbonyl group. Acquisition of an ¹H-NMR spectrum indicates a change in the environment of the protons on the methyl group in α -position to the carbonyl (**Figure 3-4 b**). Comparing the resonances *a* and *b* in **Figure 3-4 b**, one notices the shift (1.4 → 2.8 ppm) and a change in multiplicity (doublet → singlet), due to the missing hydrogen nucleus to couple with. Both techniques confirm the pathway proposed (**Figure 3-4**). Even further, ¹H-NMR spectroscopy can be used as a reliable quantitative technique for the upcoming photolysis study. To gain insights on the degradation efficiency of the *o*NB dialcohol and in order to determine the relation between absorptivity and degradation efficiency, a wavelength window is carefully probed. Since *o*NB compounds usually degrade under exposure of UV-blue visible light, this wavelength region was selected. A nanosecond pulsed laser with a tuneable light source allows the space and time-controlled irradiation of samples in solution. Tuneable laser experiments with a constant deposition of photons at specific wavelengths were carried out. Detailed descriptions of the setup and relevant calculations are appended in Chapter 8.3.1.^[185-187] Discrepancies between photochemical reactivity and photon absorbance of photochemical moieties were reported in literature which are typically captured in action plots.^[185] The action plot of the *o*NB compound **4** (**Figure 3-2** and **Figure 3-5** bottom) has been investigated for a better understanding of its photolysis and to inform future reaction design. The wavelength was tuned by employing nanosecond pulsed laser irradiation. Conversion, X_4 , and yield, Y_{4d} , were then followed by tracking the protons *a* and *b* via ¹H-NMR spectroscopy (**Figure 3-4 b** and **Figure S3-8**). The action plot of compound **4** is displayed in **Figure 3-5** along with the extinction coefficient as a function of wavelength.

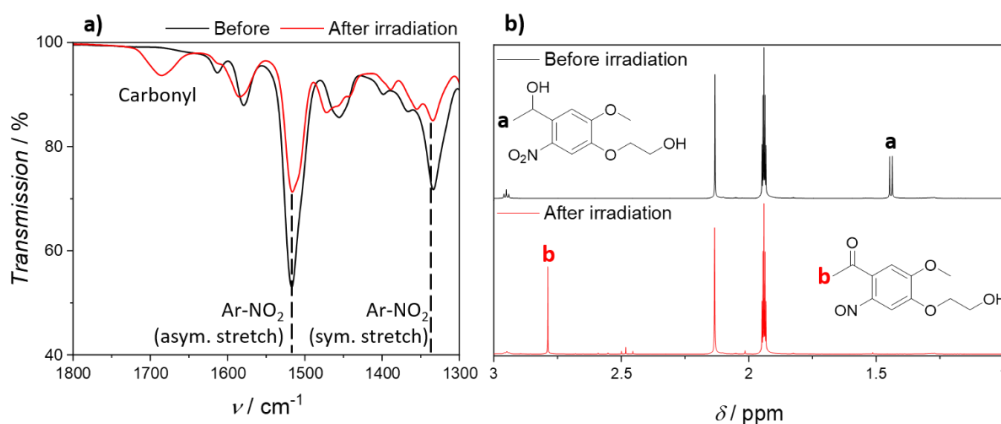


Figure 3-4: a) FT-IR spectra before (black) and after irradiation (red) of **4** in acetonitrile. Disappearance of characteristic frequency bands of nitroaromatics as well as appearance of the carbonyl frequency are highlighted. b) ¹H-NMR spectra of the *o*NB dialcohol before (top, **4**) and after (bottom, **4d**) irradiation. The protons *a* and *b* are assigned to the methyl group in alpha position of the secondary alcohol and carbonyl group, respectively. Irradiation parameters: 365 nm LED, 60 minutes, acetonitrile-*d*₃. Reproduced from Ref. 200 with permission from the Royal Society of Chemistry. Modified representation.

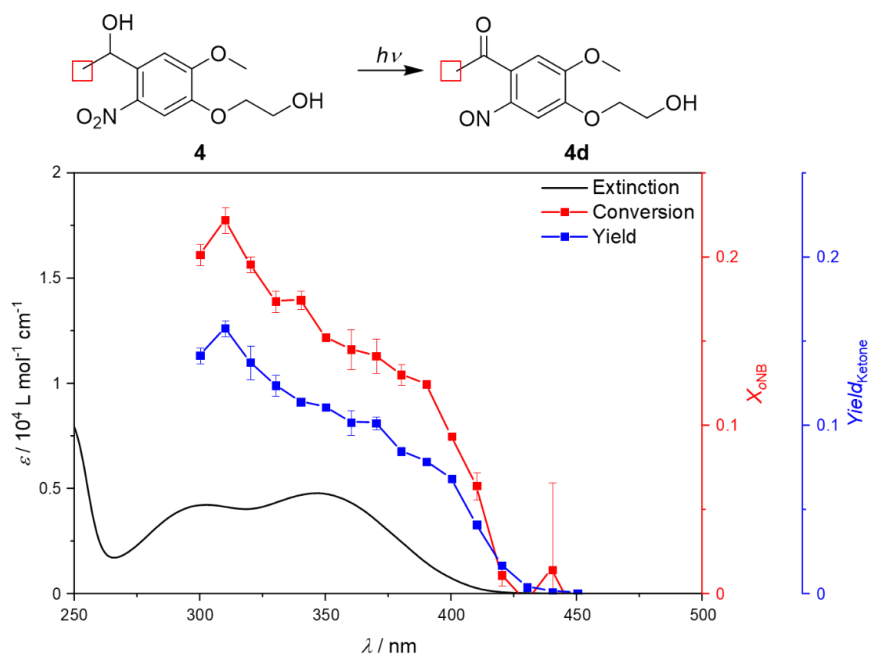


Figure 3-5: Top: Degradation reaction of **4**. The red boxes indicate the protons investigated for determination of conversion and yield. Bottom: Action plot of **4** in acetonitrile. Extinction (black), conversion X_4 (red), yield Y_{4d} (blue). Reproduced from Ref. 200 with permission from the Royal Society of Chemistry. Modified representation.

Interestingly, degradation efficiency peaks at 310 nm which does not follow its absorption maximum (λ_{max} close to 350 nm).

While the *o*NB dialcohol shows no significant absorption around 400 nm, degradation is still taking place until 425 nm, although absorption can no longer be detected. Discrepancies between the conversion and yield were found which remained almost constant until 425 nm. Indeed, given the fact that the formation of **4d** (**Figure 3-5**) is consistently less efficient than the photolysis of *o*NB dialcohol **4**, the selectivity of this reaction can be estimated. A similar trend is observed when using LEDs ranging from 340 to 415 nm. Even with such a simple method, the general trend of the degradation of **4** was reproduced. The experimental procedure was appended in Chapter 8.4.1.4 and the results provided in **Figure S3-11-Figure S3-14**).

3.3.4 Ultrafast relaxation dynamics of *o*NB dialcohol

*o*NB chemistry often finds application in polymer and material sciences. As shown in Chapter 3.3.3, UV light most efficiently triggers the photodegradation of molecule **4**. Critically however, UV light can facilitate carcinogenesis in biological tissue.^[188] The herein presented *o*NB dialcohol **4** allows for 400 nm photodegradation, thus enabling non-harmful irradiation conditions. Ultrafast relaxation dynamics of *o*NB's have been reported but were limited to UV light excitation. The following chapter will unravel the relaxation dynamics of **4** upon blue light excitation. An in-depth study of excitation wavelength and solvent influence was conducted. The acetophenone derivative **3** was studied as well and allowed for comparison with a non-reactive derivative. All investigated *o*NB compounds feature an absorption shoulder which ranges into the blue visible (~ 450 nm). One may consult the UV/Vis absorption spectra recorded in **Figure 3-2** and assign the absorption bands to electronic excited states. Using this approach, the first (lowest) excited singlet state S_1 is probably located between 300 and 400 nm, higher lying electronic states are located between 350 and 250 nm and below, as described in literature for similar systems.^[189] Particularly the extinction coefficients of **3** and **4** are low at 400 nm, $\epsilon_{3, 400 \text{ nm}} = (309 \pm 19) \text{ L mol}^{-1} \text{ cm}^{-1}$ and $\epsilon_{4, 400 \text{ nm}} = (554 \pm 5) \text{ L mol}^{-1} \text{ cm}^{-1}$ respectively (**Figure S3-15-Figure S3-18**). These conditions raise the need for employing rather uncommon conditions for transient pump-probe measurements. The concentration was chosen intentionally high which

led to oversaturation in the UV/Vis absorption spectra (*vide infra*). Further, the pump energy was adjusted to 2 μJ to ensure good signal-to-noise ratio. These high energies can lead to correlation artefacts around $t \sim 0$ ps due to occurring chirp, group velocity dispersion (GVD) and group velocity mismatch (GVM) in transparent media. Such correlation artefacts were reported^[190] and also found in the experiments conducted. **Figure 3-6** depicts single transients extracted after a pump-probe sequence with supercontinuum serving as the probe. Such artefacts are found in all following results. It is noted that the first approx. 180 fs (**Figure 3-6**) in such responses are due to GVM, GVD or cross correlation modulations phenomena and thus not relevant for further discussion.

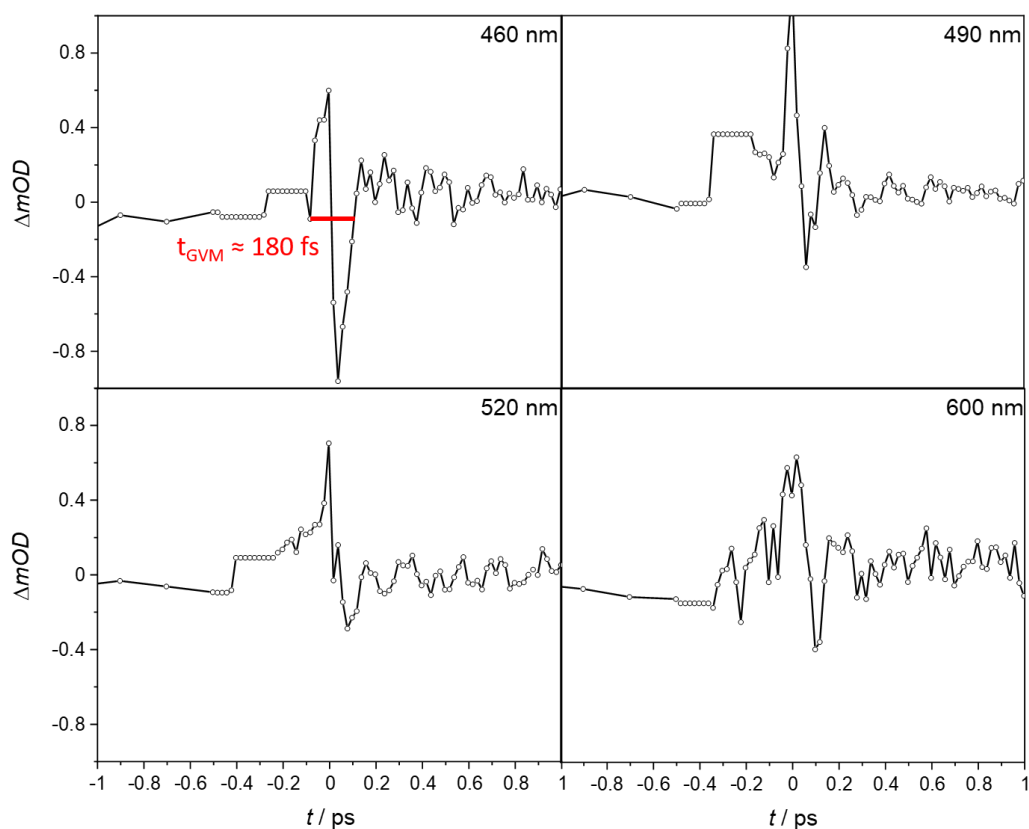


Figure 3-6: Extracted single transients from pure solvent (acetonitrile) after excitation. $\lambda_{\text{ex}} = 400$ nm, $E_{\text{ex}} = 2$ μJ , $d = 1$ mm. The transients extracted range in the entire visible spectrum and chirp can be observed in all transient responses.

3.3.4.1 Excitation with $\lambda_{\text{ex}} = 400 \text{ nm}$

In a preliminary experiment, the ultrafast relaxation dynamics of **4** were studied upon 400 nm excitation. Acetonitrile (AcN) was selected as the solvent of choice since a comparison with the previously conducted action plot is achievable. Further, acetonitrile is a common solvent used in organic synthesis and should not interfere with the relaxation dynamics due to its moderate polarity and acidity. **Figure 3-7** depicts the stationary UV/Vis absorption spectrum of the sample used. Due to low absorbance of **4** at 400 nm, the high concentration caused the absorption spectrum throughout the visible spectrum to be completely oversaturated. A resolved absorption spectrum and determination of extinction coefficient are found in **Figure S3-17** and **Figure S3-18**. Excitation with 400 nm suggests population of the first bright Singlet state, here denoted as S_1 . A recorded transient absorption (TA) contour plot allows for a first inspection of the evolution of electronic states. Contributions to ΔOD are colour-graded from red (positive) to blue (negative). Such a profile can depict a wavelength and time-resolved response simultaneously. The contour plot of **4** in AcN after excitation at 400 nm is depicted in **Figure 3-8**. Two characteristic bands are observed, one between 420 and 520 nm and one between 550 and 680 nm. Both bands have their maximum at 460 nm and 600 nm, respectively, henceforth both are referred to the ‘460 nm’ and the ‘600 nm’ response. Between the two bands, a decay at approx. 520 nm is noted which first decreases within 510 fs and is subsequently governed by negative responses after 3 ps. Interestingly, both positive signals have different evolution times. The transient response between 550 and 680 nm rises within 110 fs while the response between 420 and 520 nm increases within 510 fs. Further, the 600 nm response fully decays after 1000 ps while the 460 nm response decays to 17% its original maximum absorbance (**Figure 3-9**).

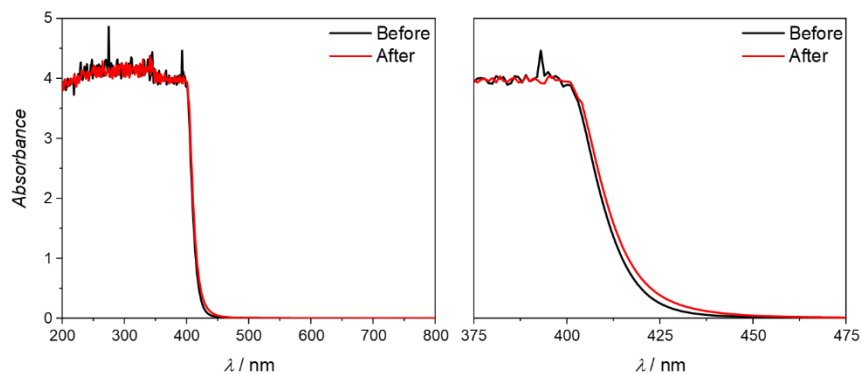


Figure 3-7: UV/Vis absorption spectrum of **4** before (black solid) and after (red solid) transient fs-laser experiment. $\lambda_{\text{ex}} = 400 \text{ nm}$, $E_{\text{ex}} = 2 \mu\text{J}$, $d = 1 \text{ mm}$, acetonitrile and zoom on the absorption shoulder

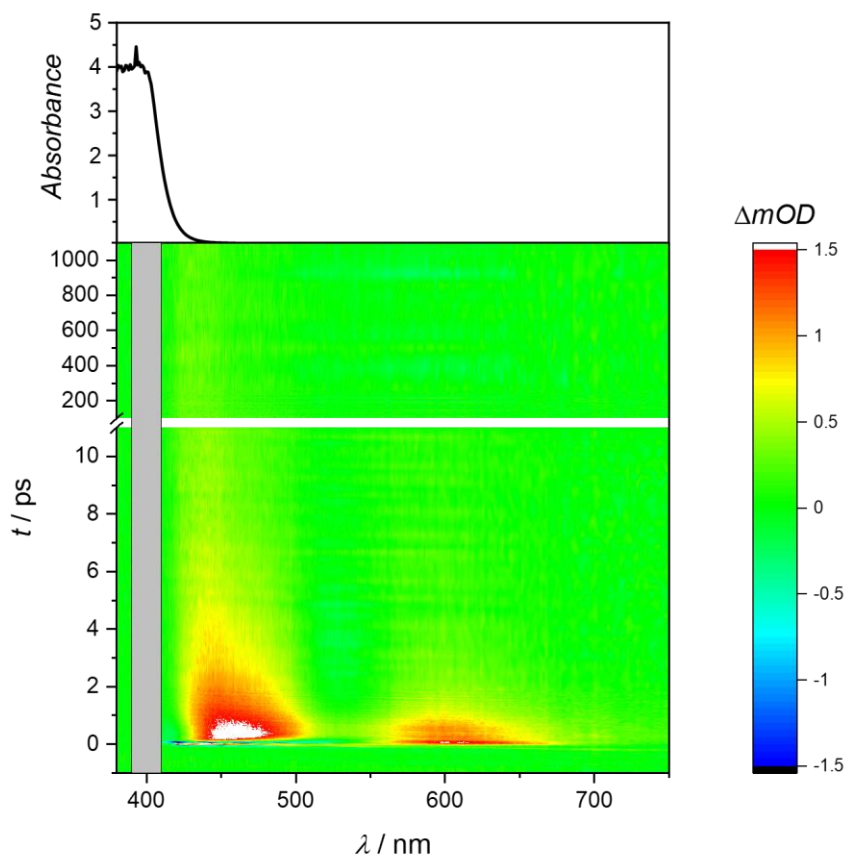


Figure 3-8: Contour plot of **4** with stationary UV/Vis absorption spectrum (top). $\lambda_{\text{ex}} = 400 \text{ nm}$, $E_{\text{ex}} = 2 \mu\text{J}$, $\lambda_{\text{probe}} = \text{supercontinuum}$, $d = 1 \text{ mm}$, $c = 72 \text{ mmol L}^{-1}$, acetonitrile. Transient response around 400 nm is neglected due to pump pulse scattering.

Weak negative responses can be found between 420 and 520 nm. Scattering phenomena are present within the first 150 fs (see **Figure S3-19**) and are attributed to

previously mentioned chirp, thus not further covered. Interestingly, all responses covered show blueshift of its maxima within the first 1 ns. The blueshift is not well pronounced but could be pinpointed to 10 nm for both the 600 nm (609 nm \rightarrow 599 nm) and 460 nm response (464 nm \rightarrow 454 nm).

TA spectra (**Figure 3-9**) confirm different rising times for the two main responses. After 0.11 ps, the 600 nm response feature is fully pronounced while the 460 nm response is fully evolved after 0.51 ps. Interestingly, the 600 nm response vanishes within 100 ps while part of the 460 nm absorption is still visible, even after 980 ps. Due to chirp phenomena, a conventionally used error function can no longer account for the deconvolution of pump and probe pulses. Bi- or triexponential fit functions were used to obtain time constants (see Equation 8-8) and were allowed to proceed from the maximum in ΔOD which is considered after approx. 0.25 ps, thus after any chirp phenomena. The respective fits are depicted in **Figure 3-10** and parameters extracted in **Table 3-1**.

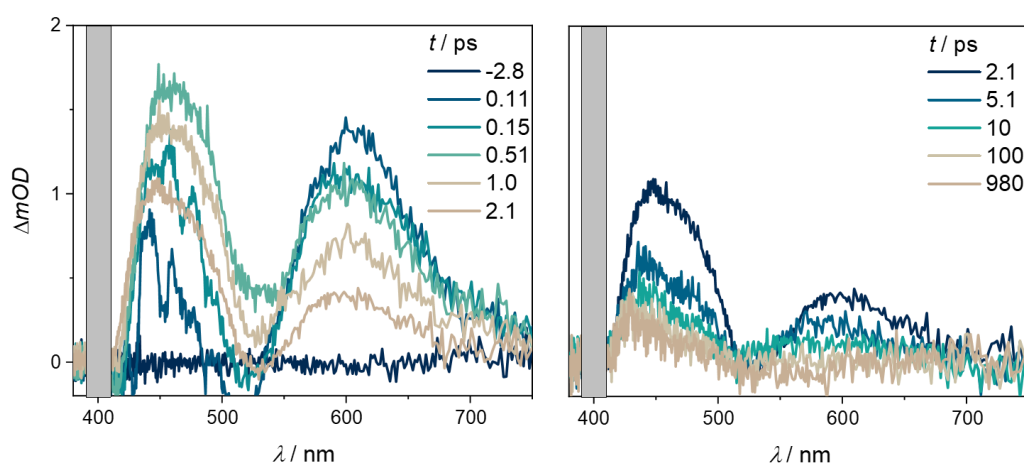
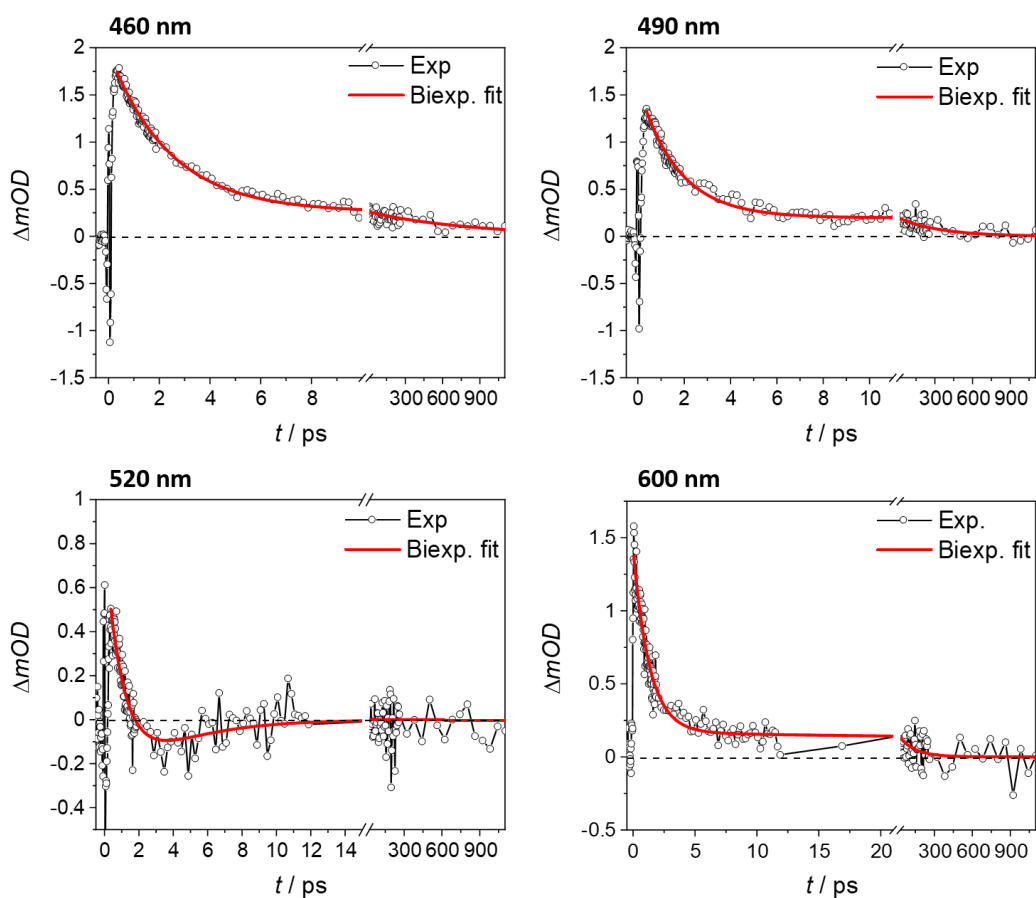


Figure 3-9: TA spectra of **4** between -2.8 and 2.1 ps (left) as well as between 2.1 and 980 ps (right). $\lambda_{\text{ex}} = 400$ nm, $E_{\text{ex}} = 2$ μJ , $\lambda_{\text{probe}} = \text{supercontinuum}$, $d = 1$ mm, $c = 72$ mmol L $^{-1}$, acetonitrile. Transient response around 400 nm is neglected due to pump pulse scattering.

Table 3-1: Extracted amplitudes and time constants from the fits shown in **Figure 3-10**.

	460 nm	490 nm	520 nm	600 nm
$A1 / 10^{-4}$	17	14	12	13
t_1 / ps	2.4 ± 0.1	1.7 ± 0.1	1.1 ± 0.1	1.3 ± 0.1
$A2 / 10^{-4}$	2.6	2.0	-3.9	1.7
t_2 / ps	856 ± 123	327 ± 56	4.23 ± 0.3	126 ± 35

**Figure 3-10:** Extracted single transient responses for the features at 460, 490, 520 and 600 nm. Experimental data was fit with a biexponential fit, starting from the maximum response.

All transient responses can be well represented with biexponential ($j = 2$) decay functions. A comparison of the amplitudes reveal that the decay predominantly consists of an ultrafast process (1.1 ps at 520 nm, 2.4 ps at 460 nm). Longer time constants (> 100 ps) may point towards several ESA processes and hints at the existence of electronic states. Several transients of the 460 nm response were studied and their biexponential fit parameters tabularized in **Table 3-2**. Interestingly, the

transients at 430 and 440 nm reveal a time constant >1000 ps which is superimposing t_2 . This phenomenon was attributed to Ground State Bleaching (GSB) since **4** still shows absorption at that wavelength.

Table 3-2: Several isolated transients of the 460 nm response. The fits are appended in **Figure S3-21**.

	430 nm	440 nm	450 nm	460 nm	470 nm	480 nm
A1 / 10 ⁻⁴	7.5	12	15	17	17	16
t_1 / ps	4.1 ± 0.3	3.8 ± 0.2	3.0 ± 0.1	2.4 ± 0.1	2.2 ± 0.1	2.0 ± 0.1
A2 / 10 ⁻⁴	3.1	3.3	3.2	2.6	2.4	2.3
t_2 / ps	>1000	>1000	795 ± 122	856 ± 123	543 ± 97	402 ± 65

However, the ultrashort time constant decreases towards longer wavelengths but still dominates the overall energy dissipation dynamics. The same approach was applied to the 600 nm response which is tabulated in **Table 3-3**.

Table 3-3: Several isolated transients of the 600 nm response. The fits are appended in **Figure S3-20**.

	580 nm	590 nm	600 nm	610 nm	620 nm
A1 / 10 ⁻⁴	10	12	13	13	11
t_1 / ps	1.3 ± 0.1	1.4 ± 0.1	1.3 ± 0.1	1.2 ± 0.1	0.94 ± 0.11
A2 / 10 ⁻⁴	1.6	1.8	1.7	1.6	3.0
t_2 / ps	58 ± 23	122 ± 27	126 ± 35	87 ± 26	7.1 ± 2.2

Again, short time constants dominate the overall energy dissipation dynamics. t_2 rise (58 → 126 ps) and fall (126 → 7.05 ps) over the spectral range of the 600 nm response. The general trend of the decrease of the longer time constant with increasing wavelength was noted at the 460 nm absorption band. This phenomenon can be explained by investigating the 520 nm response which seems to include negative contributions. Indeed, emission of **4** (in EtOH) was recorded in that spectral region. An enlarged absorption, emission and transient evolution is depicted in **Figure 3-11**:

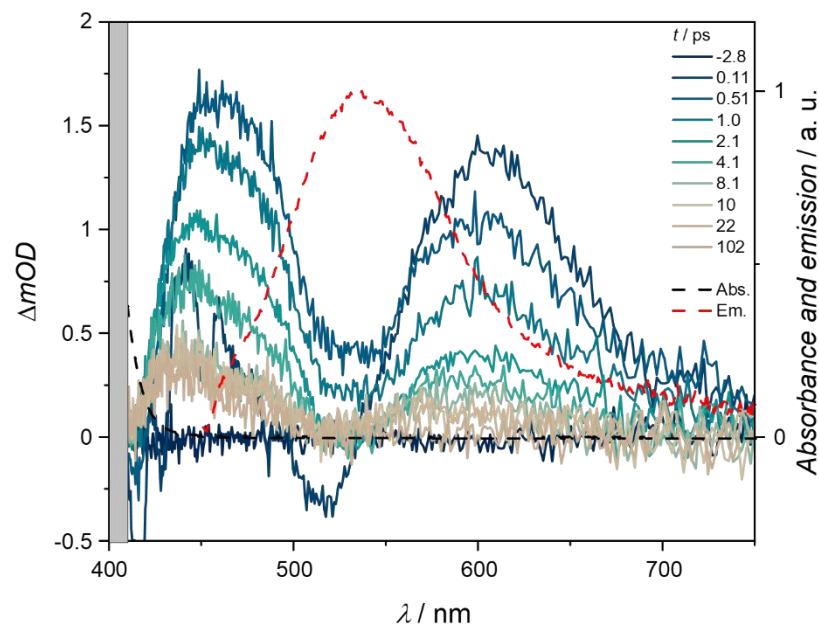


Figure 3-11: TA spectra (solid lines) of **4** between -2.8 and 100 ps. $\lambda_{\text{ex}} = 400$ nm, $E_{\text{ex}} = 2$ μJ , $\lambda_{\text{probe}} =$ supercontinuum, $d = 1$ mm, $c = 72$ mmol L⁻¹, acetonitrile. Transient response around 400 nm is neglected due to pump pulse scattering. Stationary absorption (Abs.) and emission spectra (Em.) are depicted in black and red. Parameters for acquisition emission spectrum: $\lambda_{\text{ex}} = 400$ nm, slit size = 5, EtOH.

Stimulated emission (SE) processes contribute negatively to the response in a certain spectral region. A superposition of positive ESA and negative SE processes is likely, while the ESA net response is impaired due to SE superposition. Thus, the right shoulder of the 460 nm response and the entire spectral range of 600 nm response are impacted. A wavelength-by-wavelength fit in the 520 nm spectral region was conducted as tabulated in **Table 3-4**. Negative contributions first debut at 530 nm and always contribute to the spectrum (**Table 3-4**). Triexponential decay fits are in better agreement to the experimental data, since 530 nm - 550 nm transients were approximated according to a triexponential decay. Further, the switch of algebraic sign from 540 nm to 550 nm implicates the presence of superposition of ESA (positive) and SE (negative) processes. The fact that both major responses are dominated by very short time constants (1 - 5 ps) followed by various longer time constants underlines the hypothesis that two different electronic states are populated after a short period of intramolecular vibrational redistribution (IVR) or vibrational relaxation (VR).

Table 3-4: Several isolated transients of the 520 nm response. The fits are appended in **Figure S3-22**.

	500 nm	510 nm	520 nm	530 nm	540 nm	550 nm
A1 / 10 ⁻⁴	15	14	12	34	1180	16
t ₁ / ps	0.79 ± 0.12	0.82 ± 0.05	1.1 ± 0.1	1.4 ± 18	1.3 ± 6.8	0.60 ± 0.10
A2 / 10 ⁻⁴	3.4	0.4	-3.9	-34	-1170	-29
t ₂ / ps	7.5 ± 1.9	544 ± 488	3.4 ± 0.4	1.5 ± 19	1.4 ± 6.9	16 ± 199
A3 / 10 ⁻⁴				-0.13	0.1	29
t ₃ / ps				>1000	>1000	17 ± 215

The Stokes shift from the lowest bright absorption maximum and the estimated emission maximum was calculated via Equation 8-4. Conventional S₁→S₀ fluorescence after excitation of the first bright electronic state usually occurs within 8000 cm⁻¹.^[191] Phosphorescence, twisted intramolecular charge transfer (TICT)^[192] or excited state intramolecular proton transfer (ESIPT)^[193] processes may well explain the enlarged Stokes shift, the former however requires an ISC to a triplet state.

$$\Delta\tilde{\nu}_{\text{stokes}} = \frac{10^7}{\lambda_1} - \frac{10^7}{\lambda_2} = 10\,800 \text{ cm}^{-1} \quad \text{Equation 3-1}$$

Interestingly, negative contributions of the 520 nm response occur within 1.4 - 16 ps (**Table 3-4**). The luminescence quantum yield Φ exemplarily for EtOH of **4** was determined to $\phi_4 = 0.07\%$ according to Equation 8-3. In general, the short time constants of the 600 nm response are shorter (0.94 - 1.4 ps) than the ones observed at 520 nm. It can be hypothesized that the ESA of 600 nm undergoes IVR within 1.4 ps, followed by the emissive dissipation channel. Due to superposition of all bands, the assignment remains challenging. If the observed luminescence indeed is phosphorescence or a radiative TICT or ESIPT channel cannot be clearly evidenced. Since (stimulated) phosphorescence occurs within nanoseconds to seconds, the emission does not originate from a triplet state.^[194-195] The same idea applies for biradical emissions which occur within several microseconds.^[196]

Investigation of any solvent dependencies revealed minor differences in the energy dissipation pathways. Tetrahydrofuran (THF) and ethanol (EtOH) were used as the solvent and are discussed simultaneously in the following. A shift in absorbance maxima was not observed for THF or ethanol EtOH but the extinction coefficient

exhibits some differences. Generally, the extinction coefficient is approximately 2000 L mol⁻¹ cm⁻¹ higher in EtOH than in AcN throughout the visible absorption spectrum. Extinction coefficient of **4** in THF are between those of AcN and EtOH. The respective TA profiles are depicted in **Figure 3-12**. It is stated that the general energy dissipation dynamics are very similar to the ones recorded in acetonitrile earlier. Once again, two major responses at 460 and 600 nm are observed, however, population seem to differ depending on the solvent. The state at 600 nm seems to be more populated, yet decays in THF more slowly than in EtOH. Further, a transient rise at 370 nm is observed in both solvents, although high concentration in both molecules induces complete absorption at wavelengths below 400 nm. TA spectra (**Figure 3-13**) confirm the previous claims. Single transients at particular wavelengths were extracted and fitted according to bi- or triexponential decay fit functions if applicable. Time constants and amplitudes are collated in **Table 3-5**. Interestingly, all short t_1 time constants ($\sim 1 - 2$ ps) are shorter in THF and EtOH. This applies to all investigated wavelengths but 520 nm. Negative contributions do not concur to the overall relaxation dynamics in THF and EtOH which is why the longer time constants are significantly longer. Nevertheless, emission could just not be well pronounced, thus not observed. This aligns with the low quantum yield obtained for fluorescence ($\phi_4 = 0.07\%$).

Table 3-5: Extracted transients and influence of solvent. The fits are appended in **Figure S3-24**.

λ / nm		AcN	THF	EtOH
460	t_1 / ps	2.4 ± 0.1	2.0 ± 0.1	1.5 ± 0.1
	t_2 / ps	856 ± 123	685 ± 72	> 1000
490	t_1 / ps	1.7 ± 0.1	1.4 ± 0.1	1.2 ± 0.1
	t_2 / ps	327 ± 56	867 ± 131	>1000
520	t_1 / ps	1.1 ± 0.1	1.2 ± 0.1	1.2 ± 0.1
	t_2 / ps	3.4 ± 0.4	122	>1000
600	t_1 / ps	1.3 ± 0.1	0.88 ± 0.02	0.90 ± 0.03
	t_2 / ps	126 ± 35	705 ± 312	>1000

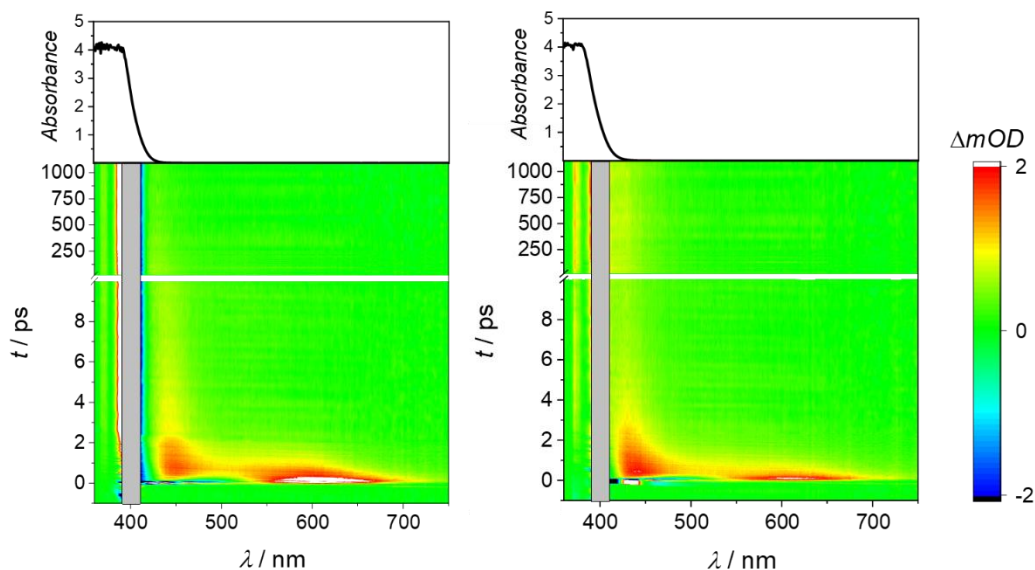


Figure 3-12: Contour plot of **4** with respective stationary UV/Vis absorption spectrum (top) in THF (left) and EtOH (right). $\lambda_{\text{ex}} = 400 \text{ nm}$, $E_{\text{ex}} = 2 \mu\text{J}$, $\lambda_{\text{probe}} = \text{supercontinuum}$, $d = 1 \text{ mm}$, $OD_{400 \text{ nm, THF}} \sim 1.2$, $OD_{400 \text{ nm, EtOH}} \sim 1.4$. Transient response around 400 nm is neglected due to pump pulse scattering. The legend on the right applies to both contour plots. Absorption spectra before and after the experiment are appended in **Figure S3-23**.

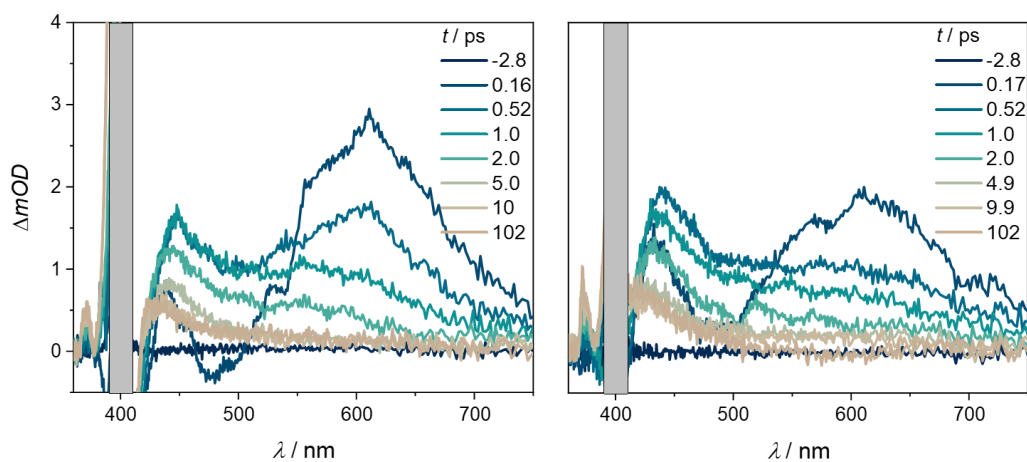


Figure 3-13: TA spectra of **4** between -2.8 and 100 ps in THF (left) and EtOH (right). $\lambda_{\text{ex}} = 400 \text{ nm}$, $E_{\text{ex}} = 2 \mu\text{J}$, $\lambda_{\text{probe}} = \text{supercontinuum}$, $d = 1 \text{ mm}$, $OD_{400 \text{ nm, THF}} \sim 1.2$, $OD_{400 \text{ nm, EtOH}} \sim 1.4$. Transient response around 400 nm is neglected due to pump pulse scattering.

Further, both solvents seem to stabilize all investigated electronic states better than AcN, hence the significantly prolonged time constant ($100 < t < 1000 \text{ ps}$) found. In EtOH, this state is even more stabilized ($t_2 > 1000 \text{ ps}$). Ultrashort processes like ISC

or VR seem to be impacted by the solvent selected but are not correlated to solvent parameters such as polarity or acidity.^[197]

3.3.4.2 Excitation with $\lambda_{\text{ex}} = 325$ nm

In order to investigate energy dissipation pathways from higher electronic states, $\lambda = 325$ nm was used to initiate population. For simplicity, these states are denoted as S_n . The respective TA profile in acetonitrile is illustrated in **Figure 3-14**, particular transient responses depicted in **Figure 3-15**.

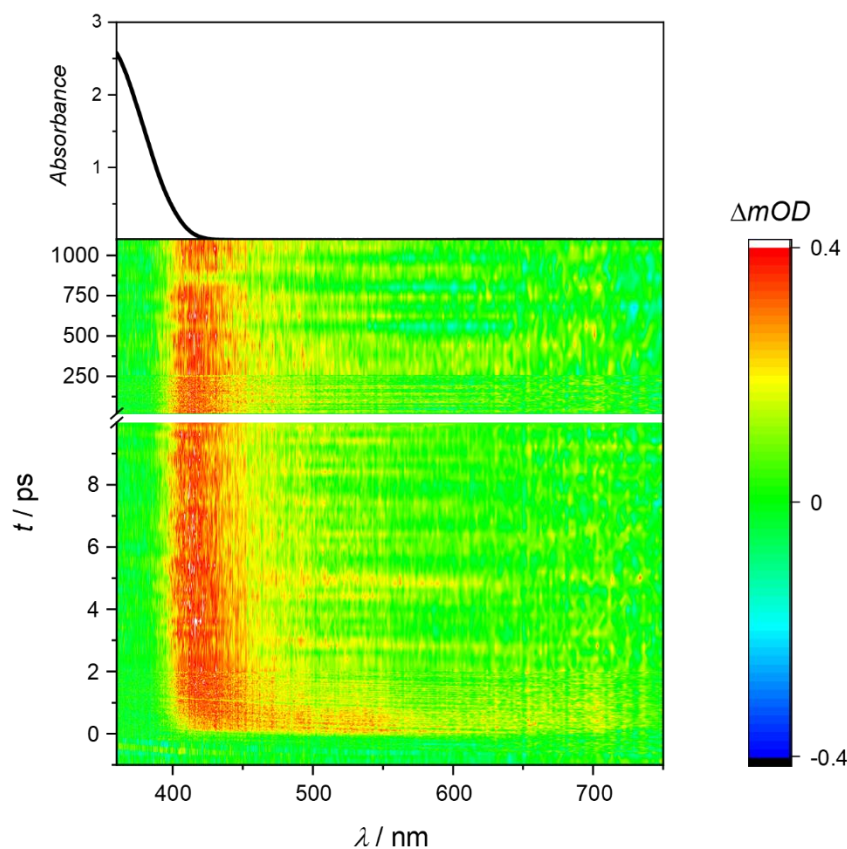


Figure 3-14: Contour plot of **4** with respective stationary UV/Vis absorption spectrum (top). $\lambda_{\text{ex}} = 325$ nm, $E_{\text{ex}} = 0.5$ μJ , $\lambda_{\text{probe}} = \text{supercontinuum}$, $d = 1$ mm, $OD_{325 \text{ nm, AcN}} \sim 2.5$, acetonitrile. UV/Vis spectra before and after acquisition are available in **Figure S3-25**.

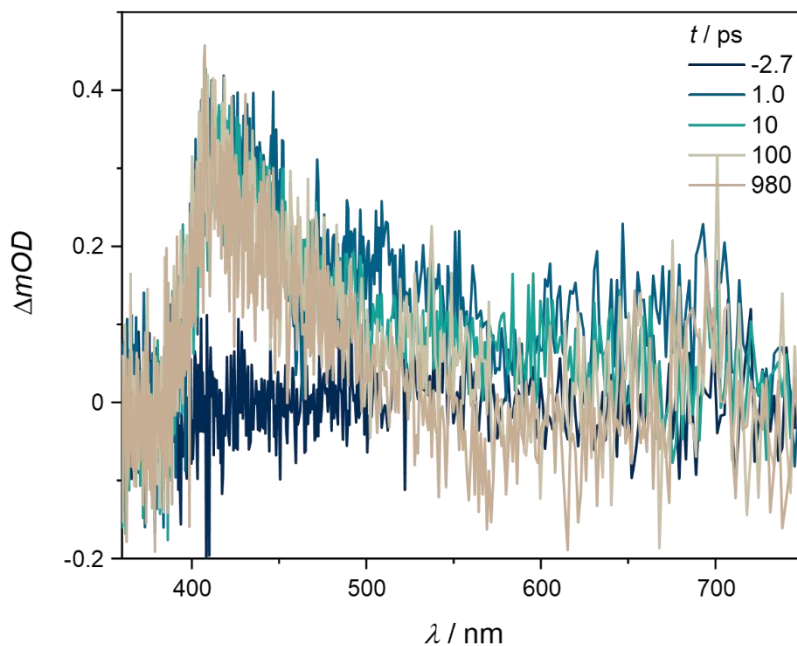


Figure 3-15: Selected TA spectra of **4**. Experimental parameters, refer to **Figure 3-14**.

First, one notes the presence of an isosbestic point in the UV/Vis spectra acquired (**Figure S3-25**) before and after treatment with 325 nm irradiation which is likely due to the formation of the respective nitrosoketone.^[198] Time constants have been retrieved and are tabulated in **Table 3-6**. All transients are governed by long-living processes ($t > 1000$ ps) but accompanied by varying short ($1 < t_1 < 15$) and moderate decays ($7.4 < t_2 < 99$). The general pattern of negative contributions at moderate decays followed by a stabilizing long time constant once again hints towards a superposition of stimulated emission and ESA. 460 nm and 520 nm transients no longer feature a $t \sim 1$ ps time constant. However, due to the low signal quality, deviations are high and the significance of obtained time constants questionable at best, thus not further discussed. In summary, the presence of a long-lasting component at 420 nm is observed here as well. However, the 460 nm and the 600 nm feature do not appear after $\lambda_{\text{ex}} = 325$ nm excitation. Considering excitation into S_n , an internal conversion (IC) to allow repopulation of S_1 does not occur which suggests a different relaxation mechanism. A possible influence of the solvent selected was investigated similarly. Time constants were evaluated in **Table S3-6** but no consistent trend was developed. Interestingly however, the 600 nm response under $\lambda_{\text{ex}} = 400$ nm was not observed.

Taking conservation of energy into account, probing the same electronic state requires detection of photons with $\lambda_{\text{probe}} = 918 \text{ nm}$ thus outside the probing window.

Table 3-6: Several isolated transients of the entire transient response of **4** in acetonitrile. The fits are appended in **Figure S3-26**.

	420 nm	460 nm	520 nm
$A1 / 10^{-4}$	-1.8	1.6	1.7
t_1 / ps	1.0 ± 0.7	13 ± 8	15 ± 3
$A2 / 10^{-4}$	0.88	-1.5	-1.0
t_2 / ps	7.4 ± 7.0	99 ± 134	50 ± 9
$A3 / 10^{-4}$	3.0	2.4	1.1
t_3 / ps	>1000	>1000	>1000

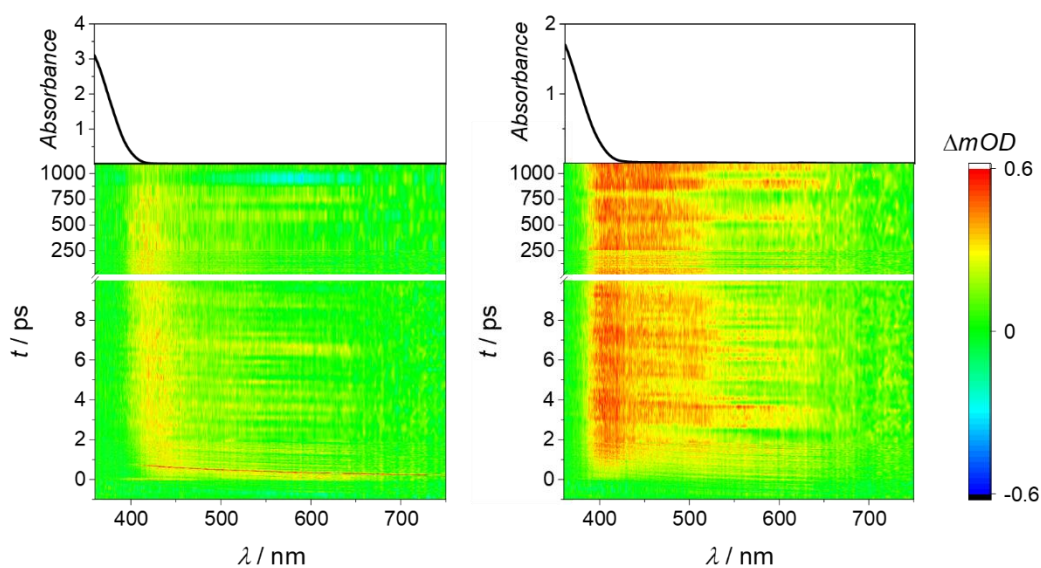
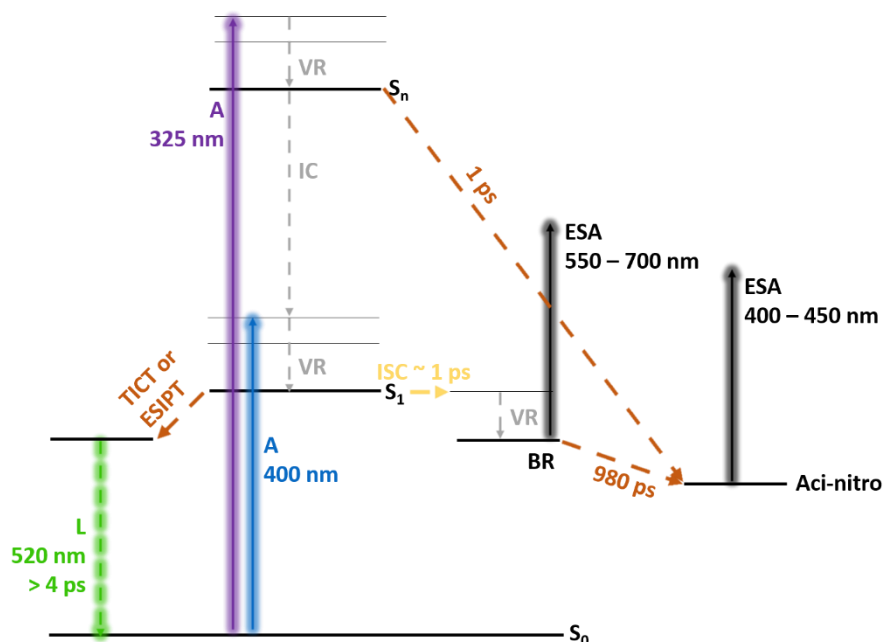


Figure 3-16: Contour plot profile of **4** with respective stationary UV/Vis absorption spectrum (top) in THF (left) and EtOH (right). $\lambda_{\text{ex}} = 325 \text{ nm}$, $E_{\text{ex}} = 0.4 \mu\text{J}$, $\lambda_{\text{probe}} = \text{supercontinuum}$, $d = 1 \text{ mm}$, $OD_{325 \text{ nm, THF}} \sim 3.1$, $OD_{325 \text{ nm, EtOH}} \sim 1.9$. The legend on the right applies to both TA profiles. Absorption spectra before and after the experiment are appended in **Figure S3-27**.

Collating the results and phenomena observed, an energy dissipation scheme is drafted in the following. Excitation at $\lambda_{\text{ex}} = 325 \text{ nm}$ conditions leads to an excitation of energetic higher states S_n compared to $\lambda_{\text{ex}} = 400 \text{ nm}$ (only S_1) due to the presence of

several absorption bands. The particular shape the spectrum obtained after 1 ps under $\lambda_{\text{ex}} = 325$ nm conditions (**Figure 3-15**) is characterized by its absorption maximum at $\lambda_{\text{max}} = 412$ nm, which is superimposed by $S_1 \leftarrow S_0$ absorption processes. This transient ($\lambda_{\text{ex}} = 325$ nm, after 1 ps, **Figure 3-15**) is remarkably similar to the transient response obtained after 980 ps under $\lambda_{\text{ex}} = 400$ nm conditions (**Figure 3-9** right). Such a 420 nm band has reportedly been attributed to the *aci*-nitro tautomer under $\lambda_{\text{ex}} = 267$ nm conditions.^[41] Given the experiments available, the population of this state can either proceed slowly ($\lambda_{\text{ex}} = 400$ nm) or rapidly ($\lambda_{\text{ex}} = 325$ nm). After $\lambda_{\text{ex}} = 325$ nm excitation, the *aci*-nitro tautomer directly forms from the S_n state while the formation after $\lambda_{\text{ex}} = 400$ nm excitation proceeds via an intermediate. As pointed out, the direct formation proceeds three orders of magnitude faster. Literature reports on the presence of triplet states at wavelengths of $400 \text{ nm} < \lambda < 450 \text{ nm}$ and $550 \text{ nm} < \lambda < 700 \text{ nm}$. The presence of such bands was observed in the experiments conducted but it is noted that appearance and dynamics of such spectral region can differ, depending on excitation conditions and dissipation pathways available.^[199] A biradical intermediate was postulated in the *o*NB degradation mechanism and experimentally evidenced,^[200] and most likely after an ISC. If this claim holds true, the time constant of $t_1 = 1.31$ ps (**Table 3-1**) for 600 nm contains the ISC and the VR processes, thus both processes occur on a similar ultrafast timescale. The assignment of the stimulated emission response arising at 520 nm (**Figure 3-10**, **Figure 3-11**) remains challenging. A negatively contributing time constant of $t_2 = 4.2$ ps was determined and could be a radiative channel from occurring excited states. Its ultrafast component, $t_1 = 1.1$ ps, is slightly faster than the one observed at 600 nm and much faster than the one at 430 nm. Consequently, SE may proceed from one of these states. Ordinary $S_1 \rightarrow S_0$ fluorescence has been excluded due to the enlarged Stokes shift observed. However, phosphorescence from its respective triplet state (with a determined ISC within 1.3 ps) is on a different timescale, ranging between nanoseconds and seconds. Critically however, it is noted that an ESIPT mechanism was reported for nitrophenols^[201] and nitrobenzaldehydes.^[202] In both instances, the hydrogen interacts with the nitro-oxygen, forming a six-membered transition state and allowing for ultrafast fluorescence. Further, the freely rotating dipolar nitro group can induce TICT or intramolecular charge transfer (ICT) processes.^[201] An efficient ISC is constrained by electron-donating character, such as the methoxy substituent in **4**.^[203] Thus, the origin

of the radiative channel cannot be clearly assigned. Radiative decay from the triplet surface absorbing at 550 – 700 nm is one possibility, thanks to the ISC within 1.3 ps (Table 3-1, Figure 3-9). The emissive channel is thus depicted in dashed lines and postulated to originate from a TICT, ESIPT or a biradical triplet state. The summary of all relaxation channels is depicted in Scheme 3-4 and a Jablonski diagram drafted. Time constants can only be given as an approximated guess, based on the exponential decay functions (see e.g. Figure 3-11). The access to the *aci*-nitro tautomer via a fast and slow channel however is obvious. The luminescence channel (L) is suggested to proceed from a TICT or ESIPT state but was not confirmed.



Scheme 3-4: Jablonski diagram correlating the energy dissipation pathways of **4** after excitation. Radiative channels are shaded in its respective colour. Absorbance (A, solid blue, purple). Vibrational Relaxation (VR, dashed grey), chemical transformations (dashed orange), Excited State Absorption (ESA, solid black), Intersystem Crossing (ISC, dashed yellow), Luminescence (L, dashed green) twisted intramolecular charge transfer (TICT) or excited state intramolecular proton transfer (ESIPT). Horizontal lines indicate distinct electronic states, biradical intermediate (BR) and *aci*-nitro tautomer (*aci*-nitro).

3.3.5 Ultrafast relaxation dynamics of *o*NB acetophenone **3**

In Chapter 3.3.4, an in this work employed *o*NB molecule was studied respecting any influence of solvent and excitation wavelength. However, the decay mechanism was

only to some level revealed, since the complex molecular structure exacerbates a full analysis of its relaxation dynamics. By locking the alcohol and the benzylic hydrogen, any decoupling of the *o*NB dynamics to the nitroaromatics relaxation mechanism is of interest. For this purpose, the precursor molecule **3** (**Figure 3-2**), an acetylic nitroaromatic, was employed and exposed to identical excitation conditions ($\lambda_{\text{ex}} = 400 \text{ nm}$, $\lambda_{\text{ex}} = 325 \text{ nm}$). Since both experiments reveal similar dynamics, they are discussed simultaneously.

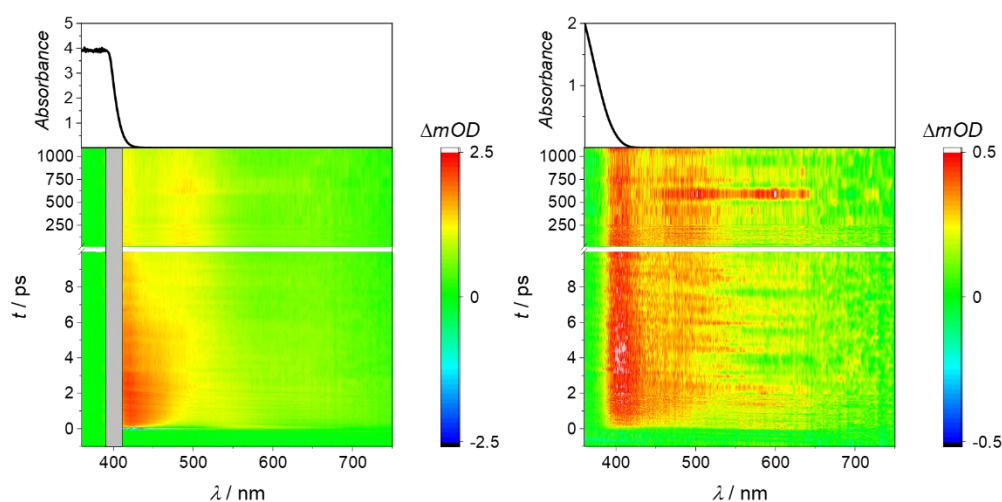


Figure 3-17: Contour plots of **3** with respective stationary UV/Vis absorption spectrum (top) in AcN. Left panel: $\lambda_{\text{ex}} = 400 \text{ nm}$, $E_{\text{ex}} = 2 \mu\text{J}$, $\lambda_{\text{probe}} = \text{supercontinuum}$, $d = 1 \text{ mm}$, $OD_{400 \text{ nm, AcN}} \sim 2.7$. Right panel: $\lambda_{\text{ex}} = 325 \text{ nm}$, $E_{\text{ex}} = 0.5 \mu\text{J}$, $\lambda_{\text{probe}} = \text{supercontinuum}$, $d = 1 \text{ mm}$, $OD_{325 \text{ nm, AcN}} \sim 0.4$. Transient response around 400 nm is neglected due to pump pulse scattering. Absorption spectra before and after the experiment are appended in **Figure S3-29**.

After excitation, absorption throughout the entire visible range is observed, as illustrated in the TA profiles in **Figure 3-17**. **Figure 3-18** depicts transient absorption spectra. After 0.5 ps, three absorption bands can be distinguished, no negative contributions are observed throughout the entire probing window. This first observation applies to both excitation wavelengths.

After excitation at 400 nm, a first approximation places maximum wavelengths of the transient absorption spectra at 430 nm, 510 nm and 640 nm, respectively. Interestingly however, the 430 nm and the 510 nm maxima seem to undergo a blueshift towards longer delay times. To investigate further, TA spectra were deconvoluted with three

gaussian functions, representing the absorption bands. **Figure 3-19** depicts the deconvolution at very short (0.5 ps) and long delay times (980 ps). The experimental spectrum was reproduced in good agreement. Indeed, the 420 nm and 520 nm response formally undergo a blue shift, shifting its maxima from 430 \rightarrow 420 nm and 510 \rightarrow 470 nm, the 640 nm response remains unaltered. The spectra obtained after 325 nm excitation depict no shift of the 410 nm maximum, a blue shift of the 460 nm maximum to 470 nm and a red shift of the 600 nm maximum to 640 nm. The low signal-to-noise ratio in the $\lambda_{\text{ex}} = 325$ nm experiment challenges any further statement. Further, all transient spectra decrease in ΔmOD within the first 10 ps but stay constant for the remaining probing window.

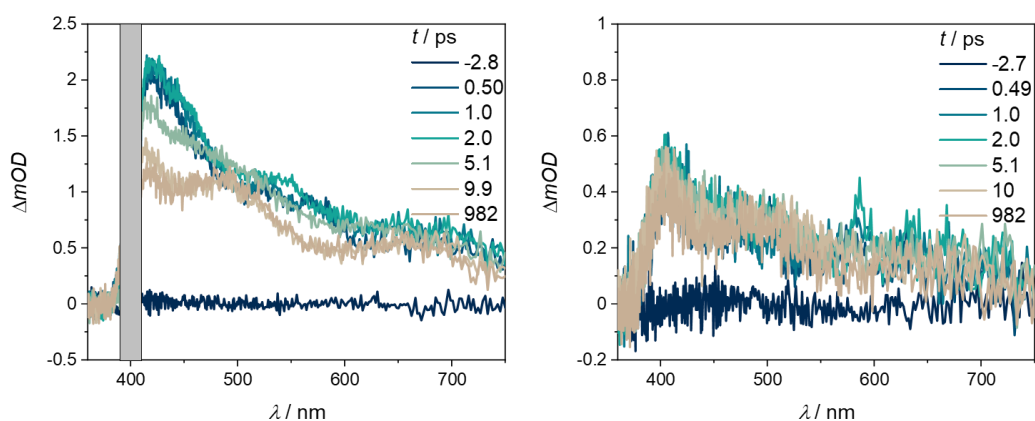


Figure 3-18: TA spectra after $\lambda_{\text{ex}} = 400$ nm (left) and $\lambda_{\text{ex}} = 325$ nm (right) in acetonitrile. Experimental parameters, refer to **Figure 3-17**.

Single transients were extracted at 430, 510 and 640 nm and tabularized in **Table 3-7**. The overall relaxation dynamics are independent of excitation wavelength; hence it is assumed that excitation leads to the population of similar electronic states to **4** but seem to decay from the first excited singlet state, denoted as S_1 . The transients are dominated by long time constants (> 1000 ps), short time constants only contribute to a smaller degree (2.3 – 34.3 ps). The opposite behaviour was observed already for **4** under comparable irradiation conditions (compare e.g. **Table 3-1**) which were dominated by short time constants. It seems that the electronic excited states populated were stabilized since all long decay constants exceed the possible delay time window.

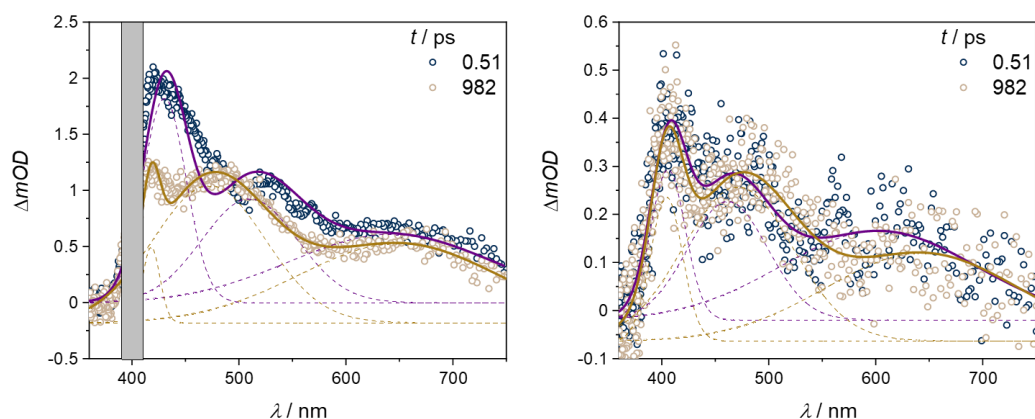


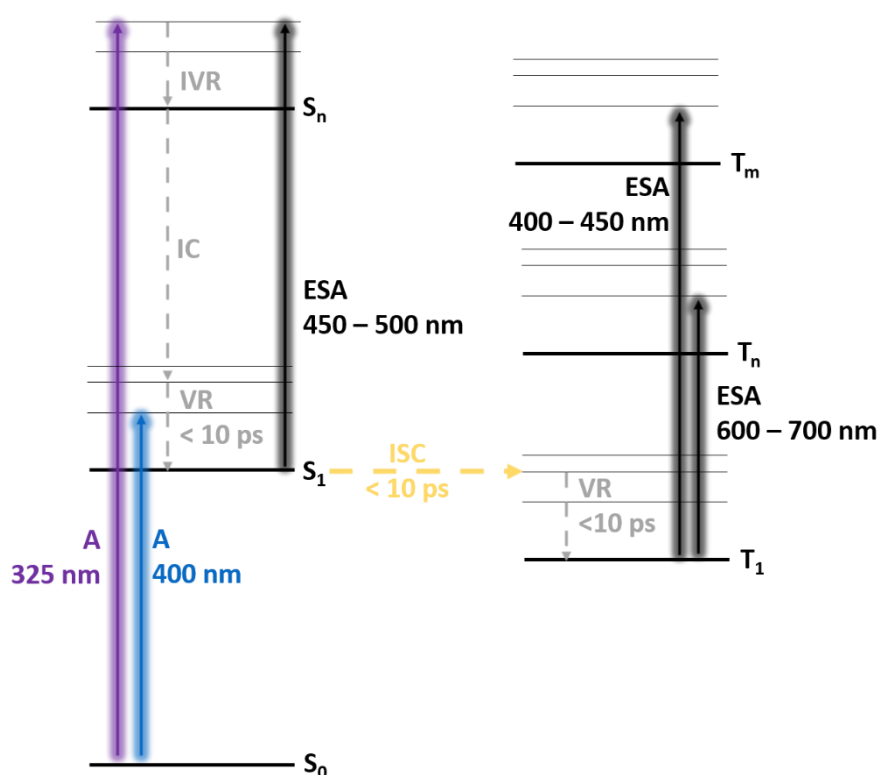
Figure 3-19: TA spectra (scattered) at 0.51 ps (purple) and 982 ps (ochre) and deconvolution with three gaussian functions (thin dashed lines). Cumulative representation is given in solid purple or ochre lines. Spectra were recorded at $\lambda_{ex} = 400$ nm (left) and $\lambda_{ex} = 325$ nm (right) in acetonitrile.

Table 3-7: Several isolated transients of the entire transient response of **3** in acetonitrile. The fits are appended in **Figure S3-30**.

λ_{ex} / nm		430 nm	510 nm	640 nm
400	A1 / 10^{-4}	11	-0.4	1.4
	t_1 / ps	6.4 ± 0.4	34 ± 54	6.4 ± 2.6
	A2 / 10^{-4}	11	11	6.3
	t_2 / ps	>1000	>1000	>1000
325	A1 / 10^{-4}	0.1	-1.1	0.2
	t_1 / ps	11 ± 54	7.7 ± 2.7	2.3 ± 7.1
	A2 / 10^{-4}	3.3	3.3	1.4
	t_2 / ps	>1000	>1000	>1000

Triplet states have been reported to occur between 400 and 450 as well as between 550 and 700 nm after UV excitation.^[199] This is consistent to the observations in **4**. Although the rise in transient absorption covers the entire spectral range, distinct ESA processes are well developed after 10 ps. Given the fact that an ISC was fulfilled in approximately 1 ps in **4**, an element must be present in **3** which cause a slower ISC process. The transient response does not decay after the first 10 ps. Compared to **4**, molecule **3** features an acetophenone-like chromophore unit. Transient absorption spectroscopy confirms the broadened response between 400 and 700 nm and attribute it to excited singlet state absorption.^[204] First and foremost luminescence was not

detected for **3**. It is stated that **3** is not able to form the critical *aci*-nitro tautomer discussed previously since such configuration would require a pentavalent carbon atom. The rising absorption band between 400-450 nm was thus assigned to a triplet state of the nitrobenzene chromophore. The acetophenone chromophore's singlet and triplet dynamic governs the entire visible range and manifests in the absorption band between 450 and 500 nm. Again, ESA between 600 and 700 nm was attributed to triplet ESA of the nitrobenzene chromophore. All relaxation channels are summarized in a Jablonski diagram and illustrated in **Scheme 3-5**.



Scheme 3-5: Jablonski diagram correlating the energy dissipation pathways of **3** after excitation. Radiative channels are shaded in its respective colour. Absorbance (A, solid blue, purple). Vibrational Relaxation (VR, dashed grey), Intramolecular vibrational redistribution (IVR, dashed grey), Excited State Absorption (ESA, solid black), Intersystem Crossing (ISC, dashed yellow). Horizontal lines indicate distinct electronic states.

After excitation into excited singlet states, a vibrational cooling period within 10 ps takes place. ISC within 10 ps then allows population of triplet states from which ESA proceed. No decay was observed; hence it is assumed that **3** does not undergo any further transformation which has been proven by studying the UV/Vis changes as well.

An overall increase in absorbance is rather related to evaporation of the solvent (**Figure S3-29**). A solvent-dependent study was not conducted.

3.3.6 Attempts for a red-shifted *o*NB reactivity plot

Although the wavelength-dependent reactivity follows an atypical shape (that is a tailing into the blue visible, **Figure 3-5**), the conversion maximum was determined to lie in the UV region. To achieve higher penetration depth at longer (blue visible) wavelengths, substantial effort was devoted to the development of red-shifted *o*NBs. Many works cover the substitution effect in *ortho* or *para* position to the nitro group as well as different leaving groups^[87] which indeed increase the degradation performance but only in the UV region. A common practice is the employment of UV light or high-intensity visible light laser for two-photon absorption.^[83] However, investigations of red-shifted *o*NB and photocleavage beyond UV light are scarcely investigated. The combination of both red shifting the molecule and achieving a higher rate of reaction was inspired by Kretshy *et al.* who reported higher absorption for sulphur substituted *o*NB's.^[205] A simple synthetic protocol involved a fluorine-thiol exchange reaction and was reported in literature.^[206] A red shift of up to 75 nm, accompanied by a higher extinction coefficient, was achieved. In the following, advances thereof are presented.

Table 3-8: Classification of molecules investigated.

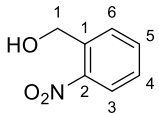
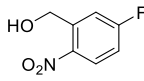
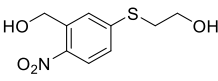
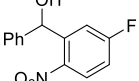
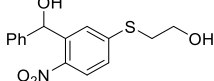
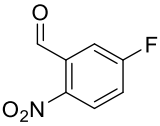
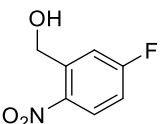
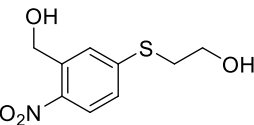
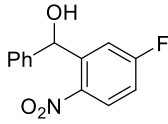
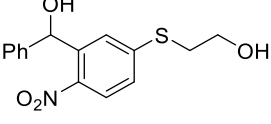
	Without donor, primary alcohol	Thioether, alcohol	primary	Without donor, secondary alcohol	Thioether, secondary alcohol
 2,5-system					

Table 3-9: Tabularized overview of chemical compounds synthesised and their names.

Investigation	Name	Structure
Starting material	2,5-H1	
	2,5-H2	
Primary alcohol	2,5-H3	
	2,5-Ph2	
Secondary alcohol, phenyl substituent	2,5-Ph3	

As depicted in **Scheme 2-3**, the general reaction is affected by many parameters. One can argue that the instability of a cleaved N=O π -bond is affected by its electron density. Consequently, this requires a donor or acceptor at the *para* position and is referred to as a ‘2,5’-system, given its aromatic position (**Table 3-8**). The herein investigated molecules are depicted in **Table 3-9** and their synthesis appended in the synthetic section (Chapter 8.5.1.5 - 8.5.1.8). Structures are confirmed by ^1H -, ^{13}C - and ^{19}F -NMR spectroscopy if appropriate (**Figure S3-31** through **Figure S3-40**). In brief, all molecular structures were synthesised according to a two-step procedure, a reduction (or Grignard) step, followed by a thiol-fluorine exchange which afforded the molecules.

First, the 2,5-primary alcohol system was investigated. Interestingly, the changes in absorptivity are significant. As depicted in **Figure 3-20**, the system **2,5-H2** does not change significantly from its precursor. Especially the lack of change in the NO_2 -absorbance region (broad absorption band around 350 nm) suggests no change in the push-pull properties. Naturally, substitution of the fluorine with a thioalkyl moiety leads to changes in absorptivity. A red shift of 76 nm was determined and accompanied by a significant rise of extinction coefficient of the Nitro absorption band

(ϵ , 1000 \rightarrow 7500 L mol⁻¹ cm⁻¹) which confirms the significance of an efficient push-pull system. UV/Vis absorption spectra of all compounds were appended in **Figure S3-41** through **Figure S3-48**. Action plot experiments of both **H2** and **H3** were performed. The wavelength window of degradation was probed to find a correlation between the existence of a push-pull configuration and molecular reactivity.

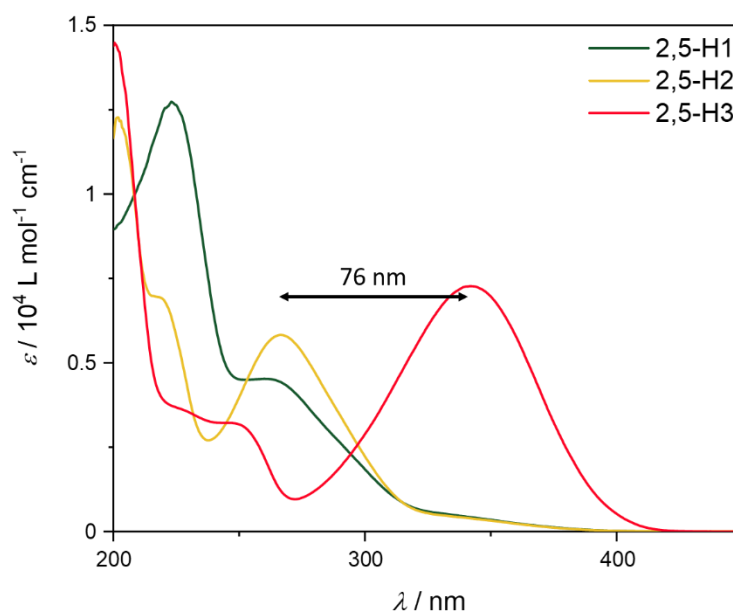


Figure 3-20: UV/Vis absorption spectra of the primary alcohol systems **2,5-H1** (green), **2,5-H2** (yellow) and **2,5-H3** (red). Spectra were recorded in acetonitrile. $d = 10$ mm.

The action plot of **2,5-H2** (experimental: Chapter 8.4.1.7) is depicted in **Figure 3-21**. Moderate degradation performance in the deep UV (~ 300 nm) is already known for *o*NB compounds and has been proven in a recent publication.^[200] However, the reactivity sharply peaks around 350 nm before subsidizing again, reaching a plateau of $\sim 2\%$ conversion at 400 nm. Interestingly, the absorptivity only tails around 350 nm but does not feature a maximum. It is critical to enhance this tailing absorption band and probe the identical wavelength window to determine a possible red shift. Surprisingly, the action plot of **2,5-H3** (**Figure 3-22**) shows a similar behaviour to the previously employed *o*NB dialcohol **4**. Instead of peaking in the UV region, a tailing behavior is observed (experimental: Chapter 8.4.1.8).

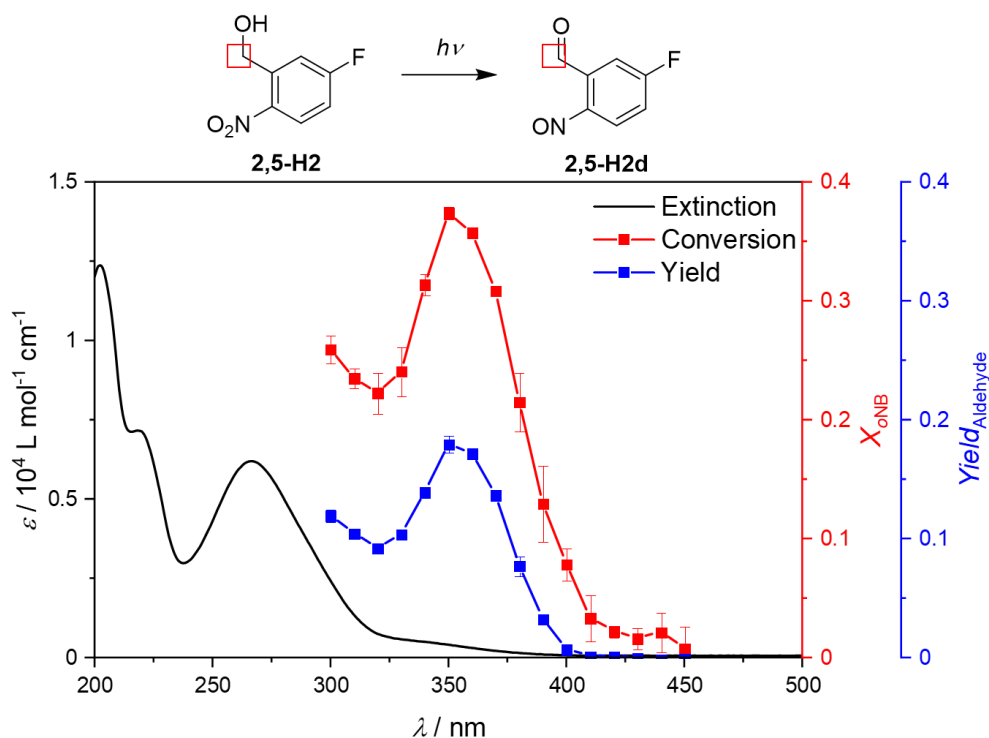


Figure 3-21: Top: Suggested degradation of **2,5-H2**. The red boxes indicate the protons investigated for determination of conversion and yield. Bottom: Action plot of **2,5-H2** measured in acetonitrile. Black solid line: absorption spectrum measured in acetonitrile ($d = 10$ mm). Red: Conversion of **2,5-H2**. Blue: Yield of **2,5-H2d**.

An atypical shape (with respect to absorptivity) and an additional shoulder in the 400 nm region is observed. This is in agreement to the previously established *o*NB-dialcohol **4**. Both molecules share a characteristic electron-donating substituent. At the *para*-position (to the nitro-group), one has to distinguish between an oxygen-atom (**4**) and a sulfur-atom (**2,5-H3**) being present. Interestingly, establishing a push-pull system, between an alkoxy or thioether substituent and the nitro group as an electron-withdrawing substituent enables a moderate degradation performance around 400 nm. The effect becomes more pronounced when sulfur is employed (compare the reactivity at 400 nm between **Figure 3-5**, **Figure 3-21** and **Figure 3-22**). Establishing a push-pull system has already been proven to amplify charge-transfer-characteristics in chromophores such as perylenes^[207] and BODIPY's.^[208] Due to the formation of a new low-lying molecular orbital, new interactions between the donor/acceptor (D/A) pair become accessible.^[209] Since a thioalkyl substituent is stronger in electron-donating strength than alkoxy substituents,^[210] introducing such motif may be beneficial for the degradation reaction of *o*NB compounds under visible light conditions. Further, the

sulfur atom additionally can induce triplet dynamics due to its heavy-atom effect. Interestingly, enhanced triplet dynamics would not be visible in the UV/Vis spectrum but observable in the reactivity plot, discrepancies are indeed well seen in **Figure 3-22**.

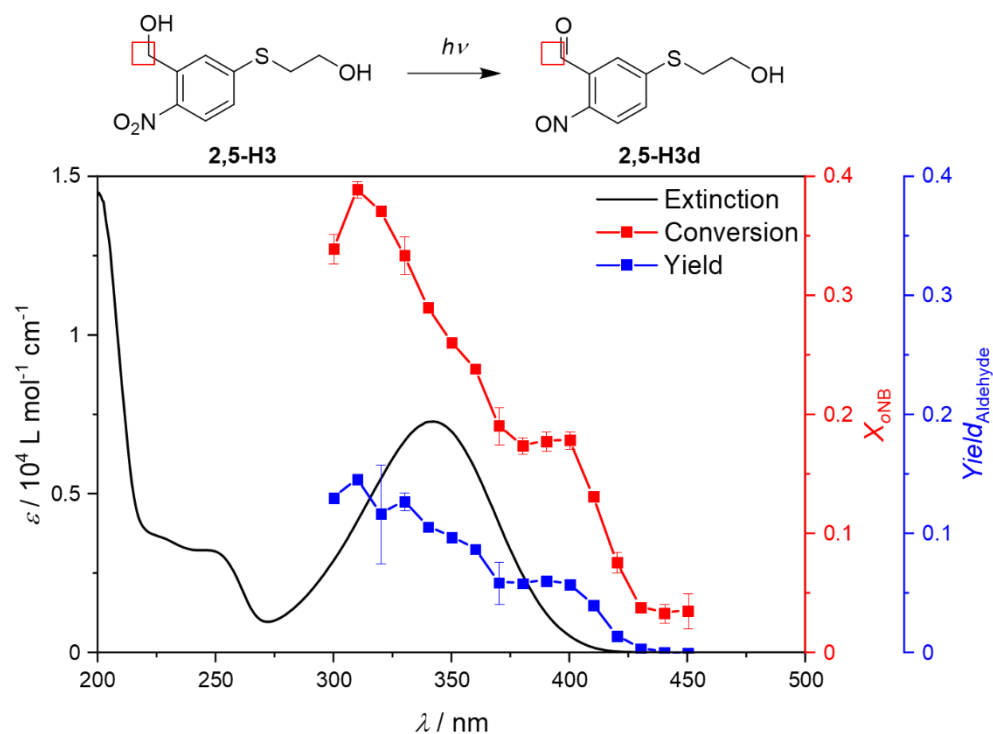


Figure 3-22: Top: Suggested degradation of **2,5-H3**. The red boxes indicate the protons investigated for determination of conversion and yield. Bottom: Action plot of **2,5-H3** measured in acetonitrile. Black solid line: absorption spectrum measured in acetonitrile ($d = 10 \text{ mm}$). Red: Conversion of **2,5-H3**. Blue: Yield of **2,5-H3d**.

Mesomeric structures with alkylic substituents at the γ -H position involve reactive radical species at terminal sites. To minimise this effect, the introduction of alkyl and aromatic systems was attempted. Such insertion can generally be achieved by Grignard reactions like phenylmagnesium bromide on the respective aldehyde site. However, the reaction with methyl magnesium bromide with nitrobenzaldehyde led predominantly to a side reaction on the nitro group. However, a phenyl ring was successfully introduced into the *o*NB structure. The synthesis of the **2,5-Ph** systems is provided in the appendix (Chapter 8.5.1.7 and 8.5.1.8). Introduction of the phenyl ring leads to a slight decrease in absorptivity of the 260 nm band (**Figure 3-23**). The differences between **2,5-H3** and **2,5-Ph3** are marginal at best, however, the extinction

coefficient of **2,5-Ph3** is higher than **2,5-H3** at the critical 350 nm absorption band. No further red-shift compared to **2,5-H3** was achieved.

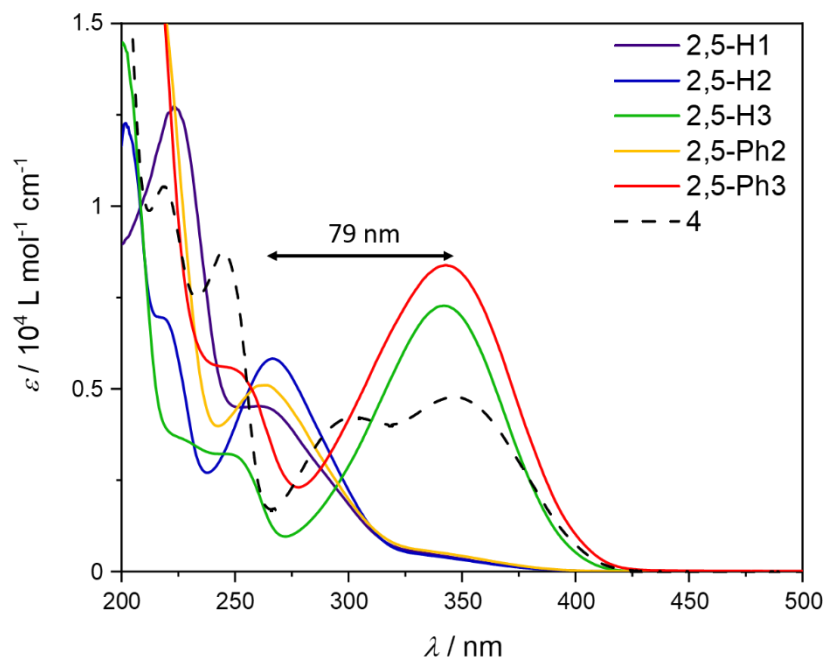


Figure 3-23: UV/Vis absorption spectra of all investigated molecules (right) in acetonitrile. $d = 10\text{mm}$. Molecular structures are listed in **Table 3-9** and **Scheme 3-2**.

The action plot of **2,5-Ph2** (**Figure 3-24**) depicts a different reactivity pattern compared to its **2,5-H2** analogon. Compared to **2,5-H2**, conversion and yield for **2,5-Ph2** diverge. This means, side reactions once again are expected. In the sub 350 nm region, yield continues to decrease while conversion increases again. However, the action plot **2,5-Ph3** (**Figure 3-25**) looks similar to the one of **2,5-H3**. Once again, tailing into 450 nm is observed but no particular reactivity maxima are pronounced. Interestingly, conversion and yield are identical which means the selectivity is almost 100%, the reaction proceeds without any side products for **2,5-Ph3**. This is in agreement to the previously established hypothesis. The incorporation of the phenyl ring was performed in order to stabilize the carbonyl-centered tertiary radical. This incorporation led to almost quantitative avoidance of side reaction.

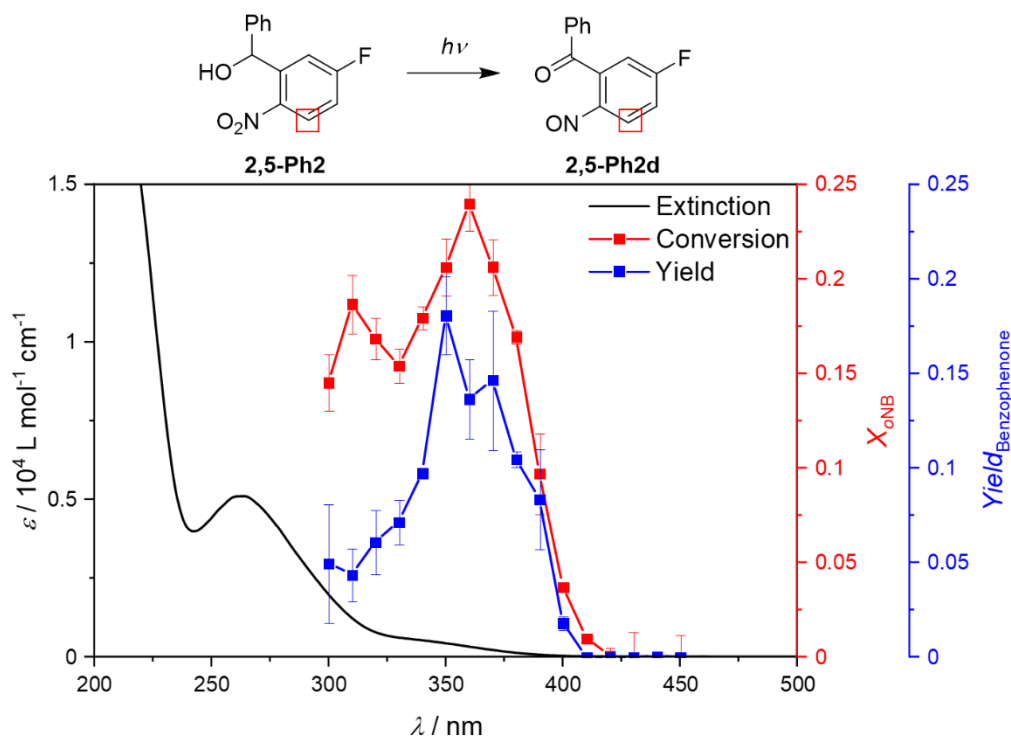


Figure 3-24: Top: Suggested degradation of **2,5-Ph2**. The red boxes indicate the protons investigated for determination of conversion and yield. Bottom: Action plot of **2,5-Ph2** measured in acetonitrile. Black solid line: absorption spectrum measured in acetonitrile ($d = 10$ mm). Red: Conversion of **2,5-Ph2**. Blue: Yield of **2,5-Ph2d**.

Figure 3-26 depicts an overarching picture of all investigated molecules. The fluorinated alcohols **2,5-H2** and **2,5-Ph2** differ in reactivity (**Figure 3-26** top) but share a similar peak at 370 nm due to a possible direct excitation of the nitro $n\pi^*$ absorption band. The phenyl derivative has a higher conversion in the probed wavelength region overall. However, all probed benzylalcohols have a somewhat significantly lower yield, compared to their conversion. This assumes a moderate selectivity ($S = X/Y$) for the intended photodegradation reaction. This general trend can be observed for all push-pull 2,5-Nitro-Sulphur configurations (**Figure 3-26** bottom). Compared to **4**, only **2,5-H3** exceeds in conversion but yield is almost identical. Further, yield and conversion only align for **2,5-Ph3** which classifies the **2,5-Ph3** degradation reaction as clean. With the 2,5-system being successfully analysed and a phenyl derivative being beneficial for the yield, the synthesis of similar structures in a 1,4-configuration was attempted. Unfortunately, no products were obtained, since the unfavorable push-pull system of 4-fluoro-2-nitrobenzaldehyde prevents any reaction at the 1 and 4 position.

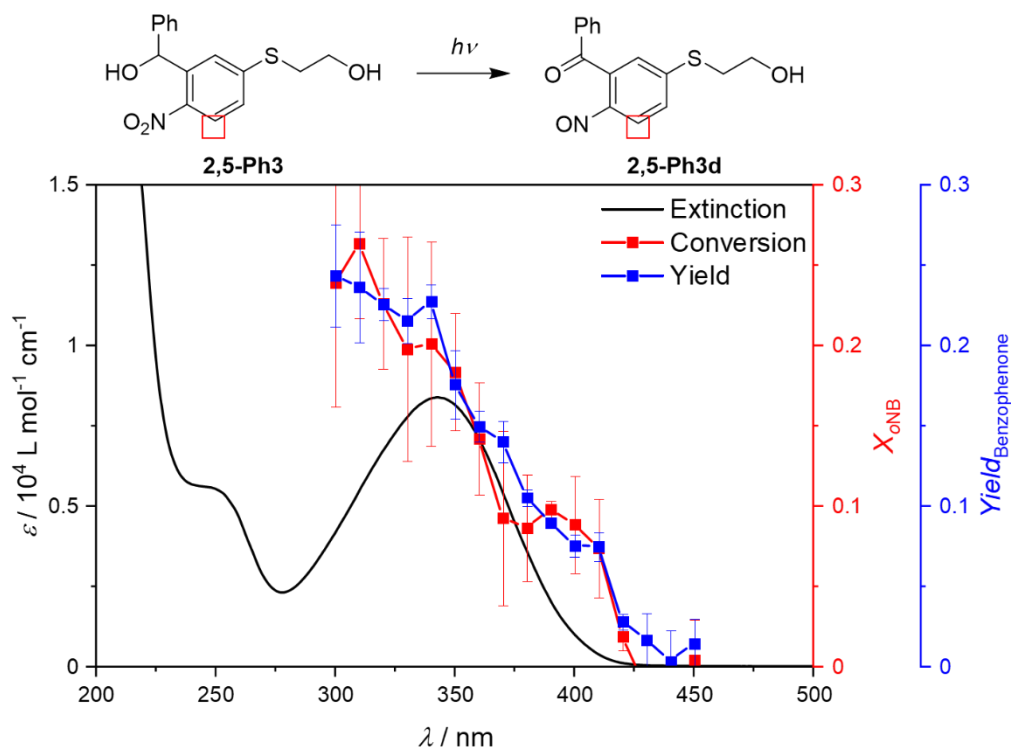


Figure 3-25: Top: Suggested degradation of **2,5-Ph3**. The red boxes indicate the protons investigated for determination of conversion and yield. Bottom: Action plot of **2,5-Ph3** measured in acetonitrile. Black solid line: absorption spectrum measured in acetonitrile ($d = 10$ mm). Red: Conversion of **2,5-Ph3**. Blue: Yield of **2,5-Ph3d**.

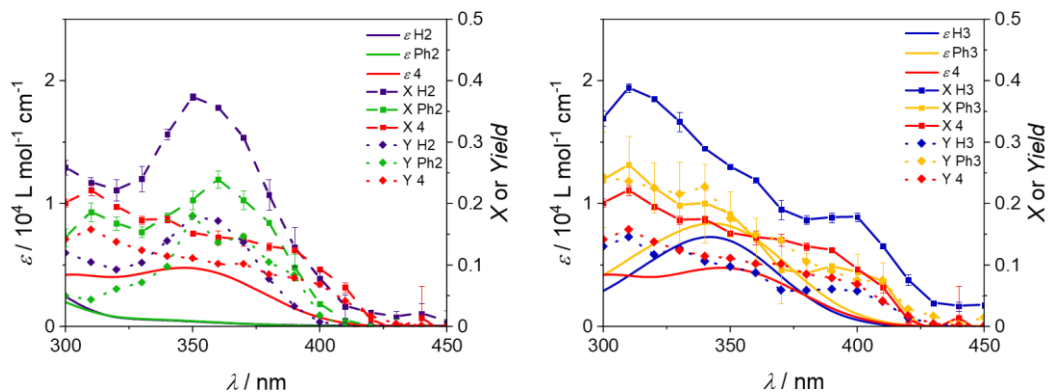
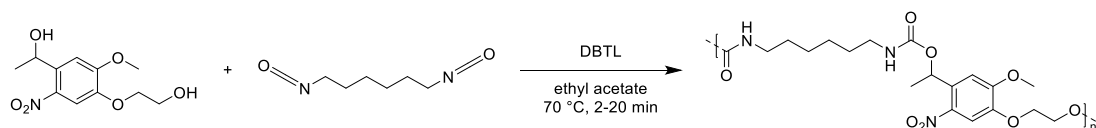


Figure 3-26: Action Plots of all compounds investigated in this chapter. Action plots were determined in acetonitrile. Solid coloured lines: extinction coefficient ϵ . Coloured Scatter-line plots: Conversion X (squares). Coloured dashed lines: Yield Y (diamonds).

3.3.7 Polymerisation of a light-degradable linker in a polycondensation reaction

The incorporation of *o*NB dialcohol **4** into polymers was naturally considered. Since two alcohol endgroups were already available, thus incorporation into a polymer

famously known for its non-degradability was attempted. Step-growth polymerisation of the *o*NB dialcohol with a diisocyanate allowed for the formation of a polyurethane (PU). The tin catalyst dibutyl tin dilaurate (DBTL) was used (**Scheme 3-6**). The addition of an equimolar amount of hexamethylene diisocyanate (HDI) and a catalytic amount of DBTL led to the formation of *o*NB-based PU after 2 to 20 min at 70 °C via a step-growth polymerisation process. Since there is no difference in stoichiometric conditions, the polymers obtained are termed according to their reaction time. The resulting polymers were initially analysed via ¹H-NMR spectroscopy. The acquired ¹H-NMR spectrum is illustrated in **Figure 3-27**. Further, full two-dimensional HSQC analysis was appended in **Figure S3-50**. Most notably, the appearance of resonances *c* and *d* confirm the successful linkage between dialcohol and diisocyanate.



Scheme 3-6: Polymerisation reaction.

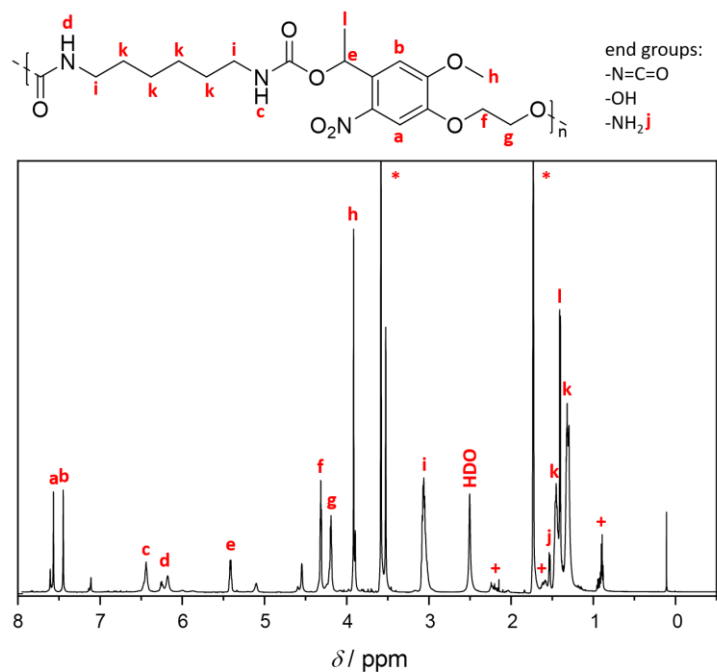


Figure 3-27: ¹H-NMR spectrum of polyurethane formed in THF-*d*₈ (*) after a reaction period of 20 minutes (see Experimental section). + marks catalyst present. Reproduced from Ref. 200 with permission from the Royal Society of Chemistry. Modified representation.

Resonance *j* suggests hydrolysis of an isocyanate terminus to an amine group (**Figure 3-27**). This would be accompanied by the release of carbon dioxide. A SEC-hyphenated mass spectrum of PU is illustrated in **Figure 3-28**.

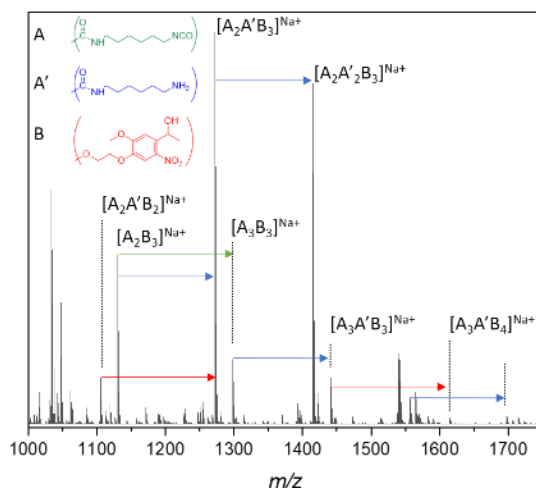


Figure 3-28: SEC-ESI mass spectra of poly(urethane-*o*NB) (20 min) averaged over retention times of single charged polymer from 18.8 to 20.6 min. The isocyanate unit ($m/z = 168.09$) is displayed in green, the hydrolysed isocyanate unit ($m/z = 142.11$) in blue and the *o*NB unit ($m/z = 257.09$) in red. Reproduced from Ref. 200 with permission from the Royal Society of Chemistry.

The successive addition of *o*NB dialcohol and hexamethyl diisocyanate can be assessed by the increase of the m/z value of 257.09 (*o*NB) and 168.09 (diisocyanate), corresponding to their respective exact masses (**Figure 3-28**). In addition, when the last monomer added is hexamethyl diisocyanate, an amine end-group has been observed. Most likely, the ESI process promotes a reaction of the isocyanate group with water, forming an unstable carbamic acid intermediate, which decomposes to an amine releasing carbon dioxide. As a result, the increase of m/z of 142.11 instead of 168.09 due to the presence of an amine instead of an isocyanate end-group (**Scheme S3-1**). The polymeric structure and successful incorporation of *o*NB have been confirmed. The shape of the obtained polyurethane polymers aligns well with expected step-growth polymerisations. Each SEC trace is a sum of Gaussian curves resulting from the successive addition of monomer units (**Figure S3-49**). 360 nm absorbance

traces were used for evaluation since the *o*NB dialcohol is photoactive in this region. With longer reaction time, the shape of polymers becomes less resolved.

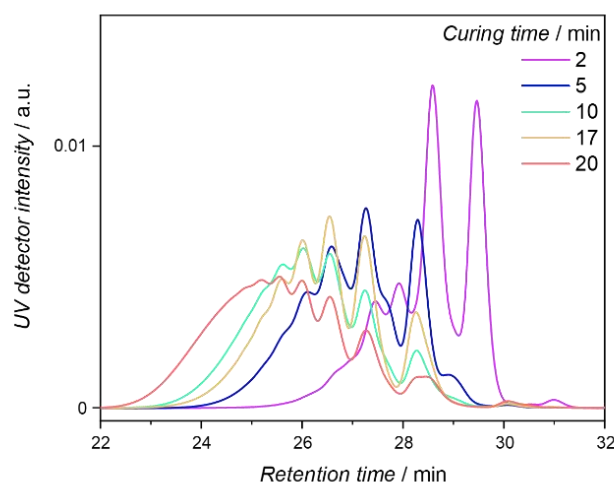
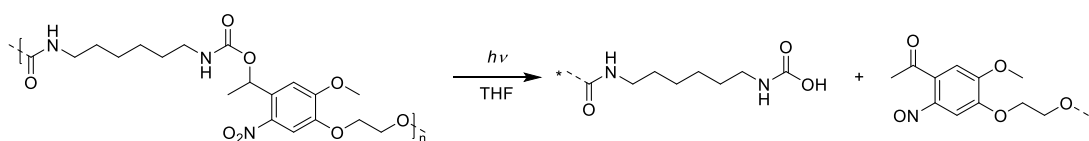


Figure 3-29. SEC traces of PUs in THF after 2 to 20 min reaction time at 70 °C. 360 nm absorbance was used for detection. Traces were normalized to the same area. Reproduced from Ref. 200 with permission from the Royal Society of Chemistry. Modified representation.

3.3.8 Depolymerisation

The here obtained polymers are exposed to irradiation conditions. Translating the findings from the small molecule study, it is suggested for **4** to form a nitrosoketone. Consequently, the leaving group features a carbamate terminus, mostly as a protonated carbamic acid. The reaction is schemed in **Scheme 3-7**.



Scheme 3-7: Degradation reaction of PUs. * mark possible sites of fractures.

LED as well as nanosecond laser light was employed to study the *o*NB dialcohol **4** on a small molecule level. Since photon doses cannot be well estimated for LED light conditions, a nanosecond laser setup was used to perform the fragmentation experiment. Briefly, a solution of polymer is exposed to a constantly rising number of photons. Then, the polymeric mixture is submitted to SEC. Pulsed-Laser-Degradation

hyphenated Size Exclusion Chromatography (PLD-SEC) enables the direct control of polymers photolysis with a precise number of photons. The degradation efficiency of the *o*NB dialcohol subsides continuously throughout the blue visible region (**Figure 3-5**), an irradiation wavelength of 365 nm was chosen in order to balance degradation efficiency and glass absorption. The photolysis experiments were performed in solution in THF, using the polymers previously synthesised (**Scheme 3-6** and **Figure 3-29**). By calculating the number of photolabile groups, the photon count was adjusted accordingly to ensure a stepwise increase of photon equivalents in each polymer. The PLD-SEC traces are depicted in **Figure 3-30**. In all polymer traces, a shift towards longer retention times (i.e. lower molecular weight) is observed. Further, the contributions high in molecular weight decrease and the contributions low in molecular weight increase. This effect is more pronounced towards polymers of higher molecular weight (compare **Figure 3-30** a) and e) for this purpose). Peaks of low molecular weight increase consistently while the broad shoulder towards the left hand side of the chromatogram decreases. The smallest fragment appears at 29.8 minutes and is of approximately 0.5 kDa which attributes well to a nitrosoketone-HDI fragment.

Thin films of PUs are supposed to bridge bulk material and solutions and are subjected to irradiation conditions. For this purpose, the photolysis of *o*NB-based PU was performed on thin films using 10 mL of a 7 mg mL⁻¹ polymer solution in dioxane or DMSO. The thickness was assessed using ellipsometry and found to be of ~10 nm (for DMSO). The photolysis of PU in thin films was assessed by performing *in situ* Quartz Crystal Microbalance (QCM) measurements employing a window module and a 365 nm light emitting diode (LED) with a constant flow of water (100 mL min⁻¹). The resonance frequency of the quartz sensor is influenced by the addition or removal of mass on or off the sensor. Indeed, the increase of averaged resonance frequencies upon light irradiation demonstrate a significant loss of material on the surface of the crystal (**Figure 3-31**). Due to an increased thickness of the dioxane spin-coated sample, a greater overall mass change was detected. In addition, X-ray photoelectron spectroscopy (XPS) was chosen to assess the chemical changes on the thin film before and after UV-irradiation (365 nm). Especially the nitrogen core level (N1s) spectrum was of high interest since the nitrogen atom of the NO₂-group is supposed to undergo significant changes but the urethane linkage has to stay intact.

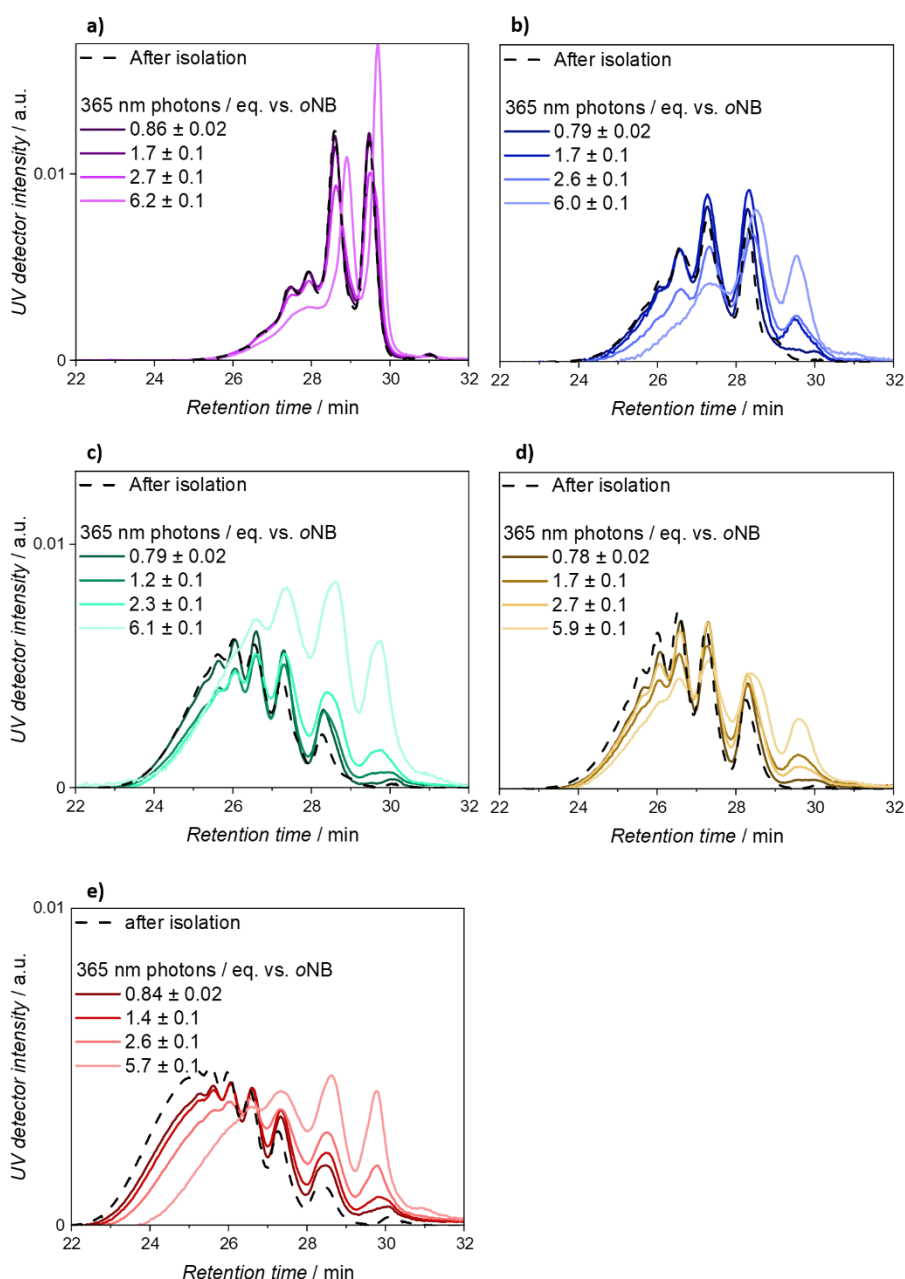


Figure 3-30: SEC traces of polymers after treatment with 365 nm photons (solid coloured lines). The polymers were allowed to form within a) two minutes, b) five minutes, c) ten minutes, d) 17 minutes, e) 20 minutes. Dashed black line resembles the isolated polymer. Reproduced from Ref. 200 with permission from the Royal Society of Chemistry. Modified representation.

The spectrum before irradiation (**Figure 3-32** black) illustrates two N1s components at 403 and 397 eV. Both components were assigned to chemical environments of NO₂ and NHR (R=C, H), respectively.^[211-212] The disappearance of the latter suggests that the urethane linkage remains intact after photolysis, given the presence of N–C bonds (397 eV) before and after both light irradiation (**Figure S3-51**, **Figure 3-32** blue). The

loss of NO₂ functions (403 eV) after photolysis however underpins photocleavage of *o*NB.

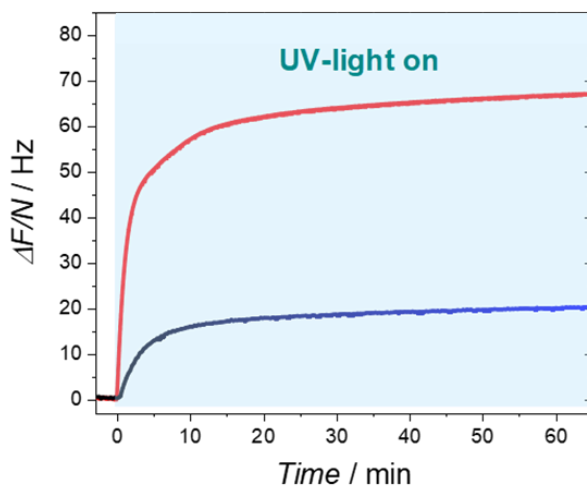


Figure 3-31: Frequency change of quartz crystal coated with 10 mL of a 7 mg mL⁻¹ polymer solution (PU-20 min) in dioxane (red) and DMSO (blue) and irradiated with a 365 nm LED from $t = 0$ min. Data obtained using a quartz crystal microbalance at 25 °C with a constant flow of water. Reproduced from Ref. 200 with permission from the Royal Society of Chemistry. Modified representation.

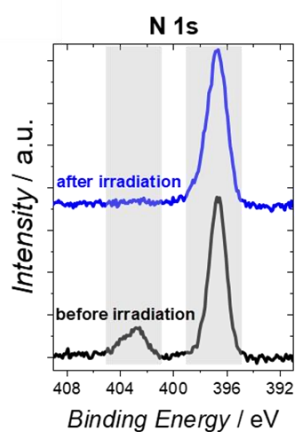


Figure 3-32: X-ray photoelectron spectroscopy of a silica slide coated with 10 mL of a 7 mg mL⁻¹ polymer solution (20 minutes cured PU) in DMSO, irradiated with a 365 nm LED and washed out with water. Wide scans are available in **Figure S3-51**. Reproduced from Ref. 200 with permission from the Royal Society of Chemistry. Modified representation.

3.4 CONCLUSION

In summary, the *o*NB functionality was explored in detail on a small molecule level. After unravelling several key features of *o*NB degradation, the relaxation dynamics of *o*NB dialcohol **4** were carefully probed and revealed identical energy dissipation pathways under $\lambda_{\text{ex}} = 400$ nm conditions than under UV light excitation. An emissive channel via an ESIPT or TICT state was found. The formation of the most prominent *aci*-nitro tautomer seems to proceed via two processes. Excitation into S_n facilitates direct transformation while excitation into S_1 is followed by generation of a biradical intermediate. The presence of such biradical intermediate has been studied via EPR methods. A detailed study on the effect of donor-acceptor configurations was conducted and revealed important insights on the stability and degradation efficiency of red-shifted *o*NB's. The formation of linear polyurethanes bearing *o*NB moieties was performed via step-growth polymerisation ensuring the presence of a cleaving point after every second monomer unit, as proven with high resolution mass spectrometry. The in-depth study of the photodegradability of the *o*NB-comonomer and linear PU in solution allowed for a better understanding of the expected chemical functions on the thin film after photolysis. The degradation of PU was successfully achieved both in solution and in thin films as proven via XPS and QCM.

Chapter 4: Chain-Length-Dependent Photolysis of *ortho*-nitrobenzyl- Centered Polymers

Parts of this chapter were adapted and reproduced with permission from J. Bachmann, C. Petit, L. Michalek, Y. Catel, E. Blasco, J. P. Blinco, A.-N. Unterreiner, C. Barner-Kowollik *ACS Macro Lett.* **2021**, *10*, 4, 447-452. Copyright 2021 American Chemical Society. The candidate conceptualized research and experimental design, performed all small molecule syntheses, performed all polymer syntheses, performed all small molecule and polymer analytical experiments, executed all light-mediated degradation experiments on a small molecule and polymer level, drafted the kinetic model, analysed and interpreted all acquired datasets, contributed to writing the initial draft and editing the original manuscript, processed revisions. Charlotte Petit assisted in all stages

4.1 ABSTRACT

Polymer chains containing *o*NB motifs seem to influence its degradation efficiency. As pointed out in Chapter 3, longer polymer chains seem to fragment more rapidly. The impact of chain length on the *o*NB degradation efficiency was questionable thus studied in the following. It is demonstrated that the photochemical cleavage of linear polymers containing a midchain photocleavable moiety strongly depends on its chain length. Based on an *ortho*-nitrobenzyl (*o*NB) difunctional RAFT agent, poly(methyl acrylate)s ($M_n = 1.59\text{--}67.6 \text{ kg mol}^{-1}$, $D = 1.3\text{--}1.4$) were synthesised in a well-defined manner. Photolysis at $\lambda_{\text{max}} = 350 \text{ nm}$ of the *ortho*-nitrobenzyl moiety led to the generation of equally sized polymer segments. The rate of *o*NB-driven polymer fragmentation, which can be well described by first-order kinetics, strongly increases with increasing molecular weight in a nonlinear fashion. Comparison to the ideal chain model shows good agreement to the experimental and suggests a possible link between entropy and degradation rate. The current chapter demonstrates a dependency of

polymer photolysis on the polymer chain length, with possible implications for photocleavable network design.

4.2 INTRODUCTION

Adaptable materials attracted much interest over the past few years.^[213-216] Such materials can undergo (de-)crosslinking and exploit reversible reactions, such as (retro-) Diels-Alder chemistry. The amount of stimuli and sophisticated chemistry has only expanded since and utilizing orthogonal chemistry gave rise to a multitude of applications, such as adaptable adhesives and self-healing materials.^[217-220] The driving force of such adaptability lies in the synergy between enthalpic and entropic contributions, which are captured by the Gibbs–Helmholtz relation, Equation 4-1.^[221]

$$\Delta_R G = \Delta_R H - T \Delta_R S \quad \text{Equation 4-1}$$

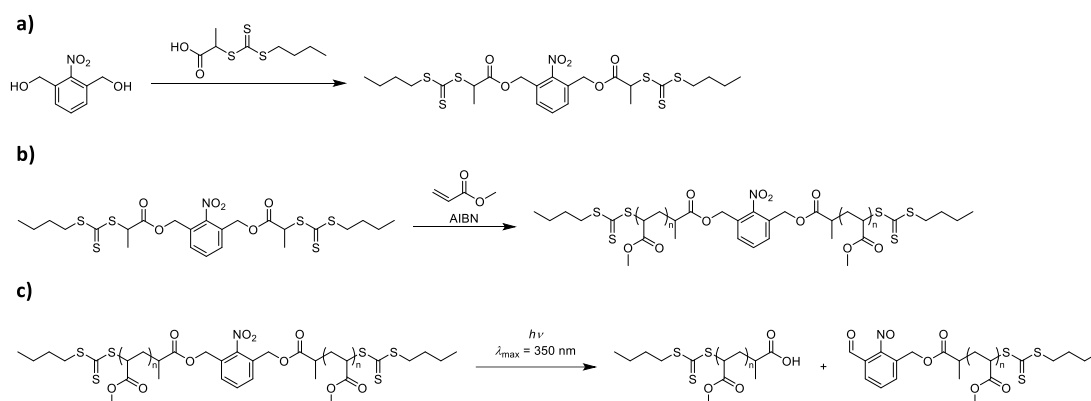
Diels-Alder chemistry is adduced once again to provide some context in the field of reversibility. Often, forward reactions are performed under ambient or mild conditions, exploiting the exothermic nature of such [4+2] cycloadditions. The reverse reaction then requires elevated temperatures. From a thermodynamic point of view, the entropic term is now favoured with rising temperature.^[222-223] Indeed, entropy has a strategic impact on designing debonding systems.^[224] In general, such (de-)bonding systems can respond to a variety of different stimuli such as light,^[225-227] heat,^[228] or pH-value.^[229-230] While emphasis is often placed on temperature-dependent (de-)bonding processes,^[231-232] little focus has been directed onto the entropy term itself. Changing the entropy gain in any isolated system will drive the Gibbs energy further into the negative ($\Delta_R G < 0$). Ultimately, entropy is the driving force in the propensity of polymers to cleave at a well-defined midchain scission point^[233-234] which has been reported in literature for thermally driven systems.^[235-236] However, the mechanisms of temperature- and photodriven cleavage differ significantly. An increase in temperature facilitates the population of higher levels of vibration and rotation, while light allows for population of electronic excited states.^[237] The impact of entropy can barely be assessed since entropy or its manifestation are not directly measurable. However, the interpretation of entropy as a macroscopic thermodynamic quantity describing the number of possible states of a system was established.^[238] Expanding this picture, it becomes understandable that mechanical stress affects the molecular

morphology. However, the influence of stress on photochemical reactivity is not fully understood.^[239] Further, as far as the author is concerned, no quantitative relationship between stress and photodegradation rate has been established yet.^[239] Interestingly, in ultrasonication-induced cleavage, a clear trend of chain length affecting the cleavage rate was also observed.^[240-241] Upon midpoint cleavage, it is critical to assess if chain length is the driving parameter for accelerated photocleavage. Literature suggests that conformational entropy or the increase of stress on the centred moiety may be responsible for this phenomenon.^[242-243] Unravelling the possibly intricate mechanism at play is beyond the scope of the current letter, which focuses on reporting an important experimental finding. To the best of the author's knowledge, there is no evidence on how chain length influences photochemical cleavage reactions in polymer systems, despite the importance of the spatial and temporal control that photosensitive units impart on degradable materials.

4.3 RESULTS AND DISCUSSION

4.3.1 Approach

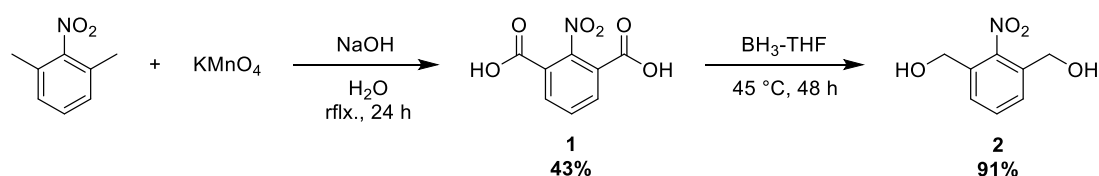
This critical gap is closed and the effects of chain length on the photolysis of poly(methyl acrylate)s containing a photolabile unit elucidated. Critically, the chain-length dependence was investigated by employing a two-arm polymer entailing a light-degradable core and a bifunctional RAFT agent for chain length control (**Scheme 4-1**). Pahnke *et al.* demonstrated in a theoretical study that the scission in the middle of molecules is entropically favoured over scission at the end.^[244] An *o*NB unit was selected as the photolabile core using alcohol groups to functionalize and further allow for incorporation into a RAFT agent. *o*NB chemistry has been widely studied over the last years and its mechanism of photolysis even explored in this thesis.^[179, 245-247] Briefly, fragmentation after light excitation will occur at the center of the polymer as the *o*NB unit undergoes a cleavage reaction, generating a nitrosobenzaldehyde and detached carboxylic acid moieties.



Scheme 4-1: Overall Strategy to evidence light-induced chain length dependent polymer cleavage. a) Synthesis of a photocleavable RAFT agent **4**. b) RAFT polymerisation with methyl acrylate. c) Irradiation of light cleavable polymers allowing fragmentation in mid chain position.

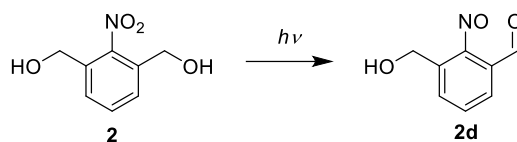
4.3.2 Probing the reactivity of the critical Bis-RAFT-degradable linker

The *o*NB core is of critical importance, as it represents the locus of photodegradation. Although cleavage of a small molecules significantly differs from polymer cleavage, the response of this functionality to light has to be initially addressed. Thus, a symmetrical *o*NB motif **2** was synthesised (**Scheme 4-2**). Synthetical protocols are appended in Chapter 8.5.2 and NMR spectra provided in **Figure S4-1-Figure S4-12**.



Scheme 4-2: Synthesis of symmetric *o*NB **2**.

Its mechanism of action was investigated in a small molecule study and the wavelength-dependent cleavage efficiency of the *o*NB unit explored. Unlike the *o*NB linker in previous Chapter 3, the here employed *o*NB unit does not feature electron donating groups, extending absorbance to the blue-visible region. The cleavage reaction is illustrated in **Scheme 4-3**.



Scheme 4-3: Degradation reaction of **2** under light exposure.

2 is converted to the nitrosobenzaldehyde **2d** under exposure to light. Indeed, the most indicative motive is the presence of aldehyde which can be monitored via $^1\text{H-NMR}$ spectroscopy. The $^1\text{H-NMR}$ spectrum before and after exposure to 340 nm light is depicted in **Figure 4-1**. Due to the symmetric structure of **2**, aromatic resonances (denoted as resonance *a*) appear as one signal around 7.6 ppm. After one hour of irradiation, this symmetry is no longer present, and several resonances appear around this region (*e*). Naturally, the aldehyde resonance *d* (10 ppm) and a disappearance of alcoholic protons was observed and indicate a conversion to the proposed nitrosobenzaldehyde structure **2d** but show further decomposition to unidentifiable byproducts as well.

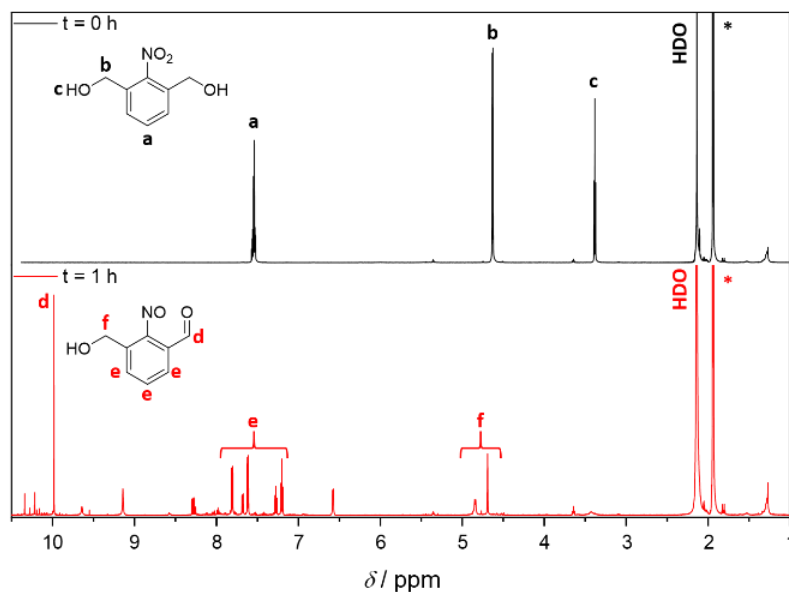


Figure 4-1: $^1\text{H-NMR}$ spectra of sample **2** in acetonitrile- d_3 before (black) and after (red) irradiation. $\lambda = 340$ nm, $U = 4.2$ V, $I = 0.25$ A, $dist = 0.5$ cm. Reprinted with permission from J. Bachmann *et al.* *ACS Macro Lett.* **2021**, *10*, 4, 447-452. Copyright 2021 American Chemical Society. Modified representation.

The UV/Vis absorption spectrum of **2** (**Figure 4-2**) reveals only a minor absorption feature centred at 257 nm with a molar extinction coefficient of $(1601 \pm 6) \text{ L mol}^{-1} \text{ cm}^{-1}$ in acetonitrile (**Figure S4-13**, **Figure S4-14**). Further extinction shows continuous tailing until 400 nm with a broadened shoulder at 350 nm and with an extinction coefficient of $(225.1 \pm 2.5) \text{ L mol}^{-1} \text{ cm}^{-1}$. After irradiation, a rise of an absorption band at around 340 nm is observed, confirming a characteristic absorption band of nitrosoaromatic compounds.^[248] It has been previously established that in many cases the UV/Vis spectrum of a given photoreactive compound is of limited value in predicting its reactivity.^[120, 249] As the highest conversion of *o*NB cleavage is preferred, an action plot of **2** (**Figure 4-3**) was generated.^[185] The full action plot analysis is included in the experimental procedures (Chapter 8.4.2.3) as well as the appendix (**Figure S4-16**).

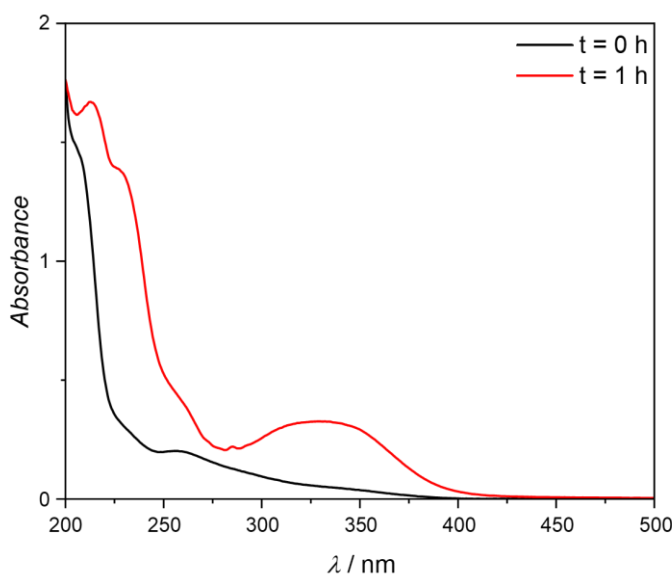


Figure 4-2: UV/Vis spectra of irradiated sample **2** in acetonitrile-*d*₃ before (black) and after (red) irradiation. $\lambda = 340 \text{ nm}$, $U = 4.2 \text{ V}$, $I = 0.25 \text{ A}$, $dist = 0.5 \text{ cm}$, $d = 10 \text{ mm}$. Reprinted with permission from J. Bachmann *et al.* *ACS Macro Lett.* **2021**, *10*, 4, 447-452. Copyright 2021 American Chemical Society. Modified representation.

Interestingly, the conversion pattern does not follow extinction of **2**, but instead peaks close to 360 nm before subsiding again until 400 nm (**Figure 4-3**). The action plot is instructive for selecting the optimum wavelength, which is in the 350 to 360 nm region

and is conveniently afforded as the maximum emission wavelength by the employed photoreactor (**Figure S4-15**). Interestingly, conversion and yield do match in their general trend but yield reaches 50% of the conversion value. The selectivity towards **2d** seems to be limited, and side reactions must be considered.

As an action plot is only distinctive for wavelength dependent response and brief light exposures, prolonged irradiation of **2** was undertaken to monitor the efficient conversion to the suggested aldehyde **2d**. As depicted in **Figure 4-2**, the degradation leads to a rise in absorbance around 350 nm. This results in an internal filter effect, preventing light to pass through absorbing layers efficiently. A reaction yield, the quotient of moles product and photons deposited can be calculated for brief irradiation times. As depicted in **Figure 4-4**, deviation from linear behaviour already at brief exposure times are observed, and thus, the reaction quantum yield estimated only for small photon numbers. The quantum yield of the photolysis reaction was determined to an upper limit of $\phi_{2 \rightarrow 2d} = (1.75 \pm 0.05)\%$ (**Table 8-9** and **Figure 4-4**) in acetonitrile- d_3 .

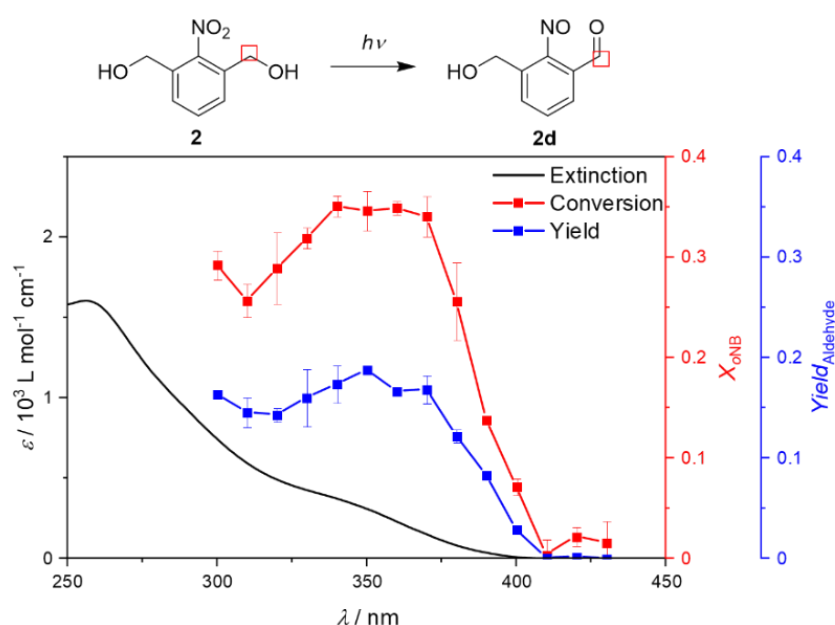


Figure 4-3: Top: Photodegradation of **2** leading to the nitrosobenzaldehyde **2d**. Bottom: Action plot of **2** in acetonitrile- d_3 showing the Conversion X_2 (red) and Yield Y_{2d} (blue). Reprinted with permission from J. Bachmann *et al.* *ACS Macro Lett.* **2021**, *10*, 4, 447-452. Copyright 2021 American Chemical Society. Modified representation.

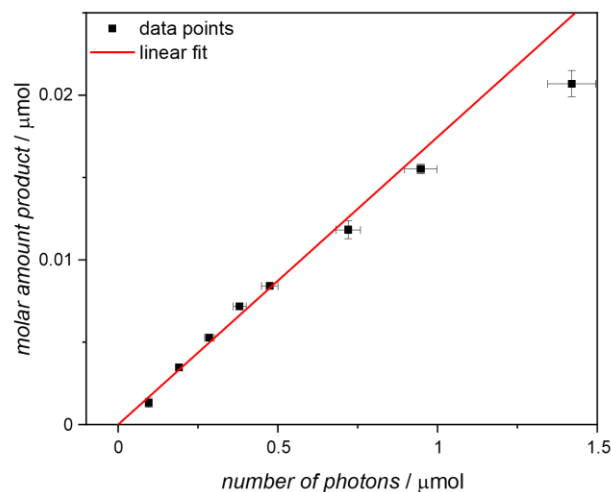
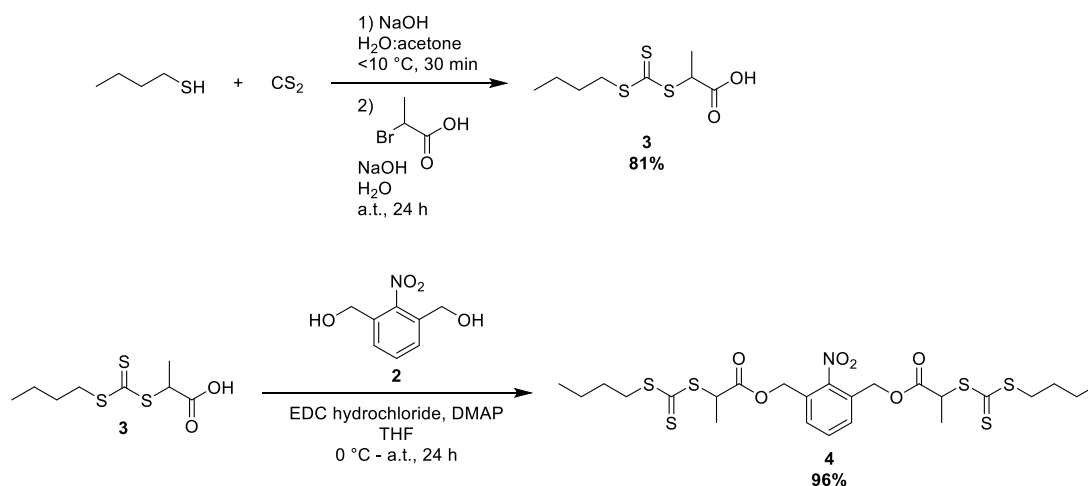


Figure 4-4: Plot of molar amount of photoproduct **2d** versus the number of incident photons. The linear fit (red) describes the experimental data well, but deviation at prolonged exposure can be observed. The intercept of the fit was set to zero. Reprinted with permission from J. Bachmann *et al.* *ACS Macro Lett.* **2021**, *10*, 4, 447-452. Copyright 2021 American Chemical Society. Modified representation.

4.3.3 Incorporation via RAFT polymerisation

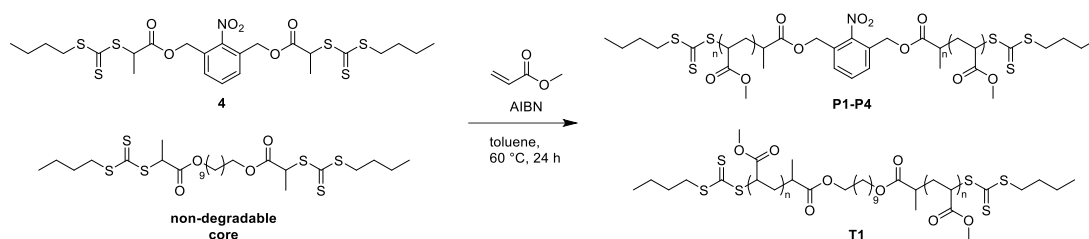
A two-arm RAFT core with a degradable *o*NB moiety (**4**) was synthesised from the previously investigated **2** (Scheme 4-4).



Scheme 4-4: Synthesis of RAFT agent **4**.

Additionally, a non-degradable RAFT agent starting from decanediol was synthesised in a similar fashion. The synthetic protocols and analyses of the RAFT agents are

appended in Chapter 8.5.2. RAFT polymerisation exploiting **4** was found to give a wide range of number average molecular weights (ranging from 1.6 to 68 kg mol⁻¹). **Scheme 4-5** depicts the reaction scheme starting from the two RAFT agents. To minimize biradical coupling during the polymerisation process, methyl acrylate (MA) was used as a fast-propagating monomer.^[153, 250] In addition, the polymerisation was performed at high dilution conditions with low equivalents of initiator (0.01 equiv.) and at low temperature (60 °C), affording **P1–P4**. Four polymers were prepared with weight- average molecular weights ranging from 1.6 to 68 kg mol⁻¹ (**Table 4-1**, **Figure 4-5**) in good dispersity ($\mathcal{D} = 1.21 - 1.44$).



Scheme 4-5: Two-arm RAFT polymerisation.

Table 4-1: Molecular data of the polymers **T1** and **P1–P4**.

Entry	M_n / kg mol ⁻¹	M_w / kg mol ⁻¹	\mathcal{D}	Core
T1	22.6	27.2	1.21	Decane
P1	1.59	2.29	1.44	<i>o</i> NB
P2	3.12	3.96	1.27	<i>o</i> NB
P3	10.5	14.0	1.33	<i>o</i> NB
P4	67.6	91.8	1.36	<i>o</i> NB

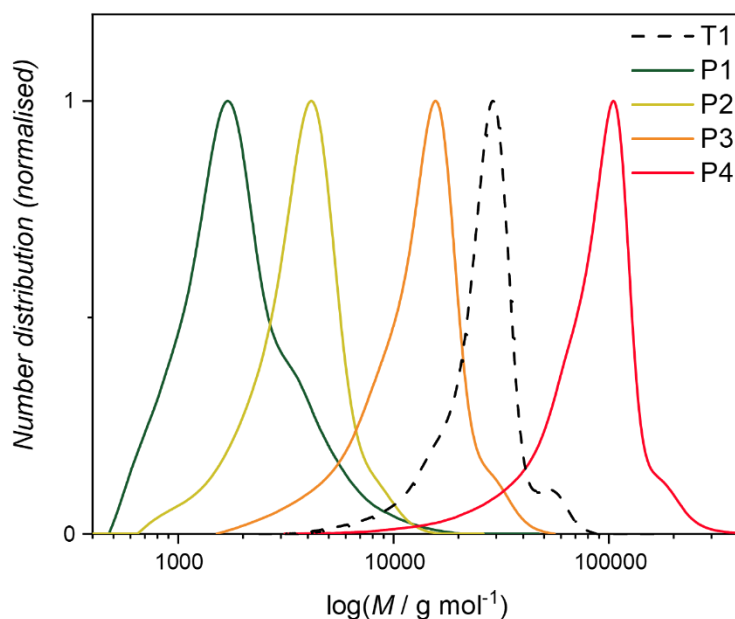


Figure 4-5: Molecular weight distributions of **T1** and **P1** to **P4** in DMAc. Molecular weight averages and polydispersity indices are collated in **Table 4-1**. Reprinted with permission from J. Bachmann *et al.* *ACS Macro Lett.* **2021**, *10*, 4, 447-452. Copyright 2021 American Chemical Society. Modified representation.

Although the polymer synthesis was carefully conducted, one will notice minor contributions of fragment species which occurred during polymerisation. This was confirmed via SEC-ESI-MS (**Figure S4-30**–**Figure S4-32**). Further, a control polymer (**T1**) with a nondegradable decane chain as a core, was synthesised (**Table 8-30**) to investigate the influence of solvent and possible ester hydrolysis in the system (**Scheme S4-3**). In order to assess solvent and general light stability, control experiments for **P1**–**P4** were conducted, as it is well-known that ester bonds can undergo hydrolysis, which may lead to bond cleavage within the RAFT agent. The stability of the ester bonds toward light irradiation and the stability of the *o*NB moiety in the employed solvent were assessed. Control polymer **T1** was irradiated for 4 h under UV-A light in dimethylacetamide (DMAc). The resulting traces obtained via size exclusion chromatography before and after irradiation of **T1** are displayed in **Figure 4-6** and show no significant change, thus suggesting the absence of photolysis of the ester bond. Although the general refractive response decreases throughout the chromatogram, no secondary species appears. In addition, the stability of an *o*NB bearing polymer (**P4**) in DMAc was monitored via SEC over the course of 216 h

(**Figure 4-6**). As for **T1**, no changes in SEC traces are observed, confirming the overall stability of the polymers in DMAc.

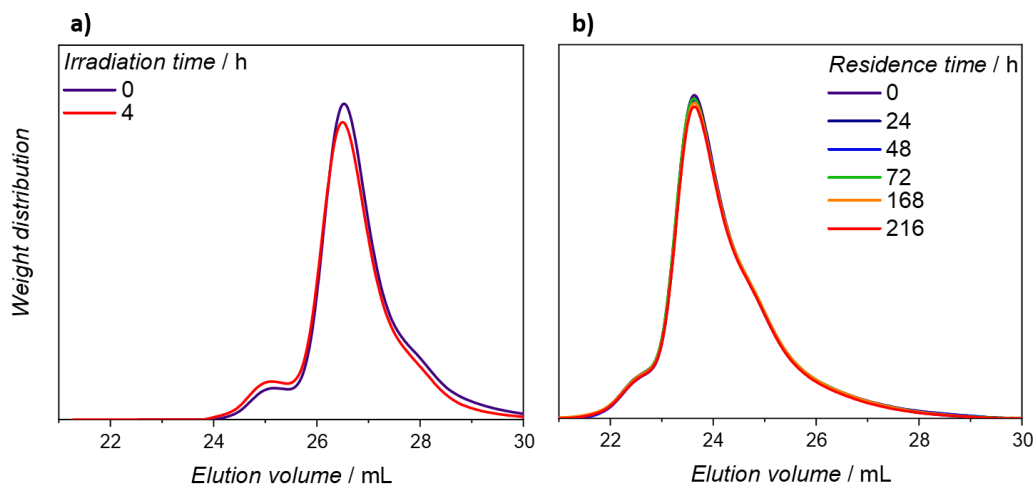
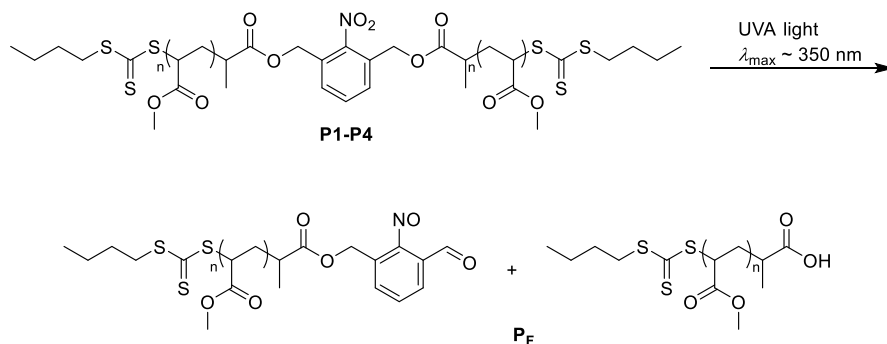


Figure 4-6: a) SEC traces of **T1** before and after irradiation (UV-A) in DMAc. b) SEC traces of **P4** at different residence times in DMAc. Reprinted with permission from J. Bachmann *et al. ACS Macro Lett.* **2021**, *10*, 4, 447-452. Copyright 2021 American Chemical Society. Modified representation.

4.3.4 Photolysis of *o*NB-centered polymers and modelling

Subsequently, photolysis of the degradable polymers **P1–P4** was performed using a photoreactor setup equipped with UV-A lamps (**Figure 8-2**, **Figure 8-3**). The formation of poly(methyl acrylate) fragments via a Norrish type II photoreaction generated two fragments with a nitrosobenzaldehyde and pending carboxylic acid termini (**Scheme 4-6**).



Scheme 4-6: Fragmentation reaction.

Exemplarily, polymer **P4** was analysed to establish the analytical procedure, while further analytical details on the other polymers can be found in the appendix (**Figure S4-19** through **Figure S4-22**, **Table 8-10** through **Table 8-13**).

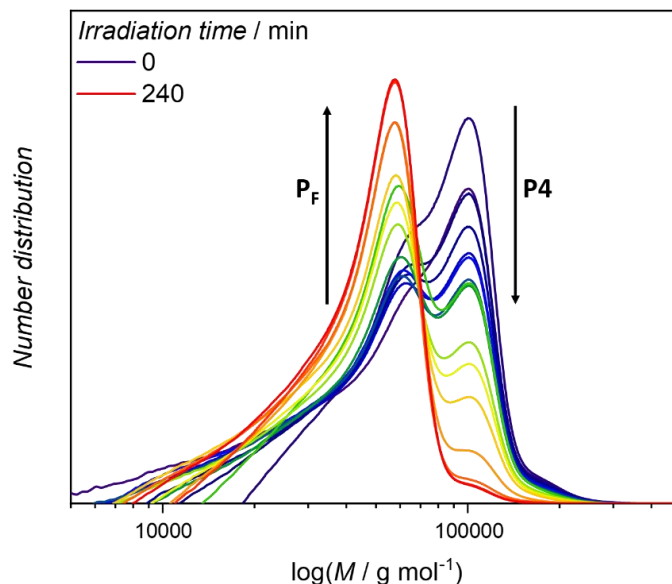


Figure 4-7: Evolution of number distribution of **P4** during irradiation in DMAc. The decrease of the species with higher molecular weight and the increase of the species of lower molecular weight is noted. Reprinted with permission from J. Bachmann *et al.* *ACS Macro Lett.* **2021**, *10*, 4, 447-452. Copyright 2021 American Chemical Society. Modified representation.

As illustrated in **Figure 4-7**, a monomodal parent polymer (dark blue trace, right hand side) rapidly fragments under light irradiation. A rise of a second species is observed and a bimodal shape in the SEC traces is noted. The rise appears at approximately half the initial molecular weight. Following the evolution of the molecular weight distribution (**Figure 4-7**) over time allows for the tracking of the scission of the parent polymer into fragments of half the original weight, until the ratio parent/fragment is constant. The presence of fragment species was confirmed via size-exclusion hyphenated electrospray ionization mass spectrometry (SEC-ESI-MS) (**Figure S4-30**-**Figure S4-32**, **Scheme S4-5**, **Table S4-1**-**Table S4-3**).

Due to convolution, the exact molecular weight is challenging to assess. Extracting the area evolution of parental and fragment was performed by assuming a bimodal Lorentzian behaviour. It was found that a convolution of Gaussian did not represent

the experimental data in sufficient accuracy. The deconvolutional analysis is illustrated in **Figure 4-8 a)**, exemplarily for an irradiation increment of 150 seconds.

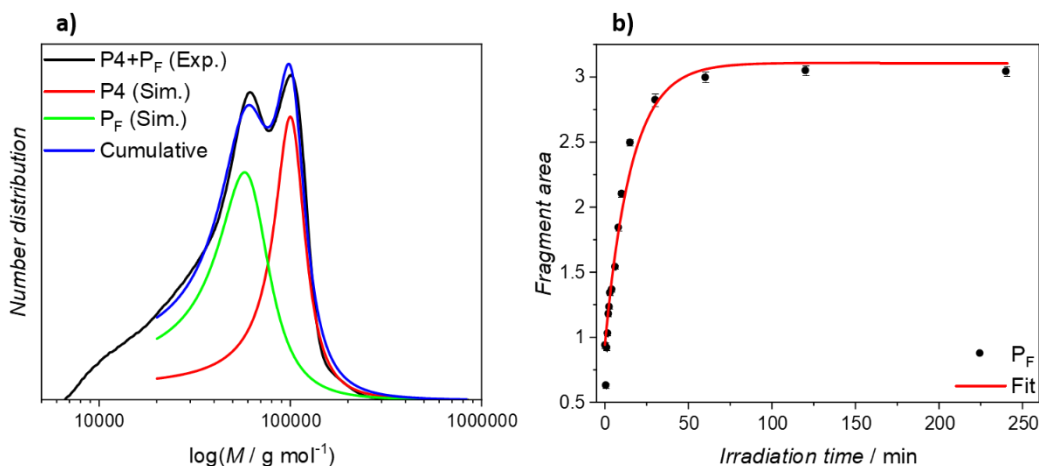


Figure 4-8: a) Exemplarily deconvolutional analysis of **P4** after 2.5 min of UV-A irradiation. Depicted are the experimental (black), and deconvoluted Lorentzian functions of assigned **P4** (red) and **P_F** (green). The cumulative trace is indicated in blue colour. b) Evolution of area of **P_F** during UV-A irradiation in DMAc for the full irradiation period. The fit described in the text is coloured in red. Reprinted with permission from J. Bachmann *et al.* *ACS Macro Lett.* **2021**, *10*, 4, 447-452. Copyright 2021 American Chemical Society. Modified representation.

Two Lorentzian functions were found to represent the experimental trace in good agreement (**Figure 4-8**). The evolution of the fragment area versus irradiation time gives access to the kinetic analysis (**Figure 4-8 b**). The decay for the parent polymer appears to follow first-order kinetics, which was further enhanced by a compensation of mass expression due to the presence of a fragment in the initial sample at t_0 . The rate law used states Equation 8-21 and its derivation is appended in Chapter 8.4.2.6

$$[F](t) = d \cdot \left[-[P]_{t=t_0} \cdot \left[\exp(-k_{app}t) - 1 \right] \right] + [F]_{t=t_0} \quad \text{Equation 8-21}$$

The area of each Lorentzian shape is easily accessible and it is assumed to relate to the concentration of each species, denoted as i.e. $[F](t)$. The fragment area $[F](t)$ is plotted against the irradiation time t , and k_{app} obtained. Such a plot is exemplarily depicted in **Figure 4-8 b**. The fit obtained based on a first-order rate law equation (Equation 8-21) and represents the experimental data in good agreement for the irradiation period.

Photolysis of the polymers **P1–P4** was conducted in the same fashion as described above and their kinetics of degradation were compared.

It is noted that the area of polymer species is a function of its molecular weight which limits a comparison of absolute values such as $[F](t)$. Thus, the relative fragment abundance, $RFA = \frac{[F]}{[F]+[P]}$ is introduced, with $[F]$ and $[P]$ being the areas of the fragment P_F and parent polymer, respectively (**Table 8-10-Table 8-13**).

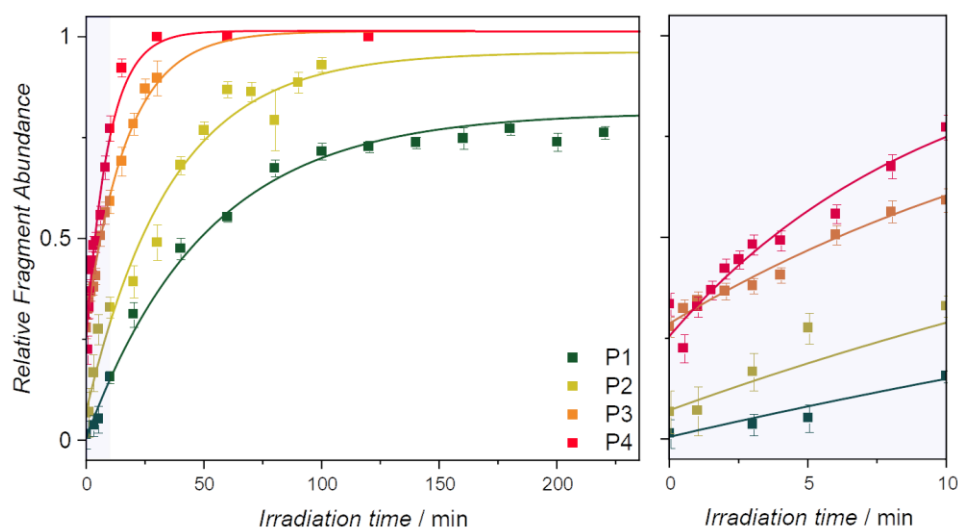


Figure 4-9: Relative fragment area evolution of **P1** to **P4** under UV-A irradiation in DMAc. The shaded zoom shows the evolution over the first 10 minutes. The solid lines are to guide the eye and do not represent the first-order decay. Reprinted with permission from J. Bachmann *et al. ACS Macro Lett.* **2021**, *10*, 4, 447-452. Copyright 2021 American Chemical Society. Modified representation.

Figure 4-9 shows the evolution of RFA for all polymers. All polymers but **P1** reach almost unity ($RFA = 1$) after the irradiation period. Indeed, parental **P1** polymer is still present in the irradiated mixture after 4h, according to deconvolutional analysis. Interestingly, the degradation of **P2** and **P3** reaches unity after 70 and 200 minutes, respectively, while **P4** cleaves completely within the first 30 minutes. This early observation suggests that *o*NB-centered polymers cleave faster with increasing molecular weight.

The apparent rate coefficients for photolysis k_{apparent} were plotted against the respective number-average molecular weights of the investigated polymer, as depicted in **Figure 4-10**.

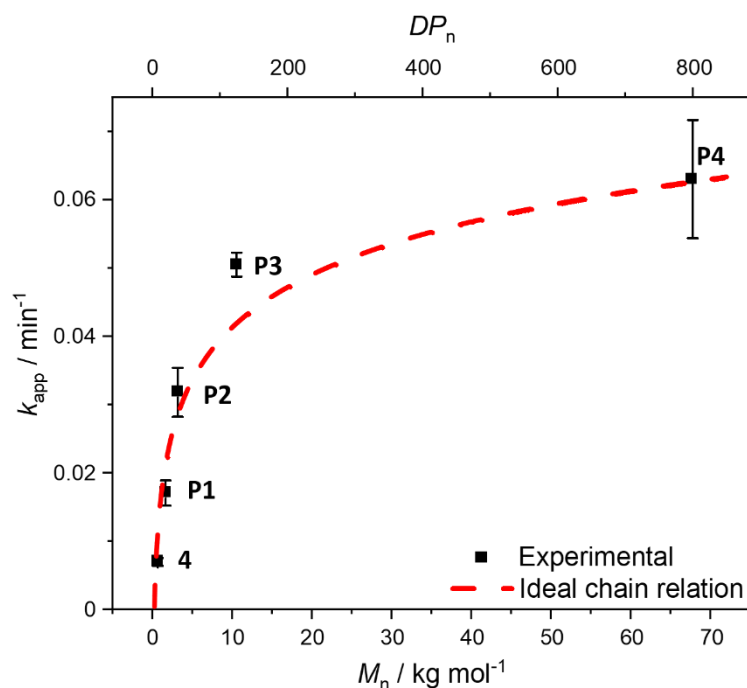


Figure 4-10: Evolution of apparent rate coefficient k_{apparent} for a first order decay versus the experimental M_n for the polymers **P1-P4** (2.0 mg mL^{-1}). The fit result for the small molecule **4** was added. It is noted that k_{app} for **4** was not determined via deconvolutional SEC analysis but via $^1\text{H-NMR}$ spectroscopy ($\text{DMSO-}d_6$) instead. Reprinted with permission from J. Bachmann *et al.* *ACS Macro Lett.* **2021**, *10*, 4, 447-452. Copyright 2021 American Chemical Society. Modified representation.

Interestingly, for the lowest molecular weights, the rate coefficient increases rapidly until it reaches a plateau for higher M_n ($> 30 \text{ kg mol}^{-1}$). As noted earlier in this chapter, an entropically driven increase in the rate coefficient k_{apparent} is a potential explanation for an accelerated degradation of larger polymer chains. In a simple comparative fashion, the determined apparent rate coefficients were fitted with a logarithmic relation on the degree of polymerisation, DP_n , in order to explore a possible proportionality toward the entropy of an ideal chain (**Figure 4-10**, red dashed line, further details: Chapter 8.4.2.8). The entropy of an ideal chain increases logarithmically with the probability density function, which is proportional to the

length of a polymer chain. Indeed, the displayed proportionality of the degree of polymerisation can be readily observed, however, the model only applies under ideal conditions. The logarithmic increase of entropy with DP_n seems to follow a similar scaling evolution as the rise of k_{apparent} with increasing molecular weight. The small molecule **4** with a DP_n of zero fits into this model (**Figure 4-10**) in excellent agreement. It is however noted that k_{apparent} of **4** has been determined with $^1\text{H-NMR}$ spectroscopy (**Figure S4-17**).

It is important to note that all degradation experiments were conducted in an equal mass concentration of 2.0 mg mL^{-1} . This naturally lowers the concentration of available *o*NB groups to undergo cleavage. An internal filter effect was observed earlier in this chapter with a rise of absorbance during photodegradation of small molecule **2** (refer to e.g. **Figure 4-2**). Several concentration dependent irradiation experiments were conducted and no clear tendency towards a concentration effect was observed (**Figure S4-23-Figure S4-28, Table 8-14-Table 8-19**).

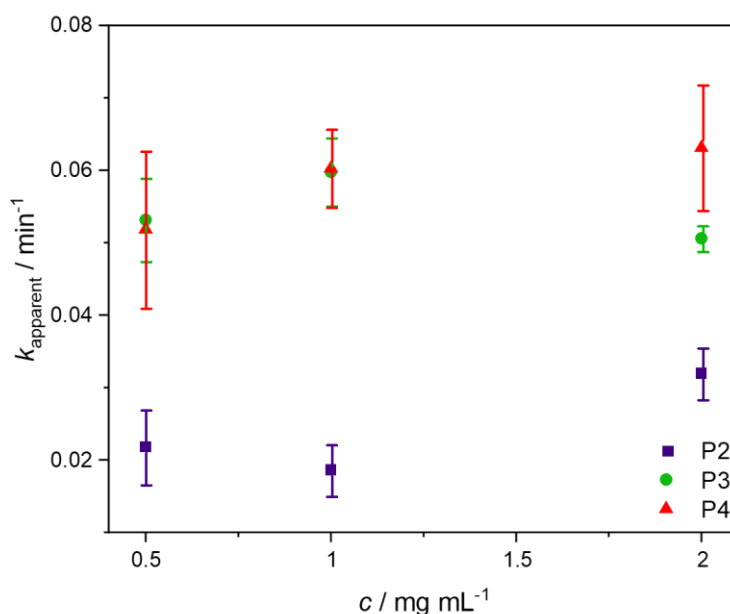


Figure 4-11: Obtained k_{apparent} for **P2-P4** versus the used mass concentrations. Note that the values for 2.0 mg mL^{-1} have been derived from **Figure S4-19-Figure S4-22**. Reprinted with permission from J. Bachmann *et al. ACS Macro Lett.* **2021**, *10*, 4, 447-452. Copyright 2021 American Chemical Society.

4.4 CONCLUSION

Experimental insight into a chain length effect in photodriven cleavage reactions was provided. The photolabile motif, the symmetric *o*NB dialcohol **2** was subjected to a thorough degradation study. It was found that **2** undergoes photolysis most efficiently at UV-A irradiation wavelengths. Transformation into a RAFT agent and subsequent two-arm polymerisation with methyl acrylate afforded a wide range of polymers. All polymers were subjected to UV-A irradiation conditions and their SEC traces deconvoluted. It was demonstrated that increasing the chain length of polymers carrying a midchain photocleavable unit leads to faster photolysis. It is thus to some extent comparable to heat-responsive reversible systems earlier reported, where the chain-length-dependent scission propensity has been shown experimentally and on a quantum chemical basis.^[234, 244] The cleavage rate rises nonlinearly with the chain length and may be directly correlated to entropic contributions as deduced with the ideal chain relation. Mechanical stress, i.e. the weakening of the critical ester bond might lead to one manifestation of entropy. Alternatively, the number of accessible microstates (of conformation), i.e. the interpretation of entropy as a degree of disorder may also be responsible for this trend. The terminology ‘conformational entropy’ can be used to describe this phenomenon. Its manifestation however, i.e. mechanical stress or its interpretation in statistics, cannot be further elucidated. Still, these findings are critical for the design and future advances of photolabile networks in which the segment lengths between the photocleavable functions constituting the network may have a significant influence on the network degradation kinetics.

Chapter 5: Peroxide-accelerated photodegradation of tetrazine- bearing thiol-acrylate polymers via green light

5.1 ABSTRACT

A tetrazine-diacrylate was synthesised and photoinitiated degradation was investigated both on the small molecule and on a polymeric system when incorporated via crosslinking. It was found that tetrazines prevent the polymer backbone from undergoing degradation under oxidative conditions but facilitated the rapid degradation under green light irradiation conditions. Hereby, the main chain undergoes ring-opening of the tetrazine motives, allowing for a nitrogen-oxygen exchange reaction. The main chain is still intact but significantly oxidised in the process. Further, the thiol-acrylate joint is oxidised as well which is observed by suggestibly a change in polarity. Both phenomena are observed as a shift in the polymer SEC traces while still retaining its original molecular weight distribution.

5.2 INTRODUCTION

1,2,4,5-tetrazines (s-tetrazines) are a class of high-energy heterocycles bearing four nitrogen atoms that were first isolated and reported by Pinner in the 19th century.^[95] Surprisingly, s-tetrazines attracted only moderate interest over the last decades despite their rather uncommon aromatic structure.^[251] Due to the arrangement of the nitrogen atoms within the aromatic system at positions 1,2 and 4,5, s-tetrazines usually express an highly electron-deficient character. This renders s-tetrazines remarkable enophiles capable of inverse electron demand Diels-Alder (iEDDA) cycloadditions which are classified as one of the fastest click reaction between dienes and dienophiles to this date.^[100, 252-253] Interestingly, tetrazine-involving iEDDA reactions are bioorthogonal and find use in a range of applications

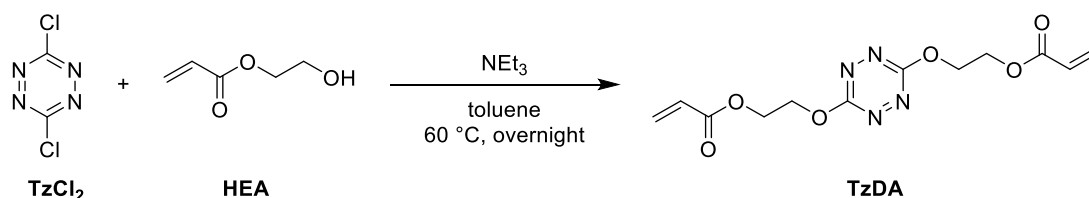
such as hydrogel design,^[254-255] drug release^[256] and biolabeling.^[257] With this, much of the interest in the tetrazine moiety is attributed to constructive ligation or linking. However, tetrazines also find usage in high-energy material such as propellants and explosives, thanks to its high nitrogen content.^[258-260] Interestingly, degradation of the tetrazine motif can also be phototriggered^[261-262] under visible light conditions which initiated the here presented study. Herein, a tetrazine motif was probed to its light uptake and subsequently incorporated into linear polymers which underwent backbone modification upon green light ($\lambda = 525$ nm) irradiation in an oxidative environment. Tetrazine bearing hydrogel networks have been probed for degradation previously^[263] but hydrogelation often implies nucleophilic substitution of a tetrazine dichloride and a thiol-linker which prevents incorporation into more complex network strategies. In this chapter, a tetrazine diacrylate was purposefully employed which hypothetically allows further incorporation into a variety of (meth-)acrylic-based polymeric material. Additionally, its accelerated degradation in the presence of hydrogen peroxide was investigated and aims to expand the usability of tetrazines in light-degradable polymers.

5.3 RESULTS AND DISCUSSION

5.3.1 Approach, design and assessment of a tetrazine-bearing monomer

Naturally, substantial effort was directed towards investigating the photochemistry of a tetrazine-bearing monomer. In a simple one-step synthesis (**Scheme 5-1**), s-tetrazine dichloride (TzCl_2) was reacted with hydroxyethyl acrylate (HEA) in the presence of triethylamine (NEt_3) to obtain tetrazine diacrylate (**TzDA**). The synthetic protocols are appended (Chapter 8.5.3) as well as NMR spectra provided (**Figure S5-1**, **Figure S5-2**). Generally, most tetrazine have an orange to red appearance, due to the presence of their weak $n\pi^*$ absorption band in the visible region (500-550 nm), followed by a $\pi\pi^*$ transition in the UV region (approx. 350 nm). The exact position and degree of extinction depends on the nature of 3,6-substituents.^[264-265] Indeed, the presented red-coloured **TzDA** exhibits a low-lying transition, centred at $\lambda_{\text{max}} = 511$ nm ($\epsilon = 570$ $\text{L}\cdot\text{mol}^{-1}\cdot\text{cm}^{-1}$ in acetonitrile), followed by a transition centred at $\lambda_{\text{max}} = 344$ nm ($\epsilon = 3500$ $\text{L}\cdot\text{mol}^{-1}\cdot\text{cm}^{-1}$ in acetonitrile). Further, **TzDA** does not undergo a significant bathochromic shift (**Figure S5-13**) for a variety of solvents tested. Usually, the $n\pi^*$

band shifts up to 10 nm, while the presence of hydrogen peroxide does not induce any significant change. A possible photodegradation pathway reported in literature results in the release of bimolecular nitrogen, followed by cleavage of the remaining N-N bond.^[266] Here, photoexcitation into the first excited electronic state (S_1), followed by Internal Conversion (IC) into a hot electronic ground state (S_0) has been postulated and experimentally shown.^[106, 267-268] Thus, the loss of the $n\pi^*$ absorption band is a useful indicator for the degradation efficiency of **TzDA**. It is important to note that mostly two different heterojunctions of s-tetrazines exist throughout the literature, i.e. thio- and an oxo-substituted derivatives besides the carbon-linked derivatives. The former has been reported to undergo degradation, releasing two equivalents of thiocyanate.^[107] However, the synthesis of a thio-tetrazine and acrylate termini was not achieved. A conversion of an epoxide to a thiirane via thiourea was successful, however, the ring-opening reaction afforded no product (see Chapter 8.5.3.5 and 8.5.3.6, **Figure S5-7**, **Figure S5-8**) which suggested autopolymerisation. An oxo-derivative upon substitution with a primary alcohol was chosen instead, affording **TzDA**. Since the absorption spectrum is not representative to the reaction profile (rather more indicative), a detailed wavelength screening for the optimum degradation wavelength was found via an established literature screening method.^[185-186, 269] In short, a wavelength-tunable nanosecond laser was employed to deposit an equal number of photons throughout the probed wavelength window. The degree of conversion was calculated by comparing respective absorbances of the $n\pi^*$ absorption band at approx. 520 nm. Experimental details are appended in Chapter 0. The corresponding action plot is depicted in **Figure 5-1**. While the absorption spectrum of **TzDA** does not change upon addition of hydrogen peroxide, the reactivity profile reveals significant differences.



Scheme 5-1: Synthesis of **TzDA** monomer.

In a nonoxidative environment (red), the conversion efficiency was estimated to approximately 7% throughout the probed wavelength window, independent on the incident light. Upon addition of hydrogen peroxide however, a significant increase of reactivity was observed (blue). While **TzDA** retains poor reactivity at 7% conversion efficiency in non-absorbing regimes such as 400 nm and beyond 600 nm, an almost six-fold increase was observed when irradiated at $\lambda = 520$ nm (39% compared to 7% for a non-oxidative environment). As expected, the shape of the reactivity profile matches the general extinction of **TzDA**, thus affirming a singlet character of photoexcitation and -degradation. Although photodegradation still occurs in a non-oxidative environment, the reaction proceeded in much higher efficiency in the presence of hydrogen peroxide.

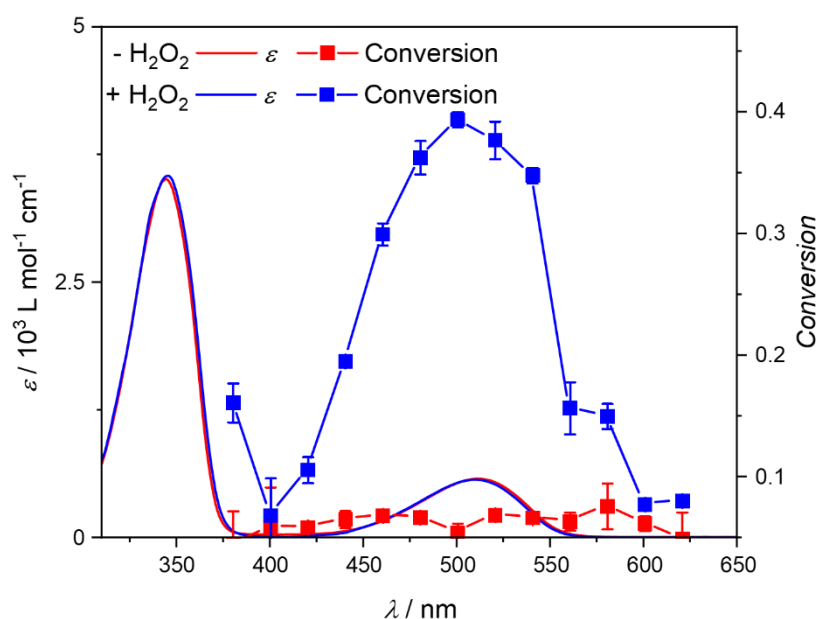


Figure 5-1: Action Plot in absence (red) and presence (blue) of hydrogen peroxide (H₂O₂). Solid lines depict the extinction coefficient and scatter illustrate conversion *X* of **TzDA**.

Identification of reaction products was achieved by a combinatory study of LC-ESI-mass spectrometry and NMR spectroscopy. Qualitative amounts of **TzDA** were subsequently submitted to oxidative conditions (+ 30wt% H₂O₂) in the dark and then irradiated under green light ($\lambda = 525$ nm) conditions. After removing all volatiles under reduced pressure, the samples were analysed via NMR and LC-ESI-MS methods.

Figure 5-2 depicts the excerpt of relevant resonances in the NMR spectra. The full NMR spectrum is appended in **Figure S5-9**. The set of ^1H -NMR resonances upon H_2O_2 exposure remains unchanged but changes when exposed to green light conditions. Interestingly, the ethylene attributed resonances *c* and *d* undergo a shift, suggesting a change in electronic density in close proximity. Resonances *a*, *b* and *c* show significant line doubling, suggesting the presence of a second species which is marginally different from the starting material, given the low shift of resonances. The resonances (**Figure 5-2 a**, ochre panel) can be no longer confidently assigned, instead relative integrals are given and confirm a structure that relates to an ethyl acrylic species. The characteristic integral pattern implies the existence of a mixture of tetrazine derivatives with an intact acrylate tail. The appended ^{13}C -NMR spectrum confirms the observations mentioned. Only under green light exposure, changes in the ^{13}C -NMR spectrum are noted. The resonances involved *a-f* are in close proximity to the tetrazine core, thus shifts in resonances are expected. The resonances *c* and *d* again show no change, indicating that change of electron density must take place at the tetrazine core. LC-ESI chromatograms are depicted in **Figure 5-3**. Once again, **TzDA** exposed to H_2O_2 only reveals minor changes. The main elution peak A remains unchanged at 8.8 min but a minor rise at 8.6 min (B) is observed. Subjectively, exposure to H_2O_2 inflicts only minor changes in molecular structure due to the low shift in retention time. However, subjecting **TzDA** to green light irradiation gives rise to peak C at 7.3 minutes, indicating significant changes in polarity. As expected for reverse-phase chromatography, a decrease in retention time is accompanied by an increase in polarity of eluting species. **Figure 5-3 b**) shows the resulting dominant species found in excellent agreement (derived error $\Delta < 2$ ppm). A complete mass spectrometric analysis is appended in **Figure S5-10**, **Table S5-1**. Panel A is mostly associated with intact **TzDA** and minor contributions of dihydrotetrazines, probably reduced due to the present electron potential.^[270] Panel B predominantly consists of a slight oxidation product but retaining the characteristic tetrazine core. Panel C confirms the absence of the prominent tetrazine structure, revealing a nitrogen-oxygen exchange. A possible degradation reaction of the tetrazine core is proposed in **Scheme 5-2**.

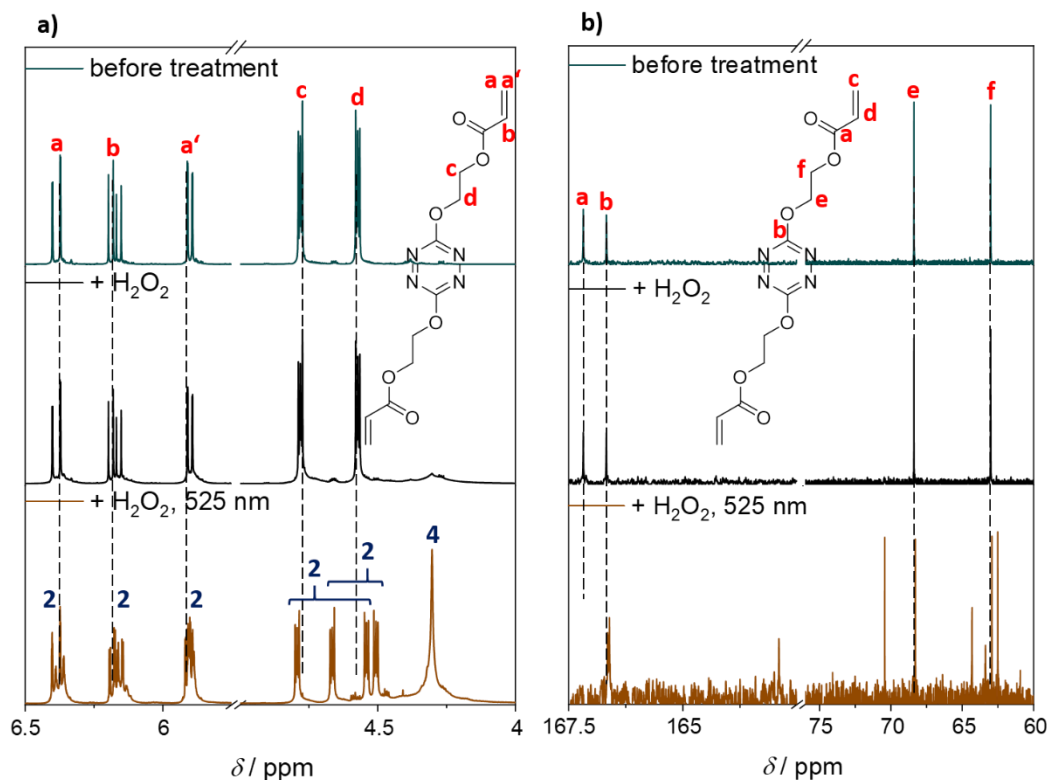


Figure 5-2: ^1H - (a) and ^{13}C - (b) NMR spectra of **TzDA** in acetonitrile- d_3 before treatment (olive), after exposure to H_2O_2 (black) and after exposure to H_2O_2 and green light ($\lambda = 525 \text{ nm}$).

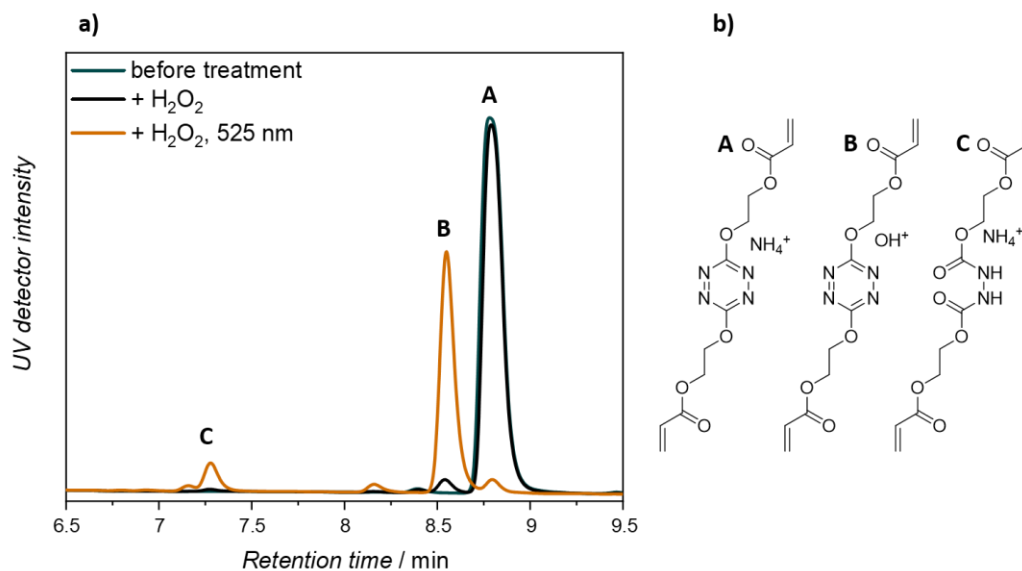
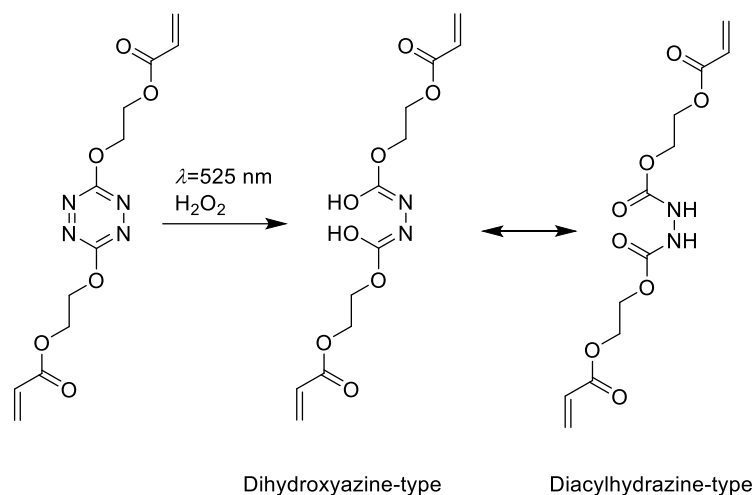


Figure 5-3: a) Liquid chromatograms of **TzDA** in acetonitrile at different conditions. Olive: before treatment, black: after exposure to H_2O_2 , ochre: After green light irradiation. b) Assigned structure of the most prominent tetrazine peak in each retention panel.

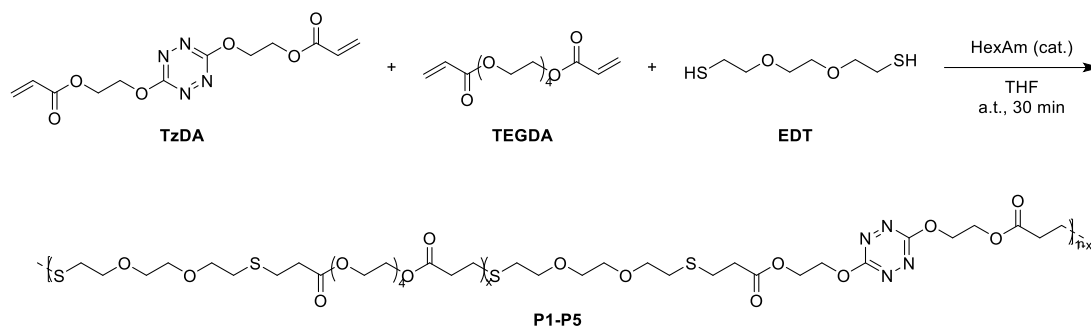
Neither mass nor NMR spectra allow for accurate identification of the product mixture as resonance structures between an azine (left) and a hydrazine (right) are suggested (**Scheme 5-2**).



Scheme 5-2: Suggested degradation reaction of **TzDA**.

5.3.2 Incorporation into thiol-acrylate copolymers

To expand the scope beyond the molecular level, **TzDA** was incorporated into linear polymers. Importantly, a non-radical involving polymerisation was preferred since tetrazines are notoriously known for their radical scavenging behaviour.^[271-273] The base-catalyzed thiol-acrylate click reaction was selected due to its high rate of reaction and simple execution.^[274] For this purpose, an aliphatic comonomer, TEGDA, was copolymerised with **TzDA** and a commercially available dithiol in the presence of catalytic amounts of hexylamine (HexAM). The general polymerisation reaction is presented in **Scheme 5-3** and detailed information are provided (Chapter 8.5.3.7).



Scheme 5-3: Thiol-Michael polymerisation procedure in the presence of hexylamine (HexAm) in catalytic amounts.

Five different polymers, **P1-P5**, were synthesised and listed in **Table 5-1**. All polymers are of similar shape and share comparable M_n , M_w and PDI values but differ in the amount of incorporated tetrazine moieties, ranging from 0% (only TEGDA incorporated) to 100% (only **TzDA** incorporated). A full analysis is included in the appendix (**Table 8-31**, **Figure S5-11**, **Figure S5-12**). An increase of reaction time did not afford polymers of higher molecular weight which suggests the completion of reaction after the time stated.

Table 5-1: Obtained tetrazine-bearing polymers and their proposition

Entry	$M_n / \text{kg mol}^{-1}$	\bar{D}	Tz in Polymer (relative)
P1	7.65	1.6	0.00
P2	6.97	1.7	0.16
P3	6.85	1.8	0.33
P4	6.41	1.8	0.60
P5	6.04	1.8	1.00

Interestingly, the increase in tetrazine incorporation seem to induce a change in the polymers' properties. Examination the amount of tetrazine incorporated, ranging from 0% (**P1**) to 100% (**P5**), a decrease in number average molecular weight is observed while \bar{D} increases. The exact amount of incorporated tetrazine has been confirmed via $^1\text{H-NMR}$ spectroscopy (**Table 8-32**, **Figure S5-11**). It is suggested that the aromatic tetrazine (compared to the aliphatic TEGDA comonomer) acts inhibitory to some extent and is less mobile, leading to a lowering of the polymerisation efficiency which

in return lowers yield and prevents efficient incorporation into the backbone. Further, oxygen-sulphur exchange reactions have been reported before^[275] and were to a small extent observed in the polymer NMR spectra which influence degradation performance. However, changing the reaction conditions, such as employing inert gas atmosphere, was not conducted, since oxygen sources would be introduced with hydrogen peroxide in any case.

5.3.3 Polymer backbone oxidation upon exposure to double triggers

As the molecular oxidation and light-response of tetrazine-diacrylate **TzDA** has been studied in detail before, the polymer degradation is investigated in the following to probe for the same effect. Michael-type thiol-ene polymers are known to be degradable under various conditions including exposure to acids and bases,^[276-280] and degradation in strong oxidative media such as hydrogen peroxide has been reported as well.^[281] As tetrazines are highly coloured, the degradation can be tracked via UV/Vis absorption spectroscopy and Size-Exclusion-Chromatography (SEC). It is noted that polymer degradation reactions usually occur along several locations along the polymer chain, often resulting in a bi- or multimodal polymer distribution.^[282] Rather than providing M_n values quantitatively, M_n is thus intended to be seen as a qualitative degree of degradation.

To investigate the influence of both triggers on the general chemical structure of a thiol-acrylate polymer and on the tetrazine motif itself, **P1** and **P5** were subjected to control experiments (**Figure 5-4** and **Figure 5-5**). **Figure 5-4 a)** does not depict any absorption bands since no chromophore was incorporated. However, **P1**, only bearing TEGDA showed a moderate shift in elution behaviour when subjected to both H₂O₂ and 525 nm light (**Figure 5-4 b**). This is believed to be due to oxidation of the thioether linkages which are inherently present in the polymer backbone (**Scheme S5-2**).

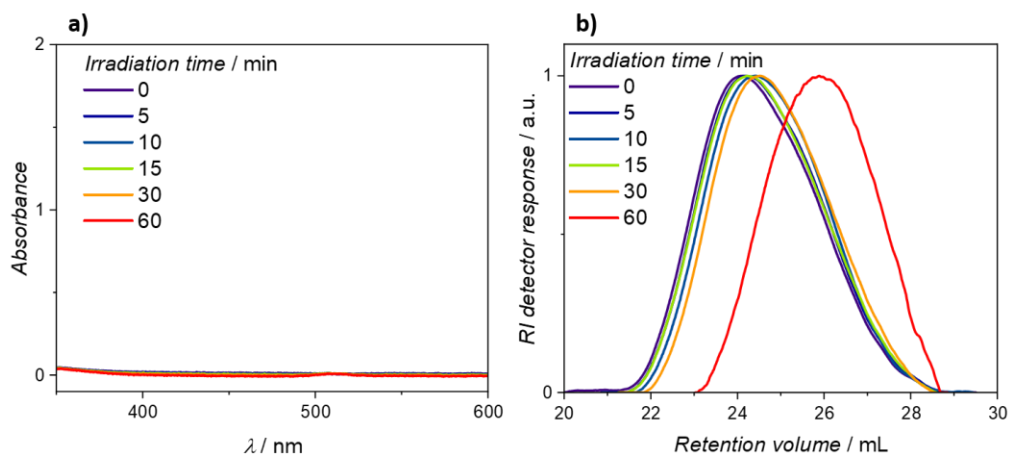


Figure 5-4: a) UV/Vis absorption spectra and b) SEC traces of P1 in THF under exposure of both hydrogen peroxide and 525 nm light.

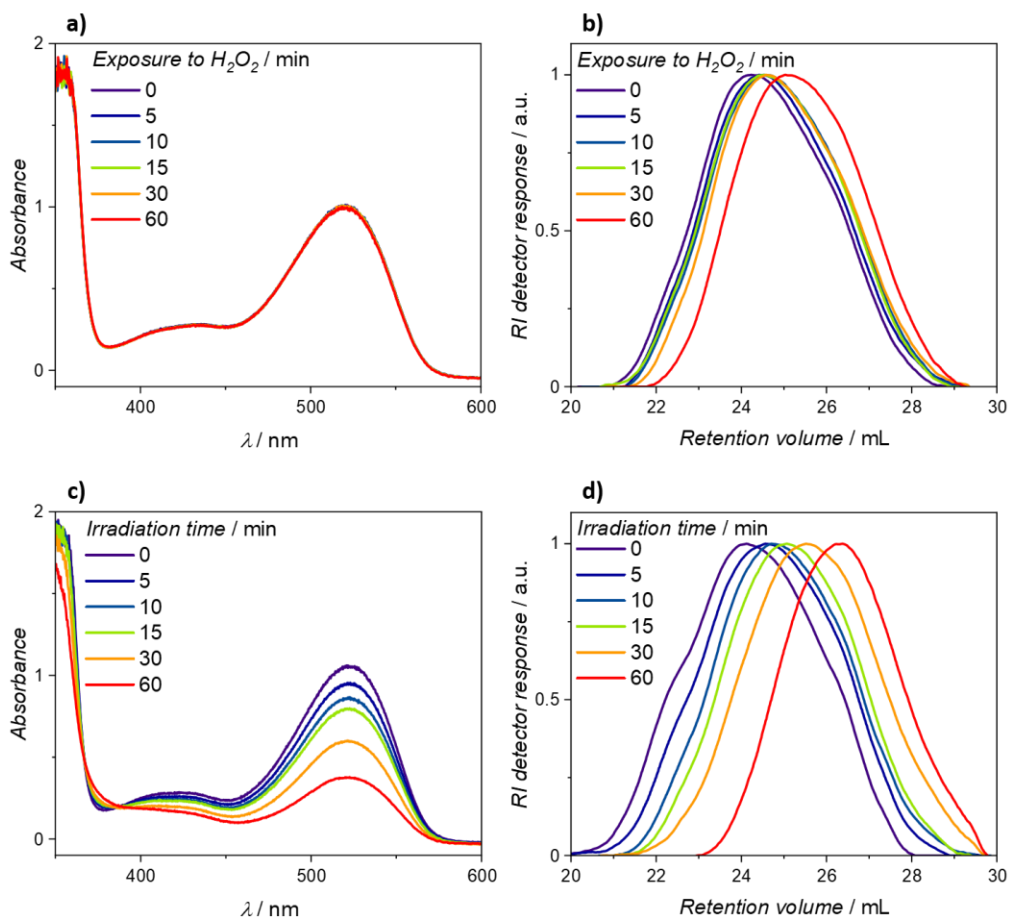


Figure 5-5: a) UV/Vis absorption spectra and b) SEC traces of P5 in THF under exposure of only hydrogen peroxide. c) UV/Vis absorption spectra and d) SEC traces of P5 in THF under exposure of only 525 nm light.

Since mass spectral analysis is not possible due to the non-ionizable nature of the polymer, the oxidation to a sulfone of the thioether functionality was proven on a test molecule level TEGASO (**Figure S5-14**, **Figure S5-15**, **Table S5-2**) and is in agreement with literature.^[283] Oxidation to the sulfone results in change of polarity, thus changing the column-polymer interaction and increasing the retention of the polymer on the column. Interestingly, fragments of TEGAS or its oxidation product have not been observed, which is in line with previous observations. Tetrazine diacrylate does not undergo cleavage either but shows nitrogen-oxygen-exchange instead. The shift in retention volume thus originates mostly from a change of polarity and not from fragmentation. This can be observed in the evolution behaviour of the SEC traces as well, i.e. the trace is only shifted but its shape does not show a bi- or multimodal pattern, which is expected in fragmentation scenarios. By subjecting **P5**, only bearing tetrazine motifs, to each of the triggers, an interesting phenomenon is observed. **P5** being subjected to only H₂O₂ revealed comparable *M_n* evolution compared to **P1** being subjected to both triggers (**Figure 5-5** a and b). This is due to thioether joint oxidation which does not affect tetrazine degradation.^[273] Interestingly, the oxidation seems to be tampered to some level, since the SEC traces in **P1** shift further towards higher retention volume (**Figure 5-4**). However, **P5** being subjected to only green light, reveals moderate degradation (**Figure 5-5** c and d). Since wavelength-independent degradation in the absence of H₂O₂ was already observed for the small molecule **TzDA**, this result agrees well.

Eventually, the degradation of tetrazine-containing polymers was observed in the presence of H₂O₂ under green light conditions. As illustrated in **Figure 5-6**, the backbone of **P5** undergoes significant and rapid changes in its absorptivity (**Figure 5-6** a) and its retention profile (**Figure 5-6** b). The *nπ** band of tetrazine completely vanishes within 15 minutes of green light ($\lambda = 525$ nm) irradiation while SEC traces confirm a shift towards longer retention times within the same time frame. This translates into an extensive acceleration of degradation. The presence of H₂O₂ causes oxidation along the thio-acrylate joint in **P1** while tetrazine acts as an antioxidant in **P5**. **Figure 5-7** depicts the changes of absorption maximum (a) and *M_n* evolution (b) throughout the series. **P1** under exposure of both triggers (squares) and **P5** only under H₂O₂ exposure (circles) reveal similar trends, while light acting on **P5** manifests in rapid photooxidation (triangles).

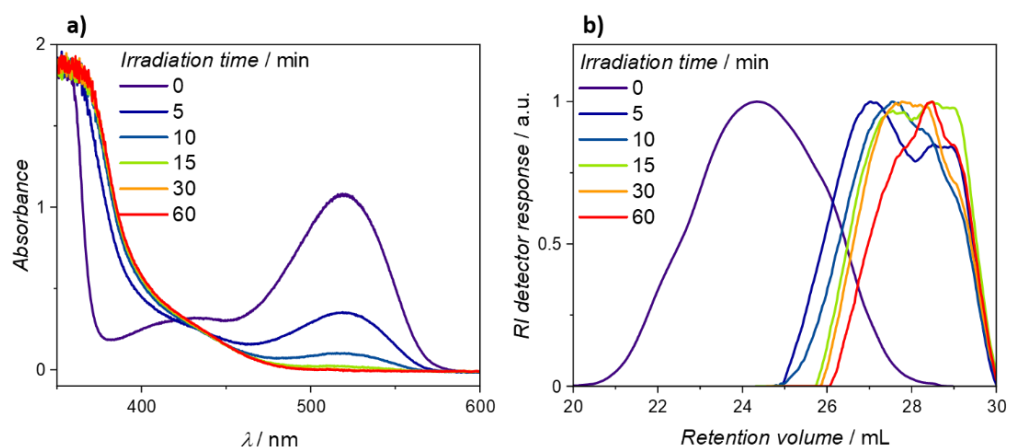


Figure 5-6: a) UV/Vis absorption spectra and b) SEC traces of **P5** in THF under exposure of both hydrogen peroxide and 525 nm light.

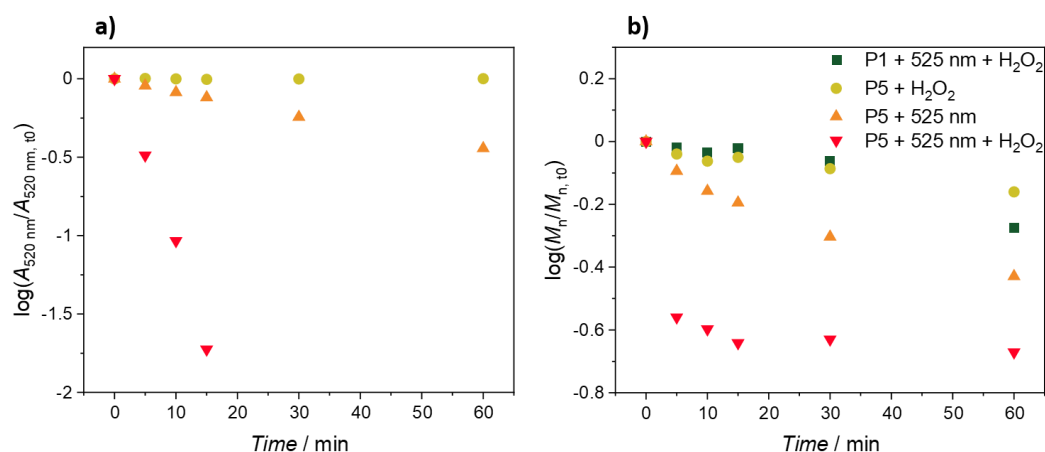


Figure 5-7: a) $A_{520\text{ nm}}$ and b) M_n evolution of **P1** and **P5** under various triggers.

The acceleration in oxidation in **P5** can only be observed in combination with green light. Interestingly, tuning the tetrazine loading in **P2-P4** (tetrazine content 16 - 60%) leads to a similar determined M_n (**Figure 5-8 b**). **P2-P4** also depict nonlinear decrease in absorptivity (**Figure 5-8 a**). Nevertheless, all degradation experiments seem to complete within 30 minutes, with **P2-P4** sharing similar elution profile after 60 minutes which is likely due to a fully oxidized backbone of the polymer. However, all tetrazine has been fully consumed as shown by the UV/Vis absorption spectra of **P1-P5** over the course of degradation (**Figure S5-16-Figure S5-18**).

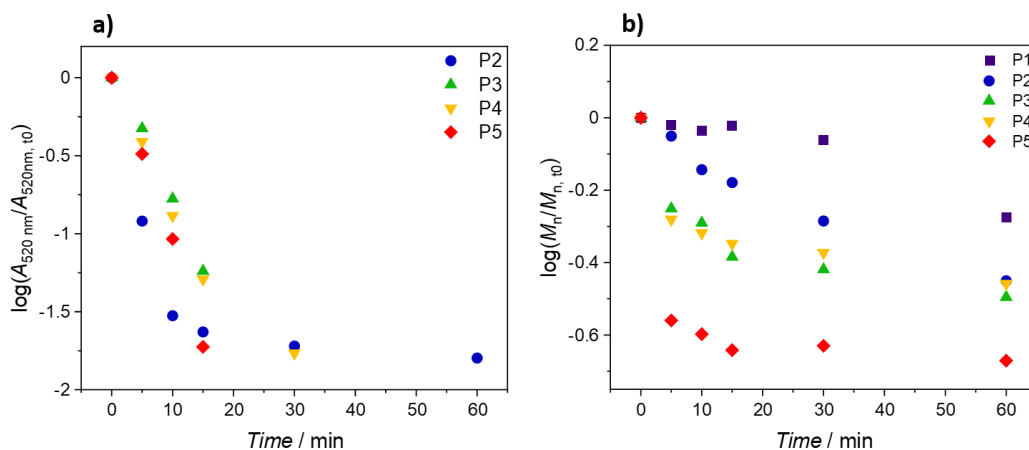
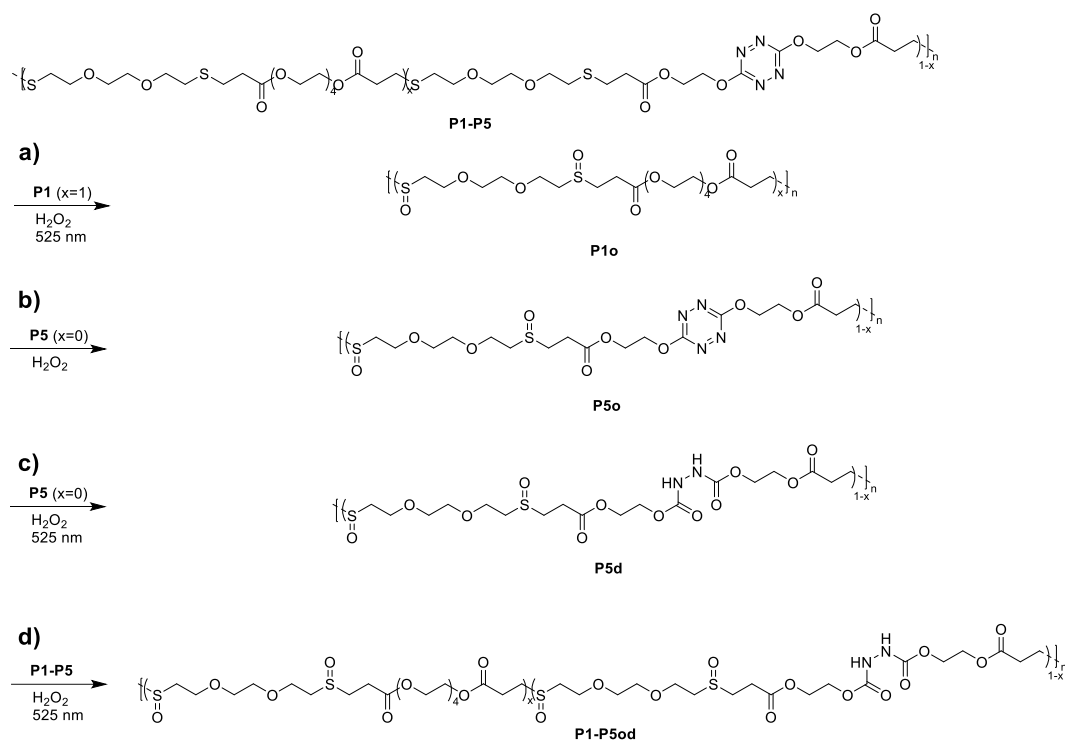


Figure 5-8: a) $A_{520\text{ nm}}$ and b) M_n evolution of **P1-P5** in presence of H_2O_2 and under green light irradiation.

Since the polymers cannot be analysed via SEC-ESI-MS methods, only knowledge from the small molecule can be applied here to these larger systems. **TzDA** undergoes intramolecular oxidation upon dual trigger exposure which was mostly proven by a change in elution behaviour, i.e. different column-matter-interactions. The same principle is also applied for the polymers which suggests a similar backbone oxidation of the thioether moiety and the tetrazine motif, thus changing polarity (**Scheme 5-4**). The backbone itself does not undergo fragmentation, i.e. the shape of the SEC traces remains unaltered (see **Figure 5-5** and **Figure 5-6**). A sequenced exposure to both triggers confirms the statements above. **P5** was subjected to first H_2O_2 and then green light irradiation, and concurrent samples were subjected to UV/Vis absorption spectroscopy and SEC. **Figure 5-9** depicts the changes in a sequence-driven exposure. UV/Vis (a) and SEC (b) traces do not significantly change (blue-green colour tones) during H_2O_2 exposure, but degrade rapidly upon 525 nm irradiation (green-shaded areas in **Figure 5-9** c and d). In contrast to a sequenced experiment, a single M_n data point recorded after 120 min H_2O_2 reveals the accelerated oxidation of the polymer backbone.



Scheme 5-4: Suggested degradation mechanisms of **P1-P5**. a) and b) depict simple thioether joint oxidation to the respective sulfone. c) expands backbone oxidation by tetrazine core degradation and d) general scheme to the suspected oxidated polymer backbone.

5.4 CONCLUSION

Tetrazine-diacrylates have been incorporated into linear thiol-acrylate polymers and probed on their light uptake and oxidation efficiency. Starting from molecular investigation, tetrazine can be triggered by any light source in the absence of H_2O_2 but revealed poor degradation efficiency. In the presence of H_2O_2 however, a significant acceleration under green light conditions was determined. This knowledge was transferred onto the polymer scale. Due to insignificant ionization potential of the obtained polymers, the degradation reaction of the small molecule **TzDA** was assumed to proceed identically to **TzDA** incorporated into linear polymers. The polymers suggestably undergo ring-opening of the tetrazine motif, allowing for a nitrogen-oxygen exchange. This way, the backbone is oxidized but the main chain remains intact. Further, the thiol-acrylate joint is oxidized in an oxidative environment which has been proven on a small molecule level with TEGASO. Both phenomena manifest in a shift of retention volume in the SEC traces, but the shape of the SEC traces remains

unaltered. This underpins the claims that the polymer backbone does not fragment but changes its polarity instead.

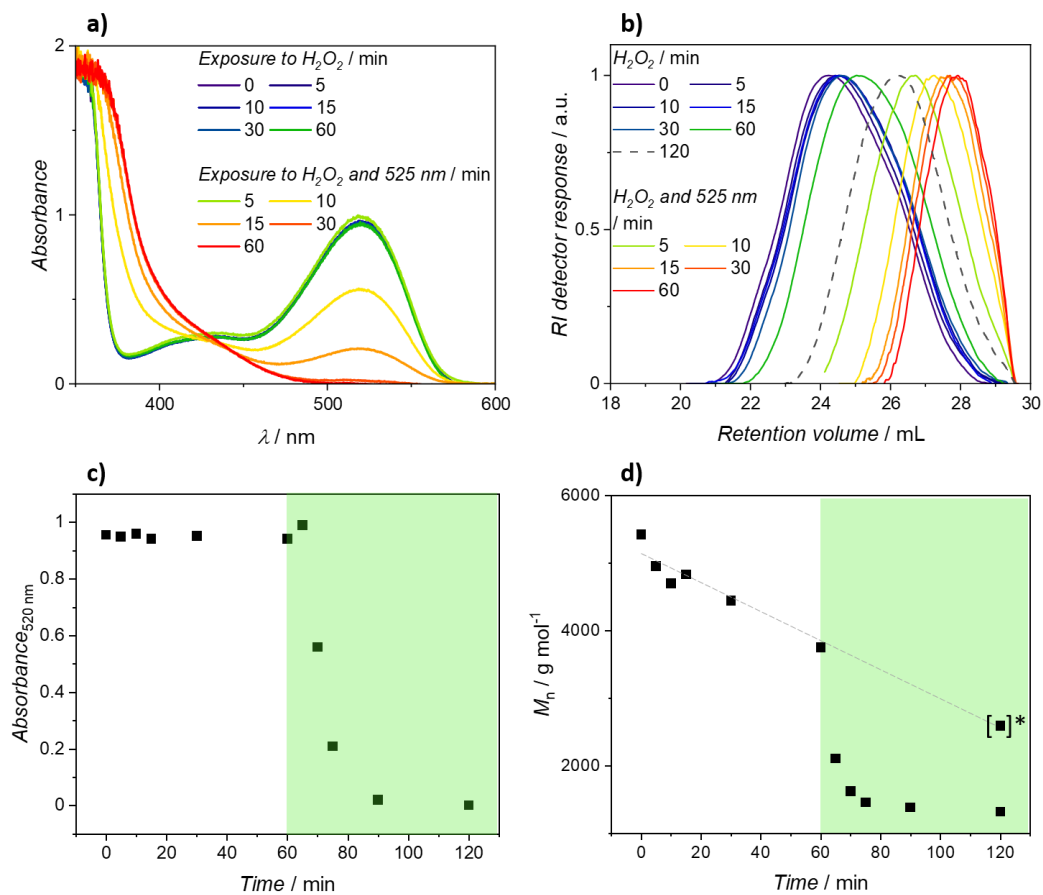


Figure 5-9: a) UV/Vis spectra and b) SEC traces of **P5** in a sequence-driven exposure experiment upon exposure to H₂O₂ and subsequently green light. Extracted absorbance at 520 nm (c) and M_n (d) during the course of exposure. The green-shaded area marks exposure with 525 nm light. *: Data point which has been exposed to H₂O₂ only for 120 minutes. The dotted line is a guide for the eye.

Chapter 6: Wavelength-Orthogonal Stiffening and Inhibition of Hydrogel Networks with Visible Light

Parts of this chapter were adapted and reproduced with permission from V. X. Truong, J. Bachmann, A.-N. Unterreiner, J. P. Blinco, C. Barner-Kowollik *Angew. Chem. Int. Ed.* **2022**, *61* (15), e202113076. Reproduced with permission. © 2022 Angewandte Chemie International Edition published by Wiley-VCH GmbH. The candidate assisted in experimental design and project execution, assisted in small molecule and polymer analytical experiments, executed all light-mediated crosslinking experiments on a molecular level in solution (Action Plots), analysed and interpreted all acquired datasets, contributed to writing the initial draft and editing the original manuscript, processed revisions. Vinh X. Truong performed the monomer and polymer synthesis, performed the material study (rheology, two-step crosslinking), analysed and interpreted the acquired datasets, contributed to writing the initial draft and editing the original manuscript, processed revisions.

6.1 ABSTRACT

The wavelength-orthogonal crosslinking of hydrogel networks using two red-shifted chromophores, i.e. acrylpyrene (AP, $\lambda_{\text{activation}} = 410 - 490 \text{ nm}$) and styrylpyrido[2,3-*b*]pyrazine (SPP, $\lambda_{\text{activation}} = 400 - 550 \text{ nm}$) was introduced. SPP chromophores are able to undergo [2+2] photocycloaddition in the visible-light regime. Interestingly, the photoreactivity of the SPP moiety is pH-dependent, whereby an acidic environment inhibits the cycloaddition. By employing a spiropyran-based photoacid generator with suitable absorption wavelength, the activation wavelength of the SPP moiety was restricted to the green light region ($\lambda_{\text{activation}} = 520 - 550 \text{ nm}$), enabling wavelength-

orthogonal activation of the AP group. The wavelength-orthogonal photochemical system was successfully applied in the design of hydrogels whose stiffness can be tuned independently by either green or blue light.

6.2 INTRODUCTION

Fragmentation or backbone modification phenomena were studied extensively in previous chapters. The former was studied in the UV-blue visible light region, while the backbone oxidation was triggered under green light conditions. However, the term degradation not only relates to intramolecular changes. Crosslinking sometimes is an undesired phenomenon in polymer science and often occurs under e.g. thermal treatment. Due to its importance in therapeutical applications, the development of photoresponsive hydrogels has gained significant momentum over the past decade and is partially owed to their dynamic viscoelastic properties and aqueous composition that highly resemble soft tissues in living systems.^[284-287] The application of light-mediated chemistries to modulate crosslinking allows for fine-tuning of their chemical and physical properties both spatially and temporally. Such light-sensitive materials are able to control signal presentation, mechanical properties and drug release.^[284] Indeed, photoresponsive hydrogels have proven to be ideal candidates for applications in advanced cell culture,^[285, 288] controlled drug delivery,^[289-290] and soft actuators.^[291] Significant efforts have been dedicated to the construction and investigation of photoresponsive hydrogels in various fields of biomedical science. In particular, photodegradable hydrogels based on *ortho*-nitrobenzyl photochemistry have been used for the differentiation of linear-specified cells^[292] and the fabrication of synthetic microvasculature.^[293-294] Recent developments in photochemistry have led to chromophores with red-shifted photoreactivity, enabling modulation of the materials by even long wavelength (low energy) visible light. More recently, the halochromic chromophore styrylquinoxaline was introduced, which can undergo photocycloaddition at $\lambda \leq 510$ nm. Exploiting an additional trigger, such as pH-value, would be beneficial for modulating the properties of hydrogels and even suppress crosslinking.^[295]

6.3 RESULTS AND DISCUSSION

6.3.1 Approach and scope

Advanced hydrogels can be modulated by several colours of light and thus enable selective control over multiple functionalities.

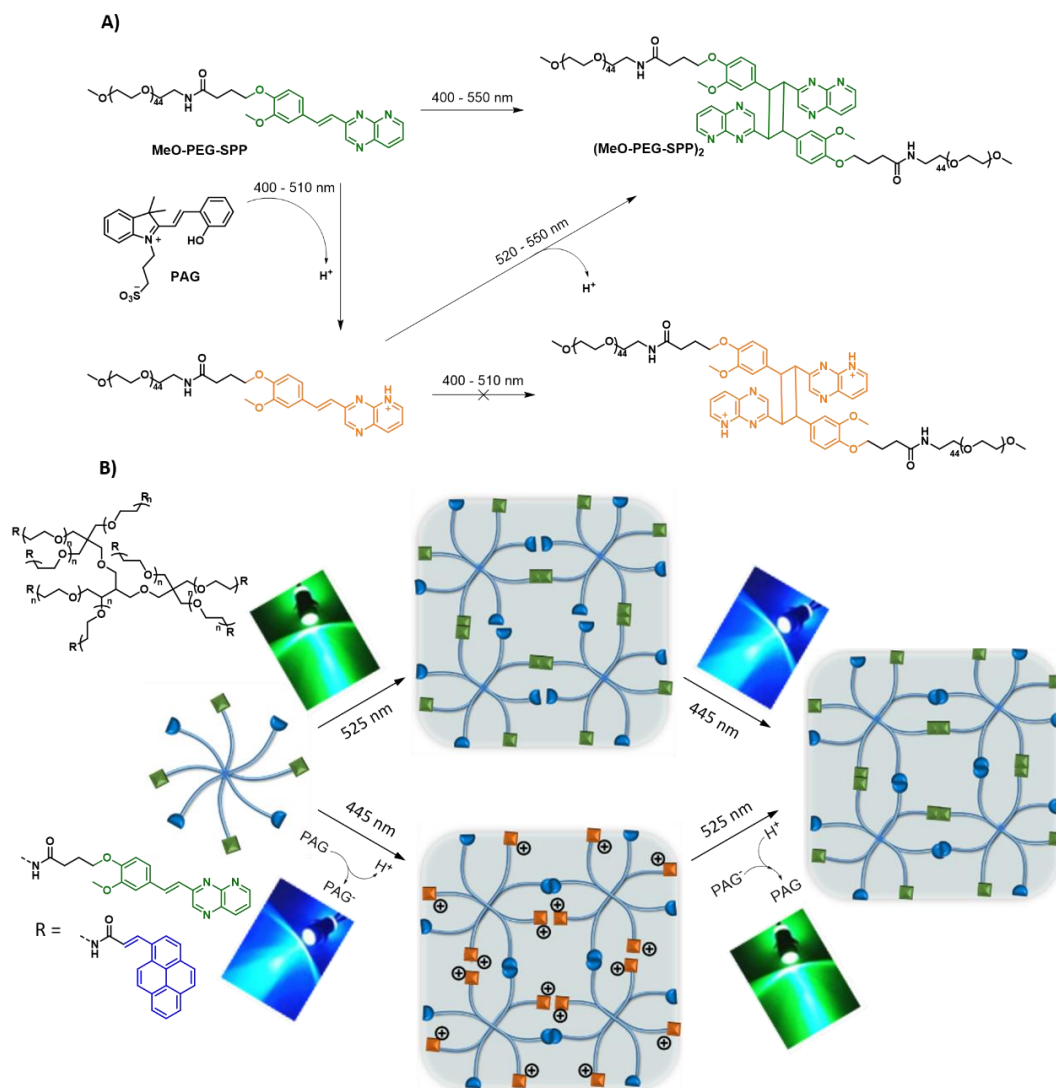


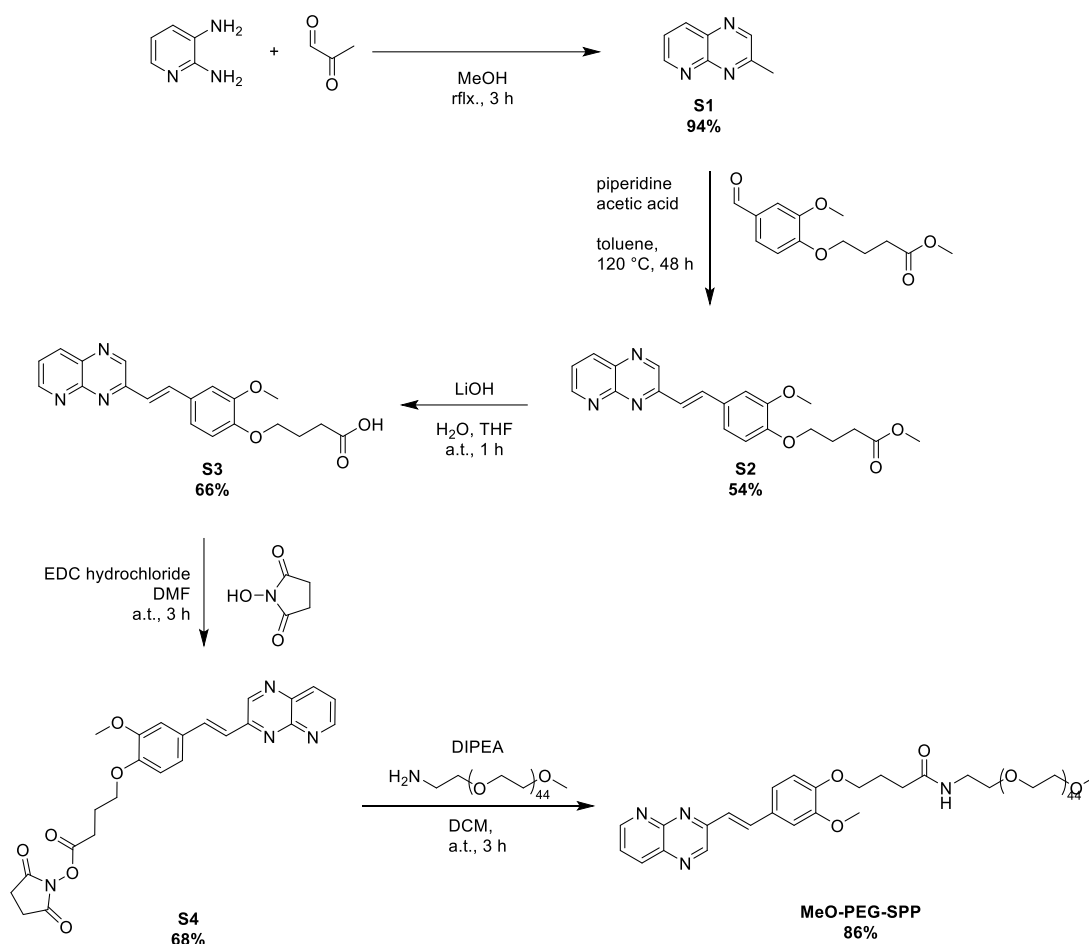
Figure 6-1: A) MeO-PEG-SPP undergoes photocycloaddition by visible light at 400–550 nm and $\text{pH} \geq 7$. In the presence of a PAG ($\lambda_{\text{activation}} = 400 - 510 \text{ nm}$), the photoreactivity of the SPP is inhibited; however, green light at 520 – 550 nm can still activate the photocycloaddition. Thus, the PAG effectively restricts the photoreactivity of MeO-PEG-SPP in the 400 – 510 nm window. B) The SPP group is attached to an 8-arm PEG together with a non-halochromic acrylamidylpyrene (AP) chromophore, which undergoes photocycloaddition by blue light ($\lambda_{\text{activation}} = 400 - 470 \text{ nm}$). The photoreactivity of AP is not compromised in presence of PAG. Thus, the 8-arm PEG-AP-SPP can crosslink by either blue or green light via photocycloaddition of the AP or SPP group, respectively. Reproduced with permission. © 2022 The Authors. *Angewandte Chemie International Edition* published by Wiley-VCH GmbH.

This can manifest in orthogonal tuning of at least two properties in a single system.^[284, 287] The adaptation of e.g. material stiffness in a well-defined manner by discrete wavelengths of visible light offers a powerful tool to explore the dynamic cell-materials interactions in biology research.^[286] Wavelength-selective photochemical design, the engineering of hydrogels networks and fabrication of photoresponsive materials were exploited many times, in which stiffness can be modulated by different colours of light.^[269, 296-297] The utility of such hydrogel platforms has been demonstrated in cell culture studies by using different colours of light. Specifically, the λ -selective stiffening of substrate induced cell detachment,^[296] while softening enhanced cell elongation and spreading, was explored.^[297] Nevertheless, the therein demonstrated λ -selectivity can only proceed in one direction, from longer to shorter wavelength. Consequently, the λ -orthogonal crosslinking of polymers via [2+2] photocycloadditions of two red-shifted chromophores, namely acrylpyrene (AP, $\lambda_{\text{activation}} = 410 - 490 \text{ nm}$) and styrylpyrido[2,3-*b*]pyrazine (SPP, $\lambda_{\text{activation}} = 400 - 550 \text{ nm}$) was studied and inhibited by introducing a photoacid generator (PAG). This way, formation of a biologically relevant hydrogel can be performed under long-wavelength visible light but crosslinking prevented under various pH-values. The photocycloaddition and halochromic properties of the SPP moiety are investigated herein for the first time. The photoreactivity of the SPP moiety in the blue light region can be inhibited by mixing the polymer with a spiropyran-based PAG ($\lambda_{\text{activation}} = 400 - 510 \text{ nm}$, **Figure 6-1 A**). The photoreactive AP group is unaffected by the PAG, thus the photocycloaddition of either AP or SPP can be activated by two discreet wavelengths in the presence of the PAG. Blue (445 nm) or green (525 nm) light can be employed, independently of each other. Afterwards the chemical design was translated into a hydrogel network, affording a hydrogel platform of which stiffness can be orthogonally influenced by irradiation with blue or green light (**Figure 6-1 B**).

6.3.2 Feasibility study

Inspired by previous works on the styrylquinoxaline-based [2+2] cycloadditions under $\lambda \leq 520 \text{ nm}$ irradiation conditions, a red shift of the photoreactivity was naturally considered. The quinoxaline motif was replaced with a pyrido[2,3-*b*]pyrazine.

Styrylpyrido[2,3-*b*]pyrazine (SPP) and easily prepared starting from pyridine-2,3-diamine in a three-step synthesis with an overall yield of 23% (refer to the synthetical procedures, Chapter 8.5.4). The synthesis is depicted in **Scheme 6-1**.

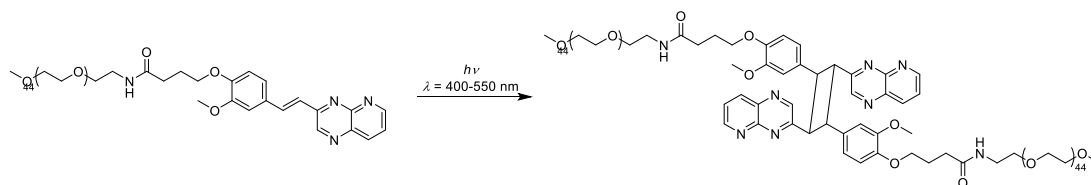


Scheme 6-1: Synthesis of MeO-PEG-SPP.

A carboxylic acid terminus allowed for conjugation to polymers, exemplarily exploited for use in polymer coupling or crosslinking. For this purpose, a poly(ethyleneglycol) with SPP end-group (MeO-PEG-SPP, **Figure 6-1 A**) was prepared and its photoreactivity investigated in water. NMR spectra are provided in **Figure S6-2-Figure S6-5**. MeO-PEG-SPP can undergo [2+2] cycloaddition which is schematized in **Scheme 6-2**.

The formation of the dimerized (MeO-PEG-SPP)₂ species was monitored by size exclusion chromatography (SEC). The SEC trace of the solution after irradiation

indicates the formation of a polymer with double molecular weight compared to the molecular weight of the starting material (**Figure 6-2 A**).



Scheme 6-2: [2+2] cycloaddition of MeO-PEG-SPP (left).

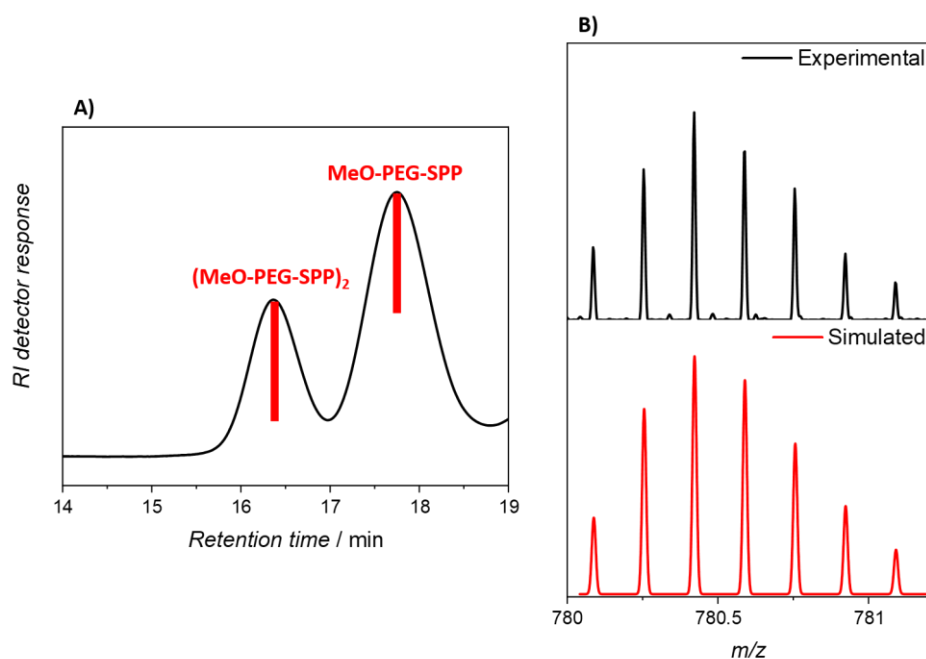


Figure 6-2: SEC data (calibrated against pMMA) of MeO-PEG-SPP and $(\text{MeO-PEG-SPP})_2$ after laser irradiation at 480 nm ($6.32 \pm 0.18 \cdot 10^{19}$ photons which result in a pulse energy of 848 μJ) in water (10 mg mL^{-1}). B) SEC-ESI-MS analysis of the dimerization of MeO-PEG-SPP after irradiation at 480 nm. Zoom into the mass spectra of experimental and simulated isotopic patterns, indicating their excellent agreement. Detailed SEC-ESI-MS analysis is appended in the appendix, **Figure S6-7**, **Figure S6-8**. Reproduced with permission. © 2022 The Authors. Angewandte Chemie International Edition published by Wiley-VCH GmbH.

Thanks to the narrow distribution of the used PEG unit, superposition of the two molecules is not observed. The presence of the $(\text{MeO-PEG-SPP})_2$ dimer is further confirmed by high resolution mass spectrometry hyphenated to SEC (**Figure 6-2 B**, **Figure S6-7** and **Figure S6-8**). The mass spectrum obtained at 16.4 minutes shows multiple patterns of the PEG repeating units with a difference of $m/z = 44.0264/7$,

corresponding to the molecular weight of one PEG repeating unit and seven sodium adducts. The obtained m/z values agree well with the simulated isotopic patterns of the photocycloaddition (MeO-PEG-SPP)₂ product.

6.3.3 Probing the pH-dependent photoreactivity of the styrylpyrido-pyrazine moiety

A tuneable nanosecond laser setup (Chapter 8.3.1) was used as a monochromatic light source, providing the same number of photons ($6.32 \cdot 10^{19}$) at each discrete wavelength in the range between 400 and 600 nm. The wavelength-dependent reactivity of SPP was thoroughly studied by exposing SPP to a constant number of photons and evaluating the product composition of cycloadduct and remaining monomer. The data were subsequently presented in the form of an action plot, displaying the conversion as a function of wavelength (**Figure 6-3**).

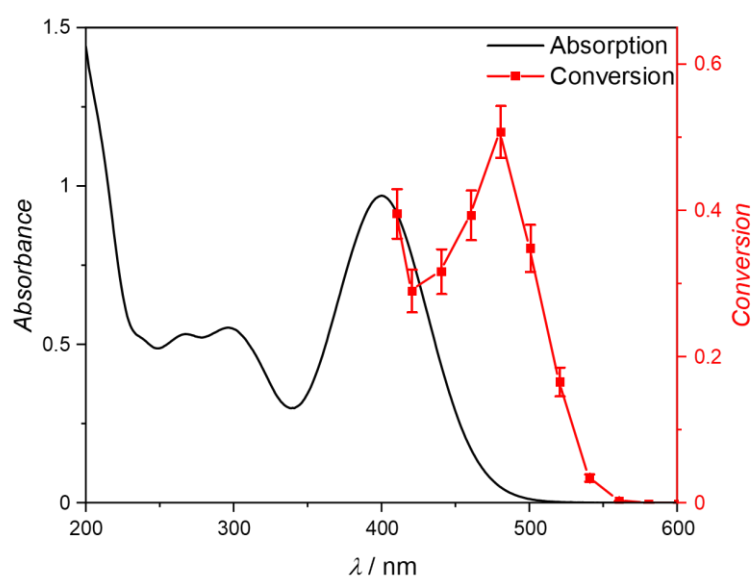


Figure 6-3: UV/Vis absorption spectrum of MeO-PEG-SPP (black solid) in water and the corresponding conversion (red solid) for the cycloaddition in water ($c = 10 \text{ mg mL}^{-1}$). Reproduced with permission. © 2022 The Authors. Angewandte Chemie International Edition published by Wiley-VCH GmbH.

Similar to previous reports on action plots of photochemical reactions in solution, [122, 298] a red shift (ca. 80 nm) in the photoreactivity of the SPP chromophore compared to its absorption spectrum was observed, indicating a maximum in absorption at 402 nm. The photoreactivity of the SPP moiety tails into the green light region (up to 540 nm), which - to the best of the author's knowledge - is the longest wavelength employed in [2+2] photocycloaddition in water. The most efficient wavelength was estimated to 480 nm (**Figure 6-3**). It is noted that the absorptivity of water in this wavelength region is negligible, dismissing any heating effects of the solvent and attributing the higher reactivity predominantly to the SPP moiety. A halochromic response of the SPP moiety is observed. Although no bathochromic shifts in the UV/Vis absorbance of the compound was determined when using several organic solvents (**Figure 6-4**), acidic solvents such as chloroform induce an additional absorption band close to 500 nm which tails up to 600 nm. The reader will note below that this aligns well with observations when decreasing the pH-value in aqueous media.

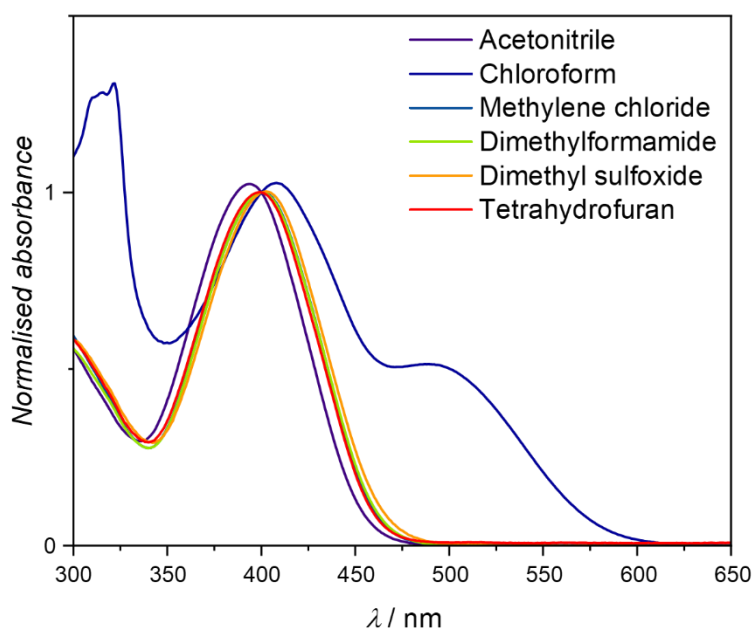


Figure 6-4: UV/Vis spectra of MeO-PEG-SPP in different organic solvents. Spectra were normalised to the absorbance at 400 nm. $d = 10$ mm. Reproduced with permission. © 2022 The Authors. *Angewandte Chemie International Edition* published by Wiley-VCH GmbH.

The pK_a of the pyrazinium moiety was determined to $pK_a = 1.15$, thus suggestibly occurs on the pyridinium nitrogen atom of the pyrido subunit.^[299] In comparison, the pK_a of quinoxalinium in water is 0.6.^[300] In aqueous environments, mild acidic conditions (pH-value 3 – 5) induce a continual decrease in absorbance of the MeO-PEG-SPP compared to the absorbance at neutral pH conditions (**Figure 6-5**). The change in UV/Vis absorbance is also associated with a significant reduction in the photoreactivity of the SPP moiety, as observed from the action plots of MeO-PEG-SPP at different pH-values (**Figure 6-5**). The conversion to dimer product decreases by more than half, from ca. 50% to ca. 20%, when the pH-value of the solution is changed to acidic condition (pH-value of 3–5).

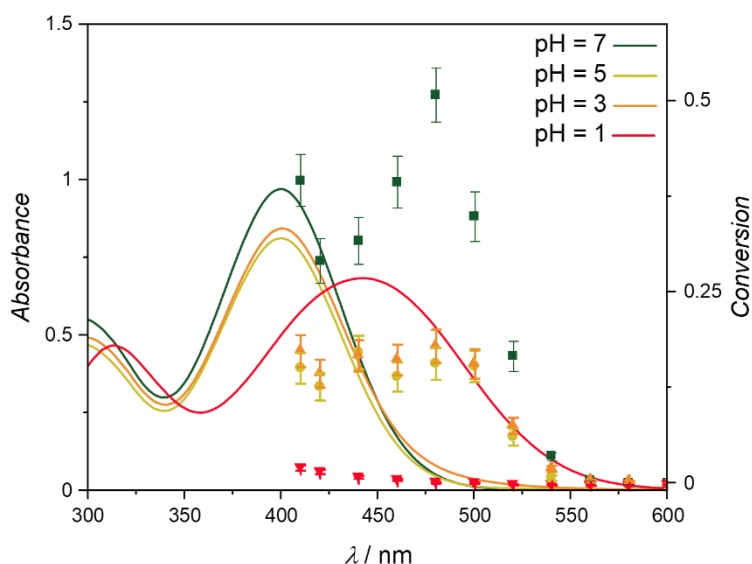


Figure 6-5: UV/Vis spectra of MeO-PEG-SPP and corresponding action plots under various pH conditions (green squares: aqueous, yellow circles: pH = 5, orange triangles: pH = 3, red diamonds: pH = 1). In all experiments, approximately 105 μmol of photons were deposited (**Table 8-23-Table 8-26**). $d = 10$ mm. Reproduced with permission. © 2022 The Authors. *Angewandte Chemie International Edition* published by Wiley-VCH GmbH.

A further decrease in $pH (\leq 1)$ completely inhibits the photoreactivity of the SPP moiety, and no cycloaddition product is observed. The inhibition of the photoreactivity correlates with a change in the UV/Vis absorbance of the solution, with a red-shift of approximately 60 nm (400 nm at $pH = 6$ and 457 nm at $pH = 0$). The pH dependent UV/Vis spectra are depicted in **Figure 6-6** and confirm the change during [2+2]

cycloaddition. Low pH-values give rise of a second absorption band at 460 nm but the absorption spectrum at low pH-values remains unaltered after (**Figure 6-6** solid and dashed) irradiation. The [2+2] cycloaddition does not – or only poorly – proceed under such low pH-values. A decrease of absorbance at 400 nm is already observed at pH-value of 2 – indicative for the cycloaddition to proceed.

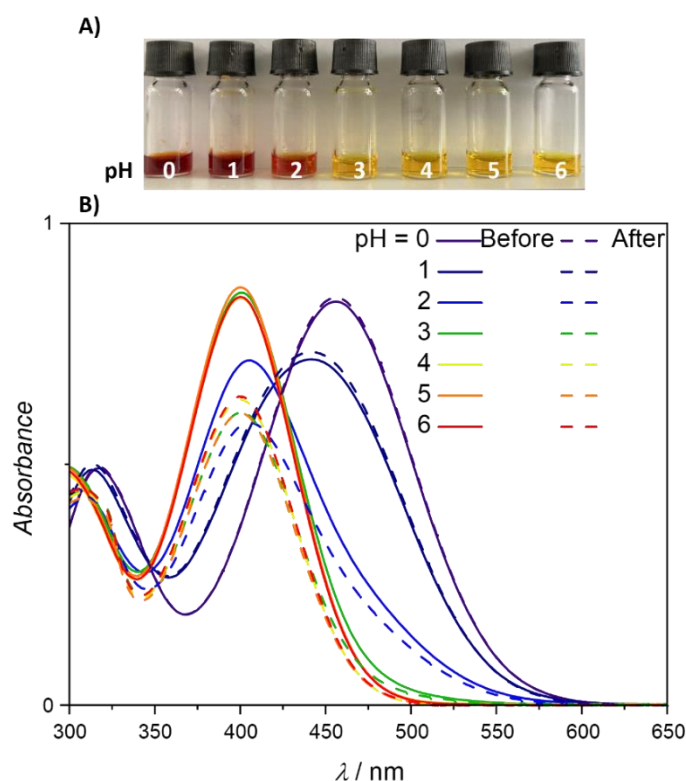


Figure 6-6: A) Picture of MeO-PEG-SPP in water at different pH values before irradiation. B) UV/Vis absorption spectra of MeO-PEG-SPP reaction mixtures in water before (solid) and after (dashed) irradiation with $\lambda = 480 \text{ nm}$ ($6.32 \pm 0.18 \cdot 10^{19}$ photons). $d = 10 \text{ mm}$. Reproduced with permission. © 2022 The Authors. *Angewandte Chemie International Edition* published by Wiley-VCH GmbH.

As a reference, the pH-dependency of a non-halochromic polymer was studied. PEG with acrylpyrene endgroup (MeO-PEG-AP, the reader is referred to Chapter 8.5.4.9), which can undergo efficient cycloaddition at $\lambda \leq 470 \text{ nm}$.^[296] 420 nm was reported as the most efficient irradiation wavelength for crosslinking. As depicted in **Figure 6-7**, no absorption at different pH-values is observed which renders AP stable against acidic environments. At pH = 0 however, a slight increase before irradiation is noted. After

irradiation, AP does not show its characteristic absorption bands, instead, a broadened shoulder is observed. Notably, the absence of the photocycloaddition adduct detected by SEC at pH = 0 under blue light irradiation is likely due to the acid-catalysed hydrolysis of the styryl group, followed by a reverse Claisen-Schmidt condensation (Scheme S6-1). The pH-dependency is illustrated in Figure 6-8.

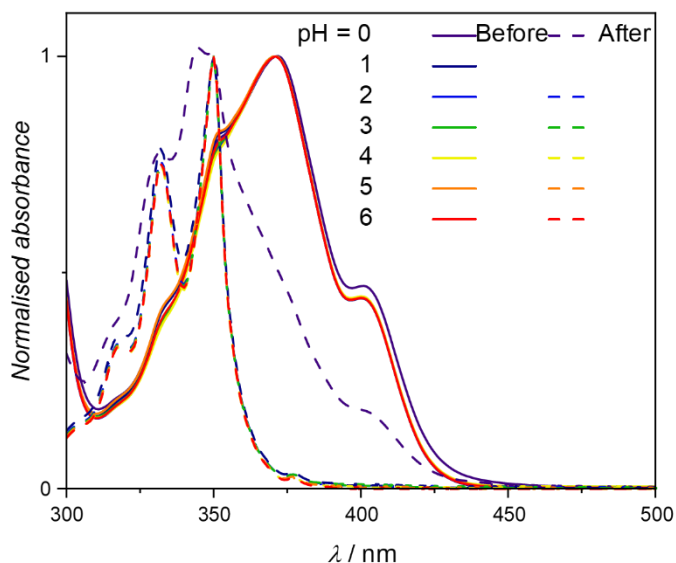


Figure 6-7: Absorption spectra of MeO-PEG-AP reaction mixtures in water before (solid) and after (dashed) irradiation with $\lambda = 420 \text{ nm}$ ($6.38 \pm 0.36 \cdot 10^{19}$ photons). Spectra were normalised to 371 nm before and 350 nm after irradiation. $d = 10 \text{ mm}$. Reproduced with permission. © 2022 The Authors. Angewandte Chemie International Edition published by Wiley-VCH GmbH.

While AP is insensitive to any pH-value, the protonation of SPP results in significant changes in reactivity. A decrease in slightly acidic media (pH = 7 \rightarrow 3-6) results in a first decline in reactivity, followed by the complete inability to form cycloproduct at pH-values below two.

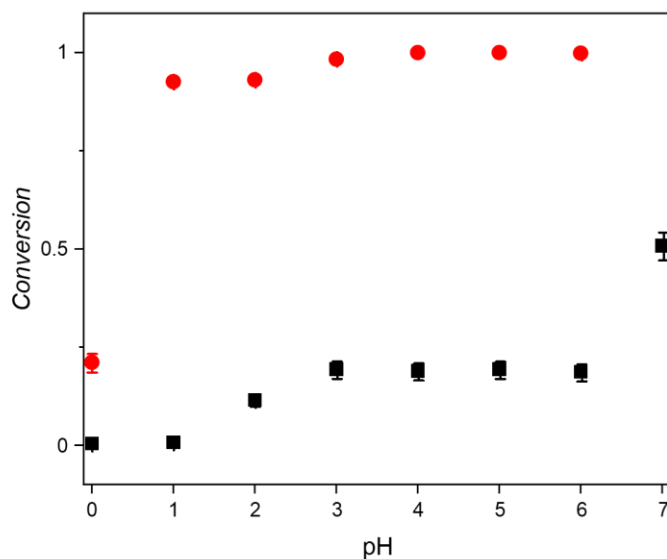
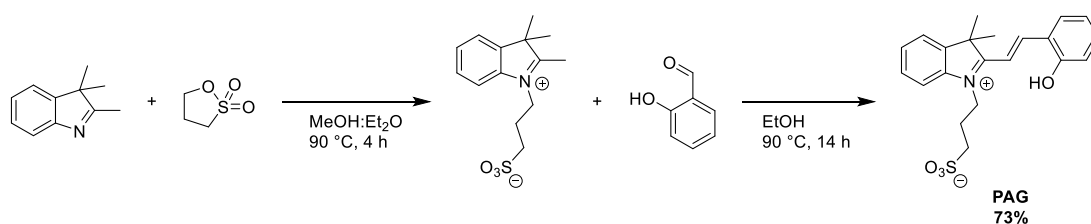


Figure 6-8: Conversion to cycloaddition products as a function of pH for MeO-PEG-SPP (black squares, $\lambda = 480$ nm, $6.32 \pm 0.18 \cdot 10^{19}$ photons) and MeO-PEG-AP (red circles, $\lambda = 420$ nm, $6.38 \pm 0.36 \cdot 10^{19}$ photons). Reproduced with permission. © 2022 The Authors. *Angewandte Chemie International Edition* published by Wiley-VCH GmbH.

6.3.4 Inhibition of photocycloaddition in presence of photoacid generator

The presence of PAG supposedly limits the photoreactivity of the SPP group and inhibits [2+2] cycloaddition in the blue light region. The synthesis of PAG is depicted in **Scheme 6-3**.



Scheme 6-3: Synthesis of PAG.

Specifically, irradiation ($\lambda = 445$ nm, $I_L = 3$ W cm⁻², $t = 1$ h) of the MeO-PEG-SPP solution resulted in the disappearance of the absorbance band characteristic of the SPP group (**Figure 6-9 A**); however, this absorbance band remains when irradiated in presence of PAG (**Figure 6-9 B**). The inhibition of the [2+2] photocycloaddition of

the SPP moiety by the PAG was further confirmed by NMR spectroscopy, indicating low formation of the dimer (ca. 5%) when a solution of MeO-PEG-SPP and PAG was exposed to blue light (**Figure 6-9 C**).

In contrast, green light ($\lambda = 525 \text{ nm}$, $I_L = 3 \text{ W cm}^{-2}$, $t = 1.5 \text{ h}$) irradiation triggers the photocycloaddition, as seen by the disappearance of the resonances corresponding to the HC=CH styryl resonances at 7 ppm and 7.5 ppm, even when PAG was present in the reaction. The UV/Vis absorption spectra of PAG and the SPP chromophore (**Figure 6-10**) reveal competitive absorption of PAG and SPP up to 500 nm. Interestingly, cycloaddition still occurs at $\lambda = 525 \text{ nm}$ (**Figure 6-9 C**, second top NMR spectrum), although only PAG absorbs photons at this wavelength. An action plot analysis for MeO-PEG-SPP in presence of PAG was performed (**Figure 6-11**). Under equimolar conditions ($[PAG]=1.71 \text{ mg mL}^{-1}$), the reactivity represents the absorptivity profile fairly well. In general, however, an inhibition effect is observed. Since the number of photons supplied to the solution in an action plot study is defined, the low conversion could be due to the competition in absorption of the PAG compound. Indeed, both compounds share a general trend of absorption in water, but PAG has a higher molar absorptivity ($39000 \text{ L mol}^{-1} \text{ cm}^{-1}$) compared to MeO-PEG-SPP ($15900 \text{ L mol}^{-1} \text{ cm}^{-1}$) at 460 nm (**Figure 6-10**).

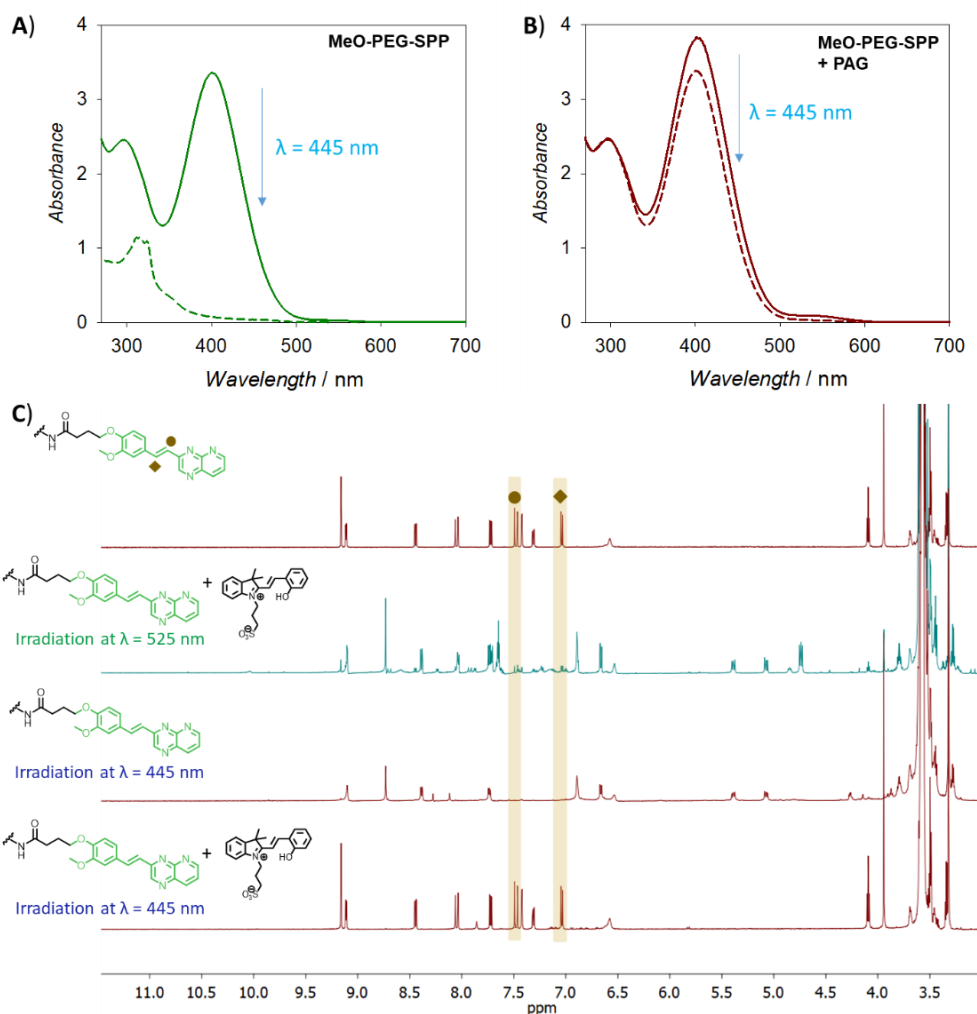


Figure 6-9: UV/Vis absorption spectra of the MeO-PEG-SPP in water in before and after irradiation with blue light at $\lambda = 445$ nm in A) absence of PAG or B) presence of PAG. C) $^1\text{H-NMR}$ spectra (600 MHz, CDCl_3) of MeO-PEG-SPP before (top spectrum) and after irradiation by green light at 525 nm with PAG, blue light at $\lambda = 445$ nm, and blue light at $\lambda = 445$ nm with PAG (bottom spectrum, irradiation conditions: $I_L = 3 \text{ W cm}^{-2}$, $t = 1 \text{ h}$); the highlighted area indicates the resonances from styryl $\text{CH}=\text{CH}$ protons. Reproduced with permission. © 2022 The Authors. *Angewandte Chemie International Edition* published by Wiley-VCH GmbH.

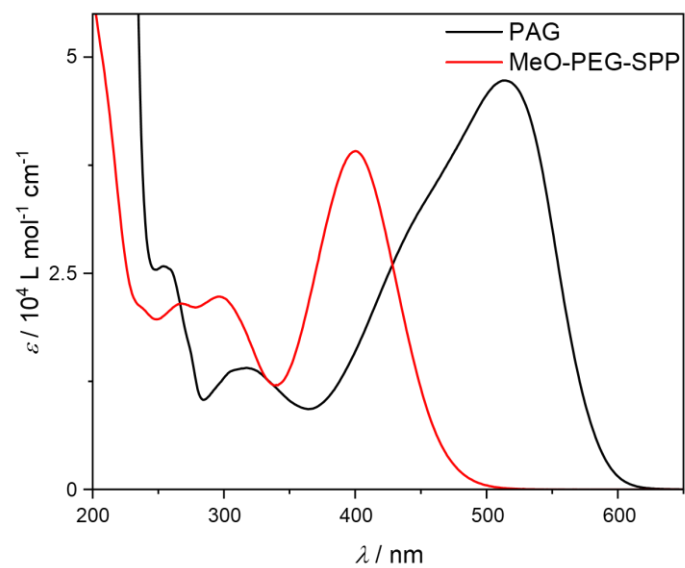


Figure 6-10: UV/Vis absorption spectra of PAG (black) and MeO-PEG-SPP (red) in water. $d = 10$ mm.

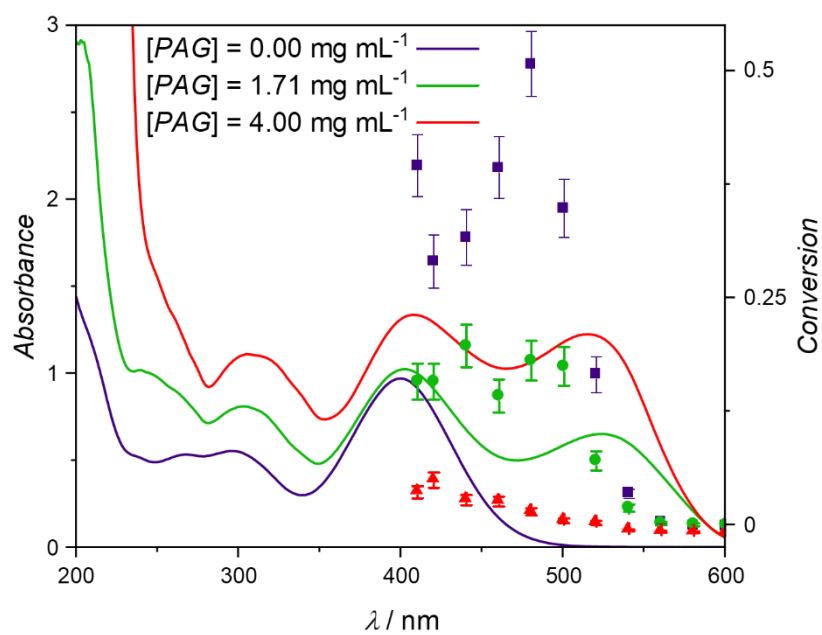


Figure 6-11: UV/Vis spectra and corresponding action plots of MeO-PEG-SPP and PAG in different concentrations of PAG in water. Violet squares: No PAG, green circles: $[PAG] = 1.71$ mg mL⁻¹, red triangles: $[PAG] = 4.00$ mg mL⁻¹. $d = 10$ mm.

6.3.5 Incorporation of the SPP moiety into a hydrogel

The halochromic photochemical ligations and inhibition with PAG are translated into materials engineering, specifically the modulation of hydrogels crosslinking density by light-mediated polymer ligation. An 8-arm PEG containing SPP endgroup (Chapter 8.5.4.7), PEG-(SPP)₈, was synthesised. Polymer solutions ($c = 5 \text{ mM}$) were exposed to blue light ($\lambda = 445 \text{ nm}$, $I_L = 20 \text{ mW cm}^{-2}$) at pH 6.8, 5 and 3 and the evolution of storage modulus investigated by *in situ* rheological measurements. The crosslinking process was followed by tracking elastic (G') and viscous (G'') moduli, with minimal disruption to the chemical reaction.^[301-302] The setup available allowed for simultaneous irradiation and characterization, by employing the irradiation source below the sample. Under neutral pH conditions, an increase in G' upon light irradiation is observed, indicating the formation of a hydrogel network via crosslinking. Gelation completed after approximately 25 min of irradiation (**Figure 6-12 B**) and no further increase in G' was observed.^[303] Acidic conditions ($\text{pH} \leq 5$) fully suppress the crosslinking and no hydrogel was formed.

8-arm PEG with non-halochromic AP endgroup, PEG-(AP)₈, displays efficient photocrosslinking under all pH conditions employed (**Figure 6-12 C**). Notably, the photocycloaddition of the AP group is more efficient than the SPP chromophore, as seen by the rapid photocrosslinking and complete gelation within 15 min of irradiation. This result agrees with the action plot study in which complete conversion of the MeO-PEG-AP was achieved, whilst only ca. 52% conversion of the MeO-PEG-SPP was recorded under similar irradiation conditions, indicating a slower reaction kinetics for the dimerization of the SPP group, and thus a slower gelation kinetics. In both systems, the G' values at complete gelation were similar and in the range of 5–7 kPa. To develop a precursor platform for the λ -orthogonal crosslinking of hydrogel networks, an eight-arm PEG containing both SPP and AP endgroups was synthesised. An NHS ester and amine coupling reaction between PEG-(NH₂)₈, SPP-NHS and AP-NHS afforded the desired eight-arm PEG with both AP and SPP.

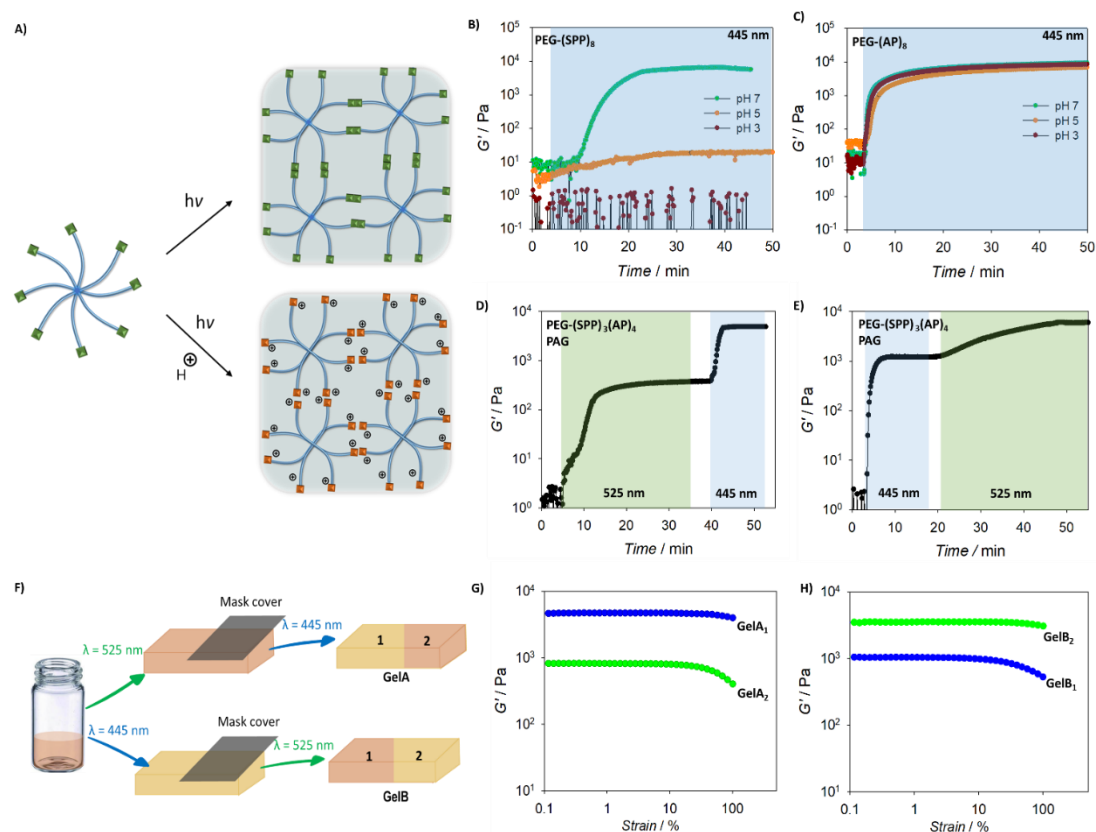
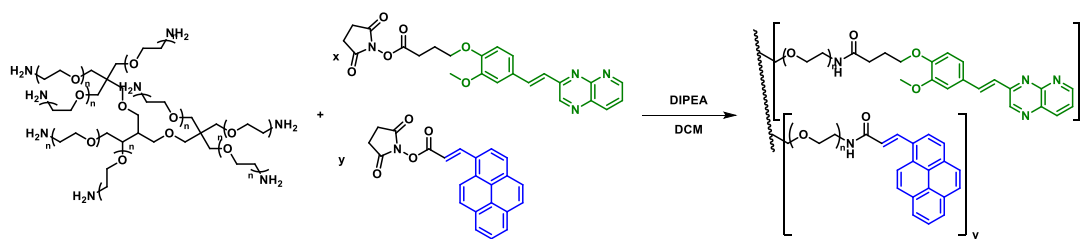


Figure 6-12: A) Schematic crosslinking of MeO-PEG-SPP in acidic environments. B) Evolution of storage modulus of PEG-(SPP)₈ solution ($c = 5$ mM) under blue light conditions ($\lambda = 445$ nm, $I_L = 20$ mW cm⁻²) at different pH values. C) Evolution of storage modulus of PEG-(AP)₈ solution ($c = 5$ mM) under blue light conditions ($\lambda = 445$ nm, $I_L = 20$ mW cm⁻²) at different pH values. D) and E) Sequence-defined irradiation conditions of PEG-(SPP)₃(AP)₄ solution ($c = 5$ mM, 10 wt%) display λ -orthogonal crosslinking of the polymer by either blue (445 nm) or green (525 nm) light ($I_L = 20$ mW cm⁻²). F) Schematic presentation of photomask experiments demonstrating the spatial control over the stiffening process. G) Strain sweep rheological data of two different areas of the hydrogel, initially formed by green light and selectively stiffened by blue light. H) Strain sweep rheological data of two different areas of the hydrogel, first formed by blue light and selectively stiffened by green light. Reproduced with permission. © 2022 The Authors. *Angewandte Chemie International Edition* published by Wiley-VCH GmbH.

It is noted that stoichiometric molar ratio of the NH₂ to the NHS group was used. The overall reaction scheme is depicted in **Scheme 6-4**. Indeed, analysis of the ¹H-NMR spectrum of the eight-arm PEG compound revealed a SPP/AP ratio of 3/4 (1.02/1.34), henceforth the polymer is referred to as PEG-(SPP)₃(AP)₄.



Scheme 6-4: Synthesis of 8-arm PEG containing SPP or AP, or both SPP and AP endgroups.

The [2+2] cycloaddition of PEG-(SPP)₃(AP)₄ solution ($c = 5$ mM, pH 6.8) in the presence of the PAG ($c = 1$ mM) was monitored. Visible light ($\lambda = 525$ nm) irradiation gave rise in the G' value, followed by a plateau at $G' = 600$ Pa after approximately 25 minutes and no further change in the G' value was observed afterwards (**Figure 6-12 D**). The crosslinking continued upon blue light (445 nm) irradiation, reaching a plateau value of $G' = 5.1$ kPa. The λ -orthogonality is demonstrated in a similar experiment, in which the solution of PEG-(SPP)₃(AP)₄ and PAG was first irradiated with blue light to achieve the first crosslinking of the AP endgroups (**Figure 6-12 E**), reaching a plateau G' value of 1.1 kPa. A second photo crosslinking step was induced when switching the light colour to green, producing a network with $G' = 6.8$ kPa. In both experiments, the recorded G' values for the initial crosslinking are 8–10 times lower than the G' values observed during the second crosslinking, despite a near equivalent amount of the photoreactive chain termini being consumed in each photocrosslinking step. The much stiffer gel formed after the second network formation may be due to enhancement effects associated with the physical interactions within the hydrophobic crosslinked structure. The increase of physical interactions within the network structure upon an increase in the number of crosslinks has been reported before for eight-arm PEG-based hydrogels crosslinked by Michael addition reactions.^[304] In the absence of PAG, the wavelength-controlled crosslinking only proceeds in one direction, and complete gelation was achieved when the solution was first irradiated with blue light (**Figure S6-9**). To further highlight the spatial control introduced, irradiation experiments with photomasks were performed. Hydrogels were formed irradiation with one colour of light, either blue ($\lambda = 445$ nm) or green ($\lambda = 525$ nm), followed by irradiation on selected areas by a different wavelength (**Figure 6-12 F** and **Figure S6-10**). As expected, each area on the hydrogels displayed well-defined mechanical properties, with the regions irradiated by two wavelengths featuring much

higher storage moduli compared to single wavelength irradiation. In particular, initial irradiation with green or blue enabled the formation of hydrogels with moduli of 980 Pa and 1020 Pa, respectively. When certain areas are exposed to the other wavelength, the moduli of those areas increased to 5.2 kPa (green then blue) and 4.8 kPa (blue then green). The slight difference in the moduli compared to the values from time sweep measurements is due to the difference in the irradiation periods.

6.4 CONCLUSION

A chemical design for the full λ -orthogonal activation of a highly red-shifted [2+2] photocycloaddition reaction was introduced. The technology is based on a halochromic styrylpyrido[2,3-b]pyrazine moiety and a non-halochromic acrylamidylpyrene function which has been reported earlier. The SPP chromophore was subjected to a thorough action plot study, and a red shift in reactivity of approximately 80 nm was determined. By using a photoacid generator with suitable activation wavelength, crosslinking of the halochromic SPP was limited to green light only, enabling its photocycloaddition to proceed independently of the photoactivation of the AP. Consequently, the bidirectional photo-stiffening of a hydrogel network was demonstrated using either blue or green light. While PAG was used as an additive, it is suggested all chromophores can be installed into a single chemical entity for the wavelength selective dynamic alteration of its materials properties. Critically, the exclusive use of visible light herein shows promise for applications in biologically relevant hydrogel design with careful 'On-Demand' crosslinking capabilities.

Chapter 7: Conclusion and Outlook

In the current thesis, several light-degradable polymers were generated and their degradation pathways carefully investigated. Photoactive molecules ($350 \text{ nm} < \lambda < 550 \text{ nm}$), i.e. *ortho*-nitrobenzyl (*o*NB), s-tetrazine and styrylpyridopyrazines (SPP) were synthesised and probed for their respective reaction pathways. All three molecule classes showed characteristic mechanisms of actions and were thus employed in different degradation scenarios. A summary was appended for each chapter, yet, the overarching findings are compiled in the following section. The chapter will close with an outlook sketching a possible trajectory in the scientific field of ‘On-Demand Light Degradable Polymers’.

ortho-nitrobenzyl is commonly used as a photolabile protecting group. In Chapter 3, the photochemistry of such *o*NB molecules was explored on a small molecule and polymeric level. The key molecule at hand, a bifunctional *o*NB dialcohol **4** (**Scheme 7-1**) was synthesised in a three-step-procedure to allow incorporation into a linear polyurethane structure. Thanks to the effect of two electron-donating alkoxy substituents on the electronic structure, the absorbance was found to extend to 400 nm. A wavelength-resolved reactivity plot (action plot) revealed a possible degradation wavelength of up to 415 nm, which was underpinned by small molecule LED irradiation experiments. *Post-mortem* analysis methods such as NMR and IR spectroscopy were employed, yet online experiments such as EPR spectroscopy revealed a critical biradical intermediate, confirming the *o*NB degradation mechanism. To shine more light on the small molecule kinetics, the critical dialcohol **4** and its precursor **3** were subjected to ultrafast transient laser spectroscopy. Using this technique, the early events of energy distribution were revealed. Although the relaxation dynamics of simple *o*NB model compounds have been reported, the energy dissipation pathways after blue light ($\lambda_{\text{ex}} = 400 \text{ nm}$) excitation have not been uncovered. It was found that 400 nm excitation allows for almost identical relaxation pathways as reported in literature for UV light excitation. However, the formation of the critical *aci*-nitro tautomer was found to proceed from two states, a triplet state with the established biradical as an intermediate and a singlet state allowing for direct transformation. Additionally, luminescence was found in **4**. A comparison with

literature suggests an ESIPT or TICT process which allows for an additional emissive channel. Introducing a carbonyl instead, it was found to slow down the ISC in **3**. Unlike **4**, **3** cannot degrade like *o*NB compounds hence no further energy dissipation pathways are revealed. Instead, excited state absorption of several triplet and singlet states were observed. The structure-reactivity relationship in *o*NB compounds was further investigated by synthesising an elaborate push-pull system. In a simple two-step synthesis, *o*NB compounds with a thioether linkage and stabilizing phenyl moieties were synthesised and probed in their reactivity pattern. Surprisingly, the incorporation of a thioether substituent induced a red shift of its furthest absorption band of approx. 75 nm. Additionally, it was shown that adjacent phenyl substituents allowed stabilization of the previously found biradical intermediate which led to higher selectivity. First, two simple primary alcohol compounds **H2** and **H3** (Scheme 7-1) were investigated. The stabilized derivative was studied in **Ph2** and **Ph3** (for a secondary alcohol with adjacent phenyl group), probed in their wavelength resolved reactivity and compared to established molecules. The action plot revealed striking similarities but also differences: Conversion of **H3** was determined highest, with the established *o*NB **4** and the **Ph3** sharing similar conversion values. However, yield and thus selectivity for the degradation of **Ph3** was determined higher compared to the other molecules **H2**, **H3** and **4**, arguably due to the increased stability of the radical. Further, all candidates showed reactivity up to 440 nm as well. Incorporation of the *o*NB dialcohol **4** was realized by forming a polyurethane with a commercially available diisocyanate. Reasonably sized linear polyurethanes were generated and submitted to pulsed-laser irradiation conditions. By exposing polymers to a controlled number of photons, the polymers' morphology change was followed via SEC methods. Depending on the deposited number of photons, the longer polymer chains underwent degradation more rapidly. Degradation was performed on small films as well, investigated via QCM methods and revealed similar results.

With the successful incorporation of *o*NB into the backbone of a polyurethane, a connection between the local position of a photolabile unit and its degradation efficiency was established. As reported for heat-driven reactions, the centre of a polymer chain is more prone to undergo a bond cleavage event than the outer areas of the chain. Due to the on-demand characteristics of light as a trigger, the question arose if the same finding applied to light-driven degradation reactions. In Chapter 4, a

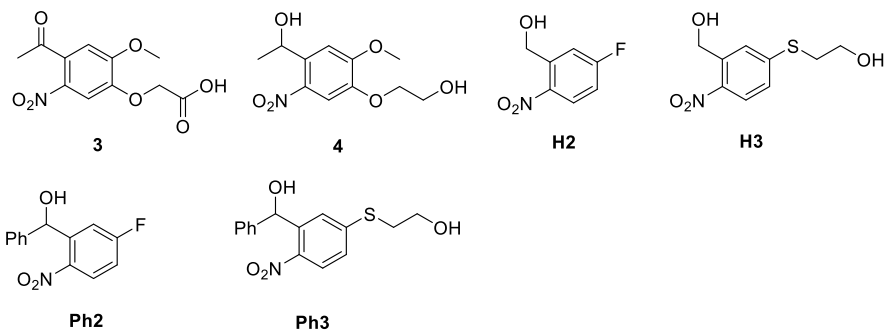
symmetric difunctional RAFT agent with photolabile traits based on the *o*NB platform was synthesised. A wavelength resolved reactivity plot revealed UV-A ($\lambda_{\text{max}} = 350 \text{ nm}$) light to be most efficient for degradation of the *o*NB motif **2** (**Scheme 7-1**). Living RAFT polymerisation with methyl acrylate allowed consistent growth with an *o*NB moiety in mid-chain position. Exposing differently sized polymer chains to UV-A irradiation conditions, a clear trend was discovered. A non-linear increase in degradation kinetics with higher (number-averaged) molecular weight was observed. A physical model relating the obtained apparent rate of reaction to its total entropy was found to be in good agreement with the experimental results.

Chapter 5 encompassed the exploitation of the molecule class tetrazine which is considered high-energetic due to the existence of four nitrogen atoms in the aromatic ring. Instead of backbone fragmentation which was previously realized with *o*NB chemistry, the oxidation of the entire backbone was anticipated. Green light irradiation conditions were employed exploiting the presence of a low-lying $n\pi^*$ absorption band, making a significant step towards visible light degradation scenarios, compared to the blue light irradiation experiments carried out with *o*NB compounds. The reaction of tetrazine dichloride with hydroxyethyl acrylate allowed for the synthesis of a tetrazine with oxygen-linked acrylate termini (**TzDA**, **Scheme 7-1**). The small molecule reactivity was probed regarding its light uptake and only poor reactivity (7%) was revealed throughout the visible light window, which did not show any wavelength dependency. Interestingly, the addition of hydrogen peroxide (H_2O_2) to the reaction mixture revealed a significant increase in light-driven degradation of tetrazine. The wavelength-resolved reactivity now features a pronounced degradation maximum at 520 nm, which seems to well represent the absorption band. The degradation of tetrazine was monitored via ^1H -, ^{13}C -NMR and LC-ESI-MS methods and a N-O exchange was found. The formed molecule was attributed to resonance structures of dihydroxyazines or diacylhydrazines. The oxidative effect was transferred into polymeric material by incorporating tetrazine diacrylate into linear thiol-acrylate polymers. A thorough study of the effect of both light and H_2O_2 on the polymer morphology was performed. It was found that H_2O_2 only oxidizes the thioether joint but leaves the tetrazine core intact. The combined exposure of light and H_2O_2 , however resulted in a dramatic increase of oxidation efficiency, due to oxidation of the tetrazine

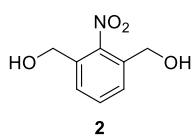
core. The reaction was completed within 15 minutes at ambient temperature and tracked via SEC and stationary UV/Vis methods.

Chapter 6 illustrates crosslinking with a newly designed chromophore unit. Styrylpyrido pyrazines (SPP) were linked to polyethylene glycol (PEG) units and allowed for [2+2] cycloaddition upon visible light irradiation. The effect of pH-value and the wavelength-resolved photon uptake on the crosslinking efficiency of **MeO-PEG-SPP (Scheme 7-1)** was investigated. The [2+2] efficiency decreased with decreasing pH-value. A photoacid generator was employed lowering the pH-value upon blue light irradiation, thus allowing the inhibition of the [2+2] cycloaddition. This technology was extended to hydrogel crosslinking by employing an 8-arm thiol. The [2+2] cycloaddition proceeded on-demand and could be turned on and off via irradiation of blue light.

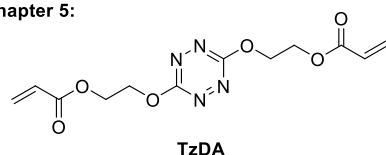
Chapter 3:



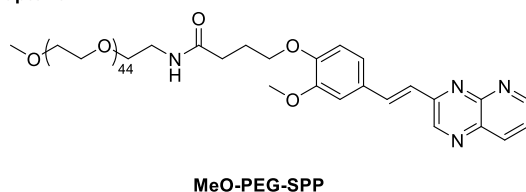
Chapter 4:



Chapter 5:



Chapter 6:



Scheme 7-1: Overview of main compounds used in this thesis.

Degradation plays a critical part in the life of plastics. It can manifest itself exemplarily as fragmentation of the backbone, with every single building block undergoing detachment or a controlled scission at several joints in the polymer chain.

It has been shown that fragmentation can be achieved under blue light irradiation conditions when a bifunctional photolabile unit is incorporated into the backbone. *o*NB chemistry hereby proved to be a promising candidate, given the synthetic ease and simple incorporation into polymers. Harsh UV light, however, renders *o*NB chemistry impracticable for any biologically relevant systems. Naturally, one considers a shift of degradation wavelength outside of the UV barrier (400 nm) an ideal approach to push reactivity into the visible range. Employing stronger electron-donating substituents can lead to a red-shifted absorption band which allows for irradiation beyond 400

nm.^[77, 86] Rate of reactions can be further improved by introducing an extended aliphatic alcohol terminus which allow for a different degradation mechanism.^[84] Exemplarily, a [2-(2-nitrophenyl)ethoxy]carbonyl (NPEOC) group allows for a photoinduced β -scission reaction instead, releasing CO₂. Even further, thio-based chemistry has been used to increase the rate of reaction as well when employing [2-(2-nitrophenyl)-propoxy]carbonyl (NPPOC) groups.^[205]

However, *o*NB chemistry also displays key disadvantages. Firstly, the degradation product absorbs photons more efficiently, thus acting as an internal filter and preventing efficient degradation. Further, the development of degradation on triplet surfaces include the presence of biradical species. The usage of *o*NB chemistry in free-radical polymers is thus challenging since degradation leads to re-crosslinking. The use of *o*NB compounds in any environment with enriched amount of radicals such as reactive oxygen species (ROS) in tumour cells may cause an *o*NB to rather terminate instead.^[305-306] Other photolabile groups such as coumarins are promising important candidates, but feature a similar blue-visible degradation window.^[307-308] Photolabile groups such as bimeane, BODIPY or 3-methylperylene allow for true visible light degradation.^[309-310] Critically however, a major drawback of photochemistry is the nature of the chromophores. Often, these chromophores are not completely consumed during a reaction but altered instead. Consequently, the total absorption efficacy might not change dramatically, or simply put, the number of chromophore units will remain constant. Surely, absorbances at specific wavelengths vanish but rises at other (red- or blue-shifted) parts of the visible spectrum are often noted.^[311] This can result in an internal filter effect which prevents efficient reaction with light since the product absorbs light necessary for the reaction simultaneously. Further, the abundance of light limits the applicability of light as useful trigger in day-to-day operation.

Polymeric material is desired to degrade ‘On-Demand’ and after use and not while using due to a random photon absorption event. One may consider the development of polymeric material which does not require many photons to trigger complete degradation. First works indicate promising results. A small amount of *o*NB groups were incorporated into side chains of an immolative linear polymer. After light excitation, the liberation of the alcohol or amine allowed for intramolecular cyclization and complete backbone fragmentation.^[312] Ultimately, one considers the deployment of a dormant photolabile group which has to evolve into the photoactive state prior.

One idea realizable is the development of dual-trigger self-immolative polymers in an AND logic gate fashion. Ideally, such a polymer is in a dormant state until usage, preventing premature or random light-driven degradation. The polymers activity is first changed, exemplarily by activating the immolative breaking point such as a carefully designed endcap. The *pro*-endcap could be activated and evolve into an active state by employing the first trigger. Subsequently, light induces complete polymer breakdown by triggering the endcap.^[313-314] Thus, ideally only one photolabile group has to be employed, avoiding the presence and formation of excessive amounts of photoactive byproduct. Thanks to the immolative capabilities, the reaction leads to a complete fragmentation of the polymer. Due to the low concentration of photolabile units, the probability of a trigger-event on-demand is high. Since degradation will technically not happen via photoinduced chemistry but rather its initiation, the total number of chromophore units will stay unaltered and low which is desired. Higher penetration depth and the absence of many photoactive units allow for true visible-light degradation. Light-mediated immolative^[315] as well as AND-gated^[314] systems have already been reported, however, the consolidation of both remains scarcely explored. Synthesis of a *pro*-endcap which can be activated with one trigger and then allow for immolation when employing light, is truly a challenge for molecular architects. But not only the endcap synthesis is challenging, it should also be noted that immolative character is limited to certain polymer architectures. Exemplarily, polylactide (PLA) and poly(lactide-*co*-glycolic acid) (PLGA) are prone to fragmentation by nucleophilic attack but may not be suitable for a variety of applications. Imprinting an ‘immolative character’ may prevent important characteristics required for plastics, such as a certain elastic modulus or toughness.

Nevertheless, not only molecular engineering should be considered. It was shown that morphological parameters, such as chain length, undeniably affect the photodriven degradation efficiency. This was explored in this thesis on a linear polymeric level.^[316] It is of high interest whether this finding can be transferred into a hydrogel design and if this dependency holds true even in a network environment. Tuning molecular reactivity with (macro-)molecular parameters such as tailored mesh size would provide excellent control over release or fragmentation scenarios. The release of monomer-sized fragments after photodegradation was observed and their nature studied. However, the obtained fragments are not of further economic value as they do not

feature any functional groups. Significant effort can be directed to photodegradable moieties which yield functional or ‘of value’ chemicals to allow for efficient recycling.^[317-318] Such goods can be used as building blocks, thus easily fuel plastic production and decrease fossil gas extraction and usage. However, not only fragmentation can be considered as a possible degradation scenario. Green light allowed tetrazine-bearing polymers to undergo oxidation under dinitrogen release. Especially in the realm of recyclability, the environmental or economic *post mortem* value of degradation products can be improved. A significantly oxidized backbone carries a higher oxygen content and may make it useful for pyrolysis application.

All in all, even the most elaborate monomer structure and polymeric architecture cannot hide the significant trade-off one has to make for degradable polymers: An efficiently degradable polymer may not possess sufficient mechanical strength or superior mechanical properties. Such a polymer platform has to be carefully designed. Many considerations will affect the selection of an appropriate photolabile unit but many photoactive groups are limited in their use. Free-radical polymerisations prevent the use of radical-based photodegradable groups since they induce recrosslinking. Aesthetically demanding polymeric material, e.g., polymers possessing a certain colour, prevent the usage of photolabile group absorbing at a different wavelength. Although light-degradable polymers are of high interest for various reasons, their implementation remains highly challenging due to the combination of factors stated previously. Selection of suitable mechanical properties was not even considered but are significantly influenced by molecular structure as well. An important step is considered to be fundamental research on a molecular and macromolecular level. Ultrafast relaxation dynamics within pico- to nanoseconds decide the fate of photolabile moieties and can be revealed by femtosecond spectroscopy. After setting a minimum performance goal for the desired application, thorough screening can reveal promising candidates. Artificial Intelligence (AI) supported screening and *de novo* design can help identify strong candidates for the project at hand.^[319] By using structure-outcome data to train an AI accordingly, a reactivity screening can proceed accelerated, thus identifying suitable candidates more rapidly.^[320] Necessarily, data quality has to be of high standards to ensure an AI’s workability and chemists have to be trained to adopt AI in their workflow. The challenges faced are multiple since so

many parameters have to be considered but the tools at hand will shine some more light in the long term.

Chapter 8: Experimental Part

8.1 MATERIALS

The following solvents were used as received without further purification:

Acetone (AR grade, AIM Scientific), acetonitrile (AcN, HPLC grade, Fisher), cyclohexane (CH, ACS, ISO grade, Suppelco), dichloromethane (DCM, analytical reagent, Fisher), diethyl ether (Et₂O, anhydrous, Ajax Finechem), *N,N*-dimethylformamide (DMF, >99%, Sigma-Aldrich), ethanol (EtOH, analytical reagent, Ajax Finechem), ethyl acetate (EA, analytical reagent, Fisher), methanol (MeOH, AR grade, AIM Scientific), n-hexane (95% AR grade, Ajax Finechem), *N,N*-dimethylacetamide (DMAc, 99%, Fisher), tetrahydrofuran (THF, HPLC grade, Fisher), toluene (HPLC grade, Fisher), acetonitrile-*d*₃ (AcN, 99.8%D, Cambridge Isotope Laboratories), dimethylsulfoxide-*d*₆ (DMSO, 99.9%D, Cambridge Isotope Laboratories), tetrahydrofuran-*d*₈ (THF, >99%D, Sigma-Aldrich).

The following chemicals were used as received without further purification:

4'-Hydroxy-3'-methoxyacetophenone (98%, Sigma-Aldrich), *tert*-butyl bromoacetate (98%, Alfa Aesar), potassium carbonate (99%, Chem-Supply), nitric acid (70%, AIM Scientific), acetic anhydride (99%, Chem-Supply), borane tetrahydrofuran complex solution (1.0 M in THF, Sigma Aldrich), hexamethylene diisocyanate (HDI, >98%, Sigma-Aldrich), dibutyltin dilaurate (DBTL, 95%, Sigma-Aldrich), amberlite® IRA743 (free base, Sigma-Aldrich), 1,3-dimethyl-2-nitrobenzene (99%, Sigma-Aldrich), potassium permanganate (AR Grade, Ajax Finechem), sodium hydroxide (AR grade, Chem-Supply), hydrochloric acid (32%, Analytical Grad, Ajax Finechem), sodium bicarbonate (NaHCO₃, 99%, Sigma-Aldrich), ammonium chloride (NH₄Cl, ACS, ISO grade, Supelco), 5-fluoro-2-nitrobenzaldehyde (98%, Combi Blocks), 2-mercaptoethanol (>99%, Sigma-Aldrich), phenylmagnesium bromide solution (3.0 M in Et₂O, Sigma-Aldrich), 1-butanethiol (99%, Sigma-Aldrich), carbon disulphide (>99%, Sigma-Aldrich), 2-bromopropionic acid (>99 %, Sigma-Aldrich), *N*-(3-dimethylaminopropyl)-*N'*-ethylcarbodiimide hydrochloride (EDC, > 98%, Sigma-Aldrich), 4-(Dimethylamino)pyridine (DMAP, >99%, Sigma-Aldrich), methyl acrylate (99%, stabilized with 15 ppm 4-methoxyphenol, Alfa Aesar), aluminium

oxide (activated, neutral, Brockmann I, Sigma-Aldrich), 3,6-Dichloro-1,2,4,5-tetrazine (TzCl₂, 97%, AmBeed), 2-Hydroxyethyl acrylate (HEA, 96%, Sigma-Aldrich), triethylamine (NEt₃, Sigma-Aldrich), tetraethylene glycol (99%, Sigma-Aldrich), acrylic acid (99%, Sigma-Aldrich), hexylamine (99%, HexAm, Sigma-Aldrich), 2-(2-(2-methoxyethoxy)ethoxy)ethyl acrylate (>90%, stabilized with MEHQ, TCI), 2,2'-(Ethylenedioxy)diethanethiol (EDT, 95%, Sigma-Aldrich), hydrogen peroxide (30% solution, Fisher), methylglyoxal solution (~40% in H₂O, Sigma-Aldrich), 2,3-Diaminopyridine (95%, Sigma-Aldrich), piperidine (synthesis grade, Sigma-Aldrich), lithium hydroxide (98%, Sigma-Aldrich), *N*-hydroxysuccinimide (98%, Sigma-Aldrich), *N,N*-diisopropylethylamine (DIPEA, >99%, Sigma-Aldrich), 8-arm PEG20k-OH (JenKem Tech, USA).

2,2-azobisisobutyronitrile (AIBN, 12 wt.% in acetone, Sigma Aldrich) was recrystallized twice from methanol prior to use.

Glassware for synthesis was first treated in a base bath (KOH in isopropanol 2 M) overnight, rinsed with water, subjected to second washing in a dishwashing machine, and dried in an oven at 70 °C for 6-12 h.

Thin-layer chromatography (TLC) was performed on silica gel 60 F254 alumina sheets (Merck) and visualized by UV light or potassium permanganate solution. Column chromatography was run on silica gel 60 (0.04-0.06 mm, 230-400 mesh ASTM, Merck).

Aqueous solutions of H₂O with different pH values were generated by subsequent dilution of water with 32% hydrochloric acid (Ajax Finechem, Analytical grade) or NaHCO₃ (Ajax Finechem, AR grade). The final pH values were recorded with an AQUAPHZ Rev. 3.1 (TPS, Australia) pH sensor after an equilibration period of 5 min. The pH sensor was calibrated against GB4 (pH=4.00) and GB7 (pH=7.01) solutions (TPS, Australia) by linear regression prior to usage.

Prior to any chromatographic purification, the crude products were deposited on celite® 545. Flash chromatography was performed on an Interchim XS420+ flash chromatography system consisting of a SP-in-line filter 20-µm, an UV-VIS detector (200-800 nm) and a SofTA Model 400 ELSD (55 °C drift tube temperature, 25 °C spray chamber temperature, filter 5, EDR gain mode) connected via a flow splitter

(Interchim Split ELSD F04590). The separations were performed using an Interchim dry load column and an Interchim Puriflash Silica HP 15 μm column.

8.2 ANALYSIS AND INSTRUMENTATION

8.2.1 Nuclear Magnetic Resonance (NMR) Spectroscopy

^1H - and ^{13}C -NMR spectra were recorded on a Bruker System 600 Ascend LH, equipped with a BBO-Probe (5 mm) with z-gradient (^1H : 600.13 MHz, ^{13}C 150.90 MHz). Resonances are reported in parts per million (ppm) relative to tetramethylsilane (TMS). The δ -scale was calibrated to the respective solvent signal of CHCl_3 , $\text{DMSO-}d_6$ or Acetonitrile- d_3 for ^1H spectra and for ^{13}C spectra on the middle signal of the CDCl_3 triplet, the DMSO quintet or the Acetonitrile septet. To analyse the spectra, the software MESTRENOVA 11.0 was used. The resonances are quoted as follows: s = singlet, bs = broad singlet, d = doublet, t = triplet, q = quartet, quin = quintet, dd = doublet of doublets and m = multiplet.

8.2.2 Stationary UV/Vis absorption Spectroscopy

UV/Vis spectra were recorded on a Shimadzu UV-2700 spectrophotometer equipped with a CPS-100 electronic temperature control cell positioner. Samples were measured in Hellma Analytics quartz high precision cell cuvettes with a path length of 10 mm at 25 $^\circ\text{C}$. If not stated otherwise, stock solutions were prepared in solvent with a concentration of 1.0 mg mL^{-1} .

Information regarding femtosecond spectroscopy setup: UV/Vis spectra in Chapter 3.3.4 and Chapter 3.3.5 were recorded on an UV/Vis/NIR spectrometer Cary 500 (Varian) between 200 and 800 nm. Samples were measured in fused silica cuvettes with a path length of 1 mm at 25 $^\circ\text{C}$.

8.2.3 Online UV/Vis absorption Spectroscopy

Online UV/Vis spectra were recorded on an in-house built-in *situ* UV/Vis apparatus. An Ocean Optics DH-MINI Deuterium-Tungsten-Halogen lamp was coupled via optic

fibres (P400-025-SR) to an Ocean Optics FLAME-T-UV-VIS spectrometer, sensitive from 200 to 850 nm, via cuvette holder. Samples were prepared in THF in varying concentrations and measured in Hellma Analytics quartz high precision cell cuvettes at 25 °C. Spectra were recorded every 50 ms (20 ms integration time).

8.2.4 Determination of extinction coefficients of compounds via stationary UV/Vis absorption spectroscopy

If not stated otherwise, extinction coefficient ϵ (L mol⁻¹ cm⁻¹) was determined by linear regression of the Beer-Lambert law. Plotting the concentration-pathlength product $c \cdot d$ versus its absorption at a distinct wavelength A_λ , the coefficient can be obtained as a slope of the linear fit. Five data points were usually generated in the range of one order of magnitude. Error bars ΔA and Δc were obtained *via* Gaussian error propagation:

$$\Delta c = \frac{1}{M \cdot V} \cdot \Delta m - \frac{m}{M \cdot V^2} \cdot \Delta V \quad \text{Equation 8-1}$$

$$\Delta A = \epsilon \cdot d \cdot \Delta c \quad \text{Equation 8-2}$$

8.2.5 Stationary Emission spectroscopy

Emission spectra were recorded on a on a Fluoromax-4 spectrofluorometer (HORIBA) with a Haake AC200 temperature control unit (Thermo Scientific). The software FluorEssence v3.5 was used to record emission spectra. Baseline was recorded in deionised water. The quantum yield Φ for emission was calculated by:^[321]

$$\Phi = \Phi_R \cdot \frac{1 - 10^{-A_R}}{1 - 10^{-A_S}} \cdot \frac{\int F_S(\lambda) d\lambda}{\int F_R(\lambda) d\lambda} \cdot \left(\frac{\eta_S}{\eta_R}\right)^2 \quad \text{Equation 8-3}$$

With A_R and A_P being the absorption maxima of reference (R) and sample (S) used for determining Φ . The second factor takes the areas of the recorded luminescence signal into account and the third factor considers refractive indices of the solvents used. 4-(Dicyanomethylene)-2-methyl-6-(4-dimethylaminostyryl)-4H-pyran was used as a reference.

8.2.6 Electron Paramagnetic Resonance (EPR) Spectroscopy

EPR spectra were recorded on a MiniScope MS400 spectrometer (Magnettech GMBH, Berlin, Germany) using CDCl_3 as the solvent and capillary tubes for liquid handling. Data simulation was performed with the MATLAB 2018a software package (The Mathworks, Natick, MA, USA) and a custom plug-in published elsewhere.^[322]

8.2.7 Fourier-transformed Infrared (FT-IR) Spectroscopy

FT-IR spectra were recorded on a Nicolet iS50 FTIR spectrometer in ATR configuration.

8.2.8 Liquid Chromatography hyphenated Electrospray Ionisation Mass Spectrometry (LC-ESI-MS)

LC-MS measurements were performed on an UltiMate 3000 UHPLC System (Dionex, Sunnyvale, CA, USA) consisting of a pump (LPG 3400SZ), autosampler (WPS 3000TSL) and a temperature controlled column compartment (TCC 3000). Separation was performed on a C18 HPLC column (Phenomenex Luna 5 μm , 100 \AA , 250 \times 2.0 mm) operating at 40 $^\circ\text{C}$. Water (containing 5 mmol L^{-1} ammonium acetate) and acetonitrile were used as eluents. A gradient of acetonitrile:H₂O 5:95 to 100:0 (v/v) in 7 min at a flow rate of 0.40 $\text{mL}\cdot\text{min}^{-1}$ was applied. The flow was split in a 9:1 ratio, where 90% of the eluent was directed through a DAD UV-detector (VWD 3400, Dionex) and 10% was infused into the electrospray source. Spectra were recorded on an LTQ Orbitrap Elite mass spectrometer (Thermo Fisher Scientific, San Jose, CA, USA) equipped with a HESI II probe. The instrument was calibrated in the m/z range 74-1822 using premixed calibration solutions (Thermo Scientific). A constant spray voltage of 3.5 kV, a dimensionless sheath gas and a dimensionless auxiliary gas flow rate of 5 and 2 were applied, respectively. The capillary temperature and was set to 300 $^\circ\text{C}$, the S-lens RF level was set to 68, and the aux gas heater temperature was set to 100 $^\circ\text{C}$. Error Δ was determined in ppm according to Equation 8-4.

$$\Delta = \frac{|m_{theo} - m_{exp}|}{m_{theo}} \cdot 10^6 \quad \text{Equation 8-4}$$

8.2.9 Size-Exclusion Chromatography hyphenated Electrospray Ionisation Mass Spectrometry (SEC-ESI-MS)

Spectra were recorded on a Q Exactive Plus (Orbitrap) mass spectrometer (Thermo Fisher Scientific, San Jose, CA, USA) equipped with an HESI II probe. The instrument was calibrated in the m/z range 74-1822 using premixed calibration solutions (Thermo Scientific) and for the high mass mode in the m/z range of 600-8000 using ammonium hexafluorophosphate solution. A constant spray voltage of 3.5 kV, a dimensionless sheath gas and a dimensionless auxiliary gas flow rate of 10 and 0 were applied, respectively. The capillary temperature and was set to 320 °C, the S-lens RF level was set to 150, and the aux gas heater temperature was set to 125 °C. The Q Exactive was coupled to an UltiMate 3000 UHPLC System (Dionex, Sunnyvale, CA, USA) consisting of a pump (LPG 3400SD), autosampler (WPS 3000TSL), and a temperature-controlled column department (TCC 3000). Separation was performed on two mixed bed size exclusion chromatography columns (Agilent, Mesopore 250 × 4.6 mm, particle diameter 3 μm) with a precolumn (Mesopore 50 × 7.5 mm) operating at 30 °C. THF at a flow rate of 0.30 mL·min⁻¹ was used as eluent. The mass spectrometer was coupled to the column in parallel to an UV detector (VWD 3400, Dionex), and a RI-detector (RefractoMax520, ERC, Japan) in a setup described earlier.^[323] 0.27 mL·min⁻¹ of the eluent were directed through the UV and RI-detector and 30 μL·min⁻¹ were infused into the electrospray source after post-column addition of a 50 μM solution of sodium iodide in methanol at 20 μL·min⁻¹ by a micro-flow HPLC syringe pump (Teledyne ISCO, Model 100DM). A 100 μL aliquot of a polymer solution with a concentration of 2 mg·mL⁻¹ was injected into the SEC system. Error Δ was determined in ppm according to Equation 8-4. SEC-ESI-MS simulation was performed with a published software package.^[324]

8.2.10 Size-Exclusion Chromatography (SEC)

Waters system (THF): In Chapter 3, SEC chromatograms were recorded on a system consisting of a 1515 Isocratic HPLC Pump, 2414 RI detector and a 717 Plus autosampler (Waters, Milford, USA), and a column set (PSS, Mainz, Germany) consisting of a guard column (50 × 8 mm, 10 μm) and two 1000 Å GRAM columns (300 × 8 mm, 10 μm). The eluent was HPLC grade THF. All molar mass data is reported relative to polystyrene standards (EasyCal, Agilent, Santa Clara, USA).

PSS system (DMAc): In Chapter 4, SEC measurements were conducted on a PSS SECurity2 system consisting of a PSS SECurity Degasser, PSS SECurity TCC6000 Column Oven (60 °C), PSS GRAM Column Set (8x150 mm 10 μm Precolumn, 8x300 mm 10 μm Analytical Columns, 1000 Å, 1000 Å and 30 Å) and an Agilent 1260 Infinity Isocratic Pump, Agilent 1260 Infinity Standard Autosampler, Agilent 1260 Infinity Diode Array and Multiple Wavelength Detector (A: 254 nm, B: 360 nm), Agilent 1260 Infinity Refractive Index Detector (35 °C). HPLC grade DMAc, 0.01 M LiBr, is used as eluent at a flow rate of 1 mL min⁻¹. Narrow disperse linear poly(styrene) (M_n : 266 g·mol⁻¹ to 2.52 · 10⁶ g mol⁻¹) and poly(methyl methacrylate) (M_n : 202 g·mol⁻¹ to 2.2 · 10⁶ g mol⁻¹) standards (PSS ReadyCal) were used as calibrants. All samples were passed over 0.22 μm PTFE membrane filters. Molecular weight and dispersity analysis were performed in PSS WinGPC UniChrom software (version 8.2).

PSS system (THF): In Chapter 5 and 6, SEC measurements were conducted on a PSS SECurity2 system consisting of a PSS SECurity Degasser, PSS SECurity TCC6000 Column Oven (35 °C), PSS SDV Column Set (8x150 mm 5 μm Precolumn, 8x300 mm 5 μm Analytical Columns, 100000 Å, 1000 Å and 100 Å) and an Agilent 1260 Infinity Isocratic Pump, Agilent 1260 Infinity Standard Autosampler, Agilent 1260 Infinity Diode Array and Multiple Wavelength Detector (A: 254 nm, B: 360 nm), Agilent 1260 Infinity Refractive Index Detector (35 °C). HPLC grade THF, stabilized with BHT, is used as eluent at a flow rate of 1 mL·min⁻¹. S-4 Narrow disperse linear poly(styrene) (M_n : 266 g·mol⁻¹ to 2.52 · 10⁶ g mol⁻¹) and poly(methyl methacrylate) (M_n : 202 g mol⁻¹ to 2.2 · 10⁶ g·mol⁻¹) standards (PSS ReadyCal) were used as calibrants. All samples were passed over 0.22 μm PTFE membrane filters. Molecular weight and dispersity analysis were performed in PSS WinGPC UniChrom software (version 8.2).

8.2.11 Chrystal Microbalance (QCM)

Measurements were performed using a Biolin Scientific QSense Explorer and window-module with 40 μ L volume above sensor and 250 μ L total volume. The temperature of the flow cell was kept at 25 °C and a flow rate of 100 μ L min⁻¹ of milli-Q water was employed. Each measurement was started by recording each sensors' fundamental frequency, recording a dry base-line for approximately 30min. Subsequently the flow cell was purged with milli-Q water and a solvent baseline was recorded for approximately 30 min (without light). Finally, the sample was irradiated with a 365 nm UV-LED to determine thin film degradation. Frequency was recorded until a stable state was reached.

8.2.12 X-Ray Photoelectron Spectroscopy (XPS)

Spectra were recorded on a KratosAxis Supra photoelectron spectrometer. During analysis, the charge compensation system was employed to prevent any localised charge build-up. For each sample, wide spectra and high-resolution spectra of individual peaks (N 1s) were recorded. All spectra were calibrated by setting the C 1s peak to 285.00 eV. Evaluation, peak deconvolution, and fitting was carried out in Casa Software LtdCasaXPS 2.3.

8.2.13 Rheological Experiments

Rheological experiments were carried out using an Anton Paar rheometer with a plate-plate configuration. The lower plate is made of quartz and the upper plate of stainless steel with a diameter of 25 mm. The LED light source (445 nm or 525 nm, intensity was tuned to 20 mW cm⁻²) was placed underneath the quartz plate. In a typical experiment, 50 μ L of an aqueous solution of polymers (10wt%, ca. 4.7 mM), was placed on the lower plate and the upper plate was brought to a measurement gap of 0.3 mm. The test was started by applying a 0.1% strain with the frequency of 1 Hz on the sample, and the light was turned on at predetermined interval. Light sources were commercially available LEDs with a 10 W power output.

8.3 LASER SETUPS

8.3.1 Action plots nanosecond laser

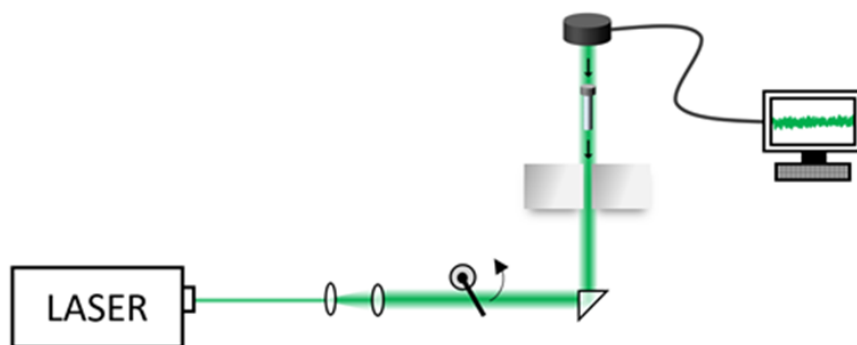
The incident light used for laser experiments (e.g. Action Plots) was generated by an Oportek Opolette 355 OPO (Coherent), producing 7 ns, 20 Hz pulses with a flat-top spatial profile. The output beam was initially passed through a beam expander (-50 mm and 100 mm lens combination) to ensure it is large enough to uniformly irradiate the entire sample volume. The beam then passes through an electronic shutter and directed upwards using a UV silica right angle prism (see **Scheme 8-1**). Finally, the beam enters the sample, suspended in an aluminium block, from below. The laser energy deposited into the sample was measured above the aluminium block before and after experiments using an EnergyMax thermopile sensor (Coherent, J-25MB-LE) to account for any power fluctuations during irradiation. Precise photon numbers were determined from the laser pulse energy using Equation 8-5:

$$N_p = \frac{E_{pulse} \cdot \lambda \cdot f_{rep} \cdot t_{irr}}{hc \cdot \frac{T_\lambda}{100}} \quad \text{Equation 8-5}$$

where E_{pulse} is the measured pulse energy above the aluminium block, λ the wavelength of the incident radiation, f_{rep} the laser repetition rate, t_{irr} the irradiation time, h Planck's constant, c the speed of light and T_λ the wavelength dependent glass transmission presented in **Figure 8-1**. For laser measurements, all samples were prepared in 0.7 mL glass crimp vials (ID 6.2 mm) capped with a rubber/PTFE septum. Once an initial measurement is completed and the photon number is known, the required energies at other wavelengths can be determined by rearranging Equation 8-5:

$$E_{pulse} = \frac{N_p \cdot hc \cdot \frac{T_\lambda}{100}}{\lambda \cdot f_{rep} \cdot t} \quad \text{Equation 8-6}$$

The transmittance values shown and used here were obtained analogously to a method reported previously.^[185] The glass vials were cut at a height of 3 mm.



Scheme 8-1: Apparatus used for the laser experiments (e.g. action plots).

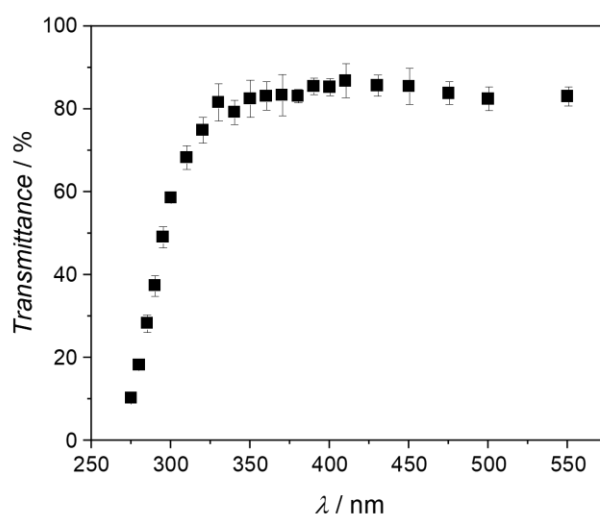


Figure 8-1: Transmittance of the bottom of the glass vials used in the current study. Transmittance of the bottom of the glass vials used in the current study.

8.3.2 Transient broadband femtosecond absorption spectroscopy

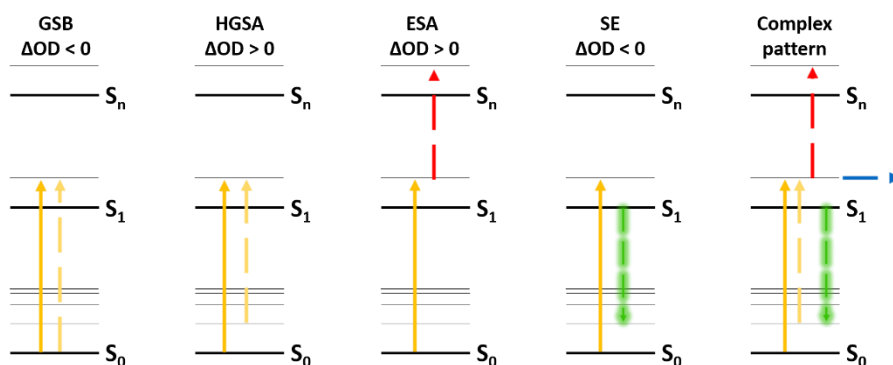
Relaxation processes after electronic excitation usually proceed on a femto- to nanosecond timescale, as described in Chapter 2.1.2 in further detail. In principle, one short laser pulse induces population of an excited states.^[47] After a certain delay time, τ , a second pulse probes the remaining population. Since the probing pulse is spectrally broadened, the almost entire visible range can be probed with one pulse. Due to the spectral broadness, the pulse is called supercontinuum. By varying the delay time, the evolution of populated states can be monitored. The change of optical density, ΔOD , is calculated by Equation 8-7:

$$\Delta OD = \log\left(\frac{I}{I_0}\right)_{with\ excitation} - \log\left(\frac{I}{I_0}\right)_{without\ excitation} \quad \text{Equation 8-7}$$

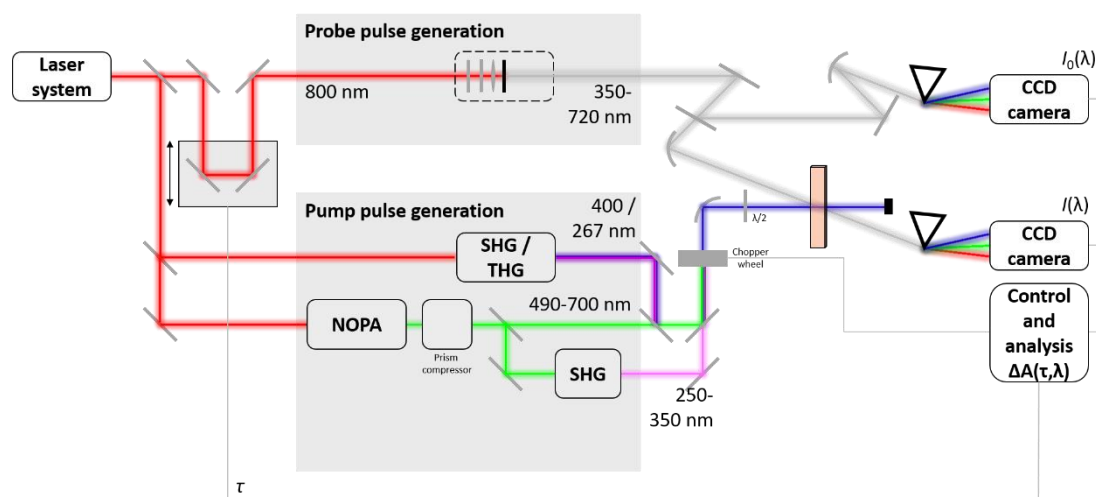
with $\log\left(\frac{I}{I_0}\right)_{with\ excitation}$ and $\log\left(\frac{I}{I_0}\right)_{without\ excitation}$ being the absorbance with and without excitation taking place, respectively. Due to the consecutive nature of the two pulses, this technique is commonly referred to ‘pump-probe-spectroscopy’.

Different relaxation process can contribute to the recorded ΔOD and are illustrated in **Scheme 8-2**. Upon absorption, the electronic ground can experience depletion if absorbing species do not repopulate the ground state before the next pump-and-probe sequence. These phenomena are referred to Ground State Bleaching (GSB) or Hot Ground State Absorption (HGSA), depending on the energetic state of the absorbing molecules. Both processes add negative contribution to ΔOD . Excited State Absorption (ESA) adds positive (> 0) contributions to ΔOD and refers to the probing of electronic excited states. Stimulated Emission (SE) adds negative contributions since an excited state is depopulated while emitting fluorescent photons. Usually, several processes happen simultaneously which give rise to a complex pattern.

The experimental setup used in this thesis is an in-house built (**Scheme 8-3**) and was described in literature before.^[39, 325-326] A regenerative Ti:Sapphire fs-laser system (Astrella, Coherent) generates ultrashort laser pulses with a duration of 35 fs at a central wavelength of 800 nm. The repetition rate of the laser system is 1 kHz with an output energy of approximately 7 mJ. After passing a set of apertures, the fundamental pulse is split into a pump and a probe line. Hereby, the pump line consists of non-collinear parametric amplifiers (NOPA’s) and further allows for simple generation of second (400 nm) and triple (267 nm) harmonics from the fundamental pulse at 800 nm. The remaining pulse is guided through a rotating 2 mm CaF₂ cell unit which generates a spectrally broad pulse between 350 and 680 nm (supercontinuum). Both pulses are aligned and focused into the sample volume. Time delay τ between pump and probe pulses was achieved by extending the optical path length of the probe pulse via a retro reflector mounted on a computer-controlled translation stage (Thorlabs). A chopper wheel (500 Hz) prevents transmission of every second pump pulse which allows separate recording of $\log\left(\frac{I}{I_0}\right)_{with\ excitation}$ and $\log\left(\frac{I}{I_0}\right)_{without\ excitation}$.



Scheme 8-2: Different processes affecting the population of excited states and ΔOD . State Bleaching (GSB), Hot Ground State Absorption (HGSA), Excited State Absorption (ESA), Stimulated Emission (SE), superposition of several processes giving rise to a complex evolution of ΔOD . For details, the reader is referred to the text.



Scheme 8-3: Experimental setup for transient UV/Vis absorption experiments. The laser system generates 800 nm femtosecond pulses which are guided into a probe pulse and a pump pulse generation unit. Both pulses are manipulated and spatial and temporal overlap was achieved in a cuvette (beige). A CCD camera records wavelength-resolved absorbances. The reader is referred to the text for details. Own illustration.

Acquisition of wavelength-resolved absorbances was achieved with a CCD streak camera. A second streak camera records the remaining supercontinuum light and accounts for any possible fluctuations during experiment. Samples were prepared in 1 mm cuvettes (Suprasil, Hellma).

Single transient responses were fit via multiexponential decay function from the respective maximum of ΔOD with $j = 2, 3$ if not stated otherwise:

$$F(t) = \sum_j A_j e^{-\frac{t}{\tau_j}} \quad \text{Equation 8-8}$$

8.4 EXPERIMENTAL PROCEDURES

8.4.1 Experimental procedures Chapter 3: Exploring the photochemistry of *ortho*-nitrobenzyl alcohols and incorporation in polyurethanes

8.4.1.1 EPR Spectroscopy of 4 and simulation of spectrum

Radical formation according to the in **Scheme 3-1** depicted mechanism was tracked via EPR. The degassed sample in CDCl₃ was irradiated with a 395 nm laser light (handheld presentation device, 5 mW), directed into the sample holder and EPR spectra were recorded. Experimental settings are listed in **Table S3-4**. The EPR spectrum was then simulated with the *garlic* function of the EasySpin package. Here, a given electron spin is simulated to couple with adjacent nuclei. The nature of the nuclei can be set. Two systems were found, one with the electron being localized at the nitrogen nucleus and coupling with the nitrogen and two hydrogen (N3) nuclei and the other being located at a carbon and coupling with this carbon nucleus only (C1). Two spectra were convoluted representing the experimental spectrum. Simulation parameters are given in **Table S3-5**. Single spectra as well as their convolution are presented in **Figure S3-7**.

8.4.1.2 General remarks for the determination of conversion and yields in Action Plots

¹H-NMR spectra were recorded in high-resolution (128 scans instead of 16). The conversion *X* and yield *Y* can then be calculated according to Equation 8-9 and Equation 8-10. Action plot studies were performed in triplets with the standard deviation as error bars.

$$X = 1 - \frac{n_\lambda}{n_{no\ irradiation}} \quad \text{Equation 8-9}$$

$$Y = \frac{n_{product,\lambda} - n_{product,no\ irradiation}}{n_{starting\ material,no\ irradiation}}$$

Equation 8-10

8.4.1.3 Action Plot of 4

Experiments were conducted in triplets (350 nm only twice). By setting the integral of the internal standard trimethoxybenzene (TMB) to 100, the integrals of **4** and **4d**, assigned to the respective resonances *a* and *b* (**Figure 3-4**) can be compared.

Table 8-1: Parameters for the Action-Plot experiment. *: When conversion is determined to < 0, resolution limit of the NMR spectrometer is assumed. *I*_{IS}: Integral internal standard, *I*₄: Integral of resonance for **4**, *I*_{4d}: Integral of resonance for **4d**, *X*₄: Conversion of **4**, *Y*_{4d}: Yield of **4d**.

λ / nm	$N_p / \mu\text{mol}$	$\Delta N_p / \mu\text{mol}$	<i>I</i> _{IS}	<i>I</i> ₄	<i>I</i> _{4d}	<i>X</i> ₄	ΔX_4	<i>Y</i> _{4d}	ΔY_{4d}
300-1			100	69.20	12.83				
300-2	0.961	0.130	100	69.60	12.06	0.201	0.006	0.142	0.005
300-3			100	70.31	12.22				
310-1			100	67.49	14.20				
310-2	0.961	0.062	100	67.56	13.38	0.222	0.008	0.158	0.005
310-3			100	68.68	13.75				
320-1			100	70.23	12.33				
320-2	0.948	0.054	100	69.79	12.69	0.196	0.005	0.138	0.010
320-3			100	70.6	11.03				
330-1			100	72.22	10.71				
330-2	0.959	0.057	100	71.51	10.34	0.174	0.006	0.124	0.006
330-3			100	72.61	11.41				
340-1			100	72.6	9.78				
340-2	0.979	0.051	100	71.84	10.02	0.175	0.006	0.114	0.002
340-3			100	71.7	10.13				
350-1			100	74.14	9.84				
350-2	0.960	0.049	100	73.82	9.55	0.153	0.003	0.111	0.002
360-1			100	74.62	9.63				
360-2	0.953	0.059	100	75.61	8.41	0.145	0.012	0.102	0.007
360-3			100	73.57	8.69				
370-1			100	74.37	9.17				
370-2	0.958	0.056	100	75.95	8.54	0.141	0.010	0.102	0.004
370-3			100	74.51	8.93				
380-1			100	76.52	7.28				
380-2	0.969	0.082	100	75.45	7.36	0.130	0.006	0.085	0.002
380-3			100	75.76	7.61				
390-1			100	76.28	6.88				
390-2	0.972	0.088	100	76.41	7.02	0.125	0.001	0.079	0.002
390-3			100	76.52	6.74				
400-1	0.960	0.083	100	79.05	6.11	0.094	0.001	0.069	0.001

400-2			100	79.15	5.87				
400-3			100	79.08	5.98				
410-1			100	82.17	3.60				
410-2	0.960	0.058	100	81.96	3.69	0.065	0.008	0.042	0.001
410-3			100	80.85	3.57				
420-1			100	86.53	1.54				
420-2	0.945	0.164	100	86.65	1.48	0.011	0.006	0.017	0.000
420-3			100	85.70	1.52				
430-1			100	88.09	0.40				
430-2	0.968	0.070	100	87.5	0.37	-0.005*	0.004	0.004	0.000
430-3			100	87.54	0.37				
440-1			100	80.84	0.09				
440-2	0.960	0.058	100	87.97	0.17	0.015	0.052	0.002	0.001
440-3			100	89.22	0.14				
450-1			100	88.26	0.09				
450-2	0.963	0.073	100	88.39	0.08	-0.014*	0.004	0.001	0.000
450-3			100	88.88	0.04				
No irradiation			100	87.29	0.00	-	-	-	-

8.4.1.4 LED Irradiation experiments

Irradiation experiments were performed using NMR tubes (for small molecule kinetics) and LEDs with an emission peak centred at 340, 365, 390 and 415 nm, respectively. The LED emission spectra are depicted in **Figure S3-10**. The LEDs were powered using a tunable (voltage U and current I) power supply. Cooling was provided via placing a fan behind the heat sink (**Figure S3-9**). Direct parameters for U , I and calculated power P_{calc} are provided in **Table 8-2**.

Table 8-2: Experimental parameters for the performed irradiation experiments. (*: performed in photovial to compensate UV absorption of ordinary glass).

λ / nm	U / V	I / A	P_{calc} / W	dist / cm
340*	0.44	4.4	1.94	2
365	3.61	0.70	2.53	2
390	3.70	0.61	2.26	2
415	14.9	0.16	2.31	2

Maintaining the same distance between the sample and the LED ensures same irradiation conditions for the sample. Different LEDs were employed (**Figure S3-10**).

After a set time, the sample is submitted to NMR spectroscopy, and afterwards exposed to further light. The conversion X , is hereby calculated by Equation 8-11.

$$X_4 = \frac{I_4}{I_4 + I_{4d}} \quad \text{Equation 8-11}$$

Analogously, the yield of **4d** is then calculated by:

$$Y_{4d} = \frac{I_{4d}}{I_4 + I_{4d}} \quad \text{Equation 8-12}$$

8.4.1.5 PLD-SEC of step growth generated PU polymers

Assuming the *o*NB dialcohol, **4**, is incorporated as every second unit, the molar amount of *o*NB for a given mixture can be calculated easily. For every cured polymer (2 – 20 minutes), four different exposure times (t1-t4) were selected. The equivalents of photons were then calculated on a case-to-case basis.

Table 8-3: Parameters for PLD-SEC experiments. Entries are denoted as curing time_ irradiation time

Entry	λ / nm	$E_{\text{pulse}} /$ μJ	$\Delta E_{\text{pulse}} /$ μJ	k	T_λ	$N_p /$ μmol	$\Delta N_p /$ μmol	$n_{o\text{NB}} /$ μmol	eq. $h\nu$ vs. <i>o</i> NB	$\Delta\text{eq. } h\nu$ vs. <i>o</i> NB
2 min_t1	340	728	16	1500	79.82	2.48	0.06	2.90	0.85	0.02
2 min_t2	340	736	18	3000	79.82	5.01	0.12	2.96	1.69	0.04
2 min_t3	340	726	16	6000	79.82	9.88	0.22	3.62	2.73	0.06
2 min_t4	340	733	16	12000	79.82	19.9	0.44	3.23	6.18	0.14
5 min_t1	340	728	16	1500	79.82	2.48	0.06	3.13	0.79	0.02
5 min_t2	340	736	18	3000	79.82	5.01	0.12	3.00	1.67	0.04
5 min_t3	340	726	16	6000	79.82	9.88	0.22	3.82	2.59	0.06
5 min_t4	340	733	16	12000	79.82	19.9	0.44	3.32	6.00	0.13
10 min_t1	340	728	16	1500	79.82	2.48	0.06	3.13	0.79	0.02
10 min_t2	340	736	18	3000	79.82	5.01	0.12	4.11	1.22	0.03
10 min_t3	340	726	16	6000	79.82	9.88	0.22	4.31	2.29	0.05
10 min_t4	340	733	16	12000	79.82	19.9	0.44	3.26	6.12	0.14
17 min_t1	340	728	16	1500	79.82	2.48	0.06	3.16	0.78	0.02
17 min_t2	340	736	18	3000	79.82	5.01	0.12	3.03	1.65	0.04
17 min_t3	340	726	16	6000	79.82	9.88	0.22	3.72	2.66	0.06
17 min_t4	340	733	16	12000	79.82	19.9	0.44	3.36	5.94	0.13
20 min_t1	340	728	16	1500	79.82	2.48	0.06	2.96	0.84	0.02
20 min_t2	340	736	18	3000	79.82	5.01	0.12	3.59	1.40	0.03
20 min_t3	340	726	16	6000	79.82	9.88	0.22	3.82	2.59	0.06
20 min_t4	340	733	16	12000	79.82	19.9	0.44	3.49	5.72	0.13

8.4.1.6 Surface experiments preparation

The QCM sensors and glass slides were plasma cleaned prior to spin coating at 1500 rpm for 2 min using 10 μL of a 7 $\mu\text{g mL}^{-1}$ polymer solution.

8.4.1.7 Action plot of 5-Fluoro-2-nitrobenzyl alcohol

Table 8-4: Irradiation parameters for the undegassed action plot of compound **2,5-H2**. I_{IS} : Integral internal standard, I_2 : Integral of resonance for **2**, $I_{2\text{d}}$: Integral of resonance for **2d**, X_2 : Conversion of **2**, $Y_{2\text{d}}$: Yield of **2d**.

λ / nm	$N_{\text{p}} / \mu\text{mol}$	$\Delta N_{\text{p}} / \mu\text{mol}$	I_{IS}	I_2	$I_{2\text{d}}$	X_2	ΔX_2	$Y_{2\text{d}}$	$\Delta Y_{2\text{d}}$
300-1			100	54.44	4.52				
300-2	0.98	0.05	100	54.81	4.60	0.259	0.012	0.120	0.005
300-3			100	56.09	4.22				
310-1			100	56.21	3.95				
310-2	1.00	0.02	100	57.29	3.88	0.235	0.008	0.105	0.001
310-3			100	57.25	3.85				
320-1			100	59.29	3.29				
320-2	0.98	0.03	100	57.25	3.52	0.223	0.017	0.092	0.003
320-3			100	56.94	3.50				
330-1			100	58.25	3.76				
330-2	0.96	0.03	100	55.85	3.96	0.241	0.021	0.104	0.003
330-3			100	55.38	3.86				
340-1			100	51.83	5.21				
340-2	0.99	0.03	100	50.54	5.20	0.313	0.009	0.139	0.001
340-3			100	50.86	5.13				
350-1			100	46.79	6.56				
350-2	0.99	0.06	100	46.13	6.98	0.374	0.005	0.180	0.007
350-3			100	46.83	6.50				
360-1			100	48.13	6.35				
360-2	0.99	0.03	100	47.50	6.53	0.357	0.004	0.172	0.003
360-3			100	47.84	6.28				
370-1			100	51.34	5.08				
370-2	0.99	0.05	100	51.20	5.17	0.308	0.004	0.137	0.002
370-3			100	51.82	5.02				
380-1			100	58.39	2.52				
380-2	0.99	0.04	100	56.56	3.04	0.215	0.025	0.077	0.008
380-3			100	60.21	3.07				
390-1			100	67.48	1.15				
390-2	0.99	0.03	100	63.23	1.24	0.130	0.032	0.033	0.002
390-3			100	63.52	1.27				
400-1	0.99	0.04	100	69.49	0.22	0.079	0.014	0.007	0.003

400-2			100	67.46	0.38				
400-3			100	68.61	0.20				
410-1			100	70.87	0.14				
410-2	0.99	0.05	100	73.55	-0.02	0.034	0.019	0.002	0.002
410-3			100	71.26	0.06				
420-1			100	72.71	0.11				
420-2	0.98	0.07	100	72.36	0.08	0.023	0.005	0.002	0.002
420-3			100	73.07	-0.02				
430-1			100	72.82	-0.02				
430-2	0.98	0.06	100	72.75	0.02	0.016	0.009	0.000	0.001
430-3			100	73.95	0.04				
440-1			100	74.02	-0.04				
440-2	0.97	0.05	100	72.76	-0.03	0.022	0.017	0.001	0.000
440-3			100	71.54	-0.04				
450-1			100	75.23	-0.06				
450-2	0.97	0.06	100	73.50	0.00	0.008	0.018	0.001	0.001
450-3			100	72.58	-0.02				
No irradiation			100	74.39	0.00				

8.4.1.8 Action plot of 5-Thioethyl-2-nitrobenzyl alcohol

Table 8-5: Irradiation parameters for the undegassed action plot of compound **2,5-H3**. I_{IS} : Integral internal standard, I_3 : Integral of resonance for **3**, I_{3d} : Integral of resonance for **3d**, X_3 : Conversion of **3**, Y_{3d} : Yield of **3d**.

λ / nm	$N_p / \mu\text{mol}$	$\Delta N_p / \mu\text{mol}$	I_{IS}	I_3	I_{3d}	X_3	ΔX_3	Y_{3d}	ΔY_{3d}
300-1			100	43.58	4.46				
300-2	0.97	0.06	100	45.03	4.49	0.339	0.012	0.130	0.004
300-3			100	45.00	4.23				
310-1			100	41.57	4.79				
310-2	0.96	0.03	100	40.65	4.96	0.389	0.007	0.146	0.003
310-3			100	41.32	4.98				
320-1			100	42.60	2.32				
320-2	0.96	0.03	100	42.34	4.75	0.371	0.003	0.117	0.042
320-3			100	42.25	4.74				
330-1			100	45.02	4.33				
330-2	0.96	0.03	100	43.77	4.52	0.334	0.016	0.127	0.008
330-3			100	45.92	4.01				
340-1			100	48.09	3.51				
340-2	0.98	0.03	100	47.60	3.61	0.290	0.004	0.106	0.002
340-3			100	47.84	3.59				
350-1			100	49.49	3.33				
350-2	0.97	0.03	100	49.90	3.30	0.261	0.004	0.097	0.002
350-3			100	50.07	3.22				
360-1	0.98	0.03	100	51.00	3.01	0.238	0.004	0.087	0.003

360-2			100	51.47	2.81				
360-3			100	51.46	3.01				
370-1			100	53.48	2.38				
370-2	0.96	0.03	100	55.58	2.29	0.191	0.016	0.059	0.018
370-3			100	54.51	1.31				
380-1			100	55.86	1.95				
380-2	0.96	0.04	100	55.12	1.93	0.174	0.007	0.059	0.002
380-3			100	55.97	2.05				
390-1			100	55.54	2.06				
390-2	0.97	0.03	100	55.85	2.02	0.178	0.008	0.061	0.001
390-3			100	54.80	2.06				
400-1			100	54.77	1.95				
400-2	0.95	0.04	100	55.55	2.01	0.179	0.007	0.057	0.002
400-3			100	55.70	1.85				
410-1			100	58.45	1.35				
410-2	0.97	0.05	100	58.75	1.34	0.131	0.003	0.040	0.001
410-3			100	58.37	1.40				
420-1			100	62.06	0.51				
420-2	0.96	0.08	100	61.76	0.48	0.076	0.009	0.014	0.001
420-3			100	62.89	0.47				
430-1			100	64.50	0.14				
430-2	0.97	0.06	100	64.82	0.12	0.039	0.004	0.004	0.000
430-3			100	65.02	0.12				
440-1			100	65.50	0.01				
440-2	0.97	0.05	100	64.53	0.02	0.034	0.008	0.001	0.000
440-3			100	65.32	0.03				
450-1			100	65.00	0.00				
450-2	0.97	0.05	100	64.01	0.01	0.035	0.015	0.000	0.000
450-3			100	65.99	0.03				
No irradiation			100	67.38	0.00				

8.4.1.9 Action plot of (5-fluoro-2-nitrophenyl)(phenyl)methanol

Table 8-6: Irradiation parameters for the undegassed action plot of compound **2,5-Ph2**. I_{IS} : Integral internal standard, I_2 : Integral of resonance for **2**, I_{2d} : Integral of resonance for **2d**, X_2 : Conversion of **2**, Y_{2d} : Yield of **2d**.

λ / nm	$N_p / \mu\text{mol}$	$\Delta N_p / \mu\text{mol}$	I_{IS}	I_2	I_{2d}	X_2	ΔX_2	Y_{2d}	ΔY_{2d}
300-1			100	23.33	0.97				
300-2	0.961	0.056	100	23.51	0.78	0.145	0.015	0.050	0.031
300-3			100	24.11	2.37				
310-1			100	22.37	0.89				
310-2	0.954	0.036	100	22.16	1.09	0.187	0.015	0.044	0.014
310-3			100	22.98	1.64				
320-1	0.991	0.046	100	22.74	1.29	0.168	0.011	0.061	0.017

320-2			100	23.34	1.56				
320-3			100	22.95	2.21				
330-1			100	23.63	2.31				
330-2	0.963	0.050	100	23.14	1.97	0.154	0.009	0.072	0.012
330-3			100	23.45	1.66				
340-1			100	22.53	2.69				
340-2	0.957	0.048	100	22.72	2.62	0.179	0.006	0.097	0.003
340-3			100	22.87	2.77				
350-1			100	21.57	4.42				
350-2	0.975	0.049	100	22.40	5.02	0.206	0.015	0.181	0.021
350-3			100	21.93	5.56				
360-1			100	21.19	4.28				
360-2	0.973	0.052	100	20.59	3.14	0.240	0.014	0.137	0.021
360-3			100	21.33	3.92				
370-1			100	21.52	2.95				
370-2	0.943	0.041	100	22.33	4.26	0.206	0.015	0.146	0.037
370-3			100	22.04	4.95				
380-1			100	23.06	2.79				
380-2	0.959	0.053	100	23.01	2.89	0.169	0.004	0.105	0.004
380-3			100	22.87	3.01				
390-1			100	24.31	1.47				
390-2	0.955	0.050	100	25.41	2.81	0.097	0.021	0.084	0.027
390-3			100	25.23	2.66				
400-1			100	26.58	0.39				
400-2	0.971	0.055	100	26.63	0.53	0.037	0.002	0.018	0.004
400-3			100	26.71	0.58				
410-1			100	27.44	0.00				
410-2	1.003	0.166	100	27.39	0.00	0.010	0.002	0.000	0.000
410-3			100	27.35	0.00				
420-1			100	27.51	0.00				
420-2	0.927	0.135	100	27.71	0.00	0.001	0.004	0.000	0.000
420-3			100	27.73	0.00				
430-1			100	27.87	0.00				
430-2	0.981	0.097	100	27.25	0.00	-0.003	0.016	0.000	0.000
430-3			100	28.13	0.00				
440-1			100	27.67	0.00				
440-2	0.991	0.092	100	27.99	0.00	-0.004	0.007	0.000	0.001
440-3			100	27.68	0.04				
450-1			100	27.48	0.00				
450-2	0.888	0.139	100	27.48	0.00	0.000	0.012	0.000	0.000
450-3			100	28.06	0.00				
No irradiation			100	27.67	0.00				

8.4.1.10 Action plot of (2-((3-(hydroxy(phenyl)methyl)-4-nitrophenyl)thio)-ethan-1-ol)

Table 8-7: Irradiation parameters for the undegassed action plot of compound **2,5-Ph3**. I_{IS} : Integral internal standard, I_3 : Integral of resonance for **3**, I_{3a} : Integral of resonance for **3d**, X_3 : Conversion of **3**, Y_{3a} : Yield of **3d**.

λ / nm	N_p / μmol	ΔN_p / μmol	I_{IS}	I_3	I_{3a}	X_3	ΔX_3	Y_{3a}	ΔY_{3a}
300-1			100	21.77	7.38				
300-2	0.987	0.084	100	18.64	9.14	0.239	0.077	0.244	0.032
300-3			100	22.72	8.33				
310-1			100	19.76	8.60				
310-2	0.961	0.063	100	21.84	6.99	0.263	0.046	0.236	0.034
310-3			100	19.51	8.67				
320-1			100	20.85	7.98				
320-2	0.995	0.042	100	20.65	7.91	0.226	0.041	0.226	0.010
320-3			100	22.69	7.47				
330-1			100	24.40	7.95				
330-2	0.993	0.057	100	21.16	7.34	0.198	0.070	0.216	0.014
330-3			100	20.98	7.24				
340-1			100	24.10	8.06				
340-2	0.984	0.060	100	21.34	7.51	0.201	0.064	0.227	0.011
340-3			100	20.83	7.95				
350-1			100	21.44	7.05				
350-2	1.003	0.085	100	22.92	5.88	0.184	0.036	0.176	0.021
350-3			100	23.36	6.30				
360-1			100	24.81	5.39				
360-2	0.968	0.095	100	23.01	5.84	0.142	0.035	0.150	0.009
360-3			100	23.33	5.84				
370-1			100	26.73	5.81				
370-2	1.015	0.092	100	23.8	5.11	0.093	0.054	0.140	0.013
370-3			100	24.73	5.36				
380-1			100	25.99	4.31				
380-2	1.028	0.105	100	24.23	4.59	0.087	0.033	0.105	0.005
380-3			100	25.54	4.50				
390-1			100	24.78	3.94				
390-2	1.010	0.098	100	24.99	4.06	0.098	0.005	0.090	0.003
390-3			100	25.05	4.10				
400-1			100	24.53	3.76				
400-2	0.982	0.109	100	26.14	3.73	0.089	0.030	0.075	0.007
400-3			100	24.92	3.42				
410-1			100	26.44	3.68				
410-2	0.968	0.092	100	25.63	3.36	0.074	0.031	0.075	0.009
410-3			100	24.74	3.84				
420-1	0.999	0.056	100	26.91	2.41	0.019	0.009	0.028	0.005

420-2			100	27.09	2.42				
420-3			100	27.38	2.18				
430-1			100	27.35	1.83				
430-2	0.999	0.053	100	29.10	2.55	-0.014	0.034	0.017	0.017
430-3			100	27.64	1.68				
440-1			100	27.58	2.20				
440-2	0.985	0.039	100	28.82	1.14	-0.023	0.023	0.004	0.019
440-3			100	28.42	1.62				
450-1			100	26.78	2.44				
450-2	0.977	0.032	100	27.65	1.78	0.004	0.025	0.015	0.015
450-3			100	28.16	1.64				
No irradiation			100	27.65	1.55				

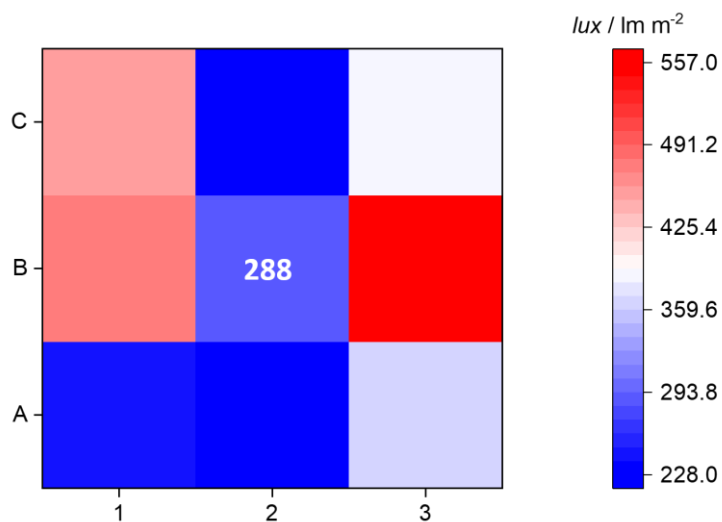
8.4.2 Experimental procedures Chapter 4: Chain-Length-Dependent Photolysis of *ortho*-nitrobenzyl-Centered Polymers

8.4.2.1 LED-based irradiation experiments

The incident light used for LED experiment of the small molecule **2** was a 340 nm UV LED. The solution was crimped, and the vial was placed above the fan-cooled LED. After a definite period of irradiation time, the solution was analysed via UV/Vis and NMR spectroscopy. Settings for the setup: $U = 4.2$ V, $I = 0.25$ A, $d = 0.5$ cm.

8.4.2.2 Photoreactor-based irradiation experiments

The samples were irradiated in a Luzchem LZC-4V photoreactor (**Figure 8-2**) using LZC-UV-A lamps, emitting at 350 nm (**Figure 8-3**). Eight lamps were installed for irradiation from the side. The internal chamber was ventilated to maintain ambient temperature during the entire experiment. Homogeneous irradiation from all directions was ensured by rotating the sample inside the reactor using the LZC-B-carousel, set at six revolutions per minute. The light intensity was measured along the bottom of the photoreactor after warming up the lamps for 5 minutes and grated in 9 equally sized squares. The carousel was set in the centre (square B2, **Scheme 8-4**). A mass concentration of 2.0 mg mL^{-1} (in DMAc) was maintained for all samples, unless stated otherwise. Over the course of the performed experiment, one SEC vial per time increment was removed from the photoreactor to ensure consecutive irradiation of all samples. The samples were filtered and immediately submitted to SEC.



Scheme 8-4: Heat map of luminous flux (lux) inside the photoreactor. The central square **B2** was illuminated with 288 lm m^{-2} for all samples subjected to irradiation (**P1-P4**, **T1** and **4**). Reprinted with permission from J. Bachmann *et al. ACS Macro Lett.* **2021**, *10*, 4, 447-452. Copyright 2021 American Chemical Society. Modified representation.



Figure 8-2: Experimental setup for the photoreactor-based irradiation experiments. Reprinted with permission from J. Bachmann *et al. ACS Macro Lett.* **2021**, *10*, 4, 447-452. Copyright 2021 American Chemical Society.

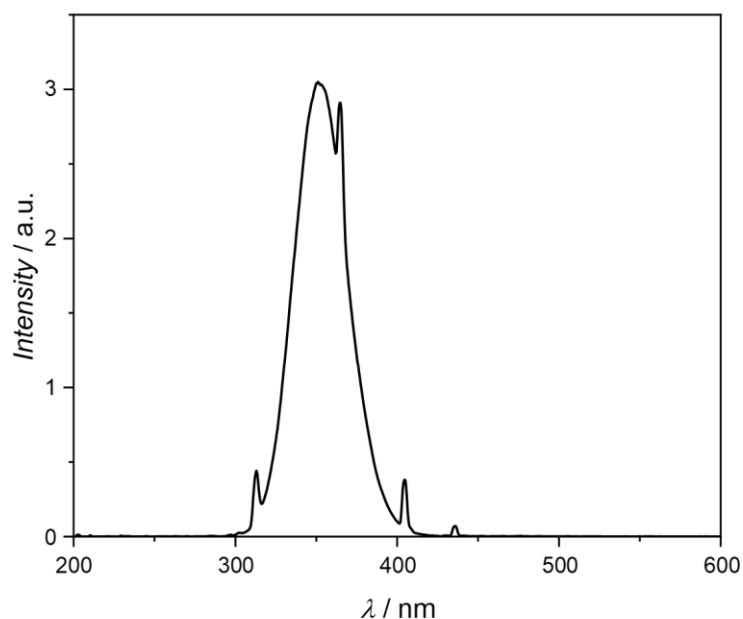


Figure 8-3: Emission spectrum of the employed UV-A lamps. Reprinted with permission from J. Bachmann *et al.* *ACS Macro Lett.* **2021**, *10*, 4, 447-452. Copyright 2021 American Chemical Society.

8.4.2.3 Action Plot of (2-nitro-1,3-phenylene)dimethanol

$^1\text{H-NMR}$ spectra were recorded in high-resolution (128 scans instead of 16). The conversion X and yield Y can then be calculated according to Equation 8-9 and Equation 8-10. Action plot studies were performed in triplets with the standard deviation as error bars. The integral of the internal standard trimethoxy benzene (TMB) was set to 100 and the integrals with and without irradiation in the respective NMR spectra (resonances b and g) were compared.

Table 8-8: Experimental parameters for the action plot of compound **2**. I_{IS} : Integral internal standard, I_b : Integral of resonance b , I_a : Integral of resonance d , X_2 : Conversion of **2**, Y_{2a} : Yield of **2d**.

λ / nm	$N_p / \mu\text{mol}$	$\Delta N_p / \mu\text{mol}$	I_{IS}	I_b	I_a	X_2	ΔX_2	Y_{2a}	ΔY_{2a}
300-1			100	97.82	5.84				
300-2	0.963	0.134	100	101.86	5.54	0.29	0.01	0.16	0.00
300-3			100	99.55	5.51				
310-1			100	107.43	5.07				
310-2	0.988	0.049	100	103.25	5.33	0.26	0.02	0.14	0.01

310-3			100	103.54	4.13				
320-1			100	98.20	4.80				
320-2	0.952	0.048	100	105.93	4.85	0.29	0.04	0.14	0.01
320-3			100	96.54	4.36				
330-1			100	95.95	5.52				
330-2	0.963	0.051	100	94.55	3.43	0.32	0.01	0.15	0.03
330-3			100	97.45	5.44				
340-1			100	91.05	5.93				
340-2	0.970	0.052	100	93.07	6.14	0.35	0.01	0.17	0.02
340-3			100	90.31	4.71				
350-1			100	90.55	6.36				
350-2	0.960	0.054	100	90.51	6.35	0.35	0.02	0.18	0.00
350-3			100	95.37	6.17				
360-1			100	91.54	5.84				
360-2	0.988	0.077	100	90.94	5.80	0.35	0.01	0.16	0.00
360-3			100	92.81	5.64				
370-1			100	95.51	6.02				
370-2	0.953	0.084	100	93.31	5.65	0.30	0.02	0.16	0.01
370-3			100	89.98	4.92				
380-1			100	98.58	4.19				
380-2	0.975	0.097	100	107.50	4.22	0.20	0.04	0.12	0.01
380-3			100	108.46	3.73				
390-1			100	121.56	1.86				
390-2	0.961	0.152	100	121.25	2.10	0.40	0.00	0.05	0.00
390-3			100	121.61	1.93				
400-1			100	132.14	0.97				
400-2	0.962	0.141	100	130.03	1.01	0.07	0.01	0.03	0.00
400-3			100	130.21	0.89				
410-1			100	140.85	0.00				
410-2	0.962	0.113	100	137.98	0.02	0.00	0.02	0.00	0.00
410-3			100	142.29	0.04				
420-1			100	138.90	0.06				
420-2	0.975	0.081	100	138.21	0.00	0.02	0.01	0.00	0.00
420-3			100	136.32	0.10				
430-1			100	135.52	0.00				
430-2	0.956	0.038	100	138.94	0.00	0.02	0.02	0.00	0.00
430-3			100	141.58	0.01				
No irradiation			100	140.90					

8.4.2.4 Quantum Yield determination of (2-nitro-1,3-phenylene)dimethanol

Quantum Yield (QY, Φ) determination for the photolysis of **2** was performed in the following manner: Equimolar samples of **2** and TMB (both $c = 0.004 \text{ mol L}^{-1}$) were briefly irradiated with the nanosecond laser setup described previously. The wavelength was set to 350 nm and exposure time consecutively increased. A volume of 250 μL in acetonitrile- d_3 was irradiated and afterwards diluted with 300 μL

acetonitrile- d_3 after irradiation. As photodegradation leads to line broadening and general increase in extinction, UV/Vis spectroscopy cannot be employed for the determination of Φ . Instead, high-resolution $^1\text{H-NMR}$ spectroscopy was employed to map the relation between incident number of photons and obtained product **2d** (Figure 4-4). The integrals shown in Figure S4-16 were used for determination. It is assumed that every photon will trigger photodegradation, which is valid for short exposure times. As can be readily seen in Figure 4-4, formation of **2d** deviates from the expected linear behaviour at long light exposure, as the photoproduct starts to absorb the light more efficiently. Thus, the QY represents a maximum estimate. The slope obtained from the linear fit is dimensionless and gives access to QY. Each incremental irradiation experiment was performed in triplicates with standard deviation as error.

Table 8-9: Irradiation data for the determination of Φ in acetonitrile- d_3 . I_{IS} : Integral internal standard, I_2 : Integral of resonance for **2**, I_{2d} : Integral of resonance for **2d**, n_{2d} : Molar amount of **2**.

Entry	$N_p / \mu\text{mol}$	$\Delta N_p / \mu\text{mol}$	I_{IS}	I_2	I_{2d}	$n_{2d} / \mu\text{mol}$	$\Delta n_{2d} / \mu\text{mol}$
			100	126.0	0.45		
350-t1	0.094	0.005	100	125.8	0.53	0.0014	0.0003
			100	123.5	0.35		
			100	121.7	1.16		
350-t2	0.189	0.010	100	121.0	1.08	0.0035	0.0001
			100	121.0	1.10		
			100	117.7	1.75		
350-t3	0.283	0.015	100	118.6	1.63	0.0053	0.0002
			100	117.6	1.67		
			100	112.9	2.32		
350-t4	0.377	0.020	100	113.9	2.30	0.0072	0.0002
			100	114.2	2.23		
			100	109.7	2.62		
350-t5	0.472	0.025	100	110.8	2.68	0.0085	0.0002
			100	110.1	2.71		
			100	105.1	3.81		
350-t6	0.717	0.038	100	104.3	3.88	0.0119	0.0006
			100	102.7	3.55		
			100	97.5	4.80		
350-t7	0.944	0.050	100	97.5	4.96	0.0156	0.0003
			100	98.0	4.95		
			100	87.5	6.25		
350-t8	1.415	0.075	100	88.6	6.63	0.0207	0.0008
			100	87.0	6.72		
No irradiation	0	0	100	130.5	0.00	0.0000	0.0000

Slope of the linear fit as shown in **Figure 4-4** is QY, $\Phi_{2 \rightarrow 2d} = (1.75 \pm 0.05)\%$.

8.4.2.5 Small molecule degradation study of (2-nitro-1,3-phenylene)bis-(methylene) bis(2-(((butylthio)carbonothioyl)thio)propanoate)

Bis-RAFT-Agent **4** was irradiated under previously established conditions, identical to the irradiation of **P1-P4** (UV-A irradiation, photoreactor, $c = 2.0 \text{ mg mL}^{-1}$). The kinetics were evaluated via $^1\text{H-NMR}$ spectroscopy and conversion was plotted versus the irradiation time. Conversion X was calculated via Equation 8-13

$$X = 1 - \frac{n_t}{n_{t=0}} \quad \text{Equation 8-13}$$

The rate constant k_{app} was obtained via monoexponential fit of X versus irradiation time (see **Figure S4-17**). $k_{\text{app}, 4, c=2.0} = (0.025 \pm 0.005) \text{ min}^{-1}$.

8.4.2.6 Deconvolutional analysis and kinetic modelling of P1-P4

For kinetic studies with a photoreactor, the polymers **P1-P4** were subjected to a deconvolution analysis to track the evolution of fragments over time. For this purpose, two Lorentzian functions were selected as a Gaussian function did not represent the appearing line-broadening adequately. Start and end SEC trace were compared for the centre of the parental and fragment peak, respectively. The centre of each function was set as constant. The area of each function and its error were of crucial importance. A physical model was fit to the **P1-P4** traces with direct representation of Area Fragment (see below). To compare **P1-P4**, the Relative Fragment Abundance, RFA , was used as expressed in Equation 8-14, Equation 8-15:

$$RFA = \frac{[F]}{[F] + [P]} \quad \text{Equation 8-14}$$

$$\Delta RFA = \left| \frac{[P]}{([F] + [P])^2} \cdot \Delta[F] \right| + \left| \frac{[F]}{([F] + [P])^2} \cdot \Delta[P] \right| \quad \text{Equation 8-15}$$

with $[F]$ being the area of fragment and $[P]$ being the area of parent polymer, obtained via deconvolution SEC analysis. ΔRFA was calculated according to maximum error estimation. The errors $\Delta[F]$ and $\Delta[P]$ were obtained via deconvolutional analysis.

The physical model originates in a first-order decay reaction (Equation 8-16) and its respective rate law (Equation 8-17). Here, the concentration was replaced with the area of species, given as $[P]$ for parental polymers and $[F]$ for fragmented polymer, respectively. An apparent rate of constant k_{app} was applied.



$$\frac{d[P]}{dt} = -k_{app} \cdot [P] \quad \text{Equation 8-17}$$

$$[P](t) = [P]_{t=t_0} \cdot \exp(-k_{app}t) \quad \text{Equation 8-18}$$

$$[P](t) = [P]_{t=t_0} + [F]_{t=t_0} - [F](t) \quad \text{Equation 8-19}$$

$$[F](t) = -[P]_{t=t_0} \cdot [\exp(-k_{app}t) - 1] + [F]_{t=t_0} \quad \text{Equation 8-20}$$

$$[F](t) = d \cdot [-[P]_{t=t_0} \cdot [\exp(-k_{app}t) - 1]] + [F]_{t=t_0} \quad \text{Equation 8-21}$$

Equation 8-18 and Equation 8-19 display the integrated rate law and the expression of mass balance. As the responsiveness of the RI detector does not scale linearly, a scaling factor d was additionally employed. Equation 8-21 is the final expression that was fitted to the experimental evolution of Fragment Area over time.

Table 8-10: Obtained areas of parent and fragment of **P1** ($c = 2.0 \text{ mg mL}^{-1}$) and calculations of the Relative Fragment Abundance, *RFA*.

Entry	$t /$ min	$M_{\text{Parent}} /$ g mol ⁻¹	$[P]$	$\Delta[P]$	$M_{\text{Fragment}} /$ g mol ⁻¹	$[F]$	$\Delta[F]$	<i>RFA</i>	ΔRFA
t ₀	0	1520	2.72	0.03	771	0.04	0.01	0.015	0.035
t ₁	3	1520	2.78	0.02	771	0.11	0.01	0.038	0.026
t ₂	5	1520	2.77	0.03	771	0.16	0.01	0.053	0.034
t ₃	10	1520	2.48	0.01	771	0.46	0.01	0.157	0.015
t ₄	20	1520	2.08	0.02	771	0.95	0.02	0.313	0.030
t ₅	40	1520	1.63	0.02	771	1.48	0.02	0.476	0.026
t ₆	60	1520	1.38	0.01	771	1.71	0.01	0.554	0.012
t ₇	80	1520	1.04	0.02	771	2.16	0.02	0.675	0.020
t ₈	100	1520	0.91	0.02	771	2.30	0.02	0.716	0.021
t ₉	120	1520	0.88	0.01	771	2.36	0.01	0.728	0.014
t ₁₀	140	1520	0.84	0.01	771	2.38	0.01	0.739	0.014
t ₁₁	160	1520	0.81	0.03	771	2.41	0.02	0.749	0.027

t ₁₂	180	1520	0.74	0.02	771	2.52	0.02	0.773	0.017
t ₁₃	200	1520	0.84	0.02	771	2.37	0.02	0.739	0.022
t ₁₄	220	1520	0.76	0.02	771	2.45	0.02	0.763	0.016
t ₁₅	240	1520	0.14	0.02	771	3.16	0.02	0.958	0.019

For a scaling factor of $d_{P1, c=2.0} = (0.967 \pm 0.035)$, an apparent rate of cleavage was determined to: $k_{app, P1, c=2.0} = (0.017 \pm 0.002) \text{ min}^{-1}$.

Table 8-11: Obtained areas of parent and fragment of **P2** ($c = 2.0 \text{ mg mL}^{-1}$) and calculations of the Relative Fragment Abundance, *RFA*.

Entry	<i>t</i> / min	<i>M</i> _{Parent} / g mol ⁻¹	[<i>P</i>]	Δ[<i>P</i>]	<i>M</i> _{Fragment} / g mol ⁻¹	[<i>F</i>]	Δ[<i>F</i>]	<i>RFA</i>	Δ <i>RFA</i>
t ₀	0	3830	2.63	0.05	1810	0.19	0.02	0.069	0.053
t ₁	1	3830	2.60	0.05	1810	0.20	0.02	0.071	0.060
t ₂	3	3830	2.38	0.04	1810	0.48	0.02	0.168	0.046
t ₃	5	3830	2.12	0.03	1810	0.81	0.02	0.276	0.038
t ₄	10	3830	1.95	0.02	1810	0.96	0.01	0.330	0.026
t ₅	20	3830	1.76	0.04	1810	1.14	0.02	0.394	0.040
t ₆	30	3830	1.49	0.04	1810	1.43	0.02	0.491	0.044
t ₇	40	3830	0.94	0.02	1810	2.02	0.01	0.682	0.022
t ₈	50	3830	0.69	0.02	1810	2.29	0.01	0.769	0.022
t ₉	60	3830	0.39	0.02	1810	2.58	0.01	0.869	0.020
t ₁₀	70	3830	0.40	0.02	1810	2.51	0.01	0.864	0.025
t ₁₁	80	3830	0.58	0.07	1810	2.25	0.04	0.794	0.075
t ₁₂	90	3830	0.32	0.03	1810	2.55	0.01	0.888	0.026
t ₁₃	100	3830	0.20	0.02	1810	2.69	0.01	0.931	0.018
t ₁₄	120	3830	0.00	0.00	1810	3.16	0.02	1.000	0.000
t ₁₅	240	3830	0.25	0.02	1810	2.62	0.01	0.914	0.021

For a scaling factor of $d_{P2, c=2.0} = (0.980 \pm 0.032)$, an apparent rate of cleavage was determined to: $k_{app, P2, c=2.0} = (0.032 \pm 0.004) \text{ min}^{-1}$.

Table 8-12: Obtained areas of parent and fragment of **P3** ($c = 2.0 \text{ mg mL}^{-1}$) and calculations of the Relative Fragment Abundance, *RFA*.

Entry	<i>t</i> / min	<i>M</i> _{Parent} / g mol ⁻¹	[<i>P</i>]	Δ[<i>P</i>]	<i>M</i> _{Fragment} / g mol ⁻¹	[<i>F</i>]	Δ[<i>F</i>]	<i>RFA</i>	Δ <i>RFA</i>
t ₀	0	14700	2.09	0.02	7530	0.81	0.02	0.279	0.025

t ₁	0.5	14700	1.95	0.02	7530	0.94	0.02	0.324	0.022
t ₂	1	14700	1.89	0.02	7530	0.99	0.02	0.345	0.022
t ₃	2	14700	1.81	0.02	7530	1.06	0.01	0.368	0.021
t ₄	3	14700	1.77	0.02	7530	1.09	0.01	0.381	0.020
t ₅	4	14700	1.69	0.02	7530	1.16	0.01	0.408	0.019
t ₆	6	14700	1.40	0.02	7530	1.44	0.02	0.507	0.024
t ₇	8	14700	1.23	0.02	7530	1.59	0.02	0.565	0.027
t ₈	10	14700	1.15	0.03	7530	1.68	0.02	0.593	0.029
t ₉	15	14700	0.87	0.03	7530	1.95	0.02	0.692	0.035
t ₁₀	20	14700	0.60	0.03	7530	2.20	0.02	0.784	0.028
t ₁₁	25	14700	0.36	0.02	7530	2.44	0.02	0.872	0.025
t ₁₂	30	14700	0.29	0.04	7530	2.53	0.02	0.898	0.042
t ₁₃	60	14700	0.00	0.00	7530	2.93	0.02	1.000	0.000
t ₁₄	120	14700	0.00	0.00	7530	3.02	0.02	1.000	0.000
t ₁₅	240	14700	0.00	0.00	7530	3.02	0.02	1.000	0.000

For a scaling factor of $d_{P3, c=2.0} = (1.065 \pm 0.015)$, an apparent rate of cleavage was determined to: $k_{app, P3, c=2.0} = (0.051 \pm 0.002) \text{ min}^{-1}$.

Table 8-13: Obtained areas of parent and fragment of **P4** ($c = 2.0 \text{ mg mL}^{-1}$) and calculations of the Relative Fragment, Abundance, *RFA*.

Entry	<i>t</i> / min	<i>M</i> _{Parent} / g mol ⁻¹	[<i>P</i>]	Δ[<i>P</i>]	<i>M</i> _{Fragment} / g mol ⁻¹	[<i>F</i>]	Δ[<i>F</i>]	<i>RFA</i>	Δ <i>RFA</i>
t ₀	0	100000	1.87	0.02	57700	0.94	0.02	0.335	0.028
t ₁	0.5	100000	2.17	0.03	57700	0.63	0.02	0.226	0.035
t ₂	1.0	100000	1.88	0.02	57700	0.92	0.02	0.329	0.025
t ₃	1.5	100000	1.76	0.02	57700	1.03	0.02	0.370	0.024
t ₄	2.0	100000	1.61	0.02	57700	1.18	0.02	0.423	0.024
t ₅	2.5	100000	1.54	0.02	57700	1.24	0.02	0.446	0.023
t ₆	3	100000	1.44	0.02	57700	1.34	0.02	0.483	0.024
t ₇	4	100000	1.41	0.02	57700	1.37	0.02	0.493	0.025
t ₈	6	100000	1.22	0.02	57700	1.54	0.01	0.558	0.023
t ₉	8	100000	0.88	0.03	57700	1.85	0.02	0.677	0.029
t ₁₀	10	100000	0.62	0.03	57700	2.10	0.02	0.773	0.031
t ₁₁	15	100000	0.21	0.02	57700	2.50	0.03	0.923	0.023
t ₁₂	30	100000	0.00	0.00	57700	2.83	0.05	1.000	0.000
t ₁₃	60	100000	0.00	0.00	57700	3.00	0.01	1.000	0.000
t ₁₄	120	100000	0.00	0.00	57700	3.05	0.04	1.000	0.000
t ₁₅	240	100000	0.00	0.00	57700	3.04	0.04	1.000	0.000

For a scaling factor of $d_{P4, c=2.0} = (1.161 \pm 0.088)$, an apparent rate of cleavage was determined to: $k_{app, P4, c=2.0} = (0.063 \pm 0.009) \text{ min}^{-1}$.

8.4.2.7 Deconvolutional analysis of P2-P4 in different mass concentrations

Table 8-14: Obtained areas of parent and fragment of **P2** ($c = 0.5 \text{ mg mL}^{-1}$).

Entry	t / min	$M_{\text{Parent}} / \text{g mol}^{-1}$	$[P]$	$\Delta[P]$	$M_{\text{Fragment}} / \text{g mol}^{-1}$	$[F]$	$\Delta[F]$
t_0	0	4200	2.76	0.05	2030	0.00	0.00
t_1	5	4200	2.46	0.11	2030	0.63	0.06
t_2	10	4200	2.90	0.05	2030	0.01	0.01
t_3	20	4200	1.53	0.14	2030	1.59	0.11
t_4	30	4200	1.73	0.13	2030	1.16	0.06
t_5	45	4200	1.22	0.17	2030	1.57	0.07
t_6	60	4200	0.44	0.17	2030	2.23	0.08
t_7	90	4200	0.00	0.00	2030	3.03	0.07
t_8	120	4200	0.00	0.00	2030	2.65	0.05
t_9	180	4200	0.00	0.00	2030	3.06	0.05
t_{10}	240	4200	0.00	0.00	2030	2.75	0.05

For a scaling factor of $d_{P2, c=0.5} = (1.085 \pm 0.091)$, an apparent rate of cleavage was determined to: $k_{app, P2, c=0.5} = (0.022 \pm 0.005) \text{ min}^{-1}$.

Table 8-15: Obtained areas of parent and fragment of **P2** ($c = 1.0 \text{ mg mL}^{-1}$).

Entry	t / min	$M_{\text{Parent}} / \text{g mol}^{-1}$	$[P]$	$\Delta[P]$	$M_{\text{Fragment}} / \text{g mol}^{-1}$	$[F]$	$\Delta[F]$
t_0	0	4100	2.69	0.04	2060	0.00	0.00
t_1	5	4100	2.90	0.04	2060	0.00	0.00
t_2	10	4100	2.85	0.07	2060	0.09	0.02
t_3	20	4100	2.56	0.09	2060	0.39	0.03
t_4	30	4100	2.17	0.11	2060	0.78	0.04
t_5	45	4100	1.46	0.14	2060	1.38	0.06
t_6	60	4100	1.23	0.16	2060	1.68	0.07
t_7	90	4100	0.89	0.14	2060	2.02	0.07
t_8	120	4100	0.98	0.16	2060	1.86	0.07
t_9	180	4100	0.80	0.17	2060	2.04	0.08
t_{10}	240	4100	0.75	0.15	2060	2.06	0.07

For a scaling factor of $d_{P2,c=1.0}=(0.810 \pm 0.058)$, an apparent rate of cleavage was determined to: $k_{app,P2,c=1.0}=(0.019 \pm 0.004) \text{ min}^{-1}$.

Table 8-16: Obtained areas of parent and fragment of **P3** ($c = 0.5 \text{ mg mL}^{-1}$).

Entry	t / min	$M_{\text{Parent}} / \text{g mol}^{-1}$	[P]	$\Delta[P]$	$M_{\text{Fragment}} / \text{g mol}^{-1}$	[F]	$\Delta[F]$
t_0	0	15100	1.58	0.06	7700	1.20	0.03
t_1	5	15100	1.21	0.08	7700	1.53	0.04
t_2	10	15100	0.84	0.09	7700	1.87	0.05
t_3	15	15100	0.51	0.08	7700	2.21	0.05
t_4	20	15100	0.14	0.04	7700	2.68	0.04
t_5	30	15100	0.06	0.04	7700	2.71	0.03
t_6	45	15100	0.00	0.00	7700	3.05	0.04
t_7	90	15100	0.00	0.00	7700	2.95	0.04
t_8	120	15100	0.00	0.00	7700	3.02	0.04
t_9	180	15100	0.00	0.00	7700	3.23	0.04
t_{10}	240	15100	0.00	0.00	7700	3.20	0.03

For a scaling factor of $d_{P3,c=0.5} = (1.225 \pm 0.039)$, an apparent rate of cleavage was determined to: $k_{app,P3,c=0.5}=(0.053 \pm 0.006) \text{ min}^{-1}$.

Table 8-17: Obtained areas of parent and fragment of **P3** ($c = 1.0 \text{ mg mL}^{-1}$).

Entry	t / min	$M_{\text{Parent}} / \text{g mol}^{-1}$	[P]	$\Delta[P]$	$M_{\text{Fragment}} / \text{g mol}^{-1}$	[F]	$\Delta[F]$
t_0	0	15200	1.68	0.05	7600	1.14	0.02
t_1	5	15200	1.19	0.06	7600	1.69	0.03
t_2	10	15200	0.78	0.07	7600	2.05	0.05
t_3	15	15200	0.39	0.06	7600	2.49	0.04
t_4	20	15200	0.34	0.07	7600	2.43	0.05
t_5	30	15200	0.14	0.05	7600	2.62	0.04
t_6	45	15200	0.00	0.00	7600	2.97	0.03
t_7	90	15200	0.00	0.00	7600	3.17	0.04
t_8	120	15200	0.00	0.00	7600	3.10	0.04
t_9	180	15200	0.00	0.00	7600	3.14	0.04
t_{10}	240	15200	0.00	0.00	7600	3.15	0.03

For a scaling factor of $d_{P3,c=1.0} = (1.176 \pm 0.027)$, an apparent rate of cleavage was determined to: $k_{app,P3,c=1.0} = (0.060 \pm 0.005) \text{ min}^{-1}$.

Table 8-18: Obtained areas of parent and fragment of P4 ($c = 0.5 \text{ mg mL}^{-1}$).

Entry	t / min	$M_{\text{Parent}} / \text{g mol}^{-1}$	[P]	$\Delta[P]$	$M_{\text{Fragment}} / \text{g mol}^{-1}$	[F]	$\Delta[F]$
t ₀	0	102000	1.60	0.05	58000	1.17	0.02
t ₁	0.5	102000	1.56	0.06	58000	1.19	0.03
t ₂	1.0	102000	1.50	0.07	58000	1.36	0.03
t ₃	1.5	102000	1.60	0.06	58000	1.09	0.02
t ₄	2.0	102000	1.54	0.07	58000	1.20	0.03
t ₅	2.5	102000	1.20	0.05	58000	1.54	0.03
t ₆	5	102000	1.14	0.00	58000	1.58	0.02
t ₇	10	102000	0.60	0.04	58000	2.11	0.0
t ₈	20	102000	0.13	0.00	58000	2.52	0.030
t ₉	30	102000	0.00	0.00	58000	2.72	0.02
t ₁₀	60	102000	0.00	0.00	58000	2.95	0.03

For a scaling factor of $d_{\text{P4},c=0.5} = (1.187 \pm 0.105)$, an apparent rate of cleavage was determined to: $k_{\text{app,P4},c=0.5} = (0.056 \pm 0.010) \text{ min}^{-1}$.

Table 8-19: Obtained areas of parent and fragment of P4 ($c = 1.0 \text{ mg mL}^{-1}$).

Entry	t / min	$M_{\text{Parent}} / \text{g mol}^{-1}$	[P]	$\Delta[P]$	$M_{\text{Fragment}} / \text{g mol}^{-1}$	[F]	$\Delta[F]$
t ₀	0	102000	1.57	0.04	58000	1.15	0.03
t ₁	0.5	102000	1.54	0.03	58000	1.16	0.02
t ₂	1	102000	1.52	0.04	58000	1.16	0.02
t ₃	2	102000	1.32	0.02	58000	1.43	0.02
t ₄	5	102000	1.10	0.04	58000	1.58	0.03
t ₅	10	102000	0.61	0.04	58000	2.00	0.03
t ₆	20	102000	0.16	0.03	58000	2.47	0.03
t ₇	30	102000	0.00	0.04	58000	2.71	0.03
t ₈	40	102000	0.13	0.00	58000	2.86	0.03
t ₉	50	102000	0.00	0.00	58000	2.87	0.03
t ₁₀	60	102000	0.00	0.00	58000	3.02	0.03

For a scaling factor of $d_{\text{P4},c=1.0} = (1.191 \pm 0.039)$, an apparent rate of cleavage was determined to: $k_{\text{app,P4},c=1.0} = (0.060 \pm 0.005) \text{ min}^{-1}$.

8.4.2.8 Ideal chain model

The total entropy dependent on the end-to-end vector \vec{R} of an ideal chain can be calculated by:^[327-328]

$$S(\vec{R}) = k_B \cdot \ln(\Omega(\vec{R})) \quad \text{Equation 8-22}$$

with k_B being the Boltzmann constant and $\Omega(\vec{R})$ being the number of microstates. Under assumption of $\Omega(\vec{R})$ being proportional to the ideal chain probability density function $P(\vec{R})$, Equation 8-23 reads

$$S(\vec{R}) = k_B \cdot \ln(P(\vec{R})) + C \quad \text{Equation 8-23}$$

with C being a constant. As it is known that $P(\vec{R})$ is proportional to its degree of polymerisation, DP_n , we assume that entropic contributions are to somewhat extent proportional to the chain length, according to Equation 8-24:

$$\begin{aligned} P(\vec{R}) &\propto DP_n \\ S &\propto b \cdot \ln(DP_n) + C \end{aligned} \quad \text{Equation 8-24}$$

The final expression in Equation 8-24 was fitted to the experimentally obtained scission rates in dependence of its degree of polymerisation DP_n . The experimentally obtained molecular weight was recalculated via Equation 8-25.

$$DP_n = \frac{M_n}{M_m} \quad \text{Equation 8-25}$$

With M_n being the experimentally obtained molecular weight of the polymers and M_m the molecular weight of the monomer unit (methyl acrylate, $M_m=86.09 \text{ g mol}^{-1}$). Parameters fulfilling the fit conditions were obtained:

Table 8-20: parameters fulfilling the fit conditions.

Parameter	Value
$b / \text{J K}^{-1}$	0.01191
$C / \text{J K}^{-1}$	-0.01284

8.4.3 Experimental procedures Chapter 5: Peroxide-accelerated photodegradation of tetrazine-bearing thiol-acrylate polymers via green light

8.4.3.1 LED irradiation experiments

All degradation experiments were performed in a designated photobox environment. The glass vessel was a Hellma Analytics quartz high precision cell with a path length of 10 mm. Orthogonal to the Online UV/Vis apparatus, a 525 nm LED was placed in a 3 cm distance. Voltage U and current I was adjusted with a tuneable power supply. Settings for the setup: $U = 9.1$ V, $I = 0.6$ A, $dist = 3$ cm.

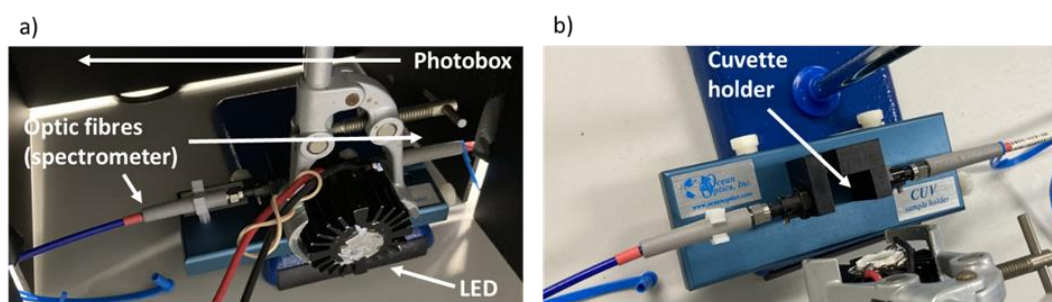


Figure 8-4: LED Irradiation setup with a) photobox enclosure and b) without enclosure.

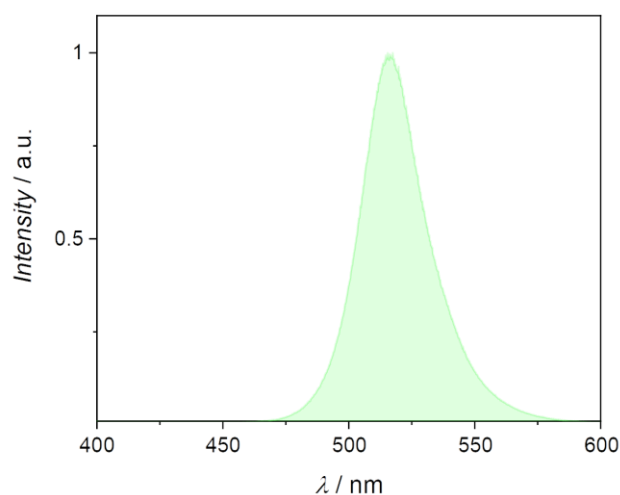


Figure 8-5: Emission spectrum of the employed green light LED.

8.4.3.2 Determination of incorporated Tz via ¹H-NMR spectroscopy

Incorporation of tetrazine was determined via ¹H-NMR spectroscopy by comparing the integral of resonances. Particularly, the ethyl groups of TzDA ($\delta = 4.51 - 4.45$, resonance *b* in **Figure S5-11** bottom) and TEGDA ($\delta = 4.18 - 4.04$, resonance *c* in **Figure S5-11** bottom) were investigated. Equation 8-26 was applied:

$$Eq_{Tz} = \frac{I_{TzDA}}{I_{TzDA} + I_{TEGDA}} \quad \text{Equation 8-26}$$

8.4.3.3 Action Plot of TzDA

A stock solution of TzDA (75 μmol , 23.3 mg) in a total volume of 12 mL of solvent was generated. The solvent was either a mixture of 3.5 mL acetonitrile and 8.5 mL 30wt% H₂O₂ solution or 3.5 mL acetonitrile and 8.5 mL H₂O. Consequently, a molar stoichiometric amount of H₂O₂ to TzDA was ensured, and solvent effects on the tetrazine degradation can be neglected. A volume of 250 μL per glass vial was prepared, thus all glass vials contained 1.56 μmol TzDA. The laser output energy was adjusted according to Equation 8-5 to ensure an equal molar amount of photons deposited into the glass vial. After irradiation, 200 μL of irradiated volume were transferred into a glass cuvette and diluted with 2300 μL of the respective solvent mixture. The conversion *X*, was then calculated via the difference of the absorption maximum (511 nm) between a non-irradiated and an irradiated sample (see Equation 8-27):

$$X = 1 - \frac{A_{511 \text{ nm, irradiated}}}{A_{511 \text{ nm, non-irradiated}}} \quad \text{Equation 8-27}$$

Table 8-21: Experimental parameters for the laser-based irradiation of TzDA in pure H₂O. λ : Wavelength of incident light; *E*: Energy per pulse; ΔE : Error in energy per pulse; *k*: Number of pulses; N_p : Number of photons deposited; $A_{511 \text{ nm}}$: Absorbance of solution at 511 nm after irradiation; *X*: Conversion; ΔX : Error in conversion.

λ / nm	<i>E</i> / μJ	ΔE / μJ	<i>k</i>	N_p / μmol	ΔN_p / μmol	$A_{511 \text{ nm}}$	<i>X</i>	ΔX
380	274	15	2120	1.56	0.09	0.2719	0.045	0.028
400	210	16	2620	1.56	0.12	0.2705	0.059	0.033

420	437	26	1200	1.57	0.09	0.2706	0.059	0.004
440	410	10	1200	1.54	0.04	0.2683	0.066	0.007
460	395	7.5	1200	1.56	0.03	0.2690	0.069	0.004
480	383	11	1200	1.57	0.05	0.2682	0.067	0.005
500	362	9.0	1200	1.55	0.04	0.2718	0.055	0.008
520	350	11	1200	1.56	0.05	0.2686	0.069	0.004
540	335	14	1200	1.55	0.07	0.2697	0.067	0.003
560	327	17	1200	1.57	0.08	0.2687	0.064	0.007
580	316	21	1200	1.57	0.10	0.2677	0.077	0.019
600	306	20	1200	1.57	0.10	0.2718	0.062	0.006
620	296	20	1200	1.57	0.11	0.2749	0.050	0.022
No irradiation	-	-	-	-	-	0.2846	-	-

Table 8-22: Experimental parameters for the laser-based irradiation of TzDA in a H₂O:H₂O₂ mixture. λ : Wavelength of incident light; E : Energy per pulse; ΔE : Error in energy per pulse; k : Number of pulses; N_p : Number of photons deposited; $A_{511\text{ nm}}$: Absorbance of solution at 511 nm after irradiation; X : Conversion; ΔX : Error in conversion.

λ / nm	$E / \mu\text{J}$	$\Delta E / \mu\text{J}$	k	$N_p / \mu\text{mol}$	$\Delta N_p / \mu\text{mol}$	$A_{511\text{nm}}$	X	ΔX
380	239	21	2440	1.56	0.14	0.2357	0.162	0.016
400	125	18	4400	1.46	0.22	0.2605	0.069	0.031
420	444	47	1200	1.59	0.17	0.2510	0.106	0.017
440	408	17	1200	1.54	0.06	0.2291	0.196	0.003
460	401	11	1200	1.58	0.04	0.1962	0.300	0.009
480	375	15	1200	1.54	0.06	0.1788	0.363	0.014
500	369	14	1200	1.58	0.06	0.1681	0.394	0.006
520	353	18	1200	1.57	0.08	0.1722	0.377	0.015
540	336	26	1200	1.55	0.12	0.1804	0.348	0.006
560	327	28	1200	1.57	0.13	0.2324	0.157	0.021
580	309	31	1200	1.54	0.15	0.2344	0.150	0.010
600	297	33	1200	1.53	0.17	0.2560	0.078	0.002
620	286	30	1200	1.52	0.16	0.2554	0.081	0.003

8.4.3.4 Polymer degradation experiment

All polymer degradation experiments were conducted in an identical manner. Usually, a polymer was dissolved in THF (and H₂O₂ where applicable). For experiments in presence of H₂O₂, 5000 μL of solution was used, 4000 μL THF and 1000 μL of a 30wt% H₂O₂ solution. For experiments in absence of H₂O₂, 5000 μL of THF was used. To ensure equal optical density around 520 nm, the following concentrations were anticipated (in mg mL⁻¹): $c_{\text{P1}} = 5.0$, $c_{\text{P2}} = 4.0$, $c_{\text{P3}} = 2.0$, $c_{\text{P4}} = 1.5$, $c_{\text{P5}} = 1.0$. The stock solution was split in two equal aliquots and immediately stored in the storage unit ($T = -20\text{ }^\circ\text{C}$). The aliquot, consisting of 2500 μL volume was subjected to online UV-Vis absorption spectroscopy while performing the degradation experiment. In a 1 cm cuvette, the absorption spectrum ($200\text{ nm} < \lambda < 800\text{ nm}$) was recorded every 60 seconds. After 60 minutes of recording, the depleted cuvette was rinsed, filled with the other aliquot and the same degradation setup was used. After each intended time increment, 500 μL of the cuvette was removed, diluted with 1300 μL THF, filtered and immediately submitted to THF-SEC. For all NMR spectra, all volatiles were removed under reduced pressure and the crude redissolved in deuterated solvent before recording the spectrum.

8.4.4 Experimental procedures Chapter 6: Wavelength-Orthogonal Stiffening and Inhibition of Hydrogel Networks with Visible Light

8.4.4.1 General Procedure for Pulsed Laser Irradiation of SPP-PEG and AP-PEG in Aqueous Solutions

The procedure was adapted according to literature.^[295-296] Stock solutions of 10 mg mL⁻¹ of MeO-PEG-SPP or MeO-PEG-AP in aqueous media were prepared. The aqueous solutions were prepared prior to use and stored at ambient temperature. 100 μL was injected into a glass vial, suitable for pulsed laser irradiation (refer to Chapter 8.3 for details). All samples were degassed with a constant stream of nitrogen for 10 min prior to irradiation. The output energy of the nanosecond laser was adjusted to ensure constant photon numbers deposited across all samples. All samples were

irradiated for 1800 seconds if not stated otherwise. After irradiation, the irradiated volume (100 μL) was split into aliquots of 25 μL volume. One aliquot was dissolved in 1775 μL THF, filtered and submitted to SEC, the other aliquot was diluted in 2475 μL of the respective solvent used for irradiation prior to submission to stationary UV/Vis spectroscopy.

8.4.4.2 General Procedure for the Calculation of Conversion from SEC data

UV traces (254 nm absorption) of each sample are used for calculation. UV absorption versus the retention volume was plotted for the entire sample set. The trace, consisting of MeO-PEG-SPP and (MeO-PEG-SPP)₂ (or MeO-PEG-AP and dimer) was deconvoluted with two Gaussian functions, representing the two species. The Conversion, X , was then calculated via Equation 8-28:

$$X = \frac{Area_{Dimer}}{Area_{Dimer} + Area_{Monomer}} \quad \text{Equation 8-28}$$

With $Area_{Dimer}$ being the area under the dimer species obtained by SEC after irradiation and $Area_{Monomer}$ being the area under the monomer species after irradiation. The error in conversion ΔX , was estimated according to a simple error propagation method:

$$\Delta X = \sqrt{\left[\frac{\partial X}{\partial Area_{Dimer}} \right]^2 \cdot \Delta Area_{Dimer}^2 + \left[\frac{\partial X}{\partial Area_{Monomer}} \right]^2 \cdot \Delta Area_{Monomer}^2} \quad \text{Equation 8-29}$$

$$\Delta X = \sqrt{\left[\frac{Area_{Monomer}}{(Area_{Monomer} + Area_{Dimer})^2} \right]^2 \cdot [0.1 Area_{Dimer}]^2 + \left[\frac{-Area_{Dimer}}{(Area_{Monomer} + Area_{Dimer})^2} \right]^2 \cdot [0.1 Area_{Monomer}]^2} \quad \text{Equation 8-30}$$

The error in the respective areas of monomer and dimer species was assumed to be 10% of the original area value. The errors are displayed in form of error bars.

8.4.4.3 Action Plot for MeO-PEG-SPP in aqueous solution (pH = 7)

Table 8-23: Experimental data for the irradiation of MeO-PEG-SPP in aqueous solution. λ : Wavelength, E_{pulse} : Measured pulse energy at the sample holder of the laser setup (**Figure 8-1**), ΔE_{pulse} : Error in measured pulse energy, t : Irradiation time, T_{λ} : Transmittance of the glass vial at respective wavelength, N_{P} : Deposited number of photons according to Equation 8-5, ΔN_{P} : Error in deposited number of photons, X : Conversion according to Equation 8-29, ΔX : Error in conversion according to Equation 8-30.

λ / nm	$E_{\text{pulse}} / \mu\text{J}$	$\Delta E_{\text{pulse}} / \mu\text{J}$	t / s	T_{λ}	$N_{\text{P}} / \mu\text{mol}$	$\Delta N_{\text{P}} / \mu\text{mol}$	X	ΔX
-	0	0	0		0	0	0.00	0.00
410	882	84	2040	85.13	104.92	9.99	0.40	0.03
420	986	54	1800	85.24	106.15	5.81	0.29	0.03
440	929	25	1800	85.36	104.93	2.82	0.32	0.03
460	890	16	1800	85.41	105.16	1.89	0.39	0.03
480	848	22	1800	85.43	104.58	2.71	0.51	0.04
500	816	20	1800	85.44	104.84	2.57	0.35	0.03
520	789	24	1800	85.45	105.43	3.21	0.17	0.02
540	755	32	1800	85.45	104.77	4.44	0.04	0.00
560	728	31	1800	85.45	104.77	4.46	0.00	0.00
580	700	44	1800	85.45	104.33	6.56	0.00	0.00
600	680	40	1800	85.45	104.85	6.17	0.00	0.00

8.4.4.4 Action Plot for MeO-PEG-SPP in aqueous solution (pH = 5)

Table 8-24: Experimental data for the irradiation of MeO-PEG-SPP in aqueous solution (pH = 5). λ : Wavelength, E_{pulse} : Measured pulse energy at the sample holder of the laser setup (**Figure 8-1**), ΔE_{pulse} : Error in measured pulse energy, t : Irradiation time, T_{λ} : Transmittance of the glass vial at respective wavelength, N_{P} : Deposited number of photons according to Equation 8-5, ΔN_{P} : Error in deposited number of photons, X : Conversion according to Equation 8-29, ΔX : Error in conversion according to Equation 8-30.

λ / nm	$E_{\text{pulse}} / \mu\text{J}$	$\Delta E_{\text{pulse}} / \mu\text{J}$	t / s	T_{λ}	$N_{\text{P}} / \mu\text{mol}$	$\Delta N_{\text{P}} / \mu\text{mol}$	X	ΔX
-	0	0	0		0	0	0	0.00
410	768	48	2340	85.13	104.80	6.55	0.15	0.02
420	981	56	1800	85.24	105.62	6.03	0.13	0.02
440	926	28	1800	85.36	104.59	3.16	0.17	0.02
460	886	17	1800	85.41	104.68	2.01	0.14	0.02
480	847	21	1800	85.43	104.46	2.59	0.16	0.02
500	813	19	1800	85.44	104.45	2.44	0.15	0.02

520	781	24	1800	85.45	104.36	3.21	0.06	0.01
540	758	30	1800	85.45	105.19	4.16	0.01	0.00
560	724	32	1800	85.45	104.19	4.61	0.01	0.00
580	704	40	1800	85.45	104.93	5.96	0.01	0.00
600	681	40	1800	85.45	105.00	6.17	0.01	0.00

8.4.4.5 Action Plot for MeO-PEG-SPP in aqueous solution (pH = 3)

Table 8-25: Experimental data for the irradiation of MeO-PEG-SPP in aqueous solution (pH = 3). λ : Wavelength, E_{pulse} : Measured pulse energy at the sample holder of the laser setup (**Figure 8-1**), ΔE_{pulse} : Error in measured pulse energy, t : Irradiation time, T_{λ} : Transmittance of the glass vial at respective wavelength, N_{P} : Deposited number of photons according to Equation 8-5, ΔN_{P} : Error in deposited number of photons, X : Conversion according to Equation 8-29, ΔX : Error in conversion according to Equation 8-30.

λ / nm	$E_{\text{pulse}} / \mu\text{J}$	$\Delta E_{\text{pulse}} / \mu\text{J}$	t / s	T_{λ}	$N_{\text{P}} / \mu\text{mol}$	$\Delta N_{\text{P}} / \mu\text{mol}$	X	ΔX
-	0	0	0		0	0	0.01	0.00
410	760	81	2360	85.13	104.59	11.15	0.18	0.02
420	972	60	1800	85.24	104.65	6.46	0.15	0.02
440	928	31	1800	85.36	104.81	3.50	0.18	0.02
460	891	18	1800	85.41	105.27	2.13	0.17	0.02
480	850	23	1800	85.43	104.83	2.84	0.19	0.02
500	814	23	1800	85.44	104.58	2.95	0.17	0.02
520	790	23	1800	85.45	105.56	3.07	0.08	0.01
540	761	35	1800	85.45	105.60	4.86	0.03	0.00
560	725	33	1800	85.45	104.33	4.75	0.01	0.00
580	702	43	1800	85.45	104.63	6.41	0.01	0.00
600	682	46	1800	85.45	105.16	7.09	0.01	0.00

8.4.4.6 Action Plot for MeO-PEG-SPP in aqueous solution (pH = 1)

Table 8-26: Experimental data for the irradiation of MeO-PEG-SPP in aqueous solution (pH = 1). λ : Wavelength, E_{pulse} : Measured pulse energy at the sample holder of the laser setup (**Figure 8-1**), ΔE_{pulse} : Error in measured pulse energy, t : Irradiation time, T_{λ} : Transmittance of the glass vial at respective wavelength, N_{P} : Deposited number of photons according to Equation 8-5, ΔN_{P} : Error in deposited number of photons, X : Conversion according to Equation 8-29, ΔX : Error in conversion according to Equation 8-30.

λ / nm	$E_{\text{pulse}} / \mu\text{J}$	$\Delta E_{\text{pulse}} / \mu\text{J}$	t / s	T_{λ}	$N_{\text{P}} / \mu\text{mol}$	$\Delta N_{\text{P}} / \mu\text{mol}$	X	ΔX
-----------------------	----------------------------------	---	----------------	---------------	--------------------------------	---------------------------------------	-----	------------

-	0	0	0		0	0	0.01	0.00
410	709	80	2540	85.13	105.01	11.85	0.03	0.00
420	976	67	1800	85.24	105.08	7.21	0.02	0.00
440	923	32	1800	85.36	104.25	3.61	0.01	0.00
460	885	18	1800	85.41	104.57	2.13	0.01	0.00
480	853	23	1800	85.43	105.20	2.84	0.01	0.00
500	821	23	1800	85.44	105.48	2.95	0.01	0.00
520	787	30	1800	85.45	105.16	4.01	0.01	0.00
540	756	41	1800	85.45	104.91	5.69	0.00	0.00
560	731	37	1800	85.45	105.20	5.32	0.00	0.00
580	702	46	1800	85.45	104.63	6.86	0.00	0.00
600	677	49	1800	85.45	104.38	7.56	0.01	0.00

8.4.4.7 Action Plot for MeO-PEG-SPP in H₂O in the presence of PAG in [PAG] = 1.71 mg mL⁻¹ (stoichiometric amount)

Table 8-27: Experimental data for the irradiation of MeO-PEG-SPP in H₂O in the presence of PAG in [PAG] = 1.71 mg mL⁻¹ (stoichiometric amount). λ : Wavelength, E_{pulse} : Measured pulse energy at the sample holder of the laser setup (**Figure 8-1**), ΔE_{pulse} : Error in measured pulse energy, t : Irradiation time, T_{λ} : Transmittance of the glass vial at respective wavelength, N_{P} : Deposited number of photons according to Equation 8-5, ΔN_{P} : Error in deposited number of photons, X : Conversion according to Equation 8-29, ΔX : Error in conversion according to Equation 8-30.

λ / nm	$E_{\text{pulse}} / \mu\text{J}$	$\Delta E_{\text{pulse}} / \mu\text{J}$	t / s	T_{λ}	$N_{\text{P}} / \mu\text{mol}$	$\Delta N_{\text{P}} / \mu\text{mol}$	X	ΔX
-	0	0	0		0	0	0.01	0.00
410	1010	91	1800	85.13	106.01	9.55	0.17	0.02
420	969	56	1800	85.24	104.32	6.03	0.17	0.02
440	930	28	1800	85.36	105.04	3.16	0.21	0.02
460	886	20	1800	85.41	104.68	2.36	0.15	0.02
480	851	27	1800	85.43	104.95	3.33	0.19	0.02
500	818	25	1800	85.44	105.10	3.21	0.18	0.02
520	780	28	1800	85.45	104.23	3.74	0.08	0.01
540	756	41	1800	85.45	104.91	5.69	0.03	0.00
560	728	41	1800	85.45	104.77	5.90	0.01	0.00
580	707	52	1800	85.45	105.38	7.75	0.01	0.00
600	682	49	1800	85.45	105.16	7.56	0.01	0.00

8.4.4.8 Action Plot for MeO-PEG-SPP in H₂O in the presence of PAG in [PAG] = 4.00 mg mL⁻¹

Table 8-28: Experimental data for the irradiation of MeO-PEG-SPP in H₂O in the presence of PAG in [PAG]=4.00 mg mL⁻¹. λ : Wavelength, E_{pulse} : Measured pulse energy at the sample holder of the laser setup (**Figure 8-1**), ΔE_{pulse} : Error in measured pulse energy, t : Irradiation time, T_{λ} : Transmittance of the glass vial at respective wavelength, N_{P} : Deposited number of photons according to Equation 8-5, ΔN_{P} : Error in deposited number of photons, X : Conversion according to Equation 8-29, ΔX : Error in conversion according to Equation 8-30.

λ / nm	E_{pulse} / μJ	ΔE_{pulse} / μJ	t / s	T_{λ}	N_{P} / μmol	ΔN_{P} / μmol	X	ΔX
-	0	0	0		0	0	0.01	0.00
410	410	1020	97	85.13	107.06	10.2	0.05	0.01
420	420	978	63	85.24	105.29	6.78	0.06	0.01
440	440	931	31	85.36	105.15	3.50	0.04	0.01
460	460	892	19	85.41	105.39	2.24	0.04	0.01
480	480	844	25	85.43	104.09	3.08	0.03	0.00
500	500	818	22	85.44	105.10	2.83	0.02	0.00
520	520	787	29	85.45	105.16	3.88	0.02	0.00
540	540	757	41	85.45	105.05	5.69	0.01	0.00
560	560	728	41	85.45	104.77	5.90	0.01	0.00
580	580	706	57	85.45	105.23	8.50	0.01	0.00
600	600	687	52	85.45	105.93	8.02	0.01	0.00

8.4.4.9 pH-dependent Single-Wavelength irradiation for MeO-PEG-SPP and MeO-PEG-AP in H₂O

Table 8-29: Conversion of MeO-PEG-SPP and MeO-PEG-AP after single-wavelength (480 nm for SPP, 420 nm for AP) irradiation in different aqueous solutions. *: Conversion value for pH = 7 for MeO-PEG-SPP was obtained from **Table 8-23**. pH: pH value determined via pH sensor, X : Conversion according to Equation 8-29, ΔX : Error in conversion according to Equation 8-30.

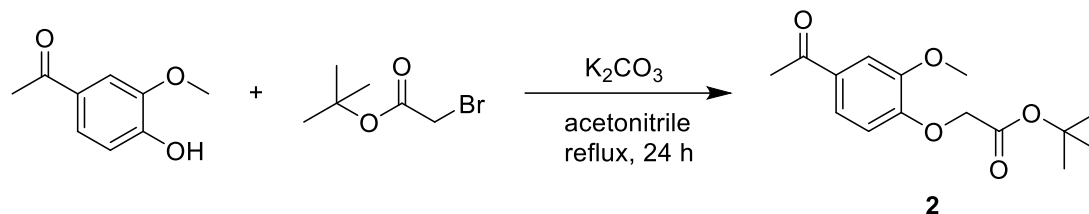
pH	X_{SPP}	ΔX_{SPP}	X_{AP}	ΔX_{AP}
0	0.00	0.00	0.21	0.02
1	0.01	0.00	0.93	0.01
2	0.11	0.01	0.93	0.01
3	0.19	0.02	0.98	0.00
4	0.19	0.02	1.00	0.00
5	0.19	0.02	1.00	0.00

6	0.18	0.02	1.00	0.00
7*	0.51	0.04	-	-

8.5 SYNTHETICAL PROCEDURES

8.5.1 Synthetical procedures Chapter 3: Exploring the photochemistry of *ortho*-nitrobenzyl alcohols and incorporation in polyurethanes

8.5.1.1 *tert*-butyl 2-(4-acetyl-2-methoxyphenoxy)acetate



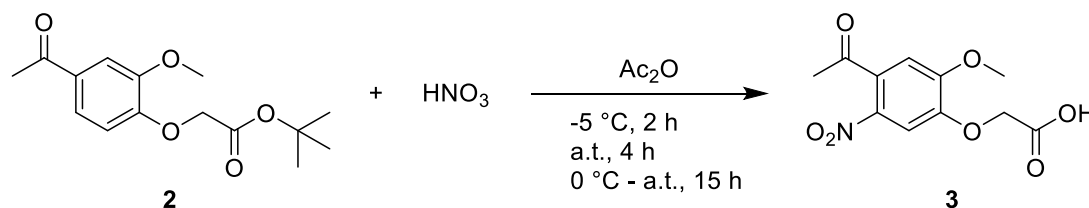
25.1 g acetovanillone (150.8 mmol, 1.20 eq.) and 59.2 g oven dried K_2CO_3 (428.0 mmol, 3.4 eq.) were dispersed in 600 mL dry acetonitrile. After freeing the flask from oxygen by flushing with argon, 18.5 mL *tert*-butyl bromoacetate (24.4 g, 125.3 mmol, 1.0 eq) was added. The solution was stirred for 24 h under reflux. The mixture was filtered, and the solvent mostly removed under reduced pressure. The residual liquid was dispersed in 100 mL saturated $NaHCO_3$ solution and exposed to an ultrasonic bath for three minutes. The aqueous phase was extracted three times with 50 mL Et_2O . The organic solvent was mostly reduced under reduced pressure and washed once with 150 mL saturated $NaHCO_3$ solution. The organic solvent was completely evaporated and **2** was isolated as pure colourless crystals. 34.3 g (98 % vs. theory).

1H -NMR, $DMSO-d_6$, 600 MHz, δ / ppm: 7.59 (d, 1H), 7.47 (dd, 1H), 6.94 (d, 1H), 4.77 (s, 2H), 3.83 (s, 3H), 2.54 (s, 3H), 1.42 (s, 9H)

^{13}C -NMR, $DMSO-d_6$, 151 MHz, δ / ppm: 196.45, 167.40, 151.34, 148.63, 130.51, 122.75, 112.10, 110.82, 81.63, 65.27, 55.66, 27.71, 26.40

LC-MS (ESI): m/z $[M+H]^+$, theo: 281.1384, exp: 281.1380, Δ / ppm: 1.42

8.5.1.2 2-(4-acetyl-2-methoxy-5-nitrophenoxy)acetic acid



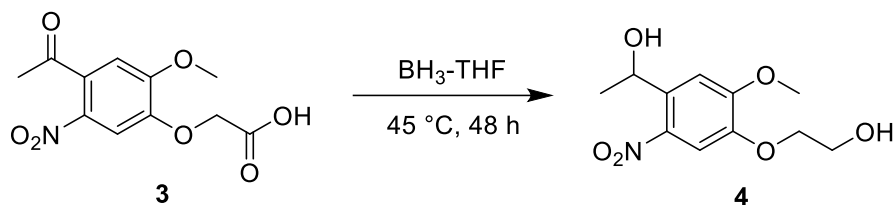
28 mL 70% HNO₃ (439.5 mmol, 12 eq.) was added dropwise into 20 mL NaCl:Ice mixture cooled acetic anhydride (21.6 g, 211.6 mmol, 5.80 eq.) under rigorous stirring. A solution of previously grinded **2** (36.3 mmol, 1.0 eq., 10.1 g) in 30 mL acetic anhydride was added slowly into the stirring mixture dropwise at -5 °C. The mixture was stirred at -5 °C for 2 h and subsequently at a.t. for 4 h. The mixture was poured into 300 mL crushed ice and allowed to reach a.t. overnight (15 h). The precipitate was filtrated and dried in vacuo at 40 °C for 24 h. Product **3** was obtained as a pale yellow amorphous solid. 5.8 g (59 % vs. theory).

¹H-NMR, DMSO-*d*₆, 600 MHz, δ / ppm: 7.59 (s, 1H), 7.25 (s, 1H), 4.90 (s, 3H), 3.94 (s, 3H), 2.52 (s, 3H)

¹³C-NMR, DMSO-*d*₆, 151 MHz, δ / ppm: 199.34, 169.67, 153.30, 147.67, 138.00, 131.77, 110.12, 108.48, 65.21, 56.71, 30.06

LC-MS (ESI): *m/z* [M+H]⁺, theo: 270.0608, exp: 270.0604, Δ / ppm: 1.48

8.5.1.3 1-(4-(2-hydroxyethoxy)-5-methoxy-2-nitrophenyl)ethan-1-ol



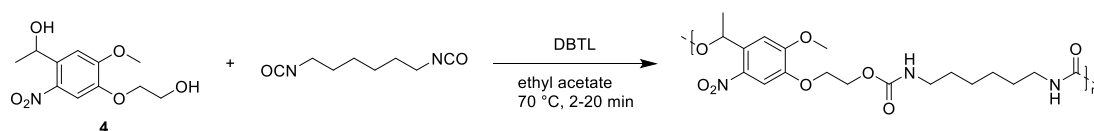
Under Schlenk conditions, 100 mL BH₃-THF solution (100 mmol, 9.9 eq.) were added into a Schlenk flask containing 2.7 g (10.1 mmol, 1.0 eq.) of **3** while stirring via a transfer canula. The mixture was warmed up to 45 °C and stirred at this temperature for 48 h. Afterwards, the reaction mixture was poured into an ice-cooled water:ethanol mixture (75:50 mL) and stirred for 5 minutes. After removing the solvent under reduced pressure, the solid residue was purified by submission to Ion-exchanging chromatography (Amberlite 743) and afterwards to chromatography (SiO₂, Et₂O/EA, 85/15 v/v). Product **4** was obtained as a yellow amorphous solid. 1.9 g (73 % vs. theory).

¹H-NMR, DMSO-*d*₆, 600 MHz, δ / ppm: 7.55 (s, 1H), 7.36 (1H), 5.47 (d, 1H), 5.26 (dq, 1H), 4.90 (t, 1H), 4.06 (t, 2H), 3.90 (s, 3H), 3.72 (q, 2H), 1.37 (d, 3H)

^{13}C -NMR, DMSO- d_6 , 151 MHz, δ / ppm: 153.41, 146.46, 138.89, 137.95, 109.07, 108.49, 70.75, 63.91, 59.36, 55.98, 25.17

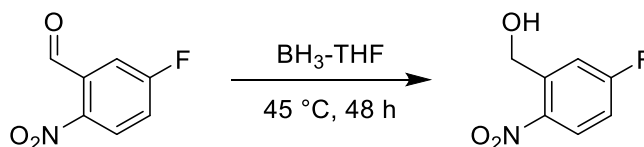
LC-MS (ESI): m/z $[\text{M}+\text{NH}_4]^+$, theo: 275.1238, exp: 275.1239, Δ / ppm: 0.36

8.5.1.4 Polymerisation coPoly(*o*NB-dialcohol-*alt*-HDI)



In a crimped vial, 500 mg of **4** (1.0 eq.) is solubilized in 2 mL of ethyl acetate in a sonication bath at 40 °C for 10 min. A solution of 354 mg of 1,6-hexamethylene diisocyanate (1.0 eq.) and 405 μL of dibutyltin dilaurate in 2 mL of EA is then added to the vial. The reaction mixture was maintained at 70 °C for 2 to 20 min. After the determined time of reaction, ethyl acetate was added, the polymer filtered off and dried overnight at 40 °C under vacuum.

8.5.1.5 5-Fluoro-2-nitrobenzyl alcohol

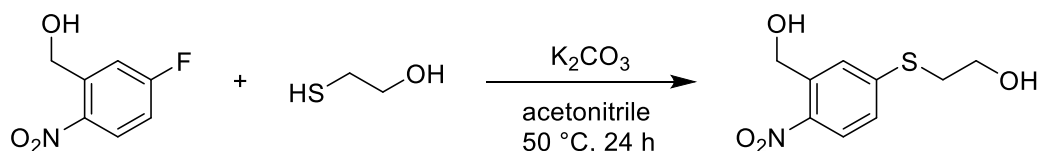


Under nitrogen atmosphere, a round bottom flask was charged with 0.4 g 5-fluoro-2-nitrobenzaldehyde (2.49 mmol, 1.0 eq.). $\text{BH}_3\text{-THF}$ solution (11 mL, 11.0 mmol, 4.4 eq.) was transferred via transfer canula. Afterwards, the mixture was allowed to proceed at 45 °C for 24 hours. Then, the reaction mixture was quenched with EtOH/ H_2O (2/1 v/v) and the solvent mostly removed. The crude was dissolved in 50 mL EA and washed with 1 M HCl once, 0.1 M NaHCO_3 twice, NH_4Cl solution twice and H_2O twice. The phases were separated, the organic solvent was removed and the compound was obtained as an off-white powder. Yield of 252 mg, 59.1 % (vs. theory).

^1H -NMR, DMSO- d_6 , 600 MHz, δ / ppm: 8.20 (m, 1H), 7.60 (dd, 1H), 7.38 (dt, 1H), 5.72 (t, 1H), 4.85 (d, 2H)

^{13}C -NMR, DMSO- d_6 , 151 MHz, δ / ppm: 164.21, 143.22, 128.02, 127.95, 114.76, 114.61, 59.76

8.5.1.6 5-[(2-Hydroxyethyl)thio]-2-nitrobenzyl alcohol



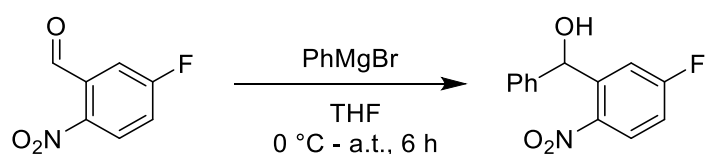
In argon atmosphere, a Schlenk flask was charged with 90 μL 2-mercaptoethanol (99 mg, 1.27 mmol, 1.1 eq.) and 259 mg K₂CO₃ (1.88 mmol, 1.6 eq.) and submerged in 10 mL dry acetonitrile. 200 mg 5-Fluoro-2-nitrobenzyl alcohol (1.17 mmol, 1.0 eq.) was dissolved in 2 mL dry acetonitrile and added to the reaction mixture via syringe pump (flow rate 2 mL hr⁻¹). The reaction was allowed to proceed at 50 °C for 24 hours. Afterwards, the reaction was diluted with 25 mL EA. The organic phase was washed with 25 mL H₂O once and 25 mL brine twice. After removing the organic solvent, flash chromatography was performed (DCM/MeOH 98/2 - 1/1 v/v). The product was obtained as a yellow powder. Yield of 163 mg (60.9% vs. theory).

^1H -NMR, DMSO- d_6 , 600 MHz, δ / ppm: 8.03 (d, 1H), 7.68 (d, 1H), 7.40 (dd, 1H), 5.58 (t, 1H), 5.06 (t, 1H), 4.84 (d, 2H), 3.65 (q, 2H), 3.19 (t, 2H)

^{13}C -NMR, DMSO- d_6 , 151 MHz, δ / ppm: 146.15, 143.13, 139.58, 125.36, 124.55, 124.19, 59.99, 59.37, 33.78

LC-MS (ESI): m/z [M+acetate]⁻, theo: 288.0536, exp: 288.0538, Δ / ppm: 0.69

8.5.1.7 (5-fluoro-2-nitrophenyl)(phenyl)methanol



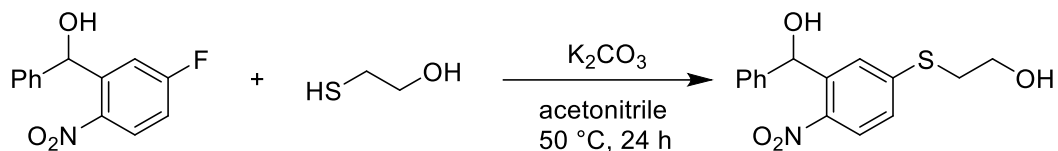
A flame-dried Schlenk flask was charged with 0.40 g 5-fluoro-2-nitrobenzaldehyde (2.37 mmol, 1.0 eq.), dissolved in 10 mL dry THF and the solution cooled down to 0 °C. 1.2 mL phenylmagnesium bromide solution (3.0 M in Et₂O) was added drop wise via syringe pump (flow rate 2.4 mL hr⁻¹). After complete addition, the reaction was

allowed to proceed at 0 °C for 6 hours. Afterwards, the solution was quenched by adding 20 mL 0.5 M HCl and diluted with 50 mL EA. The phases were separated, the organic phase was washed with H₂O once and with brine once. The organic solvent was removed, and flash chromatography (CH/EA 95/5 - 7/3 v/v) was performed. The product was isolated as yellow oil. Yield of 0.37 g, 63.5 % (vs. theory).

¹H-NMR, DMSO-*d*₆, 600 MHz, δ / ppm: 8.06 (dd, 1H), 7.64 (dd, 1H), 7.40 (dt, 1H), 7.31 (t, 2H), 7.25 (m, 3H), 6.37 (d, 1H), 6.25 (d, 1H)

¹³C-NMR, DMSO-*d*₆, 151 MHz, δ / ppm: 164.93, 163.30, 144.02, 143.30, 142.50, 128.28, 127.65, 127.55, 127.06, 115.47, 115.27, 115.10, 69.47

8.5.1.8 2-((3-(hydroxy(phenyl)methyl)-4-nitrophenyl)thio)ethan-1-ol



In an argon atmosphere, an RBF was charged with 60 μ L 2-mercaptoethanol (67 mg, 0.86 mmol, 1.1 eq.) and 169 mg K₂CO₃ (1.22 mmol, 1.5 eq.) in 10 mL dry acetonitrile. The mixture was heated up to 50 °C. 200 mg (5-fluoro-2-nitrophenyl)(phenyl)methanol (0.80 mmol, 1.0 eq.) was dissolved in 5 mL acetonitrile and added via syringe pump (flow rate 5 mL hr⁻¹). After complete addition, the reaction was allowed to proceed at 50 °C for 24 hours. Afterwards, the solution was diluted with 50 mL EA and washed with H₂O once, NH₄Cl once and brine once. The organic solvent was removed under reduced pressure, and flash chromatography (DCM/MeOH 95/5 - 8/2 v/v) was performed. The product was isolated as yellow oil. Yield of 0.15 g, 60.0 % (vs. theory).

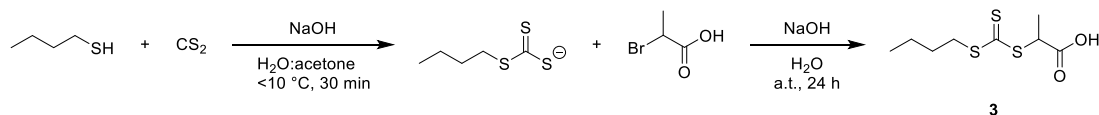
¹H-NMR, DMSO-*d*₆, 600 MHz, δ / ppm: 7.89 (d, 1H), 7.72 (d, 1H), 1.42 (dd, 1H), 7.30 (t, 2H), 7.24 (m, 3H), 6.29 (d, 1H), 6.24 (d, 1H), 5.06 (t, 1H), 3.65 (q, 2H), 3.18 (dt, 2H)

¹³C-NMR, DMSO-*d*₆, 151 MHz, δ / ppm: 33.91, 59.34, 69.49, 124.81, 125.19, 125.26, 127.02, 127.36, 128.21, 140.26, 142.96, 144.17, 145.37

LC-MS (ESI): *m/z* [M+NH₄]⁺, theo: 323.1060, exp: 323.1064, Δ / ppm=1.23

8.5.2 Synthetical procedures Chapter 4: Chain-Length-Dependent Photolysis of *ortho*-nitrobenzyl-Centered Polymers

8.5.2.1 2-(((butylthio)carbonothioyl)thio)propanoic acid

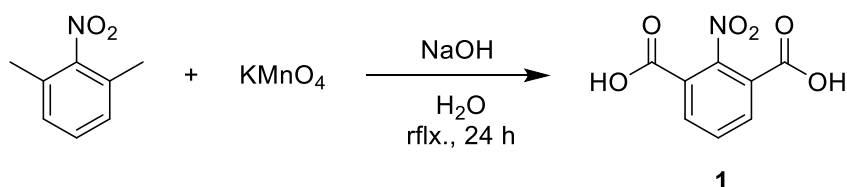


This compound was synthesised according to literature.^[329] A 50% NaOH solution (3.2 g, containing 1.6 g, 40 mmol of NaOH) was added to a stirred mixture of butanethiol (3.71 g, 41 mmol) and water (6 mL). Acetone (2 mL) was then added, and the resulting clear, colourless solution was stirred for 0.5 h then cooled to near-room temperature and treated with carbon disulphide (2.7 mL, 3.4 g, 45 mmol) to give a clear orange solution. This was stirred for 0.5 h then cooled in an ice bath to an internal temperature of <10 °C. 2-Bromopropanoic acid (6.2 g, 3.7 mL, 41 mmol) was then added at such a rate that the temperature did not exceed 30 °C followed by 50% NaOH (3.3 g, 41 mmol), also added at such a rate that the temperature did not exceed 30 °C. When the exotherm reaction had stopped, the ice bath was removed and water (6 mL) was added. The reaction was stirred at ambient temperature for 24 h then diluted with water (10 mL) and stirred and cooled in an ice bath while 10 M HCl (6 mL) was added at a rate which kept the temperature <10 °C. An orange oil precipitated. The aqueous phase was decanted and the oil was exposed to 2 mL nHexane and kept in the freezer for 60 minutes. The crystals were filtrated and recrystallized out of 5 mL nHexane twice. The compound was obtained as yellow crystals in a yield of 7.9 g (81.1%).

¹H-NMR, DMSO-*d*₆, 600 MHz, δ / ppm: 13.14 (bs, 1H), 4.67 (q, 1H), 3.38 (t, 2H), 1.62 (p, 2H), 1.52 (d, 3H), 1.36 (h, 2H), 0.89 (t, 3H)

¹³C-NMR, DMSO-*d*₆, 151 MHz, δ / ppm: 222.45, 171.55, 48.13, 36.22, 29.60, 21.44, 16.78, 13.44

8.5.2.2 2-nitroisophthalic acid



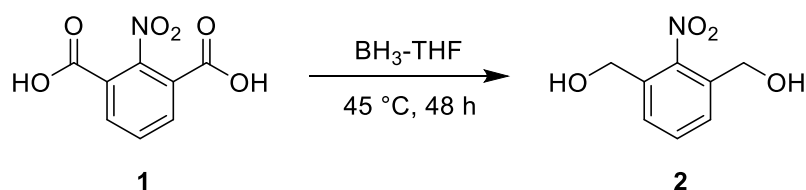
This compound was synthesised according to literature.^[330] 1,3-dimethyl nitrobenzene (9 mL, 10.0 g, 66.08 mmol, 1.0 eq.), potassium permanganate (37.3 g, 188.8 mmol, 2.9 eq.) and sodium hydroxide (3.3 g, 82.75 mmol, 1.3 eq.) were submerged in 200 mL H₂O. The mixture was refluxed for 24 hours. Afterwards, the solution was filtered and the starting material extracted in toluene (50 mL). The aqueous phase was then acidified with 100 mL 1M HCl and the white precipitate was filtered. After drying for 24 hours, a colourless powder was obtained. Yield of 6.0 g, 42.9 % (vs. theory).

¹H-NMR, DMSO-*d*₆, 600 MHz, δ / ppm: 8.18 (d, 2 H), 7.81 (t, 1H)

¹³C-NMR, DMSO-*d*₆, 151 MHz, δ / ppm: 164.11, 148.73, 134.56, 131.19, 124.91

LC-MS (ESI): *m/z* [M-H]⁻, theo: 210.0033, exp: 210.0039, Δ / ppm=2.86

8.5.2.3 (2-nitro-1,3-phenylene)dimethanol



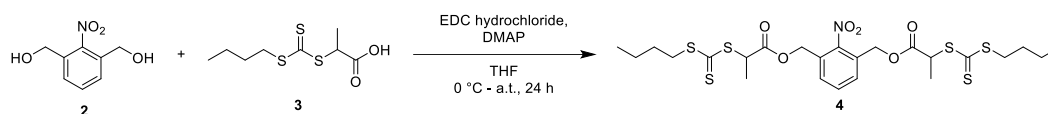
A flame dried Schlenk flask was charged with dried 2.2 g of 2-nitroisophthalic acid (10.5 mmol, 1.0 eq.). Then, 100 mL of 1 M BH₃-THF solution (37.3 mmol, 9.6 eq.) was transferred via a transfer canula. After addition, the reaction was allowed to proceed at 45 °C for 48 hours. Afterwards, the solution was quenched with 50 mL cold MeOH. The organic solvent was removed under reduced pressure, the crude redissolved in 50 mL EA and washed with 25 mL H₂O twice. Flash chromatography in CH/EA (8/2 - 1/1 v/v) afforded the product as a colorless powder. Yield of 1.75 g, 91.0 % (vs. theory).

¹H-NMR, DMSO-*d*₆, 600 MHz, δ / ppm: 7.56 (m, 3H), 5.47 (t, 2H), 4.53 (d, 4H)

¹³C-NMR, DMSO-*d*₆, 151 MHz, δ / ppm: 147.37, 134.33, 130.76, 127.52, 59.22

LC-MS (ESI): *m/z* [M+NH₄]⁺, theo: 201.0870, exp: 201.0876, Δ / ppm=2.98

8.5.2.4 (2-nitro-1,3-phenylene)bis(methylene) bis(2-(((butylthio)carbonothioyl)thio)propanoate)

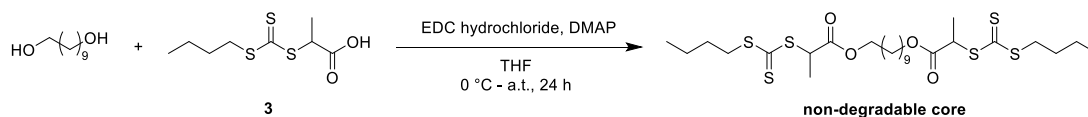


0.20 g (2-nitro-1,3-phenylene)dimethanol (1.10 mmol, 1.0 eq.), 0.70 g 2-(((butylthio)carbonothioyl)thio)propanoic acid (2.88 mmol, 2.6 eq.) and DMAP (30 mg, 0.23 mmol, 0.2 eq.) were dissolved in 10 mL dry DCM. The solution was cooled down to 0 °C with an ice bath. Then, 0.85 g EDC hydrochloride was added portion wise. After 7 hours of stirring, 0.10 g of EDC hydrochloride was additionally added (total EDC hydrochloride amount: 0.95 g, 4.94 mmol, 4.5 eq.). After a total stirring time of 24 hours, the mixture was diluted with 20 mL EA, then washed with 20 mL 0.5 M HCl, 20 mL 0.1 M NaHCO₃ and twice with 25 mL NH₄Cl. The solvent was removed under reduced pressure and flash chromatography was performed in CH/EA (95/5 - 1/1 v/v). The product was afforded as a yellow oil in a yield of 0.70 g, 96 % (vs. theory).

¹H-NMR, DMSO-*d*₆, 600 MHz, δ / ppm: 7.69 (m, 3H), 5.25 (s, 4H), 4.76 (q, 2H), 3.37 (t, 4H), 1.61 (p, 4H), 1.51 (d, 6H), 1.36 (s, 4H), 0.88 (t, 6H)

¹³C-NMR, DMSO-*d*₆, 151 MHz, δ / ppm: 221.84, 169.75, 148.08, 131.82, 130.93, 128.67, 63.16, 47.42, 36.32, 29.51, 26.33, 21.37, 16.09, 13.40

8.5.2.5 (decane-1,10-diyl bis(2-(((butylthio)carbonothioyl)thio)propanoate)



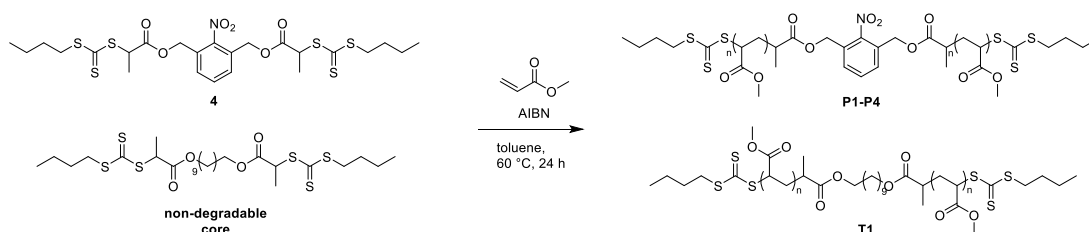
0.1 g 1,10-decanediol (0.58 mmol, 1.0 eq.), 0.7 g 2-(((butylthio)carbonothioyl)thio)propanoic acid (2.86 mmol, 4.9 eq.) and DMAP (16 mg, 0.13 mmol, 0.2 eq.) were dissolved in dry THF. The solution was cooled down with an ice bath. EDC hydrochloride (0.6 g, 3.07 mmol, 5.3 eq.) was added portion wise and the solution was kept stirring in the ice bath for five minutes. The reaction was allowed to warm up to a.t., and to proceed at a.t. for 36 hours. Afterwards, the reaction mixture was diluted with 20 mL EA and 20 mL 0.5 M HCl was added. The phases were separated, the

organic phase was washed with 25 mL 0.1 M NaHCO₃ and 20 mL H₂O. Then, the organic solvent was removed under reduced pressure and flash chromatography (95/5 CH₂Cl₂/EA v/v) was performed. The product was afforded as an orange-brown oil after drying for 24 hours. Yield of 340 mg, 95.6% (vs. theory).

¹H-NMR, DMSO-*d*₆, 600 MHz, δ / ppm: 4.74 (q, 2H), 4.07 (n, 4 H), 3.38 (q, 4H), 1.51 (d, 6H), 1.37 (m, 5H), 1.24 (bm, 15 H), 0.88 (t, 6H)

¹³C-NMR, DMSO-*d*₆, 151 MHz, δ / ppm: 13.40, 16.27, 21.40, 25.26, 27.92, 28.52, 28.81, 29.58, 36.26, 47.59, 170.25

8.5.2.6 Two-arm-RAFT polymerisation with methyl acrylate



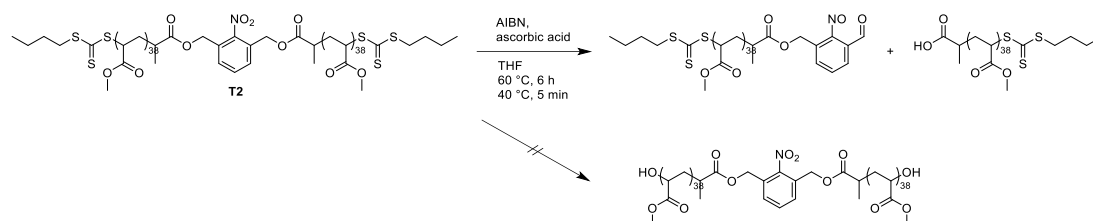
(2-nitro-1,3-phenylene)bis(methylene) bis(2-(((butylthio)carbonothioyl)thio)propanoate) (or (decane-1,10-diyl bis(2-(((butylthio)carbonothioyl)thio)propanoate))), methyl acrylate (disinhibited by passing through a short aluminium oxide plug) and AIBN were mixed in 56 mL toluene. The mixture was degassed by performing four freeze-thaw-pump cycles. The solution was sealed with argon, and the reaction mixture heated up to 60 °C and stirred for 24 hours. Afterwards, the polymer was directly precipitated three times in cold n-hexane (**T1** and **T2**, **P1-P3**) or twice in cold MeOH (**P4**). The polymer was dried *in vacuo* for 24 hours prior to further use.

Table 8-30: Polymerisation protocol. *: Only **T1** was used with a non-degradable core.

Entry	$m_{\text{RAFT-Agent}}$ / mg	Eq. RAFT-Agent	m_{MA} / mg	Eq. MA	m_{AIBN} / mg	Eq. AIBN	M_n (theo.) / kg mol ⁻¹	M_n (exp.) / kg mol ⁻¹	M_w (exp.) / kg mol ⁻¹	\bar{D}
T1*	20	1.00	560	182	1.07	0.18	17.8	22.6	27.2	1.21
T2	100	1.00	1377	100	5.26	0.20	9.27	7.13	7.79	1.09
P1	100	1.00	690	50	2.63	0.10	4.92	1.59	2.29	1.44
P2	100	1.00	1377	100	2.63	0.10	9.23	3.12	3.96	1.27

P3	100	1.00	2763	200	2.63	0.10	17.8	10.5	14.0	1.33
P4	100	1.00	13795	1000	2.63	0.10	86.7	67.6	91.8	1.36

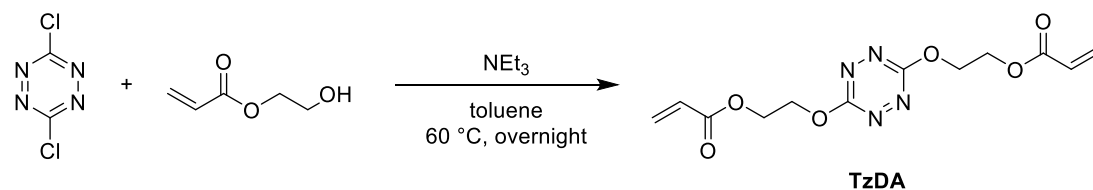
8.5.2.7 Attempted AIBN-based α,ω -endgroup removal with T2



The protocol was adapted according to literature.^[331] Briefly, in an open round bottom flask, 20 mL dry THF was heated up to 60 °C and AIBN (0.2 g, 38.0 eq.) was added portion wise. Then, **T2** ($M_{n, \text{exp}} = 7.13 \text{ kg mol}^{-1}$, 0.2 g, 1.0 eq), dissolved in dry THF, was added. The reaction mixture was stirred for 6 hours until almost complete discoloration occurred. The solution was cooled down to 40 °C and ascorbic acid (0.1 g, 12.6 eq.) was added and stirred for 5 minutes. Afterwards the solvent was mostly removed under reduced pressure and the polymer precipitated once in cold n-hexane. The polymer was dried *in vacuo* for 24 hours prior to SEC analysis. SEC traces are provided in **Figure S4-18**.

8.5.3 Synthetical procedures Chapter 5: Peroxide-accelerated photodegradation of tetrazine-bearing thiol-acrylate polymers via green light

8.5.3.1 2-((1,2,4,5-tetrazine-3,6-diyl)bis(oxy))bis(ethane-2,1-diyl) diacrylate



A flame-dried flask was charged with 1.5 g 3,6-dichloro-1,2,4,5-tetrazine (10.0 mmol, 1.0 eq.) and 3.2 mL 2-hydroxyethyl acrylate (3.5 g, 30.3 mmol, 3.0 eq.) and dissolved in 75 mL toluene. Under vigorous stirring, 4.2 mL NEt_3 (3.1 g, 30.1 mmol, 3.0 eq.) was added dropwise. After completed addition, the reaction mixture was allowed to stir at 60 °C overnight. The reaction mixture was diluted with 50 mL toluene and washed twice with brine (250 mL) and twice with water (250 mL). The organic phase

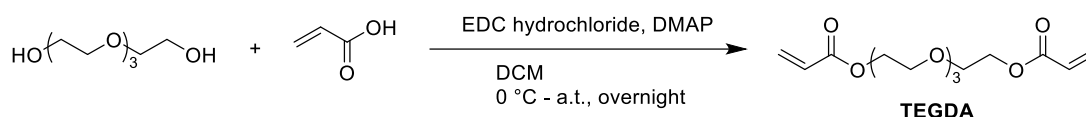
was separated, the solvent removed under reduced pressure and flash chromatography (CH/EA 75/25 - 1/1 v/v) performed. The product was afforded as a red crystalline solid (1.5 g, 48.3 % vs. theory).

¹H-NMR, DMSO-*d*₆, 600 MHz, δ / ppm: 6.36 (dd, *J* = 17.3, 1.5 Hz, 1H), 6.22 (dd, *J* = 17.3, 10.3 Hz, 1H), 5.98 (dd, *J* = 10.4, 1.5 Hz, 1H), 4.78 – 4.73 (m, 2H), 4.59 – 4.54 (m, 2H)

¹³C-NMR (151 MHz, DMSO-*d*₆) δ / ppm: 165.60, 165.38, 132.17, 127.94, 67.13, 62.10, 39.94, 39.80, 39.66, 39.52, 39.38, 39.24, 39.10

LC-MS (ESI): *m/z* [M+NH₄]⁺, theo: 328.1243, exp: 328.1252, Δ / ppm: 2.74

8.5.3.2 ((oxybis(ethane-2,1-diyl))bis(oxy))bis(ethane-2,1-diyl) diacrylate



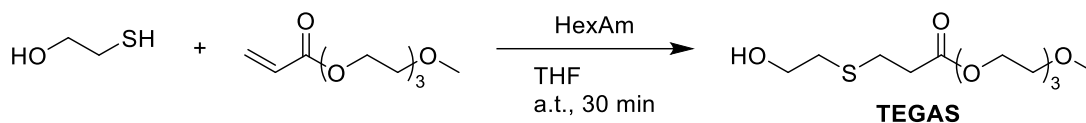
A round bottom flask was charged with 4.4 mL tetraethylene glycol (5.0 g, 26 mmol, 1.0 eq.), 4.4 mL acrylic acid (4.6 g, 64.4 mmol, 2.5 eq.) and 0.7 g DMAP (5.2 mmol, 0.2 eq.), dissolved in 100 mL DCM and cooled with an ice bath. Afterwards, 14.8 g EDC hydrochloride (77.2 mmol, 3.0 eq) was added portion wise. The ice bath was removed, and the reaction was allowed to warm up to ambient temperature and proceed overnight. Afterwards, the solution was diluted with 50 mL DCM, washed with 50 mL 0.5 M HCl, 50 mL sat. NaHCO₃, 25 mL brine and 25 mL water. The organic phase was separated, the solvent removed under reduced pressure and flash chromatography (CH/EA 6/4 v/v) was performed. The product was afforded as a colourless liquid (1.6 g, 20.1%).

¹H-NMR (600 MHz, DMSO-*d*₆) δ / ppm: 6.33 (dd, *J* = 17.2, 1.5 Hz, 2H), 6.19 (dd, *J* = 17.3, 10.4 Hz, 2H), 5.95 (dd, *J* = 10.4, 1.5 Hz, 2H), 4.23 – 4.13 (m, 4H), 3.66 – 3.62 (m, 4H), 3.55 – 3.50 (m, 8H)

¹³C-NMR (151 MHz, DMSO-*d*₆) δ / ppm: 165.48, 131.65, 128.22, 69.79, 69.76, 68.24, 63.47

LC-MS (ESI): *m/z* [M+NH₄]⁺, exp: 320.1698, theo: 320.1704, Δ / ppm: 1.87

8.5.3.3 2-(2-(2-methoxyethoxy)ethoxy)ethyl 3-((2-hydroxyethyl)thio)propanoate



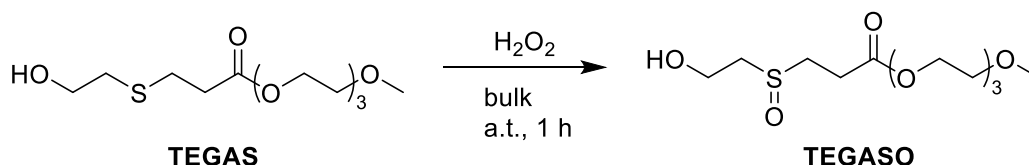
2-(2-(2-methoxyethoxy)ethoxy)ethyl acrylate was disinhibited by passing through a short aluminium oxide plug column prior to use. 2.0 g of 2-(2-(2-methoxyethoxy)ethoxy)ethyl acrylate (9.2 mmol, 1.0 eq.) and 0.9 g 2-mercaptoethanol (0.84 mL, 11.9 mmol, 1.3 eq.) were dissolved in 10 mL THF. 0.9 g Hexylamine (HexAm, 1.3 mL, 9.2 mmol, 1.0 eq.) was quickly added and the solution allowed to stir at a.t. for 30 minutes. Afterwards, all volatiles were removed under high vacuum conditions, affording TEGAS as a pale-yellow liquid (2.4 g, 89.7 %).

¹H-NMR (600 MHz, AcN-*d*₃) δ / ppm: 4.24 – 4.12 (m, 2H), 3.67 – 3.58 (m, 4H), 3.58 – 3.52 (m, 6H), 3.48 – 3.44 (m, 2H), 3.29 (s, 3H), 2.80 – 2.73 (t, 2H), 2.66 – 2.57 (m, 4H), 2.15 (s, 1H)

¹³C-NMR (151 MHz, AcN-*d*₃) δ / ppm: 172.82, 118.31, 72.62, 71.23, 71.10, 71.03, 69.66, 64.62, 62.08, 58.90, 35.70, 35.29, 27.65, 1.73, 1.60, 1.46, 1.32, 1.18, 1.04, 0.91

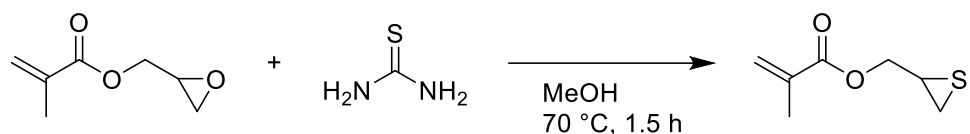
LC-MS (ESI): *m/z* [M+NH₄]⁺, theo: 314.1632, exp: 314.1627, Δ / ppm: 1.59

8.5.3.4 2-(2-(2-methoxyethoxy)ethoxy)ethyl 3-((2-hydroxyethyl)sulfinyl)propanoate



In order to assess the effects of a possible oxidation reaction on the sulphide motif, TEGAS was subjected to H₂O₂. 1 mL of 30% H₂O₂ was added to 0.1 g of TEGAS and stirred at a.t. for 1 hours. All volatiles were removed under reduced pressure. ¹H-NMR spectroscopy and LC-ESI-MS confirms the conversion to sulfinyl according to **Table S5-2**, **Figure S5-14** and **Figure S5-15**.

8.5.3.5 Thiiran-2-ylmethyl methacrylate

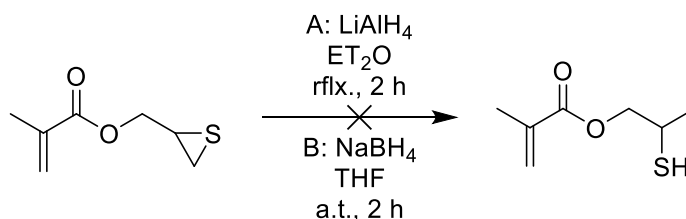


The synthesis was performed according to literature.^[332] A round bottom flask was charged with 1.4 mL glycidyl methacrylate (1.5 g, 10.54 mmol, 1.0 eq.) in 30 mL MeOH. 1.6 g thiourea (21.02 mmol, 2.0 eq.) was added portion wise while stirring at a.t. The reaction mixture was allowed to reflux for 1.5 h. Afterwards, the solvent was mostly removed under reduced pressure, 20 mL H₂O was added and the reaction mixture was extracted with 3x 15 mL CH₂Cl₂. The organic phase was dried over MgSO₄, the solvent removed under reduced pressure. The residue was purified by flash chromatography (silica gel, EA/CH 95/5 – 1/1 v/v). Product ($R_f = 0.69$, TLC CH/EA 8/2 with KMnO₄ stain) was afforded as a colourless liquid. Yield of 82.6 % (vs. theory).

¹H-NMR (600 MHz, DMSO-*d*₆) δ / ppm: 6.07 (s, 1H), 5.73 (s, 1H), 4.29 – 4.08 (dd, 2H), 3.26 (p, 1H), 2.63 (d, 1H), 2.44 (d, 1H), 1.90 (s, 3H)

¹³C-NMR (151 MHz, DMSO-*d*₆) δ / ppm: 166.21, 135.59, 126.24, 68.02, 31.62, 23.82, 17.96

8.5.3.6 2-mercaptopropyl methacrylate



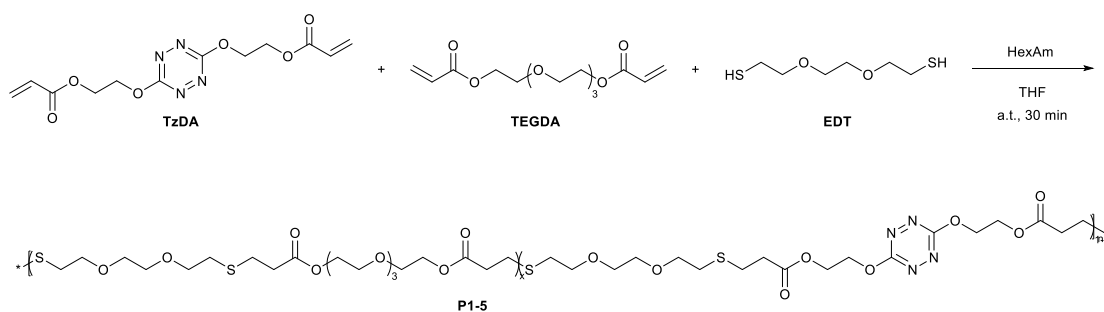
LiAlH₄ and NaBH₄ as ring opening agents were employed. Syntheses were adapted according to literature.^[333]

A: A flame-dried flask was charged with 0.2 g LiAlH₄ (5.27 mmol, 1.2 eq.) in 25 mL anhydrous Et₂O. 0.7 g thiiran-2-ylmethyl methacrylate (4.62 mmol, 1.0 eq.) in 5 mL anhydrous Et₂O was added via syringe pump (flow rate 10 mL hr⁻¹). After addition, the reaction was allowed to reflux for 2 hours. After cooling down to a.t., 30 mL of

H₂O was added slowly. Precipitated solid was redissolved in 15 mL of 10% sulfuric acid, layers were separated and the aqueous phase washed with 2x 25 mL Et₂O. All ether fractions were combined, the solvent was removed under reduced pressure, and flash chromatography performed (CH/EA 8/2-1/1 v/v). No product was isolated.

B: A flame-dried flask was charged with 0.5 g thiiran-2-ylmethyl methacrylate (3.16 mmol, 1.0 eq.) and 25 mL THF. 0.1 g NaBH₄ (3.44 mmol, 1.1 eq.) was added under continuous stirring portion wise. The reaction mixture was allowed to stir at a.t. for 2 hours. Afterwards, the reaction mixture was poured on 30 mL ice and diluted with 50 mL EA. The phases were separated, the organic solvent was removed under reduced pressure. ¹H NMR spectroscopy revealed isolation of starting material.

8.5.3.7 Polymerisation *ran*-copoly[EDT/(TzDA; TEGDA)]



A crimp vial was charged with a stirring bar, EDT and solutions of TzDA and TEGDA. TzDA and TEGDA were dissolved in THF ($c = 0.3 \text{ mg mL}^{-1}$) to ensure accurate molar amount and overall identical reaction volume used in the formulation. All formulations were agitated vigorously for 10 seconds. Hexylamine (HexAm) was added at once and the vial rapidly crimped. All solutions were stirred for exactly 30 minutes, then snap-frozen in liquid nitrogen and precipitated in cold MeOH twice. All polymers were dried in vacuo for 24 hours prior to further use. Isolated yield for all polymers was approximately 30% with the exception of **P5**.

Table 8-31: Polymerisation details. ^avalues obtained after calibration against *p*MMA standard for RI detection. ^bYield of recovered polymer.

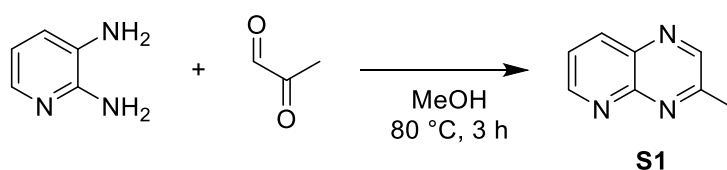
Entry	m_{TzDA} / mg	Eq. TzDA	m_{TEGDA} / mg	Eq. TEGDA	m_{EDT} / mg	Eq. EDT	m_{HEA} / mg	Eq. HEA	M_n^a / kg mol ⁻¹	M_w^a / kg mol ⁻¹	\bar{D}^a	Yield ^b / %
P1	0.0	0.00	200.0	1.00	120.6	1.00	13.4	0.20	7.65	12.0	1.6	28.7
P2	50.0	0.25	146.2	0.75	117.5	1.00	13.1	0.20	6.97	11.7	1.7	27.8
P3	100.0	0.50	97.4	0.50	117.5	1.00	13.1	0.20	6.85	12.5	1.8	30.4
P4	150.0	0.75	48.7	0.25	117.5	1.00	13.1	0.20	6.41	11.8	1.8	28.7
P5	200.0	1.00	0.0	0.00	117.5	1.00	13.1	0.20	6.04	11.1	1.8	56.7

Table 8-32: Investigation of polymer composition. ^aExperimental equivalents are provided from ¹H-NMR spectra of the respective polymer after isolation.

Entry	Eq. TzDA (theo.)	Eq. TEGDA (theo.)	Eq. TzDA (exp.) ^a	Eq. TEGDA (exp.) ^a	Eq. EDT
P1	0.00	1.00	0.00	1.00	1.00
P2	0.25	0.75	0.16	0.84	1.00
P3	0.50	0.50	0.33	0.67	1.00
P4	0.75	0.25	0.60	0.40	1.00
P5	1.00	0.00	1.00	0.00	1.00

8.5.4 Synthetical procedures Chapter 6: Wavelength-Orthogonal Stiffening and Inhibition of Hydrogel Networks with Visible Light

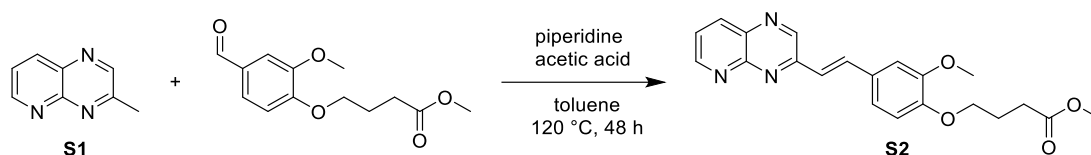
8.5.4.1 Methylpyrido[2,3-b]pyrazine



Methylglyoxal (40% in water, 5.4 g, 0.03 mmol) was added to a solution of pyridine-2,3-diamine (2.18 g, 0.02 mol) in methanol (40 mL) and the solution was heated at 80 °C with stirring under refluxing conditions for 3 h. The solution was subsequently concentrated *in vacuo* and the crude product was purified by column chromatography (n-hexane/EA 1/9 v/v) to give product as dark solid (yield: 2.7 g, 94%).

¹H-NMR, CDCl₃, 400 MHz, δ / ppm: 9.15 (dd, 1H, J = 4.2 and 1.9 Hz), 8.85 (s, 1H), 8.45 (dd, 1H, J = 8.3 and 1.9 Hz), 7.68 (dd, 1H, J = 8.3 and 4.2 Hz), 2.88 (s, 3H)
¹H-NMR is in agreement with previously published literature.^[334]

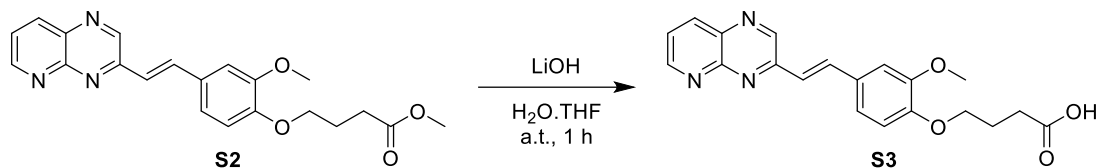
8.5.4.2 Ethyl (E)-4-(2-methoxy-4-(2-(pyrido[2,3-b]pyrazin-3-yl)vinyl)phenoxy)butanoate



To a mixture of S1 (1.4 g, 0.01 mol) and ethyl 4-(4-formyl-2-methoxyphenoxy)butanoate^[295] (4.0 g, 0.015 mol), piperidine (0.4 g, 5 mmol), acetic acid (0.4 g, 7 mmol) and dry toluene (5 mL) were added. The mixture was purged with Argon, sealed and heated at 120 °C for 48 h. The resultant solution was concentrated *in vacuo* and absorbed onto silica gel. The product was purified by column chromatography (n-hexane/EA 1/1 v/v) to give pure product as orange solid (yield: 2.1 g, 53.9%).

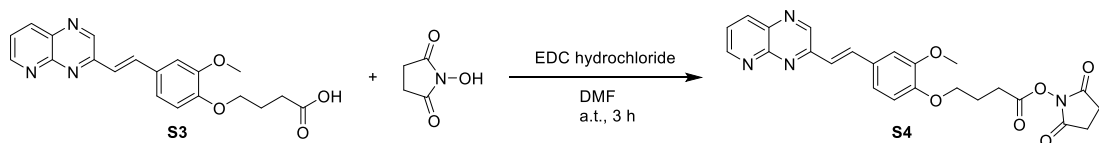
¹H-NMR, CDCl₃, 600 MHz δ / ppm: 9.14 (dd, 1H, J = 4.1 and 2.0 Hz), 9.03 (s, 1H), 8.42 (dd, 1H, J = 8.2 and 2 Hz), 8.1 (d, 1H, J = 8.4 Hz), 7.62 – 7.65 (dd, 1H, J = 8.2 and 4.2 Hz), 7.22 – 7.3 (m, 3H), 6.92 – 6.94 (d, 1H, J = 4.1 Hz), 4.13 – 4.16 (m, 4H), 3.91 (s, 3H), 2.53 – 2.57 (t, 2H, J = 7.2 Hz), 2.17 – 2.21 (m, 2H), 1.25 – 1.28 (t, 3H, J = 7.2 Hz)

8.5.4.3 (E)-4-(2-methoxy-4-(2-(pyrido[2,3-b]pyrazin-3-yl)vinyl)phenoxy)butanoic acid



Compound **S2** (1.85 g, 5 mmol) was dissolved in THF (10 mL) and to this solution was added a solution of LiOH (0.5 g, 20 mmol) in deionized water (10 mL). The solution was stirred at ambient temperature for 1 h and carefully neutralized with acetic acid. Addition of excess acetic acid resulted in the precipitation of an orange product which was filtered, washed with copious amount of water, dried *in vacuo* and used directly in the next step (yield: 1.2 g, 66.3%).

8.5.4.4 2,5-Dioxypyrrolidin-1-yl(E)-4-(2-methoxy-4-(2-(pyrido[2,3-b]pyrazin-3-yl)vinyl)phenoxy)butanoate



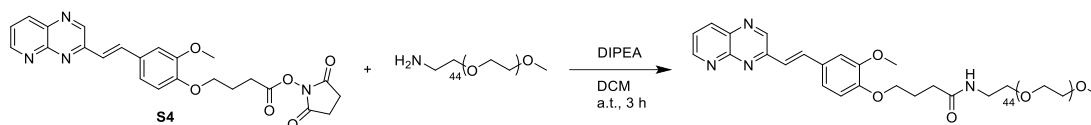
Compound **S3** (1.2 g, 3.3 mmol) was dissolved in DMF (10 mL) and to the solution was added EDC hydrochloride (0.8 g, 4.1 mmol) and N-hydroxysuccinimide (0.5 g, 4.1 mmol). The solution was stirred at ambient temperature for 3 h and DMF was concentrated *in vacuo*. The crude product was absorbed onto silica gel and purified by column chromatography eluting with n-hexane/EA (v/v = 7/3) to give product as orange crystal (yield: 1.0 g, 68%).

¹H-NMR, CD₂Cl₂, 600 MHz, δ / ppm: 9.14 (dd, 1H, J = 4.1 and 2.0 Hz), 9.03 (s, 1H), 8.42 (dd, 1H, J = 8.2 and 2 Hz), 8.1 (d, 1H, J = 8.4 Hz), 7.62 – 7.65 (dd, 1H, J = 8.2 and 4.2 Hz), 7.22 – 7.3 (m, 3H), 6.92 – 6.94 (d, 1H, J = 4.1 Hz), 4.18 – 4.2 (t, J = 7.2 Hz, 2H), 3.98 (s, 3H), 2.94 – 2.91 (t, 2H, J = 7.2 Hz), 2.86 (s, 4H), 2.28 – 2.31 (m, 2H)

¹³C-NMR, CD₂Cl₂, 151 MHz, δ / ppm: 169.74, 169.07, 154.83, 154.40, 151.76, 150.54, 150.51, 146.52, 138.75, 138.50, 137.39, 129.91, 124.67, 123.10, 122.48, 113.94, 110.69, 67.78, 56.48, 28.21, 26.21, 25.06

LC-MS (ESI): m/z [M+H]⁺, theo: 463.1612, exp: 463.1606, Δ / ppm: 1.30

8.5.4.5 MeO-PEG-SPP



MeO-PEG-NH₂ (0.5 g, 0.25 mmol) was dissolved in CH₂Cl₂ (5 mL) and compound **S4** (108 mg, 0.26 mmol) was added followed by addition of DIPEA (10 μL). The solution was stirred at ambient temperature for 3 h and precipitated into diethyl ether (100 mL) to afford the product as a yellow solid (yield: 0.5 g, 86%).

8.5.4.6 PEG-(NH₂)₈

8-arm PEG(NH₂)₈ was synthesised from 8-arm PEG20k-OH according to a previously published procedure with a degree of conversion from -OH to -NH₂ group of 98%.^[295]

8.5.4.7 PEG-(SPP)₈

PEG-(SPP)₈ was synthesised from PEG-(NH₂)₈ and compound **S4** using a similar procedure to the synthesis of MeO-PEG-SPP, affording the product as a yellow solid with a yield of 94%.

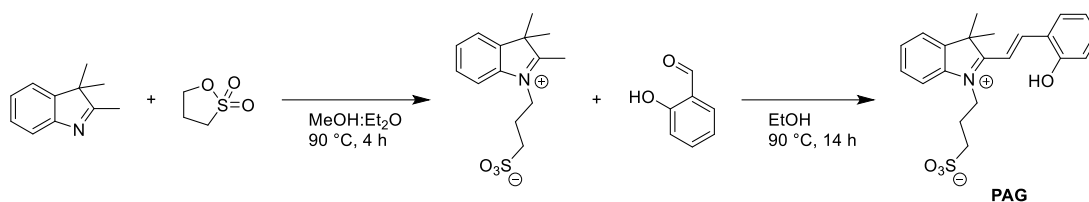
8.5.4.8 3-(pyren-1-yl)acrylate-N-hydroxysuccinimide

3-(pyren-1-yl)acrylate-N-hydroxysuccinimide was prepared according to a previously published procedure.^[335]

8.5.4.9 PEG-(AP)₈

PEG-(AP)₈ was synthesised from PEG-(NH₂)₈ and 3-(pyren-1-yl)acrylate-N-hydroxysuccinimide^[335] using a similar procedure to the synthesis of MeO-PEG-SPP, affording the product as a yellow solid with a yield of 97%.

8.5.4.10 (E)-3-(2-(2-hydroxystyryl)-3,3-dimethyl-3H-indol-1-ium-1-yl)propane-1-sulfonate (PAG)



2,3,3-trimethylindolenine (1.7 g, 0.01 mmol) was added into propane sulfone (1.3 g, 0.01 mmol) and the mixture was stirred at 90 °C for 4 h. Upon cooling to room temperature, methanol (5 mL) was added and stirred for 10 min, followed by addition of Et₂O (50 mL). The solid was filtered and washed with diethyl ether and dried *in vacuo* to give product as purple solid (yield: 2.1 g, 75%). The above solid (1.0 g, 3.6 mmol) was dissolved in ethanol (20 mL) and 2-hydroxybenzaldehyde (0.5 g, 3.9 mmol). The mixture was heated at 90 °C under refluxing condition for 14 h. Upon cooling to room temperature, the mixture was filtered and the solid was washed with ice-cold ethanol, dried *in vacuo* to give product as yellow solid (yield: 1.0 g, 73%).

¹H-NMR, DMSO-*d*₆, 600 MHz, δ / ppm: 11.03 (s, 1H), 8.62 (d, 1H, J = 16.5), 8.28 (d, 1H, J = 7.0), 8.02 (d, 1H, J = 7.0), 7.87 (m, 2H), 7.62 (m, 2H), 7.45 (t, 1H, J = 8.4), 7.04 (d, 1H, J = 8.5), 6.96 (t, 1H, J = 7.0), 4.80 (t, 2H, J = 7.5), 2.65 (t, 2H, J = 6.0), 2.15 (m, 2H), 1.78 (s, 6H).)

¹³C-NMR (DMSO-*d*₆, 151 MHz) δ / ppm: 181.77, 159.02, 148.70, 143.48, 140.93, 135.75, 129.77, 129.15, 129.13, 122.98, 121.34, 120.07, 116.62, 115.09, 111.45, 51.90, 47.33, 45.54, 26.44, 24.58

LC-MS (ESI): *m/z* [M+H]⁺, theo: 386.1421, exp: 386.1419, Δ / ppm: 0.52

Appendices

Appendix A

Supporting Information for Chapter 3: Exploring the photochemistry of *ortho*-nitrobenzyl alcohols and incorporation in polyurethanes

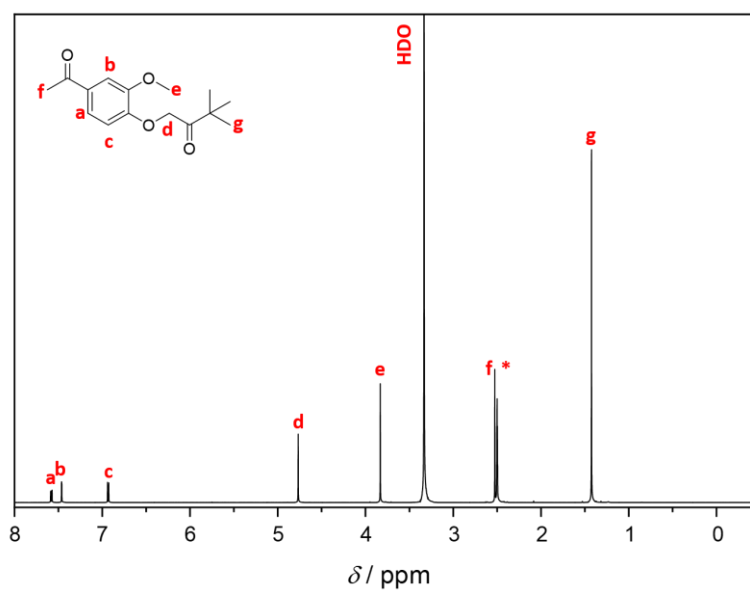


Figure S3-1: ¹H-NMR spectrum of **2** in DMSO-*d*₆ (*). Reproduced from Ref. 200 with permission from the Royal Society of Chemistry. Modified representation.

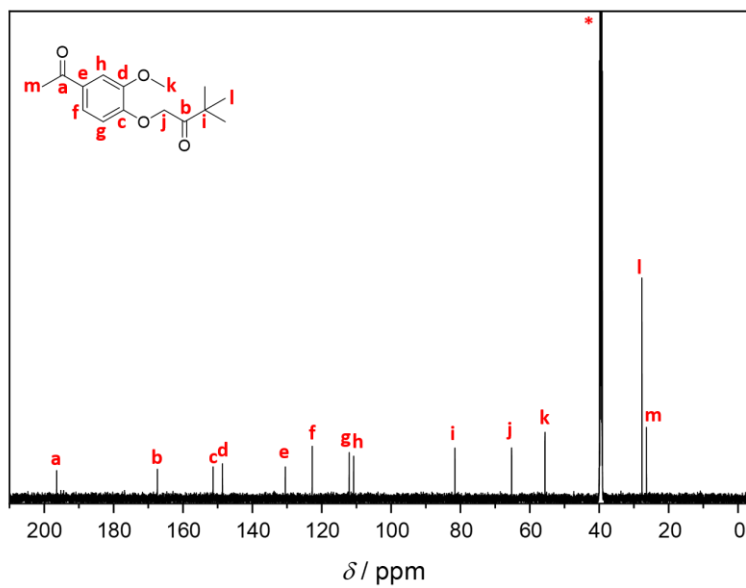


Figure S3-2: ^{13}C -NMR spectrum of **2** in $\text{DMSO-}d_6$ (*). Reproduced from Ref. 200 with permission from the Royal Society of Chemistry. Modified representation.

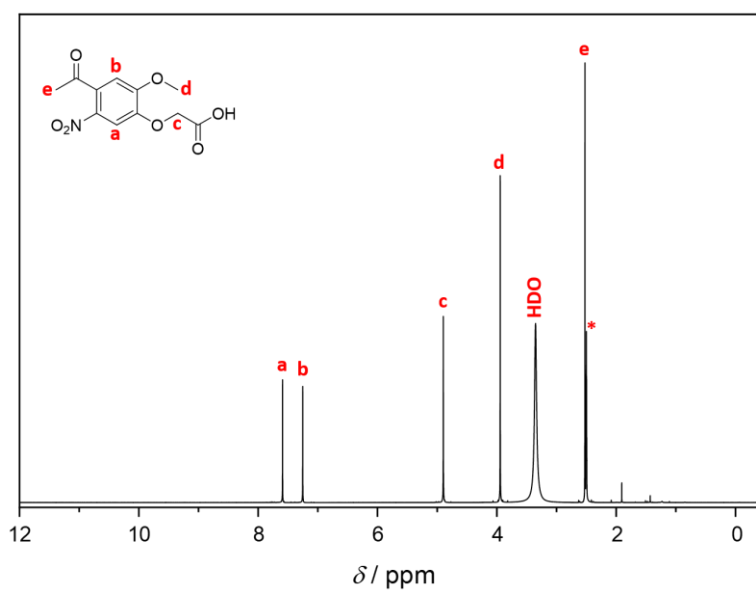


Figure S3-3: ^1H -NMR spectrum of **3** in $\text{DMSO-}d_6$ (*). Reproduced from Ref. 200 with permission from the Royal Society of Chemistry. Modified representation.

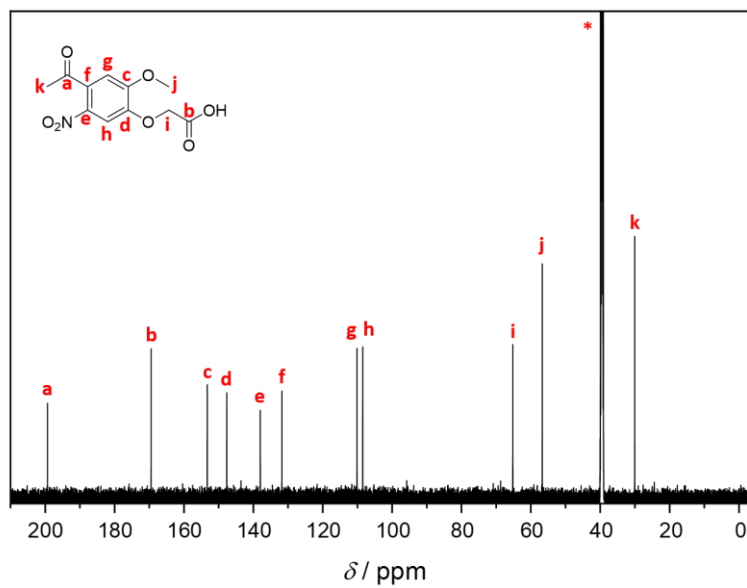


Figure S3-4: ^{13}C -NMR spectrum of **3** in $\text{DMSO-}d_6$ (*). Reproduced from Ref. 200 with permission from the Royal Society of Chemistry. Modified representation.

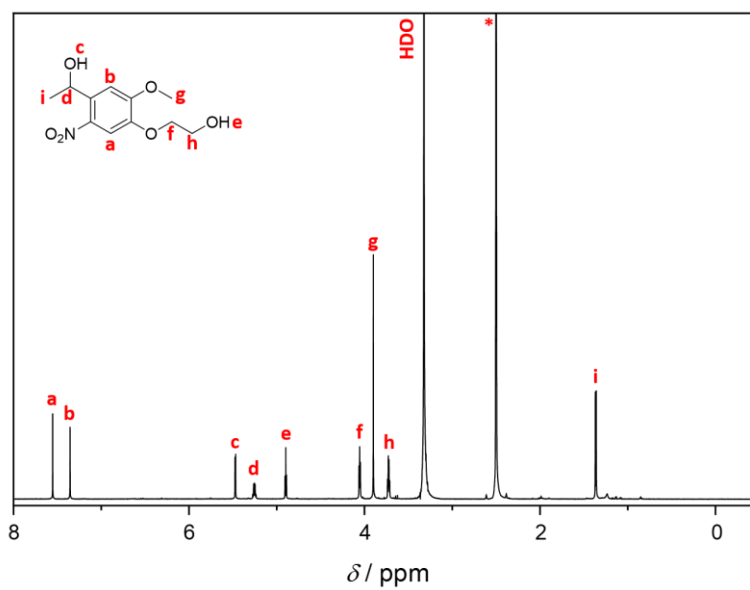


Figure S3-5: ^1H -NMR spectrum of **4** in $\text{DMSO-}d_6$ (*). Reproduced from Ref. 200 with permission from the Royal Society of Chemistry. Modified representation.

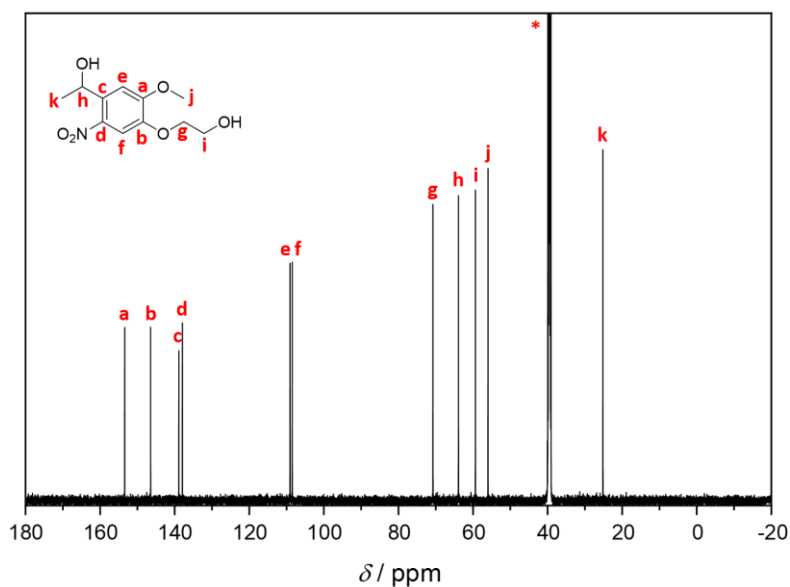


Figure S3-6: ^{13}C -NMR spectrum of **4** in $\text{DMSO-}d_6$ (*). Reproduced from Ref. 200 with permission from the Royal Society of Chemistry. Modified representation.

Table S3-1: Detailed overview of found species in the mass spectrum of **2**, comparison with theoretically expected m/z values and derived error Δ .

Assignment	m/z_{exp}	m/z_{theo}	Δ / ppm	Composition
$[\text{2M}+\text{Na}]^+$	583.2505	583.2514	1.54	$\text{C}_{30}\text{H}_{40}\text{O}_{10}\text{Na}_1^+$
$[\text{M}+\text{Na}]^+$	303.1199	303.1203	1.32	$\text{C}_{15}\text{H}_{20}\text{O}_5\text{Na}_1^+$
$[\text{M}+\text{NH}_4]^+$	298.1646	298.1649	1.01	$\text{C}_{15}\text{H}_{24}\text{O}_5\text{N}_1^+$
$[\text{M}+\text{H}]^+$	281.1384	281.1380	1.42	$\text{C}_{15}\text{H}_{21}\text{O}_5^+$
$[\text{M}^{\text{-tBu}}+\text{H}]^+$	225.0755	225.0757	0.89	$\text{C}_{11}\text{H}_{13}\text{O}_5^+$

Table S3-2: Detailed overview of found species in the mass spectrum of **3**, comparison with theoretically expected m/z values and derived error Δ .

Assignment	m/z_{exp}	m/z_{theo}	Δ / ppm	Composition
$[\text{2M}+\text{Na}]^+$	561.0968	561.0963	0.89	$\text{C}_{22}\text{H}_{22}\text{N}_2\text{O}_{14}\text{Na}_1^+$
$[\text{2M}+\text{NH}_4]^+$	556.1410	556.1409	0.18	$\text{C}_{22}\text{H}_{26}\text{N}_3\text{O}_{14}^+$
$[\text{M}+\text{Na}]^+$	292.0428	292.0428	0.00	$\text{C}_{11}\text{H}_{11}\text{N}_1\text{O}_7\text{Na}_1^+$
$[\text{M}+\text{NH}_4]^+$	287.0874	287.0874	0.00	$\text{C}_{11}\text{H}_{15}\text{N}_2\text{O}_7^+$
$[\text{M}+\text{H}]^+$	270.0609	270.0608	0.37	$\text{C}_{11}\text{H}_{12}\text{N}_1\text{O}_7^+$

Table S3-3: Detailed overview of found species in the mass spectrum of **4**, comparison with theoretically expected m/z values and derived error Δ .

Assignment	m/z_{exp}	m/z_{theo}	Δ / ppm	Composition
$[\text{M}+\text{Na}]^+$	280.0793	280.0792	0.36	$\text{C}_{11}\text{H}_{15}\text{N}_7\text{O}_6\text{Na}_1^+$
$[\text{M}+\text{NH}_4]^+$	275.1239	275.1238	0.36	$\text{C}_{11}\text{H}_{19}\text{N}_2\text{O}_6^+$
$[\text{M}-\text{H}_2\text{O}+\text{H}]^+$	240.0867	240.0866	0.42	$\text{C}_{11}\text{H}_{14}\text{N}_1\text{O}_5^+$

Table S3-4: Settings for the acquisition of shown EPR spectrum.

Setting	Value
B_0 (centre of magnetic field) / mT	336.5
R (range) / mT	5
t_{acq} (acquisition time) / s	60
N_R (Number of repetitions)	2
G_n (Gain mantisse)	7
G_e (Gain exponent)	2

Table S3-5: Parameters obtained by the simulation of two radical species via the *garlic* function.

Parameters	N3	C1
g (gyromagnetic constant)	2.01766	2.01874
S_e (electron spin)	1/2	1/2
A_H (Hyperfine coupling constant) / MHz	[6, 22, 33]	[33]
lw (line width) / MHz	0.24	0.18
Abundance	56	1

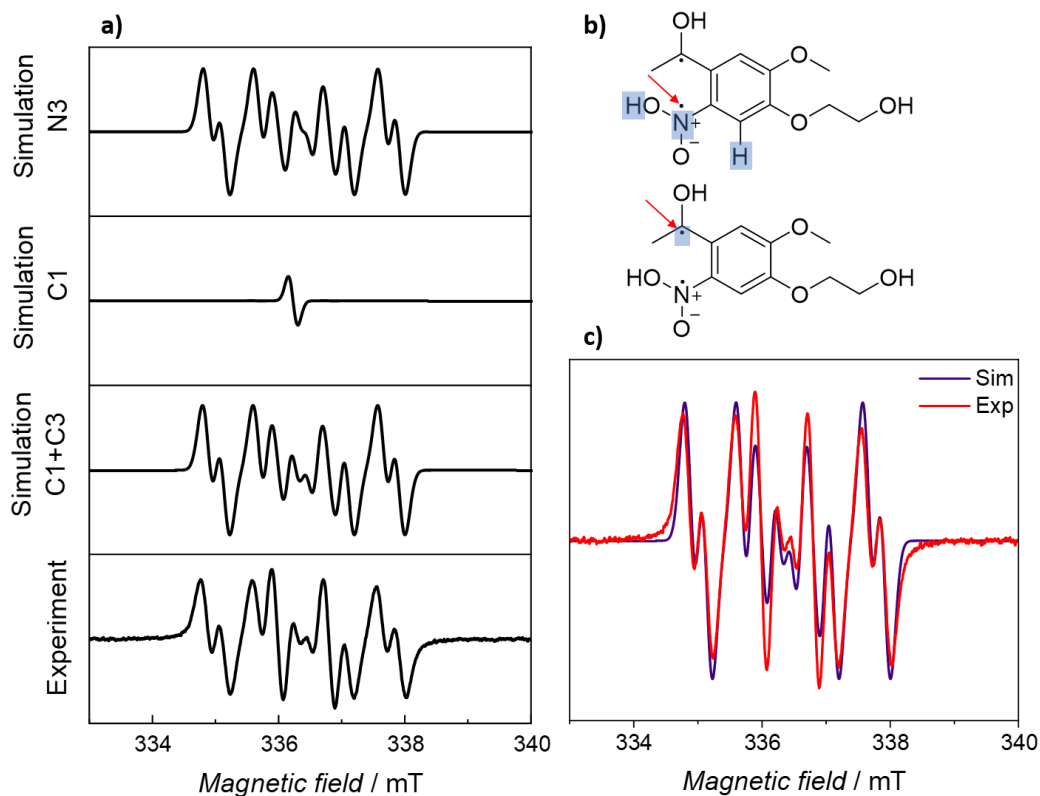


Figure S3-7: a) Extracted simulated spectra of N3, C1, the convolution of C1 and N3 and the experimental spectrum (from top to bottom). b) Assumed coupling pattern for the systems N3 (left) and C1 (right). The arrow indicates position of the radical, boxes represent coupling nuclei. c) Superimposed simulated and experimental spectra. Reproduced from Ref. 200 with permission from the Royal Society of Chemistry. Modified representation.

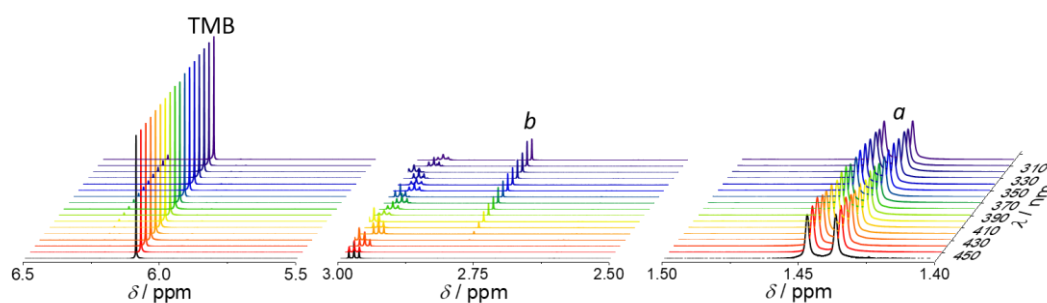


Figure S3-8: $^1\text{H-NMR}$ spectra (in acetonitrile- d_3) illustrating the analysis process for the action plot. Due to simplicity, only the first entry of every wavelength is shown. The reader is referred to **Figure 3-4 b** for emphasized resonances and Chapter 8.4.1.3 for analysis. No irradiation experiment is depicted in solid black. Reproduced from Ref. 200 with permission from the Royal Society of Chemistry. Modified representation.

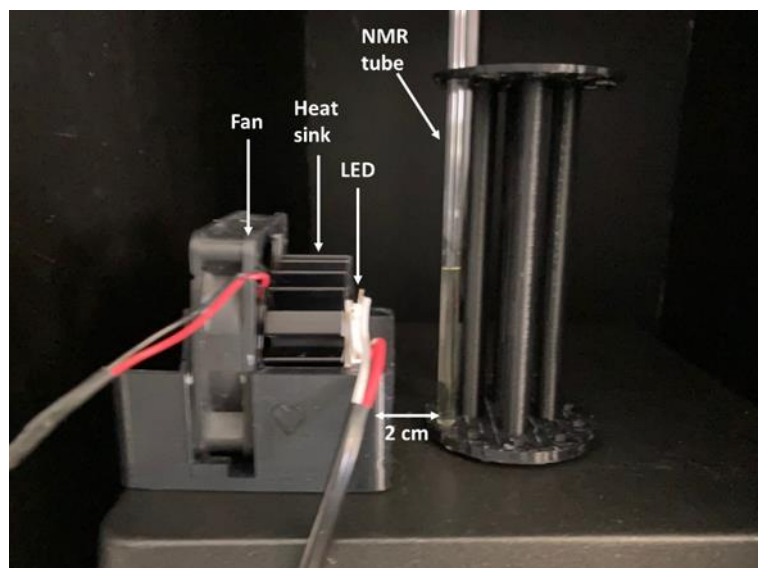


Figure S3-9: Setup for LED irradiation experiments. The heat generated by the LED is dissipated by heat sink and fan. The NMR tube is placed in 2 cm distance. Reproduced from Ref. 200 with permission from the Royal Society of Chemistry.

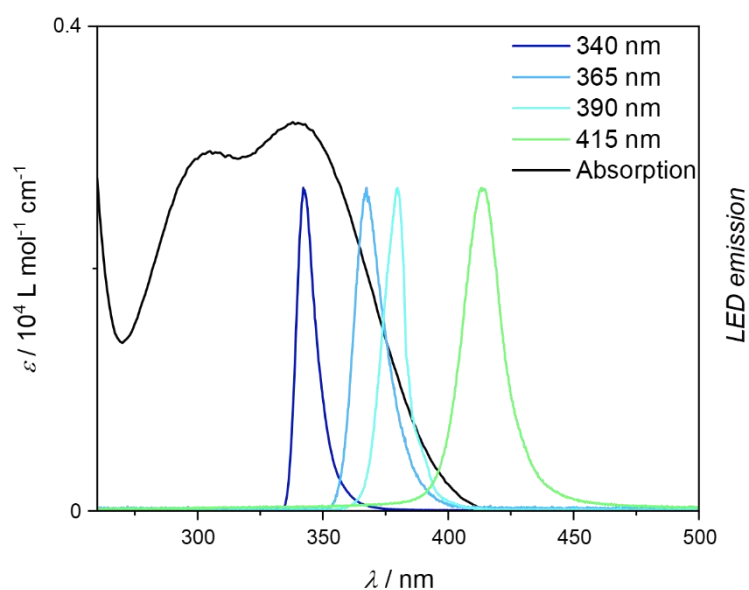


Figure S3-10: Emission spectra of the used LED's and the extinction coefficient ϵ of **4** in acetonitrile in comparison. Reproduced from Ref. 200 with permission from the Royal Society of Chemistry. Modified representation.

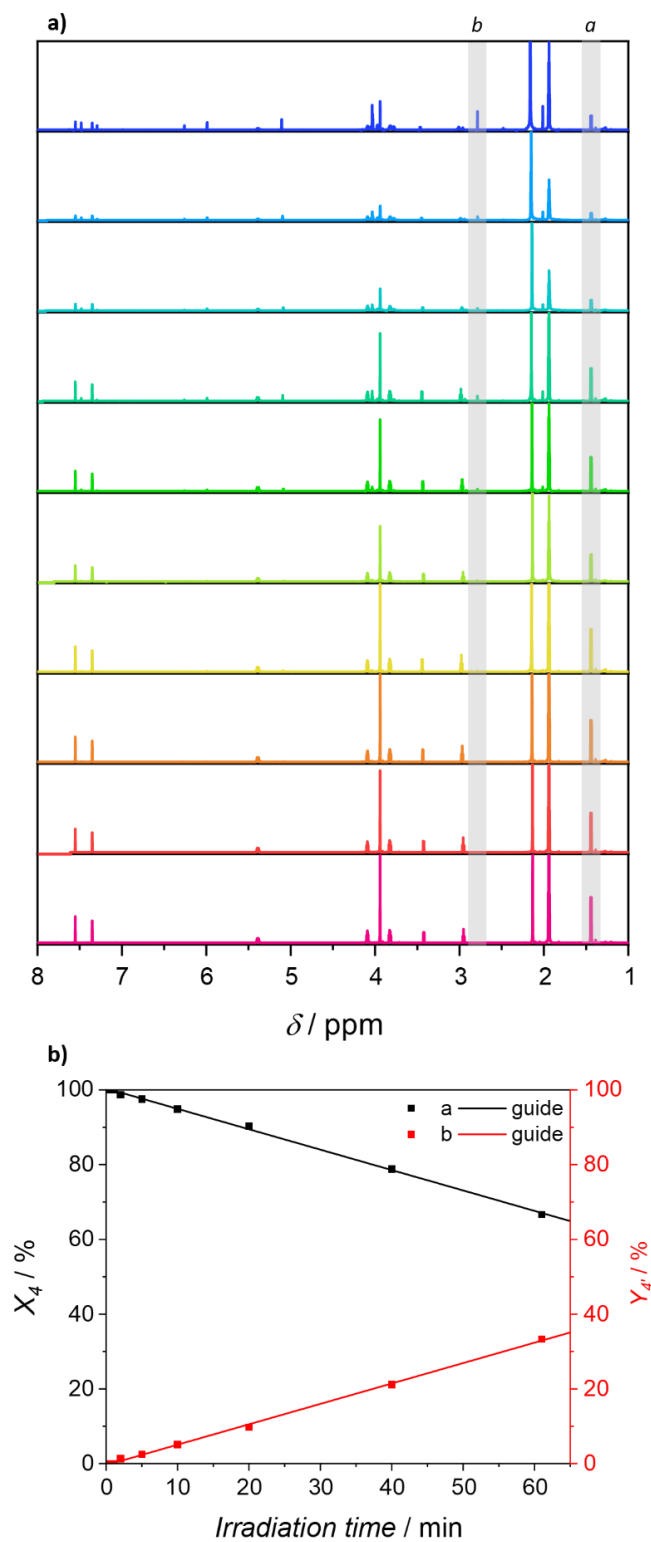


Figure S3-11: a) ¹H-NMR spectra of **4** in acetonitrile-*d*₃ with 340 nm irradiation in different exposure times. b) Plot of conversion and yield versus time for **4** (black) and **4d** (red) according to resonances *a* and *b*. Reproduced from Ref. 200 with permission from the Royal Society of Chemistry. Modified representation.

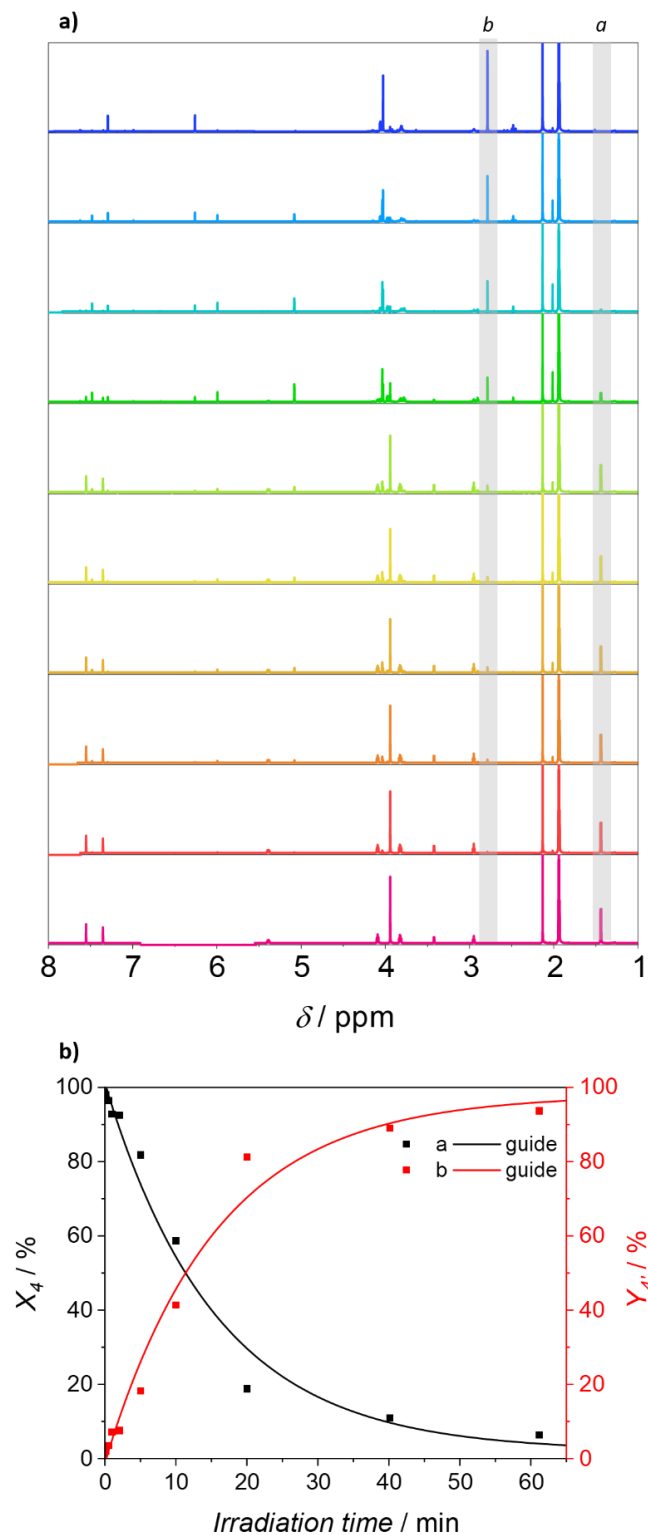


Figure S3-12: a) ¹H-NMR spectra of **4** in acetonitrile-*d*₃ with 365 nm irradiation in different exposure times. b) Plot of conversion and yield versus time for **4** (black) and **4d** (red) according to resonances *a* and *b*. Reproduced from Ref. 200 with permission from the Royal Society of Chemistry. Modified representation.

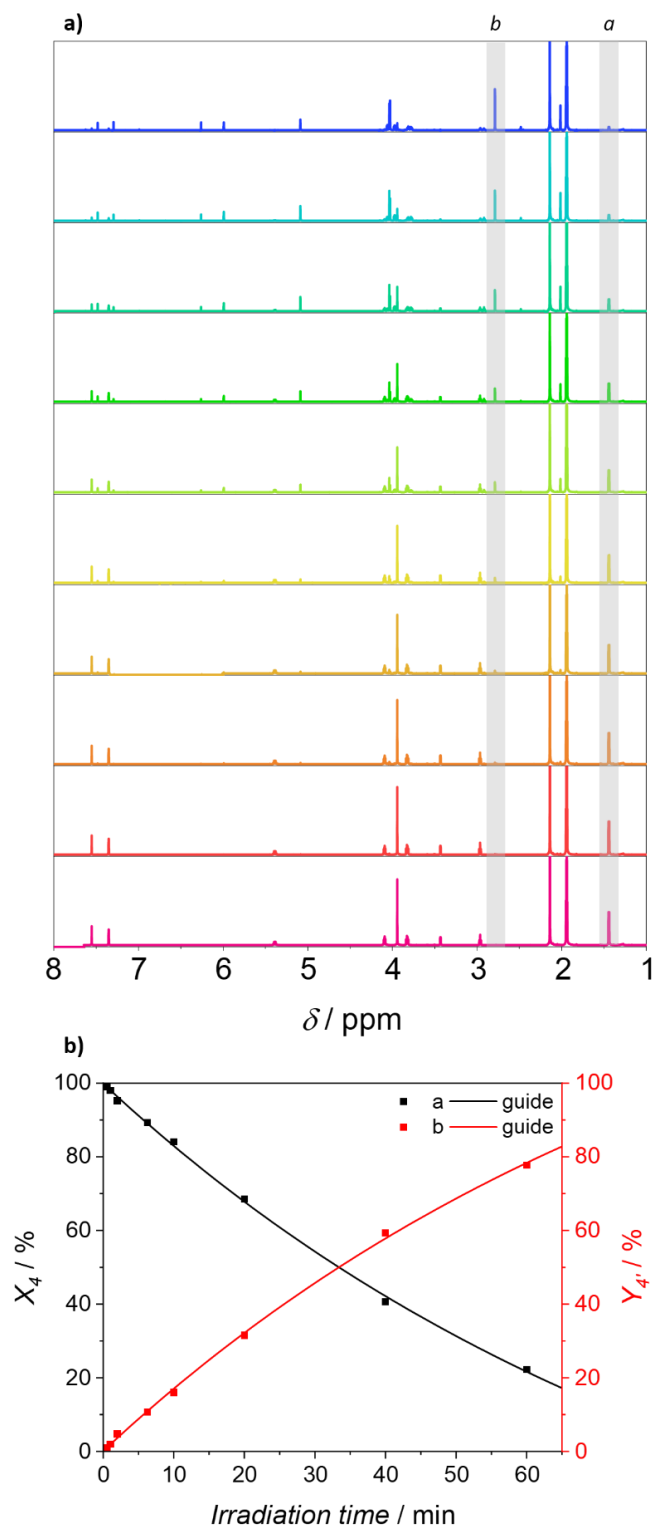


Figure S3-13: a) ¹H-NMR spectra of **4** in acetonitrile-*d*₃ with 390 nm irradiation in different exposure times. b) Plot of conversion and yield versus time for **4** (black) and **4d** (red) according to resonances *a* and *b*. Reproduced from Ref. 200 with permission from the Royal Society of Chemistry. Modified representation.

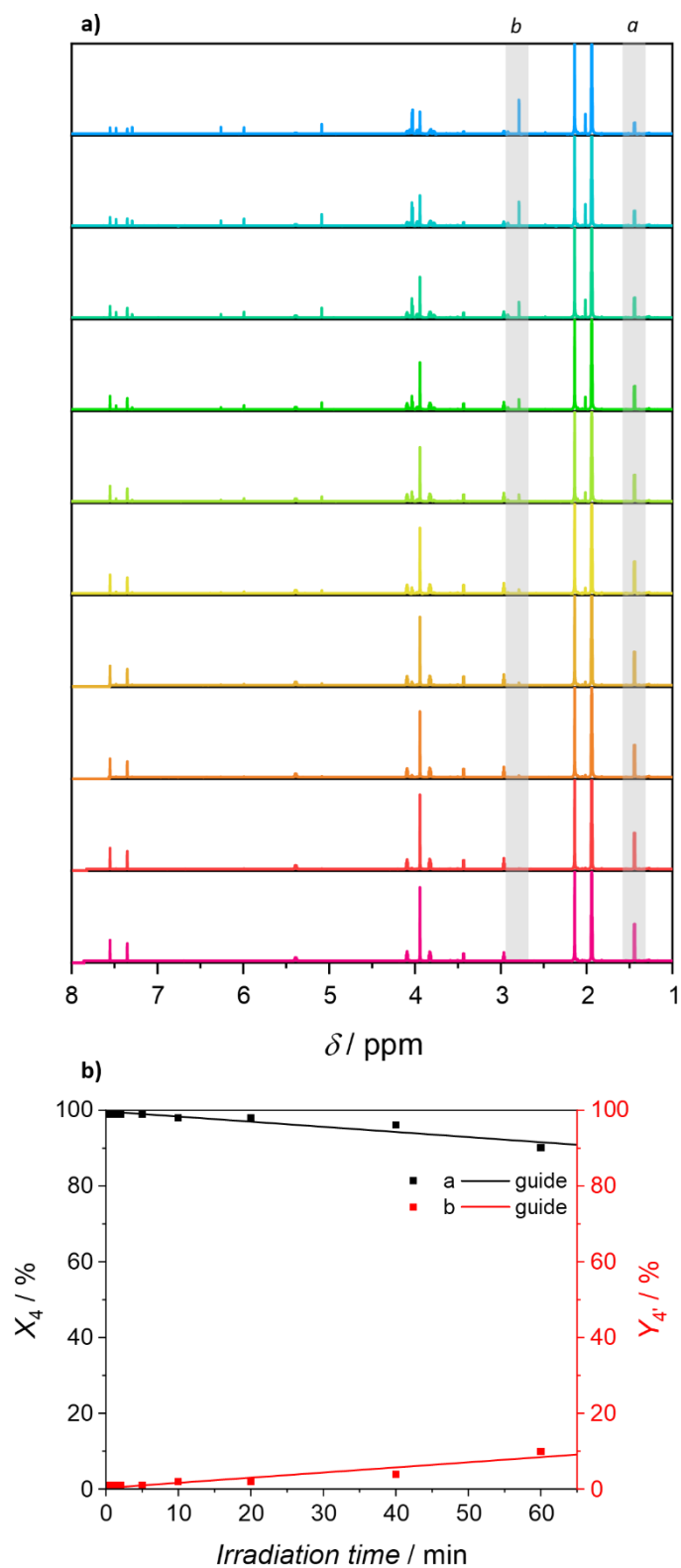


Figure S3-14: a) ¹H-NMR spectra of **4** in acetonitrile-*d*₃ with 415 nm irradiation in different exposure times. b) Plot of conversion and yield versus time for **4** (black) and **4d** (red) according to resonances *a* and *b*. Reproduced from Ref. 200 with permission from the Royal Society of Chemistry. Modified representation.

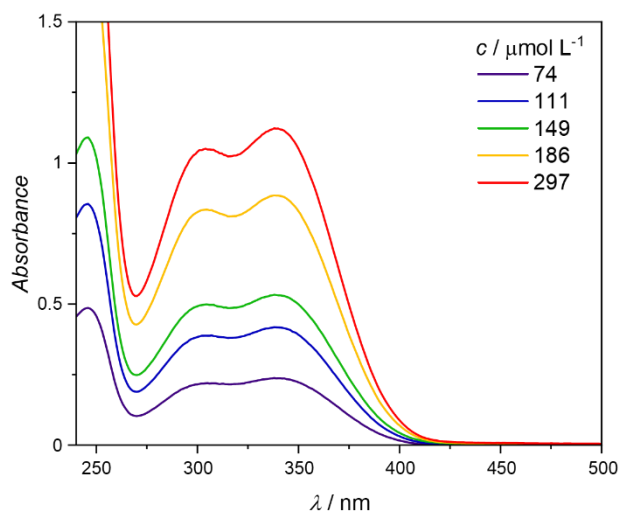


Figure S3-15: UV/Vis absorption spectra of **3** in acetonitrile. $d = 10$ mm.

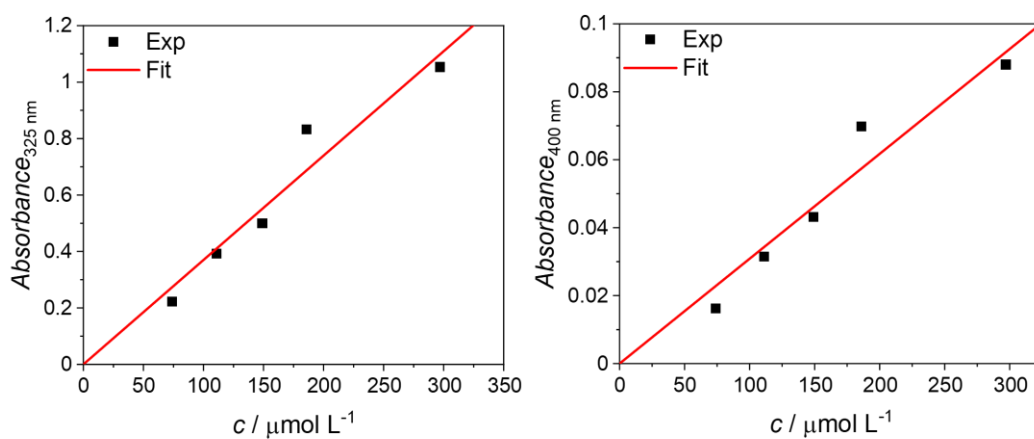


Figure S3-16: Determination of extinction coefficient ϵ of **3** in acetonitrile at 325 nm (left) and 400 nm (right). $\epsilon_{325 \text{ nm}} = (3700 \pm 210) \text{ L mol}^{-1} \text{ cm}^{-1}$, $\epsilon_{400 \text{ nm}} = (309 \pm 19) \text{ L mol}^{-1} \text{ cm}^{-1}$.

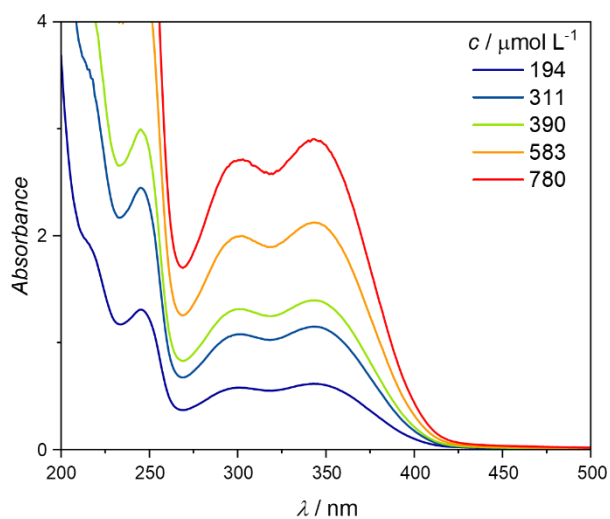


Figure S3-17: UV/Vis absorption spectra of **4** in acetonitrile. $d = 10$ mm.

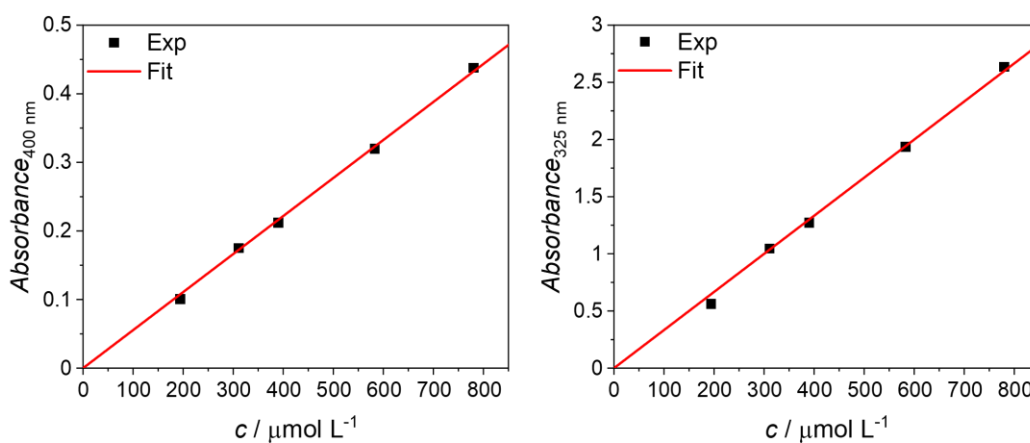


Figure S3-18: Determination of extinction coefficient ϵ of **4** in acetonitrile at 325 nm (left) and 400 nm (right). $\epsilon_{325 \text{ nm}} = (3300 \pm 40) \text{ L mol}^{-1} \text{ cm}^{-1}$, $\epsilon_{400 \text{ nm}} = (554 \pm 5) \text{ L mol}^{-1} \text{ cm}^{-1}$.

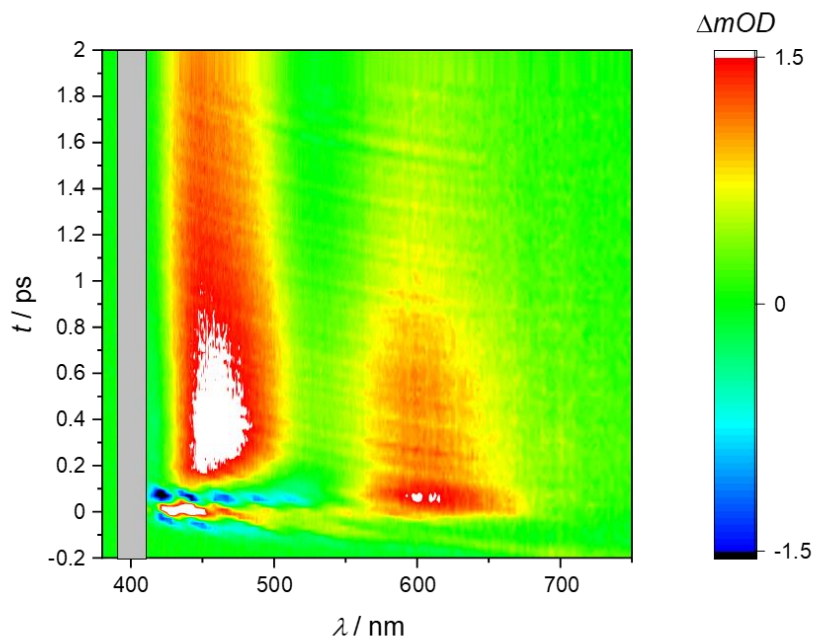


Figure S3-19: Contour plot of **4** with respective stationary in the first 2 ps. (top). $\lambda_{\text{ex}} = 400$ nm, $E_{\text{ex}} = 2 \mu\text{J}$, $\lambda_{\text{probe}} = \text{supercontinuum}$, $d = 1$ mm, acetonitrile. Transient response around 400 nm is neglected due to pump pulse scattering.

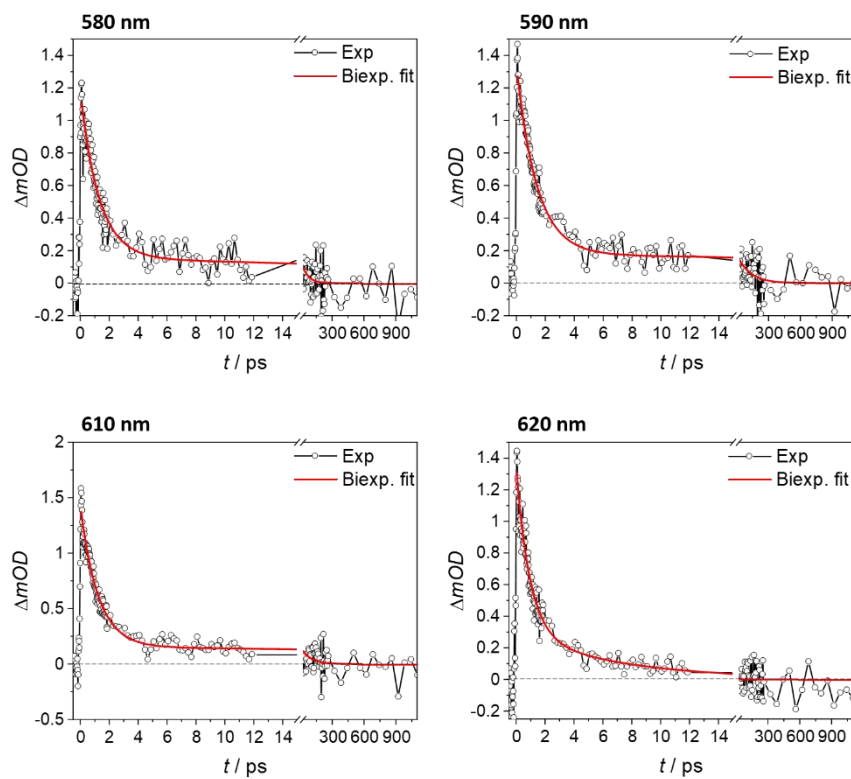


Figure S3-20: Single transients of the 600 nm response. **Figure S3-19** for parameters.

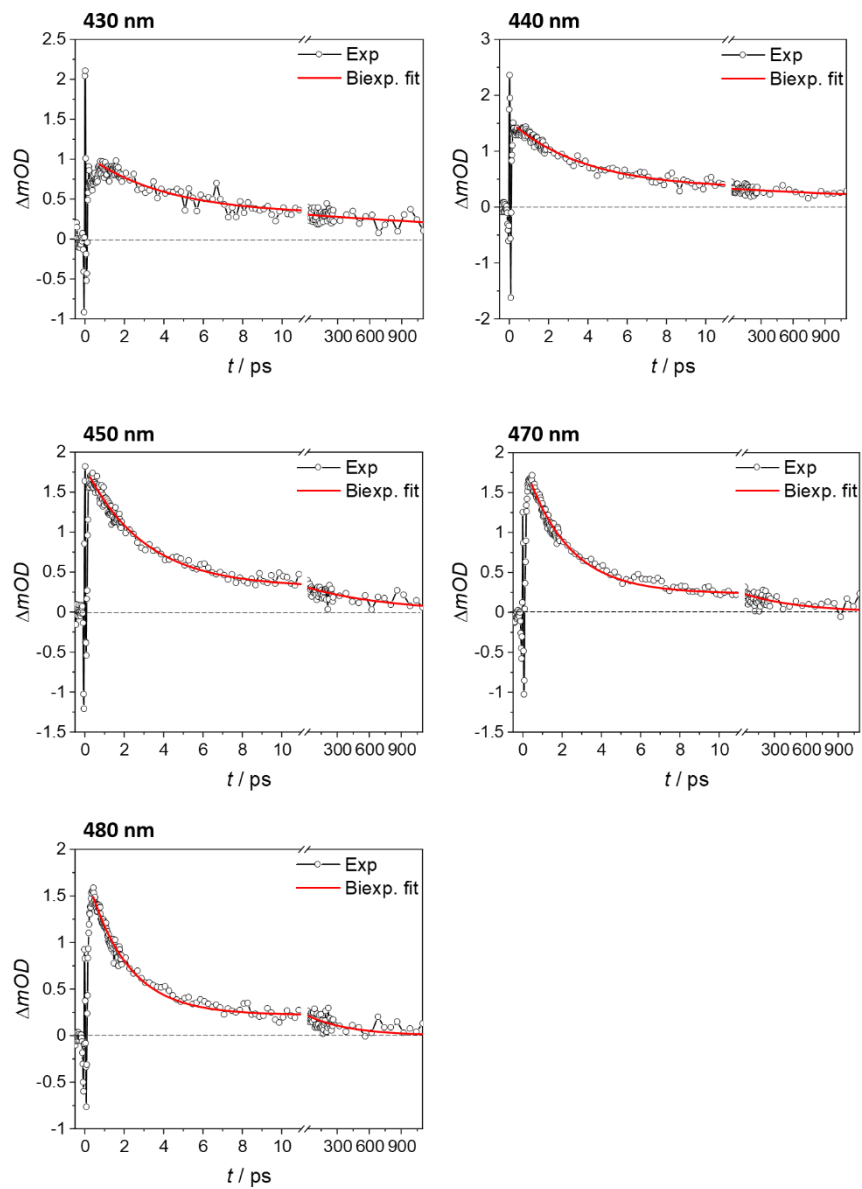


Figure S3-21: Single transients of the 460 nm response. **Figure S3-19** for parameters.

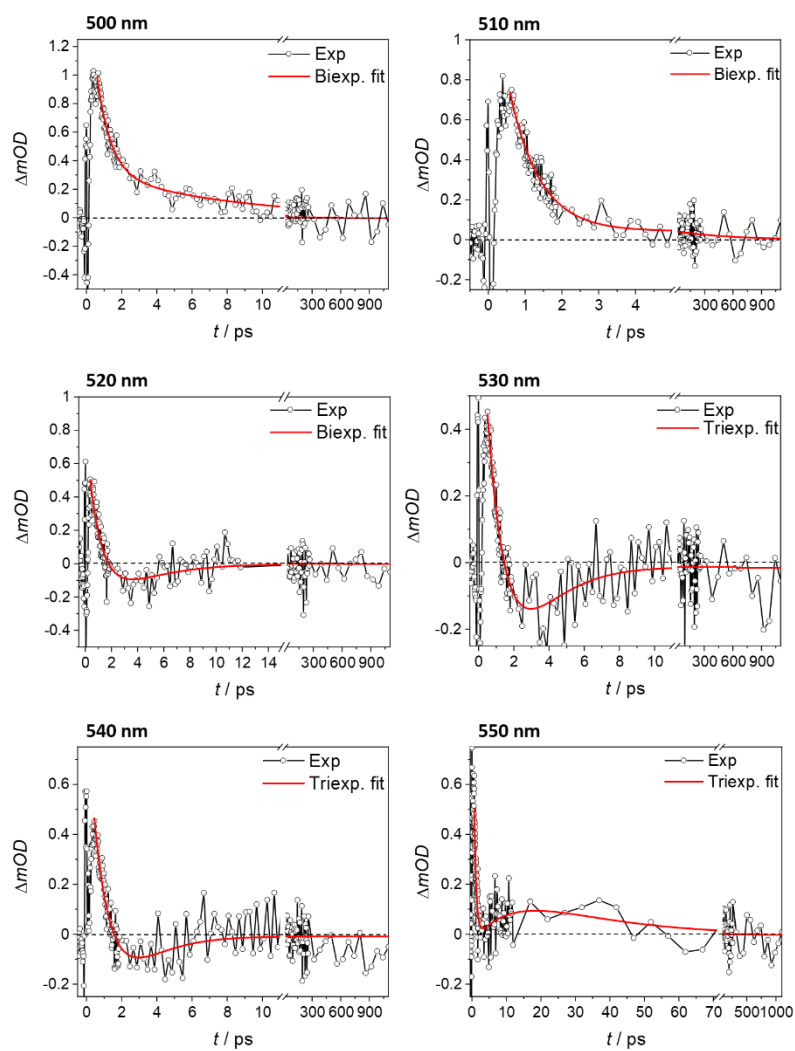


Figure S3-22: Single transients of the 520 nm response. Figure S3-19 for parameters.

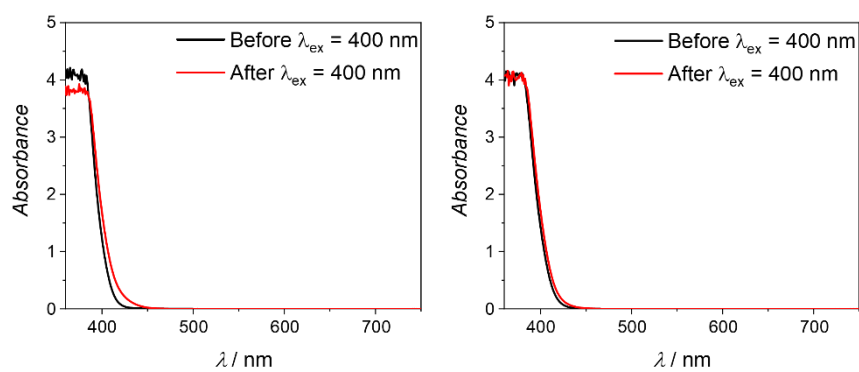


Figure S3-23: UV/Vis absorption spectra of **4** before and after transient fs-laser experiment. $\lambda_{ex} = 400 nm$, $E_{ex} = 2 \mu J$, $d = 1 mm$, THF (left), EtOH (right).

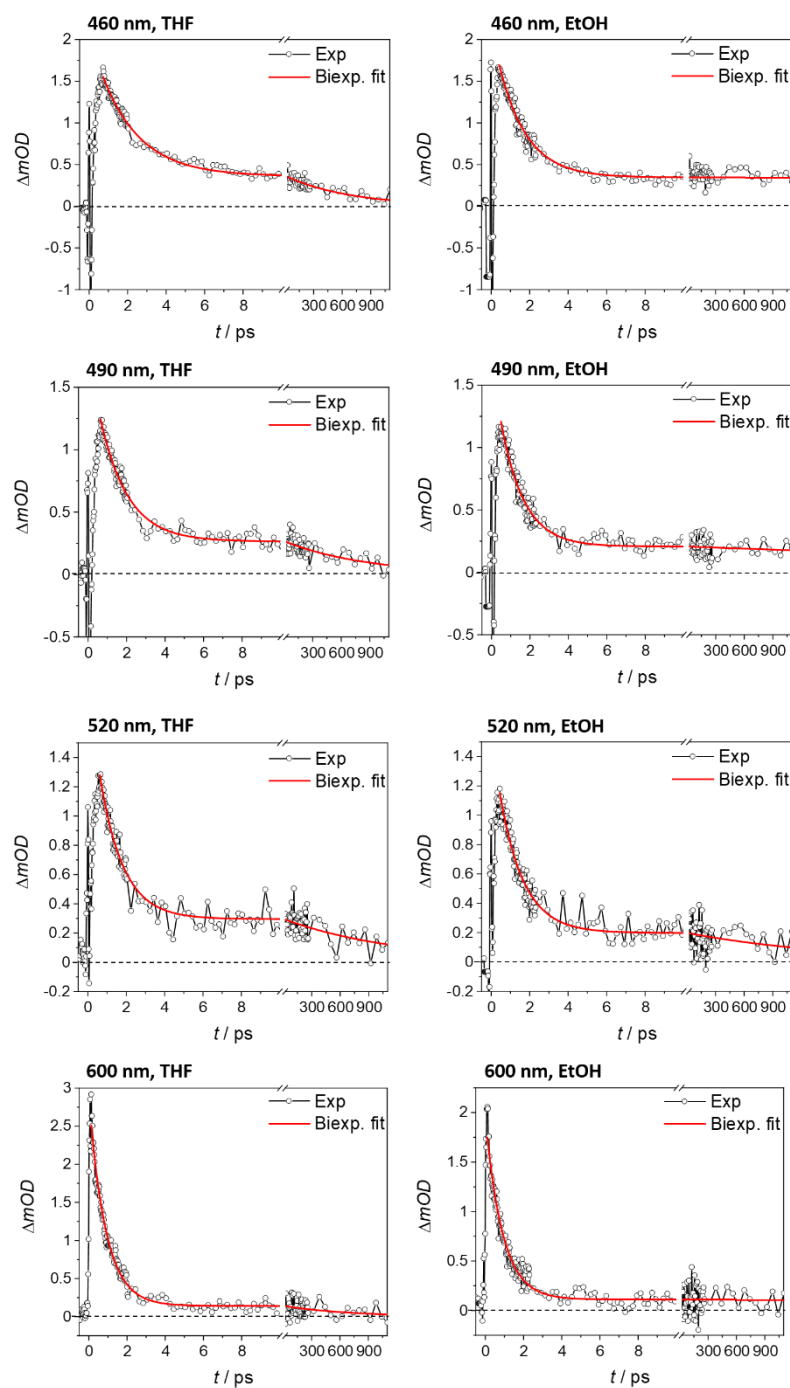


Figure S3-24: Single transients of the 460, 490, 520 and 600 nm responses in different solvents (THF left, EtOH right). **Figure 3-12** for parameters.

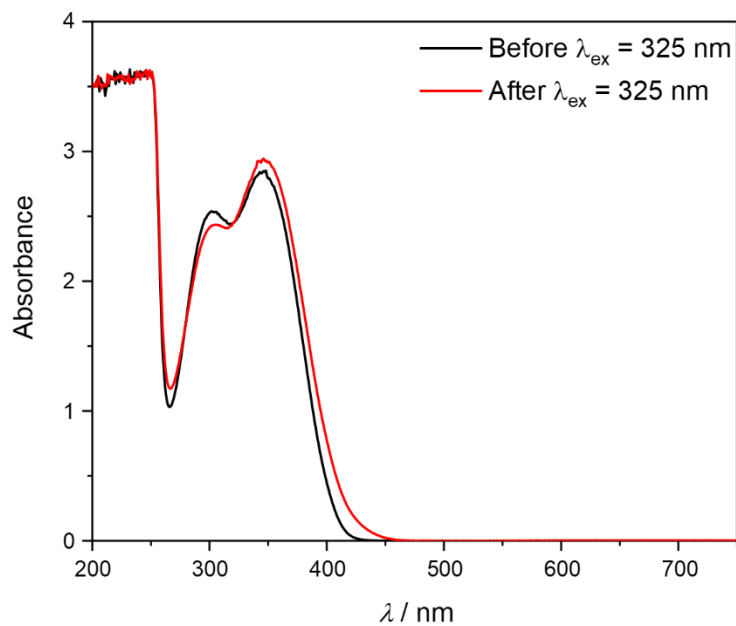


Figure S3-25: UV/Vis absorption spectrum of **4** before and after transient fs-laser experiment. $\lambda_{\text{ex}} = 325 \text{ nm}$, $E_{\text{ex}} = 0.5 \mu\text{J}$, $d = 1 \text{ mm}$, acetonitrile, $d = 1 \text{ mm}$.

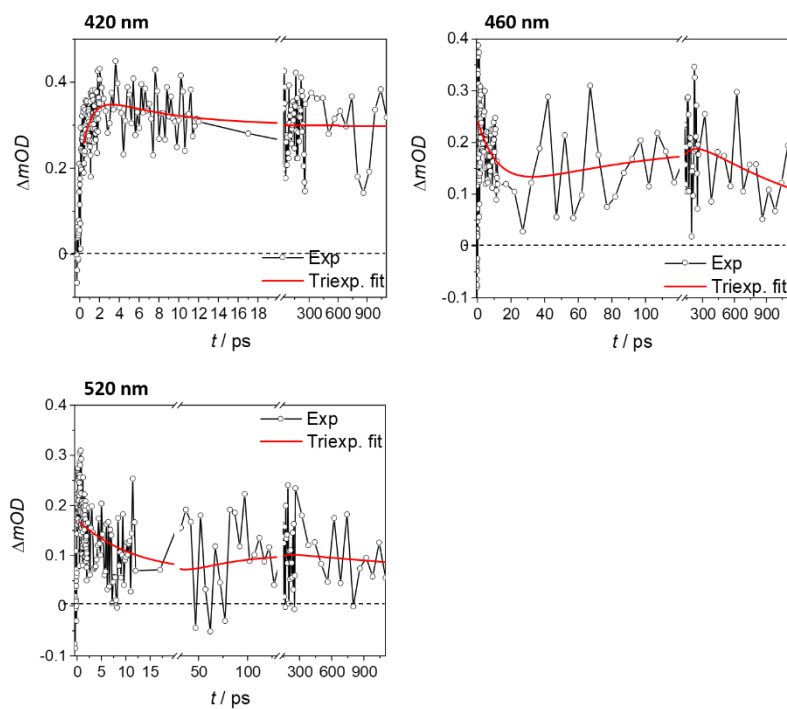


Figure S3-26: Single transients of the 420, 490 and 520 nm responses in acetonitrile. **Figure 3-14** for parameters.

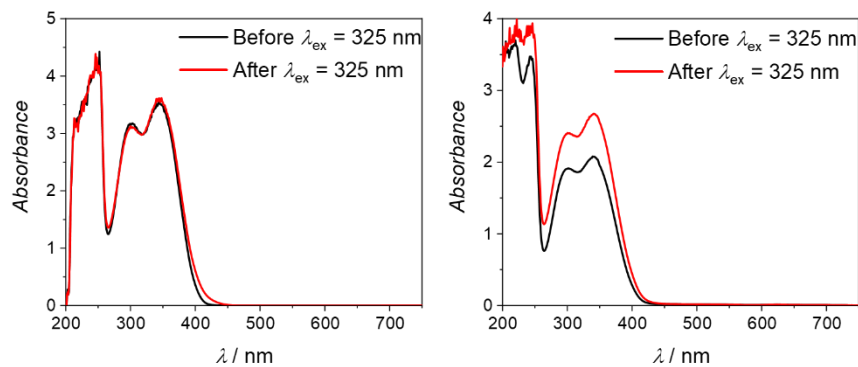


Figure S3-27: UV/Vis absorption spectra of **4** before and after transient fs-laser experiment. $\lambda_{\text{ex}} = 325$ nm, $E_{\text{ex}} = 0.4$ μJ , $d = 1$ mm, THF (left), EtOH (right).

Table S3-6: Extracted transients and influence of solvent. The fits are appended in **Figure S3-28**.

λ / nm		AcN	THF	EtOH
	t_1 / ps	1.0 ± 0.7	3.0 ± 111	88 ± 40
420	t_2 / ps	7.4 ± 7.0	3.1 ± 115	>1000
	t_3 / ps	>1000	>1000	>1000
	t_1 / ps	12.6 ± 8.3	4.5 ± 2.7	0.64 ± 0.21
460	t_2 / ps	99 ± 134	>1000	26 ± 13
	t_3 / ps	>1000	>1000	>1000
	t_1 / ps	15 ± 3	177 ± 2260	0.5 ± 47
520	t_2 / ps	50 ± 9	185 ± 2370	05 ± 47
	t_3 / ps	>1000	191 ± 1430	>1000

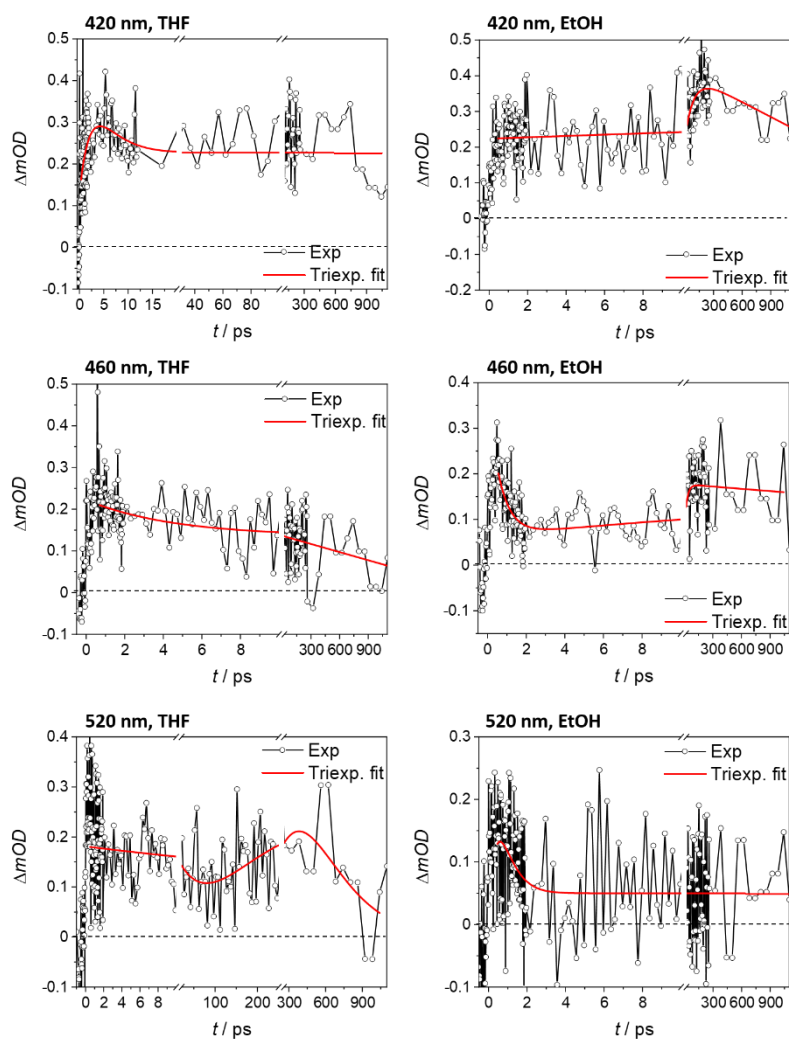


Figure S3-28: Single transients of the 460, 490, 520 and 600 nm responses in different solvents (THF left, EtOH right). **Figure 3-14** for parameters.

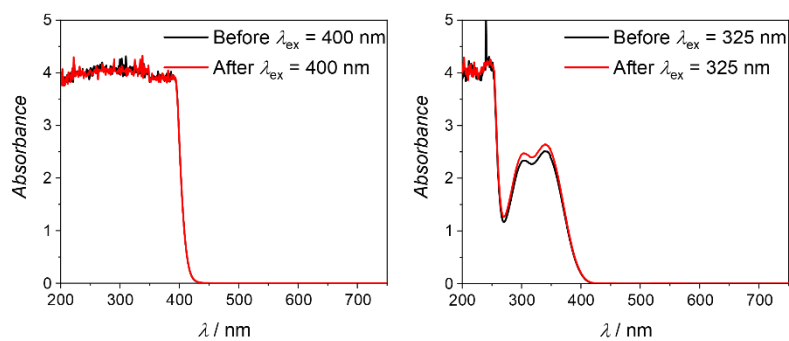


Figure S3-29: UV/Vis absorption spectra of **3** before and after transient fs-laser experiment. $\lambda_{\text{ex}} = 400$ nm, $E_{\text{ex}} = 2.0$ μJ , $d = 1$ mm (left), $\lambda_{\text{ex}} = 325$ nm, $E_{\text{ex}} = 0.5$ μJ , $d = 1$ mm (right).

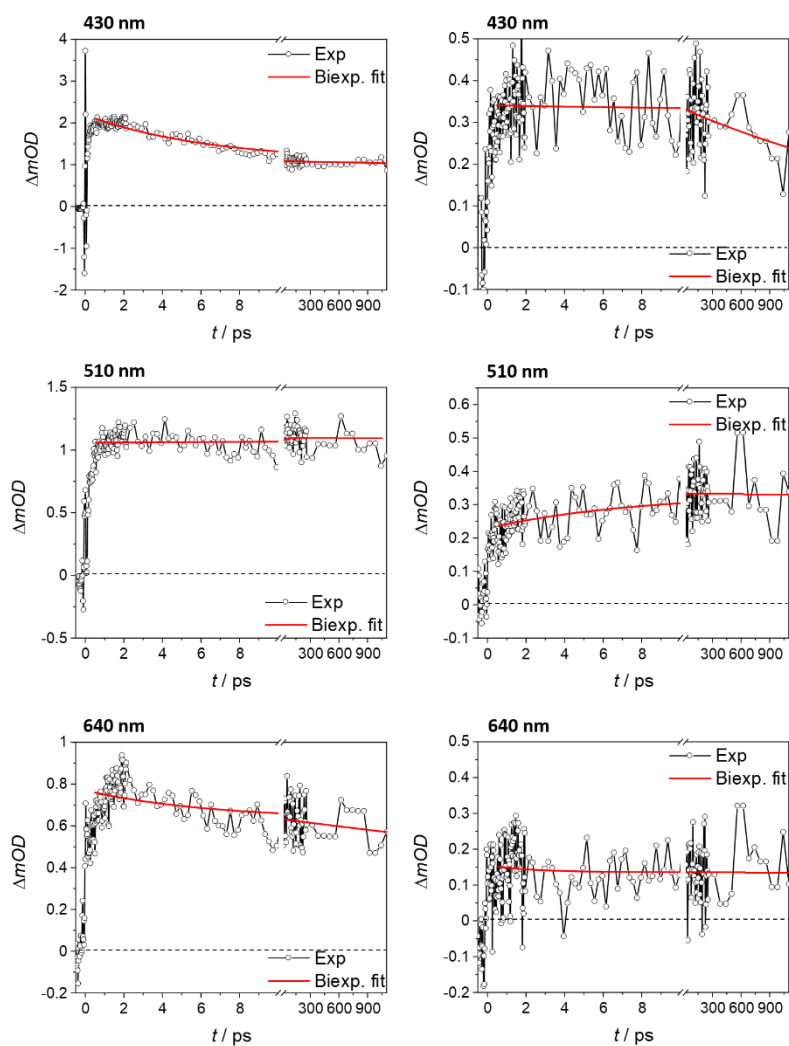


Figure S3-30: Single transients of **3** the 430, 510 and 640 nm responses at different excitation conditions. $\lambda_{ex} = 400$ nm, $E_{ex} = 2.0$ μ J, $d = 1$ mm, acetonitrile (left), $\lambda_{ex} = 325$ nm, $E_{ex} = 0.5$ μ J, $d = 1$ mm, acetonitrile (right).

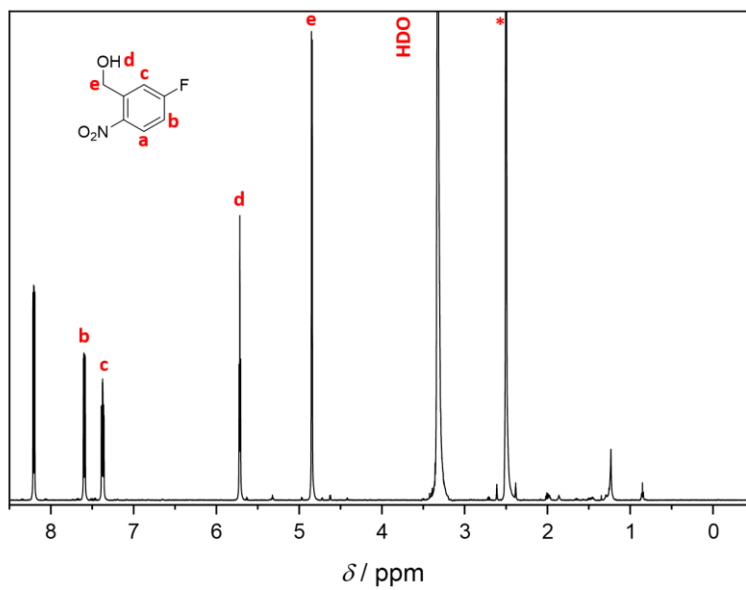


Figure S3-31: $^1\text{H-NMR}$ spectrum of **2,5-H2** in $\text{DMSO-}d_6$ (*).

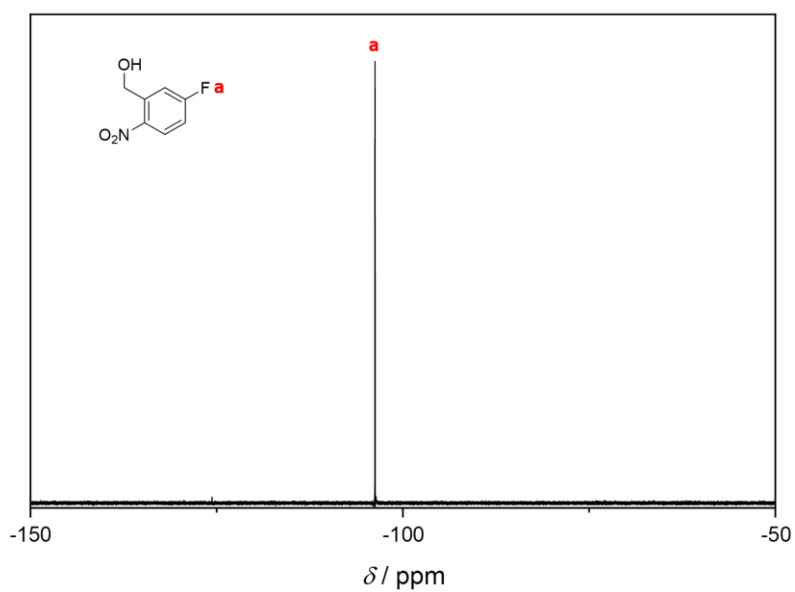


Figure S3-32: $^{19}\text{F-NMR}$ spectrum of **2,5-H2** in $\text{DMSO-}d_6$.

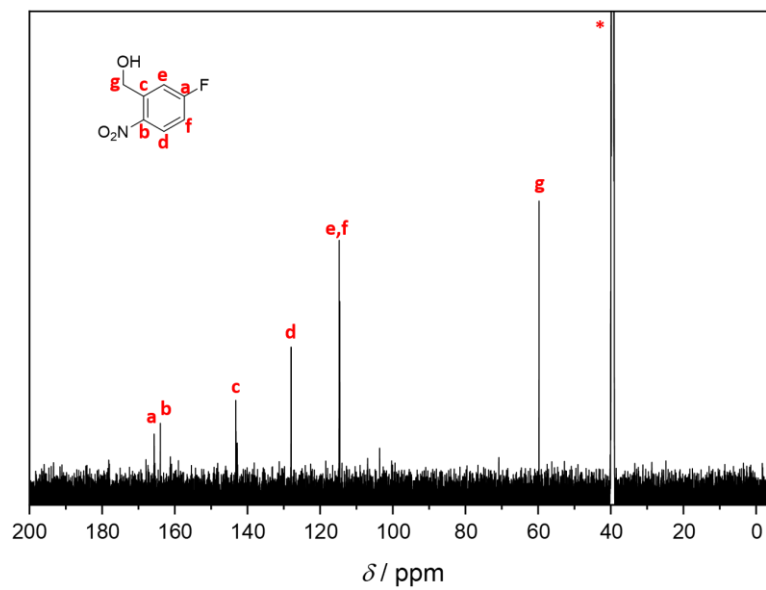


Figure S3-33: ^{13}C -NMR spectrum of 2,5-H2 in $\text{DMSO}-d_6$ (*).

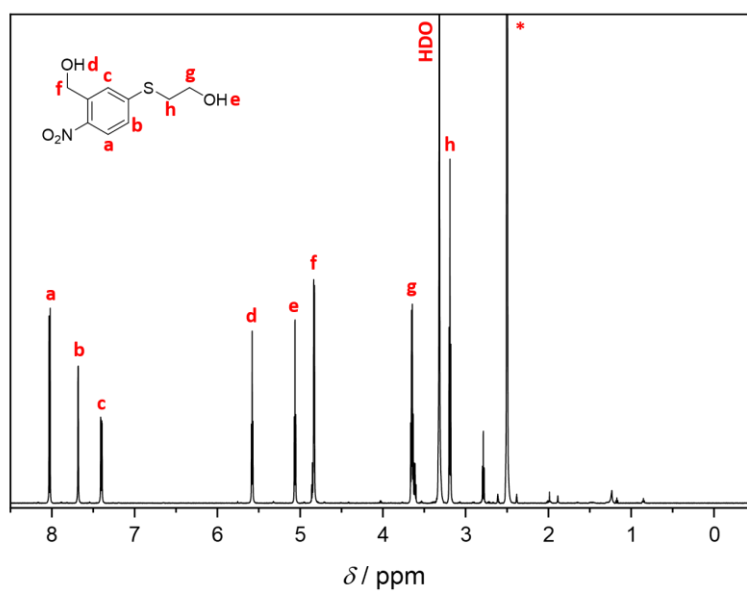


Figure S3-34: ^1H -NMR spectrum of 2,5-H3 in $\text{DMSO}-d_6$ (*).

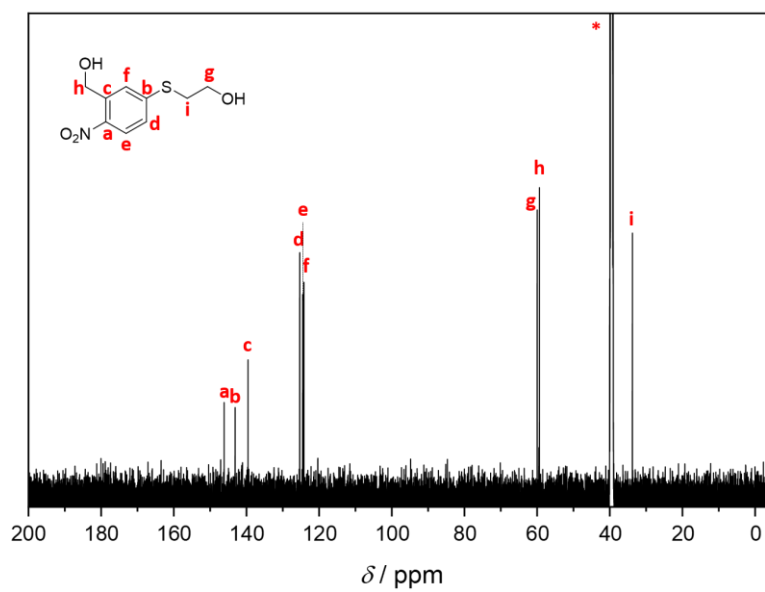


Figure S3-35: ^{13}C -NMR spectrum of **2,5-H3** in $\text{DMSO-}d_6$ (*).

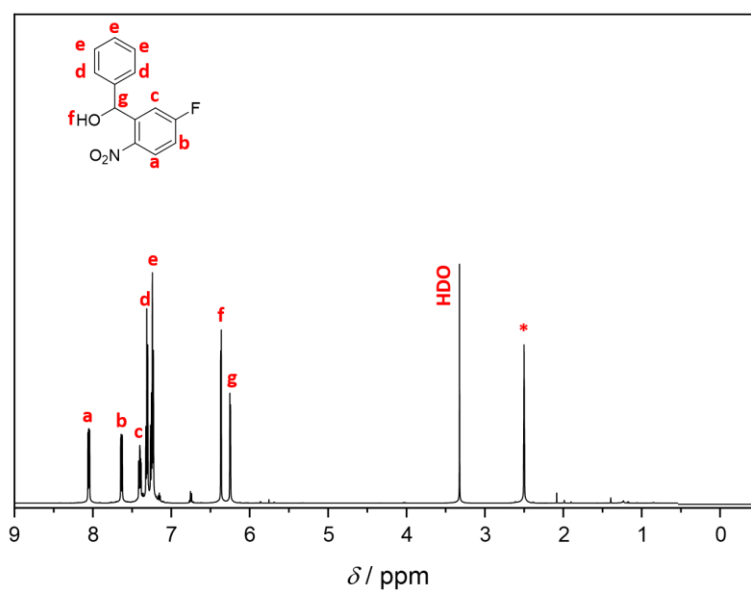


Figure S3-36: ^1H -NMR spectrum of **2,5-Ph2** in $\text{DMSO-}d_6$ (*).

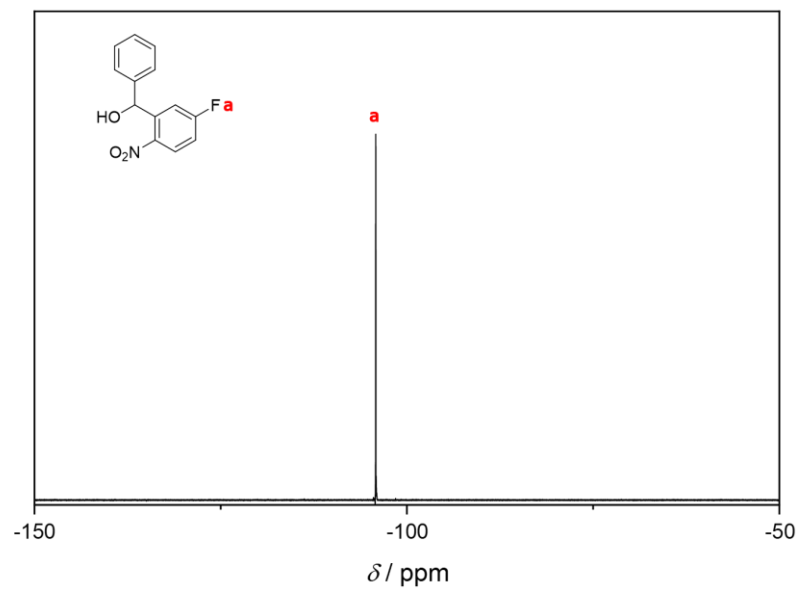


Figure S3-37: ^{19}F -NMR spectrum of 2,5-Ph₂ in DMSO-*d*₆.

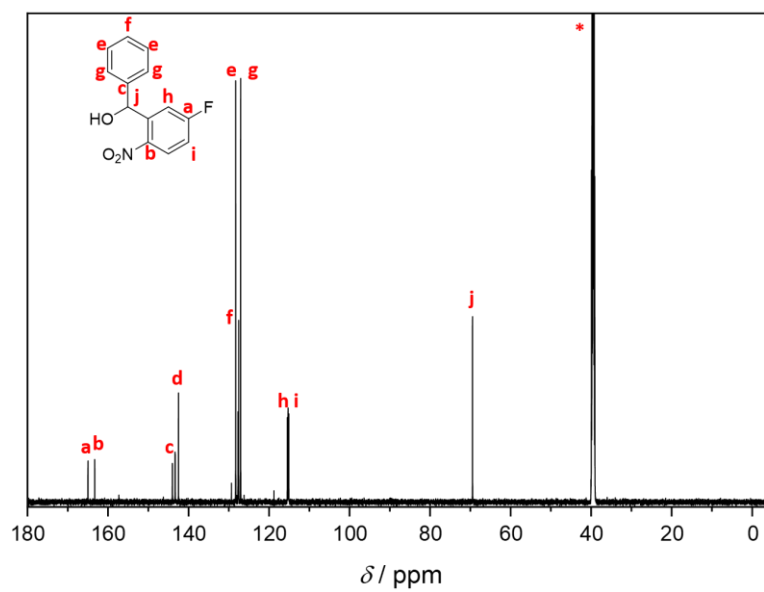


Figure S3-38: ^{13}C -NMR spectrum of 2,5-Ph₂ in DMSO-*d*₆ (*).

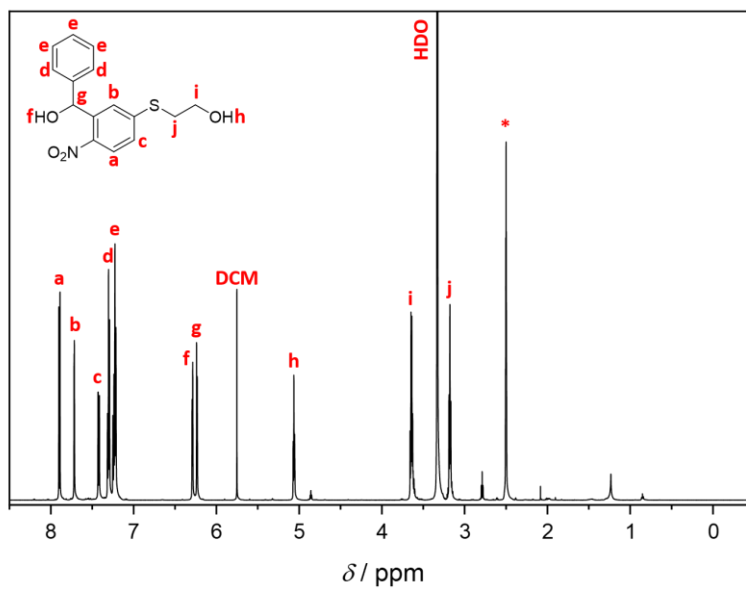


Figure S3-39: $^1\text{H-NMR}$ spectrum of **2,5-Ph3** in $\text{DMSO-}d_6$ (*).

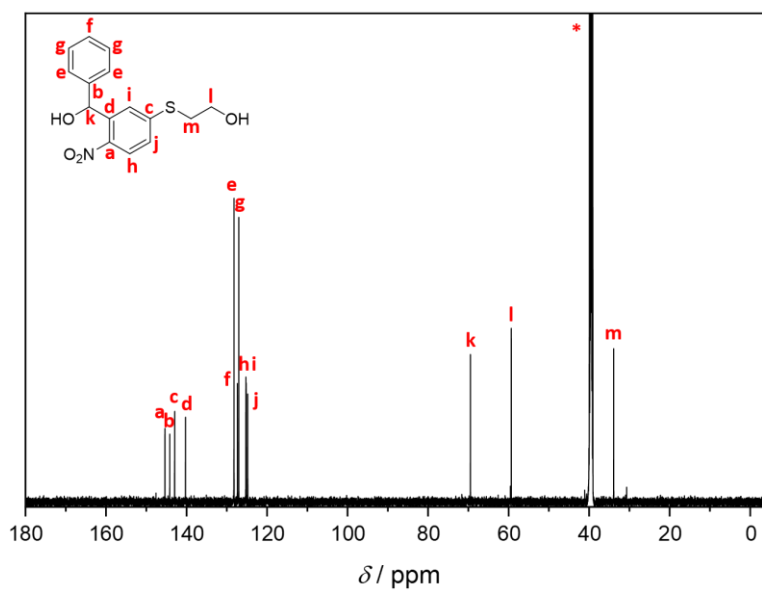


Figure S3-40: $^{13}\text{C-NMR}$ spectrum of **2,5-Ph3** in $\text{DMSO-}d_6$ (*).

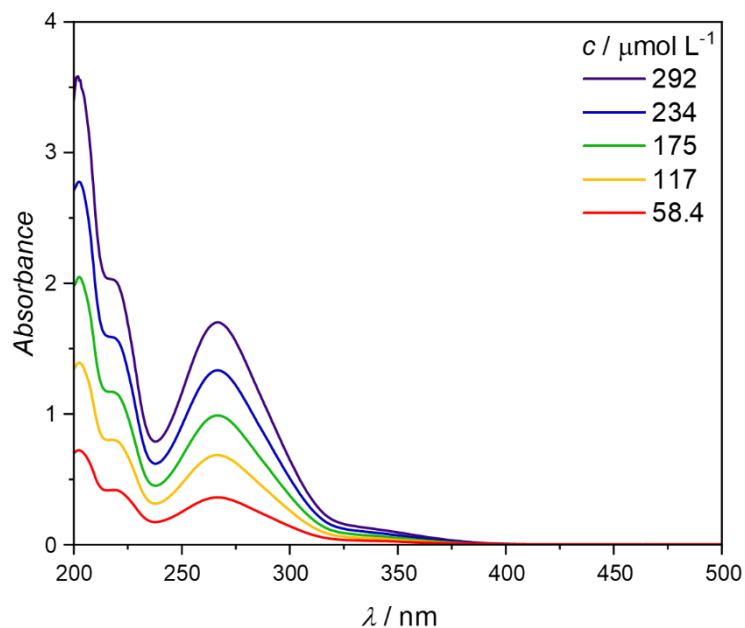


Figure S3-41: UV/Vis absorption spectra of **2,5-H2** in acetonitrile. $d = 10$ mm.

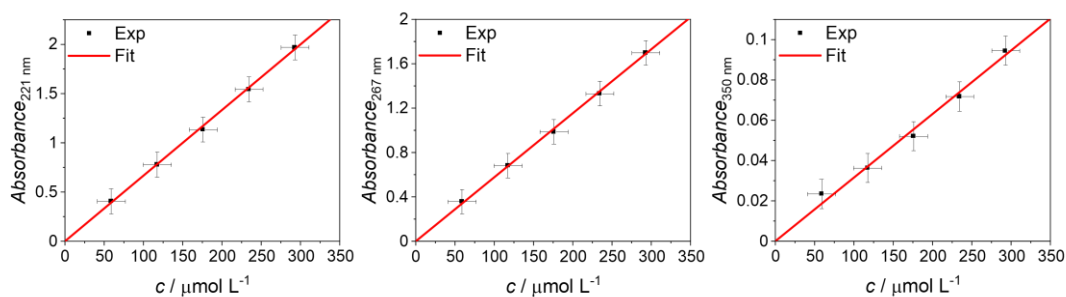


Figure S3-42: Determination of extinction coefficient ϵ of **2,5-H2** in acetonitrile at 221, 267 and 350 nm (from left to right). $\epsilon_{221 \text{ nm}} = (6670 \pm 50) \text{ L mol}^{-1} \text{ cm}^{-1}$, $\epsilon_{267 \text{ nm}} = (5770 \pm 50) \text{ L mol}^{-1} \text{ cm}^{-1}$, $\epsilon_{350 \text{ nm}} = (315 \pm 8) \text{ L mol}^{-1} \text{ cm}^{-1}$.

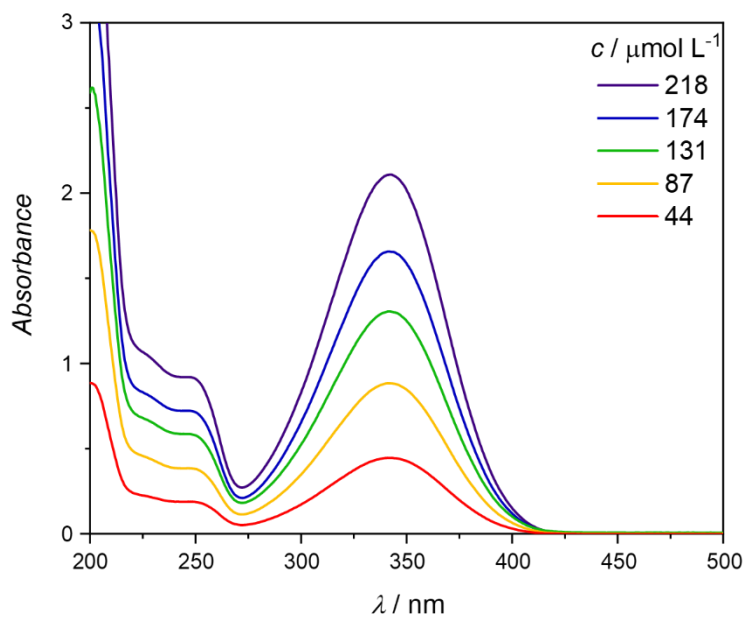


Figure S3-43: UV/Vis absorption spectra of **2,5-H3** in acetonitrile. $d = 10$ mm.

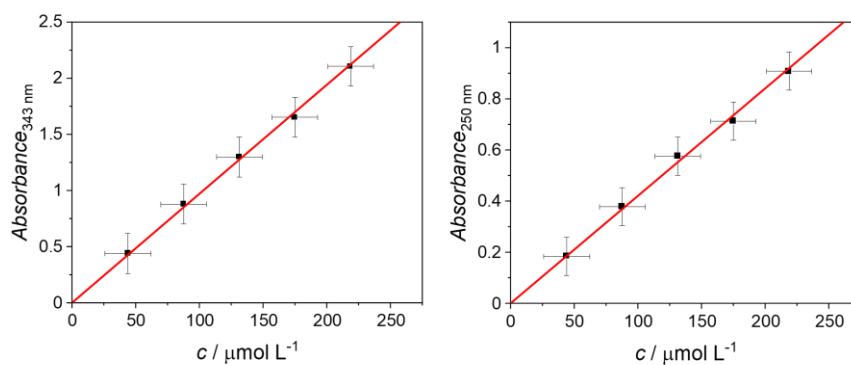


Figure S3-44: Determination of extinction coefficient ϵ of **2,5-H3** in acetonitrile at 343 (left) and 250 nm (right). $\epsilon_{343 \text{ nm}} = (9700 \pm 100) \text{ L mol}^{-1} \text{ cm}^{-1}$, $\epsilon_{250 \text{ nm}} = (4200 \pm 60) \text{ L mol}^{-1} \text{ cm}^{-1}$.

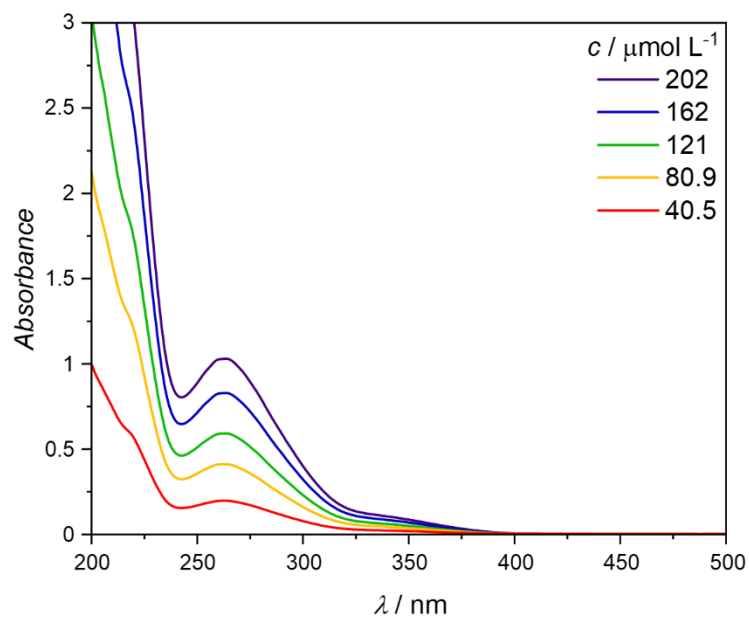


Figure S3-45: UV/Vis absorption spectra of **2,5-Ph₂** in acetonitrile. $d = 10$ mm.

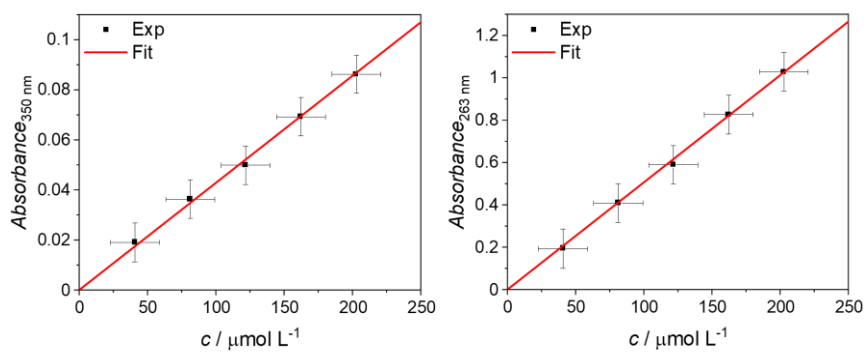


Figure S3-46: Determination of extinction coefficient ϵ of **2,5-Ph₂** in acetonitrile at 350 (left) and 263 nm (right). $\epsilon_{350 \text{ nm}} = (428 \pm 5) \text{ L mol}^{-1} \text{ cm}^{-1}$, $\epsilon_{263 \text{ nm}} = (5060 \pm 40) \text{ L mol}^{-1} \text{ cm}^{-1}$.

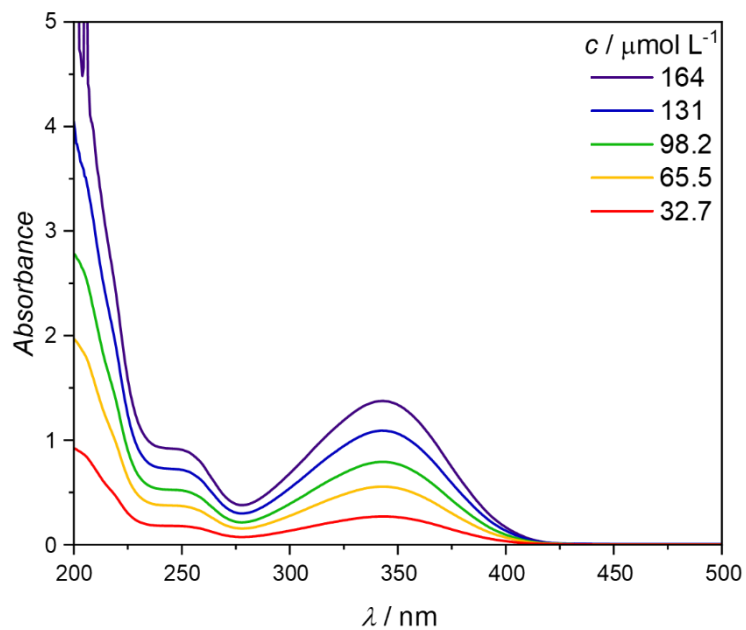


Figure S3-47: UV/Vis absorption spectra of **2,5-Ph3** in acetonitrile. $d = 10$ mm.

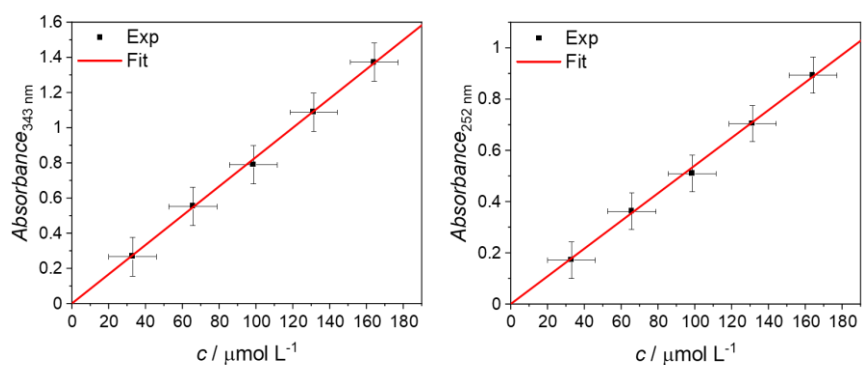


Figure S3-48: Determination of extinction coefficient ϵ of **2,5-Ph3** in acetonitrile at 343 (left) and 252 nm (right). $\epsilon_{343 \text{ nm}} = (8330 \pm 60) \text{ L mol}^{-1} \text{ cm}^{-1}$, $\epsilon_{252 \text{ nm}} = (5410 \pm 50) \text{ L mol}^{-1} \text{ cm}^{-1}$.

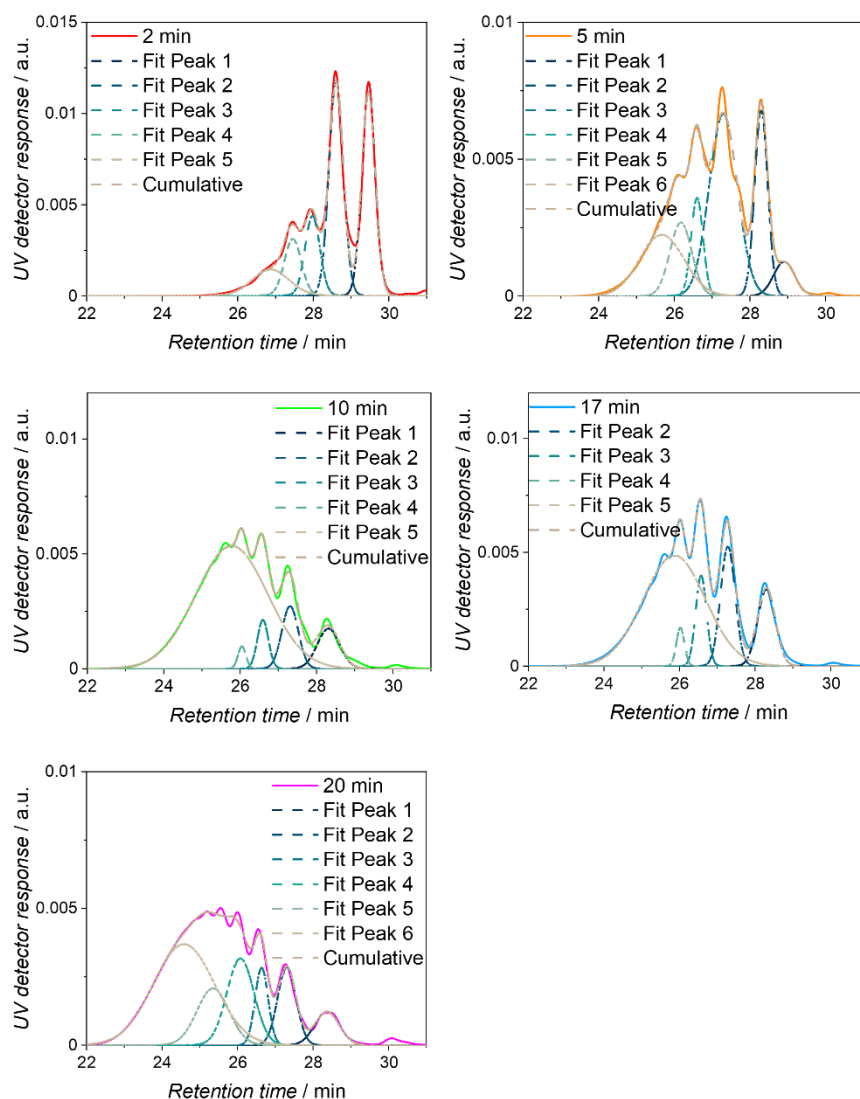
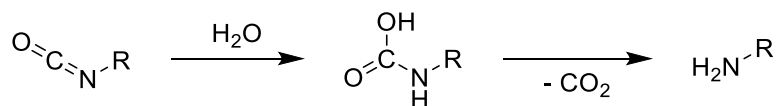


Figure S3-49: SEC traces in THF of polyurethanes formed (solid lines) and their deconvoluted Gaussians in dashed line. Reproduced from Ref. 200 with permission from the Royal Society of Chemistry. Modified representation.



Scheme S3-1: Reaction scheme of isocyanate with water, leading to the formation of an amine under liberation of carbon dioxide.

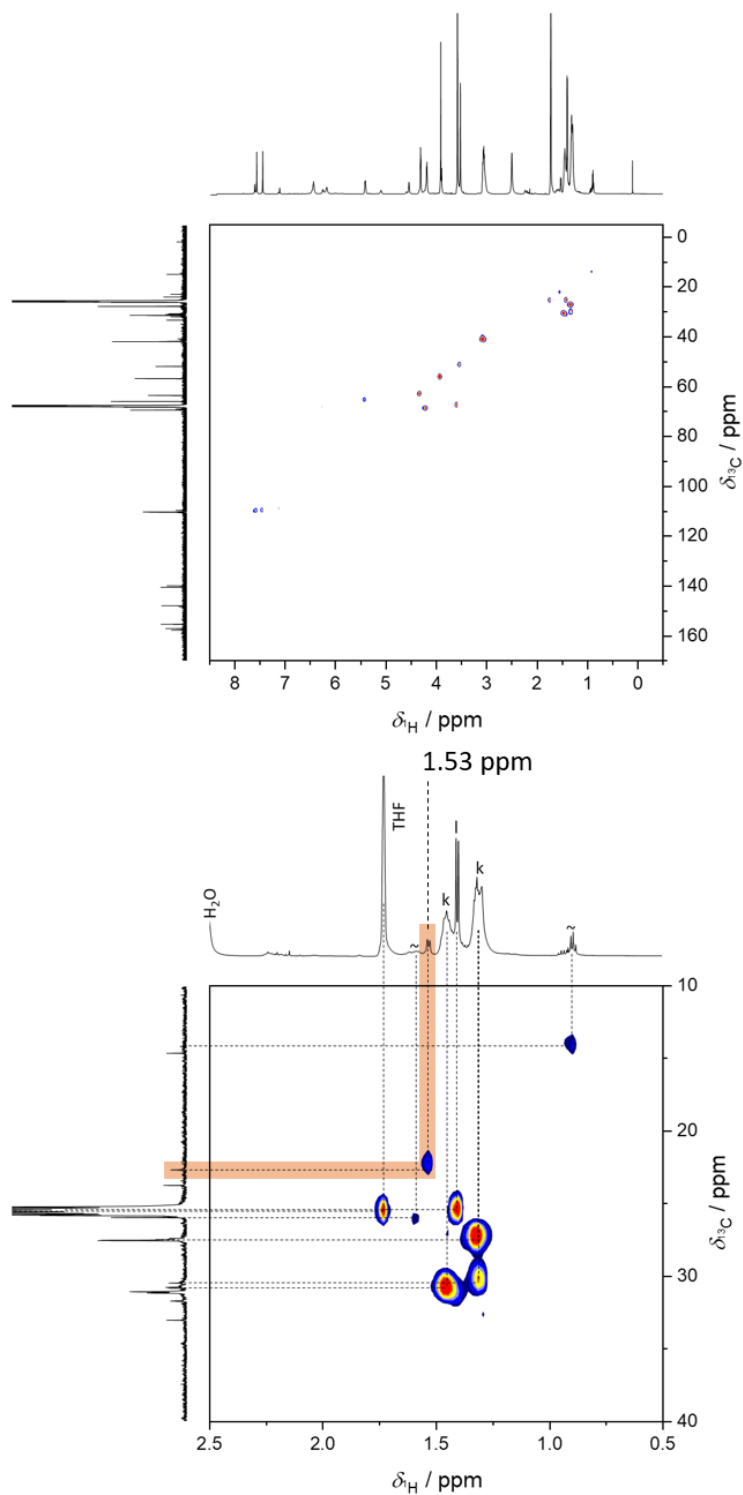


Figure S3-50: Top: Full HSQC-NMR spectrum of the 2 min cured polymer in THF- d_8 . Bottom: Zoomed spectrum between 2.5 and 0.5 ppm. The ^1H -NMR resonances at 1.53 ppm, suspected to be the result of an amine group, and its correlated ^{13}C resonance are highlighted in orange. ~ residual catalyst. Reproduced from Ref. 200 with permission from the Royal Society of Chemistry. Modified representation.

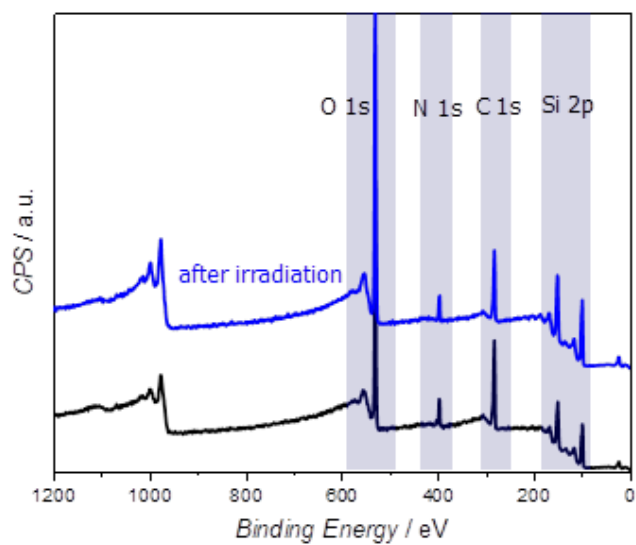


Figure S3-51: Wide scan XPS spectra of thin films of *o*NB-Polyurethane before (black) and after (blue) UV irradiation. Reproduced from Ref. 200 with permission from the Royal Society of Chemistry. Modified representation.

Appendix B

Supporting Information for Chapter 4: Chain-Length-Dependent Photolysis of *ortho*-nitrobenzyl-Centered Polymers

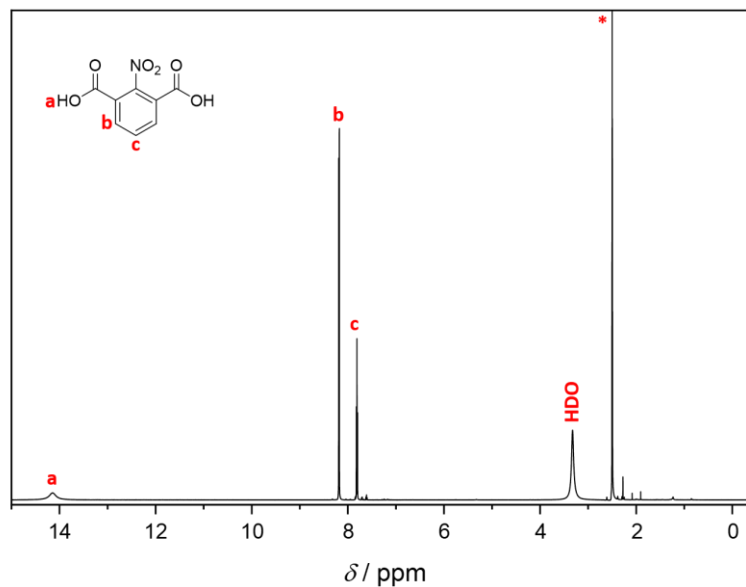


Figure S4-1: $^1\text{H-NMR}$ spectrum of **1** in $\text{DMSO-}d_6$ (*). Reprinted with permission from J. Bachmann *et al.* *ACS Macro Lett.* **2021**, *10*, 4, 447-452. Copyright 2021 American Chemical Society.

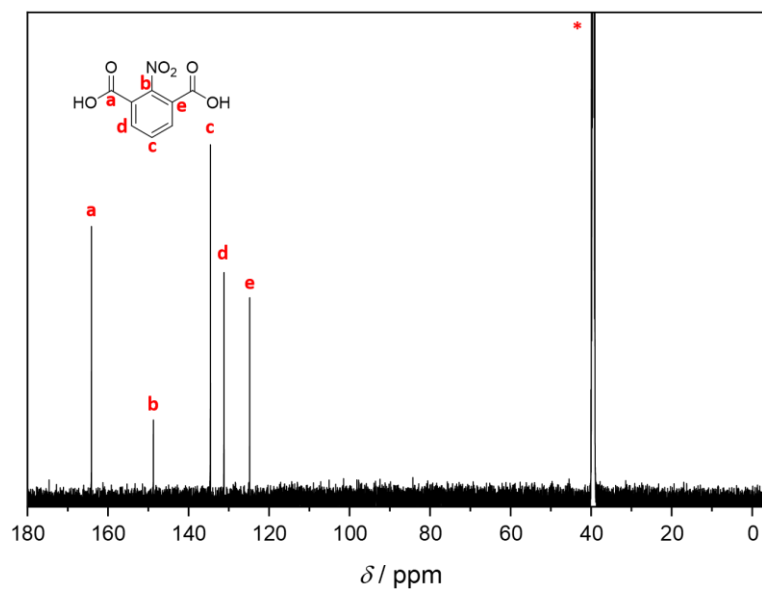


Figure S4-2: $^{13}\text{C-NMR}$ spectrum of **1** in $\text{DMSO-}d_6$ (*). Reprinted with permission from J. Bachmann *et al.* *ACS Macro Lett.* **2021**, *10*, 4, 447-452. Copyright 2021 American Chemical Society.

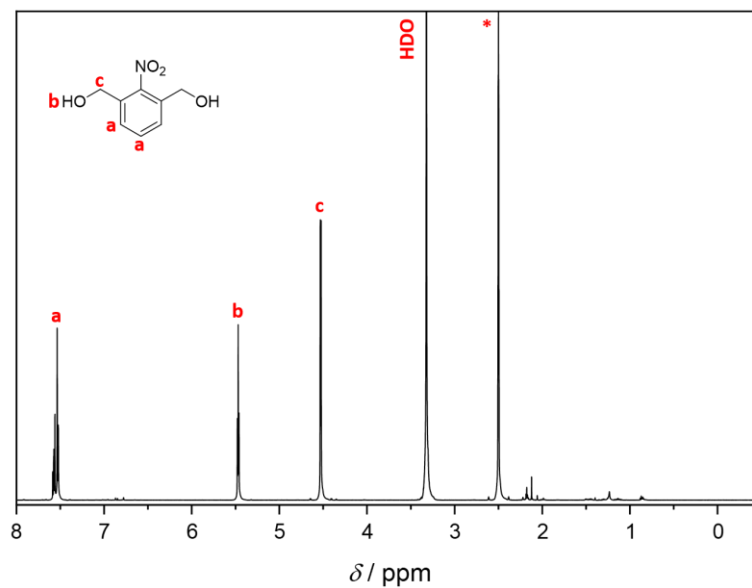


Figure S4-3: ^1H -NMR spectrum of **2** in $\text{DMSO-}d_6$ (*). Reprinted with permission from J. Bachmann *et al.* *ACS Macro Lett.* **2021**, *10*, 4, 447-452. Copyright 2021 American Chemical Society.

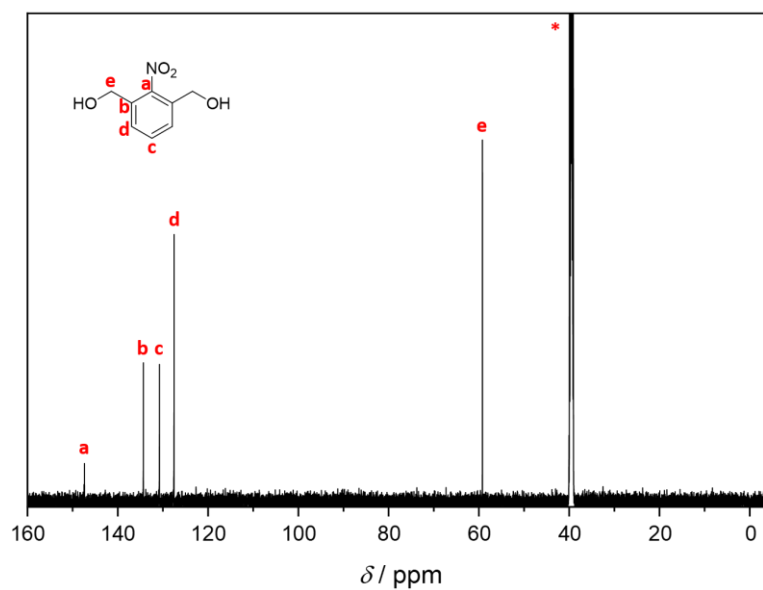


Figure S4-4: ^{13}C -NMR spectrum of **2** in $\text{DMSO-}d_6$ (*). Reprinted with permission from J. Bachmann *et al.* *ACS Macro Lett.* **2021**, *10*, 4, 447-452. Copyright 2021 American Chemical Society.

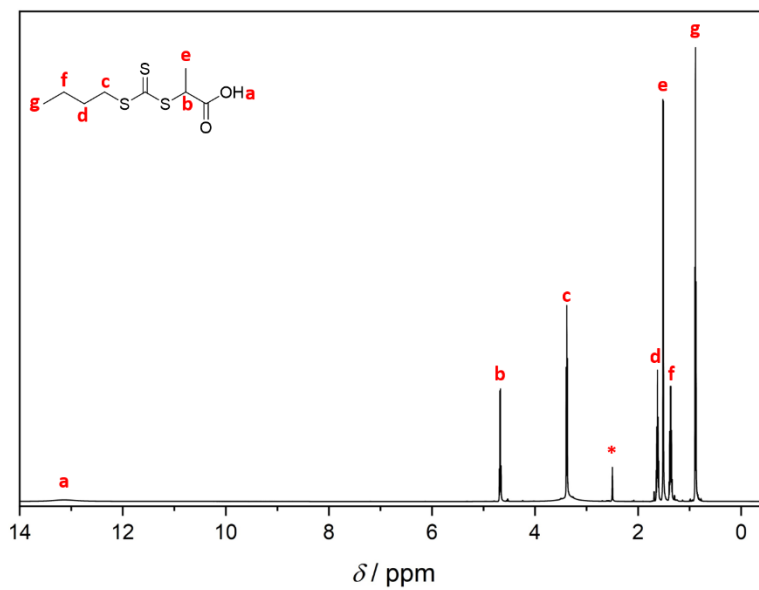


Figure S4-5: $^1\text{H-NMR}$ spectrum of **3** in $\text{DMSO-}d_6$ (*).

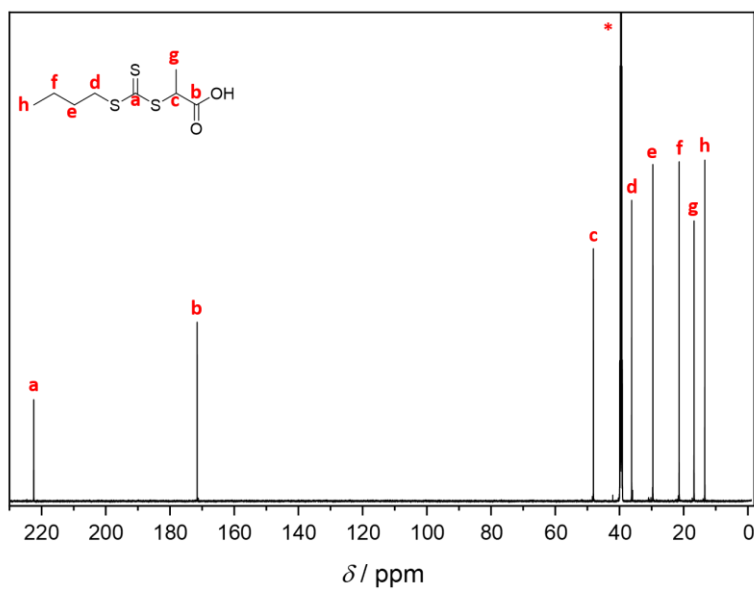


Figure S4-6: $^{13}\text{C-NMR}$ spectrum of **3** in $\text{DMSO-}d_6$ (*).

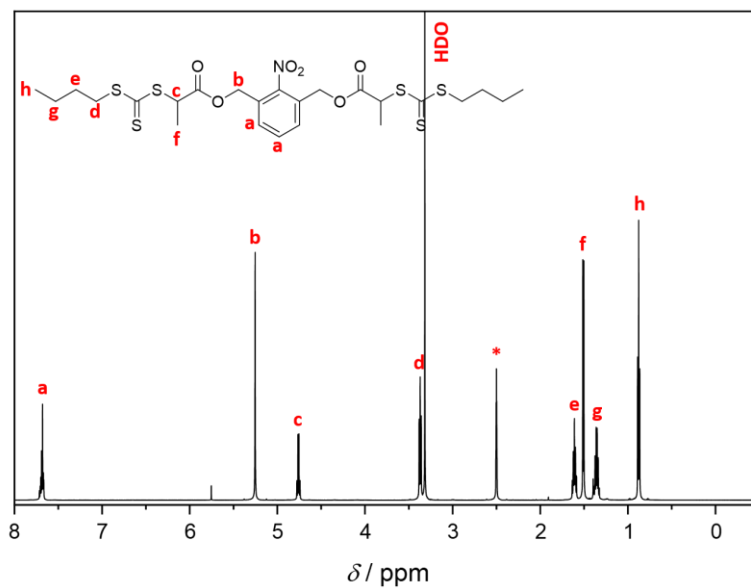


Figure S4-7: ^1H -NMR spectrum of **4** in $\text{DMSO-}d_6$ (*). Reprinted with permission from J. Bachmann *et al. ACS Macro Lett.* **2021**, *10*, 4, 447-452. Copyright 2021 American Chemical Society.

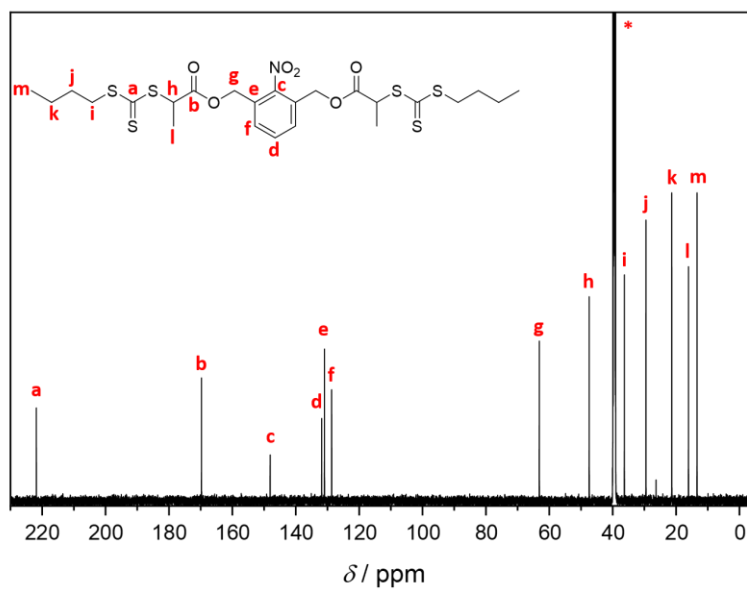


Figure S4-8: ^{13}C -NMR spectrum of **4** in $\text{DMSO-}d_6$ (*). Reprinted with permission from J. Bachmann *et al. ACS Macro Lett.* **2021**, *10*, 4, 447-452. Copyright 2021 American Chemical Society.

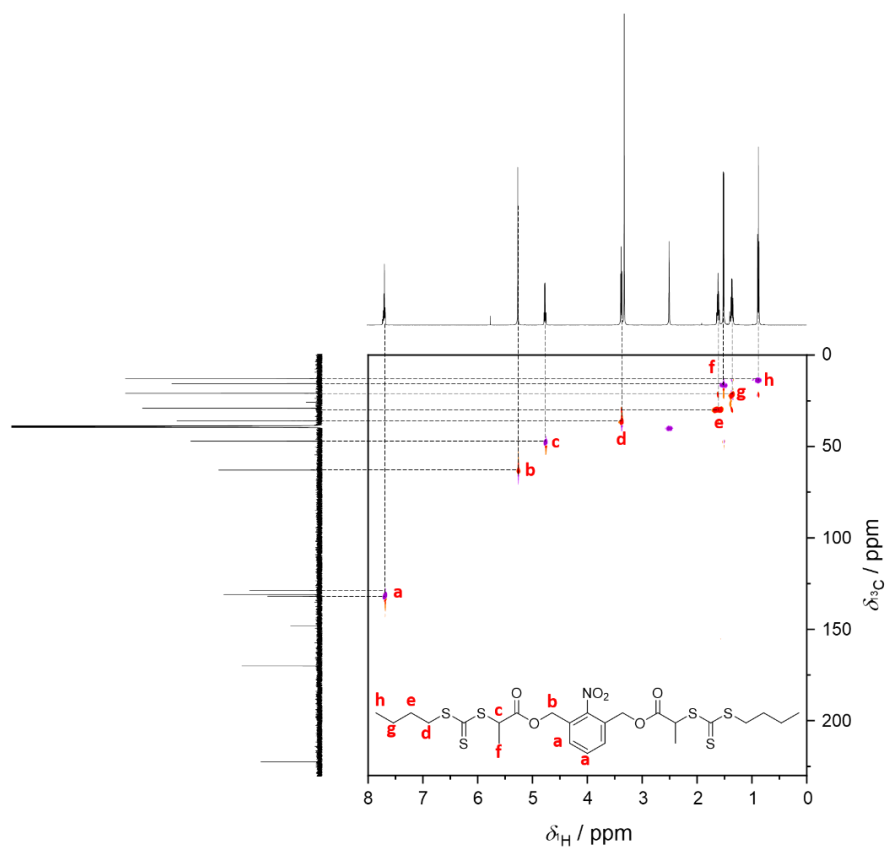


Figure S4-9: Full Gradient selected HSQC (HSQCEDET)-NMR spectrum of **4** in DMSO- d_6 (*). Reprinted with permission from J. Bachmann *et al. ACS Macro Lett.* **2021**, *10*, 4, 447-452. Copyright 2021 American Chemical Society. Modified representation.

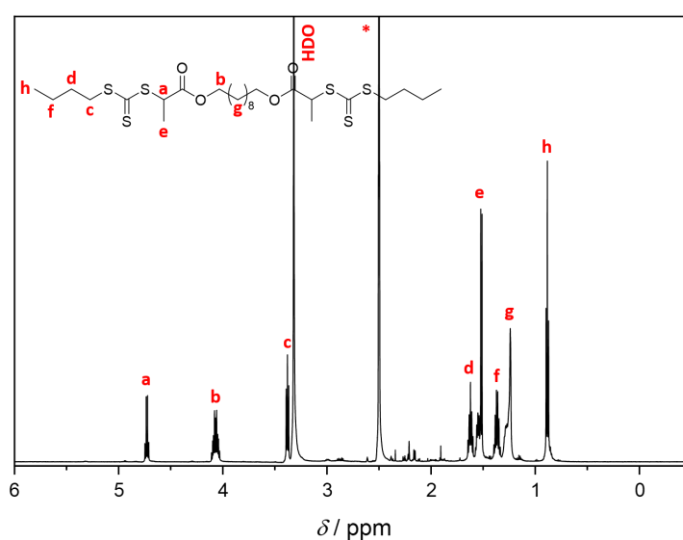


Figure S4-10: ^1H -NMR spectrum of non-degradable core in DMSO- d_6 (*). Reprinted with permission from J. Bachmann *et al. ACS Macro Lett.* **2021**, *10*, 4, 447-452. Copyright 2021 American Chemical Society.

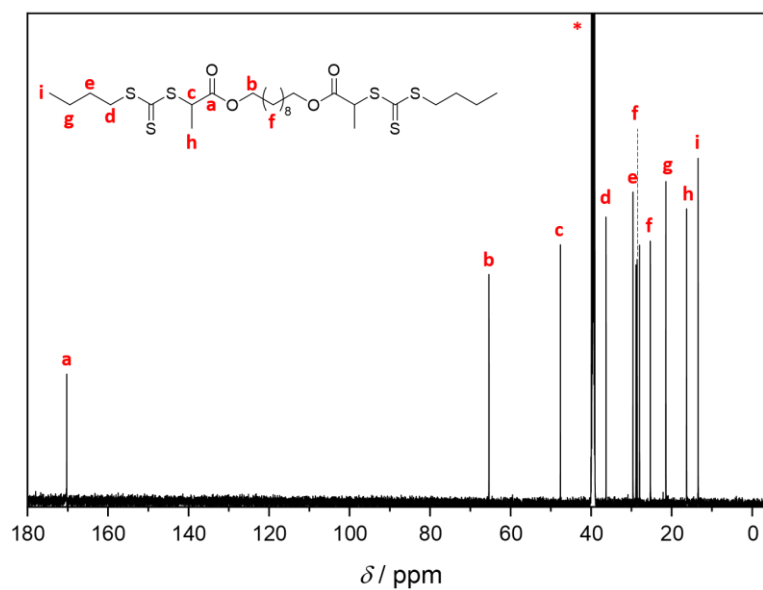


Figure S4-11: ^{13}C -NMR spectrum of non-degradable core in $\text{DMSO-}d_6$ (*). Reprinted with permission from J. Bachmann *et al. ACS Macro Lett.* **2021**, *10*, 4, 447-452. Copyright 2021 American Chemical Society.

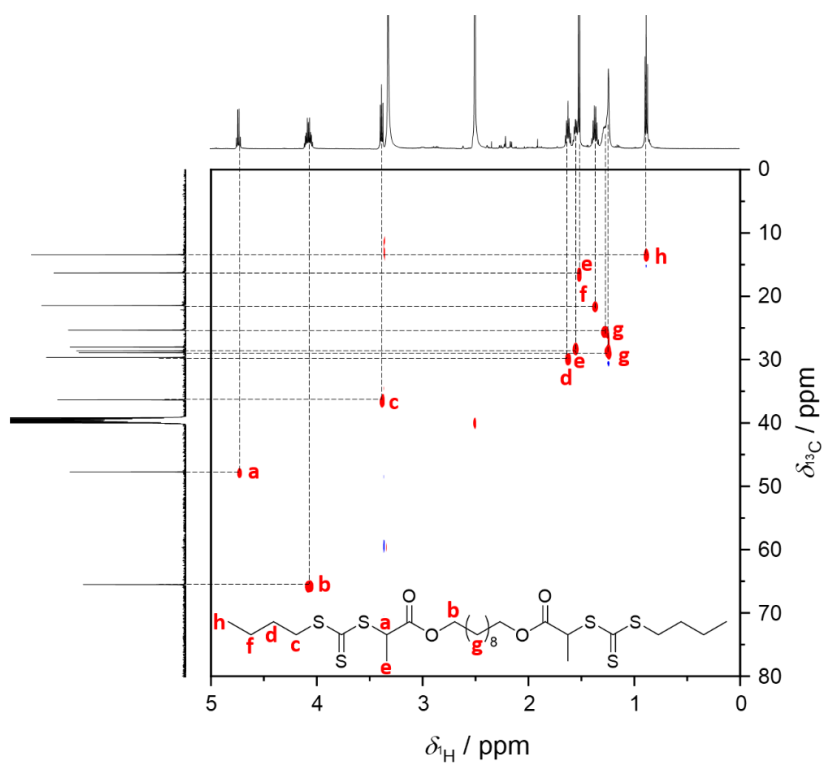
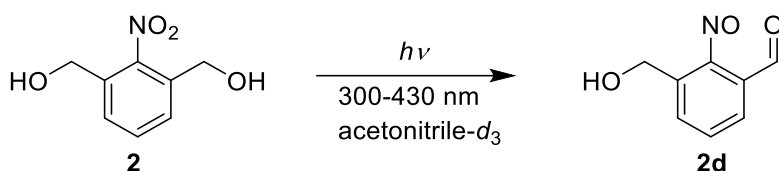


Figure S4-12: Full Gradient selected HSQC (HSQCEDET)-NMR spectrum of nondegradable core in $\text{DMSO-}d_6$ (*). Reprinted with permission from J. Bachmann *et al. ACS Macro Lett.* **2021**, *10*, 4, 447-452. Copyright 2021 American Chemical Society. Modified representation.



Scheme S4-2: Reaction scheme of the photolysis of **2** via laser irradiation (300 - 430 nm) in acetonitrile- d_3 . Reprinted with permission from J. Bachmann *et al.* *ACS Macro Lett.* **2021**, *10*, 4, 447-452. Copyright 2021 American Chemical Society.

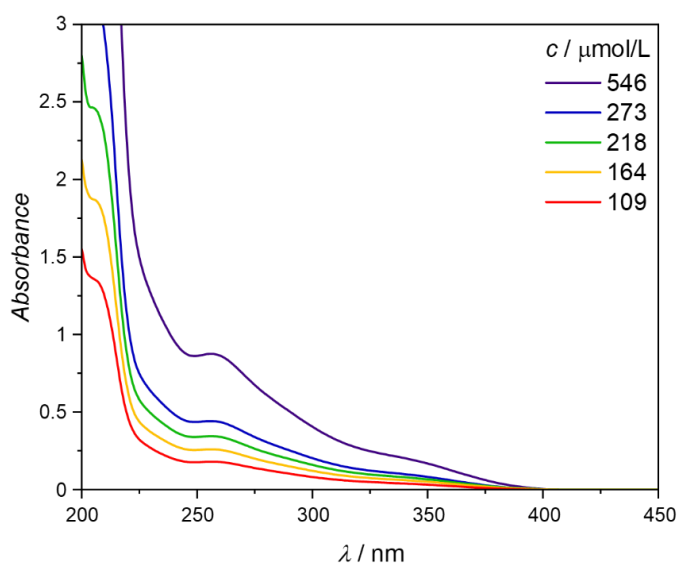


Figure S4-13: UV/Vis absorption spectra of **2** at different concentrations in acetonitrile. $d = 10$ mm. Reprinted with permission from J. Bachmann *et al.* *ACS Macro Lett.* **2021**, *10*, 4, 447-452. Copyright 2021 American Chemical Society. Modified representation.

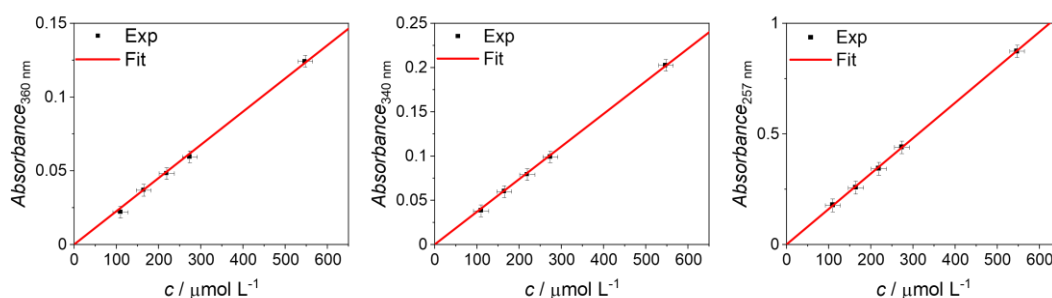


Figure S4-14: Determination of extinction coefficient ϵ of **2** in acetonitrile at 360, 340 and 257 nm (from left to right). $\epsilon_{360 \text{ nm}} = (225 \pm 2) \text{ L mol}^{-1} \text{ cm}^{-1}$, $\epsilon_{340 \text{ nm}} = (369 \pm 2) \text{ L mol}^{-1} \text{ cm}^{-1}$, $\epsilon_{257 \text{ nm}} = (1601 \pm 6) \text{ L mol}^{-1} \text{ cm}^{-1}$. Reprinted with permission from J. Bachmann *et al.* *ACS Macro Lett.* **2021**, *10*, 4, 447-452. Copyright 2021 American Chemical Society. Modified representation.

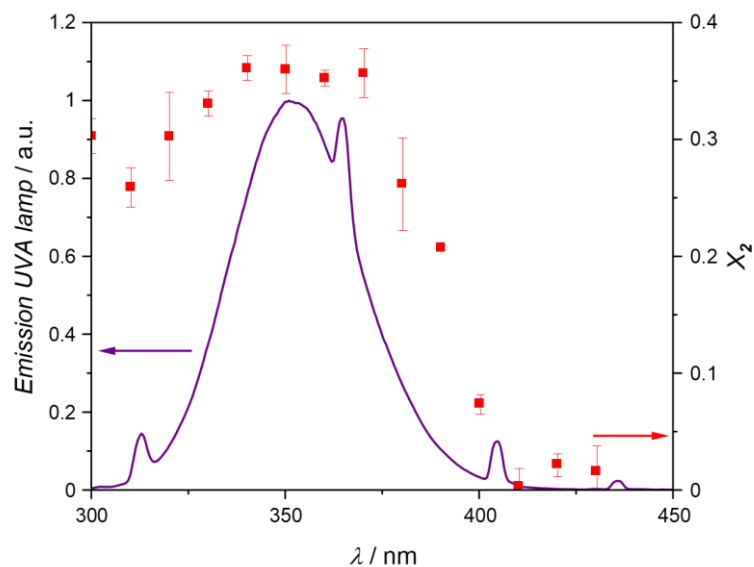


Figure S4-15: Operated UV-A photoreactor lamps. Left axis: Emission spectrum. Right axis: Conversion of **2** as a function of wavelength. Reprinted with permission from J. Bachmann *et al.* *ACS Macro Lett.* **2021**, *10*, 4, 447-452. Copyright 2021 American Chemical Society.

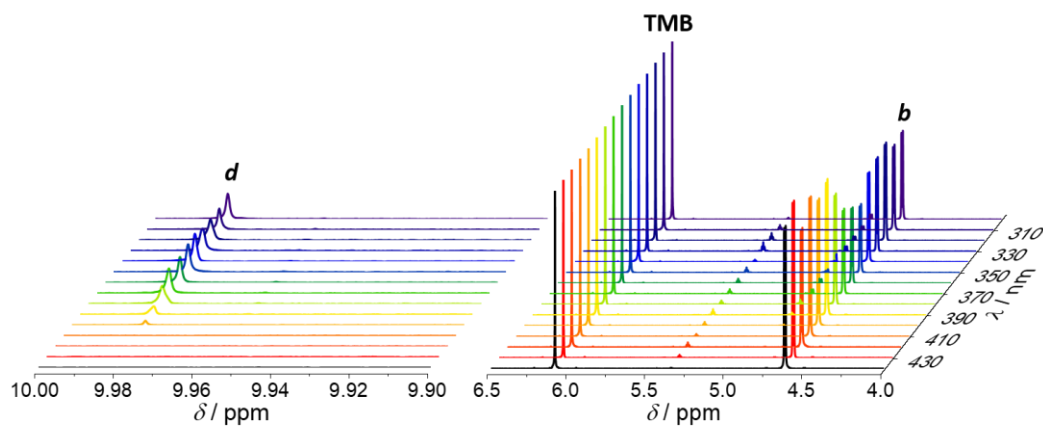
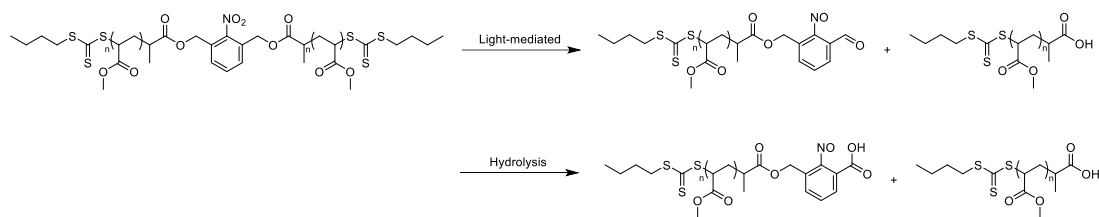


Figure S4-16: Evolution of resonances of **2** irradiated with a distinct number of photons at 350 nm in acetonitrile- d_3 . The resonances *b* and *d* relate to characteristic resonances of molecule **2** and its photoproduct as depicted in **Scheme 4-2**. All resonances were referenced to the TMB resonance. Due to simplicity, only one spectrum per time increment is shown. Reprinted with permission from J. Bachmann *et al.* *ACS Macro Lett.* **2021**, *10*, 4, 447-452. Copyright 2021 American Chemical Society. Modified representation.



Scheme S4-3: Suggested critical reaction for the general polymer structure. The critical bond is coloured in red. Top: Reaction scheme of photodegradation, generating a nitrosobenzaldehyde and the residual carboxylic acid. Bottom: Reaction scheme of the hydrolysis of the ester, generating an alcohol and a carboxylic acid. Reprinted with permission from J. Bachmann *et al. ACS Macro Lett.* **2021**, *10*, 4, 447-452. Copyright 2021 American Chemical Society.

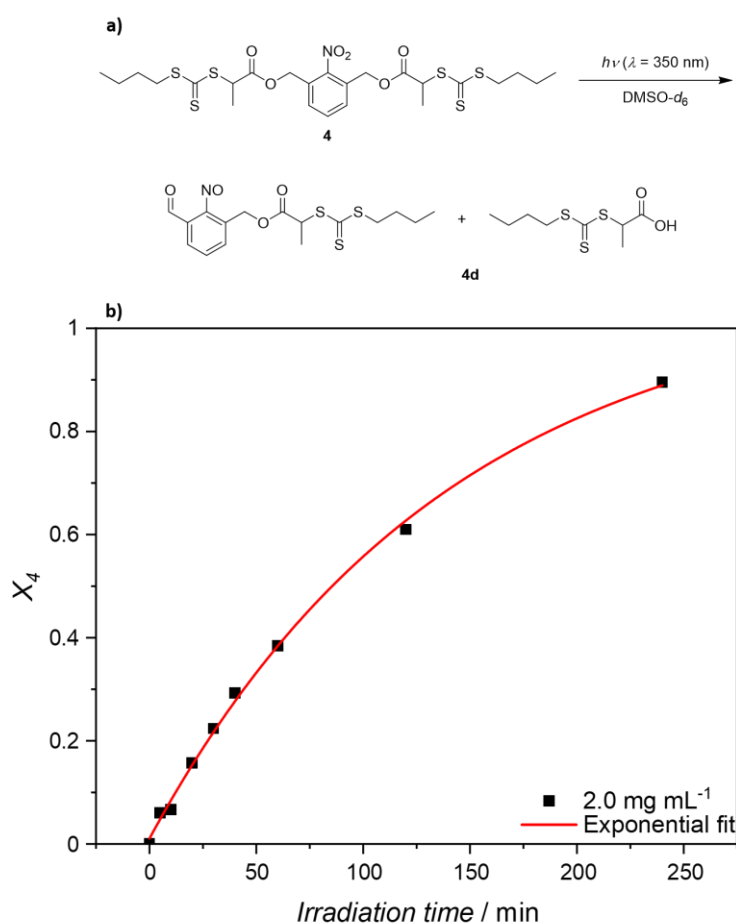


Figure S4-17: a) Proposed cleavage reaction of **4**. b) Conversion X of **4**, monitored via $^1\text{H-NMR}$ spectroscopy and monoexponential fit (line). The calculation was performed identical to the action plot studies (**Figure S4-16**) and qualitative degradation experiments. k_{apparent} was obtained as $k_{\text{app}, 4, c=2.0} = (0.025 \pm 0.005) \text{ min}^{-1}$. Reprinted with permission from J. Bachmann *et al. ACS Macro Lett.* **2021**, *10*, 4, 447-452. Copyright 2021 American Chemical Society. Modified representation.

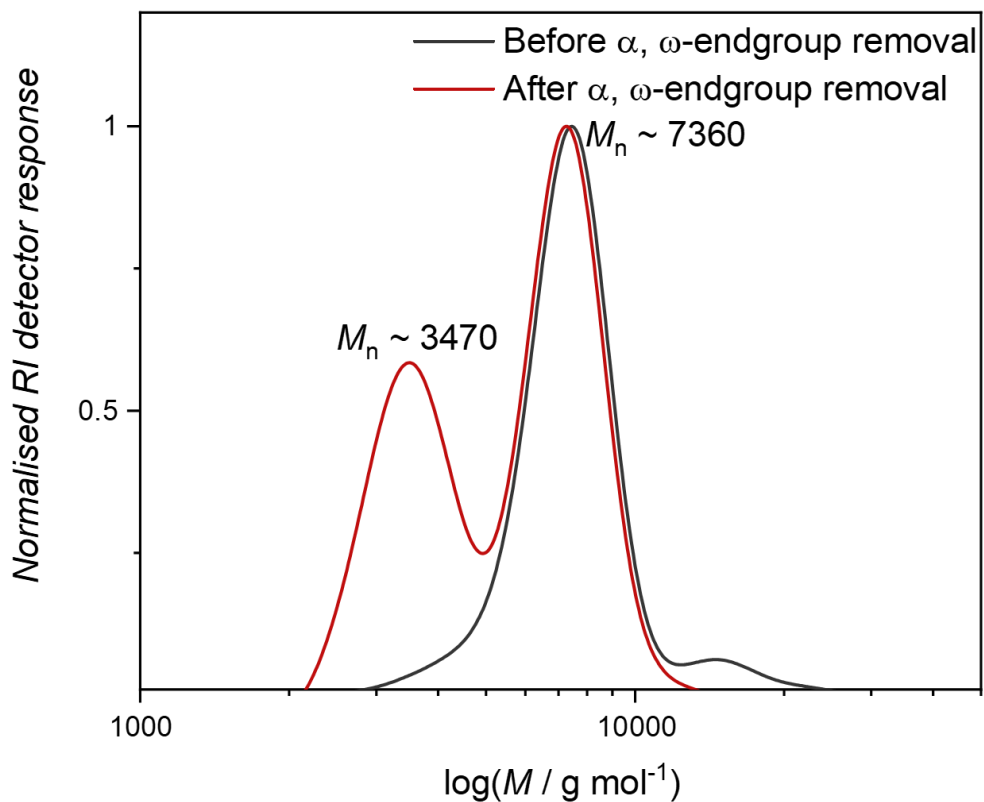


Figure S4-18: SEC traces in THF of **T2** before (black) and after (red) attempted endgroup removal. Synthetical protocol is appended in Chapter 8.5.2.7. Reprinted with permission from J. Bachmann *et al.* *ACS Macro Lett.* **2021**, *10*, 4, 447-452. Copyright 2021 American Chemical Society.

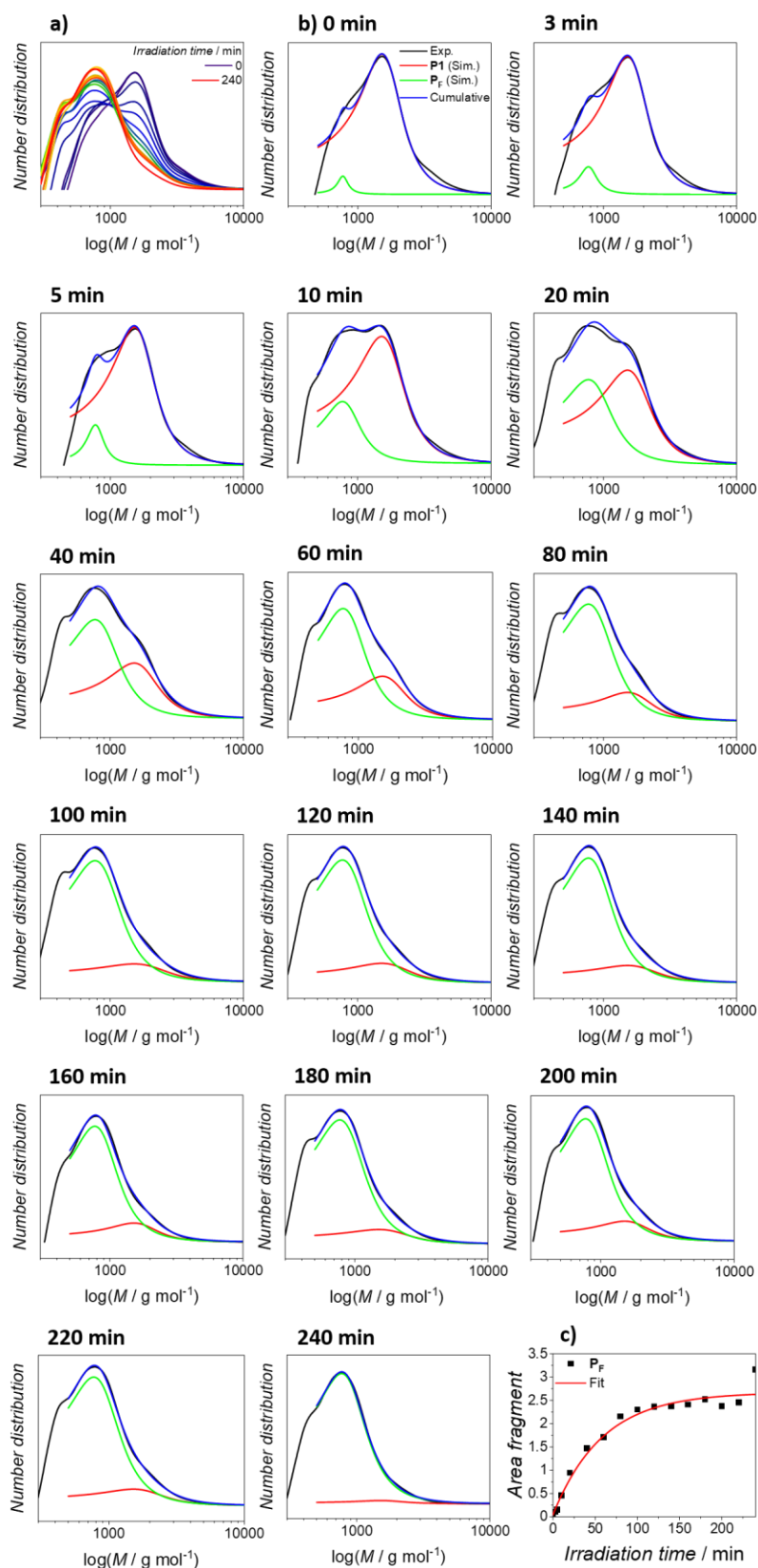


Figure S4-19: a) Number distribution of **P1** for all time periods in a mass concentration of 2.0 mg mL^{-1} . b) Deconvolution plots of single SEC traces for every time increment from 0 to 240 min. c) Evolution of Fragment area over time and fit of physical model. Reprinted with permission from J. Bachmann *et al. ACS Macro Lett.* **2021**, *10*, 4, 447-452. Copyright 2021 American Chemical Society.

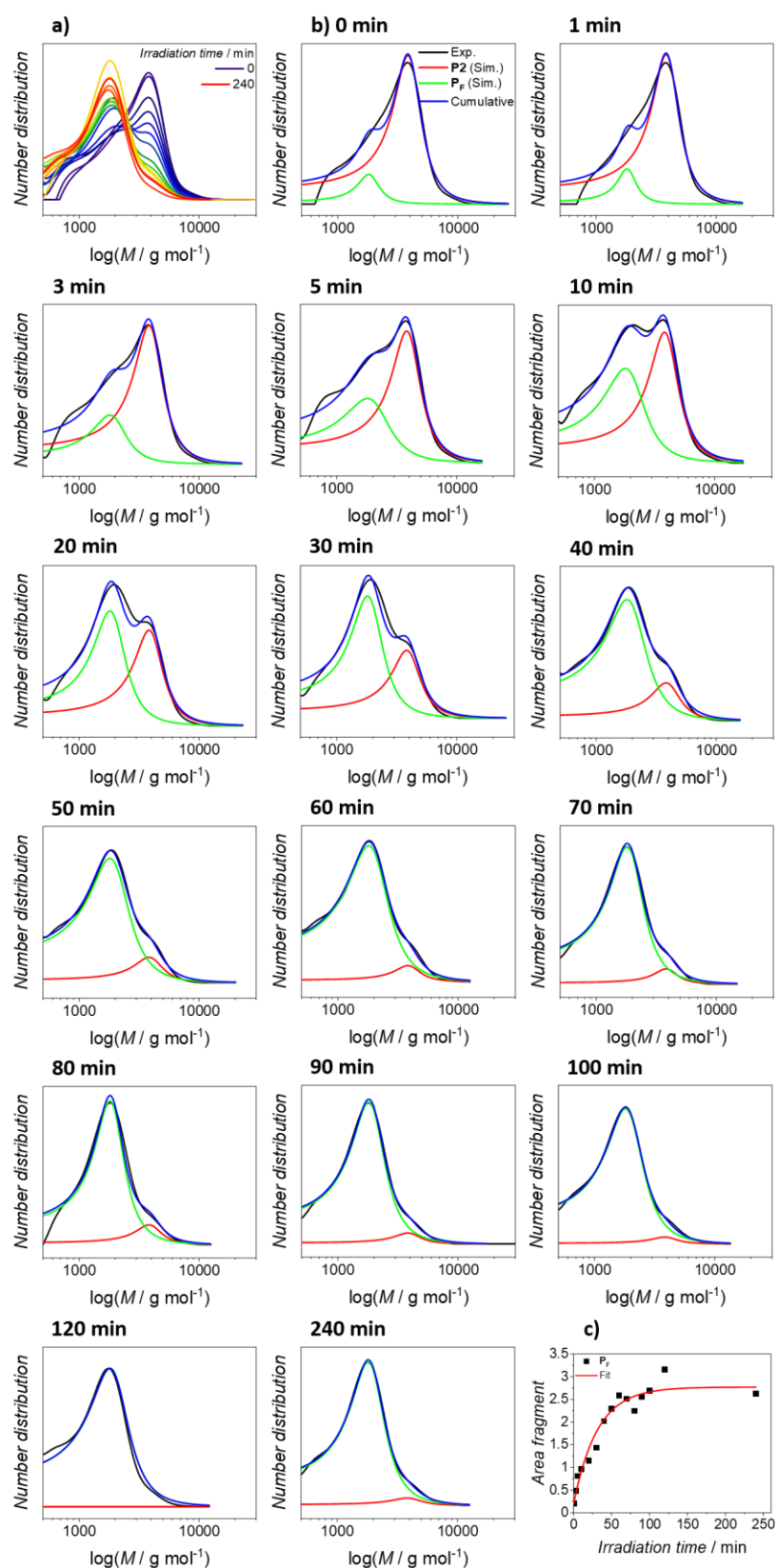


Figure S4-20: a) Number distribution of **P2** for all time periods in a mass concentration of 2.0 mg mL^{-1} . b) Deconvolution plots of single SEC traces for every time increment from 0 to 240 min. c) Evolution of Fragment area over time and fit of physical model. Reprinted with permission from J. Bachmann *et al.* *ACS Macro Lett.* **2021**, *10*, 4, 447-452. Copyright 2021 American Chemical Society.

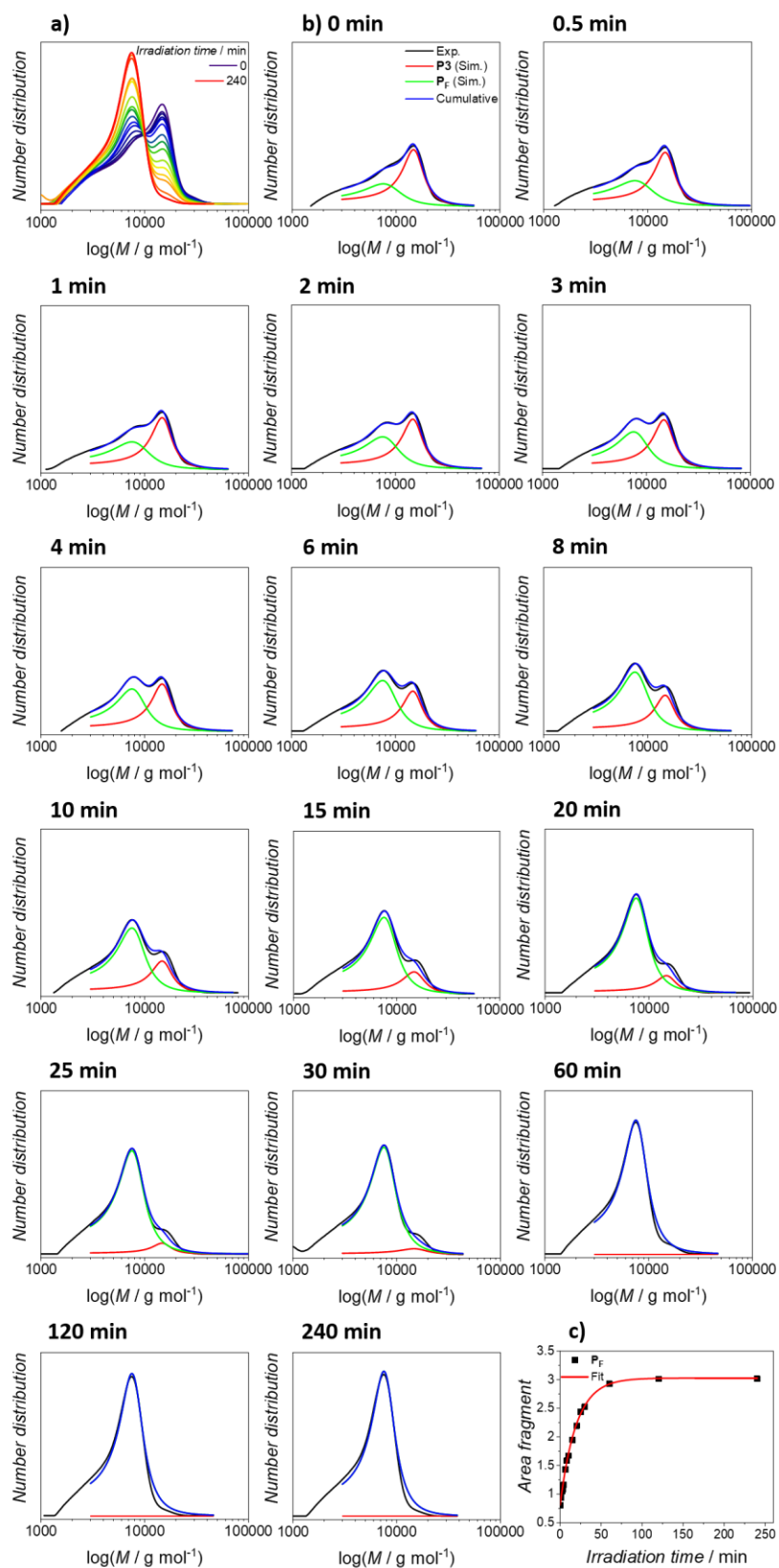


Figure S4-21: a) Number distribution of **P3** for all time periods in a mass concentration of 2.0 mg mL^{-1} . b) Deconvolution plots of single SEC traces for every time increment from 0 to 240 min. c) Evolution of Fragment area over time and fit of physical model. Reprinted with permission from J. Bachmann *et al. ACS Macro Lett.* **2021**, *10*, 4, 447-452. Copyright 2021 American Chemical Society.

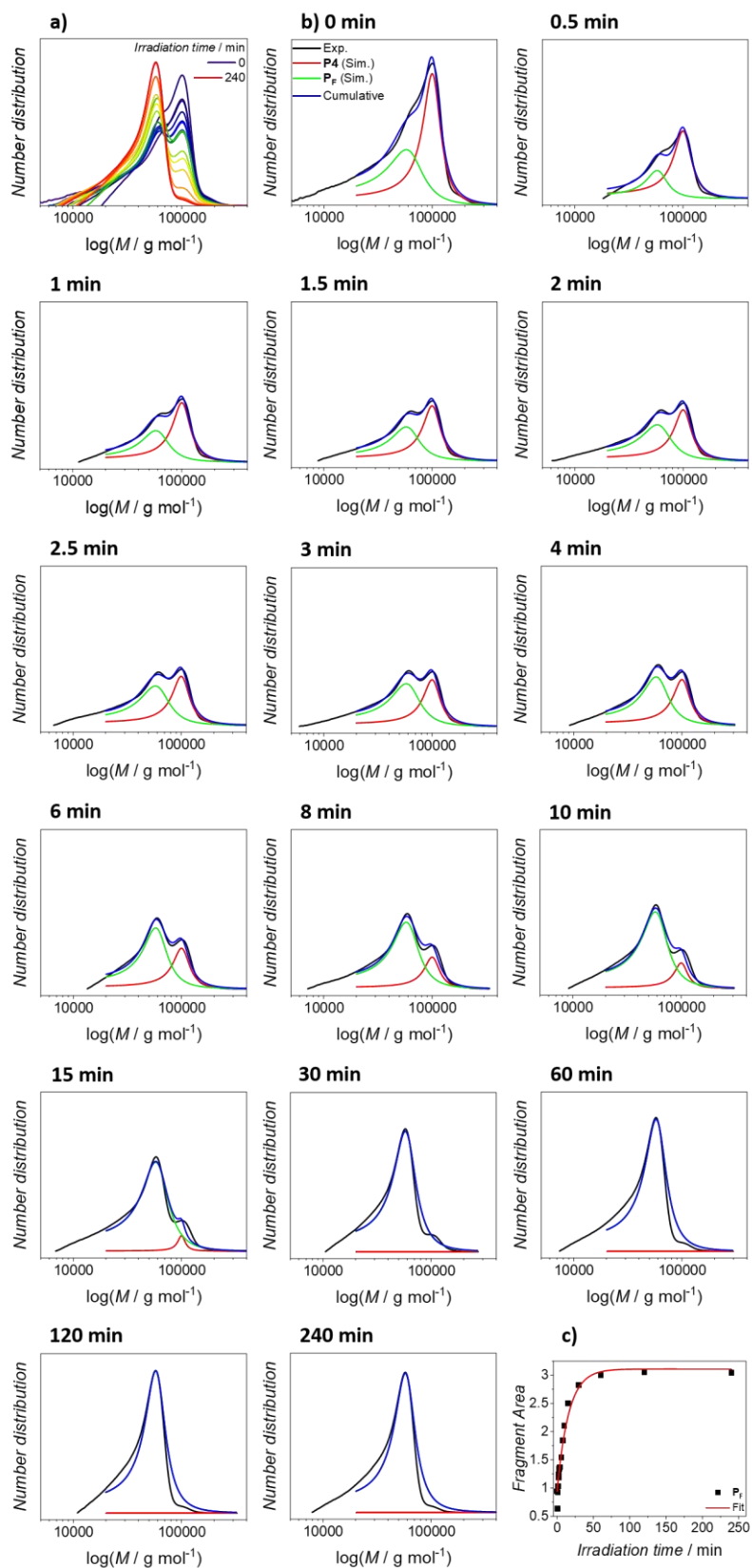


Figure S4-22: a) Number distribution of **P4** for all time periods in a mass concentration of 2.0 mg mL⁻¹. b) Deconvolution plots of single SEC traces for every time increment from 0 to 240 min. c) Evolution of Fragment area over time and fit of physical model. Reprinted with permission from J. Bachmann *et al.* *ACS Macro Lett.* **2021**, 10, 4, 447-452. Copyright 2021 American Chemical Society.

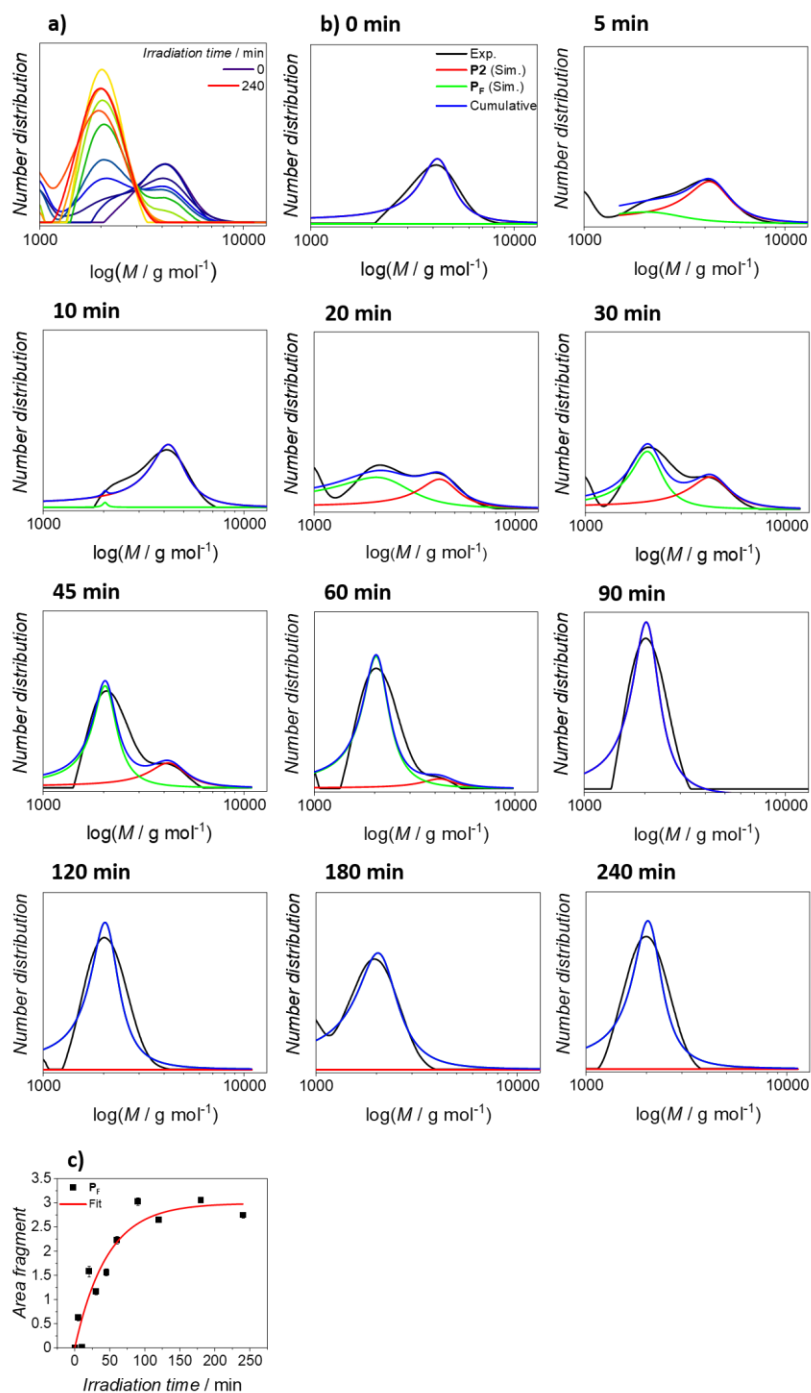


Figure S4-23: a) Number distribution of P2 in a mass concentration of 0.5 mg mL^{-1} for all time periods. b) Deconvolution plots of single SEC traces for every time increment from 0 to 240 min. c) Evolution of Fragment area over time and fit of physical model. Note that this experiment was performed during the revision process. The polymer, although stored at $5 \text{ }^\circ\text{C}$ in the dark, showed an increased level of cleavage compared to the initial polymer. Reprinted with permission from J. Bachmann *et al.* *ACS Macro Lett.* **2021**, *10*, 4, 447-452. Copyright 2021 American Chemical Society.

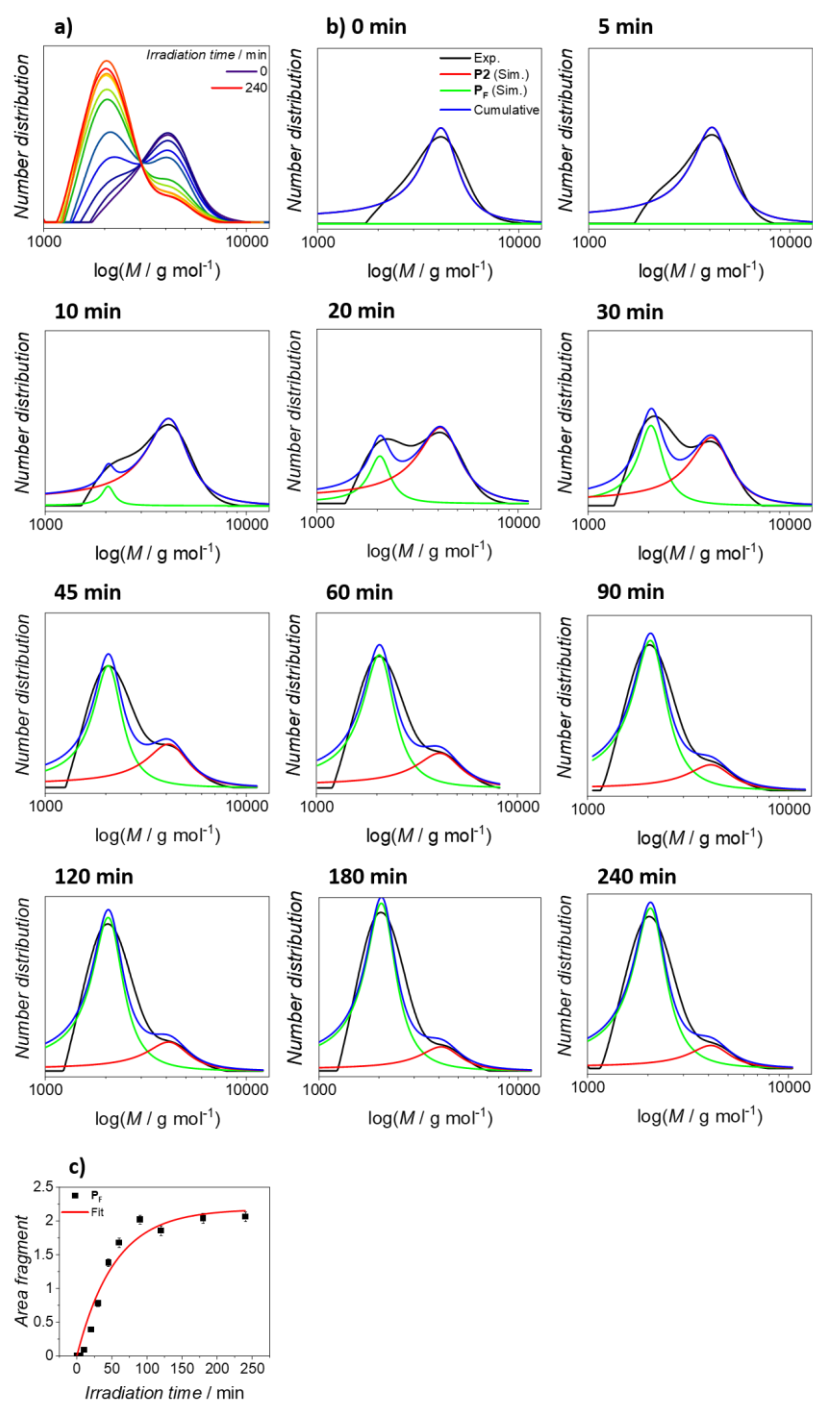


Figure S4-24: a) Number distribution of **P2** in a mass concentration of 1.0 mg mL^{-1} for all time periods. b) Deconvolution plots of single SEC traces for every time increment from 0 to 240 min. c) Evolution of Fragment area over time and fit of physical model. Note that this experiment was per-formed during the revision process. The polymer, although stored at 5°C in the dark, showed an increased level of cleavage compared to the initial polymer. Reprinted with permission from J. Bachmann *et al.* *ACS Macro Lett.* **2021**, *10*, 4, 447-452. Copyright 2021 American Chemical Society.

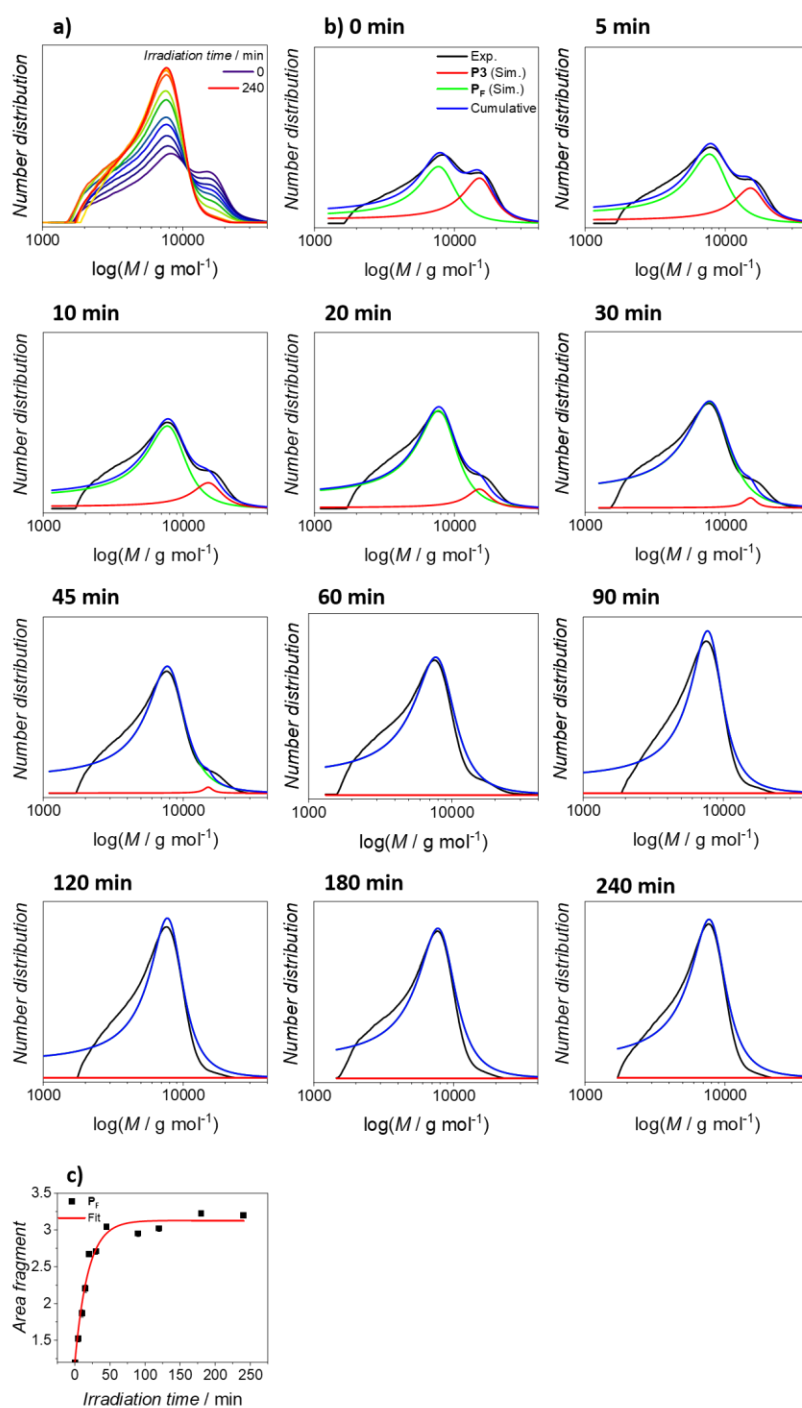


Figure S4-25: a) Number distribution of **P3** in a mass concentration of 0.5 mg mL^{-1} for all time periods. b) Deconvolution plots of single SEC traces for every time increment from 0 to 240 min. c) Evolution of Fragment area over time and fit of physical model. Note that this experiment was performed during the revision process. The polymer, although stored at $5 \text{ }^\circ\text{C}$ in the dark, showed an increased level of cleavage compared to the initial polymer. Reprinted with permission from J. Bachmann *et al.* *ACS Macro Lett.* **2021**, *10*, 4, 447-452. Copyright 2021 American Chemical Society.

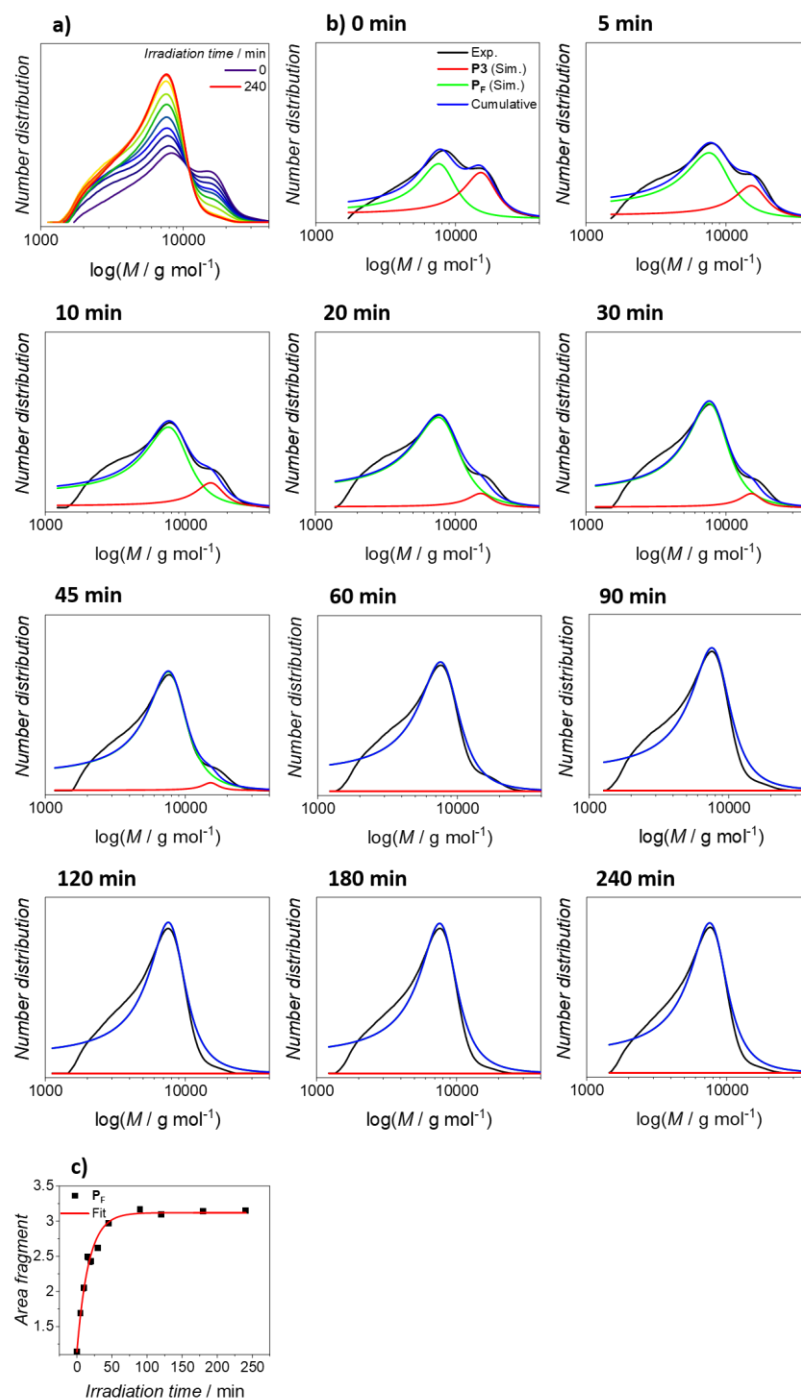


Figure S4-26: a) Number distribution of **P3** in a mass concentration of 1.0 mg mL^{-1} for all time periods. b) Deconvolution plots of single SEC traces for every time increment from 0 to 240 min. c) Evolution of Fragment area over time and fit of physical model. Note that this experiment was performed during the revision process. The polymer, although stored at 5°C in the dark, showed an increased level of cleavage compared to the initial polymer. Reprinted with permission from J. Bachmann *et al.* *ACS Macro Lett.* **2021**, *10*, 4, 447-452. Copyright 2021 American Chemical Society.

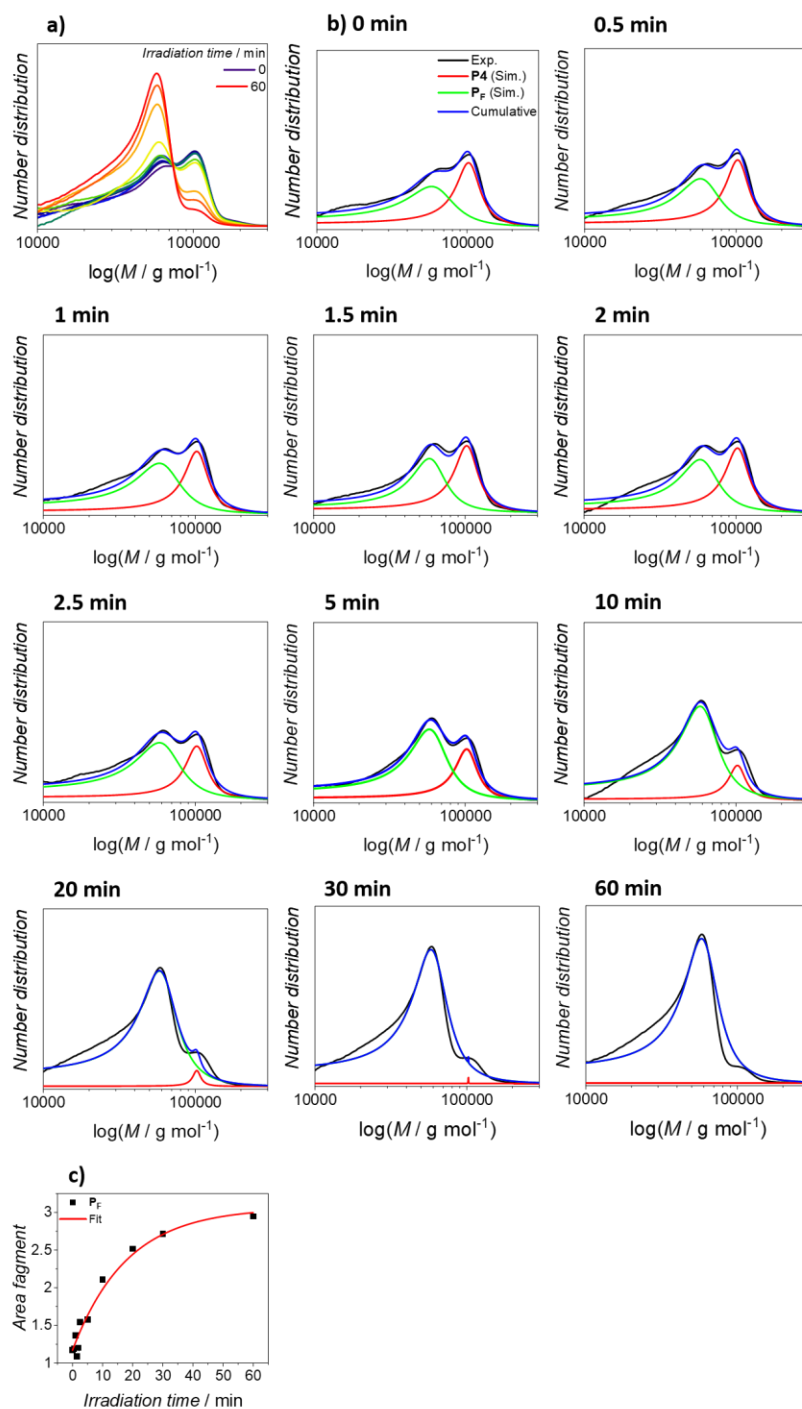


Figure S4-27: a) Number distribution of **P4** in a mass concentration of 0.5 mg mL^{-1} for all time periods. b) Deconvolution plots of single SEC traces for every time increment from 0 to 60 min. c) Evolution of Fragment area over time and fit of physical model. Note that this experiment was performed during the revision process. The polymer, although stored at 5°C in the dark, showed an increased level of cleavage compared to the initial polymer. Reprinted with permission from J. Bachmann *et al.* *ACS Macro Lett.* **2021**, *10*, 4, 447-452. Copyright 2021 American Chemical Society.

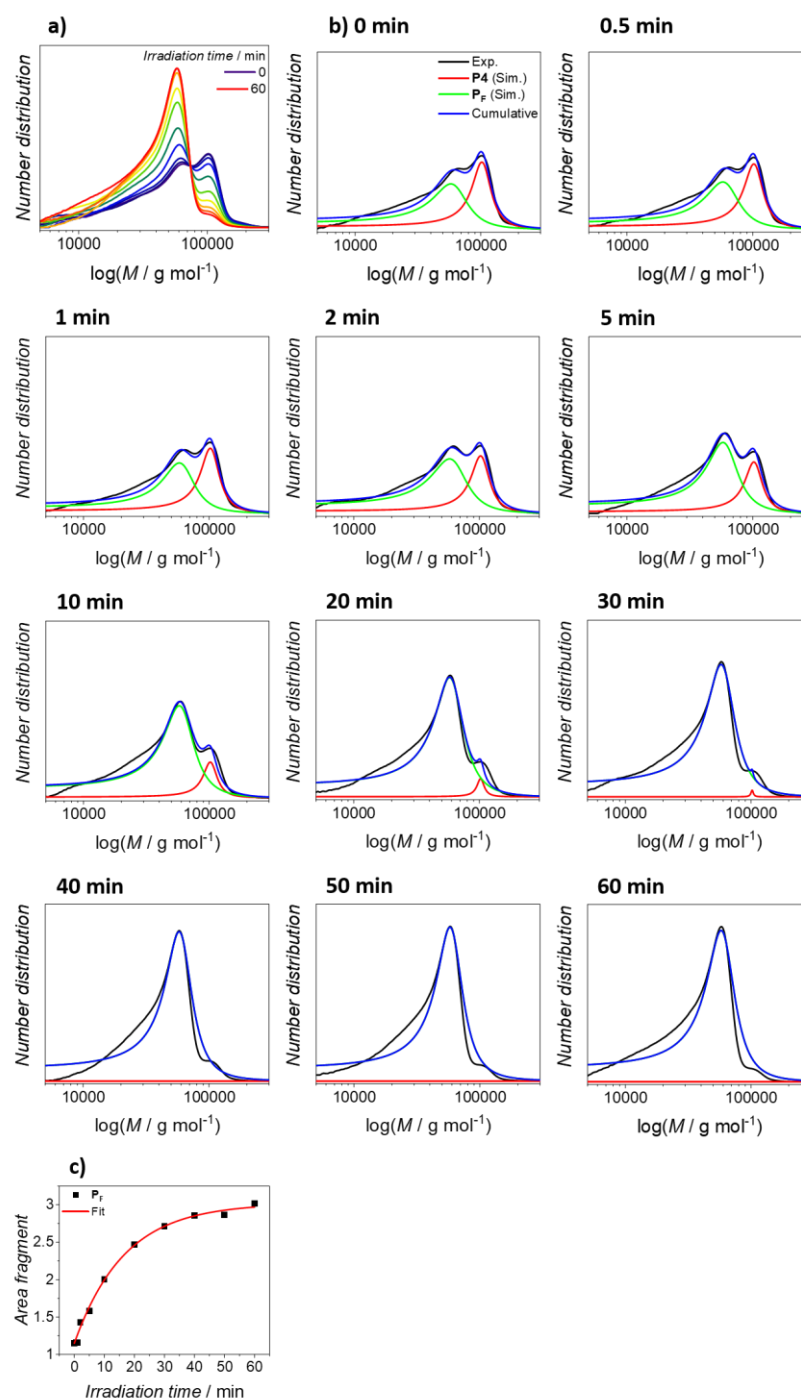


Figure S4-28: a) Number distribution of **P4** in a mass concentration of 1.0 mg mL^{-1} for all time periods. b) Deconvolution plots of single SEC traces for every time increment from 0 to 60 min. c) Evolution of Fragment area over time and fit of physical model. Note that this experiment was performed during the revision process. The polymer, although stored at 5°C in the dark, showed an increased level of cleavage compared to the initial polymer. Reprinted with permission from J. Bachmann *et al.* *ACS Macro Lett.* **2021**, *10*, 4, 447-452. Copyright 2021 American Chemical Society.

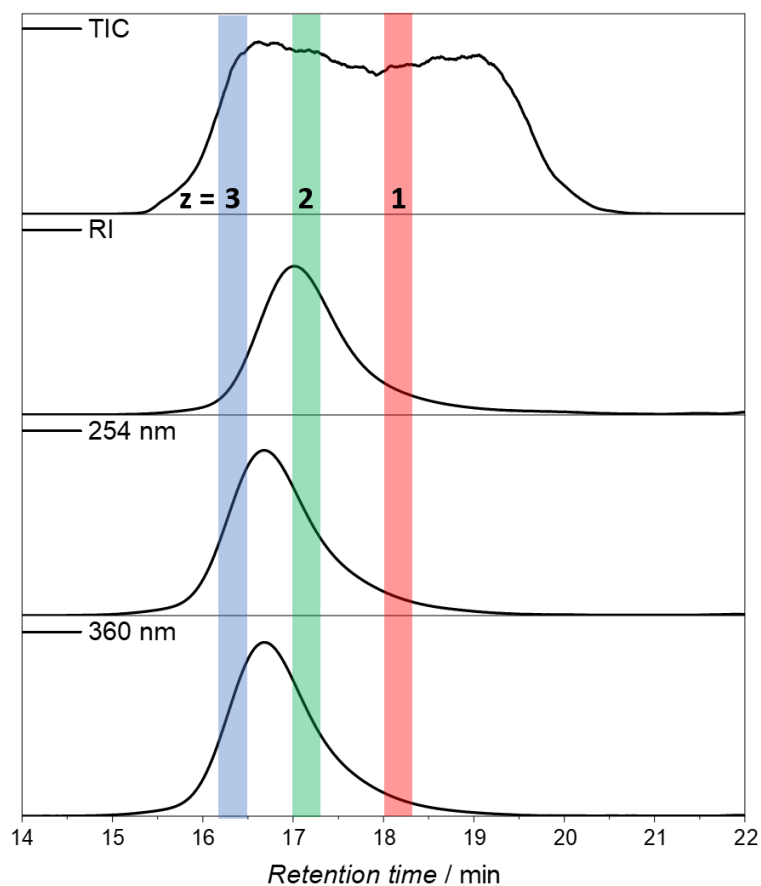
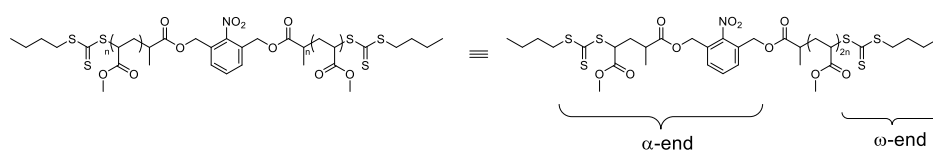


Figure S4-29: Obtained SEC-MS traces of **P2**. TIC: Total ion count, RI: Refractive index, Absorption traces at 254 and 360 nm. Different mass-to-charge regions for $z = 1, 2, 3$ are color-coded. Reprinted with permission from J. Bachmann *et al.* *ACS Macro Lett.* **2021**, *10*, 4, 447-452. Copyright 2021 American Chemical Society.



Scheme S4-4: Isobaric structure and reassignment of α - and ω -end, respectively.

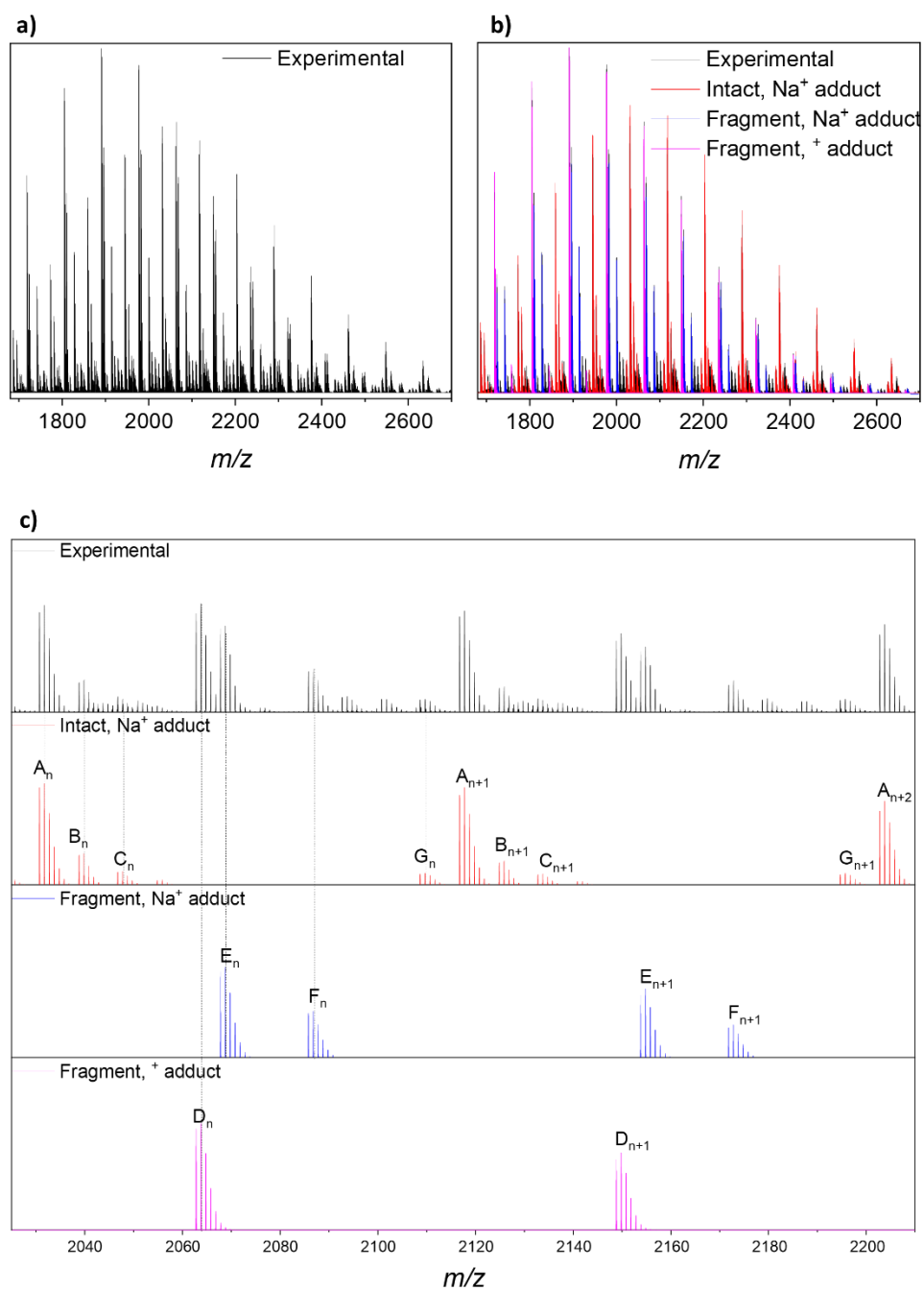
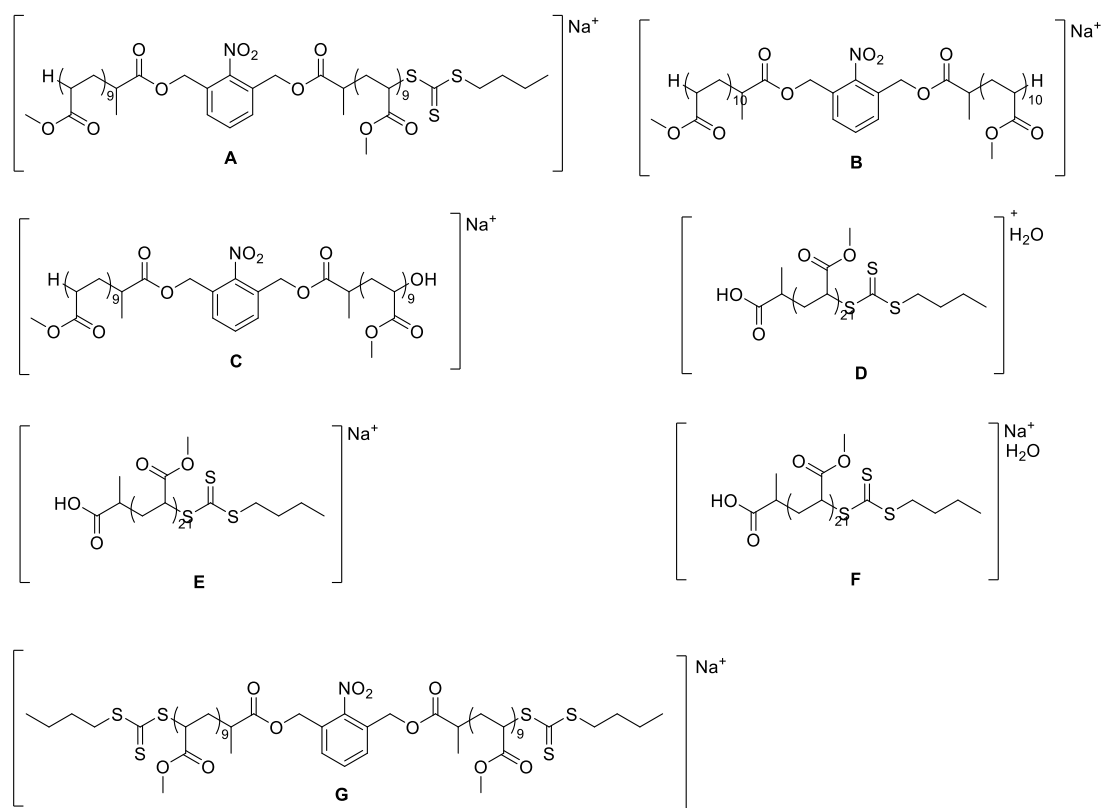


Figure S4-30: a) Experimental mass spectrum of **P2** for $z = 1$ region. b) Superimposed spectra and assigned counter ions. c) Enlarged view of the shaded area and assignment of found species. Reprinted with permission from J. Bachmann *et al.* *ACS Macro Lett.* **2021**, *10*, 4, 447-452. Copyright 2021 American Chemical Society.

Table S4-1: Detailed overview of identified signals in the mass spectrum **Figure S4-30**, comparison with theoretically expected m/z values, derived error Δ and α , ω -group.

Symbol	n	m/z_{exp}	m/z_{theo}	Δ / ppm	α , ω - group	Composition
A	18	2031.7392	2031.7389	0.15	$\alpha(\text{oNBRAFT}) \omega(\text{H})$	$[\text{C}_{91}\text{H}_{133}\text{N}_1\text{O}_{42}\text{S}_3\text{Na}_1]^+$
B	20	2039.8338	2039.8349	0.54	$\alpha(\text{oNBH}) \omega(\text{H})$	$[\text{C}_{94}\text{H}_{137}\text{N}_1\text{O}_{46}\text{Na}_1]^+$
C	18	2047.7339	2047.7351	0.59	$\alpha(\text{oNBOH}) \omega(\text{H})$	$[\text{C}_{91}\text{H}_{133}\text{N}_1\text{O}_{45}\text{S}_3\text{Na}_1]^+$
D	21	2063.8013	2063.8017	0.19	$\alpha(\text{FCOOH}) \omega(\text{RAFT})^*\text{H}_2\text{O}$	$[\text{C}_{92}\text{H}_{142}\text{O}_{45}\text{S}_3]^+$
E	21	2068.7805	2068.7802	0.15	$\alpha(\text{FCOOH}) \omega(\text{RAFT})$	$[\text{C}_{92}\text{H}_{140}\text{O}_{44}\text{S}_3\text{Na}_1]^+$
F	21	2086.7911	2086.8066	7.4	$\alpha(\text{FCOOH}) \omega(\text{RAFT})^*\text{H}_2\text{O}$	$[\text{C}_{92}\text{H}_{142}\text{O}_{45}\text{S}_3\text{Na}_1]^+$
G	17	2109.6809	2109.6818	0.43	$\alpha(\text{oNBRAFT}) \omega(\text{RAFT})$	$[\text{C}_{92}\text{H}_{135}\text{N}_1\text{O}_{40}\text{S}_6\text{Na}_1]^+$



Scheme S4-5: Assigned structures A-G for the mass-to-charge region $z = 1$. Reprinted with permission from J. Bachmann *et al.* *ACS Macro Lett.* **2021**, *10*, 4, 447-452. Copyright 2021 American Chemical Society.

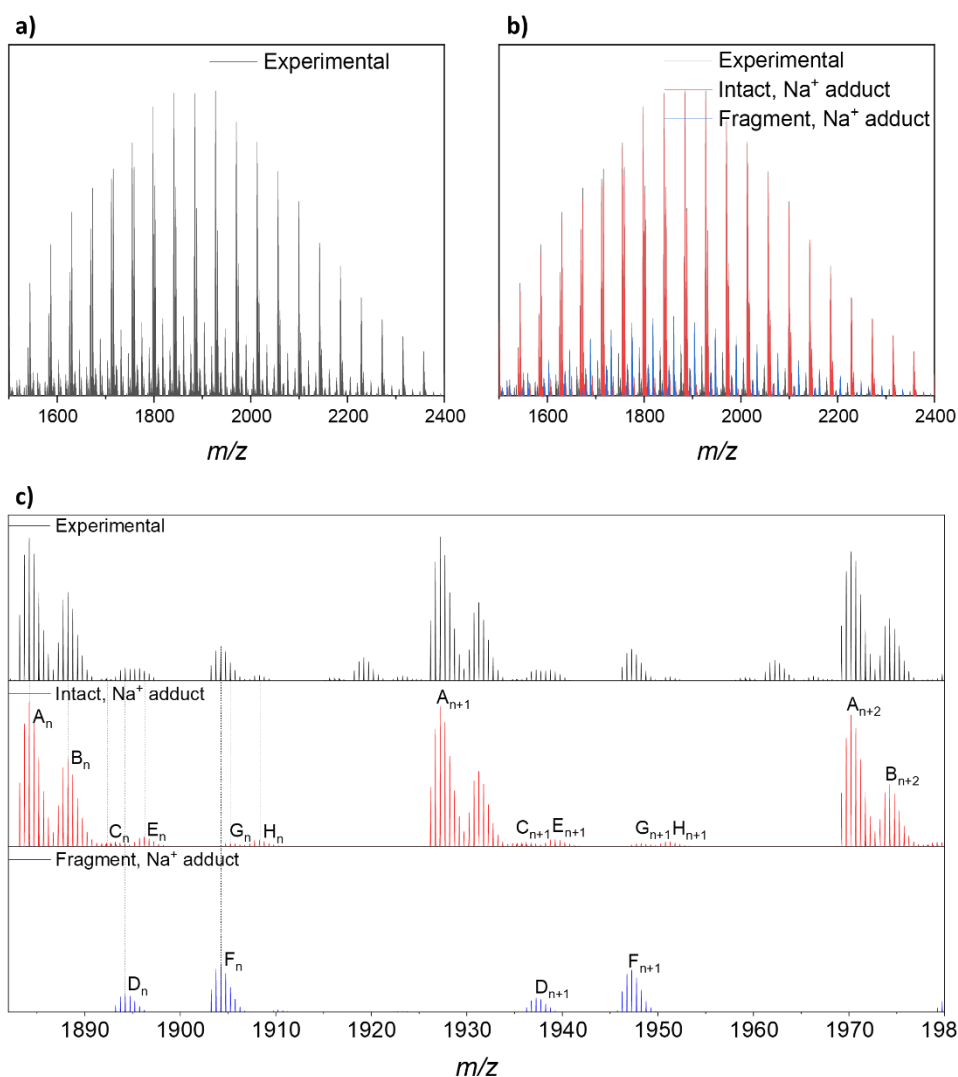
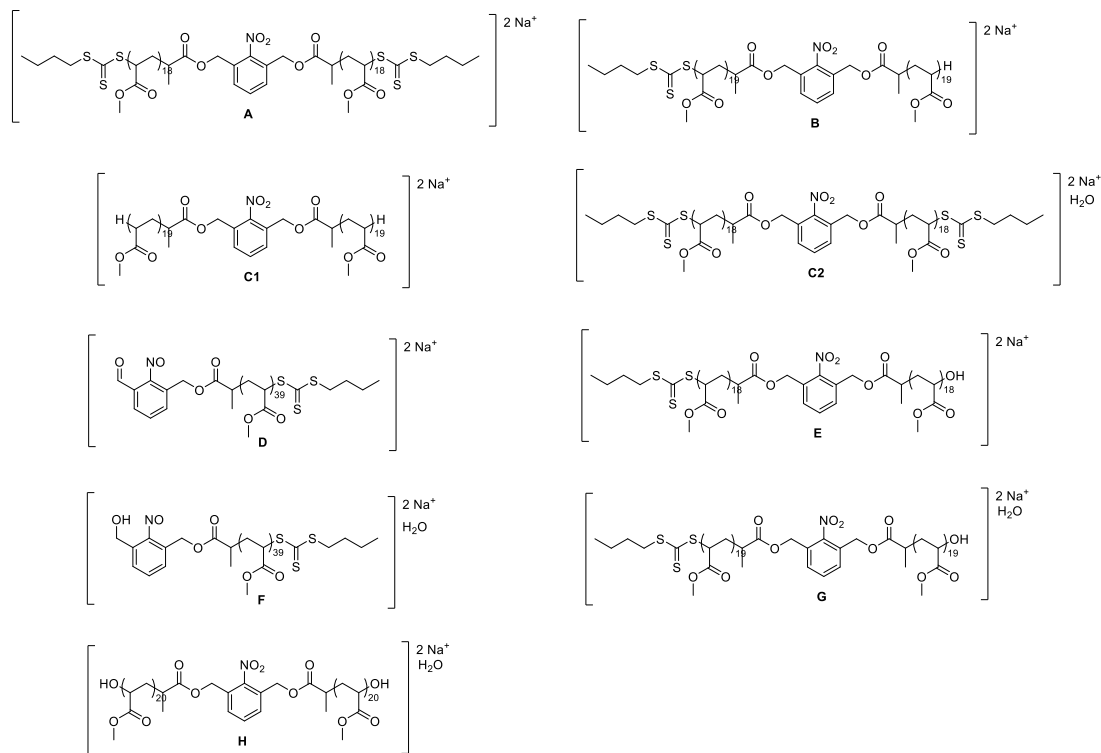


Figure S4-31: a) Experimental mass spectrum of **P2** for $z = 2$ region. b) Superimposed spectra and assigned counter ions. c) Enlarged view of the shaded area and assignment of found species. Reprinted with permission from J. Bachmann *et al.* *ACS Macro Lett.* **2021**, *10*, 4, 447-452. Copyright 2021 American Chemical Society.

Table S4-2: Detailed overview of identified signals in the mass spectrum **Figure S4-31**, comparison with theoretically expected m/z values, derived error Δ and α , ω -group.

Symbol	n	m/z_{exp}	m/z_{theo}	Δ / ppm	α , ω -group	Composition
A	36	1884.1862	1884.1854	0.42	α (oNBRAFT) ω (RAFT)	$[C_{168}H_{249}N_1O_{78}S_6Na_2]^{2+}$
B	38	1888.2332	1888.2331	0.05	α (oNBRAFT) ω (H)	$[C_{171}H_{253}N_1O_{82}S_3Na_2]^{2+}$
C1	40	1892.2843	1892.2809	1.8	α (oNBH) ω (H)	$[C_{174}H_{257}N_1O_{86}Na_2]^{2+}$
C2	36	1892.6821	1892.6898	4.1	α (oNBRAFT) ω (RAFT)*H ₂ O	$[C_{168}H_{251}N_1O_{79}S_6Na_2]^{2+}$
D	39	1894.2333	1894.2331	0.11	α (oNBd) ω (RAFT)	$[C_{172}H_{253}N_1O_{82}S_3Na_2]^{2+}$
E	38	1896.2335	1896.2306	1.5	α (oNBRAFT) ω (OH)	$[C_{171}H_{253}N_1O_{83}S_3Na_2]^{2+}$
F	39	1904.2277	1904.2463	9.8	α (oNBdr) ω (RAFT)*H ₂ O	$[C_{172}H_{257}N_1O_{83}S_3Na_2]^{2+}$
G	38	1905.2303	1905.2359	2.9	α (oNBRAFT) ω (OH)*H ₂ O	$[C_{171}H_{255}N_1O_{84}S_3Na_2]^{2+}$



Scheme 4-6: Assigned structures A-H for the mass-to-charge region $z = 2$. Reprinted with permission from J. Bachmann *et al.* *ACS Macro Lett.* **2021**, *10*, 4, 447-452. Copyright 2021 American Chemical Society.

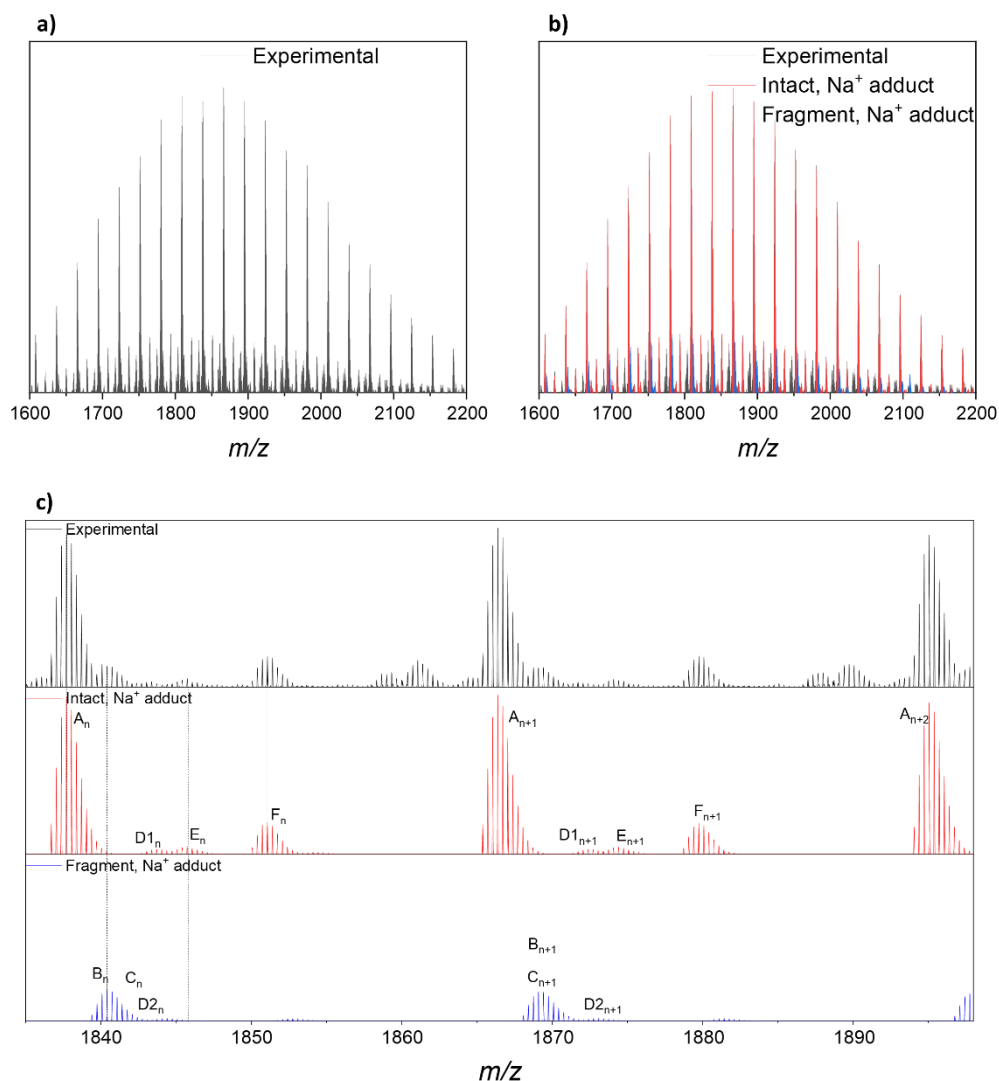
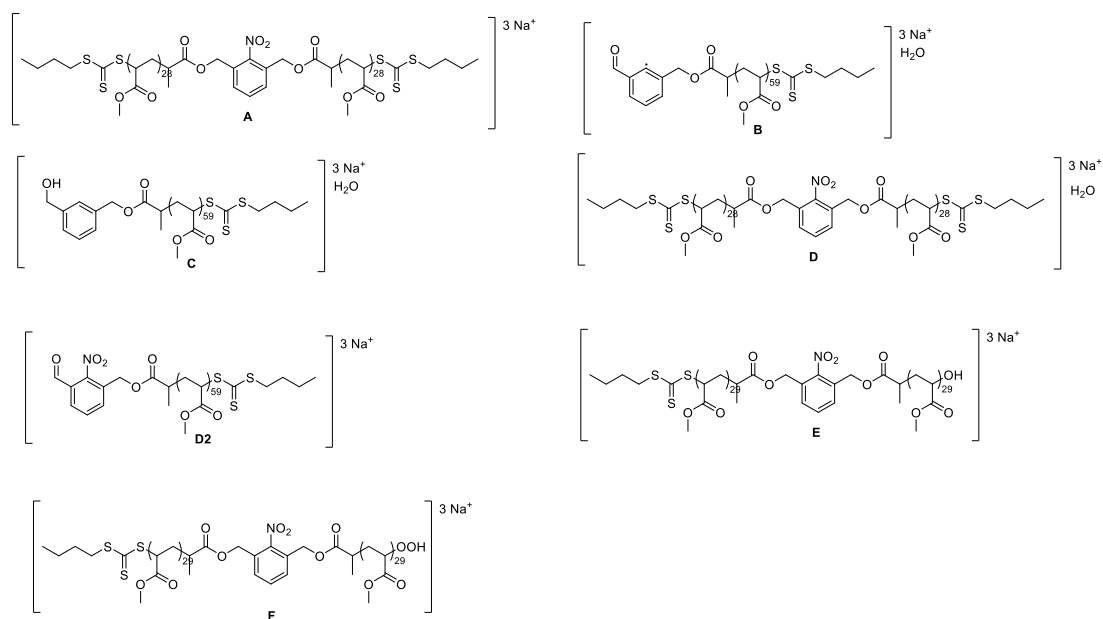


Figure S4-32: a) Experimental mass spectrum of **P2** for $z = 3$ region. b) Superimposed spectra and assigned counter ions. c) Enlarged view of the shaded area and assignment of found species. Reprinted with permission from J. Bachmann *et al.* *ACS Macro Lett.* **2021**, *10*, 4, 447-452. Copyright 2021 American Chemical Society.

Table S4-3: Detailed overview of identified signals in the mass spectrum **Figure S4-32**, comparison with theoretically expected m/z values, derived error Δ and α , ω -group.

Symbol	n	m/z_{exp}	m/z_{theo}	Δ / ppm	α , ω -group	composition
A	56	1837.7017	1837.6995	1.2	$\alpha(\text{oNBRAFT}) \omega(\text{RAFT})$	$[\text{C}_{248}\text{H}_{369}\text{N}_1\text{O}_{118}\text{S}_6\text{Na}_3]^{3+}$
B	59	1840.4010	1840.4023	0.71	$\alpha(\text{oNBd}\cdot) \omega(\text{RAFT})\cdot\text{H}_2\text{O}$	$[\text{C}_{252}\text{H}_{375}\text{O}_{122}\text{S}_3\text{Na}_3]^{3+}$
C	59	1841.4101	1841.4002	5.4	$\alpha(\text{oNBdrH}) \omega(\text{RAFT})\cdot\text{H}_2\text{O}$	$[\text{C}_{252}\text{H}_{378}\text{O}_{122}\text{S}_3\text{Na}_3]^{3+}$
D1	56	1843.7020	1843.7031	0.60	$\alpha(\text{oNBRAFT}) \omega(\text{RAFT})\cdot\text{H}_2\text{O}$	$[\text{C}_{248}\text{H}_{371}\text{N}_1\text{O}_{119}\text{S}_6\text{Na}_3]^{3+}$
D2	59	1844.4010	1844.3981	1.6	$\alpha(\text{oNBd}) \omega(\text{RAFT})$	$[\text{C}_{252}\text{H}_{373}\text{N}_1\text{O}_{122}\text{S}_3\text{Na}_3]^{3+}$
E	58	1845.7358	1845.7297	3.3	$\alpha(\text{oNBRAFT}) \omega(\text{OH})$	$[\text{C}_{251}\text{H}_{373}\text{N}_1\text{O}_{123}\text{S}_3\text{Na}_3]^{3+}$



Scheme 4-7: Assigned structures A-F for the mass-to-charge region $z = 3$. Reprinted with permission from J. Bachmann *et al.* *ACS Macro Lett.* **2021**, *10*, 4, 447-452. Copyright 2021 American Chemical Society.

Appendix C

Supporting Information for Chapter 5: Peroxide-accelerated photodegradation of tetrazine-bearing thiol-acrylate polymers via green light

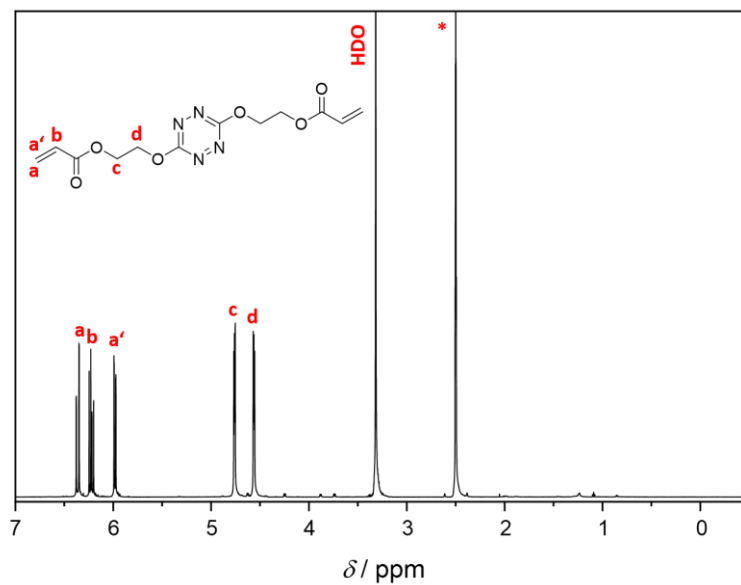


Figure S5-1: $^1\text{H-NMR}$ spectrum of TzDA in $\text{DMSO-}d_6$ (*).

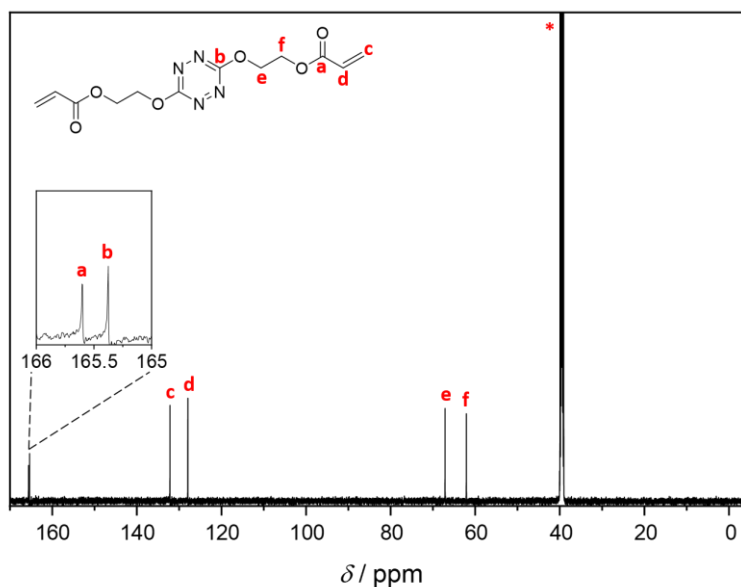


Figure S5-2: $^{13}\text{C-NMR}$ spectrum of TzDA in $\text{DMSO-}d_6$ (*). Inlet shows the two resonances at approximately 166 ppm.

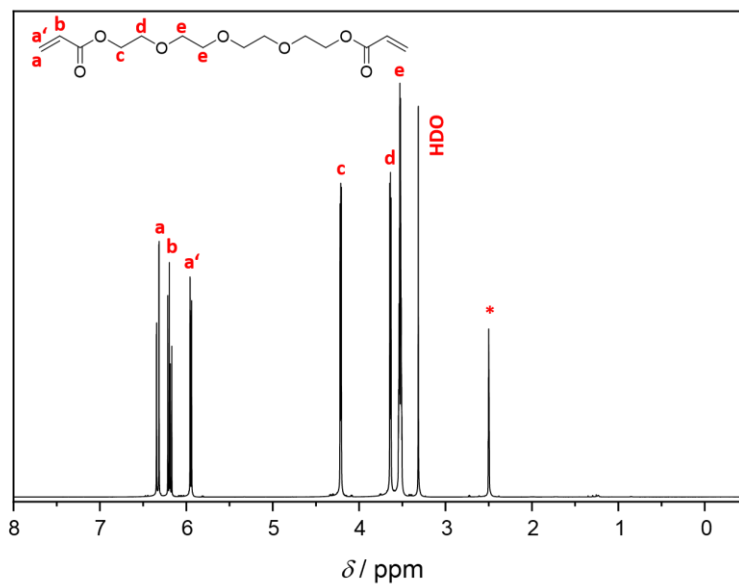


Figure S5-3: $^1\text{H-NMR}$ spectrum of TEGDA in $\text{DMSO-}d_6$ (*).

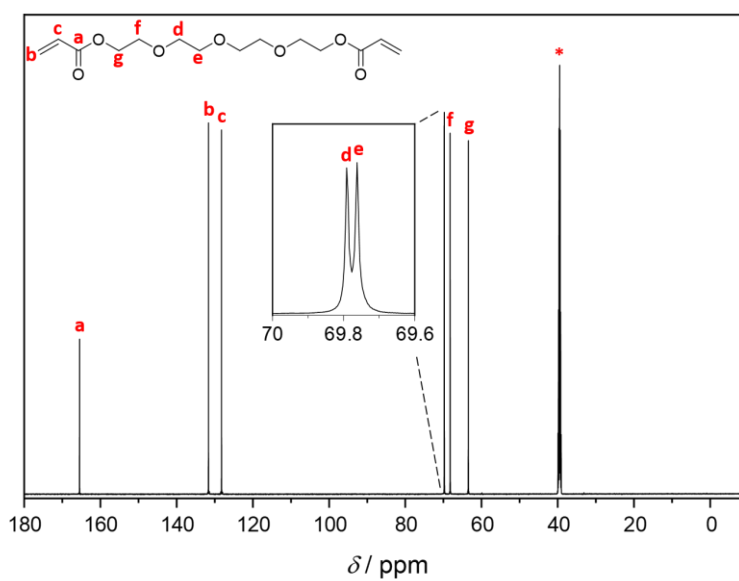


Figure S5-4: $^{13}\text{C-NMR}$ spectrum of TEGDA in $\text{DMSO-}d_6$ (*). Inlet shows the two resonances at approximately 70 ppm.

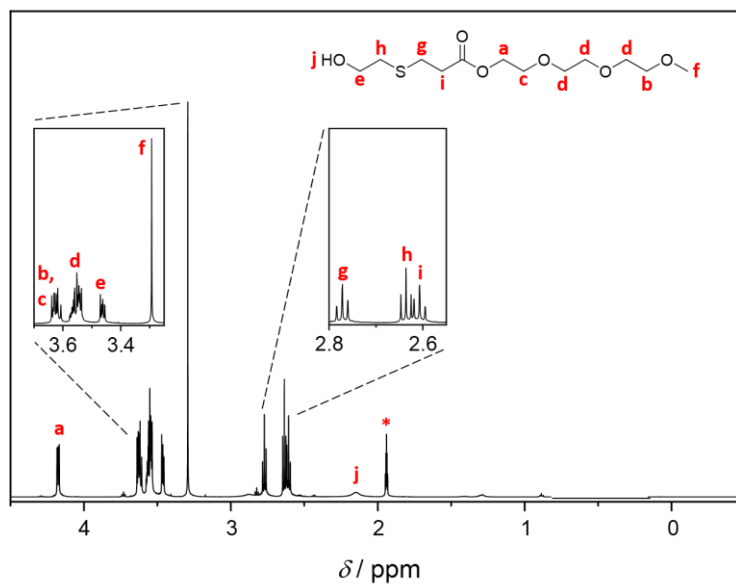


Figure S5-5: ^1H -NMR spectrum of TEGAS in acetonitrile- d_3 (*). Inlets show resonances around 3.6 (left) and 2.7 ppm (right).

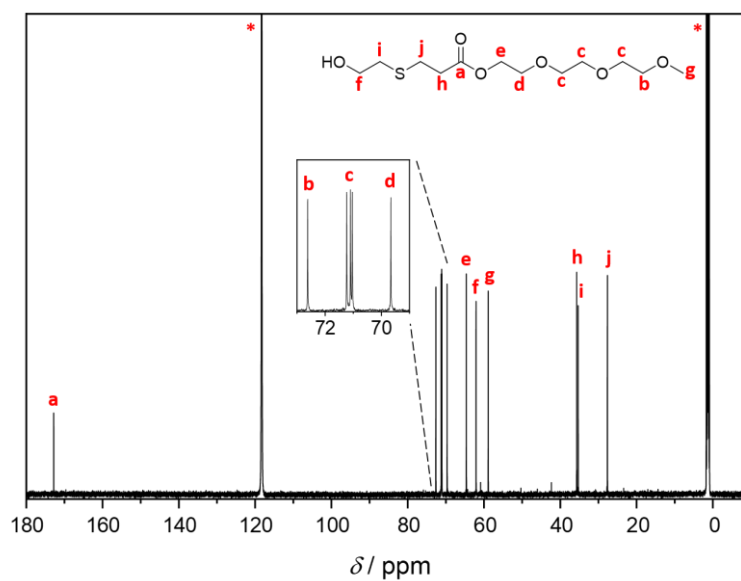


Figure S5-6: ^{13}C -NMR spectrum of TEGAS in acetonitrile- d_3 (*). Inlet shows the resonances at approximately 72 ppm.

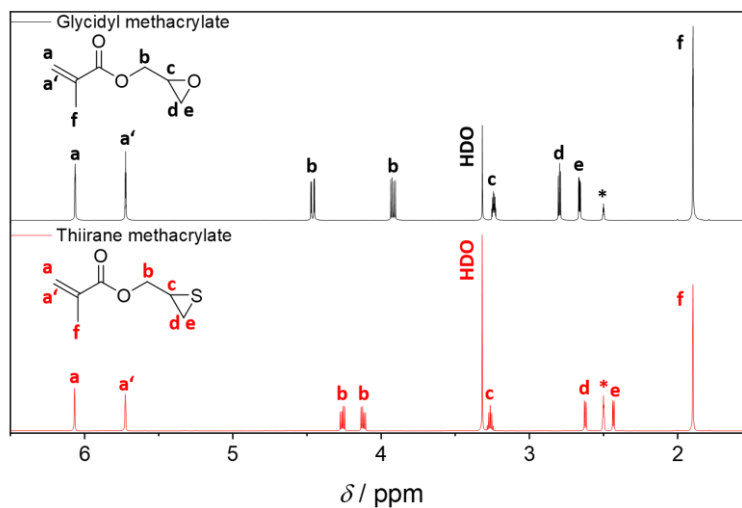


Figure S5-7: $^1\text{H-NMR}$ spectra of glycidyl methacrylate (top) and the product thirane-2-ylmethyl methacrylate (bottom) in $\text{DMSO-}d_6$ (*).

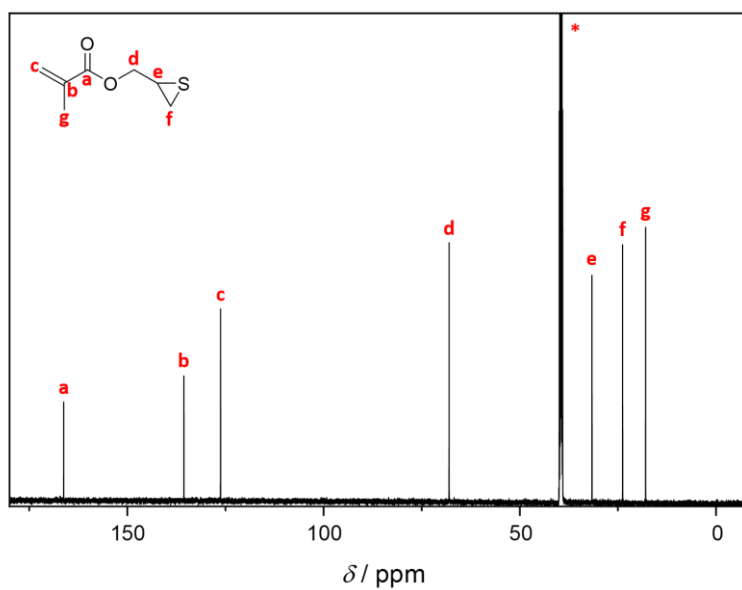


Figure S5-8: $^{13}\text{C-NMR}$ spectrum of thirane-2-ylmethyl methacrylate in $\text{DMSO-}d_6$ (*).

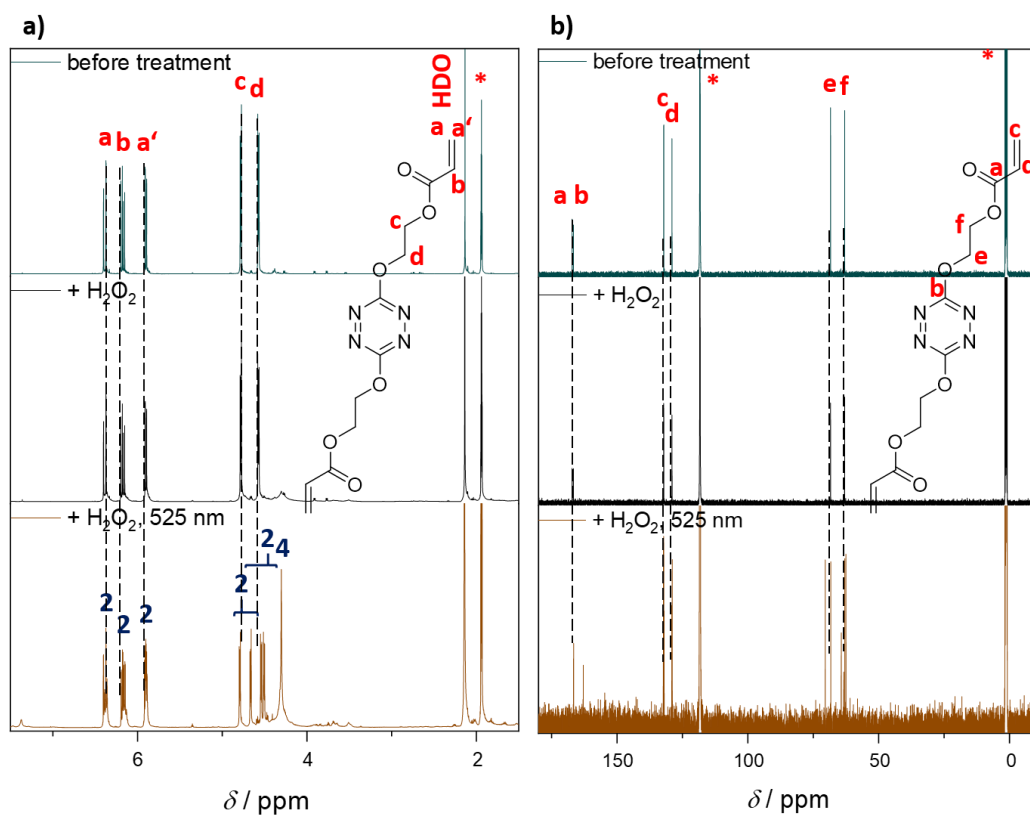
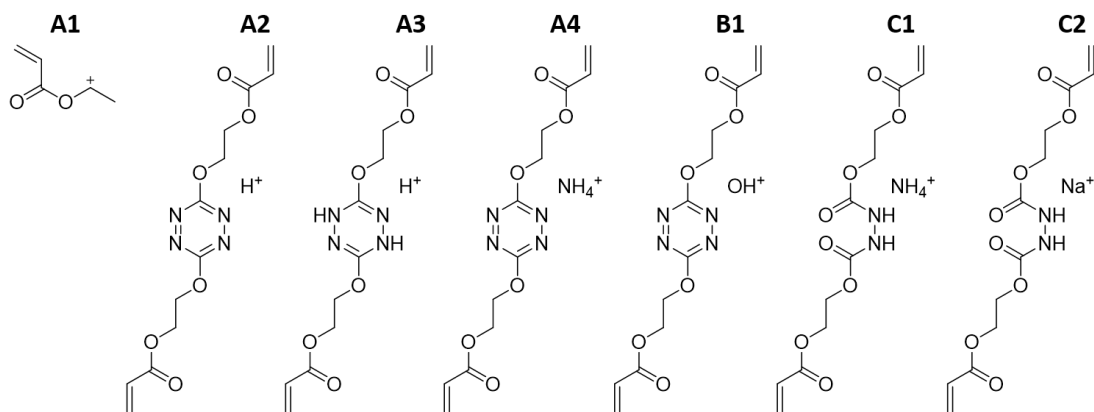


Figure S5-9: Full scale ^1H - (a) and ^{13}C - (b) NMR spectra of TzDA before treatment (olive), after exposure to H_2O_2 (black) and after green light irradiation in presence of H_2O_2 (ochre) in acetonitrile- d_3 .



Scheme S5-1: Found species in the LC-ESI-MS analysis

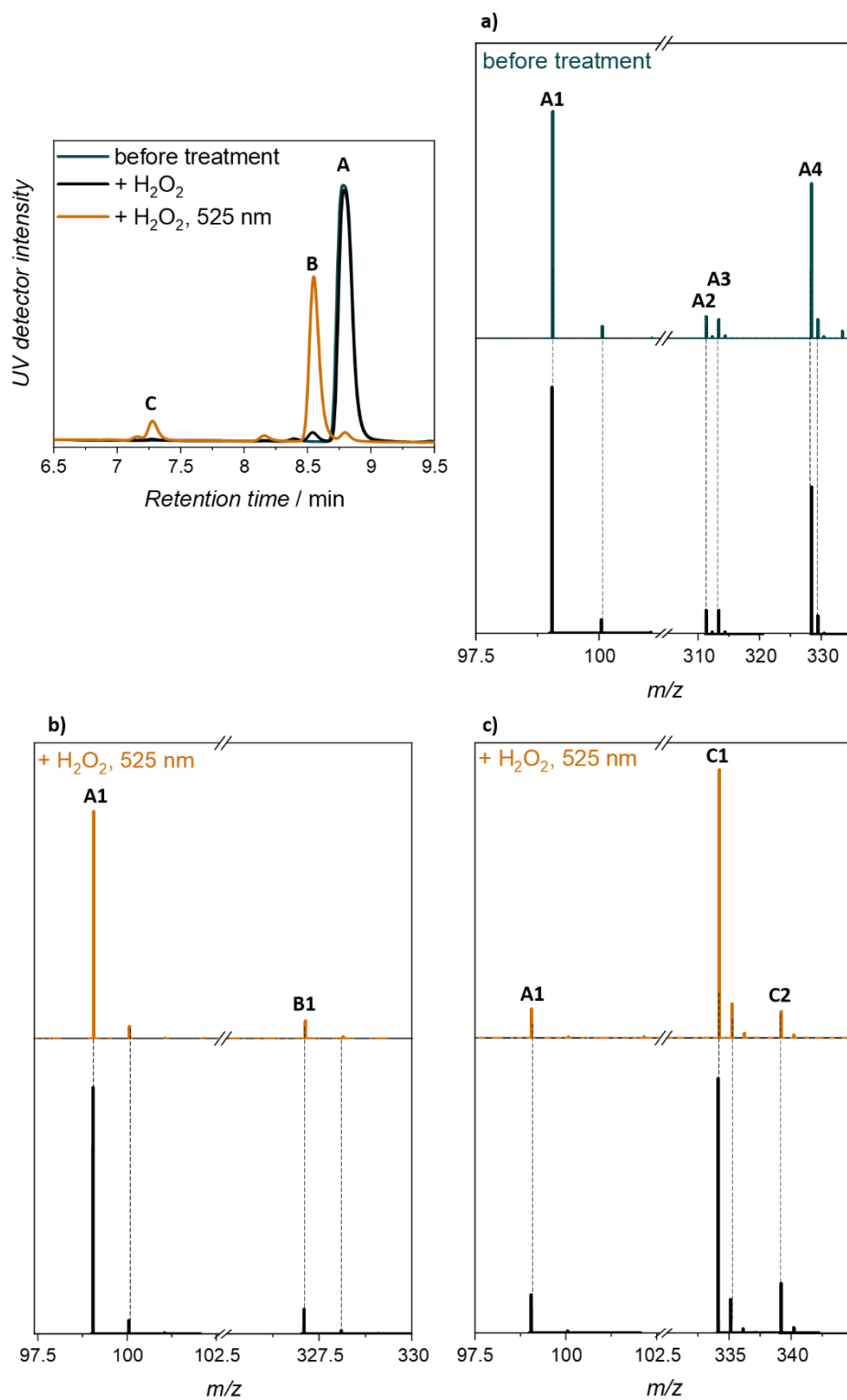


Figure S5-10: LC-ESI mass spectra of TzDA under various conditions. Olive: before treatment, black: after exposure to H₂O₂, ochre: after green light irradiation. The top left panel depicts the chromatograms of each experiment. a) Mass spectrum of peak A and assignment to theoretically derived species. b) Mass spectrum of peak B and assignment to theoretically derived species. c) Mass spectrum of peak C and assignment to theoretically derived species.

Table S5-1: Detailed overview of identified signals in mass spectra **Figure S5-10**, comparison with theoretically expected m/z values, derived error Δ and composition.

Assignment	m/z_{exp}	m/z_{theo}	Δ / ppm	Composition
A1	99.0442	99.0441	1.01	$[\text{C}_5\text{H}_7\text{O}_2]^+$
A2	311.0981	311.0986	1.61	$[\text{C}_{12}\text{H}_{14}\text{N}_4\text{O}_6+\text{H}]^+$
A3	313.1138	313.1143	1.60	$[\text{C}_{12}\text{H}_{16}\text{N}_4\text{O}_6+\text{H}]^+$
A4	328.1246	328.1252	1.83	$[\text{C}_{12}\text{H}_{14}\text{N}_4\text{O}_6+\text{NH}_4]^+$
B1	327.0931	327.0935	1.22	$[\text{C}_{12}\text{H}_{14}\text{N}_4\text{O}_6+\text{OH}]^+$
C1	334.1240	334.1245	1.50	$[\text{C}_{12}\text{H}_{16}\text{N}_2\text{O}_8+\text{NH}_4]^+$
C2	339.0793	339.0799	1.77	$[\text{C}_{12}\text{H}_{16}\text{N}_2\text{O}_8+\text{Na}]^+$

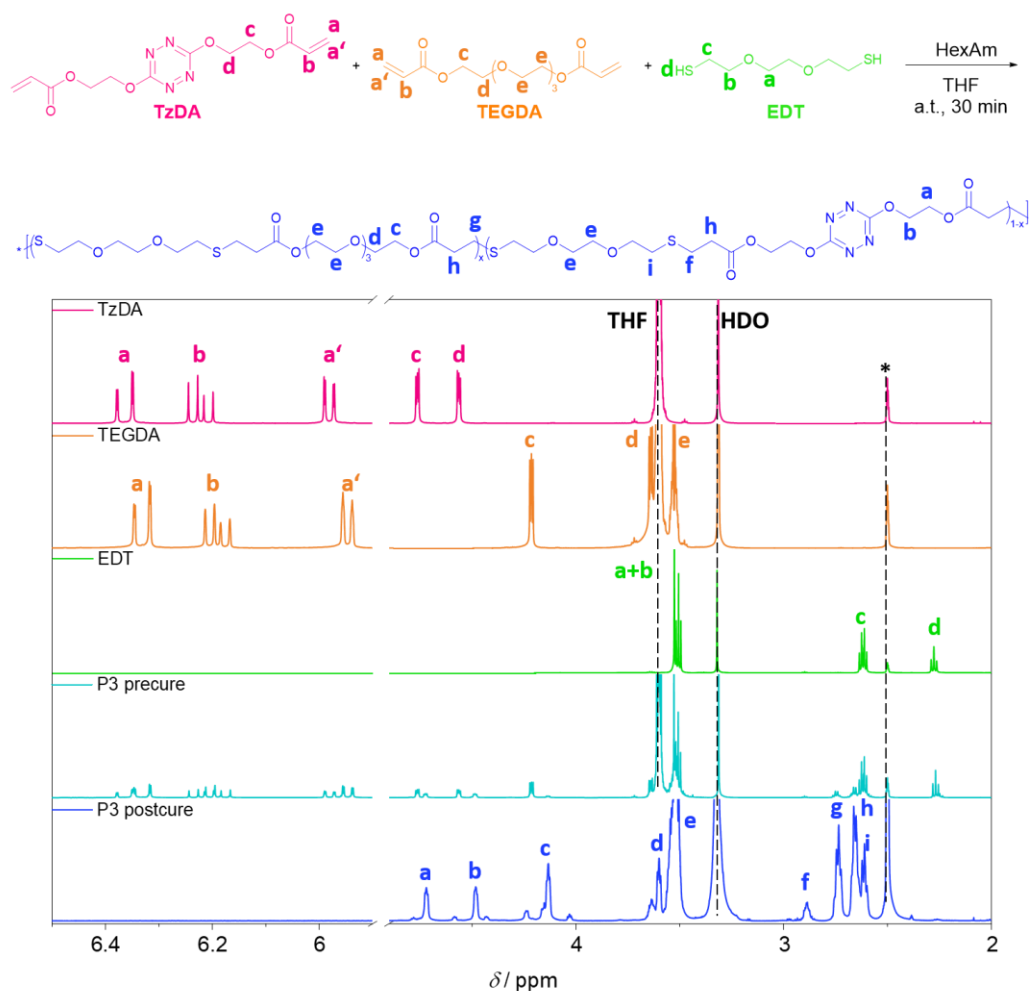


Figure S5-11: Exemplarily $^1\text{H-NMR}$ analysis of **P3** in $\text{DMSO-}d_6$ (*). Assignment of resonances of monomers, the formulation used before polymerisation and the purified polymer after drying (from top to bottom). Enlarged overview of acrylic resonances on the left hand side.

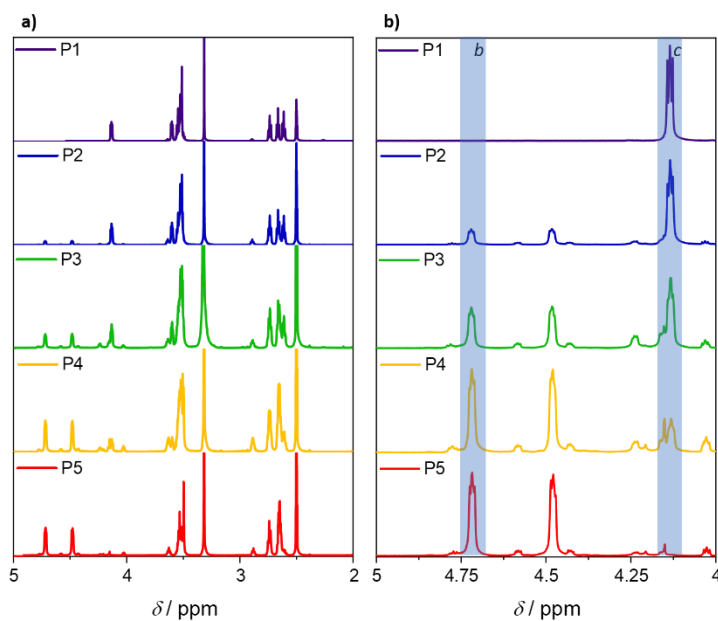


Figure S5-12: a) $^1\text{H-NMR}$ spectra of isolated polymers in $\text{DMSO-}d_6$ (*). b) Enlarged spectra with the resonances of TzDA (*b*) and TEGDA (*c*) highlighted in blue (markings are referred to **Figure S5-11** bottom).

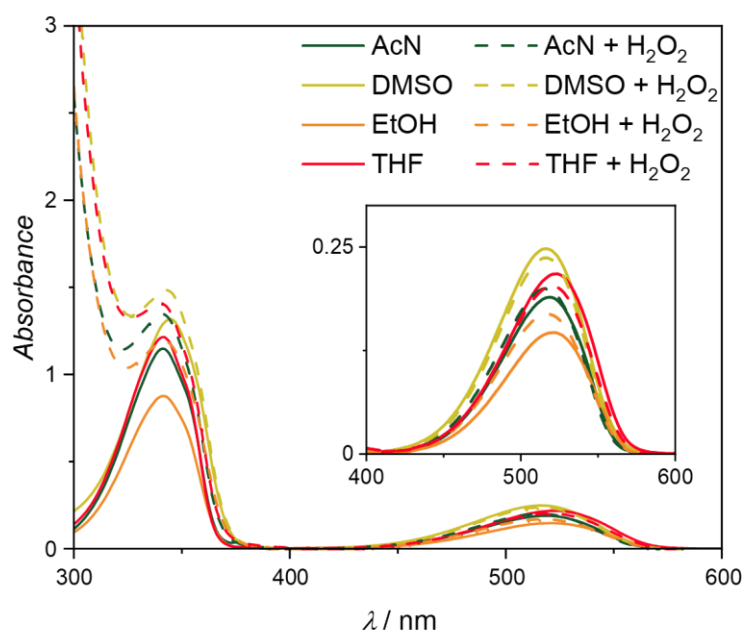


Figure S5-13: UV/Vis absorption spectra of TzDA in absence (solid line) and presence of hydrogen peroxide (H_2O_2 , 6 v%, dashed line). Different solvents were investigated: Acetonitrile (AcN, green), dimethyl sulfoxide (DMSO, ochre), ethanol (EtOH, orange), tetrahydrofuran (THF, red). Inset shows enlarged absorption band around 500 nm.

Table S5-2: Assignment of the experimental mass of TEGAS and TEGASO to its simulation, alongside its derived error and composition.

Assignment	$m/z_{\text{exp.}}$	$m/z_{\text{theo.}}$	Δ / ppm	composition
[TEGAS+NH ₄] ⁺	314.1627	314.1632	1.59	[C ₁₂ H ₂₈ N ₁ O ₆ S ₁] ⁺
[TEGASO+H] ⁺	313.1312	313.1316	1.28	[C ₁₂ H ₂₅ O ₇ S ₁] ⁺
[TEGASO+NH ₄] ⁺	330.1577	330.1581	1.21	[C ₁₂ H ₂₈ N ₁ O ₇ S ₁] ⁺

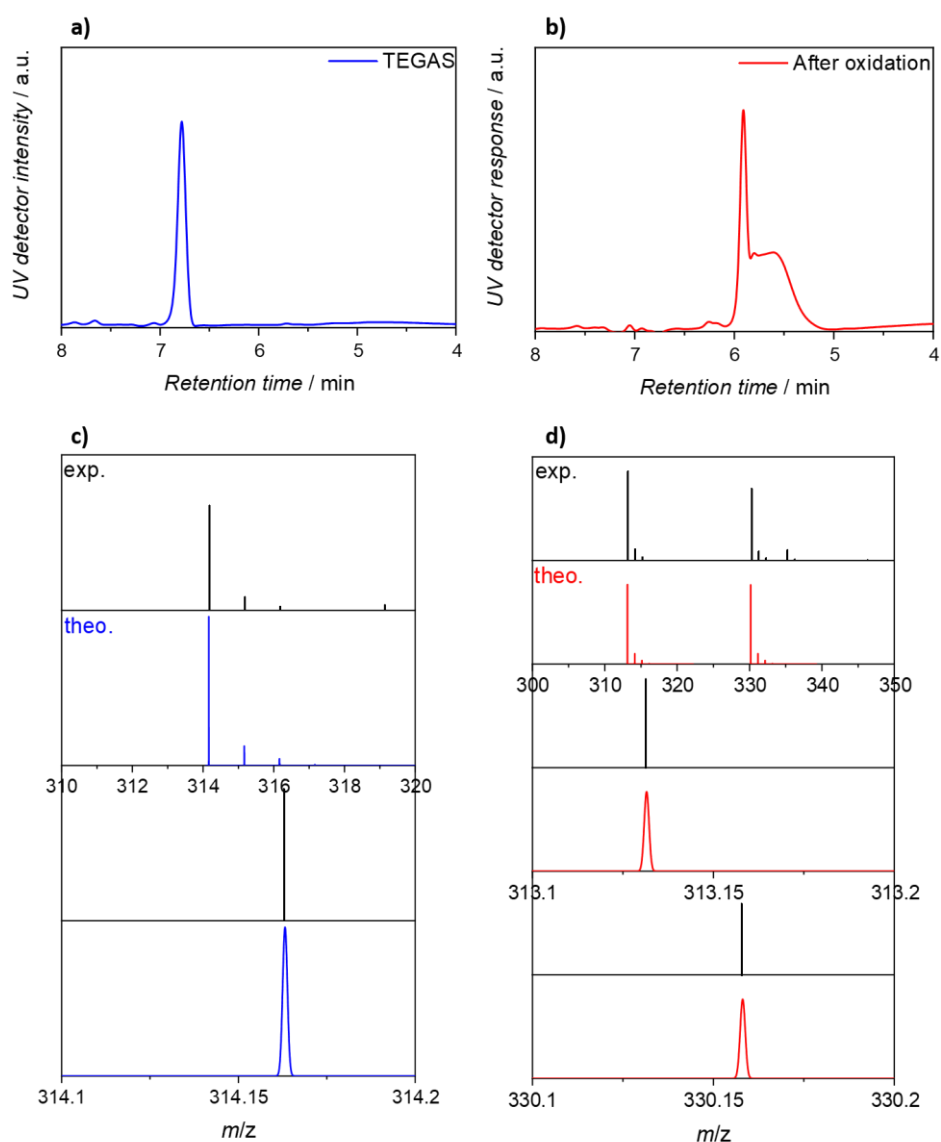


Figure S5-14: LC-ESI-MS analysis of TEGAS after oxidation. UV Chromatograms (254 nm absorbance) of a) TEGAS and b) its oxidation product. Mass spectra for c) TEGAS and d) its oxidation product. Mass spectra were extracted from the increment and compared to simulated isotopic data (top to bottom). A gaussian shape with a deviation of 5 ppm for the simulated species was assumed.

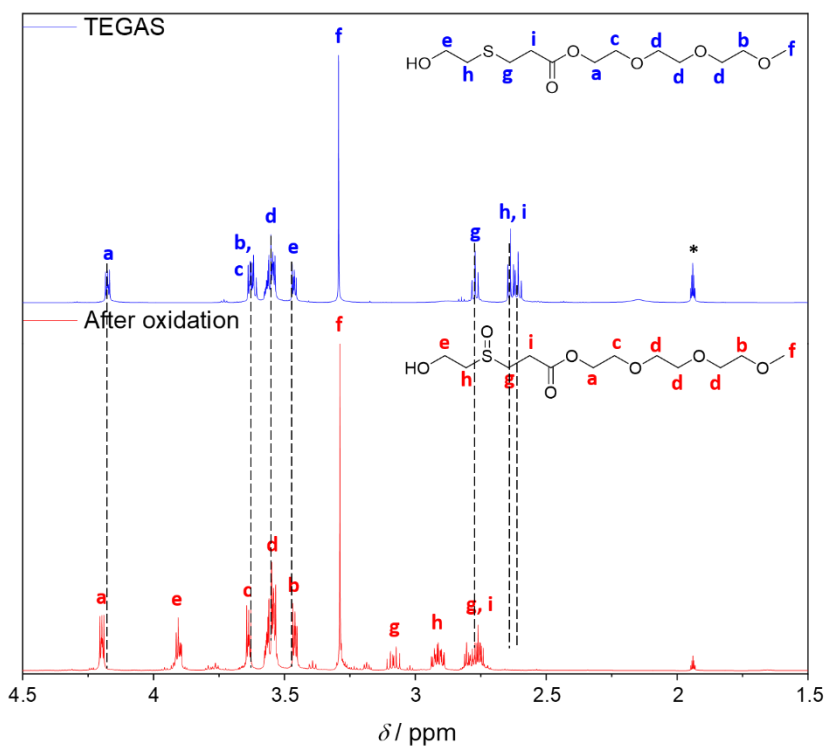
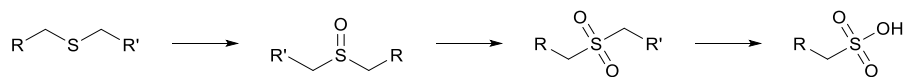


Figure S5-15: ¹H-NMR spectra of TEGAS in acetonitrile-*d*₃ (*) before (blue) and after (red) oxidation.



Scheme S5-2: Oxidative degradation reaction of sulphides. Copyright 2022 Wiley. Used with permission from D. S. Kazybayeva, G. S. Irmukhametova, V. V. Khutoryanskiy, *Polym. Adv Technol.* **2021**, *32*, 2682-2689.^[281]

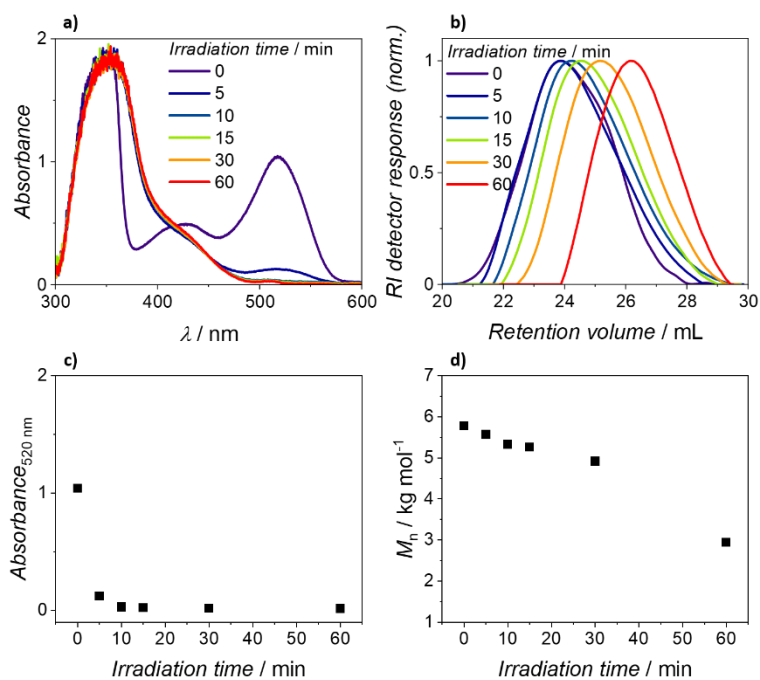


Figure S5-16: P2 in presence of H₂O₂ under green light conditions (λ = 525 nm). a) UV/Vis absorption spectra, recorded at indicated irradiation times. b) SEC traces in THF, recorded at indicated irradiation times. c) Evolution of the 520 nm absorbance. d) Evolution of M_n . M_n was determined according to pMMA calibration.

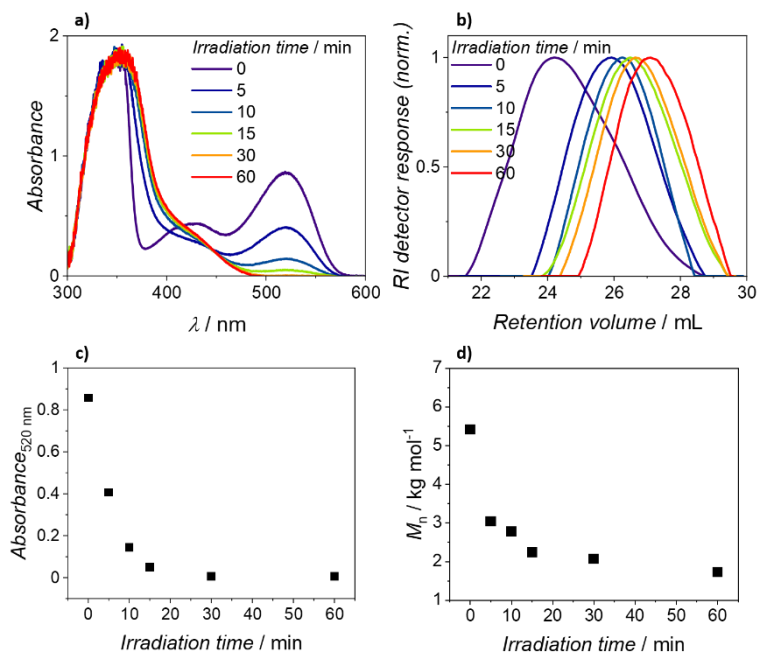


Figure S5-17: P3 in presence of H₂O₂ under green light conditions (λ = 525 nm). a) UV/Vis absorption spectra, recorded at indicated irradiation times. b) SEC traces in THF, recorded at indicated irradiation times. c) Evolution of the 520 nm absorbance. d) Evolution of M_n . M_n was determined according to pMMA calibration.

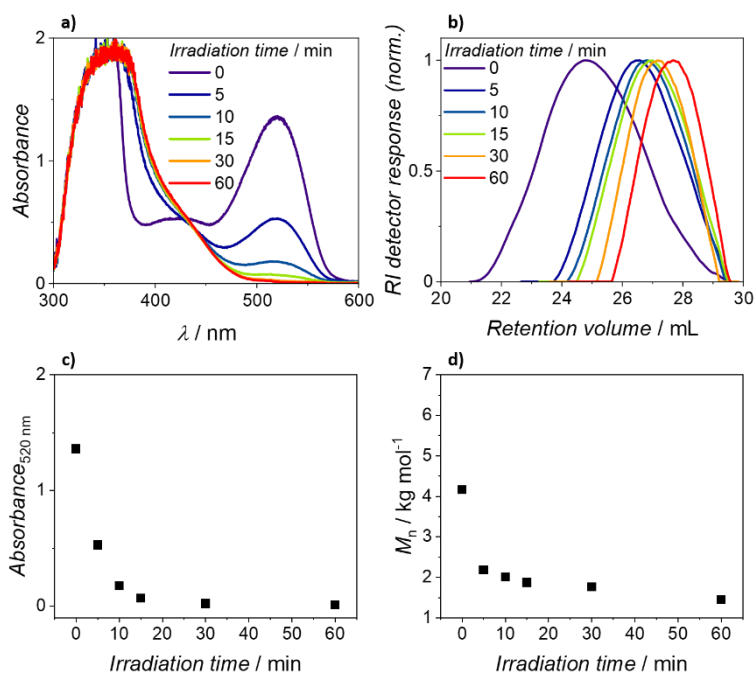


Figure S5-18: P4 in presence of H₂O₂ under green light conditions ($\lambda = 525$ nm). a) UV/Vis absorption spectra, recorded at indicated irradiation times. b) SEC traces in THF, recorded at indicated irradiation times. c) Evolution of the 520 nm absorbance. d) Evolution of M_n . M_n was determined according to pMMA calibration.

Appendix D

Supporting Information for Chapter 6: Wavelength-Orthogonal Stiffening and Inhibition of Hydrogel Networks with Visible Light

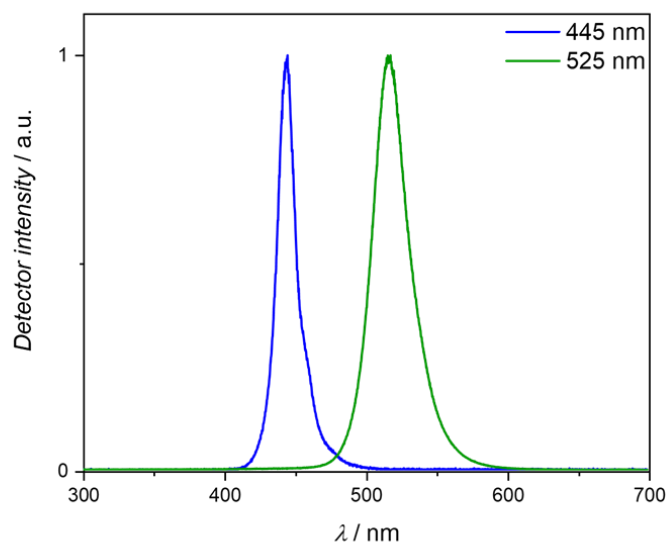


Figure S6-1: Emission spectra of the LED lights used in the rheometer irradiation experiments. Reproduced with permission. © 2022 The Authors. *Angewandte Chemie International Edition* published by Wiley-VCH GmbH.

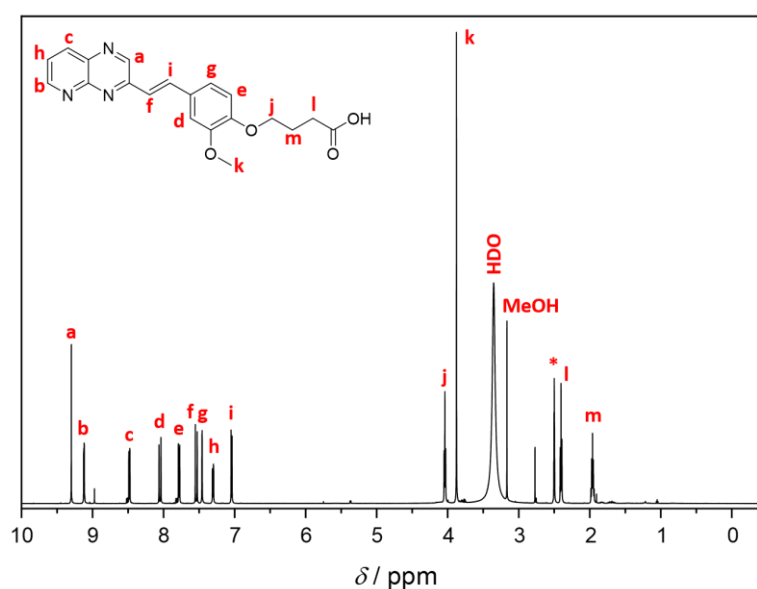


Figure S6-2: $^1\text{H-NMR}$ spectrum of **S3** in $\text{DMSO-}d_6$ (*). Reproduced with permission. © 2022 The Authors. *Angewandte Chemie International Edition* published by Wiley-VCH GmbH.

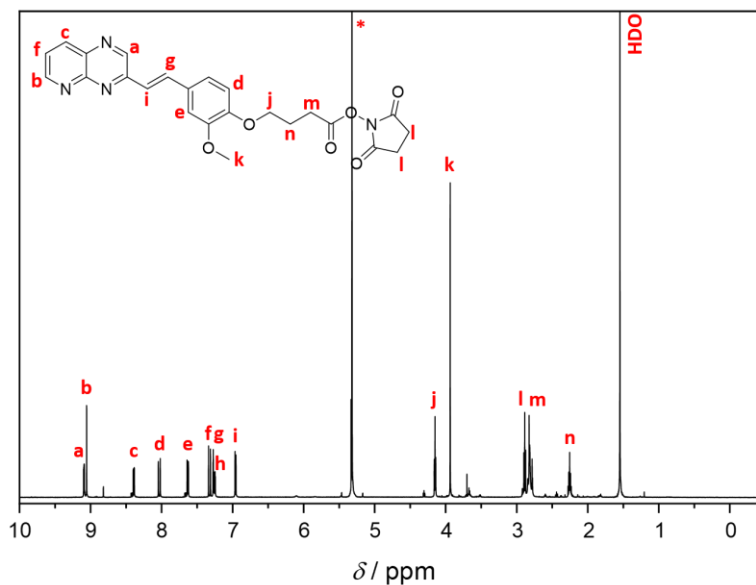


Figure S6-3: $^1\text{H-NMR}$ spectrum of **S4** in CD_2Cl_2 (*). Reproduced with permission. © 2022 The Authors. *Angewandte Chemie International Edition* published by Wiley-VCH GmbH.

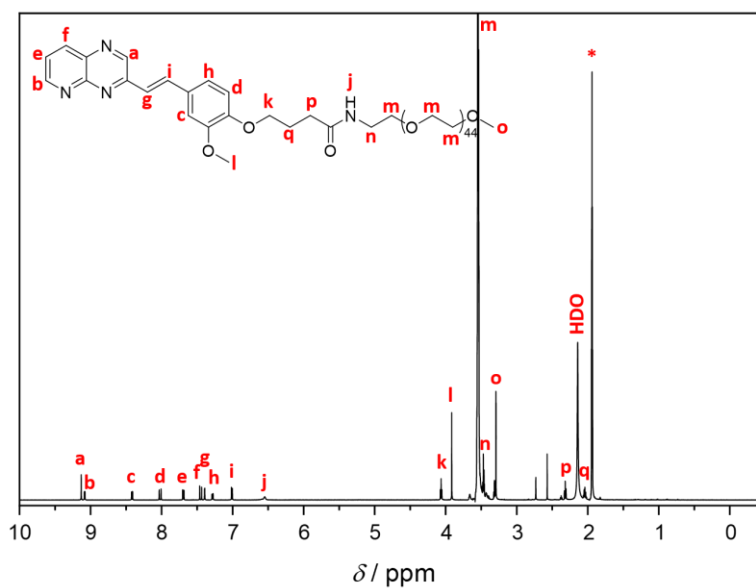


Figure S6-4: $^1\text{H-NMR}$ spectrum of MeO-PEG-SPP in acetonitrile- d_3 (*). Reproduced with permission. © 2022 The Authors. *Angewandte Chemie International Edition* published by Wiley-VCH GmbH.

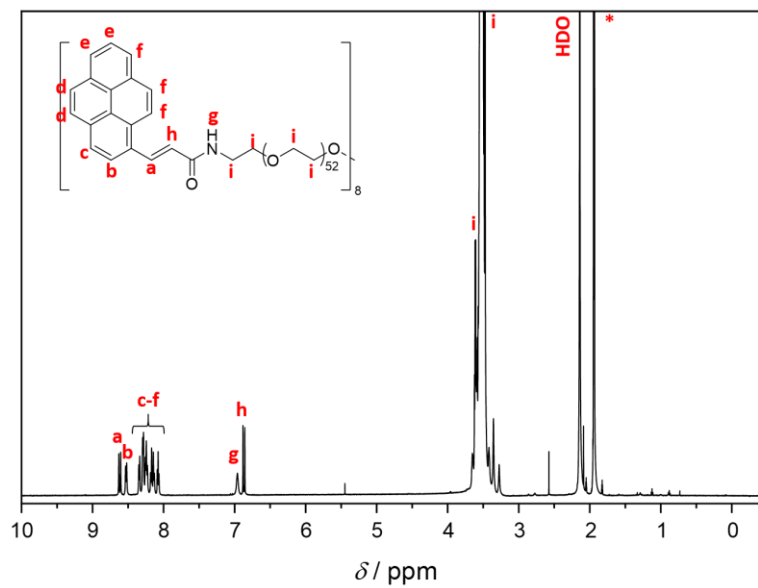


Figure S6-5: $^1\text{H-NMR}$ spectrum of PEG-(AP) $_8$ in acetonitrile- d_3 (*). Reproduced with permission. © 2022 The Authors. Angewandte Chemie International Edition published by Wiley-VCH GmbH.

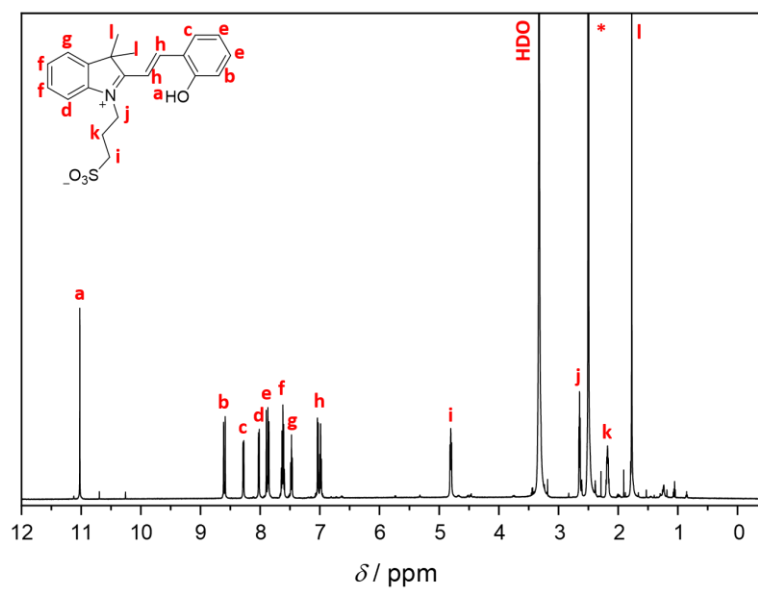


Figure S6-6: $^1\text{H-NMR}$ spectrum of PAG in DMSO- d_6 (*). Reproduced with permission. © 2022 The Authors. Angewandte Chemie International Edition published by Wiley-VCH GmbH.

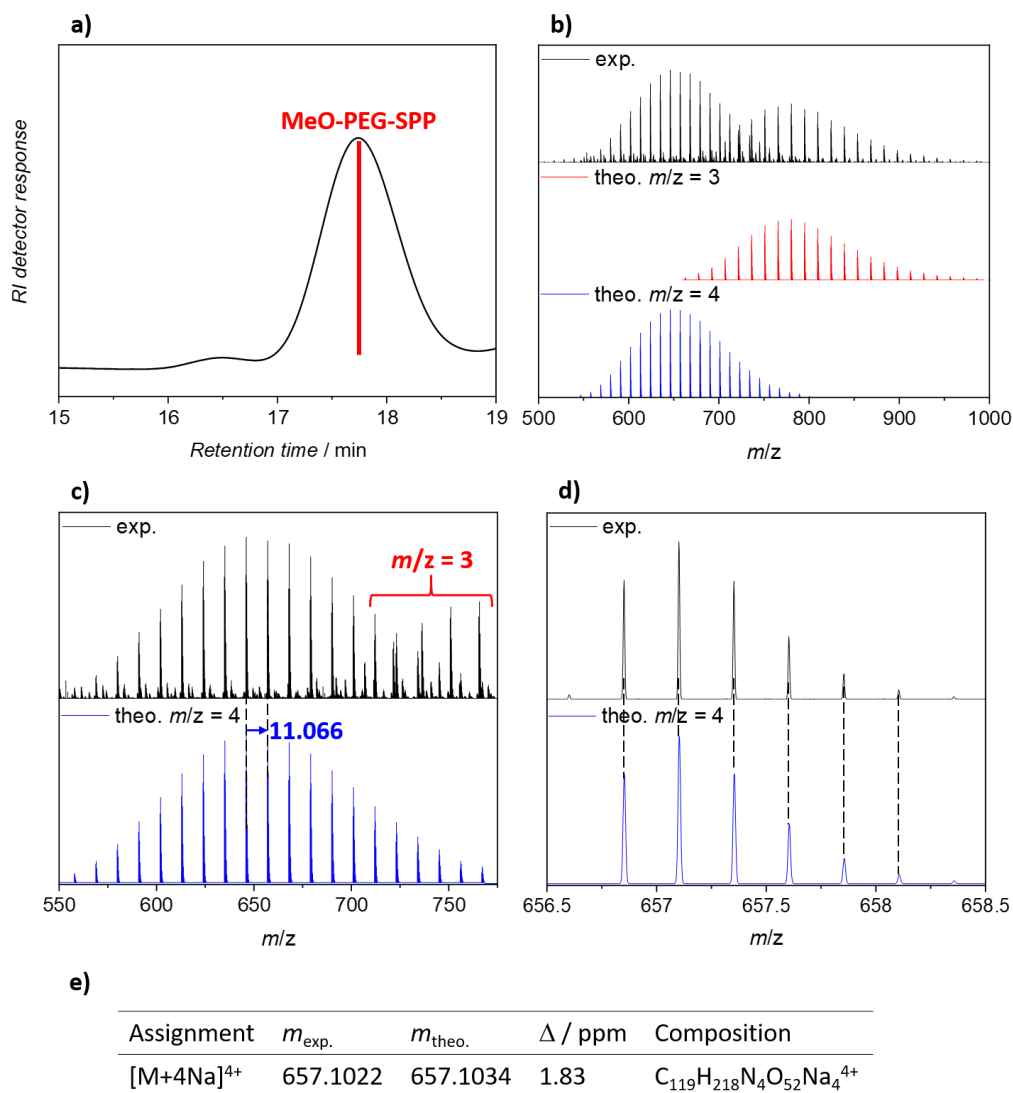


Figure S6-7: a) Refractive Index (RI) SEC trace of MeO-PEG-SPP before irradiation. b) Extracted mass spectrum from the increment and assigned species with $m/z = 3$ and $m/z = 4$. c) Enlarged mass spectrum of the most abundant $m/z = 4$ species and comparison with simulated isotopic data. d) Enlarged mass spectrum of the most abundant peak close to 657 and comparison with isotopic data. e) Assignment of the experimental mass of intact MeO-PEG-SPP to its simulation, alongside its derived error and composition. Reproduced with permission. © 2022 The Authors. Angewandte Chemie International Edition published by Wiley-VCH GmbH.

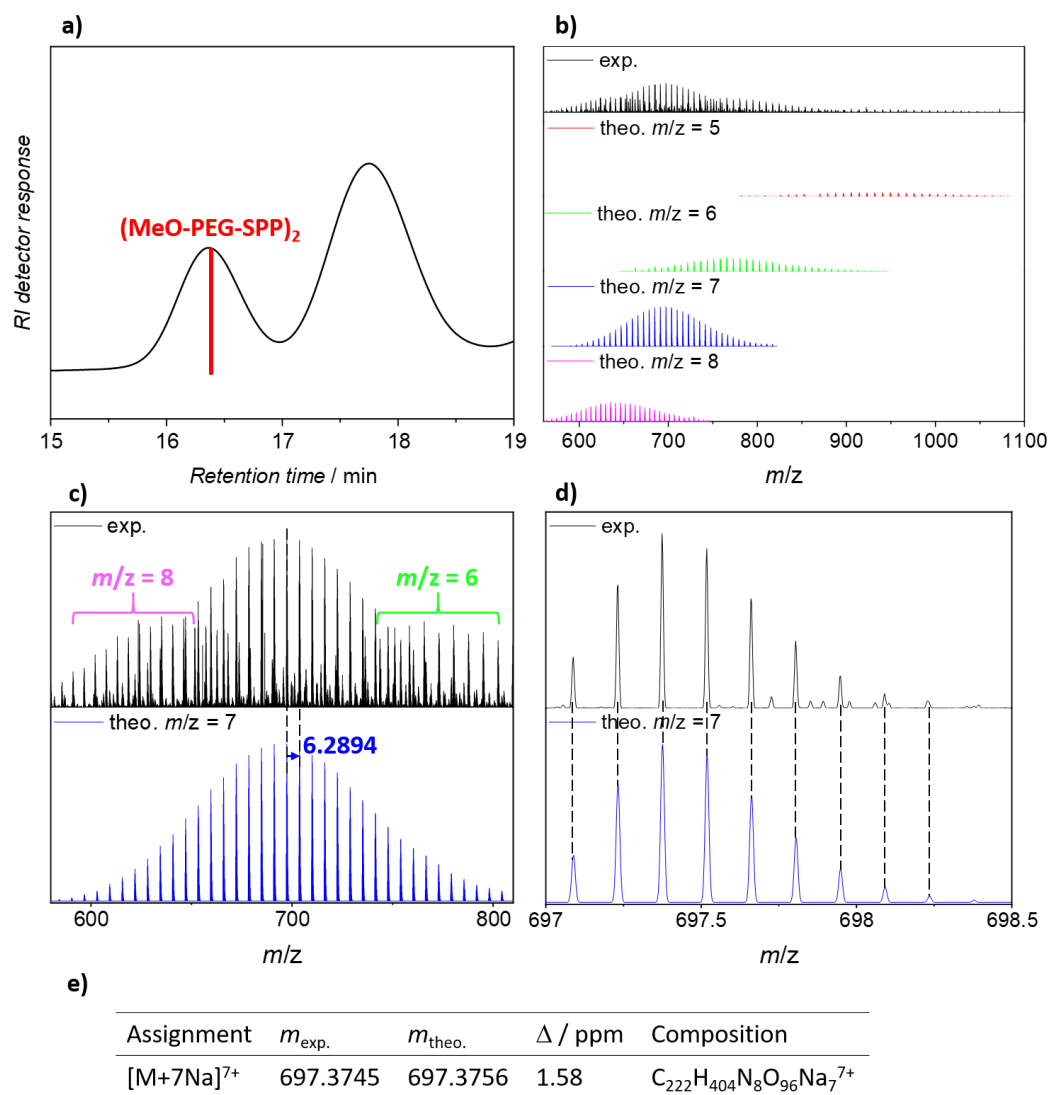
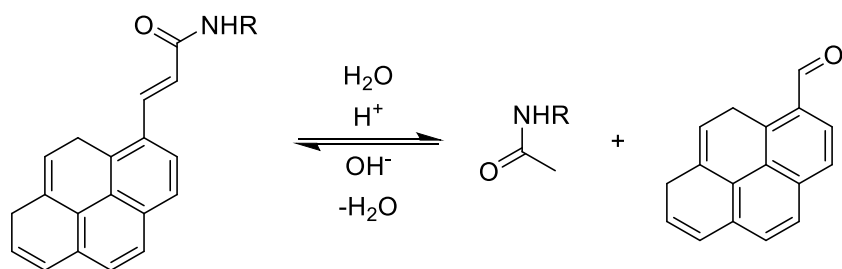


Figure S6-8: A) Refractive Index (RI) SEC trace of MeO-PEG-SPP and (MeO-PEG-SPP)₂ after irradiation. B) Extracted mass spectrum from the increment and assigned species between $m/z = 5$ and $m/z = 8$. C) Enlarged mass spectrum of the most abundant $m/z = 7$ species and comparison with simulated isotopic distribution for the same species. D) Enlarged mass spectrum of the most abundant peak close to 698 and comparison with simulated isotopic distribution for the same species. E) Assignment of the experimental mass of intact (MeO-PEG-SPP)₂ and theoretical mass, as well as its associated derived error and composition. Reproduced with permission. © 2022 The Authors. *Angewandte Chemie International Edition* published by Wiley-VCH GmbH.



Scheme S6-1: Hydrolysis of the styryl moiety under acidic conditions.

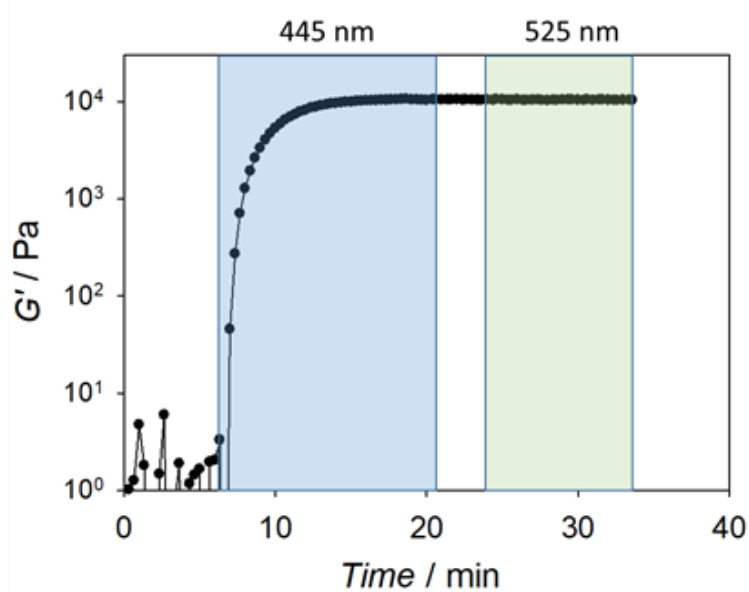


Figure S6-9: Rheology data of PEG-(SPP)₃(AP)₄ solution (5 mM) under irradiation of blue and green light ($I_L = 20 \text{ mW cm}^{-2}$). Reproduced with permission. © 2022 The Authors. *Angewandte Chemie International Edition* published by Wiley-VCH GmbH.

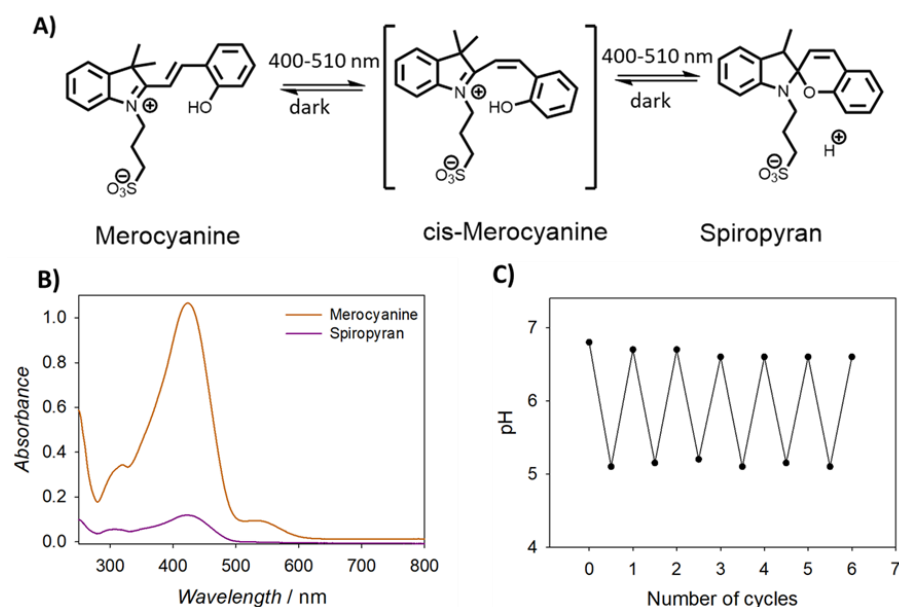


Figure S6-10: A) Photoswitching of the synthesised merocyanine PAG generator by visible light (400-510 nm) to its spiropyran form, releasing a proton during the process. The spiropyran form is rapidly reversed (in 5 min) to the merocyanine form in the dark. B) UV/Vis absorbance spectra of the PAG in the merocyanine and spiropyran forms, respectively. C) The reversible switching of the PAG by light (at 445 nm, 2 min of irradiation) and in the dark (30 min) for up to 6 cycles in a solution having initial pH value of 6.8, displaying the changes in pH after each switch. Reproduced with permission. © 2022 The Authors. *Angewandte Chemie International Edition* published by Wiley-VCH GmbH.

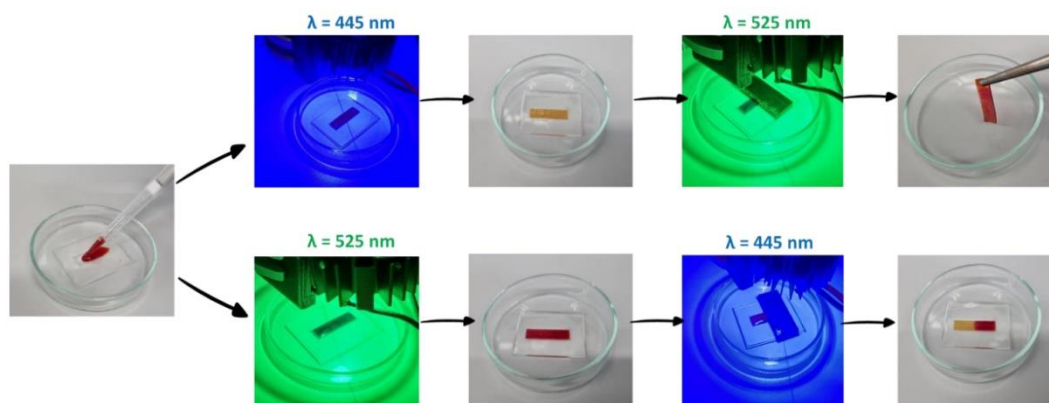


Figure S6-11: From left to right: In the first experiment, hydrogel was formed by irradiating the PEG-(SPP)₃(AP)₄ solution (10wt%, ca. 4.7 mM) and PAG (0.5 mM) with blue light, during which the PAG was switched from its merocyanine form (red) to its spiropyran form (colourless), revealing the yellow colour of the AP and SPP dimer; irradiation of green light, partly covered by a mask, enabling the stiffening of the gel only on the irradiated part, during this time the spiropyran form was reverted back to the merocyanine form. In the second experiment, the gel was initially formed by irradiation with green light, causing no change to the merocyanine; blue light irradiation on the selected part of the gel triggered the second gelation and photobleaching of PAG. Reproduced with permission. © 2022 The Authors. *Angewandte Chemie International Edition* published by Wiley-VCH GmbH.

Bibliography

- [1] A. S. Abd-El-Aziz, M. Antonietti, C. Barner-Kowollik, W. H. Binder, A. Böker, C. Boyer, M. R. Buchmeiser, S. Z. D. Cheng, F. D'Agosto, G. Floudas, H. Frey, G. Galli, J. Genzer, L. Hartmann, R. Hoogenboom, T. Ishizone, D. L. Kaplan, M. Leclerc, A. Lendlein, B. Liu, T. E. Long, S. Ludwigs, J.-F. Lutz, K. Matyjaszewski, M. A. R. Meier, K. Müllen, M. Müllner, B. Rieger, T. P. Russell, D. A. Savin, A. D. Schlüter, U. S. Schubert, S. Seiffert, K. Severing, J. B. P. Soares, M. Staffilani, B. S. Sumerlin, Y. Sun, B. Z. Tang, C. Tang, P. Théato, N. Tirelli, O. K. C. Tsui, M. M. Unterlass, P. Vana, B. Voit, S. Vyazovkin, C. Weder, U. Wiesner, W.-Y. Wong, C. Wu, Y. Yagci, J. Yuan, G. Zhang, *Macromolecular Chemistry and Physics* **2020**, *221*, 2000216.
- [2] R. J. Young, P. A. Lovell, *Introduction to Polymers*, 3rd ed., CRC Press, Boca Raton, USA, **2011**.
- [3] A. Sionkowska, *Progress in Polymer Science* **2011**, *36*, 1254-1276.
- [4] B. Zhu, D. Wang, N. Wei, *Trends in Biotechnology* **2022**, *40*, 22-37.
- [5] Z. Khurshid, M. Zafar, S. Qasim, S. Shahab, M. Naseem, A. AbuReqaiba, *Materials* **2015**, *8*, 717-731.
- [6] L. Lebreton, A. Andrady, *Palgrave Communications* **2019**, *5*, 6.
- [7] T. R. Walker, *Marine Pollution Bulletin* **2022**, *176*, 113447.
- [8] S. B. Borrelle, J. Ringma, K. L. Law, C. C. Monnahan, L. Lebreton, A. McGivern, E. Murphy, J. Jambeck, G. H. Leonard, M. A. Hilleary, M. Eriksen, H. P. Possingham, H. De Frond, L. R. Gerber, B. Polidoro, A. Tahir, M. Bernard, N. Mallos, M. Barnes, C. M. Rochman, *Science* **2020**, *369*, 1515-1518.
- [9] A. Egüez, *Journal of Environmental Management* **2021**, *280*, 111672.
- [10] F. R. Wurm, S. Spierling, H.-J. Endres, L. Barner, *Macromolecular Rapid Communications* **2020**, *41*, 2000351.
- [11] G. Brennan, M. Tennant, F. Blomsma, *Business and production solutions: closing loops and the circular economy*, 1st ed., Routledge, Oxforshire, UK, **2015**.

- [12] B. Singh, N. Sharma, *Polymer Degradation and Stability* **2008**, 93, 561-584.
- [13] Y. He, H. Li, X. Xiao, X. Zhao, *E3S Web Conf.* **2021**, 290, 01012.
- [14] D. J. Carlsson, D. M. Wiles, *Journal of Macromolecular Science, Part C* **1976**, 14, 65-106.
- [15] C. Fei Guo, T. Sun, F. Cao, Q. Liu, Z. Ren, *Light: Science & Applications* **2014**, 3, e161-e161.
- [16] E. F. Schubert, J. K. Kim, *Science* **2005**, 308, 1274-1278.
- [17] R. Wehner, *Scientific American* **1976**, 235, 106-115.
- [18] M. F. Hohmann-Marriott, R. E. Blankenship, *Annual Review of Plant Biology* **2011**, 62, 515-548.
- [19] D. Polli, P. Altoè, O. Weingart, K. M. Spillane, C. Manzoni, D. Brida, G. Tomasello, G. Orlandi, P. Kukura, R. A. Mathies, M. Garavelli, G. Cerullo, *Nature* **2010**, 467, 440-443.
- [20] S. Aubert, M. Bezagu, A. C. Spivey, S. Arseniyadis, *Nature Reviews Chemistry* **2019**, 3, 706-722.
- [21] R. J. Marcus, J. A. Kent, G. O. Schenck, *Industrial & Engineering Chemistry* **1962**, 54, 20-28.
- [22] J. L. Schnapf, T. W. Kraft, D. A. Baylor, *Nature* **1987**, 325, 439-441.
- [23] B. Valeur, M. N. Berberan-Santos, *Molecular Fluorescence: Principles and Applications*, 2nd ed., WILEY-VCH Verlag GmbH & Co. KGaA, Weinheim, Germany, **2012**.
- [24] M. Oelgemöller, N. Hoffmann, *Organic & Biomolecular Chemistry* **2016**, 14, 7392-7442.
- [25] P. W. Atkins, R. S. Friedman, *Molecular Quantum Mechanics*, OUP Oxford, **2011**.
- [26] N. J. Turro, V. Ramamurthy, J. Scaiano, *Modern Molecular Photochemistry of Organic Molecules*, University Science Books, Sausalito, USA, **2010**.
- [27] G. F. Wedler, Hans-Joachim, *Lehr- und Arbeitsbuch physikalische Chemie*, 7th ed., Wiley-VCH, Weinheim, Germany, **2018**.
- [28] A. Jablonski, *Nature* **1933**, 131, 839-840.
- [29] R. K. Venkatraman, A. J. Orr-Ewing, *Accounts of Chemical Research* **2021**, 54, 4383-4394.
- [30] V. Balevičius Jr, T. Wei, D. Di Tommaso, D. Abramavicius, J. Hauer, T. Polívka, C. D. P. Duffy, *Chemical Science* **2019**, 10, 4792-4804.

- [31] C. M. Marian, *WIREs Computational Molecular Science* **2012**, 2, 187-203.
- [32] V. G. Plotnikov, *International Journal of Quantum Chemistry* **1979**, 16, 527-541.
- [33] M. Kasha, *Discussions of the Faraday Society* **1950**, 9, 14-19.
- [34] M. Y. Berezin, S. Achilefu, *Chemical Reviews* **2010**, 110, 2641-2684.
- [35] H.-T. Feng, J. Zeng, P.-A. Yin, X.-D. Wang, Q. Peng, Z. Zhao, J. W. Y. Lam, B. Z. Tang, *Nature Communications* **2020**, 11, 2617.
- [36] J. K. McCusker, *Accounts of Chemical Research* **2003**, 36, 876-887.
- [37] M. A. El-Sayed, *The Journal of Chemical Physics* **1963**, 38, 2834-2838.
- [38] G. N. Lewis, M. Kasha, *Journal of the American Chemical Society* **1945**, 67, 994-1003.
- [39] P. Jöckle, C. Schweigert, I. Lamparth, N. Moszner, A.-N. Unterreiner, C. Barner-Kowollik, *Macromolecules* **2017**, 50, 8894-8906.
- [40] P. Jöckle, P. W. Kamm, I. Lamparth, N. Moszner, A.-N. Unterreiner, C. Barner-Kowollik, *Macromolecules* **2019**, 52, 281-291.
- [41] T. Schmierer, F. Bley, K. Schaper, P. Gilch, *Journal of Photochemistry and Photobiology A: Chemistry* **2011**, 217, 363-368.
- [42] D. Gravel, R. Giasson, D. Blanchet, R. W. Yip, D. K. Sharma, *Canadian Journal of Chemistry* **1991**, 69, 1193-1200.
- [43] S. Poplata, A. Tröster, Y.-Q. Zou, T. Bach, *Chemical Reviews* **2016**, 116, 9748-9815.
- [44] D. I. Schuster, G. Lem, N. A. Kaprinidis, *Chemical reviews* **1993**, 93, 3-22.
- [45] T. Wolff, H. Görner, *Physical Chemistry Chemical Physics* **2004**, 6, 368-376.
- [46] C. Li, *Nonlinear Optics*, Shanghai Jiao Tong University Press, Shanghai, China, **2015**.
- [47] W. Demtröder, *Laser Spectroscopy*, 3rd ed., Springer Berlin, Heidelberg, New York, USA, **2003**.
- [48] E. Riedle, M. Beutter, S. Lochbrunner, J. Piel, S. Schenkl, S. Spörlein, W. Zinth, *Applied Physics B* **2000**, 71, 457-465.
- [49] R. R. Alfano, *The Supercontinuum Laser Source*, 3rd ed., Springer Science+Business Media, New York, USA, **2016**.
- [50] P. J. M. Johnson, V. I. Prokhorenko, R. J. D. Miller, *Opt. Express* **2009**, 17, 21488-21496.
- [51] J. A. Barltrop, P. J. Plant, P. Schofield, *Chem. Commun.* **1966**, 822-823.

- [52] J. K. Kochi, *Accounts of Chemical Research* **1992**, 25, 39-47.
- [53] E. D. Hughes, C. K. Ingold, R. I. Reed, *Journal of the Chemical Society (Resumed)* **1950**, 2400-2440.
- [54] Y. Nieves-Quinones, D. A. Singleton, *Journal of the American Chemical Society* **2016**, 138, 15167-15176.
- [55] G. A. Olah, H. C. Lin, J. A. Olah, S. C. Narang, *Proceedings of the National Academy of Sciences* **1978**, 75, 545-548.
- [56] D. J. Belson, A. N. Strachan, *Journal of the Chemical Society, Perkin Transactions 2* **1989**, 15-19.
- [57] C. L. Coon, W. G. Blucher, M. E. Hill, *The Journal of Organic Chemistry* **1973**, 38, 4243-4248.
- [58] R. W. Millar, M. E. Colclough, P. Golding, P. J. Honey, N. C. Paul, A. J. Sanderson, M. J. Stewart, F. Volk, B. J. Thomson, J. E. Field, P. Gray, *Philosophical Transactions of the Royal Society of London. Series A: Physical and Engineering Sciences* **1992**, 339, 305-319.
- [59] C. C. Price, C. A. Sears, *Journal of the American Chemical Society* **1953**, 75, 3276-3277.
- [60] T. C. Bruice, M. J. Gregory, S. L. Walters, *Journal of the American Chemical Society* **1968**, 90, 1612-1619.
- [61] M. Sokolovsky, J. F. Riordan, B. L. Vallee, *Biochemistry* **1966**, 5, 3582-3589.
- [62] C. A. Cupas, R. L. Pearson, *Journal of the American Chemical Society* **1968**, 90, 4742-4743.
- [63] S. J. Kuhn, G. A. Olah, *Journal of the American Chemical Society* **1961**, 83, 4564-4571.
- [64] G. Wettermark, *The Journal of Physical Chemistry* **1962**, 66, 2560-2562.
- [65] M. V. George, J. C. Scaiano, *The Journal of Physical Chemistry* **1980**, 84, 492-495.
- [66] D. Gravel, J. Hebert, D. Thoraval, *Canadian Journal of Chemistry* **1983**, 61, 400-410.
- [67] T. Schmierer, S. Laimgruber, K. Haiser, K. Kiewisch, J. Neugebauer, P. Gilch, *Physical Chemistry Chemical Physics* **2010**, 12, 15653-15664.
- [68] C. G. Bochet, *Journal of the Chemical Society, Perkin Transactions 1* **2002**, 125-142.

- [69] C. H. Bamford, R. G. W. Norrish, *Journal of the Chemical Society (Resumed)* **1935**, 1504-1511.
- [70] W. Ried, M. Wilk, *Justus Liebigs Annalen der Chemie* **1954**, 590, 91-110.
- [71] K. Schaper, *Magnetic Resonance in Chemistry* **2008**, 46, 1163-1167.
- [72] B. G. Gowenlock, M. J. Maidment, K. G. Orrell, I. Prokě, J. R. Roberts, *Journal of the Chemical Society, Perkin Transactions 2* **2001**, 1904-1911.
- [73] W. Horspool, F. Lenci, 2nd ed., CRC Press LLC, Boca Raton, USA, **2000**.
- [74] Y. V. Il'ichev, M. A. Schwörer, J. Wirz, *Journal of the American Chemical Society* **2004**, 126, 4581-4595.
- [75] C. Marinzi, J. Offer, R. Longhi, P. E. Dawson, *Bioorganic & Medicinal Chemistry* **2004**, 12, 2749-2757.
- [76] A.-D. Guo, D. Wei, H.-J. Nie, H. Hu, C. Peng, S.-T. Li, K.-N. Yan, B.-S. Zhou, L. Feng, C. Fang, M. Tan, R. Huang, X.-H. Chen, *Nature Communications* **2020**, 11, 5472.
- [77] E. Abou Nakad, F. Bolze, A. Specht, *Organic & Biomolecular Chemistry* **2018**, 16, 6115-6122.
- [78] X. Hu, J. Shi, S. W. Thomas, *Polymer Chemistry* **2015**, 6, 4966-4971.
- [79] M. Kim, H. Chung, *Polym. Chem. UK* **2017**, 8, 6300-6308.
- [80] D. Klinger, K. Landfester, *Soft Matter* **2011**, 7, 1426-1440.
- [81] O. Bertrand, J.-M. Schumers, C. Kuppen, J. Marchand-Brynaert, C.-A. Fustin, J.-F. Gohy, *Soft Matter* **2011**, 7, 6891-6896.
- [82] B. E. Tebikachew, K. Börjesson, N. Kann, K. Moth-Poulsen, *Bioconjugate Chemistry* **2018**, 29, 1178-1185.
- [83] D. Kehrloesser, P. J. Behrendt, N. Hampp, *J. Photoch. Photobio. A* **2012**, 248, 8-14.
- [84] S. Bühler, I. Lagoja, H. Giegrich, K.-P. Stengele, W. Pfeleiderer, *Helvetica Chimica Acta* **2004**, 87, 620-659.
- [85] L. Donato, A. Mourrot, C. M. Davenport, C. Herbivo, D. Warther, J. Léonard, F. Bolze, J.-F. Nicoud, R. H. Kramer, M. Goeldner, A. Specht, *Angewandte Chemie International Edition* **2012**, 51, 1840-1843.
- [86] L. García-Fernández, C. Herbivo, V. S. M. Arranz, D. Warther, L. Donato, A. Specht, A. del Campo, *Advanced Materials* **2014**, 26, 5012-5017.
- [87] C. P. Holmes, *The Journal of Organic Chemistry* **1997**, 62, 2370-2380.

- [88] G. N. Lipunova, E. V. Nosova, G. V. Zyryanov, V. N. Charushin, O. N. Chupakhin, *Organic Chemistry Frontiers* **2021**, *8*, 5182-5205.
- [89] A. M. Churakov, V. A. Tartakovsky, *Chemical Reviews* **2004**, *104*, 2601-2616.
- [90] R. N. Butler, D. Cunningham, P. McArdle, G. A. O'Halloran, *Journal of the Chemical Society, Chemical Communications* **1988**, 232-234.
- [91] Y. Gao, Y. Lam, *Journal of Combinatorial Chemistry* **2010**, *12*, 69-74.
- [92] T. Kaihoh, T. Itoh, K. Yamaguchi, A. Ohsawa, *Journal of the Chemical Society, Chemical Communications* **1988**, 1608-1609.
- [93] A. E. Baydar, G. V. Boyd, P. F. Lindley, A. R. Walton, *Journal of the Chemical Society, Perkin Transactions 1* **1985**, 415-418.
- [94] Z.-C. Wu, D. L. Boger, *Journal of the American Chemical Society* **2019**, *141*, 16388-16397.
- [95] A. Pinner, *Berichte der deutschen chemischen Gesellschaft* **1893**, *26*, 2126-2135.
- [96] M. R. Karver, R. Weissleder, S. A. Hilderbrand, *Bioconjugate Chemistry* **2011**, *22*, 2263-2270.
- [97] W. Chen, D. Wang, C. Dai, D. Hamelberg, B. Wang, *Chemical Communications* **2012**, *48*, 1736-1738.
- [98] J. Zhu, J. Hiltz, R. B. Lennox, R. Schirmacher, *Chemical Communications* **2013**, *49*, 10275-10277.
- [99] H. Wu, N. K. Devaraj, *Accounts of Chemical Research* **2018**, *51*, 1249-1259.
- [100] D. L. Boger, S. M. Sakya, *The Journal of Organic Chemistry* **1988**, *53*, 1415-1423.
- [101] A. R. Katritzky, C. A. Ramsden, J. A. Joule, V. V. Zhdankin, V. V. Zhdankin, *Handbook of Heterocyclic Chemistry*, Elsevier, London, UNITED KINGDOM, **2010**.
- [102] S. Mayer, K. Lang, *Synthesis* **2017**, *49*, 830-848.
- [103] D. Wang, W. Chen, Y. Zheng, C. Dai, K. Wang, B. Ke, B. Wang, *Organic & Biomolecular Chemistry* **2014**, *12*, 3950-3955.
- [104] J. Waluk, J. Spanget-Larsen, E. W. Thulstrup, *Chemical Physics* **1995**, *200*, 201-213.
- [105] A. C. Scheiner, G. E. Scuseria, H. F. Schaefer, *Journal of the American Chemical Society* **1986**, *108*, 8160-8162.

- [106] V. L. Windisch, A. B. Smith, R. M. Hochstrasser, *The Journal of Physical Chemistry* **1988**, *92*, 5366-5370.
- [107] M. J. Tucker, J. R. Courter, J. Chen, O. Atasoylu, A. B. Smith III, R. M. Hochstrasser, *Angewandte Chemie International Edition* **2010**, *49*, 3612-3616.
- [108] M. J. Tucker, M. Abdo, J. R. Courter, J. Chen, A. B. Smith, R. M. Hochstrasser, *Journal of Photochemistry and Photobiology A: Chemistry* **2012**, *234*, 156-163.
- [109] D. E. Chavez, M. A. Hiskey, R. D. Gilardi, *Angewandte Chemie International Edition* **2000**, *39*, 1791-1793.
- [110] D. E. Chavez, S. K. Hanson, J. M. Veauthier, D. A. Parrish, *Angewandte Chemie International Edition* **2013**, *52*, 6876-6879.
- [111] R. B. Woodward, R. Hoffmann, *Angewandte Chemie International Edition in English* **1969**, *8*, 781-853.
- [112] C. W. David, *Journal of Chemical Education* **1999**, *76*, 999.
- [113] I. Fleming, *Molecular Orbitals and Organic Chemical Reactions: Reference edition*, Wiley & Sons, Ltd, Chichester, United Kingdom, **2010**.
- [114] Y. Inaki, H. Hiratsuka, *Journal of Photopolymer Science and Technology* **2000**, *13*, 739-744.
- [115] W. G. Kim, *Journal of Applied Polymer Science* **2008**, *107*, 3615-3624.
- [116] S. R. Trenor, T. E. Long, B. J. Love, *Macromolecular Chemistry and Physics* **2004**, *205*, 715-723.
- [117] N. Yonezawa, T. Yoshida, M. Hasegawa, *Journal of the Chemical Society, Perkin Transactions 1* **1983**, 1083-1086.
- [118] G. M. Wyman, *Chemical Reviews* **1955**, *55*, 625-657.
- [119] S. Takeuchi, S. Ruhman, T. Tsuneda, M. Chiba, T. Taketsugu, T. Tahara, *Science* **2008**, *322*, 1073-1077.
- [120] D. E. Marschner, H. Frisch, J. T. Offenloch, B. T. Tuten, C. R. Becer, A. Walther, A. S. Goldmann, P. Tzvetkova, C. Barner-Kowollik, *Macromolecules* **2018**, *51*, 3802-3807.
- [121] N. P. Kovalenko, A. Abdulkadirov, V. I. Gerko, M. V. Alfimov, *Journal of Applied Spectroscopy* **1980**, *32*, 607-612.
- [122] I. M. Irshadeen, K. De Bruycker, A. S. Micallef, S. L. Walden, H. Frisch, C. Barner-Kowollik, *Polymer Chemistry* **2021**, *12*, 4903-4909.

- [123] V. X. Truong, J. Bachmann, A.-N. Unterreiner, J. P. Blinco, C. Barner-Kowollik, *Angewandte Chemie International Edition* **2022**, *61*, e202113076.
- [124] V. X. Truong, F. Li, F. Ercole, J. S. Forsythe, *ACS Macro Letters* **2018**, *7*, 464-469.
- [125] H. Staudinger, M. Brunner, K. Frey, P. Garbsch, R. Signer, S. Wehrli, *Berichte der deutschen chemischen Gesellschaft (A and B Series)* **1929**, *62*, 241-263.
- [126] H. Staudinger, E. Geiger, E. Huber, *Berichte der deutschen chemischen Gesellschaft (A and B Series)* **1929**, *62*, 263-267.
- [127] R. Mülhaupt, *Angewandte Chemie International Edition* **2004**, *43*, 1054-1063.
- [128] C. A. I. Guise-Richardson, *Technology and Culture* **2010**, *51*, 357-387.
- [129] C. J. Rhodes, *Science Progress* **2018**, *101*, 207-260.
- [130] R. U. Halden, *Annual Review of Public Health* **2010**, *31*, 179-194.
- [131] S. Koltzenburg, M. Maskos, O. Nuyken, *Polymer Chemistry*, Springer-Verlag Berlin Heidelberg, Berlin, Germany, **2017**.
- [132] G. Mei, P. Herben, C. Cagnani, A. Mazzucco, *Macromolecular Symposia* **2006**, *245-246*, 677-680.
- [133] K. Leach, *Journal of Microencapsulation* **1999**, *16*, 153-167.
- [134] K. W. Suh, C. P. Park, M. J. Maurer, M. H. Tusim, R. D. Genova, R. Broos, D. P. Sophia, *Advanced Materials* **2000**, *12*, 1779-1789.
- [135] A. L. Andradý, M. A. Neal, *Philosophical Transactions of the Royal Society B: Biological Sciences* **2009**, *364*, 1977-1984.
- [136] S. Liu, R. Maheshwari, K. L. Kiick, *Macromolecules* **2009**, *42*, 3-13.
- [137] P. J. Flory, *Chemical Reviews* **1946**, *39*, 137-197.
- [138] W. H. Carothers, *Chemical Reviews* **1931**, *8*, 353-426.
- [139] G. Odian, *Principles of polymerization*, John Wiley & Sons, Inc., Hoboken, USA, **2004**.
- [140] B. Vollmert, *Polymer Chemistry*, Springer-Verlag Berlin Heidelberg, New York, USA, **1973**.
- [141] D. A. Shipp, *Polymer Reviews* **2011**, *51*, 99-103.
- [142] N. Corrigan, K. Jung, G. Moad, C. J. Hawker, K. Matyjaszewski, C. Boyer, *Progress in Polymer Science* **2020**, *111*, 101311.
- [143] D. A. Shipp, *Journal of Macromolecular Science, Part C* **2005**, *45*, 171-194.
- [144] F. Lorandi, M. Fantin, K. Matyjaszewski, *Journal of the American Chemical Society* **2022**, *144*, 15413-15430.

- [145] C. J. Hawker, A. W. Bosman, E. Harth, *Chemical Reviews* **2001**, *101*, 3661-3688.
- [146] R. B. Grubbs, *Polymer Reviews* **2011**, *51*, 104-137.
- [147] G. Moad, E. Rizzardo, in *Nitroxide Mediated Polymerization: From Fundamentals to Applications in Materials Science*, The Royal Society of Chemistry, **2016**, pp. 1-44.
- [148] K. Matyjaszewski, *Macromolecules* **2012**, *45*, 4015-4039.
- [149] T. E. Patten, K. Matyjaszewski, *Advanced Materials* **1998**, *10*, 901-915.
- [150] D. J. Siegart, J. K. Oh, K. Matyjaszewski, *Progress in Polymer Science* **2012**, *37*, 18-37.
- [151] W. Tang, K. Matyjaszewski, *Macromolecules* **2007**, *40*, 1858-1863.
- [152] G. Moad, E. Rizzardo, S. H. Thang, *Chemistry – An Asian Journal* **2013**, *8*, 1634-1644.
- [153] E. Rizzardo, J. Chiefari, R. T. A. Mayadunne, G. Moad, S. H. Thang, in *Controlled/Living Radical Polymerization, Vol. 768*, American Chemical Society, **2000**, pp. 278-296.
- [154] C. Barner-Kowollik, WILEY-VCH Verlag GmbH & Co. KGaA, Weinheim, Germany, **2008**.
- [155] J. Chiefari, Y. K. Chong, F. Ercole, J. Krstina, J. Jeffery, T. P. T. Le, R. T. A. Mayadunne, G. F. Meijs, C. L. Moad, G. Moad, E. Rizzardo, S. H. Thang, *Macromolecules* **1998**, *31*, 5559-5562.
- [156] K. G. E. Bradford, L. M. Petit, R. Whitfield, A. Anastasaki, C. Barner-Kowollik, D. Konkolewicz, *Journal of the American Chemical Society* **2021**, *143*, 17769-17777.
- [157] D. J. Keddie, G. Moad, E. Rizzardo, S. H. Thang, *Macromolecules* **2012**, *45*, 5321-5342.
- [158] A. Feldermann, M. L. Coote, M. H. Stenzel, T. P. Davis, C. Barner-Kowollik, *Journal of the American Chemical Society* **2004**, *126*, 15915-15923.
- [159] Z. Li, R. Zhang, K.-S. Moon, Y. Liu, K. Hansen, T. Le, C. P. Wong, *Advanced Functional Materials* **2013**, *23*, 1459-1465.
- [160] M. R. Patel, J. M. Shukla, N. K. Patel, K. H. Patel, *Mat. Res.* **2009**, *12*.
- [161] G. Ciardelli, A. Rechichi, P. Cerrai, M. Tricoli, N. Barbani, P. Giusti, *Macromolecular Symposia* **2004**, *218*, 261-272.

- [162] M. Nouman, E. Jubeli, J. Saunier, N. Yagoubi, *Journal of Biomedical Materials Research Part A* **2016**, *104*, 2954-2967.
- [163] B. D. Ratner, K. W. Gladhill, T. A. Horbett, *Journal of Biomedical Materials Research* **1988**, *22*, 509-527.
- [164] L. Zhou, D. Liang, X. He, J. Li, H. Tan, J. Li, Q. Fu, Q. Gu, *Biomaterials* **2012**, *33*, 2734-2745.
- [165] L. Zhou, L. Yu, M. Ding, J. Li, H. Tan, Z. Wang, Q. Fu, *Macromolecules* **2011**, *44*, 857-864.
- [166] Z. Wang, P. Wan, M. Ding, X. Yi, J. Li, Q. Fu, H. Tan, *Journal of Polymer Science Part A: Polymer Chemistry* **2011**, *49*, 2033-2042.
- [167] O. Bayer, *Angew. Chem.* **1947**, *59*, 257-288.
- [168] S. Awasthi, D. Agarwal, *Journal of Coatings Technology and Research* **2007**, *4*, 67-73.
- [169] D. K. Schneiderman, M. E. Vanderlaan, A. M. Mannion, T. R. Panthani, D. C. Batiste, J. Z. Wang, F. S. Bates, C. W. Macosko, M. A. Hillmyer, *ACS Macro Letters* **2016**, *5*, 515-518.
- [170] W. Yang, Q. Dong, S. Liu, H. Xie, L. Liu, J. Li, *Procedia Environmental Sciences* **2012**, *16*, 167-175.
- [171] D. R. Griffin, A. M. Kasko, *J. Am. Chem. Soc.* **2012**, *134*, 13103-13107.
- [172] P. Klán, T. Šolomek, C. G. Bochet, A. Blanc, R. Givens, M. Rubina, V. Popik, A. Kostikov, J. Wirz, *Chem. Rev.* **2013**, *113*, 119-191.
- [173] K. J. R. Lewis, M. W. Tibbitt, Y. Zhao, K. Branchfield, X. Sun, V. Balasubramaniam, K. S. Anseth, *Biomaterials Science* **2015**, *3*, 821-832.
- [174] L. Li, X.-X. Deng, Z.-L. Li, F.-S. Du, Z.-C. Li, *Macromolecules* **2014**, *47*, 4660-4667.
- [175] A. M. Rosales, S. L. Vega, F. W. DelRio, J. A. Burdick, K. S. Anseth, *Angewandte Chemie International Edition* **2017**, *56*, 12132-12136.
- [176] J.-M. Schumers, O. Bertrand, C.-A. Fustin, J.-F. Gohy, *Journal of Polymer Science Part A: Polymer Chemistry* **2012**, *50*, 599-608.
- [177] B. Yan, J.-C. Boyer, N. R. Branda, Y. Zhao, *Journal of the American Chemical Society* **2011**, *133*, 19714-19717.
- [178] H. Zhao, W. Gu, E. Sterner, T. P. Russell, E. B. Coughlin, P. Theato, *Macromolecules* **2011**, *44*, 6433-6440.

- [179] H. Zhao, E. S. Sterner, E. B. Coughlin, P. Theato, *Macromolecules* **2012**, *45*, 1723-1736.
- [180] M. Kyrish, U. Utzinger, M. R. Descour, B. K. Baggett, T. S. Tkaczyk, *Opt. Express* **2011**, *19*, 7603-7615.
- [181] P. L. Kolker, W. A. Waters, *Journal of the Chemical Society (Resumed)* **1964**, 1136-1141.
- [182] V. Jagannadham, S. Steenken, *Journal of the American Chemical Society* **1984**, *106*, 6542-6551.
- [183] E. T. Strom, J. Weinstein, *The Journal of Organic Chemistry* **1967**, *32*, 3705-3706.
- [184] J. E. T. Corrie, B. C. Gilbert, V. R. N. Munasinghe, A. C. Whitwood, *Journal of the Chemical Society, Perkin Transactions 2* **2000**, 2483-2491.
- [185] D. E. Fast, A. Lauer, J. P. Menzel, A.-M. Kelterer, G. Gescheidt, C. Barner-Kowollik, *Macromolecules* **2017**, *50*, 1815-1823.
- [186] J. P. Menzel, B. B. Noble, A. Lauer, M. L. Coote, J. P. Blinco, C. Barner-Kowollik, *J. Am. Chem. Soc.* **2017**, *139*, 15812-15820.
- [187] B. T. Tuten, J. P. Menzel, K. Pahnke, J. P. Blinco, C. Barner-Kowollik, *Chemical Communications* **2017**, *53*, 4501-4504.
- [188] A. J. Ridley, J. R. Whiteside, T. J. McMillan, S. L. Allinson, *International Journal of Radiation Biology* **2009**, *85*, 177-195.
- [189] V. Leyva, I. Corral, T. Schmierer, B. Heinz, F. Feixas, A. Migani, L. Blancafort, P. Gilch, L. González, *The Journal of Physical Chemistry A* **2008**, *112*, 5046-5053.
- [190] S. A. Kovalenko, A. L. Dobryakov, J. Ruthmann, N. P. Ernsting, *Physical Review A* **1999**, *59*, 2369-2384.
- [191] B. Czaplínska, K. Malarz, A. Mrozek-Wilczkiewicz, A. Slodek, M. Korzec, R. Musiol, *Molecules* **2020**, *25*, 2488.
- [192] M. Jiang, X. Gu, J. W. Y. Lam, Y. Zhang, R. T. K. Kwok, K. S. Wong, B. Z. Tang, *Chemical Science* **2017**, *8*, 5440-5446.
- [193] A. C. Sedgwick, L. Wu, H.-H. Han, S. D. Bull, X.-P. He, T. D. James, J. L. Sessler, B. Z. Tang, H. Tian, J. Yoon, *Chemical Society Reviews* **2018**, *47*, 8842-8880.
- [194] G. C. W. S. Wheeler, *Quaternary Science Reviews* **1988**, *7*, 407-410.

- [195] C. Ankjærgaard, M. Jain, *Journal of Physics D: Applied Physics* **2010**, *43*, 255502.
- [196] Y. Matsui, D. Kawahara, E. Ohta, H. Ikeda, *Physical Chemistry Chemical Physics* **2013**, *15*, 7064-7069.
- [197] C. Reichardt, T. Welton, *Solvents and Solvent Effects in Organic Chemistry*, 4th ed., WILEY-VCH GmbH & Co. KGaA, Weinheim, Germany, **2011**.
- [198] S. Shrivastava, H. Matsuoka, *Colloid and Polymer Science* **2016**, *294*, 879-887.
- [199] R. W. Yip, D. K. Sharma, R. Giasson, D. Gravel, *The Journal of Physical Chemistry* **1985**, *89*, 5328-5330.
- [200] C. Petit, J. Bachmann, L. Michalek, Y. Catel, E. Blasco, J. P. Blinco, A.-N. Unterreiner, C. Barner-Kowollik, *Chemical Communications* **2021**, *57*, 2911-2914.
- [201] H. A. Ernst, T. J. A. Wolf, O. Schalk, N. González-García, A. E. Boguslavskiy, A. Stolow, M. Olzmann, A.-N. Unterreiner, *The Journal of Physical Chemistry A* **2015**, *119*, 9225-9235.
- [202] B. Heinz, T. Schmierer, S. Laimgruber, P. Gilch, *Journal of Photochemistry and Photobiology A: Chemistry* **2008**, *199*, 274-281.
- [203] Y. M. Poronik, B. Sadowski, K. Szychta, F. H. Quina, V. I. Vullev, D. T. Gryko, *Journal of Materials Chemistry C* **2022**, *10*, 2870-2904.
- [204] P. A. Robertson, H. M. Bishop, A. J. Orr-Ewing, *The Journal of Physical Chemistry Letters* **2021**, *12*, 5473-5478.
- [205] N. Kretschy, A.-K. Holik, V. Somoza, K.-P. Stengele, M. M. Somoza, *Angewandte Chemie International Edition* **2015**, *54*, 8555-8559.
- [206] F. Feist, J. P. Menzel, T. Weil, J. P. Blinco, C. Barner-Kowollik, *Journal of the American Chemical Society* **2018**, *140*, 11848-11854.
- [207] M. Ahn, M.-J. Kim, D. W. Cho, K.-R. Wee, *The Journal of Organic Chemistry* **2021**, *86*, 403-413.
- [208] W.-J. Shi, P.-C. Lo, A. Singh, I. Ledoux-Rak, D. K. P. Ng, *Tetrahedron* **2012**, *68*, 8712-8718.
- [209] F. Bureš, *RSC Advances* **2014**, *4*, 58826-58851.
- [210] J. K. Pau, M. B. Ruggera, J. K. Kim, M. C. Caserio, *Journal of the American Chemical Society* **1978**, *100*, 4242-4248.

- [211] R. Hunger, W. Jaegermann, A. Merson, Y. Shapira, C. Pettenkofer, J. Rappich, *The Journal of Physical Chemistry B* **2006**, *110*, 15432-15441.
- [212] K. Roodenko, M. Gensch, J. Rappich, K. Hinrichs, N. Esser, R. Hunger, *The Journal of Physical Chemistry B* **2007**, *111*, 7541-7549.
- [213] J.-F. Lutz, *Advanced Materials* **2011**, *23*, 2237-2243.
- [214] Y. Wang, E. L. Runnerstrom, D. J. Milliron, *Annual Review of Chemical and Biomolecular Engineering* **2016**, *7*, 283-304.
- [215] D. Wang, F. Schellenberger, J. T. Pham, H.-J. Butt, S. Wu, *Chemical Communications* **2018**, *54*, 3403-3406.
- [216] S. P. Anthony, *ChemPlusChem* **2012**, *77*, 518-531.
- [217] H. Wang, S. C. Heilshorn, *Advanced Materials* **2015**, *27*, 3717-3736.
- [218] D. K. Hohl, C. Weder, *Advanced Optical Materials* **2019**, *7*, 1900230.
- [219] P. Froimowicz, H. Frey, K. Landfester, *Macromolecular Rapid Communications* **2011**, *32*, 468-473.
- [220] K. K. Oehlenschlaeger, J. O. Mueller, J. Brandt, S. Hilf, A. Lederer, M. Wilhelm, R. Graf, M. L. Coote, F. G. Schmidt, C. Barner-Kowollik, *Advanced Materials* **2014**, *26*, 3561-3566.
- [221] W. B. Jensen, *ChemTexts* **2016**, *2*, 1.
- [222] S. Billiet, K. De Bruycker, F. Driessen, H. Goossens, V. Van Speybroeck, J. M. Winne, F. E. Du Prez, *Nature Chemistry* **2014**, *6*, 815-821.
- [223] A. Gandini, A. Silvestre, D. Coelho, *Polymer Chemistry* **2013**, *4*, 1364-1371.
- [224] J. M. Winne, L. Leibler, F. E. Du Prez, *Polymer Chemistry* **2019**, *10*, 6091-6108.
- [225] D. Bléger, S. Hecht, *Angewandte Chemie International Edition* **2015**, *54*, 11338-11349.
- [226] S. Wang, L. Yue, Z.-Y. Li, J. Zhang, H. Tian, I. Willner, *Angewandte Chemie International Edition* **2018**, *57*, 8105-8109.
- [227] J. Zhang, Q. Zou, H. Tian, *Advanced Materials* **2013**, *25*, 378-399.
- [228] R. Nemoto, K. Fujieda, Y. Hiruta, M. Hishida, E. Ayano, Y. Maitani, K. Nagase, H. Kanazawa, *Colloids and Surfaces B: Biointerfaces* **2019**, *176*, 309-316.
- [229] S. C. Lee, K. J. Kim, Y.-K. Jeong, J. H. Chang, J. Choi, *Macromolecules* **2005**, *38*, 9291-9297.

- [230] L. N. Green, A. Amodio, H. K. K. Subramanian, F. Ricci, E. Franco, *Nano Letters* **2017**, *17*, 7283-7288.
- [231] A. J. Inglis, L. Nebhani, O. Altintas, F. G. Schmidt, C. Barner-Kowollik, *Macromolecules* **2010**, *43*, 5515-5520.
- [232] K. I. Papathomas, A. C. Bhatt, *Journal of Applied Polymer Science* **1996**, *59*, 2029-2037.
- [233] K. Pahnke, J. Brandt, G. Gryn'ova, P. Lindner, R. Schweins, F. G. Schmidt, A. Lederer, M. L. Coote, C. Barner-Kowollik, *Chemical Science* **2015**, *6*, 1061-1074.
- [234] N. K. Guimard, J. Ho, J. Brandt, C. Y. Lin, M. Namazian, J. O. Mueller, K. K. Oehlenschlaeger, S. Hilf, A. Lederer, F. G. Schmidt, M. L. Coote, C. Barner-Kowollik, *Chemical Science* **2013**, *4*, 2752-2759.
- [235] J. T. Manka, A. G. Douglass, P. Kaszynski, A. C. Friedli, *The Journal of Organic Chemistry* **2000**, *65*, 5202-5206.
- [236] B. R. Beno, S. Wilsey, K. N. Houk, *Journal of the American Chemical Society* **1999**, *121*, 4816-4826.
- [237] J. Vohlídal, *Chemistry Teacher International* **2020**.
- [238] C. Basaran, C.-Y. Yan, *Journal of Electronic Packaging* **1998**, *120*, 379-384.
- [239] D. R. Tyler, *Journal of Macromolecular Science, Part C* **2004**, *44*, 351-388.
- [240] M. Schaefer, B. Icli, C. Weder, M. Lattuada, A. F. M. Kilbinger, Y. C. Simon, *Macromolecules* **2016**, *49*, 1630-1636.
- [241] P. A. May, N. F. Munaretto, M. B. Hamoy, M. J. Robb, J. S. Moore, *ACS Macro Letters* **2016**, *5*, 177-180.
- [242] E. Wang, J. Lu, F. S. Bates, T. P. Lodge, *Macromolecules* **2018**, *51*, 3563-3571.
- [243] A. P. Wiita, S. R. K. Ainavarapu, H. H. Huang, J. M. Fernandez, *Proceedings of the National Academy of Sciences* **2006**, *103*, 7222.
- [244] K. Pahnke, J. Brandt, G. Gryn'ova, C. Y. Lin, O. Altintas, F. G. Schmidt, A. Lederer, M. L. Coote, C. Barner-Kowollik, *Angewandte Chemie International Edition* **2016**, *55*, 1514-1518.
- [245] H. Y. Huang, A. Skripka, L. Zaroubi, B. L. Findlay, F. Vetrone, C. Skinner, J. K. Oh, L. A. Cuccia, *ACS Applied Bio Materials* **2020**, *3*, 7219-7227.
- [246] B. Schmatz, Z. Yuan, A. W. Lang, J. L. Hernandez, E. Reichmanis, J. R. Reynolds, *ACS Central Science* **2017**, *3*, 961-967.

- [247] A. M. Kloxin, A. M. Kasko, C. N. Salinas, K. S. Anseth, *Science* **2009**, *324*, 59.
- [248] M. Gaplovsky, Y. V. Il'ichev, Y. Kamdzhilov, S. V. Kombarova, M. Mac, M. A. Schwörer, J. Wirz, *Photochemical & Photobiological Sciences* **2005**, *4*, 33-42.
- [249] D. E. Marschner, P. W. Kamm, H. Frisch, A.-N. Unterreiner, C. Barner-Kowollik, *Chemical Communications* **2020**, *56*, 14043-14046.
- [250] H. Chaffey-Millar, M. H. Stenzel, T. P. Davis, M. L. Coote, C. Barner-Kowollik, *Macromolecules* **2006**, *39*, 6406-6419.
- [251] G. Clavier, P. Audebert, *Chemical Reviews* **2010**, *110*, 3299-3314.
- [252] A.-C. Knall, C. Slugovc, *Chemical Society Reviews* **2013**, *42*, 5131-5142.
- [253] J. Sauer, D. K. Heldmann, J. Hetzenegger, J. Krauthan, H. Sichert, J. Schuster, *European Journal of Organic Chemistry* **1998**, *1998*, 2885-2896.
- [254] R. M. Desai, S. T. Koshy, S. A. Hilderbrand, D. J. Mooney, N. S. Joshi, *Biomaterials* **2015**, *50*, 30-37.
- [255] F. Jivan, R. Yegappan, H. Pearce, J. K. Carrow, M. McShane, A. K. Gaharwar, D. L. Alge, *Biomacromolecules* **2016**, *17*, 3516-3523.
- [256] R. M. Versteegen, R. Rossin, W. ten Hoeve, H. M. Janssen, M. S. Robillard, *Angewandte Chemie International Edition* **2013**, *52*, 14112-14116.
- [257] S. Stairs, A. A. Neves, H. Stöckmann, Y. A. Wainman, H. Ireland-Zecchini, K. M. Brindle, F. J. Leeper, *ChemBioChem* **2013**, *14*, 1063-1067.
- [258] M. B. Talawar, R. Sivabalan, N. Senthilkumar, G. Prabhu, S. N. Asthana, *Journal of Hazardous Materials* **2004**, *113*, 11-25.
- [259] T. Wei, W. Zhu, X. Zhang, Y.-F. Li, H. Xiao, *The Journal of Physical Chemistry A* **2009**, *113*, 9404-9412.
- [260] Q.-L. Yan, L.-L. Liu, W. He, C. Luo, A. Shlomovich, P.-J. Liu, J. Kong, M. Gozin, *Thermochimica Acta* **2018**, *667*, 19-26.
- [261] M. T. Greenfield, S. D. McGrane, C. A. Bolme, J. A. Bjorgaard, T. R. Nelson, S. Tretiak, R. J. Scharff, *The Journal of Physical Chemistry A* **2015**, *119*, 4846-4855.
- [262] S. D. McGrane, C. A. Bolme, M. T. Greenfield, D. E. Chavez, S. K. Hanson, R. J. Scharff, *The Journal of Physical Chemistry A* **2016**, *120*, 895-902.
- [263] C. Wang, C. Liu, Q. Wei, L. Yang, P. Yang, Y. Li, Y. Cheng, *Research* **2020**, *2020*, 6563091.

- [264] M. Plugge, V. Alain-Rizzo, P. Audebert, A. M. Brouwer, *Journal of Photochemistry and Photobiology A: Chemistry* **2012**, *234*, 12-20.
- [265] A.-C. Knall, M. Hollauf, C. Slugovc, *Tetrahedron Letters* **2014**, *55*, 4763-4766.
- [266] J. C. Oxley, J. L. Smith, J. Zhang, *The Journal of Physical Chemistry A* **2000**, *104*, 6764-6777.
- [267] X. Zhao, W. B. Miller, E. J. Hints, Y. T. Lee, *The Journal of Chemical Physics* **1989**, *90*, 5527-5535.
- [268] E. R. T. Kerstel, M. Becucci, G. Pietraprazia, E. Castellucci, *The Journal of Chemical Physics* **1997**, *106*, 1318-1325.
- [269] I. M. Irshadeen, S. L. Walden, M. Wegener, V. X. Truong, H. Frisch, J. P. Blinco, C. Barner-Kowollik, *Journal of the American Chemical Society* **2021**, *143*, 21113-21126.
- [270] F. Miomandre, P. Audebert, *Journal of Photochemistry and Photobiology C: Photochemistry Reviews* **2020**, *44*, 100372.
- [271] M. A. Al-Omar, A. R. Sayed, M. M. Youssef, *Molecules* **2015**, *20*, 2591-2610.
- [272] T. Le, T. Courant, J. Merad, C. Allain, P. Audebert, G. Masson, *The Journal of Organic Chemistry* **2019**, *84*, 16139-16146.
- [273] S. Jaiswal, P. C. R. Varma, L. O'Neill, B. Duffy, P. McHale, *Materials Science and Engineering: C* **2013**, *33*, 1925-1934.
- [274] J. Vandenberg, K. Ranieri, T. Junkers, *Macromolecular Chemistry and Physics* **2012**, *213*, 2611-2617.
- [275] T. Santos, D. S. Rivero, Y. Pérez-Pérez, E. Martín-Encinas, J. Pasán, A. H. Daranas, R. Carrillo, *Angewandte Chemie International Edition* **2021**, *60*, 18783-18791.
- [276] G. Burke, Z. Cao, D. M. Devine, I. Major, *Polymers* **2019**, *11*, 1339.
- [277] A. E. Rydholm, S. K. Reddy, K. S. Anseth, C. N. Bowman, *Polymer* **2007**, *48*, 4589-4600.
- [278] H. Shih, C.-C. Lin, *Biomacromolecules* **2012**, *13*, 2003-2012.
- [279] J. Vandenberg, M. Peeters, T. Kretschmer, P. Wagner, T. Junkers, *Polymer* **2014**, *55*, 3525-3532.
- [280] M. Steinmann, F. R. Wurm, *Polymer Degradation and Stability* **2020**, *179*, 109224.

- [281] D. S. Kazybayeva, G. S. Irmukhametova, V. V. Khutoryanskiy, *Polymers for Advanced Technologies* **2021**, *32*, 2682-2689.
- [282] P. Hu, A. Kumar, R. Gharibi, S. Agarwal, *Polymer Chemistry* **2022**.
- [283] B. Hendriks, O. van den Berg, F. E. Du Prez, *Progress in Organic Coatings* **2019**, *136*, 105215.
- [284] L. Li, J. M. Scheiger, P. A. Levkin, *Advanced Materials* **2019**, *31*, 1807333.
- [285] Y. Dong, G. Jin, Y. Hong, H. Zhu, T. J. Lu, F. Xu, D. Bai, M. Lin, *ACS Applied Materials & Interfaces* **2018**, *10*, 12374-12389.
- [286] T. L. Rapp, C. A. DeForest, *Advanced Healthcare Materials* **2020**, *9*, 1901553.
- [287] P. Lu, D. Ahn, R. Yunis, L. Delafresnaye, N. Corrigan, C. Boyer, C. Barner-Kowollik, Z. A. Page, *Matter* **2021**, *4*, 2172-2229.
- [288] A. M. Kloxin, M. W. Tibbitt, K. S. Anseth, *Nature Protocols* **2010**, *5*, 1867-1887.
- [289] R. Wang, Z. Yang, J. Luo, I.-M. Hsing, F. Sun, *Proceedings of the National Academy of Sciences* **2017**, *114*, 5912-5917.
- [290] E. M. Nehls, A. M. Rosales, K. S. Anseth, *Journal of Materials Chemistry B* **2016**, *4*, 1035-1039.
- [291] L. Ionov, *Materials Today* **2014**, *17*, 494-503.
- [292] A. Y. Chen, Z. Deng, A. N. Billings, U. O. S. Seker, Michelle Y. Lu, R. J. Citorik, B. Zakeri, T. K. Lu, *Nature Materials* **2014**, *13*, 515-523.
- [293] N. Brandenberg, M. P. Lutolf, *Advanced Materials* **2016**, *28*, 7450-7456.
- [294] C. K. Arakawa, B. A. Badeau, Y. Zheng, C. A. DeForest, *Advanced Materials* **2017**, *29*, 1703156.
- [295] K. Kalayci, H. Frisch, V. X. Truong, C. Barner-Kowollik, *Nature Communications* **2020**, *11*, 4193.
- [296] K. Kalayci, H. Frisch, C. Barner-Kowollik, V. X. Truong, *Advanced Functional Materials* **2020**, *30*, 1908171.
- [297] J. L. Pelloth, P. A. Tran, A. Walther, A. S. Goldmann, H. Frisch, V. X. Truong, C. Barner-Kowollik, *Advanced Materials* **2021**, *33*, 2102184.
- [298] P. W. Kamm, J. P. Blinco, A.-N. Unterreiner, C. Barner-Kowollik, *Chemical Communications* **2021**, *57*, 3991-3994.
- [299] A. Albert, G. B. Barlin, *Journal of the Chemical Society (Resumed)* **1963**, 5737-5741.

- [300] J. A. Pereira, A. M. Pessoa, M. N. D. S. Cordeiro, R. Fernandes, C. Prudêncio, J. P. Noronha, M. Vieira, *European Journal of Medicinal Chemistry* **2015**, *97*, 664-672.
- [301] C. A. Bonino, J. E. Samorezov, O. Jeon, E. Alsberg, S. A. Khan, *Soft Matter* **2011**, *7*, 11510-11517.
- [302] C. D. O'Connell, B. Zhang, C. Onofrillo, S. Duchi, R. Blanchard, A. Quigley, J. Bourke, S. Gambhir, R. Kapsa, C. Di Bella, P. Choong, G. G. Wallace, *Soft Matter* **2018**, *14*, 2142-2151.
- [303] M. Li, A. P. Dove, V. X. Truong, *Angewandte Chemie International Edition* **2020**, *59*, 2284-2288.
- [304] K. J. Jeong, A. Panitch, *Biomacromolecules* **2009**, *10*, 1090-1099.
- [305] R. M. Sainz, F. Lombo, J. C. Mayo, *Cancers* **2012**, *4*, 442-474.
- [306] H. Bayr, *Critical Care Medicine* **2005**, *33*, S498-S501.
- [307] A. Iturmendi, S. Theis, D. Maderegger, U. Monkowius, I. Teasdale, *Macromolecular Rapid Communications* **2018**, *39*, 1800377.
- [308] M. A. Azagarsamy, D. D. McKinnon, D. L. Alge, K. S. Anseth, *ACS Macro Letters* **2014**, *3*, 515-519.
- [309] V. X. Truong, F. Li, J. S. Forsythe, *ACS Applied Materials & Interfaces* **2017**, *9*, 32441-32445.
- [310] V. X. Truong, *ChemPhotoChem* **2020**, *4*, 564-570.
- [311] J. Cusido, E. Deniz, F. M. Raymo, *European Journal of Organic Chemistry* **2009**, *2009*, 2031-2045.
- [312] J. Olejniczak, M. Chan, A. Almutairi, *Macromolecules* **2015**, *48*, 3166-3172.
- [313] A. Alouane, R. Labruère, T. Le Saux, F. Schmidt, L. Jullien, *Angewandte Chemie International Edition* **2015**, *54*, 7492-7509.
- [314] S. Huvelle, T. Le Saux, L. Jullien, F. Schmidt, *Organic & Biomolecular Chemistry* **2022**, *20*, 240-246.
- [315] X. Tan, B. B. Li, X. Lu, F. Jia, C. Santori, P. Menon, H. Li, B. Zhang, J. J. Zhao, K. Zhang, *Journal of the American Chemical Society* **2015**, *137*, 6112-6115.
- [316] J. Bachmann, C. Petit, L. Michalek, Y. Catel, E. Blasco, J. P. Blinco, A.-N. Unterreiner, C. Barner-Kowollik, *ACS Macro Letters* **2021**, *10*, 447-452.

- [317] S. Rajendran, R. Raghunathan, I. Hevus, R. Krishnan, A. Ugrinov, M. P. Sibi, D. C. Webster, J. Sivaguru, *Angewandte Chemie International Edition* **2015**, *54*, 1159-1163.
- [318] S. Tian, Q. Yue, C. Liu, M. Li, M. Yin, Y. Gao, F. Meng, B. Z. Tang, L. Luo, *Journal of the American Chemical Society* **2021**, *143*, 10054-10058.
- [319] P. Schneider, G. Schneider, *Journal of Medicinal Chemistry* **2016**, *59*, 4077-4086.
- [320] Z. J. Baum, X. Yu, P. Y. Ayala, Y. Zhao, S. P. Watkins, Q. Zhou, *Journal of Chemical Information and Modeling* **2021**, *61*, 3197-3212.
- [321] I. Aujard, C. Benbrahim, M. Gouget, O. Ruel, J.-B. Baudin, P. Neveu, L. Jullien, *Chemistry – A European Journal* **2006**, *12*, 6865-6879.
- [322] S. Stoll, A. Schweiger, *Journal of Magnetic Resonance* **2006**, *178*, 42-55.
- [323] T. Gruending, M. Guilhaus, C. Barner-Kowollik, *Macromolecules* **2009**, *42*, 6366-6374.
- [324] K. De Bruycker, T. Krappitz, C. Barner-Kowollik, *ACS Macro Letters* **2018**, *7*, 1443-1447.
- [325] C. Schweigert, O. Babii, S. Afonin, T. Schober, J. Leier, N. C. Michenfelder, I. V. Komarov, A. S. Ulrich, A. N. Unterreiner, *ChemPhotoChem* **2019**, *0*.
- [326] P. Jöckle, I. Lamparth, N. Moszner, C. Barner-Kowollik, A.-N. Unterreiner, *Polymer Chemistry* **2020**, *11*, 3972-3979.
- [327] K. Freed, S. Edwards, *J. Phys. A (Gen. Phys.)* **1969**, *2*, 145-150.
- [328] I. Teraoka, *Polymer Solutions: An Introduction to Physical Properties*, John Wiley, **2002**.
- [329] C. J. Ferguson, R. J. Hughes, D. Nguyen, B. T. T. Pham, R. G. Gilbert, A. K. Serelis, C. H. Such, B. S. Hawkett, *Macromolecules* **2005**, *38*, 2191-2204.
- [330] G. Morandi, W. Thielemans, *Polymer Chemistry* **2012**, *3*, 1402-1407.
- [331] A. F. Hirschbiel, B. V. K. J. Schmidt, P. Krolla-Sidenstein, J. P. Blinco, C. Barner-Kowollik, *Macromolecules* **2015**, *48*, 4410-4420.
- [332] H. Yu, S. Cao, L. Zhang, G. Liu, J. Xu, *Synthesis* **2009**, *2009*, 2205-2209.
- [333] F. G. Bordwell, H. M. Andersen, B. M. Pitt, *Journal of the American Chemical Society* **1954**, *76*, 1082-1085.
- [334] S. Shee, K. Ganguli, K. Jana, S. Kundu, *Chemical Communications* **2018**, *54*, 6883-6886.

- [335] M. Op de Beeck, A. Madder, *Journal of the American Chemical Society* **2012**, *134*, 10737-10740.